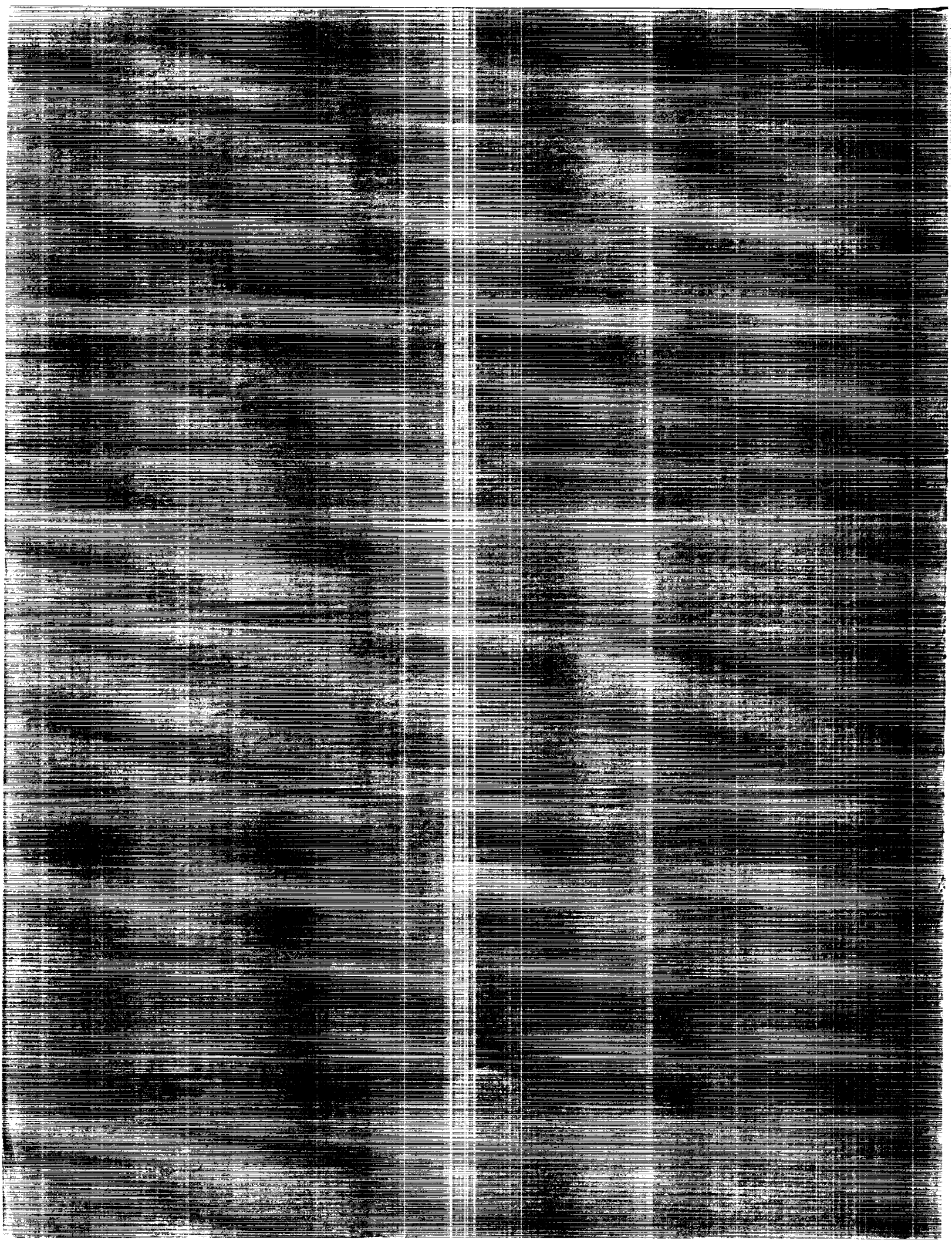


(NASA-CP-3050) FLIGHT MECHANICS/ESTIMATION
THEORY SYMPOSIUM, 1989 (NASA) 466 p
CSCL 22A

N90-13415
--THRU--
N90-13440
Unclas
0239224

H1/13



NASA Conference Publication 3050

Flight Mechanics/Estimation Theory Symposium 1989

Thomas Stengle, *Editor*
Goddard Space Flight Center
Greenbelt, Maryland

Proceedings of a symposium sponsored by
NASA Goddard Space Flight Center and held at
Goddard Space Flight Center
Greenbelt, Maryland
May 23–24, 1989

NASA

National Aeronautics and
Space Administration
Office of Management
Scientific and Technical
Information Division

1989



FOREWORD

The papers presented here have been derived primarily from speakers' summaries of talks presented at the Flight Mechanics/Estimation Theory Symposium held May 23-24, 1989 at the Goddard Space Flight Center. Papers included in this document are presented as received from the authors with little or no editing.

PRECEDING PAGE BLANK NOT FILMED



CONTENTS

Page

SESSION 1

The Effects of Seasonal and Latitudinal Earth Infrared Radiance Variations on ERBS Attitude Control M. Phenneger, J. Dehen, D. Foch, E. Harvie, M. Viridy (CSC)	3
Autonomous Spacecraft Attitude Control Using Magnetic Torquing Only K. Musser, W. Ebert (APL)	23
Periodic-Disturbance Accommodating Control of the Space Station for Asymptotic Momentum Management W. Warren, B. Wie (Univ. Texas/Austin), D. Geller (NASA/JSC)	39
Simultaneous Quaternion Estimation (QUEST)- and Bias Determination L. Markley (NASA/GSFC)	51
COBE Nonspinning Attitude Propagation D. Chu (CSC)	65
Simulation of Spacecraft Attitude Dynamics Using TREETOPS and Model-Specific Computer Codes J. Cochran, T. No, N. Fitz-Coy (Auburn)	75

SESSION 2

Orbit and Attitude Determination Results During Launch Support Operations for SBS-5 K. Hartman, P. Iano (MCI)	97
GOES-I/M Ascent Maneuvers From Transfer Orbit to Station S. Abeyagunawardene, S. Devlin, D. Elkin (CSC), R. DeFazio (NASA/GSFC)	117
GOES I-M Image Navigation and Registration J. Fiorello, I. Oh (CSC), K. Kelly, L. Ranne (NOAA).....	129
Shuttle Relative Navigation of a Tethered Satellite Mission With Current On Board Software K. Lee (MDSSC)	149

PRECEDING PAGE BLANK NOT FILMED

Impact of Tether Cutting on Onboard Navigation During the Tethered Satellite Mission - 1 D. Pirker (MDSSC)	169
Shuttle Tethered Operations: The Effect on Orbital Trajectory and Inertial Navigation M. Lardas (MDSSC)	181
Temperature Dependence of Attitude Sensor Coalignments on the Solar Maximum Mission (SMM) D. Pitone, A. Eudell (CSC), F. Patt (APC)	201

SESSION 3

True Covariance Simulation of the EUVE Update Filter I. Bar-Itzhack (NRC), R. Harman (NASA/GSFC)	223
A Gyroscope Calibration Analysis for the Gamma Ray Observatory (GRO) E. Ketchum (NASA/GSFC), M. Lee (CSC)	237
Spacecraft Attitude Determination Using the Earth's Magnetic Field D. Simpson (OAO)	255
Bilinear Modeling and Nonlinear Estimation T. Dwyer, F. Karray (Univ. Illinois), W. Bennett (TSI)	275
Extension of Euler's Theorem to n-Dimensional Spaces I. Bar-Itzhack (NRC)	299
Analysis of the Flight Dynamics of the Solar Maximum Mission (SMM) Off-Sun Scientific Pointing D. Pitone, J. Klein (CSC)	317
Extended Kalman Filter for Attitude Estimation of the Earth Radiation Budget Satellite J. Deutschmann (NASA/GSFC), I. Bar-Itzhack (NRC)	333

SESSION 4

Automation of Orbit Determination Functions for National Aeronautics and Space Administration (NASA)- Supported Satellite Missions H. Mardirossian, K. Heuerman, A. Beri, M. Samii (CSC), C. Doll (NASA/GSFC)	349
---	-----

Calculation of Double-Lunar Swingby Trajectories:	
I. Keplerian Formulation	
S. Stalos (CSC)	367
Active Rendezvous Between a Low-Earth Orbit User Spacecraft and the Space Transportation System (STS) Shuttle	
H. Hooper, J. Herrnstein (CSC)	381
Optimum Data Weighting and Error Calibration for Estimation of Gravitational Parameters	
F. Lerch (NASA/GSFC)	403
The Controllability of the Aeroassist Flight Experiment Atmospheric Skip Trajectory	
R. Wood (MDSSC)	431
Atmospheric Drag Model Calibrations for Spacecraft Lifetime Prediction	
A. Binebrink, M. Radomski, M. Samii (CSC)	445
Lifetime Predictions for the Solar Maximum Mission (SMM) and San Marco Spacecraft	
E. Smith, M. Schmitt, M. Phenneger, D. Ward (CSC), M. Lupisella, F. Vaughn (NASA/GSFC)	459



FLIGHT MECHANICS/ESTIMATION THEORY SYMPOSIUM

SESSION 1



THE EFFECTS OF SEASONAL AND LATITUDINAL EARTH INFRARED RADIANCE VARIATIONS ON ERBS ATTITUDE CONTROL*

M. Phenneger, J. Dehen, D. Foch, E. Harvie, M. Viridy
Computer Sciences Corporation

ABSTRACT

Analysis performed in the Flight Dynamics Facility by the Earth Radiation Budget Satellite (ERBS) Attitude Determination Support team illustrates the pitch attitude control motion and roll attitude errors induced by Earth infrared (IR) horizon radiance variations. IR scanner and inertial reference unit (IRU) pitch and roll flight data spanning 4 years of the ERBS mission are analyzed to illustrate the changes in the magnitude of the errors on time scales of the orbital period, months, and seasons.

The analysis represents a unique opportunity to compare prelaunch estimates of radiance-induced attitude errors with flight measurements. As a consequence of this work the following additional information is obtained: an assessment of an average model of these errors and its standard deviation, a measurement to determine and verify previously proposed corrections to the current Earth IR radiance data base, and the possibility of a mean motion model derived from flight data in place of IRU data for ERBS fine attitude determination.

* This work was supported by the National Aeronautics and Space Administration (NASA)/Goddard Space Flight Center (GSFC), under Contract NAS 5-31500.

1.0 INTRODUCTION

This paper presents analysis performed in the Goddard Space Flight Center (GSFC) Flight Dynamics Division (FDD) by the Earth Radiation Budget Satellite (ERBS) Attitude Determination Support team. The analysis was performed to measure the ERBS infrared (IR) horizon scanner sensing errors induced by seasonal and latitudinal variations in the Earth's IR horizons. The ERBS mission attitude data offers a unique opportunity to compare prelaunch and early postlaunch estimates of radiance-induced attitude errors with flight measurements of these errors. In addition, this analysis attempts to corroborate the conclusions about the FDD Earth Horizon Radiance Data Base (HRDB) from earlier analysis of data from the Nimbus-7 Limb Infrared Monitor of the Stratosphere (LIMS) experiment. The effects on estimates of these errors, due to adjustments to the radiance data base derived from the earlier LIMS analysis, are evaluated. Radiance errors are derived by a difference between pitch and roll angles obtained from processed IR scanner telemetry and pitch and roll propagations from batch least squares estimates of pitch and roll reference attitudes using the inertial reference unit (IRU). Averages of these differences are used to illustrate the changes in the magnitude of the horizon radiance-induced pitch and roll errors on time scales of the orbital period, a month, and 1 year.

The remaining sections of this paper are as follows. Section 2 is an overview relating this analysis to earlier analysis of IR radiance errors, a description of the ERBS orbit characteristics and attitude system, and a brief description of the ERBS IR scanner sensing geometry and Earth pulse processing. Section 3 describes how the errors are caused by seasonal radiance variations, explains the concept and procedures applied here to extract the errors using the ERBS flight system telemetry data, and presents and describes the flight data errors. Section 4 provides a brief explanation of the IR sensor modeling software system and the result of attempts to model the flight data with this system using two schemes for rescaling the original ERBS radiance profiles. Section 5 is a summary with conclusions about the results and future applications of this analysis.

2.0 OVERVIEW

Analysis performed between 1977 and 1984 evaluated the methods of applying an Earth IR horizon radiance model to correct IR scanner flight data (Ref. 1). Flight data from 12 spacecraft, including early postlaunch data from the ERBS, were used to compare the actual IR scanner response to the modeled response using the Horizon Radiance Modeling Utility (HRMU) (Ref. 2). Differences in the actual Earth horizon radiance pitch and roll errors relative to the model were found to occur due to limitations in the Earth IR model and IR scanner sensitivity to short duration cold cloud effects.

Data from the Nimbus-7 LIMS experiment, which included horizon radiance measurements in two IR spectral passbands similar to those used for IR horizon scanners, were compared with a model of the LIMS data using a data base of Earth IR spectra referred to here as the HRDB (Ref. 3). The HRDB was developed using the LOWTRAN computer program (Ref. 4) and a data base of worldwide balloon and rocketsonde temperature profiles (Ref. 5). The LIMS comparison indicated that the modeled IR horizon intensities

for the polar latitudes were underestimated for the summer season and overestimated for the winter season.

An overview of the ERBS attitude system and orbital characteristics is provided in Table 1.

Table 1. ERBS Orbit and Attitude Characteristics

Orbit:

Semimajor axis: 6891 km

Inclination: 57 deg

Eccentricity: 0.0014 (near-frozen orbit)

Attitude Parameters:

Angular momentum biased, Earth oriented, 1 revolution per orbit

Nominal geodetic pitch and roll = 0.0 deg

Nominal yaw = 0.0 or 180.0 deg for solar array illumination

Attitude Sensors:

Two Adcole fine Sun sensors 64x64 deg 0.004 deg (l.s.b.)

Two ITHACO Scanwheel IR sensors 0.025 deg (l.s.b.)

One Schoenstedt three-axis fluxgate magnetometer 4.68 mg (l.s.b.)

Two IRUs with three Northrop rate gyros 0.001 deg/sec (l.s.b.)

One gyrocompass onboard analog processor 0.03125 deg (l.s.b.)

Attitude Actuators:

One pitch momentum wheel

Two ITHACO scanwheels

Four orbit adjust and pitch/roll hydrazine thrusters

Two pairs of yaw turn hydrazine thrusters

One roll axis and one yaw axis, 50-ampere turn meter squared (ATm²) magnetic dipole torque rods for pitch momentum control

Two pitch axis 50 ATm² dipole torque rods for roll control

2.1 ERBS IR SCANNER DESCRIPTION

The ITHACO IR scanwheels employ a rotating prism lens and a single-flake thermistor bolometer to sense the Earth with a 1x2-deg field of view (FOV), which sweeps along a 45-deg scan cone at 2000 revolutions per minute (rpm). The IR passband is between 14 and 16.1 microns. The scanner cone axes are on opposite sides of the spacecraft in the pitch-yaw plane and are canted 10 deg down from the pitch axis. Figure 1 illustrates the inflight geometry of the scanner optics for nominal attitude (Ref. 6).

The IR scanner uses normalized threshold locator logic. For this, the Earth IR pulse is averaged between 15 and 20 deg and 20 and 25 deg, respectively, from the inward

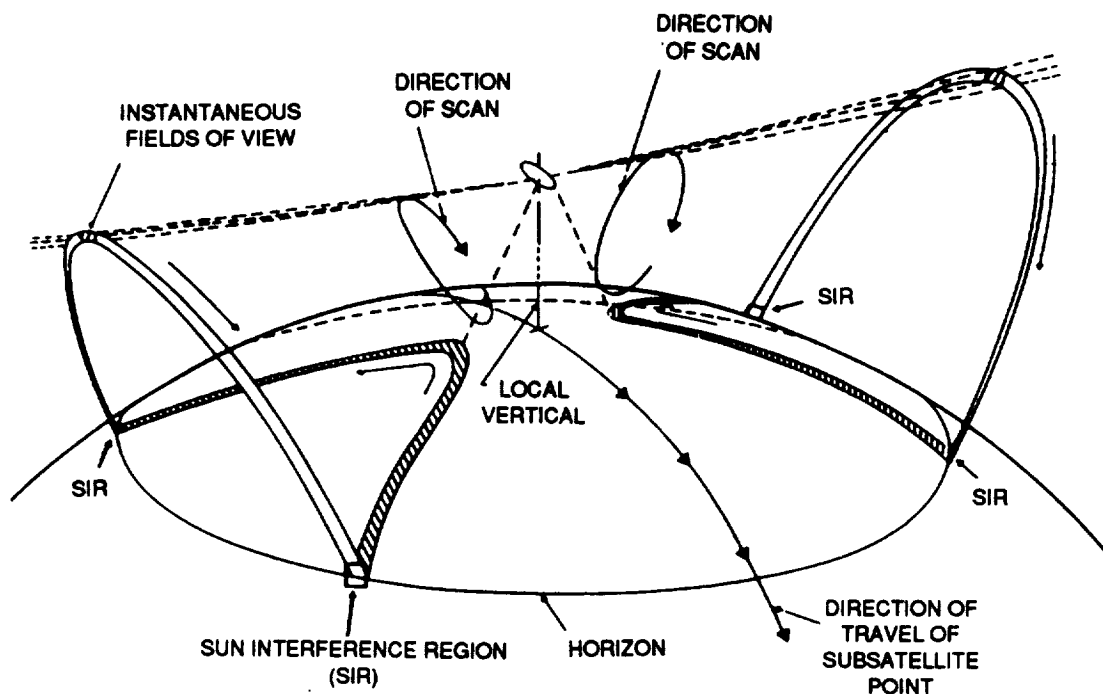


Figure 1. In-Flight Geometry of the ERBS IR Horizon Sensing System for Pitch = 0, Roll = 0, Yaw = 0

and outward horizons to determine the horizon triggering threshold voltage. A typical Earth pulse is shown in Figure 2. A magnetic pickoff mounted on the sensor body provides a reference pulse from which the acquisition of signal (AOS) and loss of signal (LOS) to index angles are computed (Ω_{in} and Ω_{out} in Figure 2). The pitch angle is computed as

$$P = \pm K_p [(\Omega_{los}^R - \Omega_{aos}^R) + (\Omega_{los}^L - \Omega_{aos}^L)] \quad (1)$$

where R and L designate the right and left side scanner angles, respectively, and where K_p is a geometry-dependent constant. For ERBS $K_p \approx 0.2462$.

Roll is computed as

$$R = K_r (\Omega^R - \Omega^L) \quad (2)$$

and

$$\Omega^{R,L} = (\Omega_{aos}^{R,L} + \Omega_{los}^{R,L})$$

where $K_r \approx 0.247$.

Figure 3 shows the scanner ground traces at 5-minute intervals for both an equatorial and a polar view of the Earth. It can be seen that the AOS and LOS threshold computation regions (indicated by hashmarks in the figure) are separated by a wide range of latitudes

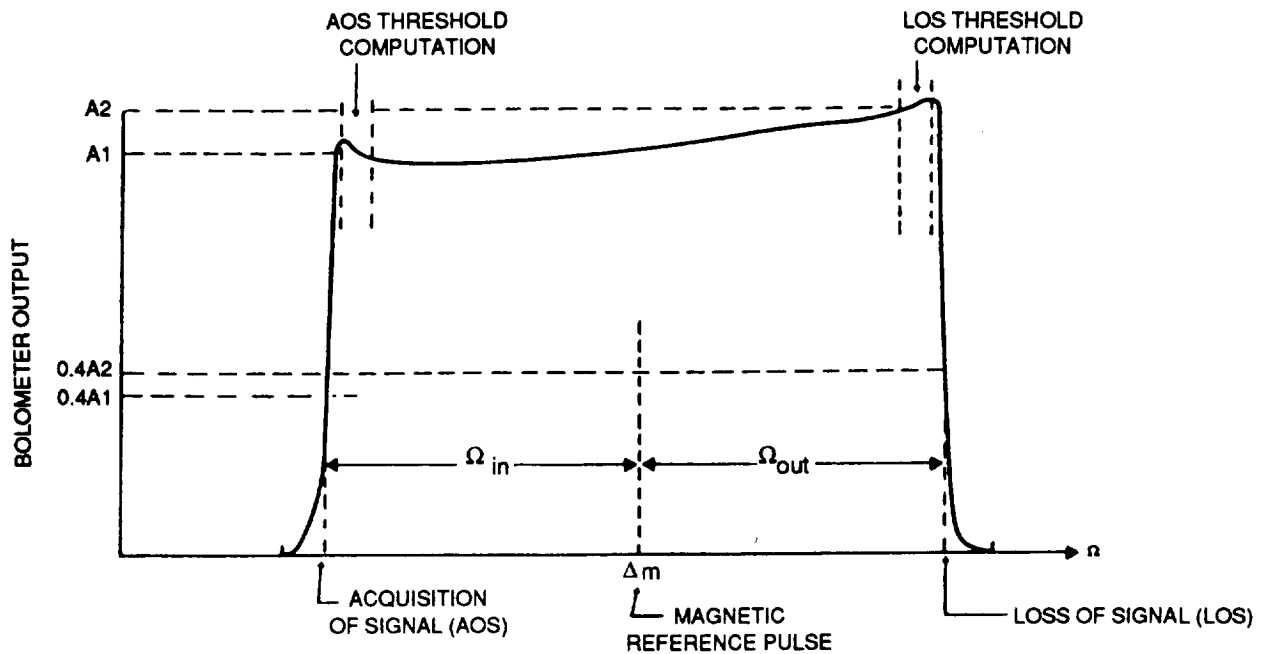
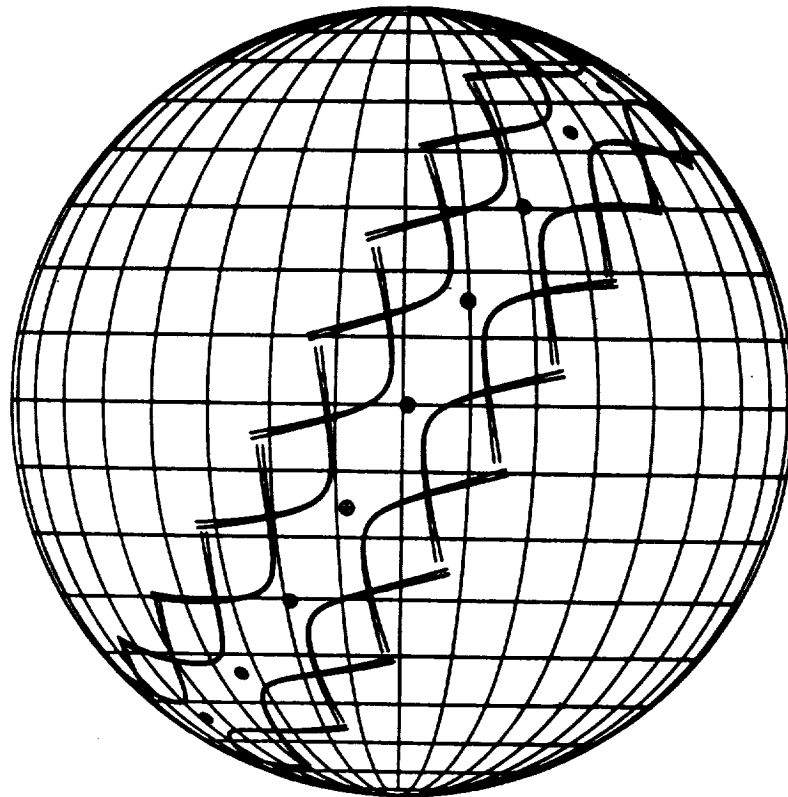


Figure 2. The Horizon Locator Logic and the IR Scanner Earth Pulse

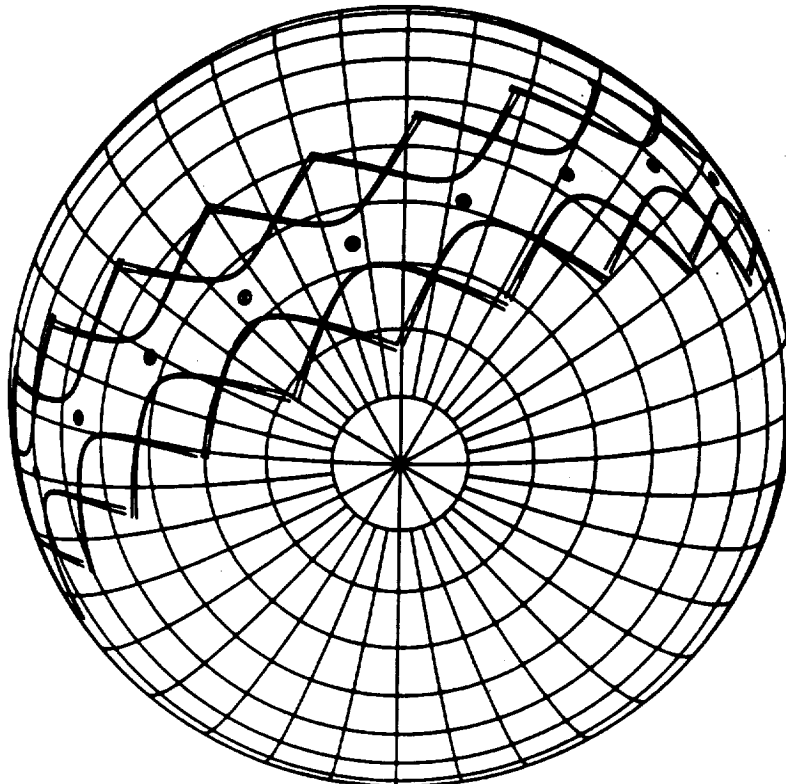
in the equatorial regions, and that the left and right scanners are widely separated at the northern and southern extremes of the orbit.

3.0 HORIZON RADIANCE ERRORS FROM FLIGHT DATA

The horizon radiance-induced pitch and roll errors in the IR scanner input to the ERBS magnetic control system (MCS) control loop are caused by radiance gradients along the scan ground traces. The gradients are most severe in the winter and summer seasons between the polar latitudes and the temperate latitudes. The gradient causes the threshold normalization region intensity and the rising edge of the Earth pulse intensity to vary relatively. A brightening at the horizon causes an increased Earth width for a given threshold voltage. Likewise, a diminished radiance at the horizon will decrease the sensed Earth width. When the ERBS is on the Equator, a minimal north-south gradient occurs for any month and pitch errors are near zero. Roll errors at this location are dependent on east-west gradients that on the average will be zero. At the midlatitudes, near 40 deg, the AOS and LOS horizons for either scanner are at maximum latitudinal separation and include the latitude regions where the stratosphere experiences the greatest seasonal radiance variation. These are latitudes between 40 deg and the poles. Thus, the pitch errors will be maximum. At the highest and lowest latitudes, the left and right scanner traces are at north and south extremes, where differences between the 80 deg and 40 deg radiance intensities will determine the peak roll errors. At these points the latitudes of the AOS and LOS horizon points are the same for each scanner and pitch errors are expected to be near zero.



EQUATORIAL VIEW



POLAR VIEW

Figure 3. ERBS IR Horizon Scanner Ground Tracks on the Earth at 5-Minute Intervals

3.1 ERROR COMPUTATION CONCEPTS

The flight system horizon radiance-induced errors are computed by subtracting IRU-based pitch and roll determined by the ERBS Attitude Ground Support System (AGSS) (Ref. 6) Fine Attitude Determination Subsystem (FADS) from the IR scanner pitch and roll. The IR scanner pitch error is the error input to the ERBS pitch control loop. Horizon radiance-induced pitch errors from the IR scanner thus cause pitch motion to null the IR scanner error signal that is received in the downlink telemetry. However, this motion is sensed by the pitch IRU. The difference, IR scanner pitch minus FADS-IRU pitch, is approximately equal to the radiance-induced pitch error in IR scanner output.

The IR scanner roll error signal is not used for continuous roll control, but for intermittent activation of the magnetic dipoles for nutation and precession control. These torques cause the spacecraft pitch axis to precess along the 33-deg latitude line at a daily average rate of 4-deg per day, which is the ascending node rate. IR scanner roll minus FADS-IRU roll is approximately equal to the radiance-induced roll error in IR scanner output.

In summary, the IR scanner pitch error is continuously nulled by the reaction wheels, and therefore does not unambiguously indicate attitude motion. The IR scanner roll error signal should vary with the radiance induced error, with periodic steps to a null roll caused by magnetic dipole precession activity. The subtraction of IRU pitch and roll attitude data from IR scanner pitch and roll thus isolates IR horizon radiance errors. Since true spacecraft motion caused by control system and environmental torques is registered by both the IR scanners and the IRUs, this motion will not contribute to the difference. Similarly, the pitch rotation that occurs in response to the high-gain antenna transponder activation for Tracking and Data Relay Satellite (TDRS) contacts, will not appear in the data.

3.2 ERROR COMPUTATION PROCEDURE

The analysis procedure begins by processing selected orbits of ERBS attitude telemetry from archived data spanning 4 years of mission operations, between 1984 and 1988. The Data Adjuster subsystem of the AGSS is used to write processed IR scanner pitch and roll data to the Processed Engineering data set. After further processing, the IRU pitch and roll solutions are derived in the FADS and written to the Attitude History File (AHF). A FORTRAN utility program, written for this analysis, then subtracts the IRU pitch and roll angles from the IR scanner pitch and roll angles to produce the IR scanner horizon radiance-induced errors. These errors are averaged over 1-deg latitude bins on the northward and southward sides of each orbit to statistically improve the accuracy and reduce the data volume. To remove the effect of IR scanner and AGSS processing biases, the monthly averaged error representations are shifted to be zero at 0-deg latitude, where these errors are expected to be zero due to orbital geometry and radiance profile symmetry. The bias values were determined by the averaged pitch and roll errors between -5 and +5 deg latitude. The one-orbit representations of the latitude averaged errors were again averaged with three to five orbits for each month in each of the 4 years to form an overall average for each month.

3.3 FLIGHT DATA ANALYSIS RESULTS

The pitch and roll errors obtained from flight data analysis for each month of the year are plotted versus subsatellite latitude in Figures 4a and 4b. The standard deviations from the mean and the northward (N) and southward (S) direction of flight are indicated by the size and type of the plot symbols. The number of orbits averaged is noted to the right of each plot. The tick marks on the ordinate at 0 deg latitude are at intervals of 0.1 deg.

The following characteristics should be noted. For most of the months the pattern of the IR radiance-induced pitch and roll errors is as expected. December and February pitch errors are unusual when compared with adjacent months. The magnitude of the pitch and roll errors in the winter and summer seasons is two to five times higher than the pre-launch analysis predicted. The Southern Hemisphere summer and winter errors are significantly different from their Northern Hemisphere counterparts. The effects of the gradual change in the radiance with season is clearly evident in this 4 year averaged data that indicates a high level of annual similarity in the stratosphere. Finally for June and July, the months when the errors are the largest, the standard deviations do not exceed the error amplitude. The next section describes the results of analysis to simulate these data using the HRMU.

4.0 MODELING THE FLIGHT DATA WITH THE HORIZON RADIANCE MODELING UTILITY

The horizon radiance errors modeled by the HRMU are derived from a detailed computation using an Earth IR model and an IR scanner model composed of the orbital geometry, the IR scanner optics, and the signal processing electronics. The input characteristics of the IR scanner electronics include threshold normalization parameters and time constants, scanner mounting tilt angles and FOV, and orbital radius and inclination. HRMU input is the IR horizon profile of brightness versus FOV tangent height and angle of incidence to the Earth data. These data are in a set of nine profiles for each month in 20-deg latitude bins between -90 and +90 deg latitude. This horizon profile data set is derived from the HRDB by integrating the HRDB Earth IR spectra over the optical IR passband for each of the 51 viewing angles represented in the profile. The HRMU computes sensor response to the Earth radiance by integrating the IR radiance, from a latitude interpolated function of the profiles, incident on the scanner optics. As the scanner FOV sweeps across the Earth, a model of the bolometer energy pulse is computed. The scanner step response function is convolved with the pulsed input radiance signal to compute the electronics output Earth pulse signal. The horizon crossing angle is determined from this output pulse as is done onboard the spacecraft in the actual IR scanner electronics. The pitch and roll error signals expected over one orbit for a specific month of the year are computed using the horizon crossing angles according to Equations (1) and (2). The HRMU model of the ERBS IR scanner is not precise, and experience has shown that the following approximations made do not significantly alter the results:

- Two components of the electronics transfer functions are not included
- Nonlinear components in the electronics are not modeled; these are voltage limiting components

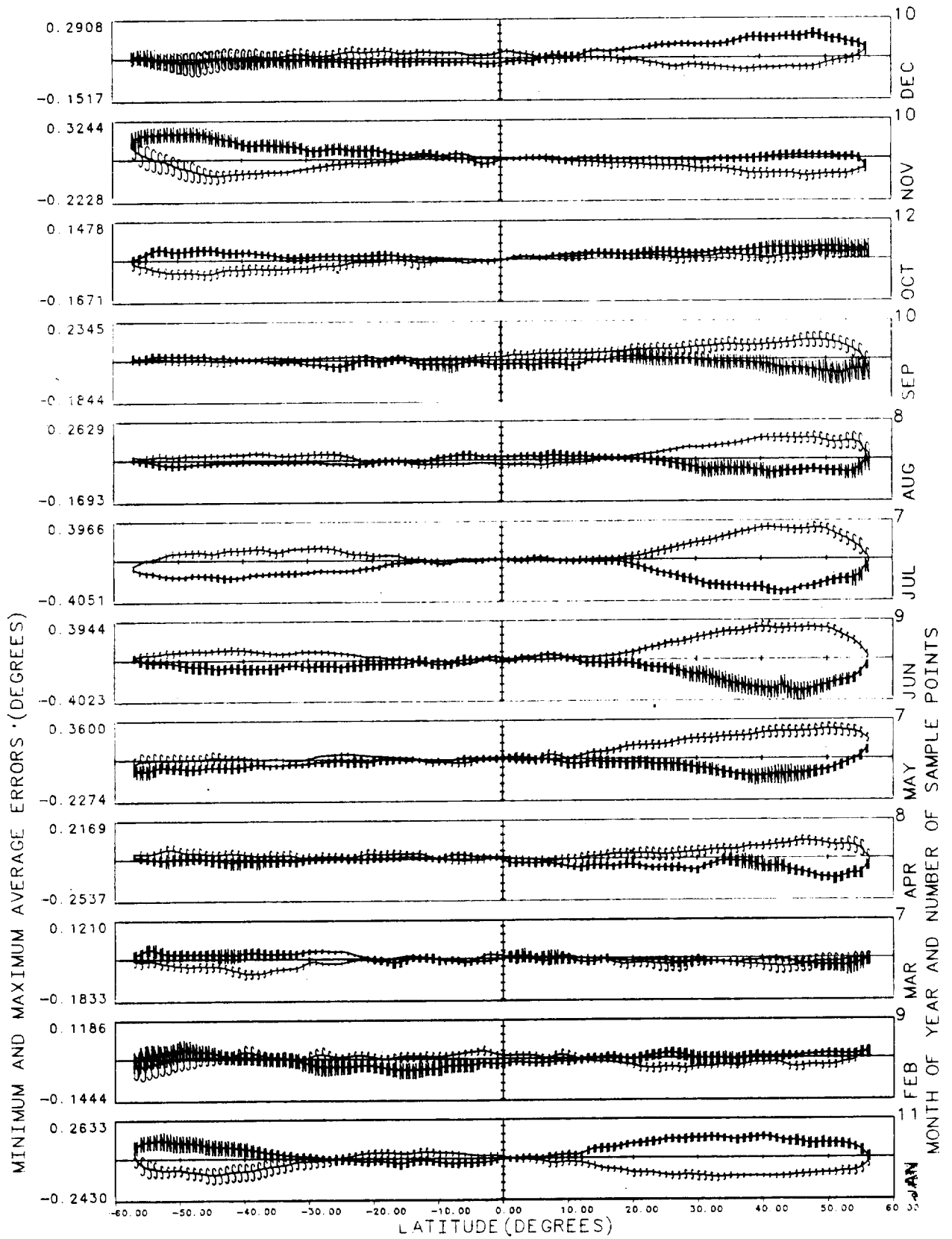


Figure 4a. Flight Data Pitch Errors Versus Latitude and Month
(With Standard Deviations)

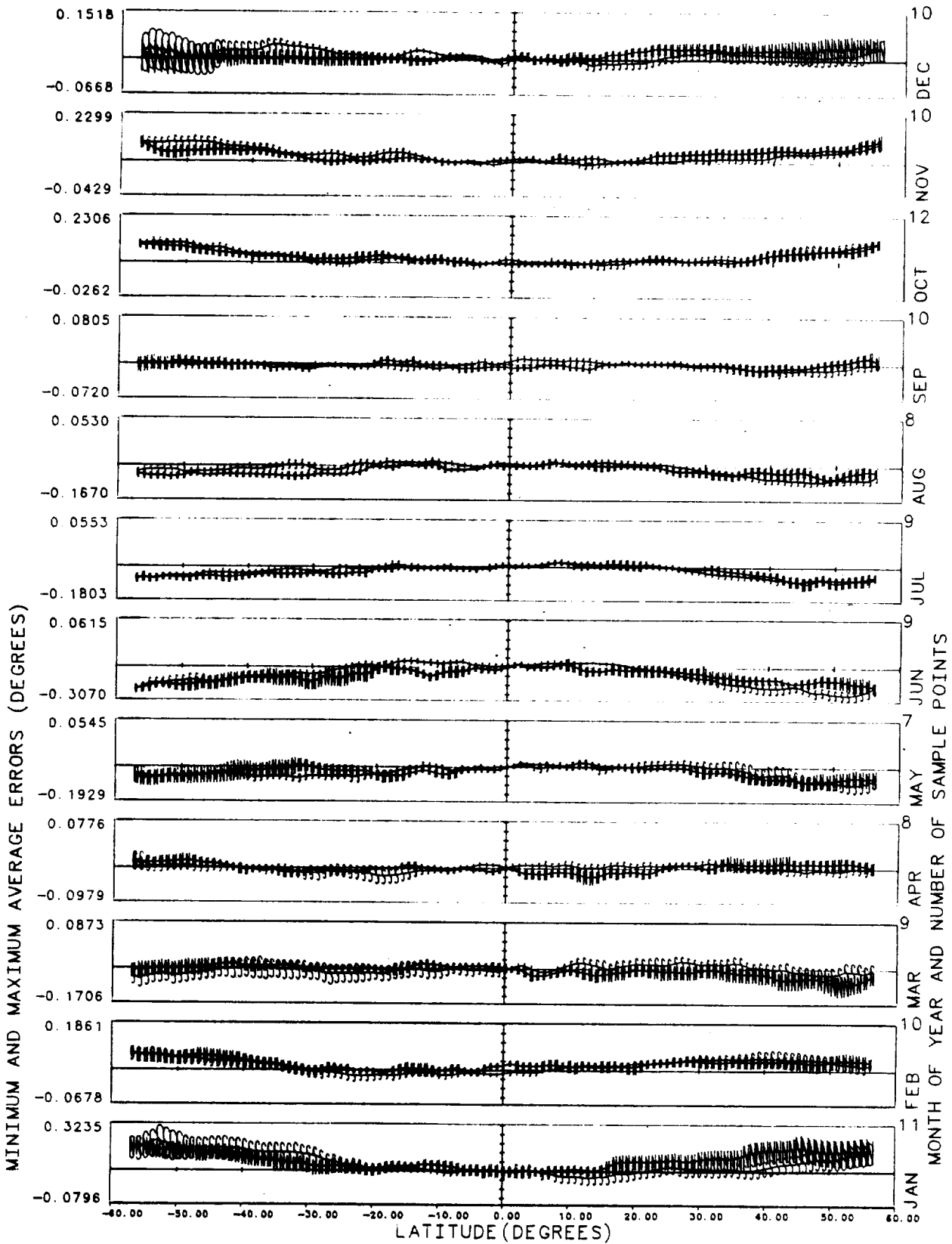


Figure 4b. Flight Data Roll Errors Versus Latitude and Month (With Standard Deviations)

- The Earth pulse processing branch of the actual ERBS IR horizon scanner circuit for threshold normalization is not modeled. Instead, the Earth detection pulse processing transfer function is also used for threshold computation.
- The optics are modeled by a square FOV without distortion due to the prism-lens optics.

The pitch and roll errors expected for ERBS as a result of prelaunch analysis using the HRMU and HRDB are illustrated in Figures 5a and 5b. The HRMU was also run on the radiance profile data adjusted using two schemes. The first uses LIMS analysis results; the second adjusts the profiles until a reasonable match to the flight data is obtained.

4.1 HORIZON RADIANCE ANALYSIS USING LIMS DATA

Analysis of the HRDB, in comparison with Nimbus/LIMS Earth radiance data, indicated that the (HRDB) model underestimates horizon radiance errors in the summer latitudes and overestimates the errors in the winter latitudes, causing the HRMU to underestimate the corresponding pitch and roll errors. This result is also verified by the comparison of the roll and pitch errors measured in this work with errors predicted by the HRMU using original horizon radiance profile data as input. To investigate the cause of the difference between the prelaunch predictions and the flight measurements of the errors, modifications were made to the HRMU input radiance profiles.

Profile adjustment scale factors were determined from plots of 0-kilometer tangent height radiance intensities from LIMS and HRDB models of LIMS profiles, illustrated in Figure 6 from Reference 3. For the months in which LIMS data were not available, the radiance profiles in the Northern and Southern Hemispheres were assumed to be seasonally symmetric. The pitch and roll errors resulting from this rescaled profile data are illustrated in Figures 7a and 7b. Improved agreement between predicted and measured pitch and roll errors for ERBS is demonstrated; however, the differences in the error magnitudes of 0.2 deg still remained. Because of this the second adjustment scheme was tried.

4.2 ADJUSTING THE RADIANCE PROFILES TO MATCH THE FLIGHT DATA ERRORS

The monthly errors from this process are illustrated in Figures 8a and 8b. The match is approximate; in most cases the model agrees with the average flight errors within the standard deviation of the flight data. During this exercise the following understanding was obtained. Efforts to raise the pitch errors relative to the LIMS profile renormalization scheme by raising and lowering the 60 and 80 deg latitude radiance profile intensities caused roll errors to exceed 0.5 deg. Thus it was determined that the pitch error in the model is controlled by changing the radiance gradient between 20, 40, and 60 deg latitudes and that to avoid excessive roll errors the gradient between 40, 60, and 80 deg latitudes must be moderated. For the summer months the radiance increases at 80 deg latitude appear to lag behind those at 60 deg latitude, as these latitudes receive increasing amounts of sunlight with the approaching solstice. Similarly, the winter 80-deg profiles are near and not much dimmer than the 60-deg profiles. Thus, roll errors were moderated

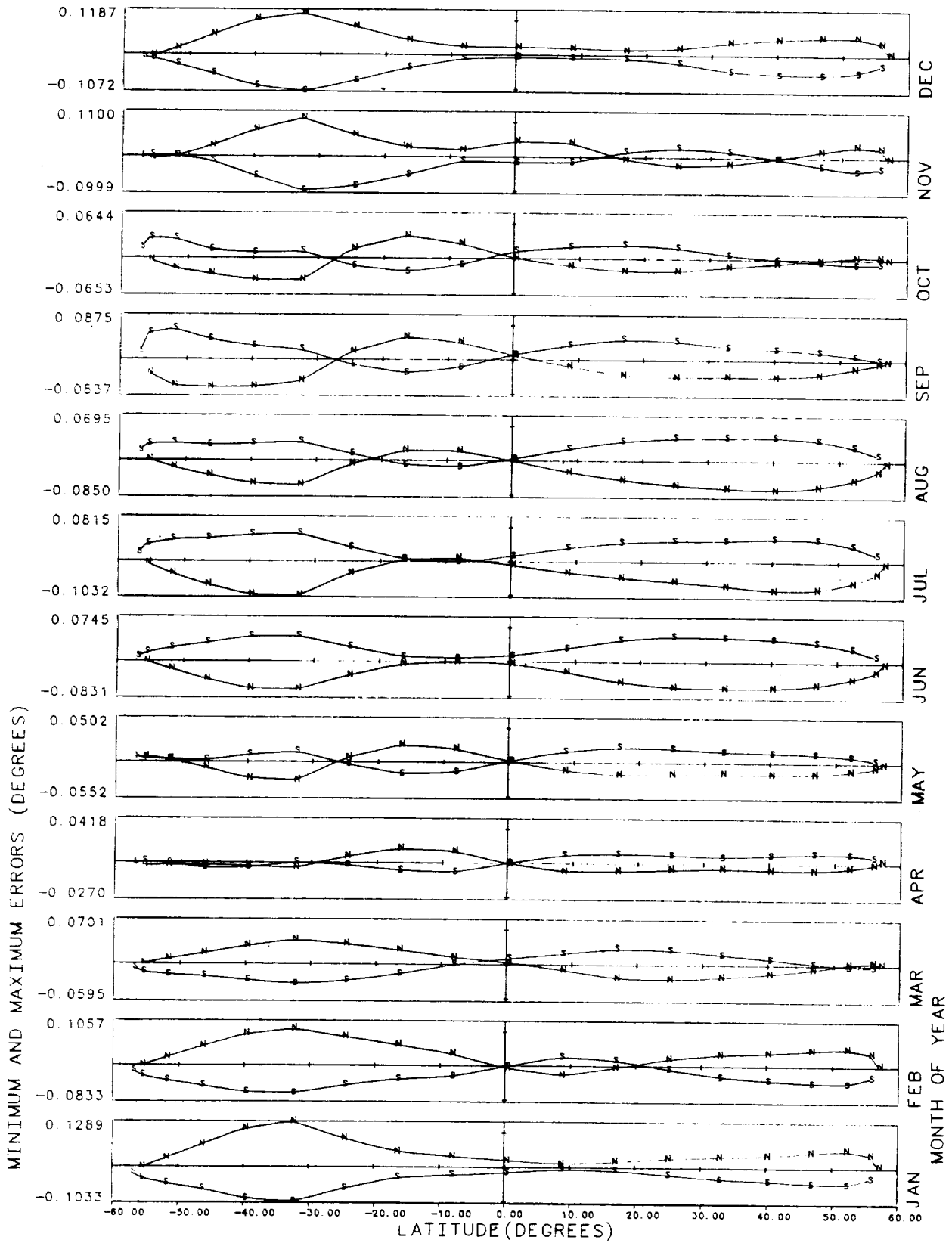


Figure 5a. Pitch Errors Versus Latitude and Month (Original Model)

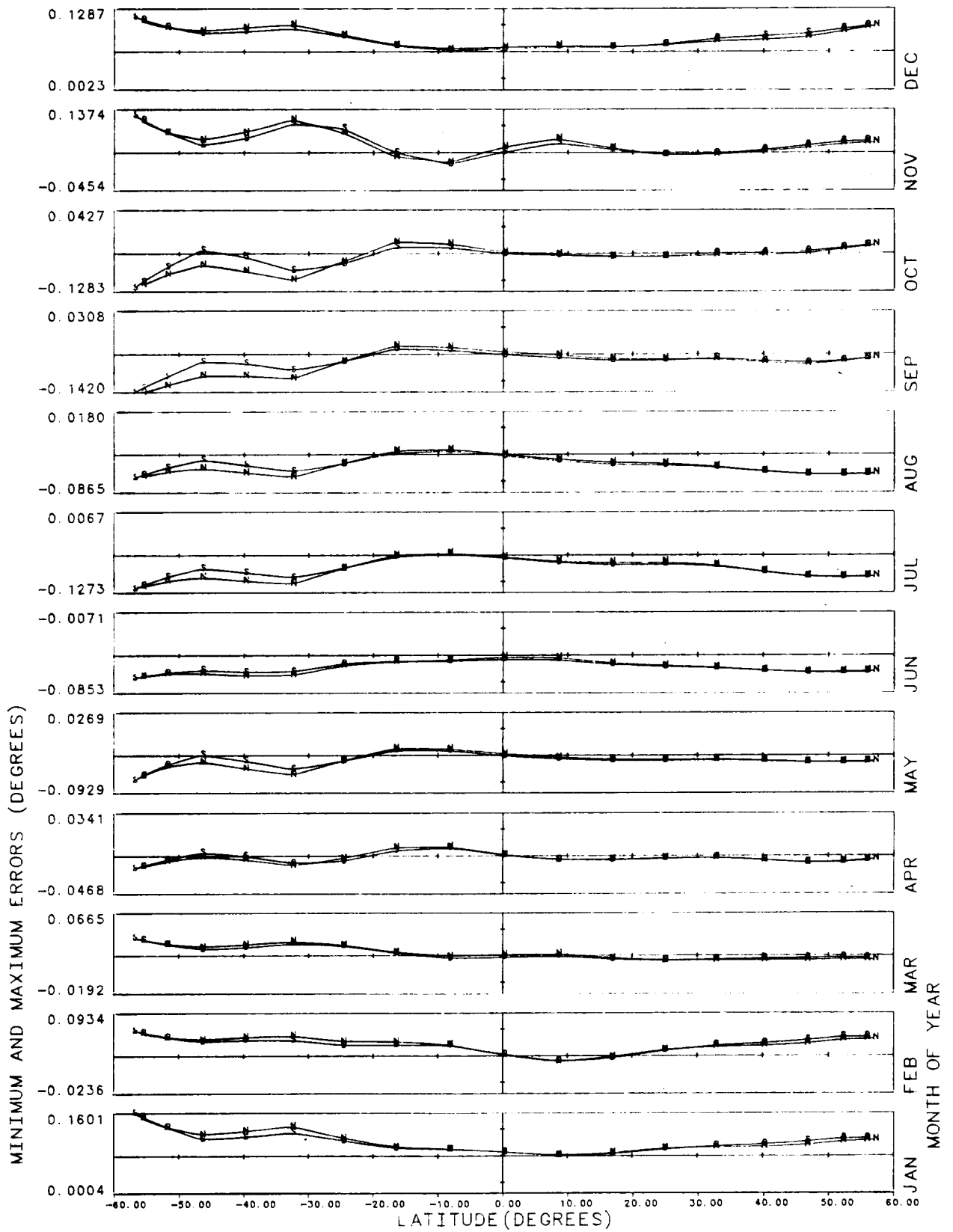


Figure 5b. Roll Errors Versus Latitude and Month (Original Model)

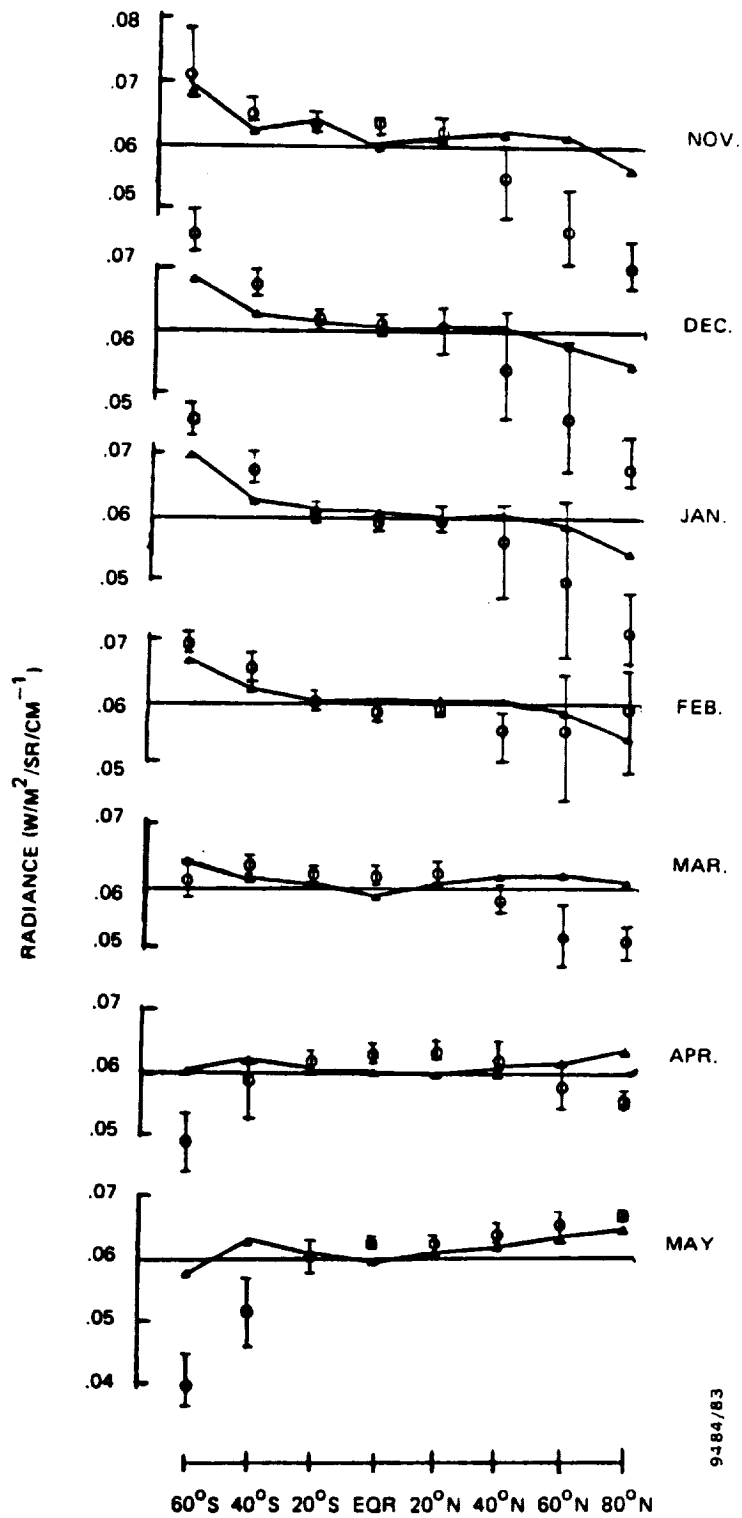


Figure 6. CO₂N Radiance Intensities at a 0-Kilometer Tangent Height Observed by LIMS (O) and Predicted by the HRDB (▲) (Bars Indicate Maximum and Minimum LIMS Values)

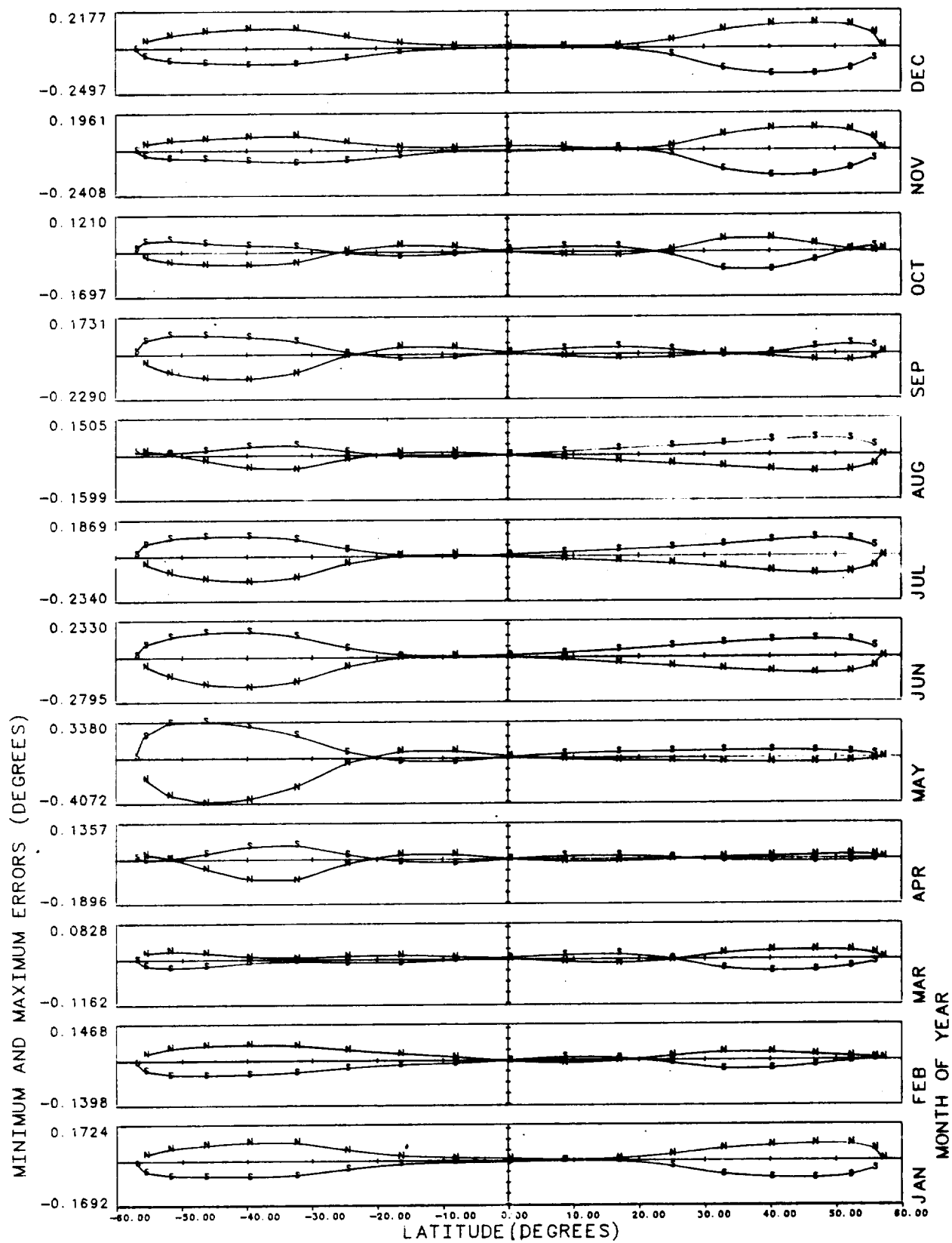


Figure 7a. Pitch Errors Versus Latitude and Month
(LIMS Modified Model)

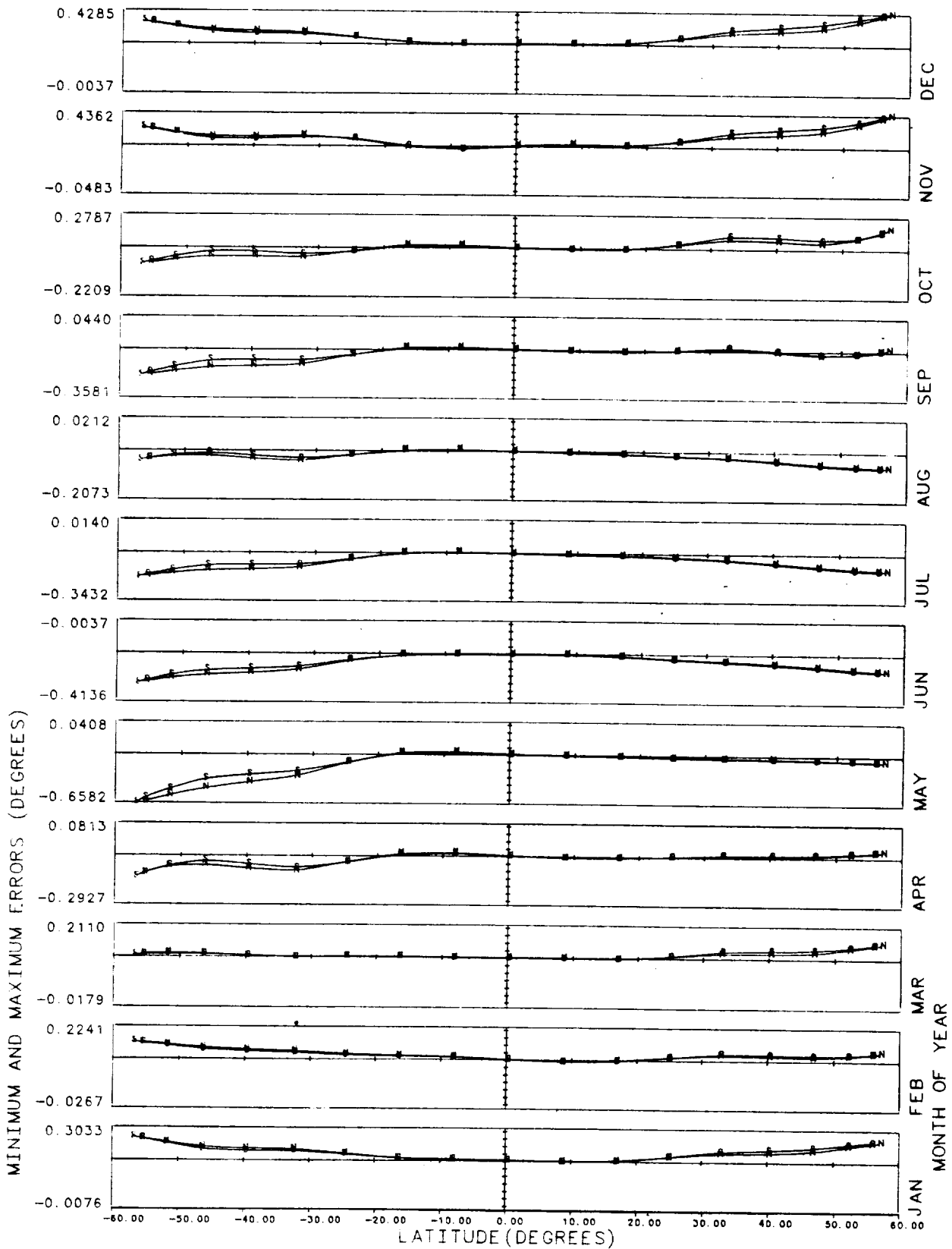


Figure 7b. Roll Errors Versus Latitude and Month (LIMS Modified Model)

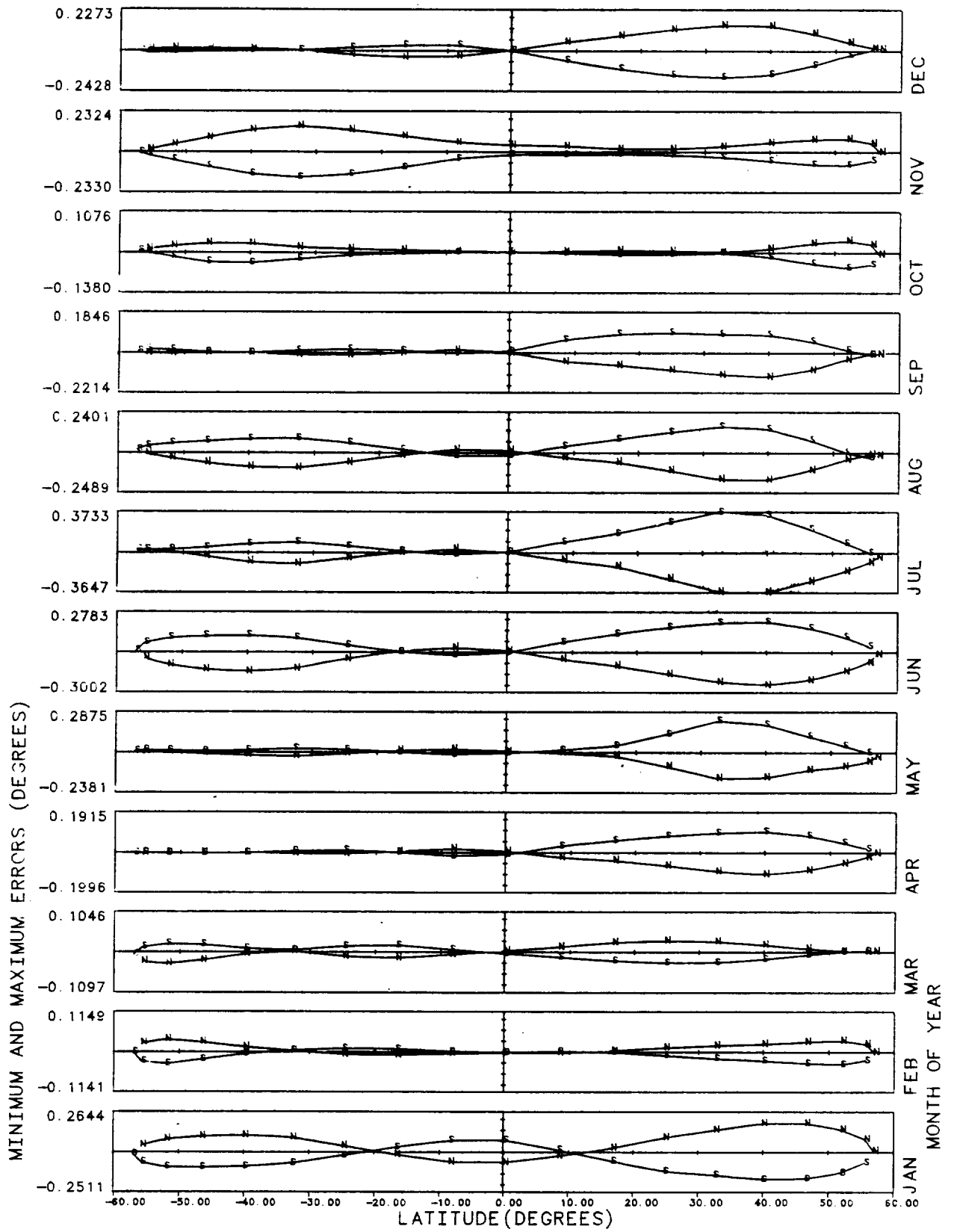


Figure 8a. Pitch Errors Versus Latitude and Month
(Flight Data Modified Model)

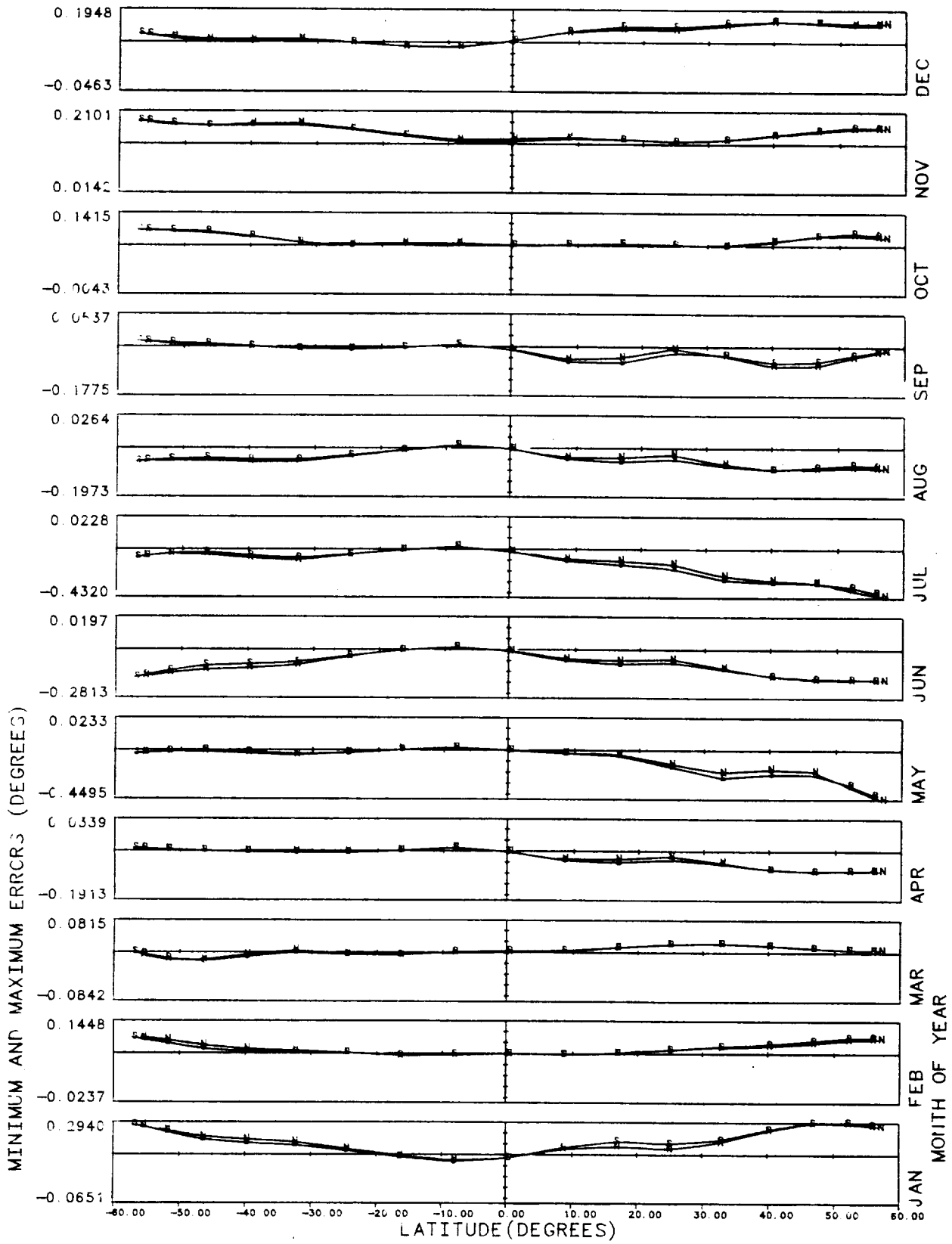


Figure 8b. Roll Errors Versus Latitude and Month
(Flight Data Modified Model)

by flattening the gradients in the high latitudes, making 40 and 80 deg radiance differences smaller in the summer and winter seasons.

5.0 CONCLUSIONS

The results of this analysis contribute significantly to the understanding of the effect of horizon radiance-induced errors in IR scanner systems and complement earlier work performed in the GSFC/FDD. The flight data measurements of the effect provide an important comparison to and calibration of the Earth horizon radiance model. The results also answer questions about the significance of the horizon radiance effect for attitude determination pointing control accuracy and about the chances of improving the accuracy of attitude measurements and pointing performance using horizon radiance modeling techniques. They also demonstrate an additional modeling technique using spacecraft flight data. In particular, the measurements indicate that the measured horizon radiance effect for ERBS exceeds the original HRMU-modeled value by as much as a factor of five. Measured values of 0.45 deg compare to 0.1 deg from the model of pitch errors for the midlatitudes in July. A possible source of this difference was known in 1984. It was reported then that the HRDB underestimated brightness contrast in the horizon radiance profiles for the polar latitudes in the winter and summer hemispheres. ERBS pitch and roll attitude information obtained from pure IR scanner telemetry thus requires the removal of errors as large as 0.45 deg. The accuracy of the model of these errors can be assessed from the results in three ways:

1. Applying no correction for radiance effects to the IR scanner pitch and roll limits the accuracy of the IR scanner attitude to 0.5 deg, ignoring all other errors due to biases, alignments, and electronic, optical, and mechanical noise.
2. Comparing the accuracy of pitch attitude results corrected using errors modeled from the original HRDB, there is a maximum 0.3 deg systematic error. However, applying the original horizon radiance correction model results in less error than no correction at all.
3. Comparing the results of IR pitch accuracy using the horizon radiance errors derived from a corrected IR Earth model, based on this work, to those from the uncorrected model shows that a significant component of the systematic error associated with latitude and season is eliminated. The resulting IR pitch attitude solution accuracy is then limited by the variance of the average error measured in this work and by the extremes exhibited by the longitudinal variations. The results indicate that the improved model will compensate for errors as large as 0.45 deg, with a 3σ error in the model of these values of approximately 0.3 deg.

The results of this analysis may be used for attitude determination support of ERBS in the future as a replacement for the spacecraft attitude motion model currently provided by the IRU. Additional enhancements can be made to this motion model by adding the effects of control loop magnetic torquing in response to spacecraft nutation and precession.

REFERENCES

1. NASA Technical Memorandum 86181, *Infrared Horizon Sensor Modeling for Attitude Determination and Control: Analysis and Mission Experience*, M. Phenneger, S. P. Singhal, T. H. Lee, T. Stengle, March 1985
2. Computer Sciences Corporation, CSC/SD-84/6007, *Earth Radiation Budget Satellite (ERBS) Horizon Radiance Modeling Utility (HRMU) User's Guide and System Description*, E. Burgess, June 1984
3. --, CSC/TM-83/6177, *Evaluation of the Horizon Radiance Data Base (HRDB)*, M. Phenneger, S. P. Singhal, November 1983
4. Air Force Geophysical Laboratory, Report AFGL-TR-80-0067, *Atmospheric Transmittance/Radiance: Computer Code LOWTRAN-5*, F. X. Kneizys, E. P. Shuttle, et al., February 1980
5. Computer Sciences Corporation, CSC/TM-77/6133, *A Comparison of Radiosonde Temperature and Humidity Profile Data Bases*, R. A. Nieman, August 1977
6. --, CSC/SD-83/6118, *Earth Radiation Budget Satellite (ERBS) Attitude Analysis and Support Plan*, M. Phenneger, et al., September 1983
7. --, CSC/SD-82/6013, *Earth Radiation Budget Satellite (ERBS) Attitude Ground Support System (AGSS) Functional Specifications and Requirements*, G. Nair, et al., September 1982
8. --, CSC/SD-86/6756, *Earth Radiation Budget Satellite (ERBS) Pitch and Roll Error Analysis*, J. Kronenwetter, et al., November 1986
9. Astrophysics and Space Science Library, Volume 73, *Spacecraft Attitude Determination and Control*, J. Wertz, Editor, 1978
10. Computer Sciences Corporation, CSC/SD-84/6005, *Earth Radiation Budget Satellite (ERBS) Definitive Attitude Determination System (DADS) User's Guide and System Description*, Y. Teng, July 1984
11. --, CSC/SD-84/6004UD2, *Earth Radiation Budget Satellite (ERBS) Attitude Determination System (ADS) User's Guide and System Description*, Revision 1, Update 2, R. Boyer, June 1988
12. --, CSC/SD-86/6012, *Horizon Radiance Modeling Utility Requirements and Specifications*, J. Hashmall, March 1986

**AUTONOMOUS SPACECRAFT ATTITUDE CONTROL
USING MAGNETIC TORQUING ONLY**

Keith L. Musser
Ward L. Ebert
The Johns Hopkins University
Applied Physics Laboratory
Laurel, Maryland 20707

ABSTRACT

Magnetic torquing of spacecraft has been an important mechanism for attitude control since the earliest satellites were launched. Typically a magnetic control system has been used for precession/nutation damping for gravity-gradient stabilized satellites, momentum dumping for systems equipped with reaction wheels, or momentum-axis pointing for spinning and momentum-biased spacecraft. Although within the small satellite community there has always been interest in inexpensive, light-weight, and low-power attitude control systems, completely magnetic control systems have not been used for autonomous three-axis stabilized spacecraft due to the large computational requirements involved. As increasingly more powerful microprocessors have become available, this has become less of an impediment. These facts have motivated consideration of the all-magnetic attitude control system presented here.

The problem of controlling spacecraft attitude using only magnetic torquing is cast into the form of the Linear Quadratic Regulator (LQR), resulting in a linear feedback control law. Since the geomagnetic field along a satellite trajectory is not constant, the system equations are time varying. As a result the optimal feedback gains are time-varying. Orbit geometry is exploited to treat feedback gains as a function of position rather than time, making feasible the onboard solution of the optimal control problem. In simulations performed to date, the control laws have shown themselves to be fairly robust and a good candidate for an onboard attitude control system.

INTRODUCTION

Magnetic torquing has been used for spacecraft attitude control since the launch of the earliest satellites. There are many operational spacecraft which use magnetics for precession/nutation damping, momentum dumping, and large angle maneuvers [1-4]. Also, there are existing three-axis control systems which use magnetic torquing to maintain spin axis orientation of a pitch reaction wheel [5]. Use of magnetics has recently been suggested for libration damping and arbitrary yaw angle control of a gravity gradient stabilized satellite [7].

Complete three-axis attitude control has not been used because of the large computational requirements involved. As increasingly more powerful microprocessors have become available, computation has become less of an impediment. This has motivated consideration of the all-magnetic attitude control system presented here.

We consider a rigid spacecraft without a gravity gradient boom. For the present discussion, we assume a perfect knowledge of the spacecraft attitude is available. Finally, we assume the spacecraft is in a near circular orbit and has a nadir pointing nominal attitude.

The geomagnetic field, while essentially constant in an earth-fixed reference frame, is time-varying in the nominal body reference frame. This introduces a time-varying element into the linearized system of equations. Because the magnetic torque vector is constrained to always lie perpendicular to the local geomagnetic field vector, the system appears uncontrollable if fixed at any instant in time. (When considered over time, it is completely controllable.) This does, however, limit the achievable closed loop transient reaction speed to the order of magnitude of the magnetic field time variation. For a nadir pointing satellite in a polar orbit, this is about two cycles per orbit. The reaction speed should decrease with decreasing orbit inclination because the geomagnetic field variation decreases in magnitude.

FORMULATION OF THE EQUATIONS OF MOTION

Nomenclature

LQR	Linear Quadratic Regulator
P, R, Y	Pitch, Roll, Yaw (2-1-3 Euler angles)
ω_o	Mean angular rate of the local vertical reference frame.
$R_i(\theta)$	Rotation matrix for an angle θ about the i-axis.
$C_{B \leftarrow S}$	Rotation matrix from inertial (space) to actual body coordinates.
$C_{N \leftarrow S}$	Rotation matrix from inertial (space) to nominal body coordinates.
$C_{B \leftarrow N}$	Rotation matrix from nominal body to actual body coordinates.
ω_B	Angular velocity of spacecraft with respect to inertial frame, represented in the body frame.
τ_B	Total external torque acting on spacecraft body, in body frame.

$\mathbf{I}_{dist,B}$	External disturbance torque, excluding gravity gradient torque, represented in the body frame.
$\mathbf{I}_{con,B}$	Control torque acting on spacecraft body, represented in body frame.
R_s	Magnitude of spacecraft position vector in Earth centered coordinates.
$\hat{\mathbf{R}}_B$	Unit vector from center of Earth to spacecraft, represented in the body frame.
J	Spacecraft inertia tensor, represented in the body frame.
$J_i \{J_1, J_2, J_3\}$	i^{th} diagonal element of inertia matrix J .
$\mathbf{d}_B(t)$	Control dipole moment of spacecraft, represented in the body frame.
\mathbf{H}_B	Local geomagnetic field intensity, represented in the body frame.
$\mathbf{H}_N(t)$	Local geomagnetic field intensity, represented in the nominal body frame.
μ	Geocentric gravitational constant, $GM_E = \mu = 3.986 \times 10^{14} \text{ m}^3/\text{s}^2$.
$h_i(t) \{h_1(t), h_2(t), h_3(t)\}$	i^{th} component of $\mathbf{H}_N(t)$.
$d_i(t) \{d_1(t), d_2(t), d_3(t)\}$	i^{th} component of $\mathbf{d}_B(t)$.
$\mathbf{x}(t)$	State vector $[\mathbf{R}, \mathbf{P}, \mathbf{Y}, \dot{\mathbf{R}}, \dot{\mathbf{P}}, \dot{\mathbf{Y}}]^T$.
F	System matrix of linearized equations.
$G(t)$	Input coupling matrix of linearized equations.
$J(\mathbf{d}_B(t))$	Quadratic cost functional.
S_f	Final time state cost matrix.
A	State cost weighting matrix.
B	Control cost weighting matrix.
$S(t)$	Solution of the matrix Riccati equation.
$K(t)$	Feedback gain matrix, parameterized by time.
$K(\beta, \lambda)$	Feedback gain matrix, parameterized by (β, λ) .
a	Orbit semi-major axis
e	Orbit eccentricity.
i	Orbit inclination.

Ω	Argument of the ascending node.
ω	Argument of perigee.
ω_E	Angular rate of the Earth $\approx 2\pi$ radians/24 hours.
λ	Earth fixed longitude of the ascending node.
β	Argument of latitude (defined in Figure 4).

FORMULATION OF THE EQUATIONS OF MOTION

For the problem at hand, we have considered the rigid-body equations of motion of a nadir-pointing spacecraft in a circular orbit. Referring to Figure 1, where (S) subscripts indicate inertial frame, (N) indicates nominal body frame, and (B) indicates actual body frame, we can represent attitude using 2-1-3 Euler angles as

$$C_{B \leftarrow S} = R_3(Y) R_1(R) R_2(\omega_0 t + P) \quad (1)$$

$$C_{B \leftarrow S} = R_3(Y) R_1(R) R_2(P) R_2(\omega_0 t) \quad (2)$$

where $R_i(\theta)$ is a rotation about axis i through angle θ . Since the desired trajectory has Y , R , and P all zero, we can define an intermediate "nominal" attitude (to be used later) as

$$C_{N \leftarrow S} = R_2(\omega_0 t) \quad , \quad (3)$$

which gives

$$C_{B \leftarrow N} = R_3(Y) R_1(R) R_2(P) \quad . \quad (4)$$

The angular velocity of the body frame with respect to the inertial frame can be expressed as

$$\underline{\omega}_B = \dot{Y} \begin{bmatrix} 0 \\ 0 \\ 1 \end{bmatrix} + R_3(Y) \dot{R} \begin{bmatrix} 1 \\ 0 \\ 0 \end{bmatrix} + R_3(Y) R_1(R) (\omega_0 + \dot{P}) \begin{bmatrix} 0 \\ 1 \\ 0 \end{bmatrix} \quad . \quad (5)$$

To first order in angles and rates this is

$$\underline{\omega}_B = \begin{bmatrix} \dot{R} + \omega_0 Y \\ \omega_0 + \dot{P} \\ \dot{Y} - \omega_0 R \end{bmatrix} \quad . \quad (6)$$

To obtain the first-order approximations to Euler's equations we write

$$\underline{\tau}_B = \frac{d}{dt} (J \underline{\omega}_B) + \underline{\omega}_B \times J \underline{\omega}_B \quad , \quad (7)$$

which, assuming a diagonal inertia matrix, gives

$$\underline{\mathbf{I}}_B \approx \begin{bmatrix} J_1 \ddot{R} + \omega_o(J_1 + J_3 - J_2) \dot{Y} + \omega_o^2(J_2 - J_3) R \\ J_2 \ddot{P} \\ J_3 \ddot{Y} - \omega_o(J_1 + J_3 - J_2) \dot{R} + \omega_o^2(J_2 - J_1) Y \end{bmatrix} \quad (8)$$

The applied torque $\underline{\mathbf{I}}_B$ consists of the gravity gradient, control, and disturbance torques, and can be represented as

$$\underline{\mathbf{I}}_B = \underline{\mathbf{I}}_{\text{dist},B} + \underline{\mathbf{I}}_{\text{con},B} + \frac{3\mu}{R_s^3} [\hat{\underline{\mathbf{R}}}_B \times (J \hat{\underline{\mathbf{R}}}_B)] , \quad (9)$$

where R_s is the geocentric radius, and $\hat{\underline{\mathbf{R}}}_B$ is the unit vector from the earth to the spacecraft, represented in the body frame. Since $\hat{\underline{\mathbf{R}}}_B$ corresponds to the z-axis in the nominal reference frame, we can use the first-order approximation

$$\hat{\underline{\mathbf{R}}}_B = \begin{bmatrix} -P \\ R \\ 1 \end{bmatrix} , \quad (10)$$

giving

$$\underline{\mathbf{I}}_B = \underline{\mathbf{I}}_{\text{dist},B} + \underline{\mathbf{I}}_{\text{con},B} - \frac{3\mu}{R_s^3} \begin{bmatrix} (J_2 - J_3) R \\ (J_1 - J_3) P \\ 0 \end{bmatrix} . \quad (11)$$

Finally, we examine the control torque $\underline{\mathbf{I}}_{\text{con},B}$. This torque is obtained from the commanded dipole $\underline{\mathbf{d}}_B(t)$ as

$$\underline{\mathbf{I}}_{\text{con},B} = \underline{\mathbf{d}}_B(t) \times \underline{\mathbf{H}}_B \quad (12)$$

where $\underline{\mathbf{H}}_B$ is the ambient field intensity represented in the body frame. We also have

$$\underline{\mathbf{H}}_B = \mathbf{C}_{B \leftarrow N} \underline{\mathbf{H}}_N(t) \approx \underline{\mathbf{H}}_N(t) \quad (13)$$

where the explicit time dependence applied to $\underline{\mathbf{H}}_N(t)$ emphasizes that its value is attitude independent. We would like to replace $\underline{\mathbf{H}}_B$ in equation (12) with $\underline{\mathbf{H}}_N(t)$. This is valid as a first-order approximation because we will later be assigning a control law for $\underline{\mathbf{d}}_B(t)$ which is linear in angles and rates.

Combining equations (8), (11), and (12) with the approximation (13), we obtain the complete linearized equations of motion as follows:

$$\dot{\underline{\mathbf{x}}}(t) = \frac{d}{dt} \begin{bmatrix} R \\ P \\ Y \\ \dot{R} \\ \dot{P} \\ \dot{Y} \end{bmatrix} \begin{bmatrix} 0 & 0 & 0 & 1 & 0 & 0 \\ 0 & 0 & 0 & 0 & 1 & 0 \\ 0 & 0 & 0 & 0 & 0 & 1 \\ F41 & 0 & 0 & 0 & 0 & F46 \\ 0 & F52 & 0 & 0 & 0 & 0 \\ 0 & 0 & F63 & F64 & 0 & 0 \end{bmatrix} \begin{bmatrix} R \\ P \\ Y \\ \dot{R} \\ \dot{P} \\ \dot{Y} \end{bmatrix} +$$

$$\begin{bmatrix} 0 & 0 & 0 \\ 0 & 0 & 0 \\ 0 & 0 & 0 \\ 0 & G42(t) & G43(t) \\ G51(t) & 0 & G53(t) \\ G61(t) & G62(t) & 0 \end{bmatrix} \begin{bmatrix} d_1(t) \\ d_2(t) \\ d_3(t) \end{bmatrix} + \mathcal{I}_{dist,B}$$

where

$$\begin{aligned} F41 &= -\frac{J_2 J_3}{J_1} \left(\omega_0^2 + \frac{3\mu}{R_s^3} \right) & G51(t) &= -h_3(t) J_2^{-1} \\ F52 &= -\frac{3\mu}{R_s^3} \left(\frac{J_1 - J_3}{J_2} \right) & G61(t) &= h_2(t) J_3^{-1} \\ F63 &= -\omega_0^2 \left(\frac{J_2 - J_1}{J_3} \right) & G42(t) &= h_3(t) J_1^{-1} \\ F64 &= \omega_0 \left(\frac{J_1 + J_3 - J_2}{J_3} \right) & G62(t) &= -h_1(t) J_3^{-1} \\ F46 &= -\omega_0 \left(\frac{J_1 + J_3 - J_2}{J_1} \right) & G43(t) &= -h_2(t) J_1^{-1} \\ & & G53(t) &= h_1(t) J_2^{-1} \end{aligned}$$

where

$h_1(t), h_2(t), h_3(t)$ are the components of $\underline{H}_N(t)$,

$d_1(t), d_2(t), d_3(t)$ are the components of $\underline{d}_B(t)$.

or, in more compact notation,

$$\frac{d}{dt} \underline{x} = F \underline{x} + G(t) \underline{d}_B(t) + \mathcal{I}_{dist,B} \quad (14)$$

APPLICATION OF THE LINEAR QUADRATIC REGULATOR (LQR)

Since it is desirable to maintain R, P, and Y as close to zero as possible over time, a reasonable cost function is the standard quadratic performance index [6]. We wish to minimize

In all cases tested, the closed loop system was stable. A simple check of controller sensitivity was made by using a slightly different model for the closed loop simulation than was assumed in computing the feedback gain. Moments of inertia, orbit eccentricity, and perigee position were varied, and in each case the system remained stable, though performance was degraded slightly, as expected.

The satellite mass properties, orbit, and disturbance parameters used in evaluations are given in Table 1. The disturbance torques used are based on a 2 m² area and a 30 cm center of pressure to center of mass offset. This is conservative for a satellite with a maximum moment of inertia of 27 kg-m². Figures 2A through 2E show time histories of Euler angles for several configurations.

APPLICATION OF GEOMETRIC PROPERTIES

Direct implementation of the time-varying linear-feedback control law described above requires a numerical solution of the matrix Riccati differential equation. Since the equation is solved backward from a future time to compute feedback gains at the present time, the integration must be restarted repetitively, each starting at a point later in time, as illustrated in Figure 3.

Obviously, integration backward in time is not ideal for real-time implementation. Fortunately, however, we can utilize the quasi-periodicity due to orbit geometry to advantage, making real-time implementation feasible.

We wish to parameterize the feedback gain $K(t)$ in terms of position rather than time. First, we make certain assumptions about the orbit:

- | | |
|--|------------------|
| (1) Orbit has a known semi-major axis, | a |
| (2) Orbit is circular, | $e = 0$ |
| (3) Orbit has known inclination, | i |
| (4) Node is inertially fixed, | $d\Omega/dt = 0$ |
| (5) Perigee is inertially fixed, | $d\omega/dt = 0$ |
| (6) Orbital angular rate is known, | ω_o |
| (7) Earth rotational rate is known, | ω_E |

These assumptions will typically be valid over several days, which is adequate for our purposes. Referring to Figure 4, it becomes simple to describe an entire satellite trajectory, $\mathbf{r}(t)$, in Earth fixed coordinates, in terms of only $\beta(t_o)$ and $\lambda(t_o)$ at any fixed time t_o :

$$\mathbf{r}(t) = R_3(\omega_E(t-t_o) - \lambda(t_o)) R_1(-i) R_3(-\beta(t_o) - \omega_o(t-t_o)) \begin{bmatrix} 1 \\ 0 \\ 0 \end{bmatrix} \quad (18)$$

The insight to be gained here is that if the trajectory can be completely parameterized in terms of the ordered pair $(\beta(t_o), \lambda(t_o))$ then the geomagnetic field history, $\underline{H}_N(t)$ can be similarly expressed in terms of (β, λ) . Hence the feedback gain matrix $K(t_o)$, which depends on $\underline{H}_N(t)$ from $t_o < t < \infty$, can be written as a function of $(\beta(t_o), \lambda(t_o))$ only. This function, $K(\beta, \lambda)$, is not time varying. Thus, $K(\beta, \lambda)$ can be computed once and will remain valid permanently.

A real orbit will not satisfy the assumptions exactly. We can, however, drop the assumption of a circular orbit; the expression in equation (18) then becomes much more tedious, but the conclusion is the same. That is, the trajectory can be completely characterized by (β, λ) .

When assumptions (4) and (5) are violated by a small amount, the effect is to add a slow time variation to $K(\beta,\lambda)$. In an implementation of this system, $K(\beta,\lambda)$ must be recomputed periodically. It is expected that recomputing once every three days will be adequate for a typical perigee drift rate of three degrees/day. This requires much less CPU time than the continuous gain computation of Figure 3.

The feedback gain function $K(\beta,\lambda)$ has been computed for several cases. It appears to be reasonably well behaved and can be represented with a modest investment in computer memory. Interestingly, a secondary advantage of using (β,λ) to parameterize $K(\bullet)$, rather than another position representation scheme, is that $K(\beta,\lambda)$ is periodic in both β and λ with a period of 2π . It may be possible to reduce data storage requirements by representing $K(\beta,\lambda)$ in terms of Fourier coefficients.

FLIGHT SOFTWARE CONFIGURATION

A suggested flight software configuration is given in Figure 5. The infrequent updating of the feedback gains is run as a background task, and the Real Time Control operation is the high priority task.

Since both tasks require a model of the orbit, periodic orbit updates from a ground station will be necessary. It is believed that updates on the order of once every seven days should be adequate for most applications.

CONCLUSIONS

The feasibility of spacecraft attitude control using only magnetic torquing has been demonstrated. Although the closed-loop transient reaction speed possible with such a system is fundamentally limited, the attitude requirements of many missions appear attainable. An algorithm for flight computer implementation has been simulated, demonstrating the feasibility of using this system with a typical onboard microprocessor. The mechanical simplicity inherent in using electromagnetics only for control promises to make such a system both cost effective and mechanically reliable.

REFERENCES

- [1] Junkins, J. L., C. K. Carrington, and C. E. Williams, "Time Optimal Magnetic Attitude Maneuvers," presented at AIAA/AAS Astrodynamics Conference, Danvers, Massachusetts, August 1980.
- [2] Glaese, J. R., et al, "Low-Cost Space Telescope Pointing Control System," *Journal of Spacecraft and Rockets*, Volume 13, No. 7, pp. 400-405, July 1976.
- [3] Carlucci, D., et al, "Attitude Estimation and Satellite Detumbling by Active Magnetic Controls," *Journal of Control and Computers*, Volume 12, No. 3, pp. 100-103, 1984.
- [4] Schmidt, G. E., Jr., "The Application of Magnetic Attitude Control to a Momentum Biased Synchronous Communications Satellite," presented at AIAA Guidance and Control Conference, Boston, Massachusetts, August 1975.
- [5] Bruderle, E., and A. Reindler, "Magnetic Roll/Yaw Attitude Control of a Momentum Biased Near Polar Orbit Satellite," IFAC Automatic Control in Space 1982, Proceedings of the Ninth Symposium, Noordwijkerhout, Netherlands, July 1982.
- [6] Elbert, T. F., Estimation and Control of Systems, Van Nostrand Reinhold Company, New York, pp. 304-319, 1984.
- [7] Martel, F., P. K. Pal, and M. Psiaki, "Active Magnetic Control System for Gravity Gradient Stabilized Spacecraft," Proceedings of the Second Annual AIAA/USU Conference on Small Satellites, September 1988.
- [8] Kalman, R. E., "Contributions to the Theory of Optimal Control," *Bol. Soc. Mat. Mexicana*, pp. 102-119, 1960.
- [9] Wertz, J. R., ed., Spacecraft Attitude Determination and Control, D. Reidel Publishing Company, Boston, Massachusetts, pp. 117-123, 1985.

Table 1

System Parameters Used in Test Cases of Table 2

Moments of Inertia

I_1	27	kg-m ²
I_2	27	kg-m ²
I_3	10	kg-m ₂

Orbital Rate

ω_o	1.0473E-3	rad/s
------------	-----------	-------

Orbit

Semi-major axis	a	1.15537	earth radii
Eccentricity	e	0.004119	
Inclination	i	89.547	degrees
Right ascension of the ascending node	Ω_N	111.167	degrees
Arg. of perigee	ω_p	71.0035	degrees
Node drift rate	$d\Omega_N/dt$	-0.047522	deg/day
Per. drift rate	$d\omega_p/dt$	-3.004395	deg/day
Epoch day		130	
Time of day		78194.5	sec
Year		87	

Orbobservation Time Span

Simulations start at 1987, day 131, time = 100 sec.

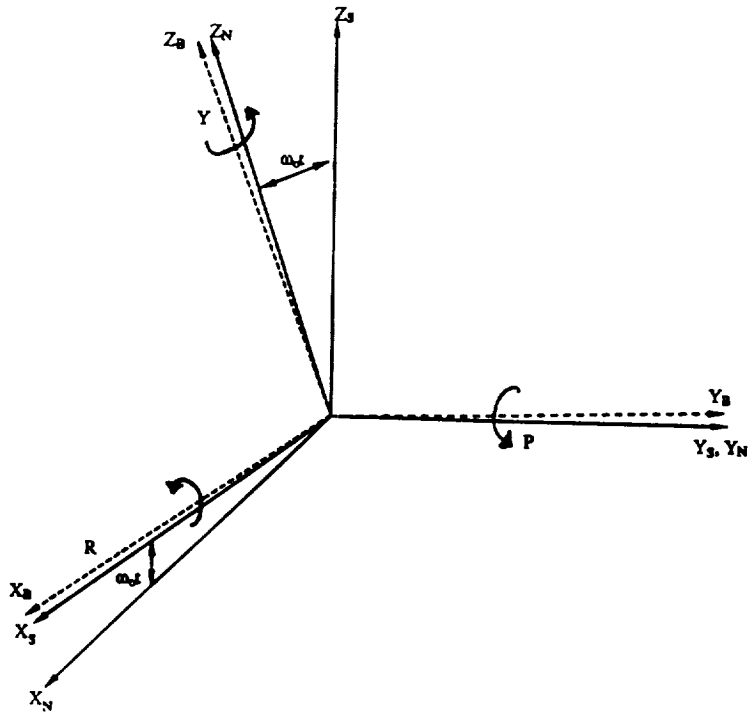
Disturbances Used in Performance Analysis

Torque (constant in body frame)

± 55	dyne-cm	in Roll
± 100	dyne-cm	in Pitch
± 10	dyne-cm	in Yaw

Residual Magnetic Dipole (constant in body frame)

200	pole-cm	in body x-axis
200	pole-cm	in body y-axis
200	pole-cm	in body z-axis



$$X_S = Y_S \times Z_S$$

Y_S = orbit normal

Z_S = center of earth to S/C position at time $t=0$

$$X_N = Y_N \times Z_N$$

Y_N = orbit normal

Z_N = local vertical (up)

P = Pitch

Y = Yaw

Figure 1: Coordinate System and Small 2-1-3 Euler Angle Definitions

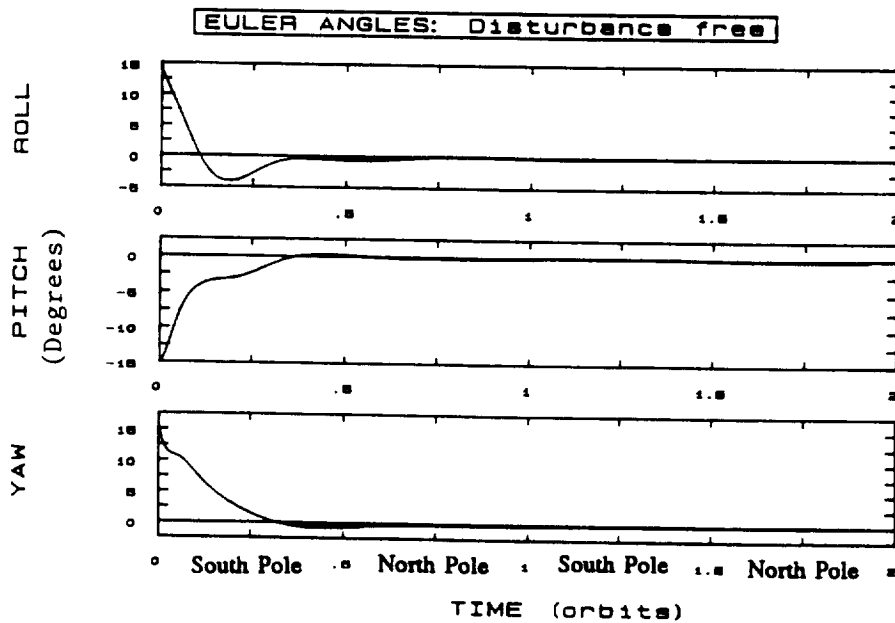


Figure 2a: Time history of Euler angles for a case without any disturbance torques or a residual dipole. Note that angles do not decay precisely to zero because the orbit is not perfectly circular.

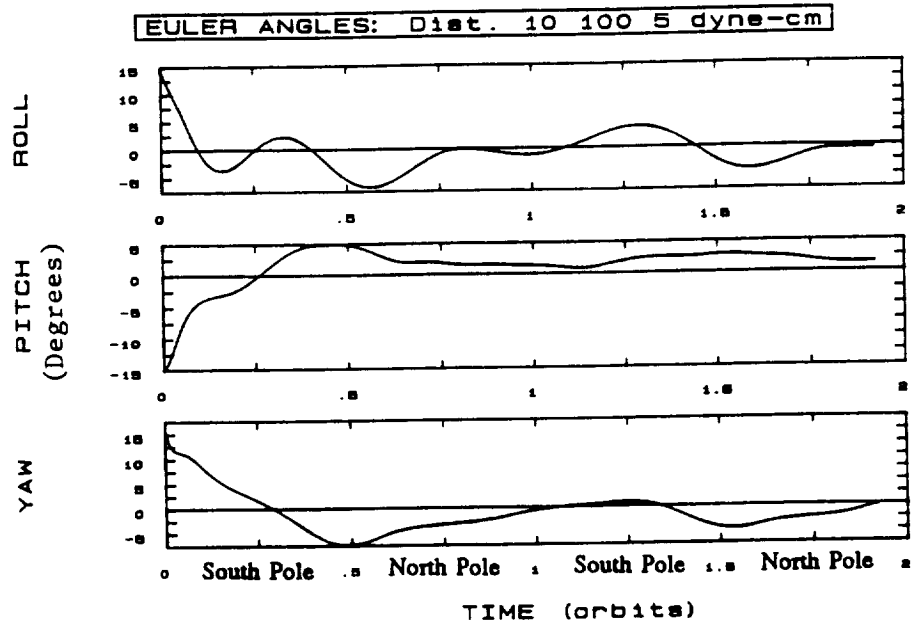


Figure 2b: Case where disturbance torque is a constant +10 dyne-cm in roll, +100 dyne-cm in pitch, and +5 dyne-cm in yaw. A residual dipole of $200 i + 200 j + 200 k$ pole-cm is also assumed.

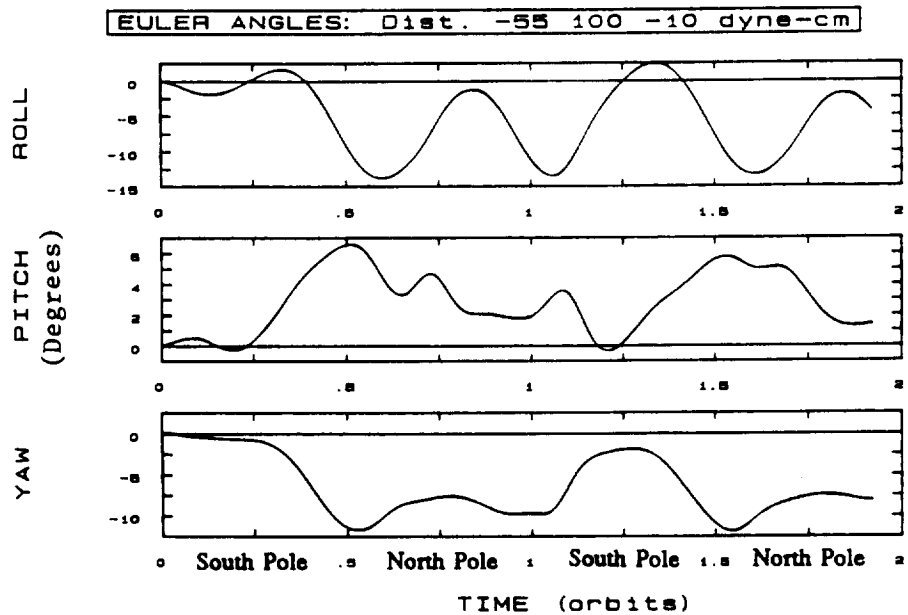


Figure 2c: Disturbance torque for this case is a constant -55 dyne-cm in roll, +100 dyne-cm in pitch, and -10 dyne-cm in yaw. A residual dipole of $200 i + 200 j + 200 k$ pole-cm is also assumed.

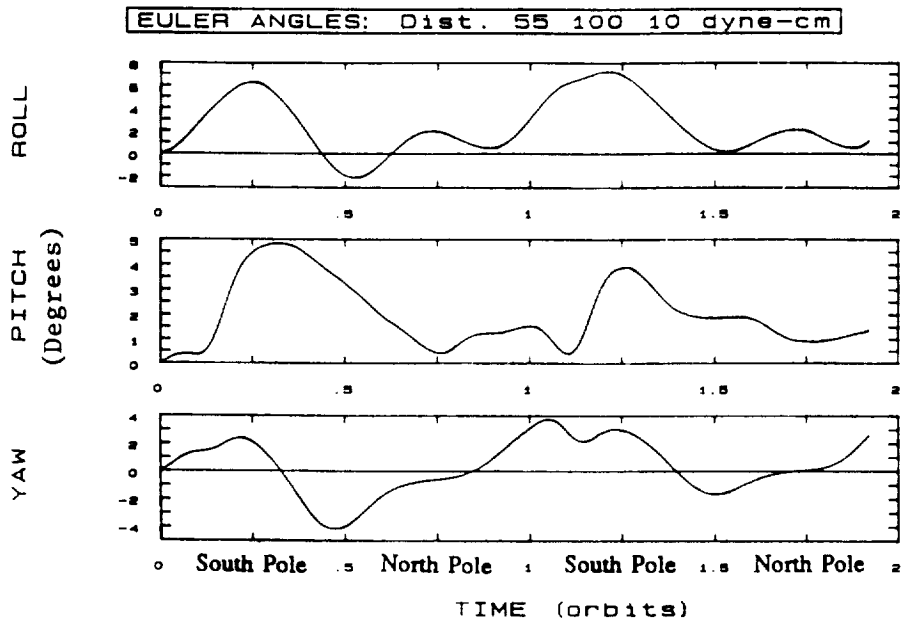


Figure 2d: The disturbance torque assumed for this case is +55 dyne-cm in roll, +100 dyne-cm in pitch, and +10 dyne-cm in yaw. A residual dipole of $200 i + 200 j + 200 k$ pole-cm is also assumed.

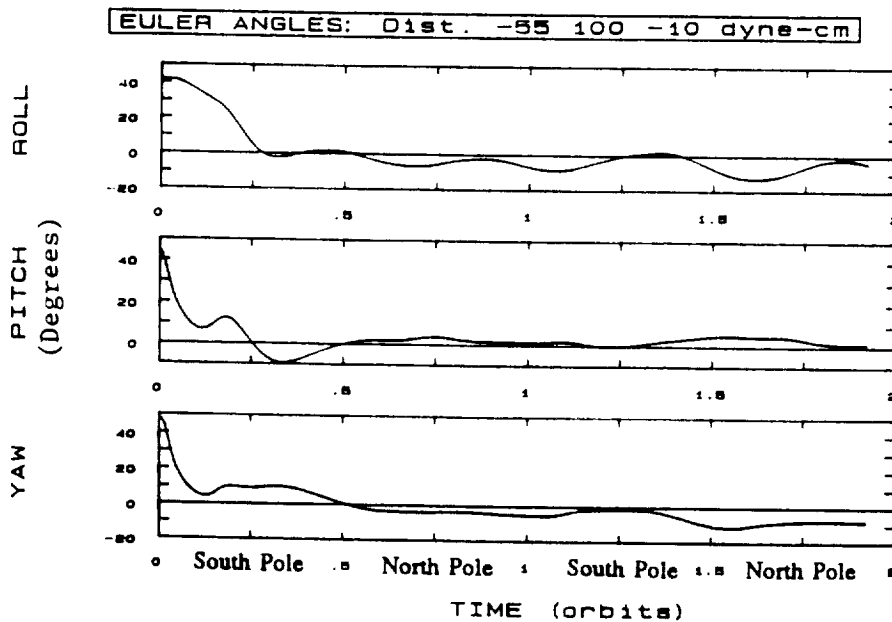


Figure 2e: Disturbance torque is a constant -55 dyne-cm in roll, +100 dyne-cm in pitch, and -10 dyne-cm in yaw. A residual dipole of $200 i + 200 j + 200 k$ pole-cm is also assumed. The closed loop system will not capture reliably at initial angles larger than 40° .

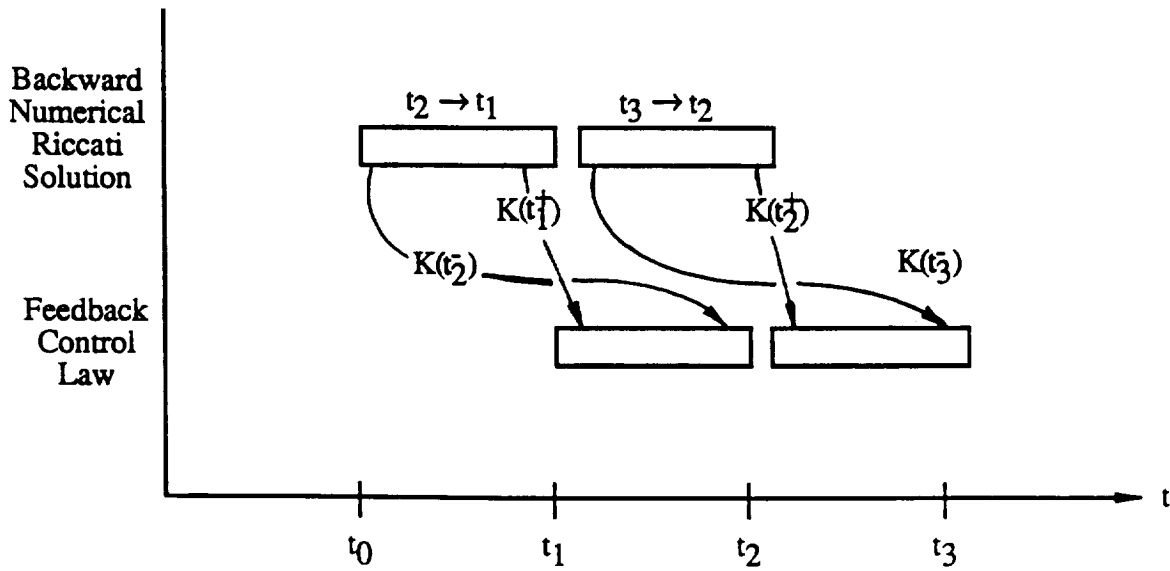
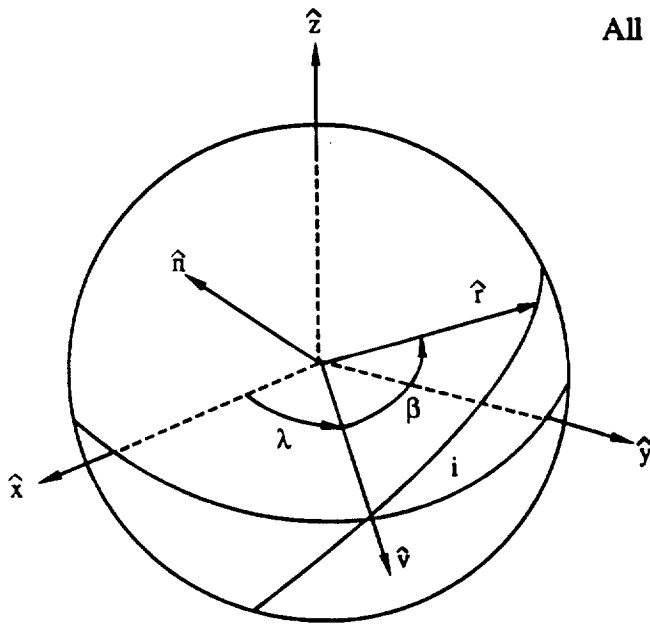


Figure 3: Iteration necessary when using backward Riccati equation integration in real time.



All vectors represented in Earth-fixed coordinates.

\hat{n} = positive orbit normal

\hat{r} = direction to spacecraft

$\hat{v} = \frac{\hat{z} \times \hat{n}}{|\hat{z} \times \hat{n}|}$ = direction of ascending node

$$\beta = \tan^{-1} \left(\frac{\hat{r} \cdot (\hat{n} \times \hat{v})}{\hat{r} \cdot \hat{v}} \right)$$

$$\lambda = \tan^{-1} \left(\frac{\hat{v} \cdot \hat{y}}{\hat{v} \cdot \hat{x}} \right)$$

\hat{x} , \hat{y} , \hat{z} Earth-fixed coordinate axes, with \hat{z} = north

Notes:

(1) $\frac{d\lambda}{dt} = -\omega_E$, $\omega_E = 2\pi$ radians/24 hours

(2) For near circular orbit, $\frac{d\beta}{dt} = \omega_o$, ω_o = orbital angular rate (rad/sec)

Figure 4: Definition of position parameters β and λ .

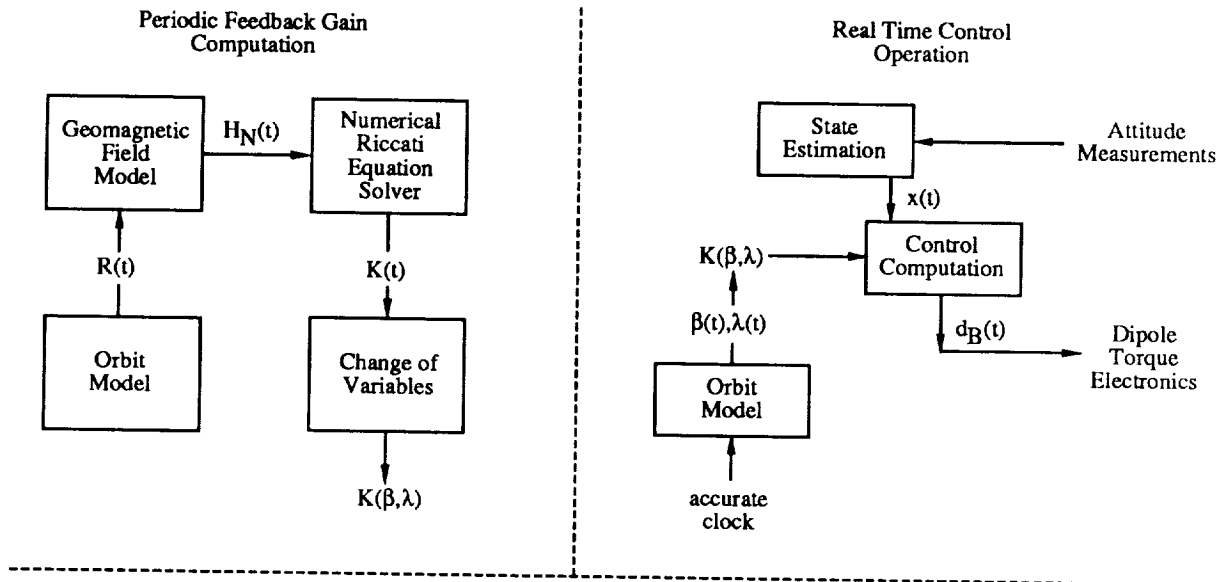


Figure 5: Control Software Structure

Periodic-Disturbance Accommodating Control of the Space Station for Asymptotic Momentum Management *

Wayne Warren[†] and Bong Wie[‡]
The University of Texas at Austin
Austin, Texas

David Geller[§]
NASA Johnson Space Center
Houston, Texas

Abstract

Periodic-disturbance accommodating control is investigated for asymptotic momentum management of control moment gyros used as primary actuating devices for the Space Station. The proposed controller utilizes the concepts of quaternion feedback control and periodic-disturbance accommodation to achieve oscillations about the constant torque equilibrium attitude, while minimizing the control effort required. Three-axis coupled equations of motion, written in terms of quaternions, are derived for roll/yaw controller design and stability analysis. The quaternion feedback controller designed using the linear-quadratic regulator synthesis technique is shown to be robust for a wide range of pitch angles. It is also shown that the proposed controller tunes the open-loop unstable vehicle to a stable oscillatory motion which minimizes the control effort needed for steady-state operations.

Introduction

The Space Station will employ CMGs (control moment gyros) as primary actuating devices during normal flight mode operation. Gravity-gradient torques will be used for CMG momentum management (unloading). The effect of a constant aerodynamic torque on a gravitationally stabilized spacecraft was first studied by Garber [1]. Such a torque produces a constant attitude angle for which aerody-

dynamic and gravitational torques are balanced. Garber [1] has shown that small roll/yaw librational motions are affected by large pitch angles. The aerodynamic disturbance torques acting on the Space Station are expected to have constant values plus periodic components caused mostly by the effects of solar panel rotations and Earth's diurnal bulge. As a result, attitude and CMG momentum oscillation about the torque equilibrium attitude will occur. A recent study [2] demonstrates the usefulness of the linear-quadratic-regulator synthesis technique and the concept of periodic-disturbance accommodation in minimizing attitude and/or CMG momentum oscillations as needed for mission requirements.

This paper is primarily concerned with attitude control and CMG periodic-disturbance rejection for large-angle pitch maneuvers of the Space Station. New results are presented expanding on the control scheme developed in [2]. Pitch-coupled roll/yaw equations of motion, first discussed in [1], and written in terms of Euler angles, are derived here in terms of quaternions. It is shown that these equations are well suited for use in designing a roll/yaw controller for large pitch motions of the Space Station. A simple concept of using quaternions for the control of spacecraft large-angle maneuvers has been developed in [3, 4]. The concept is extended here to a more complicated case of controlling both the attitude and CMG momentum of the Space Station. Furthermore, this paper presents a new control concept of asymptotic momentum management of the CMGs, which tunes the open-loop unstable vehicle to a stable oscillatory motion during steady-state operations, while minimizing the control effort needed.

Figure 1 is a functional block diagram representation of a quaternion feedback control system proposed for the Space Station. The attitude determination system utilizes rate gyros and star trackers to compute inertial quaternions and the absolute angu-

*This work was supported by the NASA Johnson Space Center through the RICIS program of the University of Houston at Clear Lake.

[†]Graduate Research Assistant, Member AIAA.

[‡]Assistant Professor, Dept. of Aerospace Engineering and Engineering Mechanics, Member AIAA.

[§]Aerospace Engineer, Mission Planning and Analysis Division.

lar velocity of the Space Station. Relative quaternions with respect to a local reference frame are then computed for control purposes. The proposed attitude/momentum controller utilizes relative quaternions, body rates (or relative quaternion rates), and CMG momenta to generate proper control torque commands to the CMGs.

Mathematical Models

In this section, equations of motion for the Space Station in a circular orbit are derived in terms of quaternions. For simplicity, the Space Station is assumed to be a single rigid body. Emphasis is on the use of quaternions in the equations of motion and in feedback control. Quaternions define the rigid body attitude as an Euler-axis rotation. The vector part of the quaternions indicates the direction of the Euler axis. The scalar part of the quaternions is related to the rotation angle about the Euler axis. Detailed discussion of the kinematics associated with quaternions and Euler angles can be found in [5, 6].

The relationships between quaternions and Euler angles, for the pitch-yaw-roll body-axis rotation sequence used in this paper, are

$$\begin{bmatrix} q_1 \\ q_2 \\ q_3 \\ q_4 \end{bmatrix} = \begin{bmatrix} C_1 S_2 S_3 + S_1 C_2 C_3 \\ C_1 S_2 C_3 + S_1 C_2 S_3 \\ C_1 C_2 S_3 - S_1 S_2 C_3 \\ C_1 C_2 C_3 - S_1 S_2 S_3 \end{bmatrix} \quad (1)$$

where $C_i \triangleq \cos(\theta_i/2)$, $S_i \triangleq \sin(\theta_i/2)$ for $i = 1, 2, 3$, $(\theta_1, \theta_2, \theta_3)$ are the roll, pitch, and yaw Euler angles of the body axes with respect to the local vertical and local horizontal (LVLH) axes, which rotate with the orbital angular velocity; and (q_1, q_2, q_3) are the vector parts of the quaternions which indicate the direction of the Euler axis while q_4 is the scalar part of the quaternions and is related to the angle of rotation about the Euler axis. Inverse relations may also be written as:

$$\begin{aligned} \theta_1 &= \tan^{-1} \left[\frac{2(q_1 q_4 - q_2 q_3)}{1 - 2q_1^2 - 2q_3^2} \right] \\ \theta_2 &= \tan^{-1} \left[\frac{2(q_2 q_4 - q_1 q_3)}{1 - 2q_2^2 - 2q_3^2} \right] \\ \theta_3 &= \sin^{-1} [2(q_1 q_2 + q_3 q_4)] \end{aligned} \quad (2)$$

The nonlinear equations of motion and attitude kinematics for the Space Station are as follows:

Space Station Dynamics:

$$\begin{aligned} & \begin{bmatrix} I_{11} & I_{12} & I_{13} \\ I_{21} & I_{22} & I_{23} \\ I_{31} & I_{32} & I_{33} \end{bmatrix} \begin{bmatrix} \dot{\omega}_1 \\ \dot{\omega}_2 \\ \dot{\omega}_3 \end{bmatrix} = \\ & -\tilde{\omega} \begin{bmatrix} I_{11} & I_{12} & I_{13} \\ I_{21} & I_{22} & I_{23} \\ I_{31} & I_{32} & I_{33} \end{bmatrix} \begin{bmatrix} \omega_1 \\ \omega_2 \\ \omega_3 \end{bmatrix} \\ & + 3n^2 \tilde{c} \begin{bmatrix} I_{11} & I_{12} & I_{13} \\ I_{21} & I_{22} & I_{23} \\ I_{31} & I_{32} & I_{33} \end{bmatrix} \begin{bmatrix} c_1 \\ c_2 \\ c_3 \end{bmatrix} \\ & + \begin{bmatrix} -u_1 + w_1 \\ -u_2 + w_2 \\ -u_3 + w_3 \end{bmatrix} \end{aligned} \quad (3)$$

where

$$\begin{aligned} \tilde{\omega} &\triangleq \begin{bmatrix} 0 & -\omega_3 & \omega_2 \\ \omega_3 & 0 & -\omega_1 \\ -\omega_2 & \omega_1 & 0 \end{bmatrix} \\ \tilde{c} &\triangleq \begin{bmatrix} 0 & -c_3 & c_2 \\ c_3 & 0 & -c_1 \\ -c_2 & c_1 & 0 \end{bmatrix} \\ c_1 &\triangleq 2(q_1 q_3 - q_2 q_4) \\ c_2 &\triangleq 2(q_1 q_4 + q_2 q_3) \\ c_3 &\triangleq 1 - 2q_1^2 - 2q_2^2 \end{aligned}$$

Attitude Kinematics (with respect to LVLH):

$$\begin{bmatrix} \dot{q}_1 \\ \dot{q}_2 \\ \dot{q}_3 \\ \dot{q}_4 \end{bmatrix} = \frac{1}{2} \Omega \begin{bmatrix} q_1 \\ q_2 \\ q_3 \\ q_4 \end{bmatrix} \quad (4)$$

where

$$\Omega \triangleq \begin{bmatrix} 0 & \omega_3 & -\omega_2 + n & \omega_1 \\ -\omega_3 & 0 & \omega_1 & \omega_2 + n \\ \omega_2 - n & -\omega_1 & 0 & \omega_3 \\ -\omega_1 & -\omega_2 - n & -\omega_3 & 0 \end{bmatrix}$$

CMG Momentum:

$$\begin{bmatrix} \dot{h}_1 \\ \dot{h}_2 \\ \dot{h}_3 \end{bmatrix} + \tilde{\omega} \begin{bmatrix} h_1 \\ h_2 \\ h_3 \end{bmatrix} = \begin{bmatrix} u_1 \\ u_2 \\ u_3 \end{bmatrix} \quad (5)$$

and $(\omega_1, \omega_2, \omega_3)$ are the body-axis components of the absolute angular velocity of the Space Station; I_{ij} ($i = j$) are the moments of inertia; I_{ij} ($i \neq j$) are the products of inertia; (h_1, h_2, h_3) are the body-axis components of the CMG momentum; (u_1, u_2, u_3) are the body-axis components of the control

torque; (w_1, w_2, w_3) are the body-axis components of the external disturbance torque; and n is the orbital rate of 0.0011 rad/sec.

When body and control axes are aligned with the principal axes of the Space Station ($I_1 \triangleq I_{11}, I_2 \triangleq I_{22}, I_3 \triangleq I_{33}$), Eqs. (3) become

$$\begin{aligned}
& I_1 \dot{\omega}_1 - (I_2 - I_3) \omega_2 \omega_3 \\
& + 6n^2(I_2 - I_3)(q_1 q_4 + q_2 q_3)(1 - 2q_1^2 - 2q_2^2) \\
& = -u_1 + w_1 \\
& I_2 \dot{\omega}_2 - (I_3 - I_1) \omega_1 \omega_3 \\
& + 6n^2(I_3 - I_1)(q_1 q_3 - q_2 q_4)(1 - 2q_1^2 - 2q_2^2) \\
& = -u_2 + w_2 \\
& I_3 \dot{\omega}_3 - (I_1 - I_2) \omega_1 \omega_2 \\
& + 12n^2(I_1 - I_2)(q_1 q_3 - q_2 q_4)(q_1 q_4 + q_2 q_3) \\
& = -u_3 + w_3.
\end{aligned} \tag{6}$$

which can be found in [5]. In this paper, however, we present a new set of equations determined by linearizing the above equations for the case of large pitch angles with small roll/yaw attitude changes. In this case, Eqs. (4), (5), and (6) can be linearized with respect to q_1 and q_3 as follows:

Space Station Dynamics:

$$I_1 \dot{\omega}_1 + n(I_2 - I_3) \omega_3 + 6n^2(I_2 - I_3)(q_4 - 2q_4 q_2^2) q_1 + 6n^2(I_2 - I_3)(2q_2 q_4^2 - q_2) q_3 = -u_1 + w_1 \tag{7a}$$

$$I_2 \dot{\omega}_2 + 6n^2(I_1 - I_3)(q_2 q_4 - 2q_4 q_2^3) = -u_2 + w_2 \tag{7b}$$

$$I_3 \dot{\omega}_3 + n(I_1 - I_2) \omega_1 - 12n^2(I_1 - I_2)(q_2 q_4^2) q_1 - 12n^2(I_1 - I_2)(q_4 q_2^2) q_3 = -u_3 + w_3 \tag{7c}$$

Attitude Kinematics (with respect to LVLH):

$$\dot{q}_1 = \frac{q_4}{2} \omega_1 + \frac{q_2}{2} \omega_3 + n q_3 \tag{8a}$$

$$\dot{q}_2 = \frac{q_4}{2} (\omega_2 + n) \tag{8b}$$

$$\dot{q}_3 = -\frac{q_2}{2} \omega_1 + \frac{q_4}{2} \omega_3 - n q_1 \tag{8c}$$

$$\dot{q}_4 = -\frac{q_2}{2} (\omega_2 + n) \tag{8d}$$

CMG Momentum:

$$\begin{aligned}
h_1 - n h_3 &= u_1 \\
h_2 &= u_2 \\
h_3 + n h_1 &= u_3.
\end{aligned} \tag{9}$$

For the case with large pitch angles and small roll/yaw attitude changes, the relationships between quaternions and Euler angles can be simplified by

linearizing with respect to θ_1 and θ_3 . Equations (1) then reduce to

$$q_2 = \sin \frac{\theta_2}{2} \tag{10a}$$

$$q_4 = \cos \frac{\theta_2}{2} \tag{10b}$$

$$\begin{bmatrix} q_1 \\ q_3 \end{bmatrix} = \frac{1}{2} \begin{bmatrix} q_4 & q_2 \\ -q_2 & q_4 \end{bmatrix} \begin{bmatrix} \theta_1 \\ \theta_3 \end{bmatrix}. \tag{10c}$$

Inverse relations for Eqs. (10c) are written as

$$\begin{bmatrix} \theta_1 \\ \theta_3 \end{bmatrix} = 2 \begin{bmatrix} q_4 & -q_2 \\ q_2 & q_4 \end{bmatrix} \begin{bmatrix} q_1 \\ q_3 \end{bmatrix}. \tag{11}$$

Equations (7) and (8) may be used to derive the Space Station equations of motion in terms of quaternions, written as follows:

$$\begin{aligned}
& \begin{bmatrix} I_1 q_4 & -I_1 q_2 \\ I_3 q_2 & I_3 q_4 \end{bmatrix} \begin{bmatrix} \ddot{q}_1 \\ \ddot{q}_3 \end{bmatrix} \\
& + n(I_1 - I_2 + I_3) \begin{bmatrix} -q_2 & -q_4 \\ q_4 & -q_2 \end{bmatrix} \begin{bmatrix} \dot{q}_1 \\ \dot{q}_3 \end{bmatrix} \\
& + n^2 \begin{bmatrix} (I_2 - I_3) & 0 \\ 0 & (I_2 - I_1) \end{bmatrix} \\
& \times \begin{bmatrix} (4q_4 - 6q_4 q_2^2) & (6q_2 q_4^2 - 4q_2) \\ (q_2 + 6q_2 q_4^2) & (q_4 + 6q_4 q_2^2) \end{bmatrix} \begin{bmatrix} q_1 \\ q_3 \end{bmatrix} \\
& = \frac{1}{2} \begin{bmatrix} -u_1 + w_1 \\ -u_3 + w_3 \end{bmatrix}
\end{aligned} \tag{12a}$$

$$I_2 [q_4 \ddot{q}_2 - q_2 \ddot{q}_4] + 3n^2 (I_3 - I_1) (2q_4 q_2^3 - q_4 q_2) = \frac{1}{2} (-u_2 + w_2). \tag{12b}$$

The quaternion relations of Eqs. (10) may be used to transform Eqs. (12) to the following known form [1, 6] involving only Euler angles:

$$\begin{aligned}
& I_1 \ddot{\theta}_1 + n^2 (I_2 - I_3) (1 + 3 \cos^2 \theta_2) \theta_1 \\
& - n (I_1 - I_2 + I_3) \dot{\theta}_3 + 3n^2 (I_2 - I_3) (\sin \theta_2 \cos \theta_2) \theta_3 \\
& = -u_1 + w_1
\end{aligned} \tag{13a}$$

$$\begin{aligned}
& I_2 \ddot{\theta}_2 + 3n^2 (I_1 - I_3) \sin \theta_2 \cos \theta_2 \\
& = -u_2 + w_2
\end{aligned} \tag{13b}$$

$$\begin{aligned}
& I_3 \ddot{\theta}_3 + n^2 (I_2 - I_1) (1 + 3 \sin^2 \theta_2) \theta_3 \\
& + n (I_1 - I_2 + I_3) \dot{\theta}_1 + 3n^2 (I_2 - I_1) (\sin \theta_2 \cos \theta_2) \theta_1 \\
& = -u_3 + w_3.
\end{aligned} \tag{13c}$$

A final linearization with respect to small pitch motions leads to the following well-known equations of motion:

Space Station Dynamics:

$$I_1 \ddot{\theta}_1 + 4n^2 (I_2 - I_3) \theta_1$$

$$-n(I_1 - I_2 + I_3)\dot{\theta}_3 = -u_1 + w_1 \quad (14a)$$

$$I_2\ddot{\theta}_2 + 3n^2(I_1 - I_3)\theta_2 = -u_2 + w_2 \quad (14b)$$

$$I_3\ddot{\theta}_3 + n^2(I_2 - I_1)\theta_3 + n(I_1 - I_2 + I_3)\dot{\theta}_1 = -u_3 + w_3 \quad (14c)$$

Attitude Kinematics (with respect to LVLH):

$$\dot{\theta}_1 - n\theta_3 = \omega_1 \quad (15a)$$

$$\dot{\theta}_2 - n = \omega_2 \quad (15b)$$

$$\dot{\theta}_3 + n\theta_1 = \omega_3 \quad (15c)$$

These linearized equations are used in [2] for the case of small roll, pitch, and yaw attitude changes. In this paper, emphasis is on the use of Eqs. (7) for the momentum/attitude control of the Space Station having small roll/yaw attitude changes but large-angle pitch motions.

Inertia values for the Phase 1 Space Station, as well as assembly flight 3, are listed in Table 1. Table 2 includes expected aerodynamic disturbances which are modeled as a bias plus periodic terms in the body-fixed control axes:

$$\begin{aligned} w(t) = & \text{Bias} + A_n \sin(nt + \phi_1) \\ & + A_{2n} \sin(2nt + \phi_2) \\ & + A_{3n} \sin(3nt + \phi_3) \\ & + A_{4n} \sin(4nt + \phi_4) \end{aligned}$$

The disturbance torque acting in each axis is determined from data generated at NASA Johnson Space Center by a nonlinear simulation program. The program simulates translational and rotational motions of the Space Station in orbit about an oblate Earth. It includes rotating solar panels, time-varying surface areas, and time-varying center-of-pressure locations. A Jacchia-Lineberry atmospheric model is used to compute density variations. The dominant aerodynamic torque frequencies at n and $2n$ are caused by Earth's diurnal bulge and solar panel rotation effects, respectively. Actual magnitudes and phases of these disturbance torques are assumed unknown for control design.

Control Issues

Before presenting the pitch and roll/yaw controller designs, it is important to clarify some issues related to the effects of large pitch motions and inertia value uncertainties on the stability of the controlled Space Station. A characteristic of momentum/attitude control using gravity-gradient torque is that pitch, roll, and yaw responses will settle down

to, or oscillate about, a constant torque equilibrium attitude (TEA). Primary factors involved in determining the constant pitch TEA are the magnitude of the bias in the disturbance torque and the numerical difference between roll and yaw moments of inertia. This can be seen by studying the steady-state form of Eq. (14b):

$$\bar{\theta}_2 = \frac{\bar{w}}{3n^2(I_1 - I_3)}$$

where $\bar{\theta}_2$ is the pitch TEA angle and \bar{w} is the bias of the pitch disturbance torque. Pitch gravity-gradient torque is largest when the pitch attitude is 45 degrees. This is predicted in Eq. (13b) where, at the steady-state,

$$\sin(2\bar{\theta}_2) = \frac{2\bar{w}}{3n^2(I_1 - I_3)}$$

It may be necessary to consider this worst-case pitch TEA in control system design. After switching to CMG mode from some other modes (e.g., reboost mode utilizing reaction jets), the Space Station must be able to achieve TEA in each axis without CMG momentum or commanded torque saturations.

The large motions possible in the pitch axis emphasize the importance of using Eqs. (7), (12), or (13) in designing the control system. These equations show the dependence of roll/yaw dynamics on pitch attitude. In fact, a roll/yaw closed-loop system designed for small pitch angles may become unstable at large pitch angles; therefore, roll/yaw closed-loop stability must be checked at various pitch TEA values.

Other factors affecting closed-loop stability are uncertainties and variations in moments and products of inertia. In particular, the magnitude of the pitch gravity-gradient torque depends on the difference between the roll and yaw moments of inertia. If these inertias are nearly equal (e.g., see Table 1, assembly flight 3 data), pitch gravity-gradient torque is very small and the pitch TEA (if it exists) is large. In addition, very small uncertainties in the moments of inertia can cause the system to become unstable. A discussion of the importance of checking closed-loop system robustness with respect to inertia uncertainties, by varying inertia values in an appropriate "direction", is included in the appendix of this paper.

Under normal operating conditions, the Space Station will have rotating solar arrays. This causes time-varying (sinusoidal) roll and yaw moments of inertia, and consequently, a similarly time-varying gravity-gradient torque in the pitch axis as shown

in Fig. 2. If the bias value of $I_1(t) - I_3(t)$ is such that the pitch gravity-gradient torque never changes sign, the system will remain stable. If the gravity-gradient torque does switch signs, the system may become unstable, depending upon how long the sign of the torque is changed. For sufficiently short periods of this opposite torque, the system will be stable with large, bounded responses about the TEA. If gravity-gradient torque is to ultimately be used in momentum/attitude control, the above factors will be useful in the design of the inertia configuration. Consideration should be given to defining a boundary near the point or condition corresponding to zero pitch-axis gravity-gradient torque, defined by $I_1(t) - I_3(t) = 0$. This is illustrated in Fig. 2. The boundary may be thought of as the minimum gravity-gradient torque allowed in the pitch axis for which closed-loop stability, with respect to inertia uncertainties, is maintained.

In the next sections, the pitch and roll/yaw controller designs are presented along with time simulations of the closed-loop system. In this paper, we expand on the previous study [2] by developing a periodic-disturbance accommodating controller which achieves asymptotic momentum management of the CMGs in all three axes. The Phase 1 inertia configuration listed in Table 1 is used. Effects of products of inertia are assumed negligible. The corresponding time-varying gravity-gradient torque in the pitch axis does not change sign; however, the time simulations presented here use the assumption that inertia values remain constant while periodic terms in the aerodynamic torque include solar panel rotation effects. Large pitch TEA responses are produced by introducing an appropriately large bias in the pitch-axis disturbance torque.

Pitch Control

In this section, a pitch-axis controller is developed for attitude and CMG momentum control. It is shown in [2] that disturbance rejection filters can be used to reject either attitude or CMG momentum oscillations occurring at the frequencies present in the disturbance torques. Since asymptotic momentum management of the CMGs in all three axes is of primary interest in this paper, the disturbance rejection filters for the pitch axis have the following forms:

$$\begin{aligned}\ddot{\alpha}_2 + (n)^2 \alpha_2 &= h_2 \\ \ddot{\beta}_2 + (2n)^2 \beta_2 &= h_2\end{aligned}$$

$$\begin{aligned}\ddot{\gamma}_2 + (3n)^2 \gamma_2 &= h_2 \\ \ddot{\eta}_2 + (4n)^2 \eta_2 &= h_2\end{aligned}$$

where initial conditions for the filter states can be arbitrarily selected (usually zero initial conditions). Use of filters at frequencies n , $2n$, $3n$, and $4n$ is indicated by aerodynamic torque data generated by a nonlinear simulation program written for the Space Station. The pitch-axis control logic is given by a single control input involving twelve states:

$$u_2 = \mathbf{K}_2 \mathbf{x}_2 \quad (16)$$

where

$$\begin{aligned}\mathbf{K}_2 &\triangleq \text{a } 1 \times 12 \text{ gain matrix} \\ \mathbf{x}_2 &\triangleq \begin{bmatrix} q_2 & \dot{q}_2 & h_2 & \int h_2 & \alpha_2 & \dot{\alpha}_2 \\ \beta_2 & \dot{\beta}_2 & \gamma_2 & \dot{\gamma}_2 & \eta_2 & \dot{\eta}_2 \end{bmatrix}^T.\end{aligned}$$

The control task is to find proper gains for this twelve-state feedback controller.

In order to use linear control design methodologies, Eq. (7b) must be linearized for small pitch motion. This results in Eq. (14b), which is used as the basis for pitch control analysis and design. Various techniques may be used in selecting the twelve gains of Eq. (16). These include linear-quadratic-regulator (LQR) synthesis [7] and direct assignment of closed-loop eigenvalues using a pole-placement technique. Several iterations of any method may be required to achieve satisfactory closed-loop performance and robustness. Note that gains resulting from Eqs. (14b) are for the use of θ_2 in state feedback. In order to accommodate q_2 for use in feedback, the gains corresponding to states q_2 and \dot{q}_2 are doubled since the approximation used for q_2 is $\theta_2/2$. New gains do not need to be computed for the pitch controller in the case of large pitch motion. It is mostly roll/yaw destabilization at large pitch angles which forces pitch-axis instability.

The open-loop pitch axis of the Phase 1 inertia configuration is unstable, with poles at $s = \pm 1.5n$, 0 , 0 , and filter poles at $s = \pm jn$, $\pm j2n$, $\pm j3n$, $\pm j4n$. One pole at $s = 0$ comes from the integral feedback of h_2 . After iterative use of an LQR synthesis code, available in CTRL-C software, a set of closed-loop eigenvalues have been selected and are listed in Table 3. The corresponding gain set is given in Table 4. Closed-loop pitch responses of Eq. (6), for a pitch-axis maneuver of -30 degrees (caused by a large pitch-axis torque bias), can be seen in Figs. 4, 5, and 6. Comments on the responses are reserved until after the presentation of the roll/yaw controller design.

Roll/Yaw Control

The roll/yaw controller has a structure similar to that of the pitch controller. By examining the open-loop transfer function matrix from control inputs to roll/yaw attitudes and CMG momentum, it is shown in [2] that a periodic disturbance at the orbital rate can be rejected in the yaw attitude but not in the roll attitude. The analysis is accomplished using Eqs. (9) and (14), which assume small motions in all axes. In an effort to determine if it is possible to have periodic-disturbance rejection in both roll and yaw attitudes for this different case involving large pitch motions, a similar analysis is considered here using the pitch-coupled roll/yaw dynamics described by Eqs. (13).

By combining Eqs. (9) and (13), the transfer function matrix from (u_1, u_3) to (θ_1, θ_3) can be written as

$$\begin{bmatrix} \theta_1(s) \\ \theta_3(s) \end{bmatrix} = \frac{1}{\Delta} \begin{bmatrix} G_{11}(s) & G_{13}(s) \\ G_{31}(s) & G_{33}(s) \end{bmatrix} \begin{bmatrix} u_1(s) \\ u_3(s) \end{bmatrix}$$

where

$$\begin{aligned} G_{11}(s) &= -[I_3 s^2 + (1 + 3s_2^2)n^2(I_2 - I_1)] \\ &\quad \times [s^2 + n^2] \\ G_{13}(s) &= -[n(I_1 - I_2 + I_3)s \\ &\quad - 3n^2(I_2 - I_3)s_2 c_2][s^2 + n^2] \\ G_{31}(s) &= [n(I_1 - I_2 + I_3)s \\ &\quad + 3n^2(I_2 - I_1)s_2 c_2][s^2 + n^2] \\ G_{33}(s) &= -[I_1 s^2 + (1 + 3c_2^2)n^2(I_2 - I_3)] \\ &\quad \times [s^2 + n^2] \\ \Delta &= I_1 I_3 (s^2 + n^2) \{s^4 + n^2[1 + 3k_1 + k_1 k_3 \\ &\quad + 3(k_3 - k_1)s_2^2]s^2 \\ &\quad + [3n^3(k_3 - k_1)s_2 c_2]s + 4n^4 k_1 k_3\} \end{aligned}$$

and $s_2 = \sin \theta_2$, $c_2 = \cos \theta_2$, $k_1 = (I_2 - I_3)/I_1$, and $k_3 = (I_2 - I_1)/I_3$. Transmission zeros at $\pm jn$ appear in the transfer function matrix. It would seem that periodic disturbances of frequency n cannot be rejected in either the roll or yaw attitudes; however, for CMG momentum and control torque relations defined by

$$\begin{aligned} \dot{h}_1 &= u_1 \\ \dot{h}_3 &= u_3 \end{aligned}$$

and with appropriate alterations of Eqs. (13), the transfer function matrix from (u_1, u_3) to (θ_1, θ_3) can be written as

$$\begin{bmatrix} \theta_1(s) \\ \theta_3(s) \end{bmatrix} = \frac{1}{\Delta} \begin{bmatrix} G_{11}(s) & G_{13}(s) \\ G_{31}(s) & G_{33}(s) \end{bmatrix} \begin{bmatrix} u_1(s) \\ u_3(s) \end{bmatrix}$$

where

$$\begin{aligned} G_{11} &= (s) \{-I_3 s^3 + n^2[3(I_1 - I_2)s_2^2 - I_3]s \\ &\quad + 3n^3(I_2 - I_3)s_2 c_2\} \\ G_{13} &= (ns) \{(I_2 - I_1)s^2 + [3n(I_2 - I_3)s_2 c_2]s \\ &\quad + (1 + 3s_2^2)n^2(I_2 - I_1)\} \\ G_{31} &= -(ns) \{(I_2 - I_3)s^2 + (1 + 3c_2^2)n^2(I_2 - I_3)\} \\ G_{33} &= -\{I_1 s^4 + n^2[3(I_2 - I_3)c_2^2 + I_1]s \\ &\quad + 3n^2(I_2 - I_1)s_2 c_2\} \\ \Delta &= I_1 I_3 (s^2) \{s^4 + n^2[1 + 3k_1 + k_1 k_3 \\ &\quad + 3(k_3 - k_1)s_2^2]s^2 \\ &\quad + [3n^3(k_3 - k_1)s_2 c_2]s + 4n^4 k_1 k_3\}. \end{aligned}$$

Transmission zeros are not apparent in these expressions. A numerical analysis reveals, however, that there are transmission zeros at $\pm jn$ for the transfer functions from u_1 and u_3 to roll attitude, while yaw attitude has no troublesome zeros. These results show that, even for the case of pitch-coupled roll/yaw dynamics, there is an inability to reject roll attitude oscillations occurring at the orbital rate. Hence, in this paper, periodic-disturbance rejection for CMG momentum in both the roll and yaw axes is considered. That is, a periodic control of the Space Station for asymptotic momentum management of the CMGs in all three axes is of primary interest here.

Periodic-disturbance rejection filters for the roll/yaw axes can be represented as:

$$\begin{aligned} \ddot{\alpha}_1 + (n)^2 \alpha_1 &= h_1 \\ \ddot{\beta}_1 + (2n)^2 \beta_1 &= h_1 \\ \ddot{\gamma}_1 + (3n)^2 \gamma_1 &= h_1 \\ \ddot{\eta}_1 + (4n)^2 \eta_1 &= h_1 \\ \ddot{\alpha}_3 + (n)^2 \alpha_3 &= h_3 \\ \ddot{\beta}_3 + (2n)^2 \beta_3 &= h_3 \\ \ddot{\gamma}_3 + (3n)^2 \gamma_3 &= h_3 \\ \ddot{\eta}_3 + (4n)^2 \eta_3 &= h_3. \end{aligned}$$

The roll/yaw control logic involving two control inputs and twenty-four states is expressed as

$$\begin{bmatrix} u_1 \\ u_3 \end{bmatrix} = \mathbf{K} \begin{bmatrix} \mathbf{x}_1 \\ \mathbf{x}_3 \end{bmatrix} \quad (17)$$

where

$\mathbf{K} \triangleq$ a 2×24 gain matrix

$$\begin{aligned} \mathbf{x}_1 &\triangleq \begin{bmatrix} q_1 & \omega_1 & h_1 & \int h_1 & \alpha_1 & \dot{\alpha}_1 \\ \beta_1 & \dot{\beta}_1 & \gamma_1 & \dot{\gamma}_1 & \eta_1 & \dot{\eta}_1 \end{bmatrix}^T \text{ (roll states)} \\ \mathbf{x}_3 &\triangleq \begin{bmatrix} q_3 & \omega_3 & h_3 & \int h_3 & \alpha_3 & \dot{\alpha}_3 \\ \beta_3 & \dot{\beta}_3 & \gamma_3 & \dot{\gamma}_3 & \eta_3 & \dot{\eta}_3 \end{bmatrix}^T \text{ (yaw states)}. \end{aligned}$$

The pitch-coupled roll/yaw equations described by Eqs. (7) are used as the basis for the roll/yaw controller design. It is evident in the pitch-coupled equations that roll/yaw dynamics are dependent upon pitch attitude. Consideration must be given to the pitch-axis TEA when designing the roll/yaw controller gains. Equations (7) (or Eqs. (12) or (13)) are especially useful for this purpose when q_2 and q_4 in the equations are assigned their respective values corresponding to the expected pitch TEA (see Eqs. (10a) and (10b)). As a result, Eqs. (7a) and (7c) become linear and any linear control design methodologies may be used to design the roll/yaw controller gains.

For spacecraft operating under the influence of gravity-gradient torques, it is interesting to examine the changes in roll/yaw open-loop eigenvalues that occur as the pitch bias changes. This was first studied by Garber [1]. A root locus of open-loop eigenvalues versus pitch angle, for the Phase 1 inertia configuration, is shown in Fig. 3. It can be seen that the open-loop roll/yaw dynamics are not very sensitive to pitch attitude. The Space Station is unstable with poles at $s = \pm 1.05n \pm j0.7n$, 0 , 0 , $\pm jn$, and filter poles at $s = \pm jn$, $\pm jn$, $\pm j2n$, $\pm j2n$, $\pm j3n$, $\pm j3n$, $\pm j4n$, $\pm j4n$ (for $\theta_2 = 0^\circ$ where $q_2=0$ and $q_4=1$). The double pole at $s = 0$ occur because of the integral feedback of h_1 and h_3 .

After iterative use of an LQR synthesis code, closed-loop eigenvalues have been selected and are listed in Table. 3. A gain set for Eqs. (17), corresponding to a pitch TEA of 0° , is listed in Table. 4. For these gains, the closed-loop roll/yaw axes are stable for pitch angles ranging from -21° to $+23^\circ$. Since a simulation of the large-angle pitch maneuver needed to reach a pitch TEA of -30° is desired, a different gain set is used for the simulations presented in this paper. For these gains, the closed-loop roll/yaw axes are stable for pitch angles ranging from -48° to $+3^\circ$. Closed-loop roll/yaw responses of Eqs. (6), for a pitch-axis maneuver of -30 degrees, can be seen in Figs. 4, 5, and 6. The overall closed-loop system has a 10 dB gain margin and a phase margin of 60° in each control loop.

Discussion of Simulation Results

Closed-loop responses for a simulation of the nonlinear dynamics described by Eqs. (6) are shown in Figs. 4, 5, and, 6. Quantities plotted include quaternions, CMG momenta, and control torques. Initial conditions corresponding to $\theta_1(0) = \theta_2(0) = \theta_3(0) =$

1 degree and $\dot{\theta}_1(0) = \dot{\theta}_2(0) = \dot{\theta}_3(0) = 0.001$ deg/sec are assumed. Allowable limits on CMG momentum and commanded torque are assumed to be 30,000 ft-lb-sec and 150 ft-lb, respectively.

In the roll axis, quaternion q_1 oscillates ($\pm 0.7^\circ$) about a roll TEA of -0.003 ($\theta_1 = -0.5^\circ$). Roll CMG momentum h_1 is the input to the roll-axis disturbance rejection filter and settles down to zero after reaching a maximum value near 8000 ft-lb-sec. Control torque u_1 is zero at the steady-state and has a peak value near 23 ft-lb. In the pitch axis, quaternion q_2 oscillates ($\pm 4.3^\circ$) about a pitch TEA of -0.257 ($\theta_2 = -30^\circ$). The large-angle maneuver causes the pitch CMG momentum h_2 (disturbance filter input) to become quite large at nearly 18,000 ft-lb-sec, before settling to zero. Control torque u_2 is zero at the steady-state with a maximum value near 30 ft-lb. In the yaw axis, quaternion q_3 oscillates ($\pm 1.2^\circ$) about a yaw TEA of -0.013 ($\theta_3 = -1.5^\circ$). Yaw CMG momentum h_3 (disturbance filter input) settles down to zero after reaching a maximum value close to 600 ft-lb-sec. Control torque u_3 is zero at the steady-state, and reaches a maximum value near 12 ft-lb.

The simulations show that the proposed control scheme tunes the open-loop unstable Space Station to a stable, oscillatory motion which minimizes control effort during steady-state operations. For the assumed disturbance torque models (with unknown magnitudes and phases), the stabilized Space Station needs no control torque at steady-state conditions. Analysis shows, however, that small-amplitude periodic components of frequencies $5n$ and $6n$ are present in u_1 and u_3 at the steady-state. These small residual components are caused by the coupling between the pitch and roll/yaw axes, and become particularly noticeable for large pitch biases.

There is an interesting feature of the quaternion feedback scheme which is not apparent from the simulation responses. If rejection of pitch and yaw attitude oscillations is desired, it seems natural to use q_2 and q_3 as inputs to the respective disturbance rejection filters. Even though q_2 and q_3 will become constant at the steady-state, all of the Euler angles will oscillate. A study of Eqs. (2) (or Eqs. (11)) reveals why. By assigning constant values to q_2 , q_3 , and q_4 in Eqs. (2) (or Eqs. (11)), it can be seen that θ_1 , θ_2 , and θ_3 are all functions of q_1 , which oscillates. The same may be said for q_1 , q_2 , q_3 , and q_4 if Euler angle feedback is used. For oscillations of θ_1 and constant values for θ_2 and θ_3 , Eqs. (1) show that all quaternions are functions of θ_1 and will therefore oscillate. In either case, however, these oscillations

are small. The important point is that the elimination of pitch or yaw oscillations, if needed, may be accomplished by using Euler angles θ_2 and θ_3 as disturbance rejection filter inputs (with appropriate gain changes).

A check of closed-loop robustness with respect to inertia uncertainties emphasizes an important issue associated with the Phase 1 inertia configuration. By selecting specific "directions" in which to vary the three moments of inertia (I_1, I_2, I_3), the closed-loop system can be shown to be unstable for as little as -7% uncertainty in I_3 with $+8\%$ uncertainty in I_1 . For these inertia variations, the pitch-axis gravity-gradient torque disappears ($I_1 - I_3 = 0$) and closed-loop pitch dynamics become unstable. The limitations shown in this example (and several others involving even smaller inertia uncertainties), are not related to the selection of control logic but are physical limitations inherent to the inertia configuration of the Phase 1 Space Station. A description of the inertia variation "directions" used above is presented in the appendix of this paper.

Conclusions

In this paper asymptotic momentum management of control moment gyros of the Space Station has been investigated. It was shown that the proposed controller tunes the Space Station, which has a gravitationally "unstable" inertia configuration, to a stable, oscillatory motion which minimizes the control effort needed at the steady-state. By utilizing the concepts of quaternion feedback control and periodic-disturbance rejection filters, the proposed controller provides robust control of the Space Station for large-angle pitch motions. The pitch-coupled roll/yaw equations of motion derived in this paper were shown to be particularly useful in roll/yaw controller design and stability analysis.

Appendix: Inertia Variation Directions

It is a common practice in control design to satisfy time and frequency-domain requirements first, then check for closed-loop robustness. For spacecraft, inertial properties may be very sensitive parameters in the closed-loop system. It seems reasonable to increase and decrease all inertias by the same percentage, thus checking controller effectiveness for a proportionally heavier and lighter spacecraft. This procedure may not indicate the true inertia sensi-

tivity. It is important to consider the magnitude and direction of the variation for each inertia value. Since the inertia matrix may be transformed to three principal moments of inertia by aligning the body and principal axes, suggestions for variations in the moments of inertia for the roll (I_1), pitch (I_2), and yaw (I_3) axes are presented here.

Three important relationships may be derived from the definitions for the moments of inertia. These relationships are as follows:

$$\begin{aligned} I_1 + I_2 &> I_3 \\ I_1 + I_3 &> I_2 \\ I_2 + I_3 &> I_1 \end{aligned}$$

Together, these relations define the physically possible inertia configurations. A control designer may unknowingly use inertia variations which result in inertia values that violate these constraints. Stability of the closed-loop system will be tested for a physically impossible inertia configuration. The important point is not the fictitious inertias but whether or not the control designer can redirect this extraneous stability margin to encompass more of the region of physically possible inertia values.

When gravity-gradient torque is used in the control of a rotating spacecraft, additional inertia constraints are introduced. The control scheme presented in this paper is a good example. Equations (14) show that roll-axis gravity-gradient and gyroscopic coupling torques are zero when $I_2 = I_3$, pitch-axis gravity-gradient torque is zero when $I_1 = I_3$, and the yaw-axis gyroscopic coupling torque is zero when $I_1 = I_2$.

A useful aid for visualizing the relationship between inertia constraints and inertia variations is now presented. Figure A.1 shows a three-dimensional, cubic figure defined in three "inertial" directions. The inertia constraint relations may now be visualized as planes in this "inertial" space. The planes $I_1 + I_2 = I_3$, $I_1 + I_3 = I_2$, and $I_2 + I_3 = I_1$ are labeled in Fig. A.1, and represent the physical boundaries of inertia values. The area inside the three intersecting boundaries represents all physically possible inertia configurations. A representation of the cut-away portion of the "inertia cube" is shown in Fig. A.2. Planes defining the physical and system torque boundaries are labeled. Figures A.1 and A.2 provide a three-dimensional representation of the information presented in the k_3 versus k_1 inertia ratio plots in [5-7]. It may be convenient to normalize the moments of inertia being studied by $\sqrt{I_1^2 + I_2^2 + I_3^2}$ in order to locate the position of the nominal configuration within a "unit inertia cube".

The relative positioning of the nominal inertia configuration from the constraint boundaries can then be easily determined.

Since the shortest distance from a point to a plane is in a direction perpendicular to that plane, it seems logical to check inertia variations in directions perpendicular to the inertia boundaries. In this way, the minimum variation necessary to reach a physical boundary can be found while checking the closed-loop stability of the system in question. For rotating spacecraft with gravity-gradient control systems, inertia variations perpendicular to the planes $I_1 = I_2$, $I_1 = I_3$, and $I_2 = I_3$ are needed. It may be seen in Fig. A.2 that these planes intersect inside the region of physically possible inertia values, and partition the region into several sections. It should be a control designers' goal to include the area within the physical boundaries inside a "control surface" which contains all of the inertia values for which the closed-loop system is stable.

References

1. Garber, T.B., "Influence of Constant Disturbing Torque on the Motion of Gravity-Gradient Stabilized Satellites," AIAA Journal, Vol.1, No.4, April 1963, pp. 968-969.
2. Wie, B., Byun, K.W., Warren, W., Geller, D., Long, D., and Sunkel, J., "A New Approach to Attitude/Momentum Control of the Space Station," AIAA Paper No.88-4132 (to appear in the Journal of Guidance, Control, and Dynamics).
3. Wie, B., and Barba, P.M., "Quaternion Feedback for Spacecraft Large-Angle Maneuvers," Journal of Guidance, Control, and Dynamics, Vol.8, No.3, May-June 1985, pp. 360-365.
4. Wie, B., Weiss, H., and Arapostathis, A., "Quaternion Feedback Regulator for Spacecraft Eigenaxis Rotations," AIAA Paper No.88-4117 (to appear in the Journal of Guidance, Control, and Dynamics).
5. Kane, T.R., Likins, P.W., and Levinson, D.A., Spacecraft Dynamics, McGraw-Hill, 1983, pp. 12-16, 23-25, 58-62.
6. Hughes, P.C., Spacecraft Attitude Dynamics, John-Wiley&Sons, 1986, Chapters 2 and 9.
7. Bryson, A.E., "Control of Spacecraft and Aircraft," Course Notes, Stanford University (to be published as a text).

Table 1. Space station inertia configurations

Inertia (slug-ft ²)	Assembly Flight#3	Phase 1
I_{11}	23.22E6	50.28E6
I_{22}	1.30E6	10.80E6
I_{33}	23.23E6	58.57E6
I_{12}	-0.023E6	-0.39E6
I_{13}	0.477E6	-0.24E6
I_{23}	-0.011E6	0.16E6

Table 2. Phase 1 aerodynamic torque models (in units of ft-lbs)

w_1	$1 + \sin(nt) + 0.5\sin(2nt) + 0.3\sin(3nt) + 0.5\sin(4nt)$
w_2	$13^* + 1.2\sin(nt) + 3.5\sin(2nt) + 0.3\sin(3nt) + 0.5\sin(4nt)$
w_3	$1 + \sin(nt) + 0.5\sin(2nt) + 0.3\sin(3nt) + 0.5\sin(4nt)$

* nominal pitch bias torque is 4 but 13 is used to produce a large pitch TEA

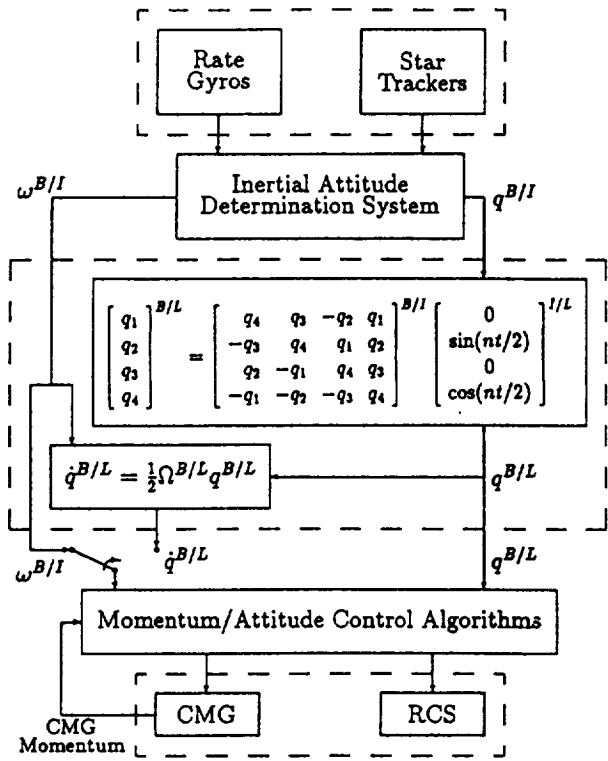
Table 3. Phase 1 closed-loop eigenvalues
(in units of orbital rate - 0.0011 rad/sec)

	Momentum/Attitude		Disturbance Filters	
Pitch	-1.0, -1.5	-1.5±j1.5	-0.3±j1.0 -0.3±j3.0	-0.3±j2.0 -0.3±j4.0
Roll/Yaw	-0.23, -0.71	-0.53±j1.54	-0.14±j0.99	-1.13±j0.75
	-1.04±j0.70	-1.06±j0.71	-0.19±j2.01	-0.47±j2.20
			-0.32±j3.02	-0.68±j3.21
			-0.53±j3.97	-0.25±j4.00

Table 4. Phase 1 controller gains

Pitch	Units	Roll/Yaw*	Units
$[K_2]^T$		$[K]^T$	
4.2425E+2	(ft-lb/rad)	3.8526E+3	3.7381E+2 (ft-lb/rad)
2.5412E+5	(ft-lb-sec/rad)	1.2003E+6	1.0126E+5 (ft-lb-sec/rad)
1.4840E-2	(ft-lb/ft-lb-sec)	1.4360E-2	1.9364E-3 (ft-lb/ft-lb-sec)
4.0150E-6	(ft-lb/ft-lb-sec ²)	-1.6361E-6	2.7852E-7 (ft-lb/ft-lb-sec ²)
-1.9064E-9	(ft-lb-rad ² /ft-lb-sec ³)	3.6578E-10	-1.8526E-10 (ft-lb-rad ² /ft-lb-sec ³)
2.1970E-6	(ft-lb-rad ² /ft-lb-sec ²)	7.6282E-7	1.1857E-7 (ft-lb-rad ² /ft-lb-sec ²)
-4.6097E-9	(ft-lb-rad ² /ft-lb-sec ³)	-3.2712E-9	-5.7517E-10 (ft-lb-rad ² /ft-lb-sec ³)
-5.2383E-7	(ft-lb-rad ² /ft-lb-sec ²)	-3.3865E-7	-1.6409E-7 (ft-lb-rad ² /ft-lb-sec ²)
-5.3793E-9	(ft-lb-rad ² /ft-lb-sec ³)	-1.0702E-8	-1.1317E-9 (ft-lb-rad ² /ft-lb-sec ³)
-1.9423E-6	(ft-lb-rad ² /ft-lb-sec ²)	-3.4827E-6	-5.3664E-7 (ft-lb-rad ² /ft-lb-sec ²)
-7.3458E-9	(ft-lb-rad ² /ft-lb-sec ³)	-1.5903E-8	-1.5491E-9 (ft-lb-rad ² /ft-lb-sec ³)
-2.6056E-6	(ft-lb-rad ² /ft-lb-sec ²)	-3.1256E-6	-4.7197E-7 (ft-lb-rad ² /ft-lb-sec ²)
		9.4016E+2	2.4994E+2 (ft-lb/rad)
		-1.2743E+5	1.1386E+5 (ft-lb-sec/rad)
		-2.4992E-3	-3.5209E-3 (ft-lb/ft-lb-sec)
		-7.3398E-7	-1.0348E-6 (ft-lb/ft-lb-sec ²)
		4.8557E-9	-5.5935E-10 (ft-lb-rad ² /ft-lb-sec ³)
		3.7017E-7	-4.2651E-6 (ft-lb-rad ² /ft-lb-sec ²)
		2.0608E-9	-6.8224E-10 (ft-lb-rad ² /ft-lb-sec ³)
		1.8854E-6	-2.4769E-6 (ft-lb-rad ² /ft-lb-sec ²)
		4.0142E-10	9.4962E-10 (ft-lb-rad ² /ft-lb-sec ³)
		1.5548E-6	-2.7820E-6 (ft-lb-rad ² /ft-lb-sec ²)
		8.3363E-10	8.3453E-10 (ft-lb-rad ² /ft-lb-sec ³)
		1.3125E-6	-2.5757E-6 (ft-lb-rad ² /ft-lb-sec ²)

* Designed for a pitch TEA of 0°



B/I indicates body frame with respect to inertial frame
 B/L indicates body frame with respect to LVLH frame
 I/L indicates inertial frame with respect to LVLH frame

Fig. 1. A quaternion feedback control system for the Space Station.

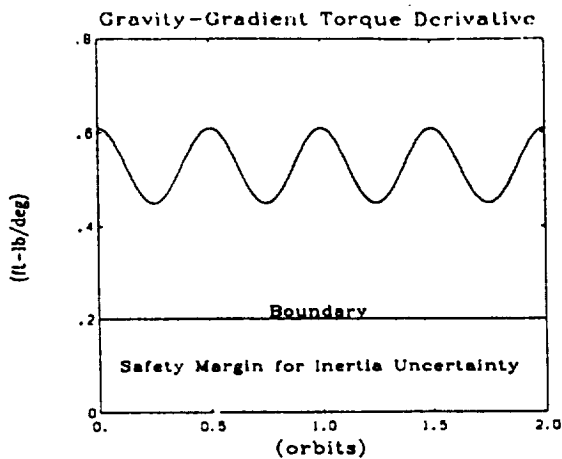


Fig. 2. Time-varying pitch-axis gravity-gradient torque derivative.

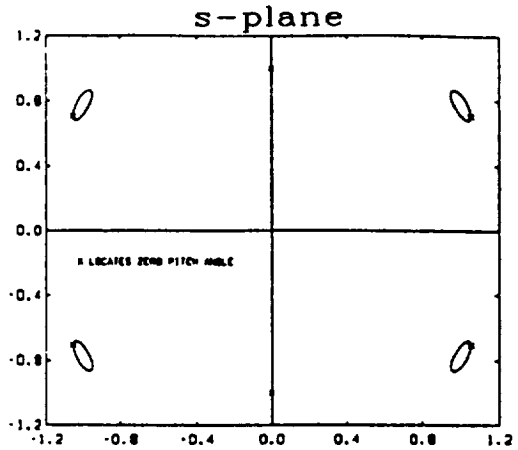


Fig. 3. Plot of roll/yaw open-loop poles versus pitch angle in the s plane (s in units of orbital rate).

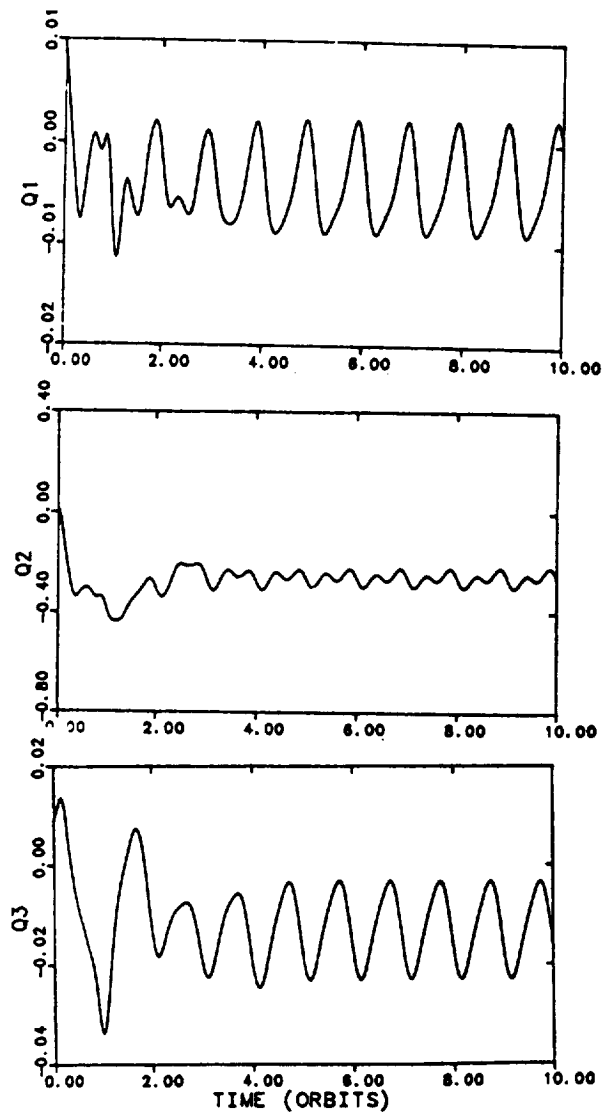


Fig. 4. Closed-loop quaternion responses.

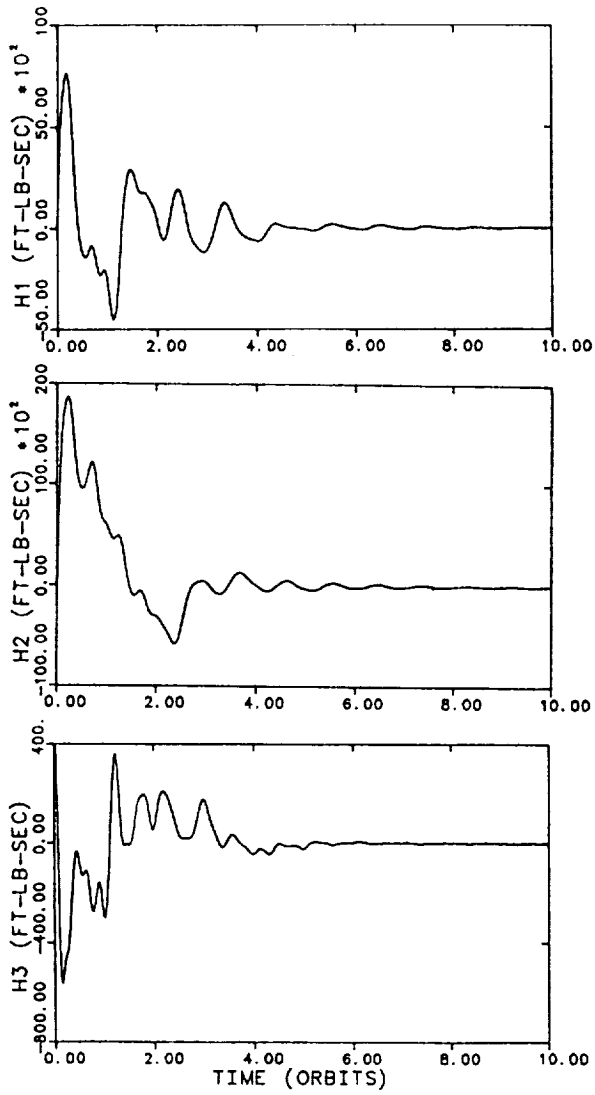


Fig. 5. CMG momentum histories.

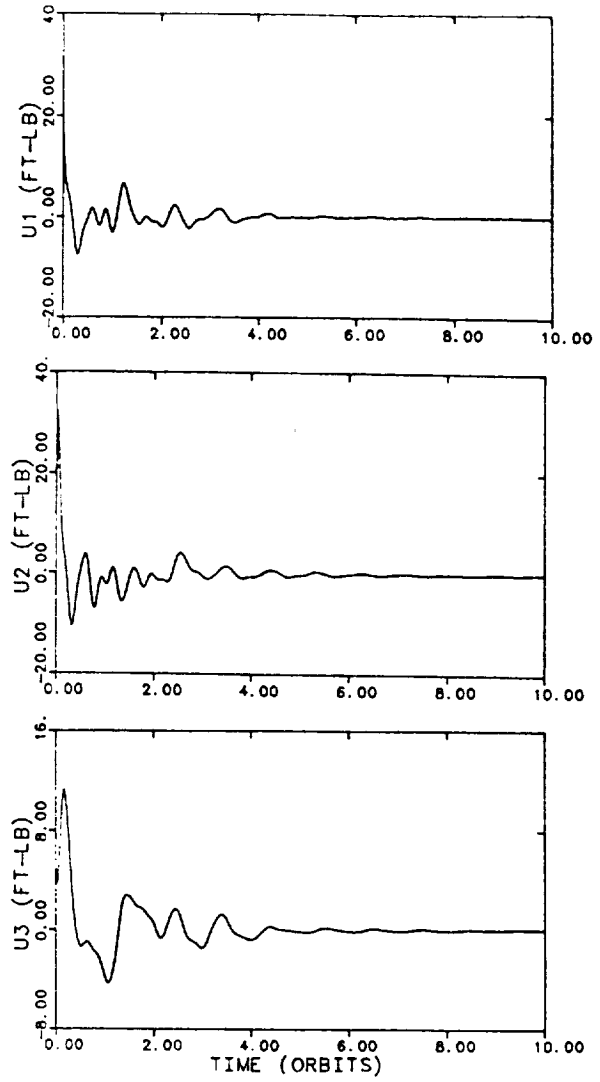


Fig. 6. Commanded torque histories.

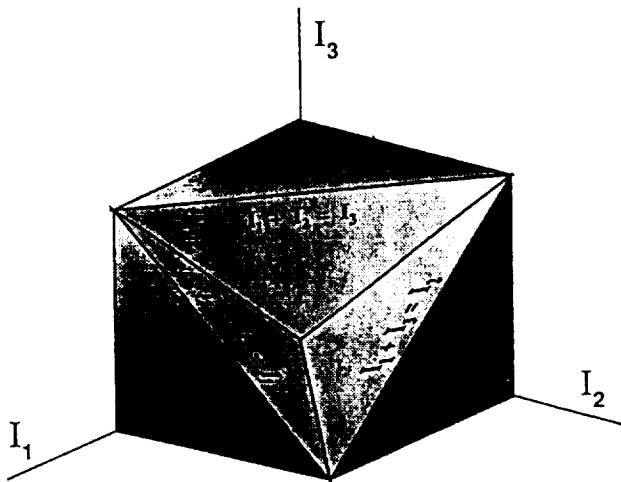


Fig. A.1. Physical boundaries of inertia values.

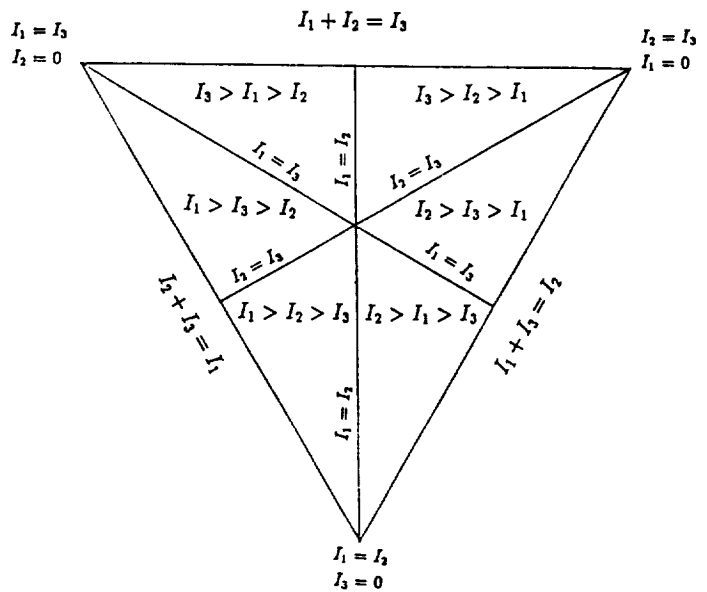


Fig. A.2. Regions within the physical boundaries.

**SIMULTANEOUS QUATERNION ESTIMATION (QUEST)
AND BIAS DETERMINATION**

F. Landis Markley
Attitude Analysis Section,
Flight Dynamics Analysis Branch, Code 554.1
Goddard Space Flight Center,
Greenbelt, MD 20771

This paper presents tests of a new method for the simultaneous estimation of spacecraft attitude and sensor biases, based on a quaternion estimation algorithm minimizing Wahba's loss function. The new method is compared with a conventional batch least-squares differential correction algorithm. The estimates are based on data from strapdown gyros and star trackers, simulated with varying levels of Gaussian noise for both inertially-fixed and Earth-pointing reference attitudes. Both algorithms solve for the spacecraft attitude and the gyro drift rate biases. They converge to the same estimates at the same rate for inertially-fixed attitude, but the new algorithm converges more slowly than the differential correction for Earth-pointing attitude. The slower convergence of the new method for non-zero attitude rates is believed to be due to the use of an inadequate approximation for a partial derivative matrix. The new method requires about twice the computational effort of the differential correction. Improving the approximation for the partial derivative matrix in the new method is expected to improve its convergence at the cost of increased computational effort.

Introduction

When determining the three-axis attitude of a spacecraft, it is often necessary to simultaneously estimate sensor biases and misalignments. An extended Kalman filter or a batch least-squares differential correction procedure is generally used for this process [1]. These methods, collectively referred to as state estimation methods, require that the nonlinear estimation problem be linearized about *a priori* estimates of the attitude, biases, and misalignments. The purpose of this paper is to compare the standard batch least-squares differential correction procedure with a new algorithm [2] based on the *q*-method for minimizing Wahba's least-squares loss function [3]. The new algorithm computes the parameters iteratively, but does not linearize about an *a priori* attitude estimate, so it is expected to be more robust than the usual state estimation methods if the problem is highly nonlinear or if initial estimates are poor.

The development of the new algorithm is presented in detail in reference 2, along with some historical background, so it will not be repeated here. The following iterative procedure estimates the attitude at time t and the vector \mathbf{x} comprising the m non-attitude parameters. An *a priori* estimate \mathbf{x}^0 of \mathbf{x} is used to compute the matrix

$$B(t, \mathbf{x}) \equiv \sum_{i=1}^n a_i \Phi(t, t_i; \mathbf{x}) \mathbf{b}_i(\mathbf{x}) \mathbf{r}_i^T(\mathbf{x}), \quad (1)$$

where the unit vectors \mathbf{r}_i are representations in an inertial reference frame of the directions to some observed objects, the \mathbf{b}_i are the unit vector representations of the corresponding observations in the spacecraft body frame, the a_i are positive weights, and n is the number of observations. The 3×3 attitude propagation matrix $\Phi(t, t_0; \mathbf{x})$ is the solution of the differential equation

$$d\Phi(t, t_0; \mathbf{x})/dt = -[\omega(t, \mathbf{x}) \times] \Phi(t, t_0; \mathbf{x}) \quad (2)$$

with initial value

$$\Phi(t_0, t_0; \mathbf{x}) = I \equiv \text{the } 3 \times 3 \text{ identity matrix}, \quad (3)$$

where the column vector $\omega(t, \mathbf{x})$ contains the components in the body frame of the spacecraft angular velocity relative to inertial space. The matrix $[\mathbf{v} \times]$ is defined for an arbitrary three-vector \mathbf{v} by

$$[\mathbf{v} \times] \equiv \begin{bmatrix} 0 & -v_3 & v_2 \\ v_3 & 0 & -v_1 \\ -v_2 & v_1 & 0 \end{bmatrix} \quad (4)$$

The parameters in \mathbf{x} may enter the matrix $B(t, \mathbf{x})$ through the kinematics expressed by $\Phi(t, t_i; \mathbf{x})$, the observation modeling in $\mathbf{b}_i(\mathbf{x})$, or the reference vector models in $\mathbf{r}_i(\mathbf{x})$. The m matrices $\partial B / \partial x_j$, and the $m(m+1)/2$ independent matrices $\partial^2 B / \partial x_j \partial x_k$ expressing the derivatives of $B(t, \mathbf{x})$ with respect to the parameters must also be computed.

Standard methods [4] are next used to compute the largest eigenvalue $\lambda_{max}(\mathbf{x})$ and corresponding normalized eigenvector $\mathbf{q}_{opt}(t, \mathbf{x})$ of the symmetric 4×4 matrix

$$K(t, \mathbf{x}) \equiv \begin{bmatrix} B(t, \mathbf{x}) + B^T(t, \mathbf{x}) - I \operatorname{tr} B(t, \mathbf{x}) & \mathbf{p}(t, \mathbf{x}) \\ \mathbf{p}^T(t, \mathbf{x}) & \operatorname{tr} B(t, \mathbf{x}) \end{bmatrix} \quad (5)$$

with the three-component column vector $\mathbf{p}(t, \mathbf{x})$ defined by

$$[\mathbf{p}(t, \mathbf{x}) \times] = B^T(t, \mathbf{x}) - B(t, \mathbf{x}). \quad (6)$$

Then the optimal attitude matrix for parameter vector \mathbf{x} , $A_{opt}(t, \mathbf{x})$, is computed from $\mathbf{q}_{opt}(t, \mathbf{x})$ by

$$A_{opt}(t, \mathbf{x}) = (q^2 - \mathbf{Q}^T \mathbf{Q}) I + 2\mathbf{Q} \mathbf{Q}^T - 2q[\mathbf{Q} \times], \quad (7)$$

where the three-vector part \mathbf{Q} and scalar part q of the quaternion $\mathbf{q}_{opt}(t, \mathbf{x})$ are given by

$$\mathbf{q}_{opt}^T(t, \mathbf{x}) = [\mathbf{Q}^T, q]. \quad (8)$$

The parameter vector update is given by

$$\delta \mathbf{x}_{opt} = W^{-1}(\mathbf{x})[\mathbf{h}(\mathbf{x}) - W^0(\mathbf{x} - \mathbf{x}^0)], \quad (9)$$

where, for $j, k = 1, \dots, m$,

$$W_{jk}(\mathbf{x}) = [W^0 - N^T(t, \mathbf{x})M^{-1}(t, \mathbf{x})N(t, \mathbf{x})]_{jk} - \text{tr}[A_{opt}^T(t, \mathbf{x})\partial^2 B(t, \mathbf{x})/\partial x_j \partial x_k], \quad (10)$$

$$h_j(\mathbf{x}) = \text{tr}\{[\partial B(t, \mathbf{x})/\partial x_j]A_{opt}^T(t, \mathbf{x})\}, \quad (11)$$

$$N_{1j}(t, \mathbf{x}) = \{[\partial B(t, \mathbf{x})/\partial x_j]A_{opt}^T(t, \mathbf{x})\}_{23} - \{[\partial B(t, \mathbf{x})/\partial x_j]A_{opt}^T(t, \mathbf{x})\}_{32}, \quad (12a)$$

$$N_{2j}(t, \mathbf{x}) = \{[\partial B(t, \mathbf{x})/\partial x_j]A_{opt}^T(t, \mathbf{x})\}_{31} - \{[\partial B(t, \mathbf{x})/\partial x_j]A_{opt}^T(t, \mathbf{x})\}_{13}, \quad (12b)$$

$$N_{3j}(t, \mathbf{x}) = \{[\partial B(t, \mathbf{x})/\partial x_j]A_{opt}^T(t, \mathbf{x})\}_{12} - \{[\partial B(t, \mathbf{x})/\partial x_j]A_{opt}^T(t, \mathbf{x})\}_{21}, \quad (12c)$$

and

$$M(t, \mathbf{x}) = \lambda_{max}(\mathbf{x}) I - B(t, \mathbf{x})A_{opt}^T(t, \mathbf{x}). \quad (13)$$

In these equations \mathbf{x}^0 is the *a priori* estimate of \mathbf{x} and W^0 is a symmetric positive-semidefinite matrix of weights assigned to this estimate; it is permissible to assign zero weights to the *a priori* estimate by setting $W^0 = 0$. The update $\delta \mathbf{x}_{opt}$ is added to \mathbf{x} to get the new parameter estimate. If the update is small enough, the procedure is complete; otherwise the computations are repeated from equation (1) until convergence is achieved.

The attitude covariance $P_{\theta\theta}$, the parameter covariance $P_{\mathbf{xx}}$, and the cross-covariance $P_{\theta\mathbf{x}}$ of the converged estimate can be computed as follows:

$$P_{\theta\theta}(t) = \sigma_{tot}^2 [M^{-1}(t, \mathbf{x}) + M^{-1}(t, \mathbf{x})N(t, \mathbf{x})W^{-1}(\mathbf{x})N^T(t, \mathbf{x})M^{-1}(t, \mathbf{x})], \quad (14)$$

$$P_{\mathbf{xx}} = \sigma_{tot}^2 W^{-1}(\mathbf{x}), \quad (15)$$

and

$$P_{\theta\mathbf{x}}(t) = P_{\mathbf{x}\theta}^T(t) = \sigma_{tot}^2 M^{-1}(t, \mathbf{x})N(t, \mathbf{x})W^{-1}(\mathbf{x}), \quad (16)$$

where

$$\sigma_{tot}^2 \equiv \left[\sum_{i=1}^n \sigma_i^{-2} \right]^{-1} \quad (17)$$

with σ_i^2 equal to the variance of the i^{th} vector measurement. The covariance computation assumes the weights to be

$$a_i = \sigma_{tot}^2 / \sigma_i^2 \quad (18)$$

and

$$W^0 = \sigma_{tot}^2(P^0)^{-1}, \quad (19)$$

where P^0 is the covariance of the *a priori* parameter vector estimate. An expression for $M^{-1}(t, \mathbf{x})$ is derived in the Appendix, eliminating the need for a numerical matrix inversion.

Application to Gyro Drift Determination

For the application to be treated in this paper, we assume that the kinematic information for attitude propagation is obtained from three gyros aligned with the spacecraft body axes. In this case the estimation algorithm assumes that the body rate vector $\omega(t, \mathbf{x})$ is

$$\omega(t, \mathbf{x}) = \omega_g(t) - \mathbf{x}, \quad (20)$$

where $\omega_g(t)$ is the column vector of gyro outputs and \mathbf{x} , a three-component vector of gyro drifts, is the vector of parameters to be estimated. These parameters enter $B(t, \mathbf{x})$ through the attitude propagation matrices $\Phi(t, t_0; \mathbf{x})$. The first and second partial derivatives of $\Phi(t, t_0; \mathbf{x})$ with respect to the components of \mathbf{x} are needed to evaluate the corresponding partial derivatives of $B(t, \mathbf{x})$. The partial derivative of equation (2) with respect to x_j is, using equation (20),

$$d[\partial\Phi(t, t_0; \mathbf{x})/\partial x_j]/dt = -[\omega(t, \mathbf{x}) \times][\partial\Phi(t, t_0; \mathbf{x})/\partial x_j] + [\mathbf{e}_j \times] \Phi(t, t_0; \mathbf{x}), \quad (21)$$

where \mathbf{e}_j is the unit vector along the j^{th} spacecraft axis. The solution of this differential equation consistent with equations (2) and (3) is

$$\partial\Phi(t, t_0; \mathbf{x})/\partial x_j = \int_{t_0}^t \Phi(t, t'; \mathbf{x})[\mathbf{e}_j \times] \Phi(t', t_0; \mathbf{x}) dt'. \quad (22)$$

Using the group property and orthogonality of the attitude propagation matrix,

$$\Phi(t', t_0; \mathbf{x}) = \Phi(t', t; \mathbf{x})\Phi(t, t_0; \mathbf{x}) = \Phi^T(t, t'; \mathbf{x})\Phi(t, t_0; \mathbf{x}), \quad (23)$$

and the relation

$$\Phi[\mathbf{e}_j \times] \Phi^T = [(\Phi \mathbf{e}_j) \times], \quad (24)$$

which holds for any proper orthogonal matrix Φ , gives

$$\partial\Phi(t, t_0; \mathbf{x})/\partial x_j = -[\psi_j(t, t_0; \mathbf{x}) \times] \Phi(t, t_0; \mathbf{x}), \quad (25)$$

where $\psi_j(t, t_0; \mathbf{x})$ is the j^{th} column of the matrix

$$\Psi(t, t_0; \mathbf{x}) \equiv - \int_{t_0}^t \Phi(t, t'; \mathbf{x}) dt' = [\psi_1(t, t_0; \mathbf{x}) \quad \psi_2(t, t_0; \mathbf{x}) \quad \psi_3(t, t_0; \mathbf{x})]. \quad (26)$$

The matrices $\Phi(t, t_0; \mathbf{x})$ and $\Psi(t, t_0; \mathbf{x})$ are also used for the usual state estimation methods [5, 6]. They are computed by adding up contributions over time intervals $t_{i+1} - t_i$, which are chosen to be short enough that variations in ω over the interval can be neglected. Thus

$$\Phi(t_{i+1}, t_0; \mathbf{x}) = \Phi(t_{i+1}, t_i; \mathbf{x})\Phi(t_i, t_0; \mathbf{x}), \quad (27)$$

where

$$\Phi(t_{i+1}, t_i; \mathbf{x}) = I - [\mathbf{u} \times] \sin|\phi| + [\mathbf{u} \times]^2 (1 - \cos|\phi|), \quad (28)$$

\mathbf{u} is the unit vector

$$\mathbf{u} \equiv \omega/|\omega|, \quad (29)$$

and $|\phi|$ is the length of the vector

$$\phi \equiv \omega(t_{i+1} - t_i). \quad (30)$$

Similarly,

$$\Psi(t_{i+1}, t_0; \mathbf{x}) = \Psi(t_{i+1}, t_i; \mathbf{x}) + \Phi(t_{i+1}, t_i; \mathbf{x})\Psi(t_i, t_0; \mathbf{x}), \quad (31)$$

with

$$\Psi(t_{i+1}, t_i; \mathbf{x}) = -(t_{i+1} - t_i) \{ I - [\mathbf{u} \times] |\phi|^{-1} (1 - \cos|\phi|) + [\mathbf{u} \times]^2 (1 - |\phi|^{-1} \sin|\phi|) \}. \quad (32)$$

The second partial derivatives of $\Phi(t, t_0; \mathbf{x})$ only appear in $W(\mathbf{x})$ and not in $\mathbf{h}(\mathbf{x})$, so approximate forms will be used for these partials. They are also computed by adding up contributions over short time intervals $t_{i+1} - t_i$, giving

$$\begin{aligned} \partial^2 \Phi(t_{i+1}, t_0; \mathbf{x}) / \partial x_j \partial x_k &= [\partial^2 \Phi(t_{i+1}, t_i; \mathbf{x}) / \partial x_j \partial x_k] \Phi(t_i, t_0; \mathbf{x}) \\ &+ [\partial \Phi(t_{i+1}, t_i; \mathbf{x}) / \partial x_j] [\partial \Phi(t_i, t_0; \mathbf{x}) / \partial x_k] + [\partial \Phi(t_{i+1}, t_i; \mathbf{x}) / \partial x_k] [\partial \Phi(t_i, t_0; \mathbf{x}) / \partial x_j] \\ &+ \Phi(t_{i+1}, t_i; \mathbf{x}) [\partial^2 \Phi(t_i, t_0; \mathbf{x}) / \partial x_j \partial x_k], \end{aligned} \quad (33)$$

where the first partial derivatives are give by equations (25) – (32) and where

$$\begin{aligned} \partial^2 \Phi(t_{i+1}, t_i; \mathbf{x}) / \partial x_j \partial x_k &= (t_{i+1} - t_i)^2 \{ \frac{1}{2} (\mathbf{e}_j \mathbf{e}_k^T + \mathbf{e}_k \mathbf{e}_j^T - 2\delta_{jk} I) \\ &+ \frac{1}{3} (\phi_j [\mathbf{e}_k \times] + \phi_k [\mathbf{e}_j \times] + \delta_{jk} [\phi \times]) \}. \end{aligned} \quad (34)$$

The approximation is in equation (34), which is valid to first order in ϕ . Starting the iterative computations of equations (27), (31), and (33) requires initial values for the matrices: the identity for $\Phi(t_0, t_0; \mathbf{x})$ from equation (3), and zero for $\Psi(t_0, t_0; \mathbf{x})$ and $\partial^2 \Phi(t_0, t_0; \mathbf{x}) / \partial x_j \partial x_k$.

Observation Modeling

Star tracker data are used to estimate the spacecraft attitude and gyro drifts. Each star tracker measurement is a two-component vector \mathbf{y}_i giving the location of the star image in the focal plane of the sensor. For attitude estimation with the new method we need to compute the star unit vector in the spacecraft body frame \mathbf{b}_i in terms of the measurement data \mathbf{y}_i . The star unit vector in the sensor frame is

$$\mathbf{s}_i = (1 + |\mathbf{y}_i|^2)^{-1/2} [(y_i)_1, (y_i)_2, 1]^T, \quad (35)$$

and then \mathbf{b}_i is given by

$$\mathbf{b}_i = C_i^T \mathbf{s}_i, \quad (36)$$

where C_i is the proper orthogonal 3×3 matrix defining the orientation in the body frame of the star tracker making this observation.

Data Simulation

Simulated gyro data and star tracker data are used to test the algorithm. The simulation assumes a constant angular velocity vector ω_{true} . The gyro data are simulated by adding varying levels of Gaussian noise to the components of ω_{true} . A true attitude matrix is computed by integrating the angular rates;

$$dA_{true}(t)/dt = - [\omega_{true} \times] A_{true}(t), \quad (37)$$

with some specified initial attitude matrix $A_{true}(t_0)$.

A star is initially simulated for each star tracker by randomly generating a measurement vector y_i within the star tracker field of view. Equations (35) and (36) then give the star unit vector \mathbf{b}_i in the body frame, and the star unit vector in the inertial reference frame is given by

$$\mathbf{r}_i = A_{true}^T(t_i)\mathbf{b}_i, \quad (38)$$

where t_i is the simulation time. For successive simulation times t_i , the reference vector \mathbf{r}_i is held fixed and the vector in the body frame is computed as

$$\mathbf{b}_i = A_{true}(t_i)\mathbf{r}_i. \quad (39)$$

Then the corresponding vector in the star tracker reference frame is given by the inverse of equation (36),

$$\mathbf{s}_i = C_i\mathbf{b}_i; \quad (40)$$

the measurement vector y_i by the inverse of equation (35),

$$y_i = (s_i)_3^{-1}[(s_i)_1, (s_i)_2]^T, \quad (41)$$

and Gaussian noise is added to the two components of y_i . This process is continued until the star has been tracked for some fixed number of observations or until it leaves the field of view, at which time a new star is randomly placed in the field of view. Earth and Sun interference are neglected in these simulations.

Comparison Algorithm

The algorithm chosen for comparison is a batch least-squares differential correction algorithm similar to that employed in the attitude ground support system of the Upper Atmosphere Research Satellite (UARS) [6]. The algorithm provides a least-squares estimate of a six-component state vector

$$\delta\mathbf{X}^T \equiv [\delta\theta^T \delta\mathbf{x}^T], \quad (42)$$

where $\delta\theta$ is the attitude error vector at epoch, and $\delta\mathbf{x}$ is the error in the gyro drift estimates. This is updated iteratively as follows. At the start of each iteration, an estimate \mathbf{x} of the gyro drifts and $A_{est}(t_0)$ of the epoch attitude are available. For each measurement y_i , a predicted value \mathbf{g}_i is computed from the known reference vector \mathbf{r}_i by equations identical to (39) – (41), but with the unknown attitude matrix $A_{true}(t_i)$ replaced by

$$A_{est}(t_i) = \Phi(t_i, t_0; \mathbf{x})A_{est}(t_0). \quad (43)$$

The computed value \mathbf{g}_i is seen to depend on both \mathbf{x} and $A_{est}(t_0)$. The optimal state update is the solution of

$$F \delta\mathbf{X} = \sum_{i=1}^n \sigma_i^{-2} G_i^T (y_i - \mathbf{g}_i) - \begin{bmatrix} 0 \\ (P^0)^{-1}(\mathbf{x} - \mathbf{x}^0) \end{bmatrix}, \quad (44)$$

where

$$F \equiv \sum_{i=1}^n \sigma_i^{-2} G_i^T G_i + \begin{bmatrix} 0 & 0 \\ 0 & (P^0)^{-1} \end{bmatrix}, \quad (45)$$

with σ_i^{-2} , P^0 , and \mathbf{x}^0 as defined previously, and with $\mathbf{0}$ a three-vector of zeros and 0 a 3×3 matrix of zeros. The 2×6 matrix G_i of partial derivatives of the errors of the i^{th} measurement with respect to $\delta\mathbf{X}$ is given by

$$G_i = \begin{bmatrix} (y_i)_1(y_i)_2 & -1 - (y_i)_1^2 & (y_i)_2 \\ 1 + (y_i)_2^2 & -(y_i)_1(y_i)_2 & -(y_i)_1 \end{bmatrix} C_i [\Phi(t_i, t_0; \mathbf{x}) \quad \Psi(t_i, t_0; \mathbf{x})]. \quad (46)$$

This state update gives new estimates of the gyro drifts and attitude:

$$\mathbf{x}_{new} = \mathbf{x} + \delta\mathbf{x}, \quad (47)$$

and

$$A_{new}(t_0) = \{I - |\delta\theta|^{-1}[\delta\theta \times] \sin|\delta\theta| + |\delta\theta|^{-2}[\delta\theta \times]^2(1 - \cos|\delta\theta|)\} A_{est}(t_0). \quad (48)$$

This iterative procedure is repeated until convergence is achieved. An estimate of the covariance matrix is provided by

$$\begin{bmatrix} P_{\theta\theta} & P_{\theta\mathbf{x}} \\ P_{\mathbf{x}\theta} & P_{\mathbf{x}\mathbf{x}} \end{bmatrix} = F^{-1}. \quad (49)$$

The initial attitude to begin the first iteration is provided by the q -method, as embodied in equations (1) - (7).

Numerical Examples

Tests were performed for both inertially-fixed and earth-pointing spacecraft attitudes, with star tracker orientations and other parameters corresponding to the Gamma Ray Observatory (GRO) [7] and UARS [6] spacecraft, respectively. Two star trackers were modeled with 8 degree by 8 degree fields of view and with an angle of approximately 73 degrees between their boresights. Some tests were performed with perfect star tracker measurements, but the results presented in this paper all include Gaussian noise on each star tracker output with standard deviation of 8 arc seconds, or 3.88×10^{-5} radians. The time interval between star tracker measurements was 32.768 seconds, the interval used by the UARS onboard computer. The data were simulated with no gyro bias, and the estimations were performed with non-zero initial bias estimates, so the bias estimate is the same as the bias error for these tests. The initial bias error was 10^{-4} radians/sec along either the spacecraft roll or yaw axis, but only representative results with initial roll bias errors are given below.

The epoch time t_0 for the estimation was taken to be the time of the first observation. In all but four tests, the true attitude matrix at epoch was set equal to the identity matrix. The tests for one simulation case were repeated with four different true attitude matrices at epoch:

$$A_{true}(t_0) = \begin{bmatrix} 0.352 & 0.864 & 0.360 \\ -0.864 & 0.152 & 0.480 \\ 0.360 & -0.480 & 0.800 \end{bmatrix}, \quad (50a)$$

$$A_{true}(t_0) = \text{diag}[1, -1, -1], \quad (50b)$$

$$A_{true}(t_0) = \text{diag}[-1, 1, -1], \quad (50c)$$

and

$$A_{true}(t_0) = \text{diag}[-1, -1, 1], \quad (50d)$$

where $\text{diag}[\dots]$ denotes a 3×3 matrix with the given elements on the main diagonal and zeros elsewhere. The attitude and bias errors for these different initial attitudes were identical to those for $A_{true}(t_0) = I$ within the precision of the output, as they should be. The covariance P^0 of the *a priori* bias estimates was taken to be infinite for all tests.

A representative subset of the tests is presented in Tables 1-7. At least 10 iterations were performed in each case, and the errors for all the iterations after those presented are identical to the errors of the last iteration in the table, to the precision of the table. The first "iteration" in the differential correction (DC) columns is not really a DC iteration; it is an initial attitude estimation using the *q*-method, as explained above. Thus the bias error after one DC "iteration" is the *a priori* error. The last line in each table is the estimate of the error standard deviations from the covariance matrices of equations (14) and (15) or equation (49).

Tables 1-6 present the tests with inertially-fixed attitude. These are in pairs: Tables 1 and 2 give the results for the highest observability case with two star trackers and a full orbit of data, Tables 3 and 4 have two star trackers but only 10 observations in each, and Tables 5 and 6 are for the case of only 10 observations in a single star tracker. Each simulated star was observed five times in these tests, so the cases in Tables 5 and 6 contain only two stars; the angular separation between these stars was 1.3 degrees. In each pair of tables, the first (odd-numbered) presents the results with no gyro noise, and the second (even-numbered) shows the effects of Gaussian noise on each gyro with standard deviation of 1 degree/hour, or 4.848×10^{-6} rad/sec.

The most important aspect of the tests, as concerns this paper, is the comparison of the results of the new method to those of the DC. The bias and attitude errors are not the same at each iteration, but both the general rate of convergence and the final converged errors are almost identical. Where there are differences, the errors of the new method are slightly lower, but not by a significant amount.

In the cases without gyro noise, the covariance matrix is a good indicator of the estimation errors. This correspondence is especially striking in Tables 1 and 3, while the actual errors in Table 5 are about 20 times less than the covariance matrix would indicate. The errors in the latter case are remarkably small considering the poor measurement geometry, with only two reference vectors separated by 1.3 degrees. When gyro noise is included, the actual errors can exceed the covariance estimates; this is not surprising since the covariance computation does not take gyro errors into account, nor does any other part of the estimation process. When unrealistically large gyro noise with standard deviation of 100 degree/hour was included, both estimation procedures became unreliable. The new method failed catastrophically when the nominally positive-definite matrix W defined by equation (10) developed a negative element on its main diagonal. The DC did not become singular, since the matrix F of equation (45), unlike W , is manifestly positive-semidefinite; but the bias estimation error increased monotonically for the first 10 iterations. Thus the new method is somewhat less robust than the DC in this case; but this is not very significant since a Kalman filter or smoother should probably be used in the presence of large amounts of dynamic noise [5].

Table 1. Bias and Attitude Errors for Inertially-fixed Attitude
with Two Star Trackers, 95.6 Minutes of Data, and no Gyro Noise

Iteration	Batch DC		New Method	
	Bias (rad/sec)	Attitude (rad)	Bias (rad/sec)	Attitude (rad)
1	1.00D-4	2.88D-1	1.68D-6	2.88D-1
2	5.65D-7	1.50D-3	1.69D-9	4.83D-3
3	1.68D-9	5.83D-6	1.68D-9	5.82D-6
4	1.68D-9	5.81D-6	1.68D-9	5.80D-6
Covariance	2.90D-9	9.53D-6	2.91D-9	9.54D-6

Table 2. Bias and Attitude Errors for Inertially-fixed Attitude
with Two Star Trackers, 95.6 Minutes of Data, and Gyro Noise of 1 deg/hour

Iteration	Batch DC		New Method	
	Bias (rad/sec)	Attitude (rad)	Bias (rad/sec)	Attitude (rad)
1	1.00D-4	2.87D-1	1.73D-6	2.87D-1
2	6.54D-7	2.66D-3	2.90D-7	5.46D-3
3	2.90D-7	1.98D-3	2.90D-7	1.98D-3
Covariance	2.90D-9	9.53D-6	2.91D-9	9.54D-6

Table 3. Bias and Attitude Errors for Inertially-fixed Attitude
with Two Star Trackers, 5.5 Minutes of Data, and no Gyro Noise

Iteration	Batch DC		New Method	
	Bias (rad/sec)	Attitude (rad)	Bias (rad/sec)	Attitude (rad)
1	1.00D-4	1.48D-2	2.12D-7	1.48D-2
2	2.17D-7	2.95D-5	2.07D-7	3.02D-5
3	2.07D-7	2.93D-5	2.07D-7	2.93D-5
Covariance	2.10D-7	3.67D-5	2.10D-7	3.68D-5

Table 4. Bias and Attitude Errors for Inertially-fixed Attitude
with Two Star Trackers, 5.5 Minutes of Data, and Gyro Noise of 1 deg/hour

Iteration	Batch DC		New Method	
	Bias (rad/sec)	Attitude (rad)	Bias (rad/sec)	Attitude (rad)
1	1.00D-4	1.49D-2	3.50D-6	1.49D-2
2	3.50D-6	2.71D-4	3.50D-6	2.71D-4
3	3.50D-6	2.72D-4	3.50D-6	2.72D-4
Covariance	2.10D-7	3.67D-5	2.10D-7	3.68D-5

Table 5. Bias and Attitude Errors for Inertially-fixed Attitude with One Star Tracker, 5.5 Minutes of Data, and no Gyro Noise

Iteration	Batch DC		New Method	
	Bias (rad/sec)	Attitude (rad)	Bias (rad/sec)	Attitude (rad)
1	1.00D-4	1.63D-2	1.14D-4	1.63D-2
2	2.29D-5	3.25D-3	1.07D-6	5.69D-3
3	1.38D-6	2.94D-4	1.08D-6	2.49D-4
4	1.10D-6	2.55D-4	1.08D-6	2.51D-4
5	1.11D-6	2.55D-4	1.08D-6	2.51D-4
Covariance	2.39D-5	4.18D-3	2.40D-5	4.19D-3

Table 6. Bias and Attitude Errors for Inertially-fixed Attitude with One Star Tracker, 5.5 Minutes of Data, and Gyro Noise of 1 deg/hour

Iteration	Batch DC		New Method	
	Bias (rad/sec)	Attitude (rad)	Bias (rad/sec)	Attitude (rad)
1	1.00D-4	1.44D-2	1.18D-4	1.44D-2
2	2.25D-5	1.16D-2	4.39D-6	7.11D-4
3	4.51D-6	1.54D-2	4.41D-6	1.54D-2
4	4.50D-6	1.54D-2	4.41D-6	1.54D-2
Covariance	2.37D-5	4.16D-3	2.38D-5	4.18D-3

Table 7. Bias and Attitude Errors for Earth-Pointing Attitude with One Star Tracker, 5.5 Minutes of Data, and no Gyro Noise

Iteration	Batch DC		New Method	
	Bias (rad/sec)	Attitude (rad)	Bias (rad/sec)	Attitude (rad)
1	1.00D-4	3.01D-2	8.04D-5	3.01D-2
2	1.37D-5	2.54D-3	1.73D-5	3.02D-2
3	4.74D-6	8.52D-4	7.17D-6	3.05D-3
4	4.88D-6	8.76D-4	5.31D-6	1.27D-3
5	4.88D-6	8.76D-4	4.97D-6	9.48D-4
6	4.88D-6	8.76D-4	4.91D-6	8.90D-4
7	4.88D-6	8.76D-4	4.89D-6	8.79D-4
8	4.88D-6	8.76D-4	4.89D-6	8.78D-4
9	4.88D-6	8.76D-4	4.89D-6	8.77D-4
Covariance	1.24D-5	2.15D-3	1.12D-5	1.96D-3

The attitude errors in Table 2 are larger than those in Table 4, showing that estimators that do not handle dynamic noise correctly should not be used with long spans of data including the effects of dynamic noise.

The tests with Earth-pointing attitude used a constant pitch rate of -1.083073×10^{-3} rad/sec, which corresponds to an orbit period of 96.7 minutes. For these tests, a simulated star was tracked until it left the star tracker field of view. The test parameters were otherwise the same as for inertially-fixed attitude. The new method did not fare as well in these tests; it generally required more iterations than the DC to converge, although the final errors were virtually identical. This suggests the presence of errors in the matrix $W(\mathbf{x})$ that steers the estimates to their optimal values, and not in the vector $\mathbf{h}(\mathbf{x})$ that identifies the optimum once it has been reached. Table 7 presents the results of a test with a single star tracker, observing only two stars with angular separation of 7 degrees. This is a particularly discouraging example, in which the DC converged in four iterations, while the new method required nine. Since this is a low observability case, in which attitude kinematics information is more important compared to the measurements than in a high observability case, an accurate computation of $W(\mathbf{x})$ is especially important.

The greater success of the new method for inertially-fixed attitude than for non-inertial attitude suggests the inadequacy of the approximation of equation (34) for the matrix of second partial derivatives $\partial^2\Phi(t_{i+1}, t_i; \mathbf{x})/\partial x_j \partial x_k$, which appears in $W(\mathbf{x})$ and not in $\mathbf{h}(\mathbf{x})$. This approximation should be replaced by one that is valid for all values of the rotation angle ϕ , subject to the assumption that the angular rates are approximately constant between observations. This may also avoid the failure of the new method in the test with 100 degree/hour gyro noise, since this has an effect on the propagation of the partial derivative matrices similar to the effects of actual angular rates of the same size.

The computational effort required by the two algorithms was also measured. Both algorithms were implemented in double-precision Fortran and executed on a DEC VAX 11/780. The CPU times were proportional to the number of iterations performed, the times per iteration for the two methods being

$$t_{CPU, new} = 13 + 15.2 n \text{ msec} \quad (51a)$$

and

$$t_{CPU, DC} = 31 + 6.7 n \text{ msec.} \quad (51b)$$

where n is the number of observations. The coefficient of n in these times can be interpreted as the time required to process a measurement, including propagation of the attitude transition matrix, partial derivative matrices, and so forth. The n -independent term represents the end-of-iteration computations, including matrix inversions and computation of updates to the bias vector and attitude matrix. Thus equation (51) shows that the measurement processing is more expensive for the new method, while the end-of-iteration computations of the DC require more effort. The exact CPU times will vary from case to case, but the DC appears to be about twice as fast, overall, as the new method for the numbers of measurements typically processed. Improving the computation of the matrix of second partial derivatives for the new method will require even more effort to process each measurement.

Conclusions

These tests establish the validity of a new method for the simultaneous estimation of spacecraft attitude and sensor biases, based on a quaternion estimation algorithm minimizing Wahba's loss function. The new algorithm performs as well as a batch least-squares differential correction in tests with inertially-fixed attitude, in the sense of converging to equally accurate estimates in the same number of iterations. The new algorithm converges more slowly than the differential correction for Earth-pointing attitude, probably owing to the use of an inadequate approximation for a partial derivative matrix in the new method. The new method does not show any advantages in terms of robustness or speed of convergence, and in addition requires about twice the computational effort of the differential correction. It is hoped that improving the approximation for the partial derivative matrix in the new method will improve its convergence and/or robustness, without adding significantly to its computational burden.

Appendix

The matrix $B(t, \mathbf{x})$ has the singular value decomposition [8]

$$B = U_+ S' V_+^T, \quad (\text{A1})$$

where U_+ and V_+ are proper orthogonal matrices, and

$$S' = \text{diag}[S_1, S_2, S_3], \quad (\text{A2})$$

a 3×3 matrix with $S_1, S_2,$ and S_3 on the main diagonal and zeros elsewhere. The arguments t and \mathbf{x} are omitted from this and all subsequent equations for notational simplicity. The optimal attitude estimate is given in terms of these matrices by [8]

$$A_{opt} = U_+ V_+^T. \quad (\text{A3})$$

The maximum eigenvalue λ_{max} of the matrix K defined by equation (5) is related to the optimal attitude by [2]

$$\lambda_{max} = \text{tr}(A_{opt} B^T), \quad (\text{A4})$$

where tr denotes the trace. Equations (A1) – (A4) and (13) show that

$$\det B = S_1 S_2 S_3, \quad (\text{A5})$$

$$\lambda_{max} = S_1 + S_2 + S_3, \quad (\text{A6})$$

$$M = U_+ \text{diag}[S_2 + S_3, S_3 + S_1, S_1 + S_2] U_+^T. \quad (\text{A7})$$

and

$$\det M = (S_2 + S_3)(S_3 + S_1)(S_1 + S_2). \quad (\text{A8})$$

We now define the scalar

$$\kappa \equiv \frac{1}{2} [\lambda_{max}^2 - \text{tr}(B B^T)]. \quad (\text{A9})$$

A little algebra shows that

$$\kappa = S_2 S_3 + S_3 S_1 + S_1 S_2, \quad (\text{A10})$$

$$\kappa \lambda_{max} - \det B = \det M, \quad (A11)$$

and

$$\kappa I + BB^T = U_+ \text{diag}[(S_3 + S_1)(S_1 + S_2), (S_1 + S_2)(S_2 + S_3), (S_2 + S_3)(S_3 + S_1)]U_+^T = \text{adj } M, \quad (A12)$$

where adj denotes the adjoint matrix. Equations (A11) and (A12) give the desired result

$$M^{-1} = (\kappa \lambda_{max} - \det B)^{-1}(\kappa I + BB^T). \quad (A13)$$

The evaluation of M^{-1} by means of equations (A9) and (A13) does not require the singular value decomposition of B .

References

- [1] WERTZ, JAMES R. (editor) *Spacecraft Attitude Determination and Control*, D. Reidel, Dordrecht, the Netherlands, 1978
- [2] MARKLEY, F. LANDIS "Attitude Determination and Parameter Estimation using Vector Observations: Theory," *Journal of the Astronautical Sciences*, Vol. 37, No. 1, January-March, 1989
- [3] WAHBA, GRACE "A Least Squares Estimate of Spacecraft Attitude," *SIAM Review*, Vol. 7, No. 3, July 1965, p. 409.
- [4] SHUSTER, M. D. and OH, S. D. "Three-Axis Attitude Determination from Vector Observations," *Journal of Guidance and Control*, Vol. 4, No. 1, January-February 1981, pp. 70-77
- [5] LEFFERTS, E. J., MARKLEY, F. L., and SHUSTER, M. D. "Kalman Filtering for Spacecraft Attitude Estimation," *Journal of Guidance, Control, and Dynamics*, Vol. 5, No. 5, September-October 1982, pp. 417-429
- [6] KRACK, K. et al., *Upper Atmosphere Research Satellite (UARS) / Extreme Ultraviolet Explorer (EUVE) Flight Dynamics Support System (FDSS) Functional Specifications*, Computer Sciences Corporation, CSC/TR-88/6032, November 1988
- [7] BLEJER, D. et al., *Gamma Ray Observatory (GRO) Flight Dynamics Support System (FDSS) Specifications: II Functional Specifications, Update 1*, Computer Sciences Corporation CSC/TR-85/6005UD1, February 1987
- [8] MARKLEY, F. LANDIS "Attitude Determination Using Vector Observations and the Singular Value Decomposition," *Journal of the Astronautical Sciences*, Vol. 36, No.3, July-September 1988, pp. 245-258

COBE NONSPINNING ATTITUDE PROPAGATION*

D. Chu
Computer Sciences Corporation (CSC)

ABSTRACT

The Cosmic Background Explorer (COBE) spacecraft will exhibit complex attitude motion consisting of a spin rate of approximately -0.8 revolution per minute (rpm) about the x-axis and simultaneous precession of the spin axis at a rate of one revolution per orbit (rpo) about the nearly perpendicular spacecraft-to-Sun vector. The effect of the combined spinning and precession is to make accurate attitude propagation difficult and the 1-degree (3σ) solution accuracy goal problematic.

To improve this situation, an intermediate reference frame is introduced, and the angular velocity divided into two parts. The "nonspinning" part is that which would be observed if there were no rotation about the x-axis. The "spinning" part is simply the x-axis component of the angular velocity. The two are propagated independently and combined whenever the complete attitude is needed. This approach is better than the usual "one-step" method because each of the two angular velocities look nearly constant in their respective reference frames. Since the angular velocities are almost constant, the approximations made in discrete time propagation are more nearly true.

To demonstrate the advantages of this "nonspinning" method, attitude is propagated as outlined above and is then compared with the results of the one-step method. Over the 100-minute COBE orbit, the one-step error grows to several degrees while the nonspinning error remains negligible.

* This work was supported by the National Aeronautics and Space Administration (NASA)/Goddard Space Flight Center (GSFC), Greenbelt, Maryland, under Contract NAS 5-31500.

COBE ATTITUDE AND THE NEED FOR MORE ACCURATE PROPAGATION

The attitude of the Cosmic Background Explorer (COBE) is three-axis stabilized with the minus x-axis maintained 94 degrees from the Sun line (Figure 1). The spacecraft pitches about that line at a rate of 1 revolution per 100-minute orbit period. It also spins about the minus x-axis once every 75 seconds. COBE attitude can be expressed as an Euler 3-2-1 (pitch-roll-yaw) rotation sequence with respect to a rotating Earth-Sun coordinate frame with the z-axis pointing toward the Sun and the y-axis pointing along the cross product of the Sun and Earth vectors. Nominal pitch and roll are then 0 and -4 degrees, respectively.

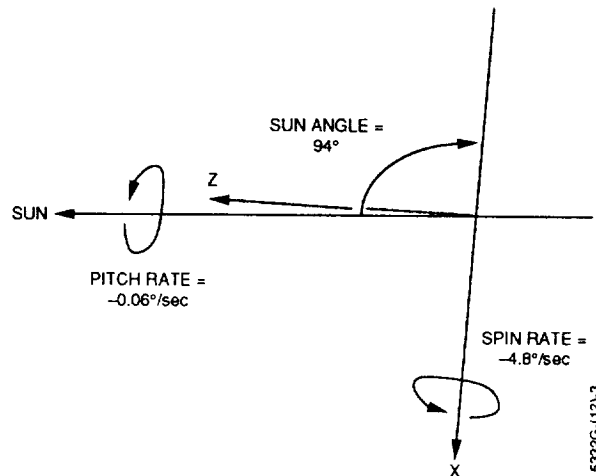


Figure 1. COBE Attitude Profile

Propagating the attitude from samples of the angular velocity assumes that the angular velocity remains constant in the body frame over the sample interval. The COBE gyro sampling intervals are 0.5, 1, 2, or 4 seconds, depending on the telemetry format and data rate. For COBE, which spins as much as 19.2 degrees per gyro sample, the pitch component of the angular velocity can change direction significantly. Under these circumstances, the usual method of propagation, which handles the total incremental rotation at once, introduces errors that accumulate over time and become unacceptably large.

This paper describes a variation on the usual one-step propagation that reduces this error by introducing an intermediate nonspinning coordinate frame. The advantage of the nonspinning frame is that the angular velocities used for its propagation and for the subsequent transformation to the body frame vary much less between gyro samples. The associated equations for gyro calibration follow along with numerical estimates of the improvement in COBE propagation accuracy.

NOTATION AND THE USUAL ONE-STEP ATTITUDE PROPAGATION

Attitude is represented here by the orthogonal inertial-to-body coordinate transformation matrix, $A_{B/I}$, and the kinematic equation for its propagation (Reference 1, p. 512) is

$$\dot{A}_{B/I} = -\underline{\omega}_B A_{B/I} \quad (1)$$

The dot ($\dot{\cdot}$) above $A_{B/I}$ indicates differentiation with respect to time. Since the angular velocity, ω_B , is not constant, Equation (1) is solved numerically. Still, a formal solution may be written as

$$A_{B/I}(t) = \Phi_{B/I}(t, t_0) A_{B/I}(t_0) \quad (2)$$

$\Phi_{B/I}$ is the attitude propagation matrix satisfying the differential equation:

$$\dot{\Phi}_{B/I} = -\underline{\omega}_B \Phi_{B/I} \quad (3)$$

and the initial condition:

$$\Phi_{B/I}(t_0, t_0) = I \quad (4)$$

where I is the identity matrix.

The subscripts I and B refer here to the inertial and body coordinates in which a vector or matrix is expressed. The vector ω_B , for example, is the angular velocity in body coordinates, and $\underline{\omega}_B$ is the antisymmetric matrix derived from it.

$$\underline{\omega}_B = \begin{bmatrix} 0 & -\omega_{B3} & \omega_{B2} \\ \omega_{B3} & 0 & -\omega_{B1} \\ -\omega_{B2} & \omega_{B1} & 0 \end{bmatrix} \quad (5)$$

The slash (/) indicates a transformation from the frame on the right to that on the left. Thus, $A_{B/I}$ is the inertial-to-body coordinate transformation matrix.

NONSPINNING INTERMEDIATE FRAME AND TWO-STEP PROPAGATION

In body coordinates, the spin component of the COBE angular velocity, ω_B'' , is constant, while the pitch component, ω_B' , varies with time:

$$\omega_B(t) = \omega_B'(t) + \omega_B'' \quad (6)$$

If the spin axis is denoted by \hat{S}_B , these two portions of the angular velocity can be computed as follows:

$$\omega_B' = (I - \hat{S}_B (\hat{S}_B)^T) \omega_B \quad (7)$$

$$\omega_B'' = \hat{S}_B (\hat{S}_B)^T \omega_B \quad (8)$$

An intermediate, nonspinning coordinate system denoted by the subscript N can be introduced that is defined by the propagation equation

$$\dot{A}_{N/I} \equiv -\underline{\omega}'_N A_{N/I} \quad (9)$$

where

$$\omega'_N \equiv (A_{B/N})^T \omega'_B \quad (10)$$

Since the magnitude of ω'_B is less than that of ω_B , ω'_B does not change as much as ω_B does between gyro samples. Thus, all other things being the same, the error in propagating $A_{N/I}$ should be less than the error in propagating $A_{B/I}$. If the propagation from the nonspinning frame to the body frame can be done perfectly, as is plausible since the spin rate is constant, the total propagation error for this two-step method should also be less than that for the usual one-step method.

To complete the propagation of $A_{B/I}$, it remains to compute $A_{B/N}$, which transforms from the nonspinning to the body frame:

$$A_{B/N} = A_{B/I} (A_{N/I})^T \quad (11)$$

By the product rule for differentiation, the $\dot{A}_{B/I}$ is

$$\dot{A}_{B/N} = \dot{A}_{B/I} (A_{N/I})^T + A_{B/I} (\dot{A}_{N/I})^T \quad (12)$$

Substituting for $\dot{A}_{B/I}$ and $\dot{A}_{N/I}$ from Equations (1), (6), and (9) and combining attitude transformations yields

$$\dot{A}_{B/N} = -(\underline{\omega}'_B + \underline{\omega}''_B) A_{B/N} + A_{B/N} \underline{\omega}'_N \quad (13)$$

Noting that $\underline{\omega}'_N$ is the similarity transformation of $\underline{\omega}'_B$,

$$\underline{\omega}'_N = (A_{B/N})^T \underline{\omega}'_B A_{B/N} \quad (14)$$

gives the differential equation for the propagation of $A_{B/N}$:

$$\dot{A}_{B/N} = -\underline{\omega}''_B A_{B/N} \quad (15)$$

With equations for both $A_{B/N}$ and $A_{N/I}$, the complete attitude, $A_{B/I}$, can be propagated.

GYRO CALIBRATION

In addition to reducing the propagation error due to the finite gyro sampling interval, it is usually necessary to calibrate the gyros to reduce systematic errors in the sensed angular

velocity. Because calibration involves the same type of computations as propagation, it is also done more accurately with a two-step method.

With one-step propagation, gyro calibration errors, $\Delta\alpha$, can be found using the solution to the following error propagation equation (Reference 2, p. 4-13):

$$\dot{\theta}_B = -\underline{\omega}_B \theta_B + \Delta\omega_B \quad (16)$$

where θ_B is the attitude error expressed in axis and angle form, and the angular velocity error, $\Delta\omega_B$, is related to the gyro calibration errors by the matrix $G(\omega_B)$.

$$\Delta\omega_B = G(\omega_B) \Delta\alpha \quad (17)$$

The solution to the error equation has the form

$$\theta_B(t) = \Gamma_{B/I}(t, t_0) \Delta\alpha + \Phi_{B/I}(t, t_0) \theta_B(t_0) \quad (18)$$

where the variational matrix, $\Gamma_{B/I}$, transforms the gyro calibration errors into contributions to the attitude error

$$\Gamma_{B/I}(t, t_0) = \int_{t_0}^t \Phi_{B/I}(t, \tau) G(\omega_B) d\tau \quad (19)$$

The matrix $\Gamma_{B/I}$ then serves as the partial derivative of the propagated attitude error with respect to the gyro parameter errors:

$$\frac{\partial \theta_B}{\partial \Delta\alpha} = \Gamma_{B/I}(t, t_0) \quad (20)$$

If one knows θ_B at times t and t_0 , $\Delta\alpha$ can be found from Equation (18).

A corresponding variational matrix is needed for calibration with the nonspinning propagation method. Because the two methods are different, there is no reason to expect the variational matrices to be the same. Both steps of the nonspinning propagation, however, follow the same kind of propagation equation as does the one-step method, and the corresponding error equations can be applied to each step separately:

$$\dot{\theta}'_N = \Delta\omega'_N - \underline{\omega}'_N \theta'_N \quad (21)$$

$$\dot{\theta}''_B = \Delta\omega''_B - \underline{\omega}''_B \theta''_B \quad (22)$$

Here, θ'_N is the error in the nonspinning propagation expressed in the nonspinning frame. θ''_B is the corresponding error in the spinning propagation expressed in body coordinates. The angular velocity errors, $\Delta\omega'_N$ and $\Delta\omega''_B$, are defined as follows:

$$\Delta\omega'_N \equiv A_{N/B} [I - \hat{S}_B (\hat{S}_B)^T] G(\omega_B) \Delta\alpha \quad (23)$$

$$\Delta\omega''_B \equiv \hat{s}_B (\hat{s}_B)^T G(\omega_B) \Delta\alpha \quad (24)$$

θ'_N and θ''_B can be solved for as in the one-step propagation to give solutions of the form

$$\theta'_N = \Gamma_{N/I} \Delta\alpha + \Phi_{N/I} \theta'_N(t_0) \quad (25)$$

$$\theta''_B = \Gamma_{B/N} \Delta\alpha + \Phi_{B/N} \theta''_B(t_0) \quad (26)$$

where the variational matrices $\Gamma_{N/I}$ and $\Gamma_{B/N}$ are computed as follows:

$$\Gamma_{N/I} = \int_{t_0}^t \Phi_{N/I}(t, \tau) \Delta\omega'_N d\tau \quad (27)$$

$$\Gamma_{B/N} = \int_{t_0}^t \Phi_{B/N}(t, \tau) \Delta\omega''_B d\tau \quad (28)$$

The total propagation error, θ_B , then equals

$$\theta_B = A_{B/N} \theta'_N + \theta''_B \quad (29)$$

This gives the partial derivative of the attitude error with respect to the gyro calibration errors as

$$\Gamma_{B/I} = \Gamma_{B/N} + \Phi_{B/N} \Gamma_{N/I} \quad (30)$$

which can be used in Equation (18) to solve for $\Delta\alpha$.

NUMERICAL SIMULATION

Although the large COBE gyro sampling interval can be expected to degrade one-step propagation accuracy, it is useful to know how much of an effect it actually has. The nonspinning method must justify its additional computation with significantly better accuracy.

To compute the propagation error for each method, the pitch rate, $\dot{\phi}$, roll rate, $\dot{\theta}$, and spin rate, $\dot{\psi}$, measured with respect to the inertial frame are assumed to be constant.

$$\dot{\phi} = -360^\circ/6000 \text{ sec} = -0.06^\circ/\text{sec} \quad (31)$$

$$\dot{\theta} = 0 \quad (32)$$

$$\dot{\psi} = -0.8 \text{ rpm} = -4.8^\circ/\text{sec} \quad (33)$$

The exact attitude is then found by first performing the pitch rotation, ϕ , followed by the roll and spin rotations, θ and ψ .

$$\phi = (t - t_0) \dot{\phi} + \phi_0 \quad (34)$$

$$\theta = -4^\circ \quad (35)$$

$$\psi = (t - t_0) \dot{\psi} + \psi_0 \quad (36)$$

The one-step attitude can be propagated from the following formula for the angular velocity (Reference 1, p. 765):

$$\omega_B(t)^T = [\dot{\psi} - \sin(\theta) \dot{\phi}, \cos(\theta) \sin(\psi) \dot{\phi}, \cos(\theta) \cos(\psi) \dot{\phi}] \quad (37)$$

The two angular velocities for the nonspinning propagation are as follows:

$$\omega'_N(t)^T = [0, \cos(\omega_{B1}t) \omega_{B2} - \sin(\omega_{B1}t) \omega_{B3}, \sin(\omega_{B1}t) \omega_{B2} + \cos(\omega_{B1}t) \omega_{B3}] \quad (38)$$

$$\omega''_B(t)^T = [\dot{\psi} - \sin(\theta) \dot{\phi}, 0, 0] \quad (39)$$

The one-step and nonspinning attitudes are then compared to the exact attitude, and the angular differences are computed. A plot of the one-step propagation error for 0.5-second sampling intervals is shown in Figure 2 for a timespan of one orbit. While the one-step error grows to a maximum value of 2.4 degrees, the nonspinning error remains less than 0.003 degree.

The results show that, even for the smallest gyro sampling interval, which is 0.5 second, the one-step propagation errors are quite large. This is counterintuitive. Since a constant spin can be propagated without error, it would be expected that adding a much smaller constant pitch rate would have a negligible effect. The flaw in that argument is that, although the spin is constant in the body frame, the pitch angular velocity is not. It is constant in the inertial frame. The assumption about the size of the error is also slightly misplaced. Small pitch rates do produce slowly growing propagation errors, but because the orbit is correspondingly longer, they have more time to grow.

Even more surprising than the size of the error is its oscillation. Rather than grow without limit, the propagation error peaks at the middle of the orbit. The reason is that while the actual pitch angular velocity moves continuously in the body frame, the sampled pitch angular velocity is fixed in the direction it has at the start of the interval. Thus, the sampled value lags the true value and introduces a roll component of angular velocity (Figure 3). Over an orbit period, the roll direction changes by 360 degrees, and the propagation error that builds up in the first half of the orbit decreases over the second half.

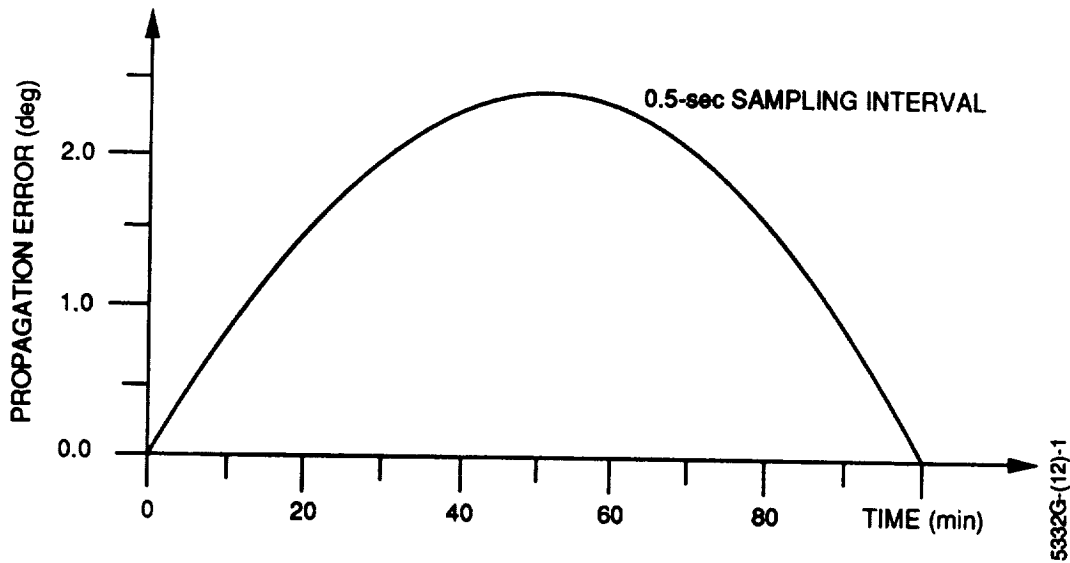


Figure 2. One-Step Propagation Error Time Dependence

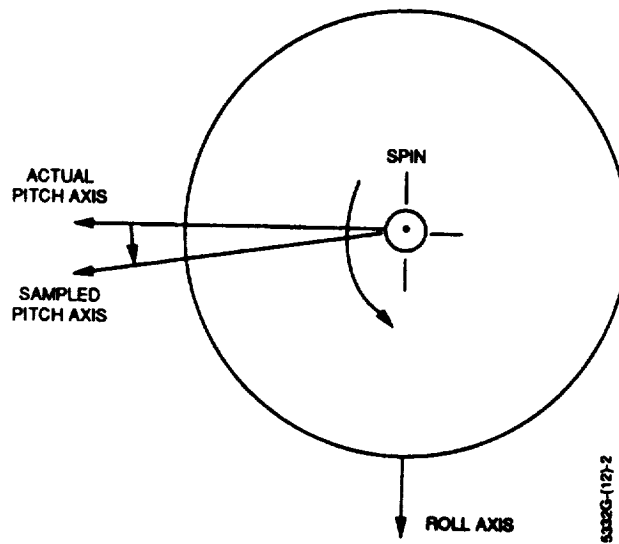


Figure 3. Sampling Introduces a Roll Angular Velocity

SUMMARY

The nonspinning propagation method described here is a means of trading computation for accuracy when the body angular velocity changes direction between gyro samples. This method is currently implemented for batch attitude determination in the COBE flight dynamics support system (Reference 3, p. 3.1.2.42-1), where it is needed to meet the attitude determination accuracy goal of 1 degree (3σ). Further investigation should still be done on understanding the effects of nonconstant roll, interpolating the angular

velocity to the midpoint of the sampling interval, and using higher order numerical integration methods.

Whether nonspinning propagation is worth the extra work for other missions depends on the magnitude and form of the angular velocity, the gyro sampling rate, and the accuracy requirements. The unexpectedly large errors that would have been observed for COBE, however, argue for consideration of this effect whenever a three-axis stabilized spacecraft undergoes a compound rotational motion, such as spinning and pitching.

ACKNOWLEDGMENTS

Nonspinning propagation was proposed for COBE by B. T. Fang, and in presenting it here, the author seeks only to make it available to a wider audience. For their help in that effort, the author wishes to acknowledge M. Nicholson and Y. Sheu of Computer Sciences Corporation and F. L. Markley of Goddard Space Flight Center.

REFERENCES

1. J. R. Wertz (ed.), *Spacecraft Attitude Determination and Control*. Dordrecht, Holland: D. Reidel Publishing Company, 1980
2. Computer Sciences Corporation, CSC/TM-88/6001, *Attitude Determination Error Analysis System (ADEAS) Mathematical Specifications Document*, M. Nicholson, October 1988
3. --, CSC/TR-87/6004, *Cosmic Background Explorer (COBE) Flight Dynamics Support System (FDSS) Specifications II. Functional Specifications*, K. Hall, June 1987

SIMULATION OF SPACECRAFT ATTITUDE DYNAMICS
USING TREETOPS AND MODEL-SPECIFIC
COMPUTER CODES

John E. Cochran, Jr.,* T. S. No[†] and
Norman G. Fitz-Coy[†]

Auburn University, Alabama 36849

ABSTRACT

The simulation of spacecraft attitude dynamics and control using the generic, multi-body code called TREETOPS and other codes written especially to simulate particular systems is discussed. Differences in the methods used to derive equations of motion--Kane's method for TREETOPS and the Lagrangian and Newton-Euler methods, respectively, for the other two codes--are considered. Simulation results from the TREETOPS code are compared with those from the other two codes for two example systems. One system is a chain of rigid bodies; the other consists of two rigid bodies attached to a flexible base body. Since the computer codes were developed independently, consistent results serve as a verification of the correctness of all the programs. Differences in the results are discussed. Results for the two-rigid-body, one-flexible-body system are useful also as information on multi-body, flexible, pointing payload dynamics.

INTRODUCTION

Since the launch of Explorer I and the realization, based on its anomalous attitude time history,¹ that a spacecraft generally could not be considered a rigid body, the field of spacecraft attitude dynamics and control has developed to the point that many methods of analysis^{2,3,4,5,6} and numerous attitude dynamics and control simulation codes^{7,8,9} are now available. The volume of literature in the area of spacecraft attitude dynamics is great enough that we will not attempt to review even the part more directly concerned with multibody spacecraft. The purpose of this paper is merely to consider some methods for developing equations of motion for multi-body spacecraft and to compare results obtained from a rather general digital simulation code called TREETOPS⁸ with those from simulations which are model-specific.

First, we will consider the use of the Newton-Euler method, the Lagrangian method with quasi-coordinates^{10,11} and Kane's method⁴ for deriving equations of motion for both rigid and flexible multi-body spacecraft models. Second, we will discuss, briefly, the computer codes used to obtain comparative results. Third, we will present some examples of results obtained from the computer codes.

*Professor, Department of Aerospace Engineering.

[†]Graduate Student, Department of Aerospace Engineering.

METHODS FOR DERIVING EQUATIONS OF MOTION

To illustrate the use of the three methods for deriving equations of motion, we adopt the simple two-body model shown in Fig. 1. Our motivation for doing this is that a chain configuration will be considered in the examples. Body B_1 , of mass m_1 , is rigid and body B_2 , of mass m_2 , is either rigid, or flexible, at our convenience. The bodies have centers of mass of C_1 and C_2 , respectively, and move with respect to an inertial frame N in which a dextral, orthogonal coordinate system, $OXYZ$, with its associated unit vectors \hat{n}_j , $j=1,2,3$, is fixed. Body B_j has a centroidal inertia dyadic \underline{I}_j . For body B_1 , \underline{I}_1 is constant. If we decide that B_2 is rigid, \underline{I}_2 is also constant. But, generally, \underline{I}_2 varies with time when B_2 is flexible.

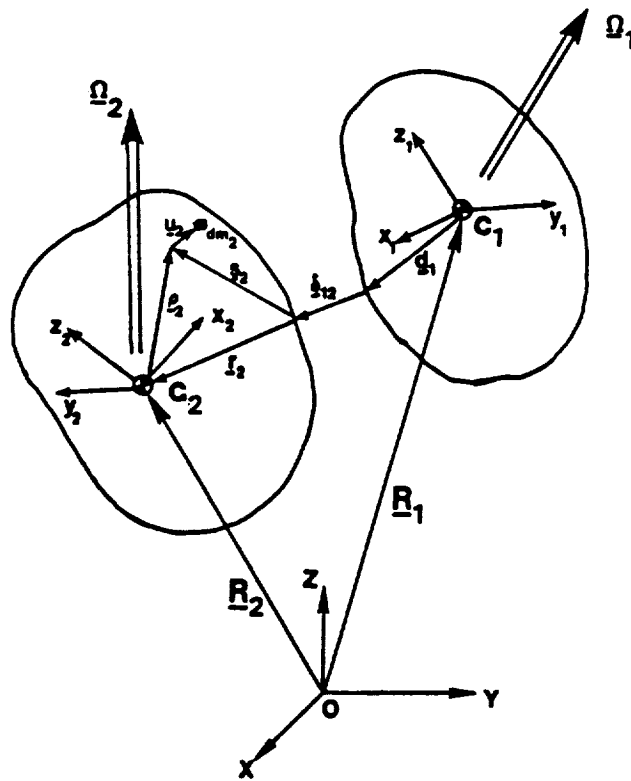


Fig. 1 Two-body system for example.

We let \underline{R}_j denote the position vector from O to C_j , $\underline{\rho}_j$ the vector from C_j to an arbitrary element of mass dm_j when that body is undeformed and \underline{u}_j denote the displacement of dm_j from the position it occupies when body B_j is deformed. In addition, we let $\underline{\Omega}_j$ denote the angular velocity of a coordinate system, $C_jx_jy_jz_j$, in body B_j . For $j=1$, the $C_1x_1y_1z_1$ coordinate system is fixed in B_1 . For $j=2$, we may let the $C_2x_2y_2z_2$ system be such that $\int \tilde{u}_2 \tilde{u}_2 dm_2$ (where \tilde{u}_2 is the skew-symmetric matrix

counterpart of $\underline{u}_2 \cdot \underline{x}$) is diagonal, or some other condition can be used to define the orientation of $C_2 x_2 y_2 z_2$ in B_2 .²

For convenience, we let $\underline{u}_2 = \sum_{k=1}^n \phi_k q_k$, where the ϕ_k are modal vectors and are functions of the undeformed coordinates of dm_2 .

Newton-Euler Equations

The Newton-Euler method is to write equations for the translation and rotation of each body subject to external, or active,⁴ forces and moments and forces and moments of constraint.

For body j , if \underline{F}_{je} and \underline{F}_{jc} are, respectively, the external force on body j and the constraint force,

$$m_j \ddot{\underline{r}}_j = \underline{F}_{je} + \underline{F}_{jc}, \quad j = 1, 2, \quad (1)$$

Also, for body 1, if \underline{M}_{1e} and \underline{M}_{1c} are the external moment and constraint moment, respectively, we have,

$$\underline{I}_1 \cdot \dot{\underline{\Omega}}_1 + \underline{\Omega}_1 \times \underline{I}_1 \cdot \underline{\Omega}_1 = \underline{M}_{1e} + \underline{M}_{1c} \quad (2)$$

The equations of motion for body B_2 are somewhat different, of course, if it is flexible. First, to obtain an independent equation for each q_ℓ , we may take the fundamental equation for the acceleration of dm_2 ,

$$(\ddot{\underline{R}}_2 + \ddot{\underline{\rho}}_2 + \ddot{\underline{u}}_2) dm_2 = d\underline{f}_2, \quad (3)$$

where $d\underline{f}_2$ is the force on dm_2 , expand $\ddot{\underline{\rho}}_2$ and $\ddot{\underline{u}}_2$, dot multiply by $\underline{\phi}_\ell$ and integrate over the mass of the body to get

$$\begin{aligned} \int \underline{\phi}_\ell dm_2 \cdot \ddot{\underline{R}}_2 &= \underline{\Omega}_2 \cdot \int \underline{\phi}_\ell \times [(\underline{\rho}_2 + \underline{u}_2) \times \underline{\Omega}_2] dm_2 \\ &- \int [\underline{\phi}_\ell \times (\underline{\rho}_2 + \underline{u}_2)] dm_2 \cdot \dot{\underline{\Omega}}_2 \\ &- 2 \int \underline{\phi}_\ell \times \dot{\underline{u}}_2 dm_2 \cdot \underline{\Omega}_2 \\ &- \int \underline{\phi}_\ell \cdot \ddot{\underline{u}}_2 dm_2 = \int \underline{\phi}_\ell \cdot d\underline{f}_2 \end{aligned} \quad (4)$$

where $\dot{\underline{u}}_2$ and $\ddot{\underline{u}}_2$ are the time derivatives of \underline{u}_2 in the coordinate system $C_2x_2y_2z_2$. Here,

$$\underline{Q}_0 = \int \underline{\phi}_0 \cdot d\underline{f}_2 \quad (5)$$

contains contributions due to the external forces on B_2 . Also, if $\underline{\phi}_0$ is not compatible with the constraints, then \underline{Q}_0 will contain terms due to the constraint forces.

An equation for the rotational motion of B_2 is also required. To find one, we may cross $\underline{\rho}_2 + \underline{u}_2$ into Eq. (4) and integrate over the mass of B_2 to get

$$\begin{aligned} & - \int (\underline{\rho}_2 + \underline{u}_2) \times [(\underline{\rho}_2 + \underline{u}_2) \times \dot{\underline{\Omega}}_2] dm_2 - \underline{\Omega}_2 \times \int (\underline{\rho}_2 + \underline{u}_2) \times [(\underline{\rho}_2 + \underline{u}_2) \times \underline{\Omega}_2] dm_2 \\ & - 2 \int (\underline{\rho}_2 + \underline{u}_2) \times (\dot{\underline{u}}_2 \times \underline{\Omega}_2) dm_2 \\ & - \int (\underline{\rho}_2 + \underline{u}_2) \times \ddot{\underline{u}}_2 dm_2 \\ & = \int (\underline{\rho}_2 + \underline{u}_2) \times d\underline{f}_2 = \underline{M}_{2e} + \underline{M}_{2c} \end{aligned} \quad (6)$$

If B_2 is rigid, we can reduce Eq. (6) to

$$\underline{I}_2 \cdot \dot{\underline{\Omega}}_2 + \underline{\Omega}_2 \times \underline{I}_2 \cdot \underline{\Omega}_2 = \underline{M}_{2e} + \underline{M}_{2c} \quad (7)$$

We will consider that B_1 and B_2 are coupled together with a hinge which allows rotation of B_2 with respect to B_1 with three degrees of freedom. In such a case, we can consider $\underline{M}_{1c} = -\underline{M}_{2c}$ to be a function of state variables such as the components of $\underline{\Omega}_{2/1} = \underline{\Omega}_2 - \underline{\Omega}_1$ and the angles used to describe the relative rotational motion.

The constraint force $\underline{F}_{1c} = -\underline{F}_{2c}$ can be found by subtracting the first of Eqs. (1) from the second and simplifying, i.e.,

$$\underline{F}_{1c} = \frac{1}{2} (\underline{F}_{1e} - \underline{F}_{2e} - m_2 \underline{\ddot{R}}_2 + m_1 \underline{\ddot{R}}_1) \quad (8)$$

From Eq. (8) and Eqs. (1) we can obtain verifications of the well known fact that the center of mass of the system, C, moves according to

$$\underline{\ddot{R}} = \frac{1}{M} (\underline{F}_{1e} + \underline{F}_{2e}) \quad (9)$$

where $\underline{R} = (m_1 \underline{R}_1 + m_2 \underline{R}_2)/M$ and $M = m_1 + m_2$.

Equations (2), (4), (6) and (9) define the motion except for that of C_2 . One way to get an equation for the motion of C_2 is to write (see Fig. 2)

$$m_2 \underline{c}_2 + m_1 \underline{c}_1 = \underline{0} \quad (10)$$

and

$$\underline{c}_1 - \underline{c}_2 = -\underline{d}_1 - \underline{r}_2 \quad (11)$$

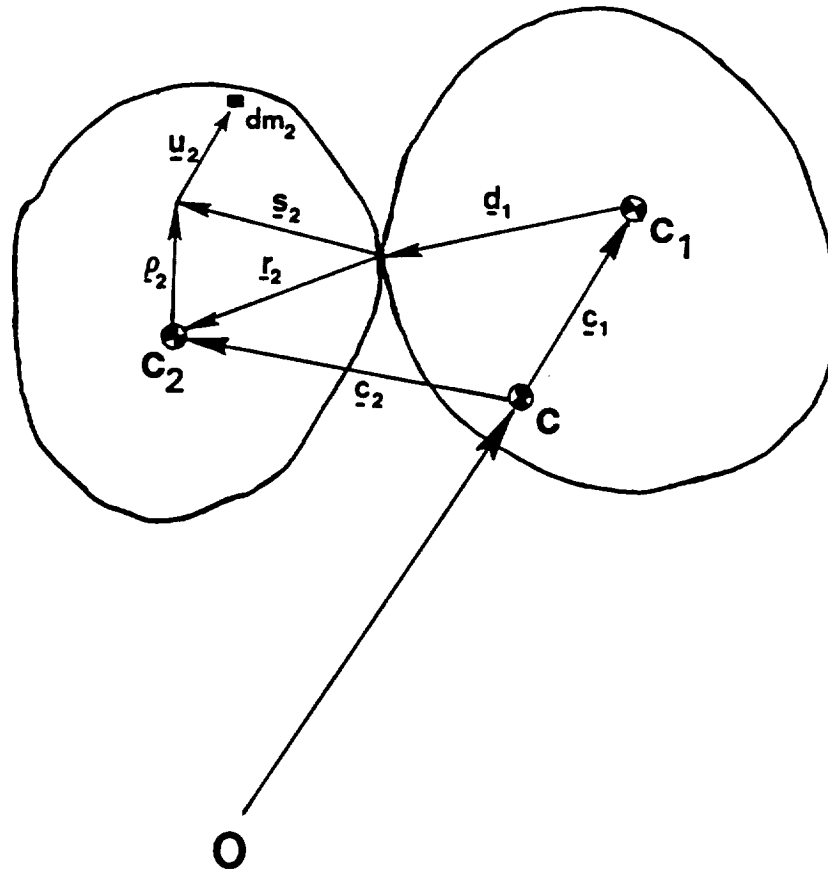


Fig. 2 Position vectors.

Then, since

$$\underline{r}_2 = \int (\underline{s}_2 + \underline{u}_2) dm_2 \quad (12)$$

and from Eq. (10),

$$\underline{c}_1 = - (m_2/m_1) \underline{c}_2, \quad (13)$$

we find that

$$M/m_1 \underline{c}_2 = \underline{d}_1 + \frac{1}{m_2} \int (\underline{s}_2 + \underline{u}_2) dm_2 \quad (14)$$

Our dependent variables are \underline{R} , $\dot{\underline{R}}$, $\underline{\Omega}_1$, $\underline{\Omega}_2$, the q_k , $k=1,2,\dots,n$, and suitable orientation variables for B_1 and the relative angular orientation of B_2 with respect to B_1 .

Lagrange's Method

An ad hoc procedure based directly on Newton's equations of motion is not as attractive to many analysts as one which includes a "recipe" for obtaining the desired result. For complex dynamical systems subject to holonomic constraints a modification of Lagrange's method often leads more easily, or at least more directly, to equations of motion which are first order in the derivatives of "quasi-coordinates." The quasi-coordinates are introduced by Whittaker by homogeneous differential forms in generalized coordinates. For our example, we can take as generalized coordinates θ_{1j} and θ_{2j} , $j=1,2,3$, Euler angles which define the attitude of B_1 with respect to the OXYZ system and the attitude of B_2 with respect to B_1 , respectively, the q_j , $j=1,2,\dots,n$, associated with the vibrational modes and the coordinates of the center of mass of B_1 and B_2 . Then, for convenience, we define

$$\underline{q}^* = (X_1 \ Y_1 \ Z_1 \ X_2 \ Y_2 \ Z_2 \ \theta_{11} \ \theta_{12} \ \theta_{13} \ \theta_{21} \ \theta_{22} \ \theta_{23} \ q_1 \ q_2 \ \dots \ q_n)^T \quad (15)$$

An $N=12 + n$ vector of quasi-coordinates, $\underline{\pi}$, can be defined by

$$d\underline{\pi} = A d\underline{q}^* \quad (16)$$

where A is a non-singular $N \times N$ matrix of functions of the q_k^* , $k=1,2,\dots,N$, and possibly the time.

In particular, the π_k can be chosen so that

$$\underline{\Omega}_1 = \begin{bmatrix} d\pi_7/dt \\ d\pi_8/dt \\ d\pi_9/dt \end{bmatrix} \quad (17)$$

and

$$\underline{\Omega}_2 = \begin{bmatrix} d\pi_{10}/dt \\ d\pi_{11}/dt \\ d\pi_{12}/dt \end{bmatrix} \quad (18)$$

The other π_k may be identical to the other original generalized coordinates, or we may take

$$\begin{aligned} d\pi_1/dt &= \dot{X}_1 \\ d\pi_2/dt &= \dot{Y}_1 \\ d\pi_3/dt &= \dot{Z}_1 \end{aligned} \quad (19)$$

and use Eqs. (10)-(14) to write the components of the vector $\underline{r} = x_{12} \hat{i}_1 + y_{12} \hat{j}_1 + z_{12} \hat{k}_1$ from C_1 to C_2 in terms of the Euler angles θ_{2j} and the q_k .

This equation would be a vector (3x1) holonomic constraint.

Lagrange's equations using the q_k^* are, in matrix form,

$$\frac{d}{dt} \left[\frac{\partial T}{\partial \dot{q}^*} \right] - \frac{\partial T}{\partial q^*} = \underline{Q}^T, \quad (20)$$

where T is the kinetic energy of the system and \underline{Q} is an N vector of generalized forces.

If we let

$$\underline{\Omega} = d\underline{\pi}/dt \quad (21)$$

and

$$\underline{B} = \underline{A}^{-1}, \quad (22)$$

then Eqs. (20) may be transformed into

$$\frac{d}{dt} \left[\frac{\partial \bar{T}}{\partial \underline{\Omega}} \right] + \left[\frac{\partial \bar{T}}{\partial \underline{\Omega}} \right] \underline{C}^T - \frac{\partial \bar{T}}{\partial q^*} \underline{D}^T = \underline{N}^T, \quad (23)$$

where \bar{T} is expressed using $\underline{\Omega}$ and \underline{q}^* , C and D are $N \times N$ matrices, and \underline{N} is a generalized force matrix. For a single rigid body of mass m_1 centroidal inertia dyadic \underline{I}_1 and center of mass velocity \underline{V}_1 ,

$$T = 1/2 \underline{\Omega}_1 \cdot \underline{I}_1 \cdot \underline{\Omega}_1 + 1/2 m_1 \underline{V}_1 \cdot \underline{V}_1. \quad (24)$$

Or, in matrix form, body-fixed basis, we have

$$T = 1/2 \underline{\Omega}_1^T \underline{I}_1 \underline{\Omega}_1 + 1/2 m_1 \underline{V}_1^T \underline{V}_1 \quad (25)$$

Thus, if we let $\underline{\Omega}^T = (\underline{\Omega}_1^T \underline{V}_1^T)$,

$$T = \frac{1}{2} \underline{\Omega}^T \begin{bmatrix} J & 0 \\ 0 & m_1 I \end{bmatrix} \underline{\Omega} \quad (26)$$

where I is the 3x3 identity matrix and J is the inertia matrix, then

$$\frac{\partial \bar{T}}{\partial \underline{\Omega}} = \underline{\Omega}^T \begin{bmatrix} J & 0 \\ 0 & m_1 I \end{bmatrix} \quad (27)$$

Note that $\partial \bar{T} / \partial \underline{\Omega}$ does not contain the q_k^* , explicitly, and

$$\frac{d}{dt} \left(\frac{\partial \bar{T}}{\partial \underline{\Omega}} \right)^T = \begin{bmatrix} J & 0 \\ 0 & m_1 I \end{bmatrix} \dot{\underline{\Omega}} \quad (28)$$

In this case, we have

$$C = \begin{bmatrix} \underline{\Omega}_1 \\ 0 \end{bmatrix} \quad (29)$$

and

$$\underline{N} = \begin{bmatrix} \underline{F} \\ \underline{M} \end{bmatrix} \quad (30)$$

For the two-body example, we get a matrix equation of the form

$$M \begin{bmatrix} \dot{\underline{v}}_{-1} \\ \dot{\underline{v}}_{-2} \\ \dot{\underline{\Omega}}_{-1} \\ \dot{\underline{\Omega}}_{-2} \\ \ddot{\underline{q}} \end{bmatrix} = \underline{N} . \quad (31)$$

Kane's Method

Kane's method for deriving equations of motion is based on the use of "partial velocities and partial angular velocities" (see Ref. 4, pp. 87-90 and Chapter Four) to extract from Newton's equations of motion a sufficient set of equations of motion in terms of chosen variables, the so-called "generalized speeds" and finding partial coordinates. Kane's procedure for a system of N particles with n degrees of freedom consists of (1) choosing generalized speeds, generalized velocities and partial angular velocities; (2) writing \underline{F}_i , the resultant force on each particle, m_i , in the system; (3) writing the acceleration, \underline{a}_i , $i=1,2,\dots,n$; (3) dotting each of the partial velocities (\underline{V}_r) in turn, into $\underline{F}_i - m_i \underline{a}_i = \underline{0}$ and summing over the particles. The basic equation used is

$$\underline{F}_r + \underline{F}_r^* = 0 \quad (r=1,\dots,n) , \quad (34)$$

where

$$\underline{F}_r = \sum_{i=1}^N \underline{V}_r \cdot \underline{R}_{-i} \quad (r=1,2,\dots,n) \quad (35)$$

are the generalized active forces and

$$\underline{F}_r^* = \sum_{i=1}^N \underline{V}_r \cdot (-m_i \underline{a}_i) \quad (r=1,2,\dots,n) \quad (36)$$

are the generalized inertia forces.

For our two-body example, we may use the equations,

$$\underline{\Omega}_{-l} = \Omega_{l1} \hat{i}_{-l} + \Omega_{l2} \hat{j}_{-l} + \Omega_{l3} \hat{k}_{-l} \quad , \quad l=1,2, \quad (37)$$

$$\underline{V} = \dot{X} \hat{n}_1 + \dot{Y} \hat{n}_2 + \dot{Z} \hat{n}_3 \quad (38)$$

and

$$\dot{\underline{u}}_2 = \sum_{k=1}^n \phi_{k1} \dot{q}_k + \underline{\Omega}_2 \times \sum_{k=1}^n \phi_{k2} q_k, \quad (39)$$

where

$$\underline{\phi}_k = \phi_{k1} \hat{i}_2 + \phi_{k2} \hat{j}_2 + \phi_{k3} \hat{k}_2, \quad (40)$$

to identify the partial velocities \hat{n}_r , $r=1,2,3$, of C; partial angular velocities $\hat{i}_\ell, \hat{j}_\ell, \hat{k}_\ell$, $\ell=1,2$, of Body ℓ ; and the partial velocities $\phi_{k1} \hat{i}_2$, $\phi_{k2} \hat{j}_2$ and $\phi_{k3} \hat{k}_2$, $k=1,2,\dots,n$, of the elements of B_2 due to deformation.

By writing the acceleration of an element in each body, as we did in the Newton-Euler method, we can obtain the \underline{V}_r to substitute into Eq. (36). The equations are basically the same in form as those found using the Newton-Euler method. However, the procedure is well defined rather than ad hoc.

COMPUTER CODES

Four digital computer programs for simulating multi-body dynamics have been used to obtain the results which follow. There is a model-specific program written to simulate the system shown in Fig. 3. The three-body satellite (actually a sounding rocket payload¹²) consists of a rigid body to which are attached two booms carrying sphere. Equations of motion¹² were obtained directly from Newton's laws and programmed in a special code.

A second program¹⁰ called MBODY was developed to model a chain of rigid bodies. The equations for this more general model were derived using Lagrange's equation with quasi-coordinates.

TREETOPS, the third program to simulate example systems, is based on equations of motion obtained by applying Kane's method. The latest version, which apparently is still in the development stage, contains rather general models of flexible bodies interconnected in a tree topology and of active control elements.

TREETOPS is intended to be useful control system analysis tool.

A fourth program, called FMBODY, has been developed along the same lines as MBODY to handle flexible as well as rigid bodies. This code has not been fully checked out, but some results from it are included in the next section.

EXAMPLES

Simulation results for several example spacecraft models have been generated using MBODY, TREETOPS, the model-specific code and FMBODY. Results for three spacecraft models are presented here.

The first model, depicted in Fig. 3, consists of a rigid body and two rigid booms. Physical data for the model, which is intended to represent the SPEAR-1 sounding rocket payload,¹² are given in Table 1.

Table 1. Physical Characteristics of Model 1.

1. Main Body

Mass: 300 kg

Moments of Inertia:

$$I_{xx} = 100 \text{ kg-m}^2$$

$$I_{yy} = 400 \text{ kg-m}^2$$

$$I_{zz} = 400 \text{ kg-m}^2$$

Distance from Boom Attachment Point to
Center of Mass of Main Body: 6 m

2. Booms

Length: 2 m

Moments of Inertia (Rods Neglected):

$$I_{xx} = I_{yy} = I_{zz} : 10 \text{ kg-m}^2$$

Table 2 gives the initial conditions for two cases in which the booms rotate from positions parallel to the main body's axis of symmetry toward orientations in which booms are perpendicular to the symmetry axis. In both cases, the system is initially spinning about its symmetry axis and the external torque is zero throughout the motion. In Case I, the deployment is symmetric, since the booms initially have equal and opposite angular velocities with respect to the main body. In Case II, the booms start with different magnitude relative angular rates.

Figure 4 shows the spin rate (Ω_{11}) time history for Case I. Although it is not representative of an actual deployment, the booms rotate through approximately 190 deg in 5 s. The results for the SPECIAL PROGRAM and MBODY are in exact agreement. The Ω_{11} from TREETOPS begins to disagree with the other results at around 2.5 s, but the values at $t = 5$ s, all look the same.

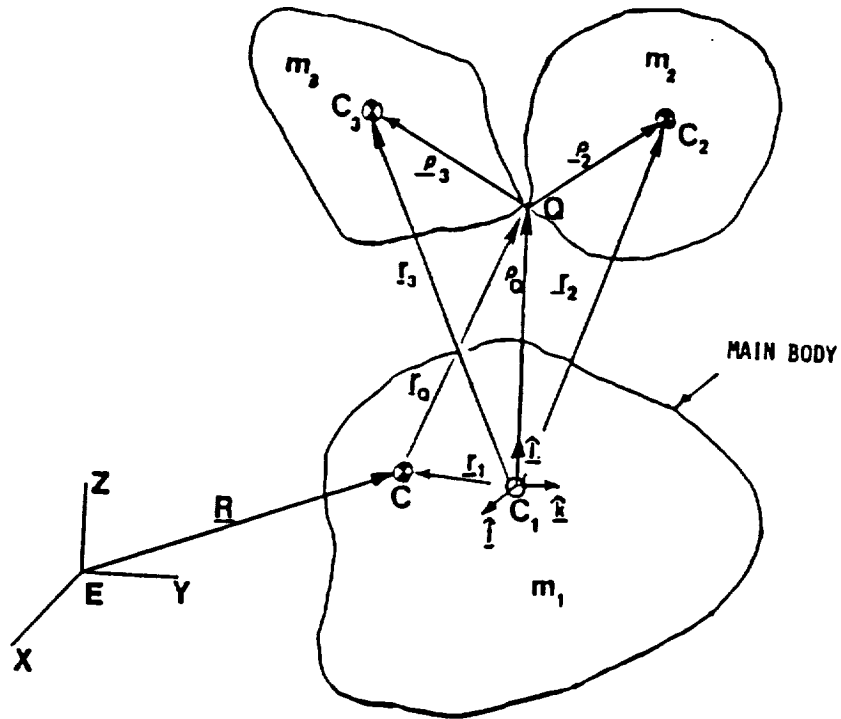


Fig. 3 SPEAR-1 rigid body model.

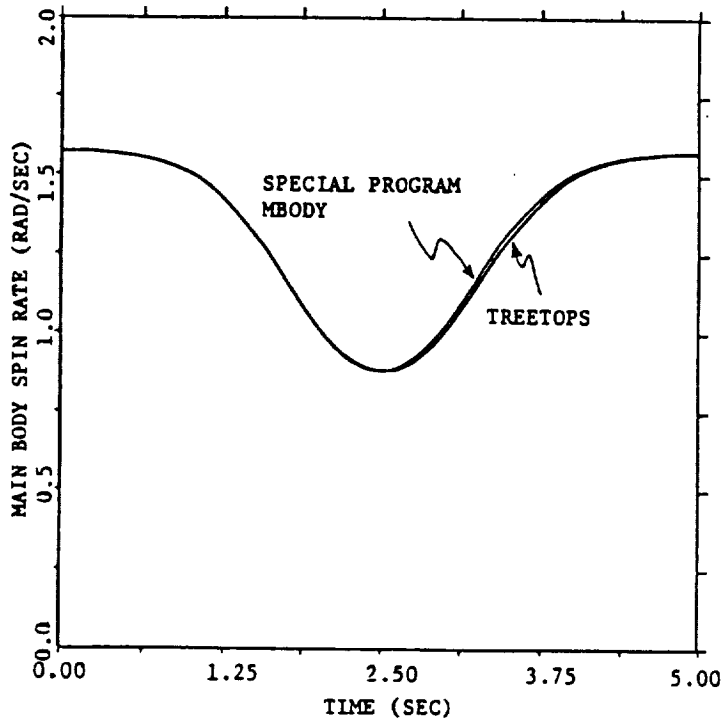


Fig. 4. Spin rate time history (Case I).

The same characteristic is seen in the deployment rate time histories shown in Fig. 5. The small differences in the TREETOPS results are reflected in

Table 2. Initial Conditions for Example 1 Results

CASE I: Main Body Spinning/Symmetric Deployment of Booms

$$\underline{\Omega}_1(0) = (90 \quad 0 \quad 0)^T \text{ deg/sec}$$

$$\Omega_{2/1}(0) = (0 \quad 0 \quad 10)^T \text{ deg/sec}$$

$$\Omega_{3/1}(0) = (0 \quad 0 \quad -10)^T \text{ deg/sec}$$

CASE II: Main Body Spinning Asymmetric Deployment of Booms

$$\underline{\Omega}_1(0) = (90 \quad 0 \quad 0)^T \text{ deg/sec}$$

$$\Omega_{2/1}(0) = (0 \quad 0 \quad 10)^T \text{ deg/sec}$$

$$\Omega_{3/1}(0) = (0 \quad 0 \quad -5)^T \text{ deg/sec}$$

the plot of H, the magnitude of the angular momentum of the system about its center of mass, versus time shown in Fig. 6. The reasons for the small variations in H have not been determined, but it is conjectured that they are due to lack of numerical precision or the way in which constraints are enforced.

Case II is an asymmetric deployment of the booms. The results for spin rate (Ω_{11}) are similar (see Figs. 7 and 8) to those for Case I and again there is some difference in the results from MBODY and the Special Program and TREETOPS. The difference is more evident in the results for H given in Fig. 9.

Example 2

The model for the second example is a uniform flexible beam to which two rigid bodies are coupled. Figure 10 shows the geometry of the system and Table 3 gives the values of system constants used to obtain the numerical results. This model is intended to represent a simple multi-body pointing spacecraft. Bodies B_2 and B_3 are those which are to be pointed. The base body, B_1 , is flexible and, for the purposes of this example is uncontrolled. Only two mode shapes were used in this example. The motion of the system is described by the inertial position of the center of mass of B_1 , the attitude of B_1 (θ_{1j} , $j=1,2,3$), the attitudes of B_2 and B_3 with respect to B_1 (θ_{2j} and θ_{3j} , $j=1,2,3$) and the generalized coordinates q_k , $k=1,2,3,4$.

The system is initially quiescent. At $t=0$, torques are applied to B_2 and B_3 about axes parallel to the y -axis and passing through the points of attachment of B_2 and B_3 , respectively.

The time histories of the angles θ_{j3} , $j=1,2,3$, are shown in Fig. 11. Figure 12 shows the time history of the two non-zero generalized coordinates q_{11} and q_{12} , for deformation in the x -direction. As expected, the base body rotated clockwise around the y -axis. It also translated in the z -direction.

Results from TREETOPS for this example have not been obtained as of this writing since a new version of TREETOPS was installed recently on a VAX 785 at Auburn University and a few problems have not been resolved. Additional results will be available soon.

Table 3. Physical Characteristics of Model for Example 2.

Body 1

Mass: 500 kg

Moments of Inertia:

$$I_{xx} = 4333.33 \text{ kg-m}^2$$

$$I_{yy} = 4333.33 \text{ kg-m}^2$$

$$I_{zz} = 333.33 \text{ kg-m}^2$$

Stiffness Characteristics:

$$EI = 100 \text{ N-m}^2 ,$$

Uniform

Dimensions:

$$a = b = 2 \text{ m}, c = 10 \text{ m}$$

$$d = 1 \text{ m}, h = 2 \text{ m}$$

$$d_1 = d_2 = 1 \text{ m}$$

Bodies 2 and 3

Mass: 100 kg

Moments of Inertia:

$$I_{xx} = 12.5 \text{ kg-m}^2$$

$$I_{yy} = 39.6 \text{ kg-m}^2$$

$$I_{zz} = 39.6 \text{ kg-m}^2$$

Dimensions:

$$d = 1 \text{ m}, h = 2 \text{ m}$$

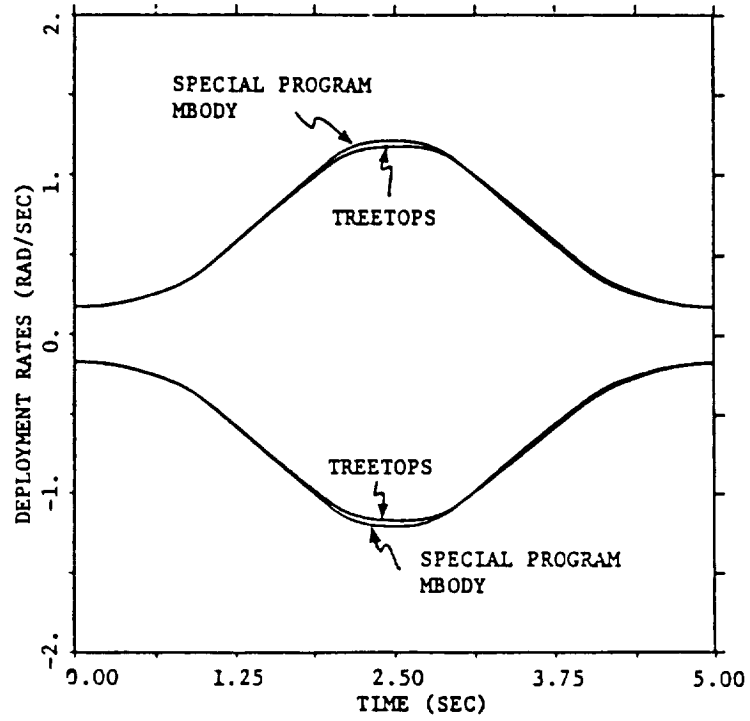


Fig. 5 Deployment rate time history (Case I).

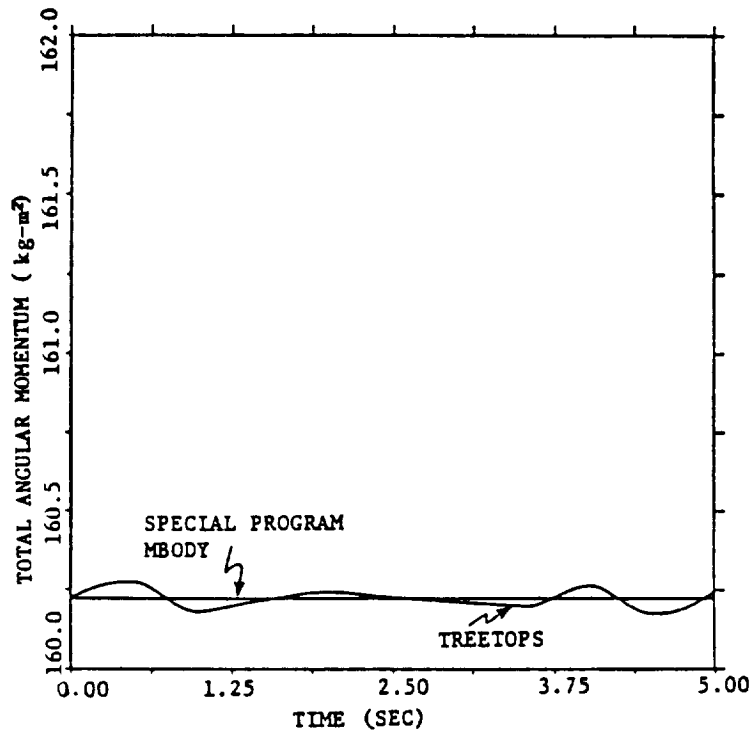


Fig. 6 Magnitude of the total angular momentum (Case I).

52

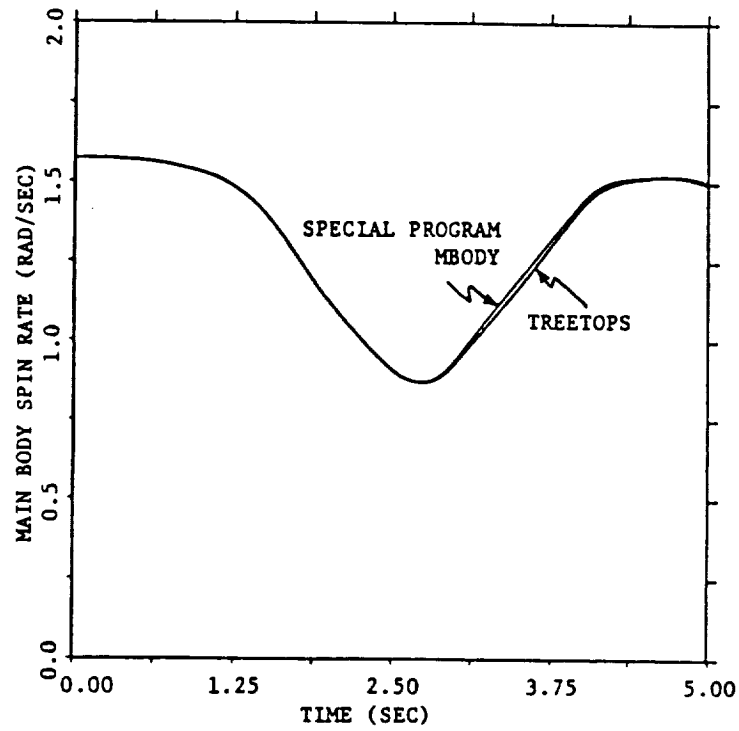


Fig. 7 Spin rate time history (Case II).

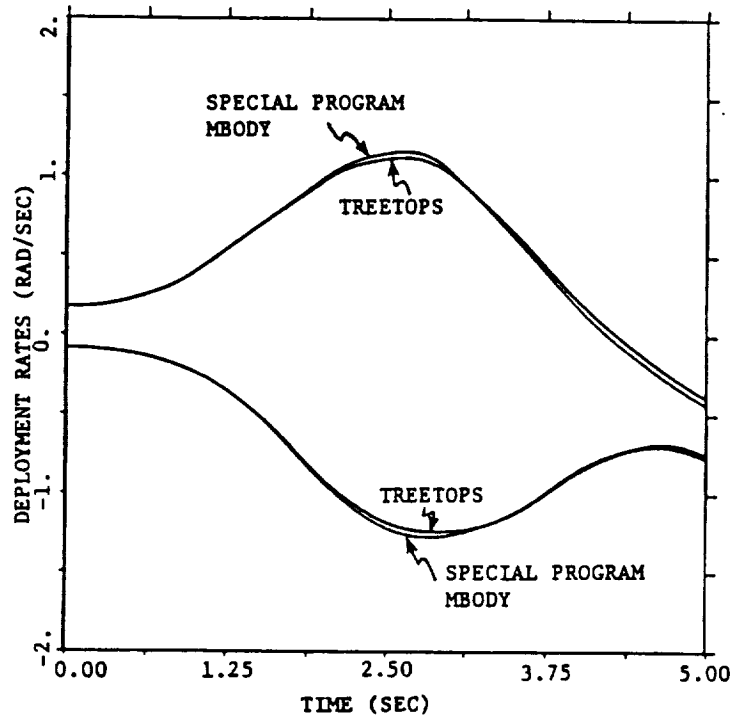


Fig. 8 Deployment rate time history (Case II).

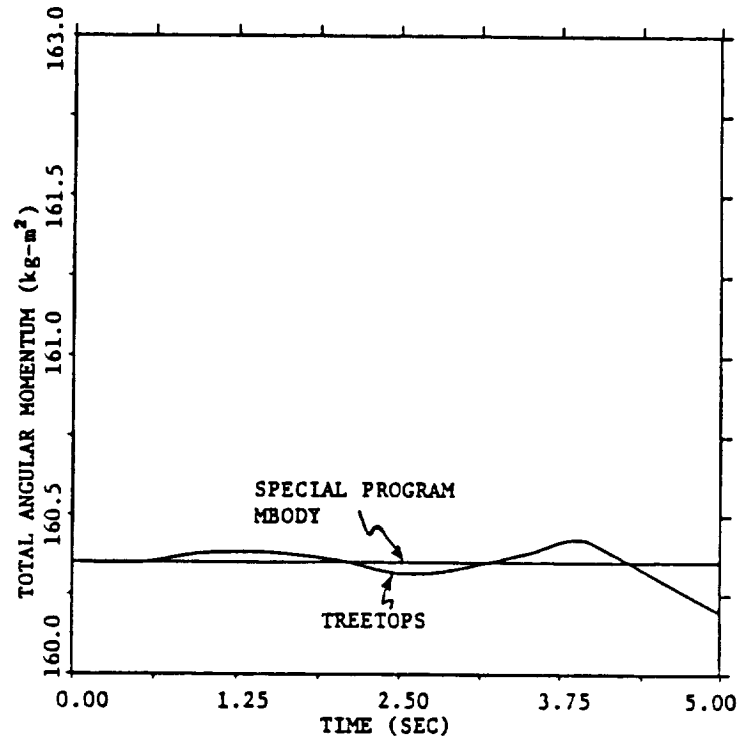


Fig. 9 Magnitude of the total angular momentum (Case II).

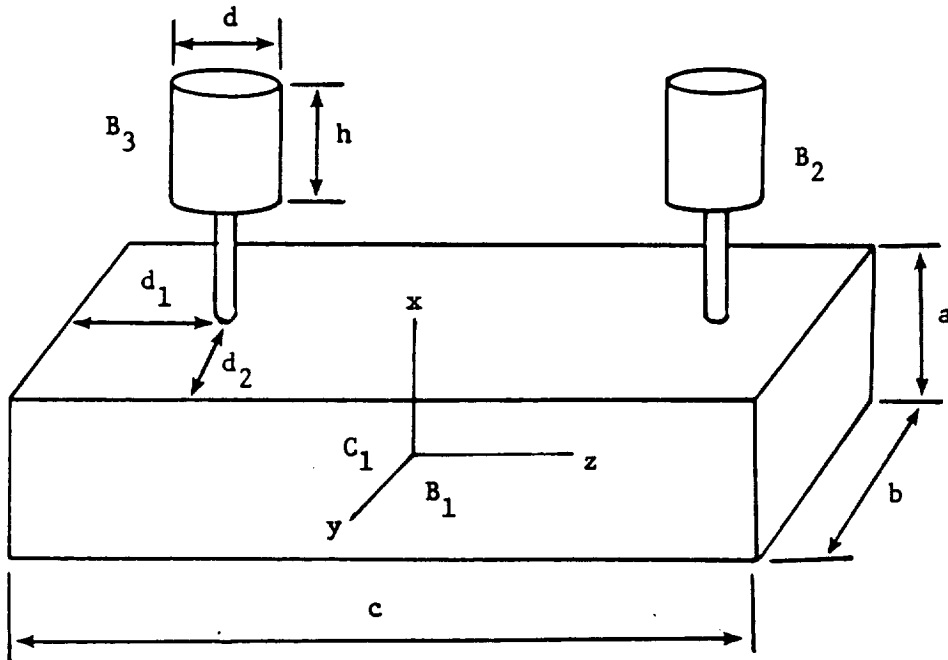


Fig. 10 Model for a multi-body pointing satellite.

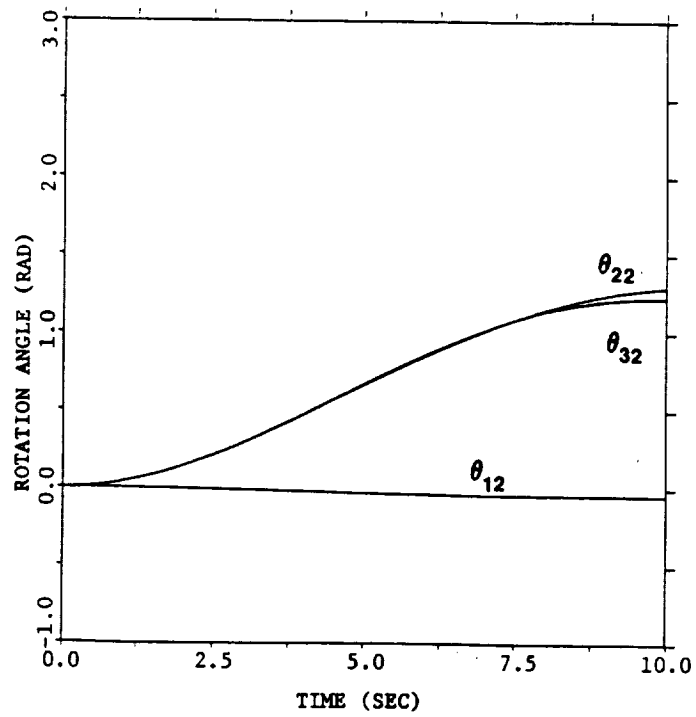


Fig. 11 Attitude angles, bodies 1, 2 and 3.

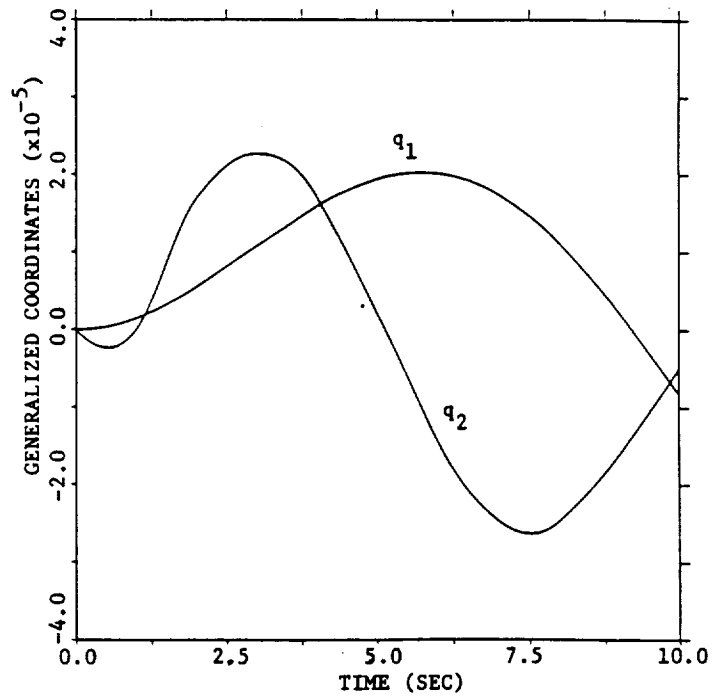


Fig. 12 Generalized coordinates associated with the modes.

CONCLUSIONS

Methods for deriving equations which mathematically model multi-body pointing spacecraft have been discussed. None of the three methods considered appear clearly superior from both the aspects of understanding the system and generating equations.

Results obtained using the model-specific code, based on Newton-Euler equations, and MBODY, based on equations derived using Lagrange's equations and quasi-coordinates, agree to within the numerical precision used. Thus, both of these programs are probably correct. The TREETOPS results differ slightly, but probably not significantly, from those obtained from the model specific code and MBODY. The reason for a non-constant computed angular momentum magnitude may lie in the method for computing the angular momentum. Addition of checking needs to be done to determine the exact course.

For the multi-body pointing spacecraft example, we obtained, and have presented here, results from a program, FMBODY, based on equations derived using Lagrange's equations with quasi-coordinates and flexible body model data. We were not able by the time this paper was submitted to get results from a new, updated TREETOPS program. However, it is expected that we will find that TREETOPS and FMBODY results agree and that TREETOPS requires less CPU time.

REFERENCES

1. Bracewell, R. N., and Garriott, O. K., "Rotation of Artificial Earth Satellites, Nature, Vol. 182, 1958, pp. 760-762.
2. Likins, P. W., "Analytical Dynamics and Nonrigid Spacecraft Simulation," Technical Report 32-1593, Jet Propulsion Laboratory, Pasadena, California, July 15, 1974.
3. Hooker, W. W., and Margulies, G., "The Dynamical Attitude Equations of an n-Body Satellite," Journal of the Astronautical Sciences, Vol. 12, No. 4, 1965, pp. 123-128.
4. Kane, T. R., Likins, P. W., and Levinson, D. A., Spacecraft Dynamics, McGraw-Hill, Inc., New York, 1983.
5. Cochran, J. E. Jr. and Shu, P. H., "Effects of Energy Addition and Dissipation on Dual-Spin Spacecraft Attitude Motion," Journal of Guidance, Control and Dynamics, Vol. 6, No. 5, 1983, pp. 368-372.
6. Modi, V. J., and Shrivastava, S. K., "Coupled Librational Motion of an Axi-Symmetric Satellite in a Circular Orbit," Aeronautical Journal, Vol. 73, No. 704, 1969, pp. 674-680.
7. Fleischer, G. E., and Likins, P. W., "Attitude Dynamics Simulation Subroutines for Systems of Hinge-Connected Rigid Bodies," Technical Report 32-1592, Jet Propulsion Laboratory, Pasadena, California, May 1, 1974.

8. "TREETOPS, User's Manual," Honeywell, Inc. (Space & Strategic Avionics Division), September 1988 (Preliminary Version).
9. Bodley, C. S., et al., "A Digital Computer Program for the Dynamic Interaction Simulation of Controls and Structure (DISCOS)," NASA Technical Paper No. 1219, 1978.
10. Whittaker, E. T., A Treatise on the Analytical Dynamics of Particles and Rigid Bodies, Fourth Edition, Cambridge University Press, London, 1944, pp. 40-44.
11. No, T. S., "Dynamic Simulation of Multi-Body Systems," Master of Science Thesis, Auburn University, Auburn, Alabama, March 1989.
12. Cochran, J. E., Jr., Fitz-Coy, N. G., and No, T. S., "Dynamics and Control of Large Space Platforms and Small Experimental Payloads," SPIE Paper 871, Presented at the IS&T Space Structures, Power and Power conditioning conference, Los Angeles, California, January 11-13, 1988.

FLIGHT MECHANICS/ESTIMATION THEORY SYMPOSIUM

SESSION 2

ORBIT AND ATTITUDE DETERMINATION RESULTS
DURING LAUNCH SUPPORT OPERATIONS FOR SBS-5

K. R. Hartman and P. J. Iano
MCI Telecommunications Corporation

ABSTRACT

Presented are orbit and attitude determination results from the launch of Satellite Business Systems (SBS)-5 satellite on September 8, 1988 by Ariane-space. SBS-5 is a Hughes Aircraft Corporation HS-376 spin-stabilized spacecraft. The launch vehicle injected the spacecraft into a low inclination transfer orbit. Apogee motor firing (AMF) attitude was achieved with trim maneuvers. An apogee kick motor placed the spacecraft into drift orbit. Postburn, reorientation and spindown maneuvers were performed during the next 25 hours. The spacecraft was on-station 19 days later.

The orbit and attitude were determined by both an extended Kalman filter and a weighted least squares batch processor. Although the orbit inclination was low and the launch was near equinox, post-AMF analysis indicated an attitude declination error of 0.034 degree, resulting in a saving of 8.5 pounds of fuel. The AMF velocity error was 0.4 percent below nominal.

The post-AMF drift rate was determined with the filter only 2.5 hours after motor firing. The filter was used to monitor and retarget the reorientation to orbit normal in real-time.

1. INTRODUCTION

SBS-5 is an HS-376 spin-stabilized communications spacecraft built by Hughes Aircraft Corporation (Reference 1). It is designed to provide voice, video, and data traffic to the United States on 14 channels in the Ku-band frequency, i.e. in the 14/12 GHz range.

Figure 1 shows an exploded view of the spacecraft components. The spacecraft remains in the stowed position until drift orbit, when the communications platform is despun and the solar panel is extended. The main sections of the spacecraft are the spinning rotor and the despun Earth-oriented platform.

The reaction control subsystem (RCS), which uses hydrazine propellant, is located on the spinning rotor. It consists of two independent systems joined by an interconnect manifold. Each system contains two conispherical tanks, one radial, and one axial thruster. A Thiokol Star 30 apogee kick motor (AKM) provides the impulse to inject the spacecraft into drift orbit.

The attitude control subsystem (ACS) provides velocity control, spin-axis attitude control and antenna pointing control. Data for attitude determination are provided by spinning Sun and Earth sensors. A thruster actuated active nutation control (ANC) subsystem is used after apogee motor firing to dampen nutation. After the communications reflector is deployed, the despin active nutation damping electronics (DANDE) controls nutation with despin motor torques. Accelerometers in the rotor sense nutation for both ANC and DANDE nutation damping. Figure 2 shows the ACS functional block diagram (Reference 1).

Telemetry, command/track, and ranging subsystems provide command capability and spacecraft information. The slant range from the ground station to the spacecraft is determined by a multiple-tone ranging system.

The Flight Dynamics group and Mission Control Facility (MCF) are located at the Clarksburg, Maryland ground station. This facility is used for tracking, telemetry and commanding (TT&C) support and contains the real-time computers for data collection and storage. In addition, the following ground stations provided support: Castle Rock, Colorado; Allan Park, Canada; Perth, Australia; Sydney, Australia; and Betzdorf, Luxembourg.

The software used to support the SBS-5 mission was written by the Flight Dynamics Department at Telesat Canada (Reference 2). The software system was used to support several Telesat missions and was modified for the SBS mission. Two Hewlett-Packard (HP)-1000 minicomputers were used as primary and backup systems for the mission. Telesat personnel also provided support during the SBS-5 mission.

SBS-5 was assigned a longitude of 123 degrees West by the Federal Communications Commission (FCC). Prelaunch mission analysis was conducted to optimize the transfer orbit and drift orbit trajectories based on a 10-year mission lifetime requirement.

SBS-5 and the GSTAR-3 spacecraft of GTE Spacenet Corporation were copassengers on the Ariane 3 launch vehicle. The launch site was Kourou, French Guiana. A combined launch window is shown in Figure 3. The SBS-5 constraints are based on Sun angle and eclipse duration restrictions.

The spacecraft sensors provide three basic measurements: Sun angle, Earth chord, and separation data, i.e. the angle between the spin axis-Sun plane and the spin axis-Earth plane. Using only Sun angle and Earth chord measurements, attitude determination errors place stringent constraints on the launch window for low inclination orbits during periods near the equinoxes. However, the spin-axis attitude is sensitive to separation angle measurements except when the Earth, the spacecraft, and the Sun are colinear. Since colinearity occurs at only one instance in the transfer orbit, and sensor data are collected for approximately two hours during each apogee pass, separation angle measurements restore attitude determination accuracy during periods near equinox (Reference 3).

Liftoff occurred at the opening of the launch window (23:00 GMT), resulting in a nominal separation time of 23:20:52 GMT. The separation Sun angle of 72.1 degrees and spin rate of 6.94 rpm were near the nominal predicted values of 70.0 degrees and 7.0 rpm respectively. The postlaunch orbit vector delivered by Ariane showed the semimajor axis 2.6-sigma below nominal. After processing tracking data through the first and second revolutions (revs), the semimajor axis was determined to be 4.8-sigma high.

A spinup maneuver was performed during the first rev to increase the spin rate to 50 rpm. Thruster functionals and ANC test firings were performed. The first attitude trim maneuver was postponed until the fourth rev due to the uncertainty in the orbit and attitude state. An attitude touchup was necessary before the apogee motor firing (AMF) on rev 7.

On September 11 at 20:17:39 GMT, the apogee motor was fired at a longitude of 150.5 degrees West. The orbit solution from the Kalman filter 2.5 hours after AMF showed that the orbital plane was achieved, but the drift rate was 3 degrees per day East instead of the nominal 1 degree per day East. This indicated a 0.4-percent underperformance of the apogee motor with negligible attitude pointing errors. The drift orbit maneuver sequence was redesigned.

At the perigee following AMF, a postburn maneuver and a reorientation (reor) maneuver to near orbit normal attitude were performed. The attitude target was planned to account for the precession expected during the spindown maneuver. The reor was monitored and retargeted in real-time with the Kalman filter. At the next apogee, the spindown maneuver was performed to reduce the spin rate to 37.4 rpm in preparation for despinning the communications platform. The spin rate increased to 55 rpm as a result of deployment activities which began on September 13.

On September 18 a series of four maneuvers were executed to reduce drift rate. Three additional orbit maneuvers were performed on September 26 and 27 to stop the drift rate at a longitude of 123 degrees West. Stationkeeping support began on September 27. The first North-South maneuver was executed on October 12.

2. MODELING

Predicting the orbital and attitude motion of a spacecraft during the transfer orbit is very complicated. This is due to the many perturbing forces on the spacecraft such as the Earth's geopotential field, atmospheric drag, and lunar and solar gravity. These forces must be accounted for to accurately predict the motion of the spacecraft. An Earth sensor model is required to predict

the output as seen from the spacecraft Earth sensors.

2.1 ORBIT DETERMINATION

An extended Kalman filter and weighted least squares batch processor were both used for orbit determination during launch support (Reference 2). The Mission Kalman Filter (MKAL) Program provided real-time orbit estimation, tracking data monitoring, and automatic deweighting of less accurate or "bad" data samples. The effects of drag at perigee on the orbit are predicted and the state covariances are corrupted appropriately. The filter equations are augmented with considered parameters, i.e. station location and range bias uncertainties to insure stability (Reference 4). The filter estimates the spacecraft position and velocity vectors, and azimuth and elevation biases. When a set of observations are averaged, the orbit state vector and covariance matrix are advanced to the average time of the observations. The data are filtered using the extended Kalman filter algorithm. The method produces a state vector which minimizes the weighted mean square residuals between the model and the measurements. The filter adjusts the covariances to account for modeling, propagation, and maneuver performance errors.

The weighted least squares algorithm with a priori statistics was used to minimize the sum of the square of the weighted residuals between actual and computed observations, while simultaneously constraining the state to satisfy an a priori state within a specified uncertainty (Reference 2). The data are averaged to the mid-interval of the observations. The mean and the root mean square are computed for each residual type. Azimuth and elevation biases for each station were adjusted with this information. Range biases for Allan Park and Perth were set to zero for the mission. Range biases for Castle Rock and Clarksburg were set to values estimated by orbit determination of on-station spacecraft.

The spacecraft position vector was propagated by numerical integration of the Encke formulation of the equations of motion. A fourth order Runge-Kutta-Gill integrator was used with variable stepsize. Stepsizes of 54 seconds at perigee, and 360 seconds at apogee, were used during transfer orbit. A stepsize of approximately 35 minutes was used during drift orbit.

The following forces were modeled: geopotential, lunar and solar gravity, and atmospheric drag. Solar radiation pressure was modeled during drift orbit. The Goddard Earth Model (GEM)-10 was used for nonspherical gravitational perturbations. The geopotential order 6 was used during the transfer orbit. Accelerations due to lunar and solar forces were computed via Encke's method. Drag acceleration was modeled analytically as outlined in Reference 5. The Jacchia-Roberts atmospheric density model was used. Lunar and solar positions were obtained from a Jet Propulsion Laboratory ephemerides tape.

The tracking data rates were as follows: The Perth and Allan Park ground stations sent 25 azimuth, elevation, and range measurements within 25 seconds; Castle Rock sent six azimuth and elevation measurements within 30 seconds, followed by 25 range tone measurements in 25 seconds; Clarksburg sent 5 range tone measurements in 5 seconds (only during the drift orbit).

2.1.1 INITIAL ASSUMPTIONS

The Ariane 3 launch vehicle injects the spacecraft into a transfer orbit with

a perigee height of 200 kilometers, an apogee height of 36,206 kilometers, and an inclination of 7 degrees. After transfer orbit injection, the attitude and roll control system (SCAR) of the Ariane vehicle begins orientation maneuvers required before separation of the GSTAR-3 and SBS-5 satellites. Separation of SBS-5 occurs about four minutes after injection.

The prelaunch nominal separation state (at injection time) was as follows:

Epoch (GMT)	- 88:252:23:16:47:241	<u>1-sigma</u>
	- September 8, 1988	
Semimajor Axis (km)	- 24554.0830	20.231
Eccentricity	- 0.73210339	0.226E-03
Inclination (deg)	- 6.998977	0.173E-01
Mean Anomaly (deg)	- 0.536041	0.157E-02
Argument of Perigee (deg)	- 177.977117	0.141
Node (deg)	- 146.985053	0.141
Mass (kg)	- 1238.9741	
Spin (rpm)	- 7.0	
RMOI (kg * m**2)	- 500.25623	

This state was used for prelaunch mission analysis and for generating nominal station prediction information. It corresponds to a seventh rev apogee bias of approximately 171.6 kilometers. A correlation matrix in spherical coordinates at spacecraft injection/separation was delivered by Ariane before launch. It contained expected launch vehicle dispersions.

2.1.2 ESTIMATION OF ORBITAL DRAG

Prelaunch analysis was conducted to develop a procedure for estimating the effect of atmospheric drag on the orbit (Reference 6). Because the spacecraft attitude was altered only slightly during transfer orbit, the angle between the spin axis and the velocity vector of the spacecraft relative to the atmosphere was the same each perigee. It was not possible to distinguish between the axial and normal drag force components, so the drag coefficients were equated.

The perigee drag coefficients were estimated with two successive revs of tracking data to independently compute the apogee height of the second of the two revs. Due to perigee drag, the apogee height computed with the second of the two revs of data should be lower than the apogee height computed with the first of the two revs. The difference in the computed apogee heights was expected to vary from a minimum of 540 meters, corresponding to drag coefficients of 1, to a maximum of 2.7 kilometers, corresponding to drag coefficients of 5.

2.2 ATTITUDE DETERMINATION

The MKAL Program was used for real-time attitude estimation and reorientation maneuver retargeting. The Mission Attitude Determination (MAD) Program was used for weighted least squares batch processing of data (Reference 2).

The attitude data were provided by the spacecraft attitude data processor (ADP), which makes time interval measurements (t-times), between occurrences of real-time reference pulses. Ten measurements made up one set of t-times, which were received approximately every 15 seconds. These pulse code modulation (PCM) data were then converted to the types needed for attitude determina-

tion. The five data types were: psi data (the spin angle separating the mid-points of the psi and psi-2 Sun pulses); north and south Earth sensor half-chord widths; and north and south Earth separation data (the angles between the psi pulse and the center of the north or south Earth sensor pulse).

Five sets of observations are averaged to the midpoint of the interval. The attitude state vector included the phi and theta angles of the spin-axis attitude vector, psi bias, Earth sensor cant angle biases, and Sun/Earth sensor separation biases. Earth sensor chord width biases were determined with the MAD Program and applied to the observation model of the filter. During large reor maneuvers, the maneuver precession rate and force centroid error are also included in the filter state vector. (The force centroid error is the difference between the desired and actual thrust direction.)

The Phi-Theta coordinate system (Reference 2) is shown in Figure 4. Theta is the angle between the planes formed by the Sun vector/Earth spin axis and the Sun vector/spacecraft spin-axis vector. Theta is positive if measured clockwise looking along the Sun vector. Phi is the angle measured from the spacecraft spin axis to the Sun vector.

Earth sensor scanning and delay models were included in the software (Reference 2). Since the Earth sensors have a 1.5-degree field of view that is diamond shaped, a point source cannot be used to accurately predict the Earth chord width. The scanning model reproduces the discrete digital waveform of the Earth sensor and uses a fixed threshold level of 31 percent to estimate the Earth chord width. Due to thermal capacitance and AC coupling in the Earth sensor amplifiers, the actual sensor output will be distorted (Reference 2). The delay model was developed to account for this effect.

2.2.1 INITIAL ASSUMPTIONS

SBS-5 was injected with an orientation near AMF attitude. This was based on an average AMF attitude over the Ariane two-month launch period. The Ariane 3-sigma error on this injection attitude was 2.8 degrees, with a contractual agreement that it be within six degrees. The prelaunch nominal attitude state was as follows:

Epoch (GMT)	- 88:252:23:16:47:241	
Spin-axis declination (deg)	- 236.428	<u>1-sigma</u> 2.00
Spin-axis right ascension (deg)	- -8.3495	2.00

The nominal AMF target attitude had a spin-axis right ascension of 238.148 degrees and declination of -7.777 degrees. An objective of this mission was to target the post-AMF plane so that the inclination was less than 0.05 degree on October 15, 1988, without North-South maneuvers.

The pre-AMF inclination was 7.0 degrees and the right ascension of the ascending node was 146.98 degrees. The target post-AMF inclination was 0.16 degree and the node was 287.57 degrees. The target plane was biased to allow for the plane change effects of the reorientation maneuver to orbit normal and the spindown maneuver.

2.2.2 ESTIMATION OF ATTITUDE PRECESSION DUE TO PERIGEE DRAG

The torque due to atmospheric drag is in the direction of $\hat{A} \times \vec{V}$, where \vec{V} is the velocity of the spacecraft with respect to the atmosphere, and \hat{A} is the spin-axis vector. At perigee, \vec{V} is normal to the spacecraft position vector \vec{R} , and \hat{A} is nearly normal to \vec{R} . Therefore, $\hat{A} \times \vec{V}$ is nearly in the direction of \vec{R} . Since the inclination of the spacecraft orbit is low, \vec{R} is directed primarily in right ascension. The change in right ascension due to perigee precession was estimated from the measured change in the Sun angle, ϕ , during perigee passage. The Sun angle is estimated from the measured rotation angle, ψ , between the midpoints of the two Sun pulses from the spacecraft Sun sensor.

3. RESULTS

A summary of both weighted least squares and real-time orbit determination results are shown in Table 1. A summary of both weighted least squares and real-time attitude determination results are shown in Table 2.

3.1 TRANSFER ORBIT

3.1.1 SEPARATION STATE VECTOR DETERMINATION

Liftoff of the Ariane 3 occurred at the opening of the September 8th launch window (23:00 GMT), resulting in a nominal SBS-5 separation time of 23:20:52 GMT.

Ariane delivered a transfer orbit solution about 23:46 GMT. It was obvious soon after launch that the SBS-5 transfer orbit was not nominal. The semimajor axis of a weighted least squares (WLS) solution was 96 kilometers above the Ariane nominal, whereas the Ariane 3-sigma error was only 61 kilometers. The nominal seventh rev apogee bias was 171.6 kilometers, whereas the WLS apogee bias was 367.1 kilometers (Table 1).

Ariane delivered an attitude solution shortly after launch. This is shown in Table 2 as the GSFC/ARIANE solution. It was 2.2 degrees from the nominal and within the Ariane 3-sigma error. However, the spacecraft attitude could only be verified in the ψ direction. The ADP on-board the spacecraft cannot send valid data at spin rates below 29 rpm. Frequency modulated (FM) real-time attitude sensor data were used to calculate a Sun sensor ψ to ψ period of 8642 milliseconds, corresponding to a spin rate of 6.9 rpm. The ϕ angle of 72.1 degrees was derived from these ψ data, and was identical to the Ariane delivery.

The MKAL Program diverged due to inaccurate starting conditions. The filter was restarted with the WLS solution. At the start of rev 2, the filter diverged again, and it was restarted with a WLS solution based on tracking data just from rev 2. The attitude covariance was reinitialized. This shows the importance of an accurate state vector and covariance matrix for starting the filter.

3.1.2 ORBITAL DRAG ESTIMATION

Since the first attitude trim maneuver was postponed until the fourth rev of the transfer orbit, an estimate of the orbital drag could be made for perigees

2 and 3. The drop in apogee due to perigee 2 was estimated to be 0.592 kilometers, which corresponded to a drag coefficient of one. The drop in apogee due to perigee 3 was estimated to be 0.013 kilometers, which corresponded to a drag coefficient of zero. The decision was made to leave the drag coefficients equal to zero throughout the transfer orbit.

3.1.3 ATTITUDE SENSOR AND DATA BIAS DETERMINATION

A procedure was developed during launch simulations to calculate sensor and data biases using the MAD Program. The psi bias was first computed with cant angle biases fixed at zero. Then the cant angle biases were computed with the psi bias fixed at its value computed in the first iteration.

A psi bias of -0.242 degree was estimated at the end of rev 1. A psi bias of 0.088 degree was estimated at the end of rev 2 and -0.067 degree during rev 3. It was apparent that the psi bias was not converging. The decision was made to fix the psi bias at zero and calculate the other biases with WLS processing for the remainder of the mission (Table 2). Chord width biases estimated with WLS processing were input to the filter.

3.1.4 ATTITUDE TOUCHUPS FOR APOGEE MOTOR FIRING

The first attitude touchup was performed on rev 4. The rear target is shown in Table 2. The rear target was biased to account for precession expected due to perigees 5, 6, and 7. The perigee precession was consistent from rev to rev. The delta psi angle was about -0.013 degree, which corresponded to a delta phi angle of 0.016 degree.

Figure 5 shows the results of the first attitude touchup. The filter solutions are designated by KF, and the WLS solutions are designated by AD. Each solution was propagated to rev 4 to account for perigee precession. The difference, 0.82 degree, between the WLS solution for revs 2 and 3 indicates a modeling error. The WLS solutions for revs 4, 5, and 6 in Table 2, show similar but smaller differences. The WLS solution for revs 4, 5, and 6 taken together (not shown in Table 2) is essentially identical to the filter solution at the end of rev 6.

The first attitude touchup was executed with 115 pulses of the axial 1 thruster and a start angle of 172.7 degrees. The expected precession was 1.68 degrees, and the expected precession phase was 334.4 degrees. Table 3 shows the precession calculated from the premaneuver and postmaneuver attitude solutions in Figure 5. The table also shows the percent difference between the measured and nominal precession, the difference between the measured and nominal precession phase, relative to the Sun's azimuth in the spacecraft spin plane, and the corresponding thrust centroid error. In each case, the postmaneuver attitude is the KF/END-REV6 solution. Of the three premaneuver solutions, the KF/END-REV3 solution was probably closest to the true attitude.

Figure 6 shows the results of the second attitude touchup. Only sensor data were provided during rev 6 which was the Luxembourg pass. The decision whether or not to do a touchup on rev 7 was based primarily on the filter solution at the end of rev 6.

As mentioned above, the discrepancy between the weighted least squares attitude state solutions for revs 2 and 3 indicates a modeling error. The attitude

solutions differ by 0.82 degree, and sensor biases differ significantly (Table 2). Most of the discrepancy between the attitude solutions can be removed by fixing the biases. Table 4 contains the weighted least squares solutions using fixed biases. For comparison, the corresponding solutions from Table 2 are also shown. To account for perigee precession, all solutions were propagated to rev 4. Table 4 shows that fixing the biases removes most of the difference between weighted least squares solutions that use data from different revs.

Figure 7 shows the Earth chord residuals for revs 2 through 6. These residuals were computed with WLS using the fixed biases from solution KF/END-REV6 (Table 2). The north Earth chord data residuals showed a different signature for the even revs than for the odd revs. The south Earth chord residuals showed an even/odd rev pattern to a lesser degree. Table 4 also shows that the weighted least squares solutions for revs 4 and 6 are much closer to each other than the solution for either rev is to the rev 5 solution.

Allan Park executed the AMF maneuver as scheduled on September 11 at 20:17:39 GMT. The apogee motor firing was successful. The burn duration was about 54.9 seconds. The predicted duration was 54.1 seconds.

The AMF delta-velocity vector was determined from pre- and post-AMF orbit solutions. The delta-velocity vector corresponded to an AMF attitude error of 0.18 degree in right ascension and 0.03 degree in declination. The magnitude of the error was well within the 3-sigma value of 0.5 degree used for dispersion fuel allocation. The AKM performance error was about 0.4 percent below nominal.

The small attitude declination error resulted in a saving of approximately 8.5 pounds of fuel, based on a prelaunch study of injection and AMF dispersion errors (Reference 7).

3.2 DRIFT ORBIT

The filter was used to monitor and confirm the results of the apogee motor firing in real-time. Three parameters were closely monitored in an effort to confirm the AMF delta-velocity and attitude, i.e. drift rate, inclination and node. A scan was made on these three parameters by varying the apogee motor delta-velocity and attitude right ascension and declination, i.e. the initial burn vector. By comparing the post-AMF results from the filter with these scans, a preliminary estimate of the initial burn vector was made.

3.2.1 REAL-TIME POST-AMF MONITORING

Allan Park sent azimuth and elevation data following AMF. About one hour later, Allan Park also sent range data. About 1.5 hours after AMF, Castle Rock sent azimuth, elevation, and range data. Coverage continued for 3.7 hours after AMF.

The post-AMF weighted least squares solution showed an inclination of 0.15 degree, in agreement with solutions received from Millstone and NORAD. The MKAL Program showed an inclination of 0.08 degree. A later Millstone solution confirmed this inclination.

Figure 8 shows the drift rate, and inclination, along with the 1-sigma errors as determined by the MKAL Program. The filter had an accurate determination

of the drift rate and inclination within 2.5 hours of AMF. The node was not accurately determined until more data were received after the six-hour ground station coverage gap. Due to an apparent 0.4-percent underperformance of the AKM, the observed drift rate, inclination, and node were different than expected.

3.2.2 REAL-TIME MONITORING OF REORIENTATION TO ORBIT NORMAL ATTITUDE

A postburn maneuver and reorientation maneuver to orbit normal attitude were performed near perigee to remove most of the drift orbit apogee bias. The reor was planned in two parts to insure Earth sensor coverage during the burn by at least one sensor. The target attitude was five degrees off orbit normal attitude to account for the precession expected during the spindown maneuver.

The first leg of the reor was performed about 15 minutes after the postburn. The second leg was performed 9 minutes later. The maneuver was terminated early due to the loss of execute pulses caused by incorrect polarization of the transmitting antenna at Allan Park. Commanding was switched to Castle Rock. Leg 3 was performed about 12 minutes later. This part of the maneuver was terminated early due to commanding constraints near Earth shadow. The attitude was about 1.5 degrees from the target. A spindown maneuver was performed about 12 hours later.

The filter was used to monitor and retarget the reor in real-time. The filter calculated a new jet start angle and maneuver duration for each leg of the reor. Because the precession error was slight, the first part of the reor was allowed to continue to its nominal end time. The MKAL Program computed a new jet start angle and duration for the second leg of the maneuver. Figure 9 shows the predicted and observed attitude motion during the reor as it was monitored in real-time with data from the MKAL Program.

3.2.3 TRANSITION FROM MISSION OPERATIONS TO STATIONKEEPING OPERATIONS

The stationkeeping Kalman filter, KALMN, estimates both the orbit vector and the spin-axis vector. KALMN models the force and torque exerted on the spacecraft due to solar radiation. KALMN uses a quadratic fit to the GEM-10 model about a specified central longitude. The force model includes the gravitational forces due to the Sun and Moon. Maneuvers are modeled as instantaneous changes in velocity and spin-axis orientation. The spacecraft state vector includes the spin-axis orientation, a correction to the solar radiation torque and force model, a psi bias, and cant angle biases.

KALMN began processing range and attitude data from 88:258 (September 14). Orbit and attitude vectors were taken from the MKAL Program. The covariances were corrupted to accommodate differences in modeling. The psi and cant angle biases were set to zero and the chord width biases were set to 0.25 degree. The corrections to the solar radiation force and torque models were set to zero. Tracking and attitude data were processed by both KALMN and MKAL until 88:262 (September 18), when MKAL processing was suspended. On 88:270 (September 26), MKAL was restarted using the KALMN state to monitor three drift and two attitude maneuvers on 88:270 and 88:271. MKAL processing was terminated on 88:272 (September 27), and normal stationkeeping operations began.

4. CONCLUSION

The source of the attitude modeling error is unknown and existed in both the Kalman filter and weighted least squares batch processor. The filter continuously estimated the attitude state vector using data from revs 2 through 6; whereas, the weighted least squares processor estimated a state vector one rev at a time, and was more sensitive to the even/odd rev modeling error.

The low orbital inclination and launch time near equinox produced poor attitude determination geometry. Attitude separation data were used to restore attitude determination accuracy. The attitude precession due to perigee drag was determined from rev to rev and this information was used to benefit the AMF attitude targeting. A Kalman filter and weighted least squares processor were used to determine the attitude and orbit. This provided a way to verify the accuracy of state vector solutions. As a result, the AMF attitude error in declination was only 0.034 degree.

Since the Kalman filter continuously updated the orbit and attitude state vector, it was possible to: (1) determine the drift rate and inclination 2.5 hours after AMF, which verified the results of the motor firing, and facilitated prompt planning of the drift orbit maneuver sequence; (2) monitor and retarget the reorientation to orbit normal attitude in real-time, which minimized pointing errors during the large maneuver.

The SBS-5 predicted end of life was extended nearly 4 months as a result of the technical expertise and dedication of the launch support team.

REFERENCES

1. Hughes Aircraft Corporation, Satellite Business Systems (SBS) F-5 System Summary, Reference D5647-SCG8700030M, February 1987.
2. Telesat Canada, Flight Dynamics System Theory Manual, SBS Edition SCS-FDS-104, Revision 1.1, August 1, 1988.
3. Telesat Canada, "Attitude Determination for Low Inclination Transfer Orbits", Memorandum from A. Grise to F. Kes, January 8, 1987.
4. Mobley, R., Rowell, L., and Smith, M., Tracking Error Propagation and Orbit Prediction Program, Rand Corporation, RM-6256-PR, July 1970.
5. Cappellari, J., Mathematical Theory of the Goddard Trajectory Determination System, Goddard Space Flight Center, Greenbelt, Maryland, April 1976, Chapter 6.
6. MCI Telecommunications Corporation, Satellite Business Systems (SBS)-5 Prelaunch Document, September, 1988.
7. MCI Telecommunications Corporation, SBS-5 Mission Analysis Review, June 30, 1986.

Table 1. SBS-5 Orbit Determination Summary

SOLN	7TH APOGEE			ARGUMENT OF PERIGEE (DEG)	8TH PERIGEE HEIGHT (KM)
	TIME(88:255) HH:MM:SS	BIAS (KM)	INC (DEG)		
NOMINAL	20:00:37	171.656	7.003	180.333	205.411
GSFC SEP SMA	19:47:26	75.099	7.007	179.912	198.305
R1003	20:24:38	366.707	7.024	177.013	200.275
R1004	20:24:41	367.094	7.014	176.992	200.365
KF-REV1	20:24:51	370.728	6.842	177.265	197.733
R1005	20:25:18	360.324	6.930	177.651	212.400
R12001	20:24:48	362.179	6.965	180.448	205.953
R12002	20:24:56	362.633	6.977	180.455	206.808
R12003	20:24:55	361.074	6.992	180.240	208.301
R123001	20:24:57	360.619	7.002	180.177	209.040
R123002	20:24:56	360.452	7.000	180.152	209.074
R123003	20:24:55	360.353	6.999	180.137	209.080
R123004	20:24:54	360.228	6.995	180.118	209.038
R123001B	20:24:56	360.195	6.998	180.119	209.592
TOUCHUP					
R12345 OD1	20:24:53	359.919	6.99	180.148	209.358
R45001	20:24:48	356.398	7.012	180.091	211.260
R123 PROPUP	20:24:56	360.220	6.995	180.115	209.596
R12345002	20:24:50	359.917	6.985	180.123	208.705
R45001B	20:24:47	354.760	7.017	180.090	212.730
TOUCHUP					
PRE-AMF	20:24:47	357.114	7.019	180.096	210.370
R1-7001	20:24:52	359.638	6.996	180.094	209.486

NOTES - The following is an explanation for the solution titles.

Example - Rn00x

- R - abbreviation for revolution
- n - revolution numbers of the tracking data used in the solution
- OD - weighted least squares orbit determination
- x - solution number
- KF - orbit determination from the filter (MKAL)

Table 2. SBS-5 Attitude Determination Summary

SOLN	SARA (DEG)	SADEC (DEG)	CANT ANGLE BIASES (DEG)		CW BIASES (DEG)		SUN-EARTH SEPARATION BIASES (DEG)		PSI BIAS (DEG)
			N	S	N	S	N	S	
NOMINAL	236.429	-8.349							
GSFC/ARIANE	238.632	-8.200							
R1AD1	238.806	-6.442	0.0000	-.0020	0.000	0.000	0.000	1.766	-.242
KF	238.782	-8.751	-.1332	.0210	0.000	0.000	1.605	1.462	.000
R2AD2	238.860	-9.120	.0068	-.0035	-.150	-.164	1.519	1.544	.088
KF/END-REV2	238.880	-8.992	.0347	.0164	-.150	-.164	1.558	1.548	.088
R3AD1	238.800	-8.296	-.0450	.0210	-.074	-.051	1.792	1.663	-.067
KF/END-REV3	238.958	-8.606	-.1724	-.1286	-.074	-.051	1.687	1.595	.093
TOUCHUP									
REOR-TARGET	237.483	-7.419							
R4AD1C	237.400	-7.736	-.0220	.0160	-.096	-.085	1.587	1.560	.000
KF/END-REV4	237.436	-7.603	-.0448	-.0059	-.096	-.085	1.643	1.594	.014
R5AD1_MAD	237.470	-7.343	-.1380	-.0780	-.104	-.082	1.827	1.708	.000
R45AD1_MAD	237.427	-7.606	-.0763	-.0345	-.100	-.084	1.671	1.609	.000
KF/END-REV5	237.462	-7.546	-.1110	-.0680	-.104	-.082	1.749	1.656	.018
R6AD1B_MAD	237.405	-7.922	-.0020	.0596	-.051	-.045	1.468	1.457	.000
KF/END-REV6	237.478	-7.608	-.0800	.0040	-.051	-.045	1.633	1.555	.025
TOUCHUP									
PREAMF-KF	237.439	-7.419	-.0084	.0421	-.051	-.045	1.694	1.579	.008
AMF-TARGET	237.47	-7.400							
AMF									
DV-VECTOR	237.292	-7.434							
POSTAMF-KFS1	238.074	-7.895	-.0330	-.0051	-.051	-.045	1.709	1.657	.019
POSTAMF-KFS3	238.070	-7.712	-.0226	-.0019	-.051	-.045	1.741	1.421	-.0096
AMF+AD1	238.149	-7.164	-.1337	.0120	-.051	-.045	1.968	1.826	-.0009

NOTES - The following is an explanation for the solution titles.

Example - RnADx

- R - abbreviation for revolution
- n - revolution numbers of the sensor data used in the solution
- AD - weighted least squares attitude determination (MAD)
- x - solution number
- KF - attitude determination from the filter (MKAL)

Table 3. Precession and Phase Errors Relative to Nominal

ATTITUDE SOLUTION		DELTA-P	DELTA-P	PHASE	CENTROID
PREMANEUVER	POSTMANEUVER	(DEG)	ERROR	ERROR	ERROR
			(%)	(DEG)	(MS)
R2AD2	END-RV6-KF	2.08	24	- 12.7	- 42
R3AD1	END-RV6-KF	1.54	- 8	6.8	23
END-RV3-KF	END-RV6-KF	1.82	8	0.3	1
R3AD1	R5AD1	1.65	-2	-1.6	-5

NOTES

DELTA-P is the angular separation between the intial and final solutions.
 DELTA-P ERROR is the difference between DELTA-P and the nominal precession.
 PHASE ERROR is the difference between the measured and nominal precession phase relative to the Sun's azimuth in the spacecraft spin plane.
 CENTROID ERROR is PHASE ERROR divided by the spin rate.
 R3AD1 and R5AD1 were the solutions used to calibrate the first rear during the mission.

Table 4. Comparison of WLS Attitude Solutions Generated with Fixed and Free Biases. (All angles are in degrees.)

REV	FREE BIASES			FIXED BIASES				
	SARA	SADEC	ANG. SEP.	SARA	SADEC	ANG. SEP.		
2	238.89	-9.12	0.82	238.87	-8.76	0.06		
3	238.82	-8.30		238.88	-8.70			
TOUCHUP								
4	237.40	-7.74	0.18	237.44	-7.66	0.04		
5	237.45	-7.34		0.40	237.42		-7.79	0.13
6	237.37	-7.92		0.59	237.44		-7.62	0.17

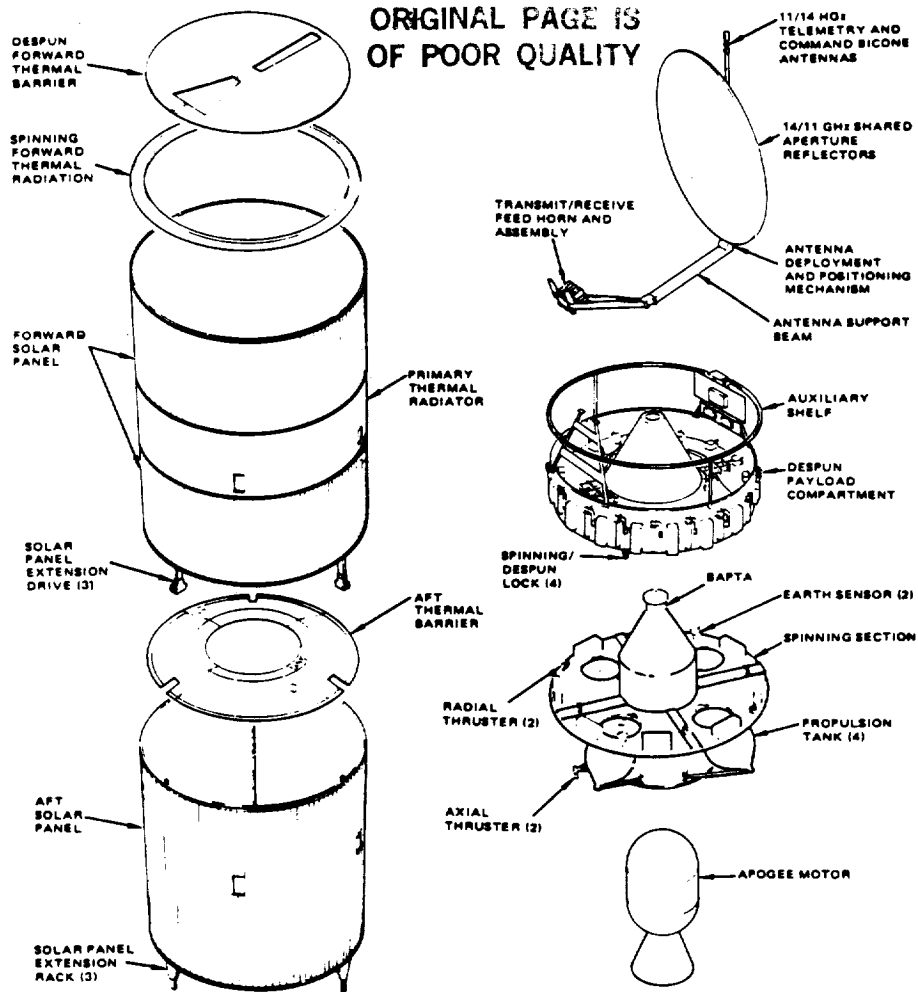


Figure 1. SBS-5 Spacecraft Components

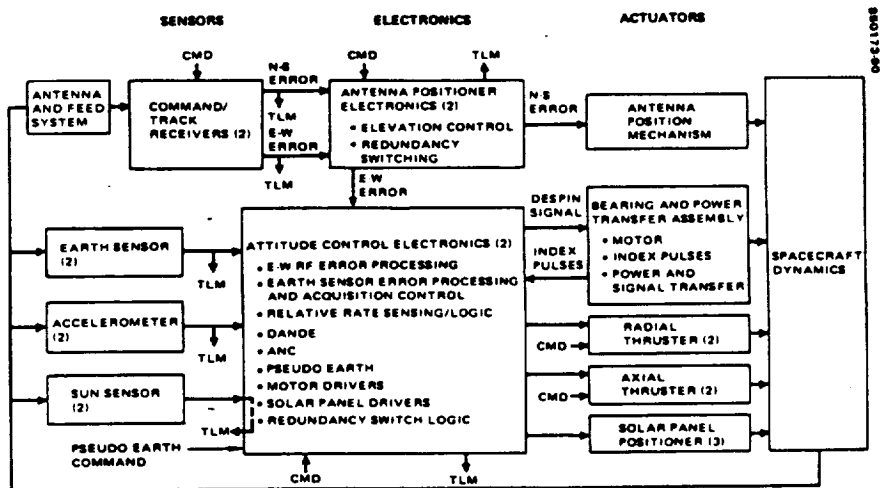


Figure 2. ACS Functional Block Diagram

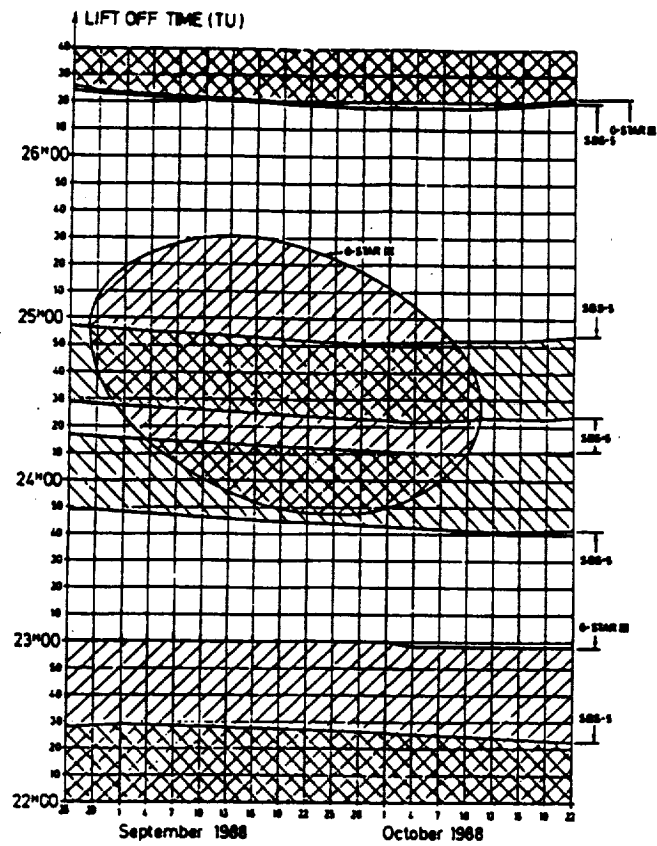


Figure 3. Combined Launch Window Universal Time at Liftoff

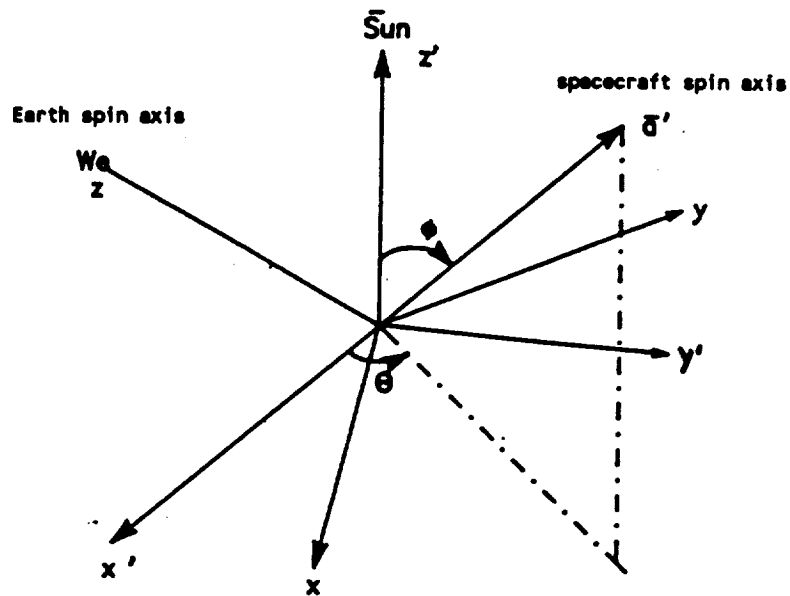
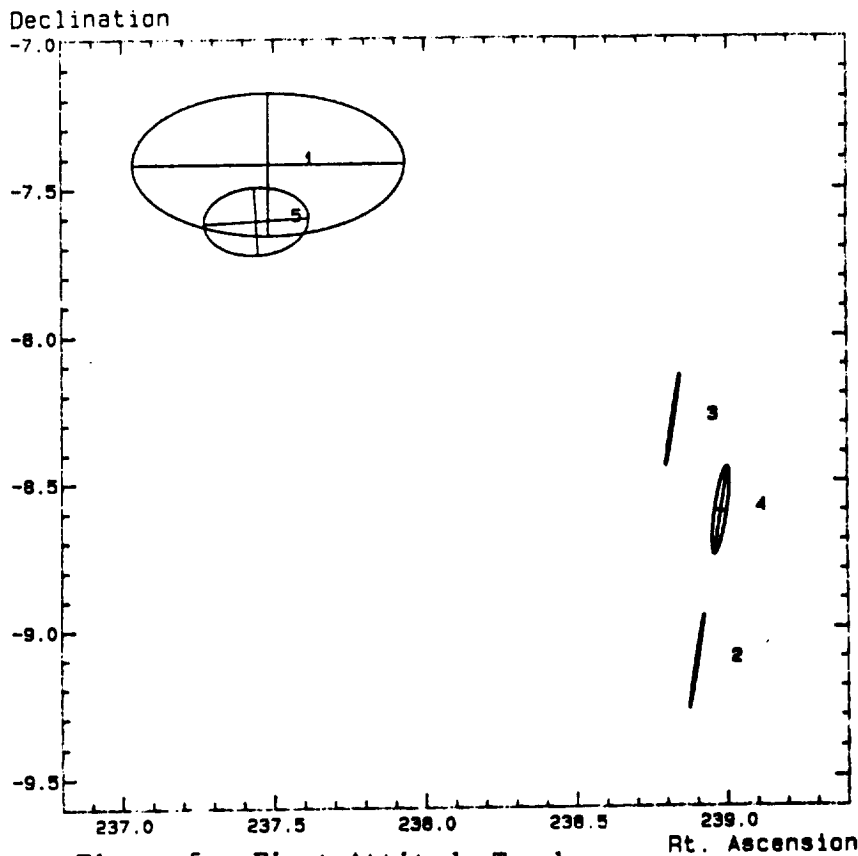


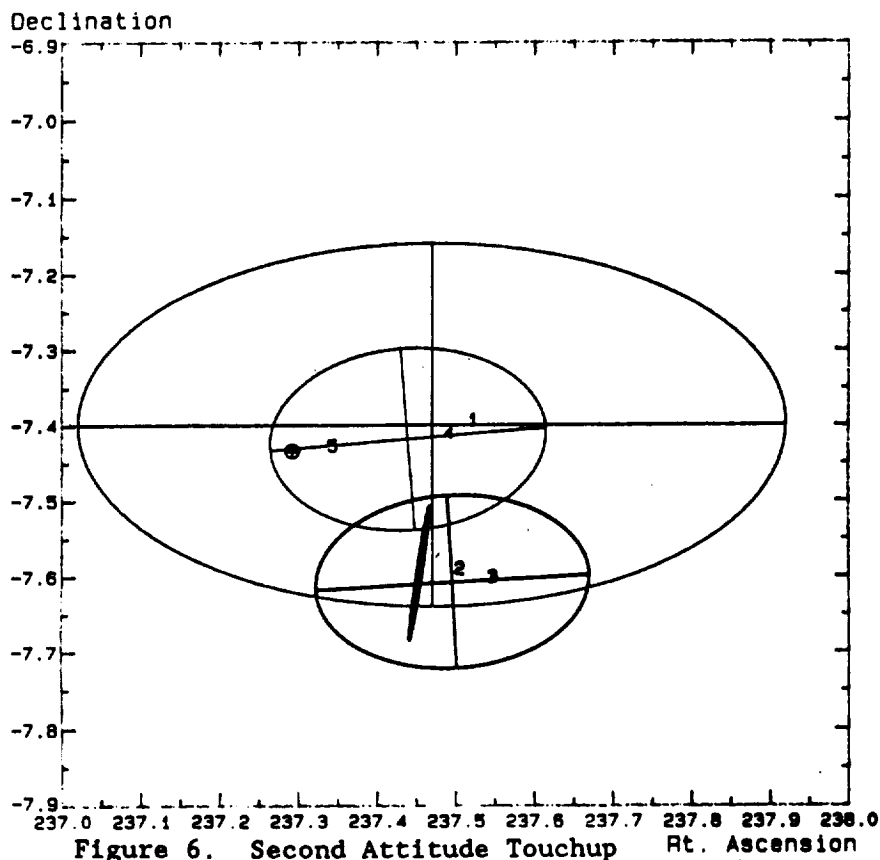
Figure 4. Phi-Theta System



Solution Index

- 1 REOR TARGET
- 2 R2A02
- 3 R3A01
- 4 END-RV3-KF
- 5 END-RV6-KF

Figure 5. First Attitude Touchup



Solution Index

- 1 AMF TARGET4
- 2 R496AD1
- 3 END-RV6-KF
- 4 PRE-AMF-KF
- 5 AMF DELTA-V

Figure 6. Second Attitude Touchup

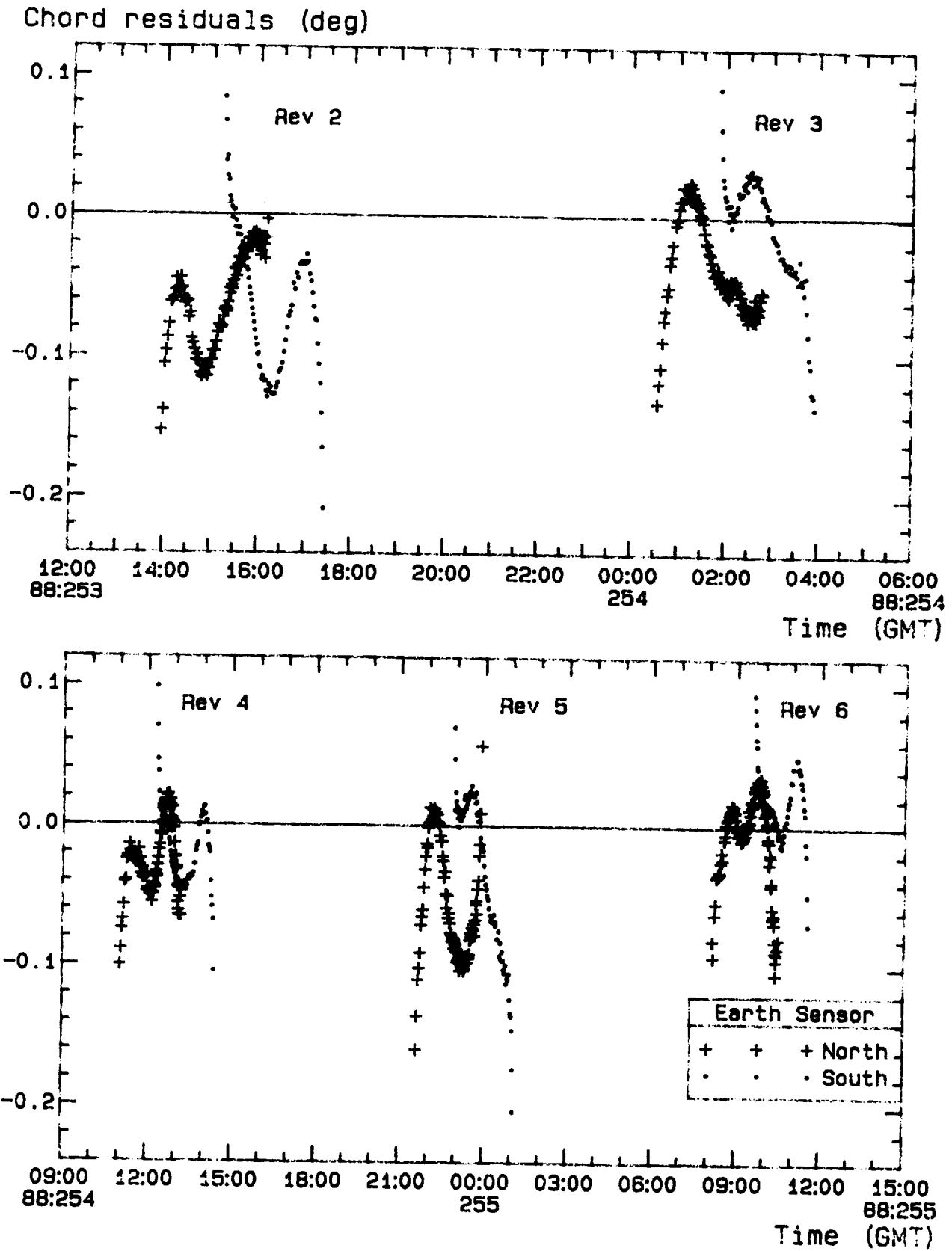
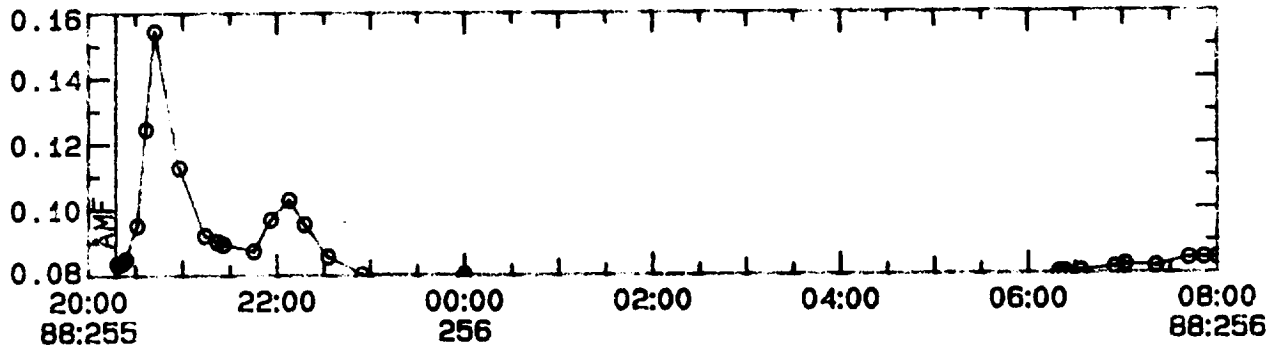
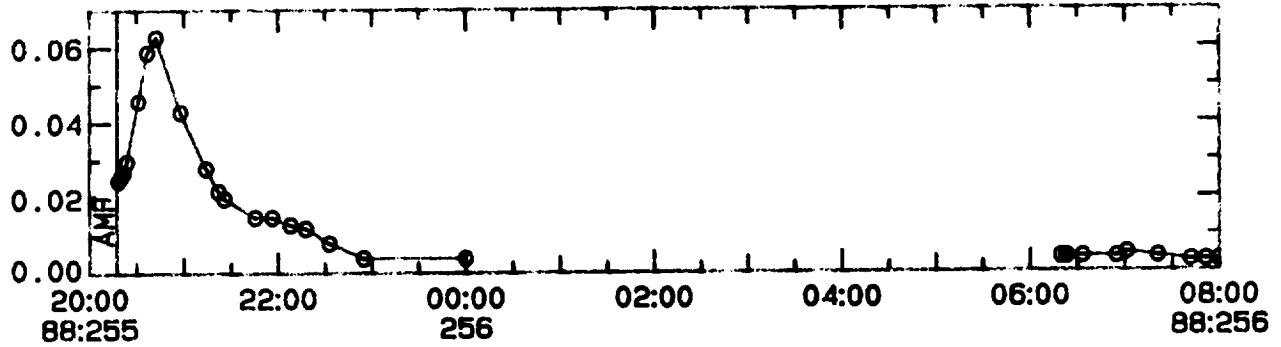


Figure 7. Earth Chord Residuals for Revs 2 Through 6

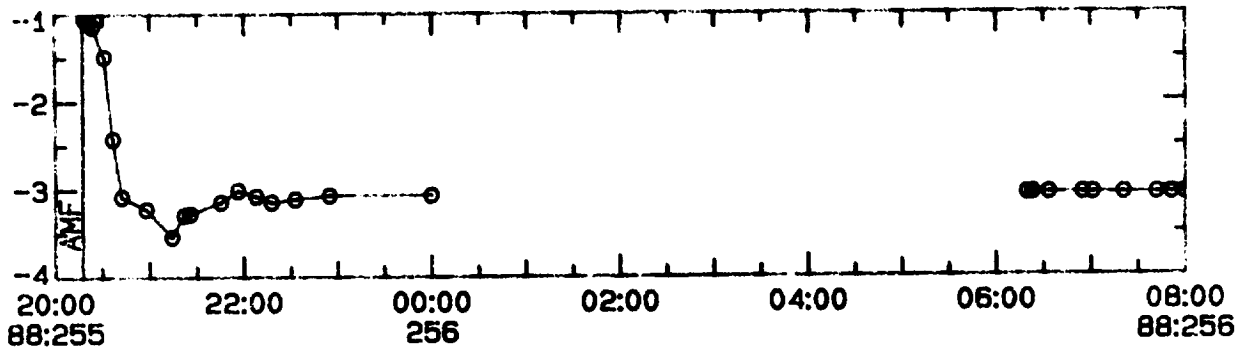
INCLINATION (DEG)



1-SIGMA INCLINATION ERROR



DRIFT RATE (DEG/DAY)



1-SIGMA DRIFT RATE ERROR

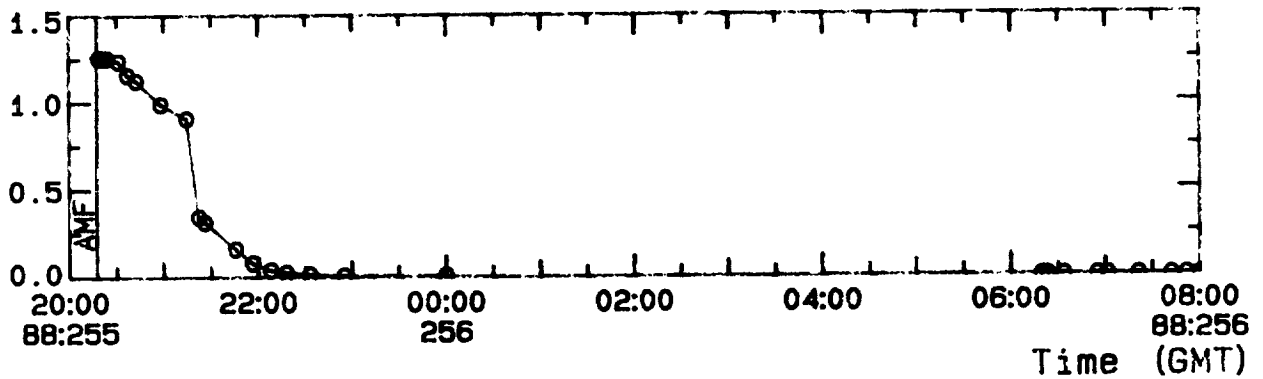


Figure 8. Observed Drift Rate, Inclination, and 1-Sigma Errors Following Apogee Motor Firing

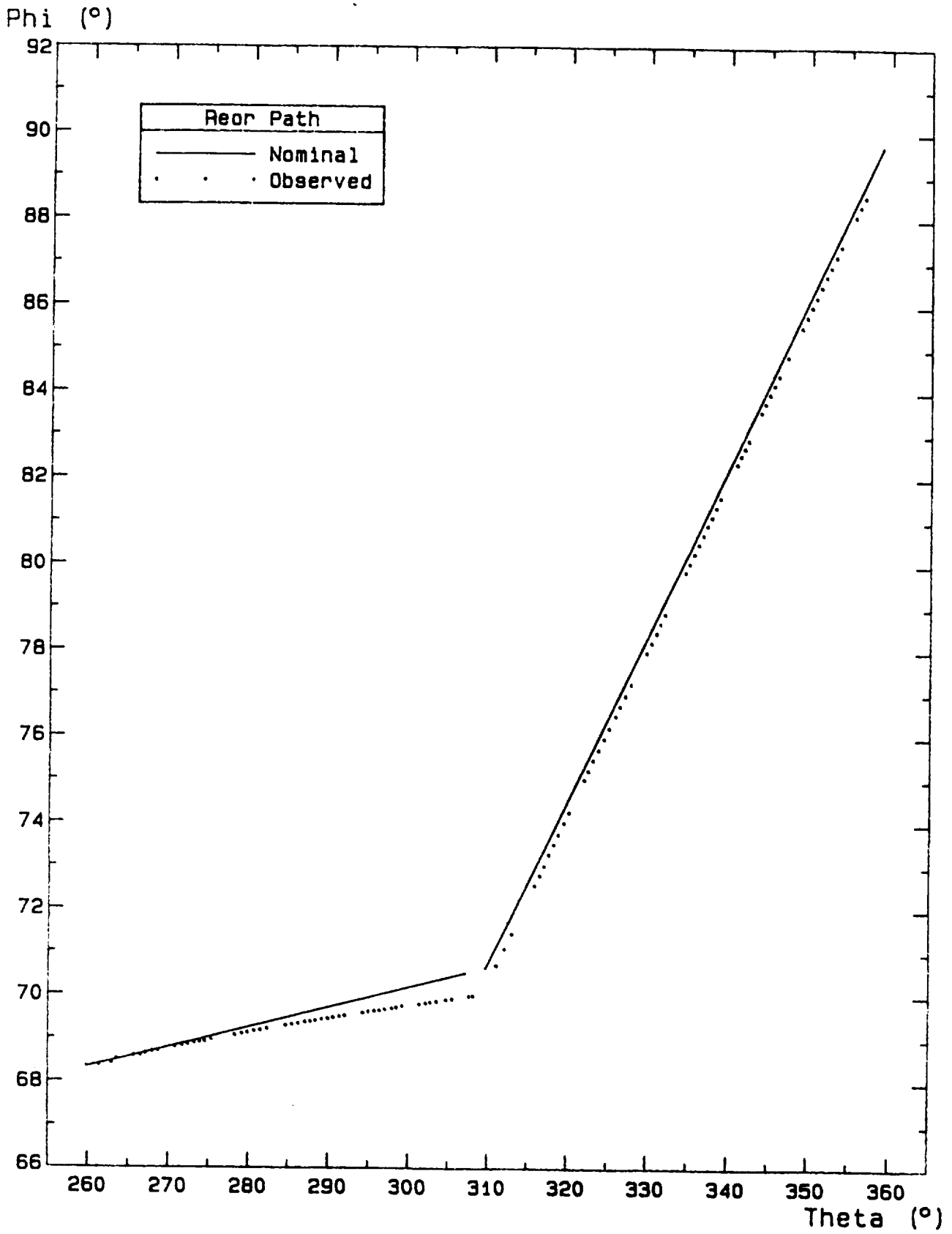


Figure 9. SBS-5 Reorientation to Orbit Normal Attitude

GOES-I/M ASCENT MANEUVERS FROM TRANSFER ORBIT TO STATION*

S. Abeyagunawardene, S. Devlin, D. Elkin
Computer Sciences Corporation

R. DeFazio
NASA/Goddard Space Flight Center

ABSTRACT

The Geostationary Operational Environmental Satellite (GOES)-I/M station acquisition sequence consists nominally of three in-plane/out-of-plane maneuvers at apogee on the line of relative nodes and a small in-plane maneuver at perigee. Existing software to determine maneuver attitude, ignition time, and burn duration required modification to optimize the out-of-plane parts and admit the noninertial, three-axis stabilized attitude.

The Modified Multiple Impulse Station Acquisition Maneuver Planning Program (SENARIO2) was developed from its predecessor, SCENARIO, to optimize the out-of-plane components of the impulsive delta-V vectors. Additional new features include computation of short-term J_2 perturbations and output of all premaneuver and postmaneuver orbit elements, coarse maneuver attitudes, propellant usage, spacecraft antenna aspect angles, and ground station coverage. The output data are intended to be used in the launch window computation and by the maneuver targeting computation (General Maneuver (GMAN) Program) software.

The maneuver targeting computation in GMAN was modified to admit the GOES-I/M maneuver attitude. Appropriate combinations of ignition time, burn duration, and attitude enable any reasonable target orbit to be achieved.

*This work was supported by the National Aeronautics and Space Administration (NASA)/Goddard Space Flight Center (GSFC), Greenbelt, Maryland, Contract NAS 5-31500.

1. INTRODUCTION

Salient features of the optimization software and targeting algorithms for the Geostationary Operational Environmental Satellite (GOES)-I/M station acquisition maneuvers are presented in this paper. Selected numerical results will be shown for maneuvers at apogee.

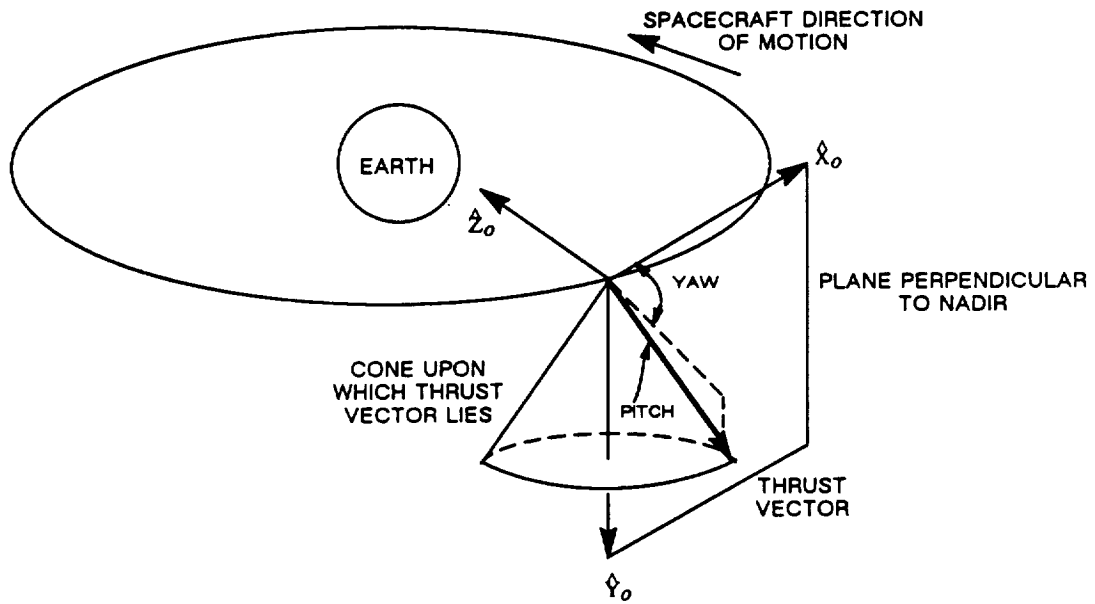
The nominal mission consists of three apogee maneuvers and one perigee maneuver. The initial orbit is an elliptic transfer orbit inclined at about 27.5 degrees. The desired orbit is geosynchronous at near-zero inclination at a desired right ascension of the ascending node (see Figure 1). The line of apsides and line of relative nodes are nearly coincident for each of the maneuvers so that in-plane and out-of-plane changes can take place simultaneously. The spacecraft is said to have acquired station when the final synchronous orbit has been achieved with the spacecraft at the desired longitude.

Using the two-body approximation, a set of impulsive delta-V vectors is first determined that enables the spacecraft to acquire station with satisfactory ground station coverage for the lowest fuel expenditure (minimum total delta-V). Elements for each of the post-maneuver orbits are then determined from the delta-V vectors. Next, ignition time, attitude, and burn duration are determined for the three-axis stabilized, noninertial maneuver attitude. The software is designed to permit quick replanning in case of contingency.

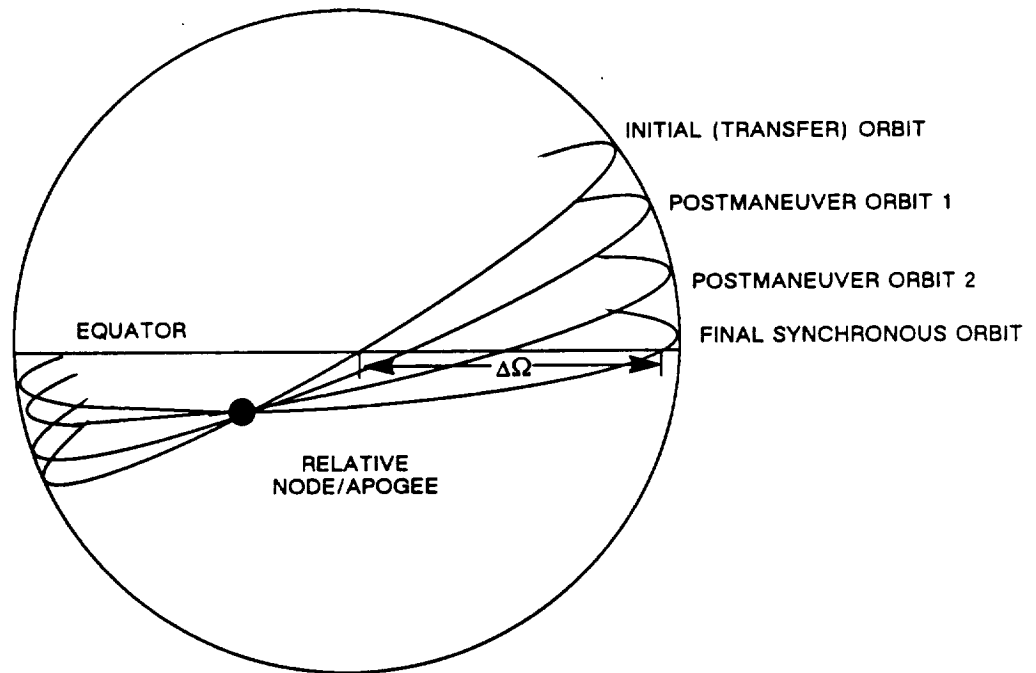
2. DESCRIPTION OF THE MANEUVER ATTITUDE AND THE STATION ACQUISITION SEQUENCE

The maneuver attitude is controlled as follows: Spacecraft pitch is held constant in the local orbital coordinate system with the Earth sensors and the thrust vector is held with the gyroscope at a fixed angle to the negative orbit normal of the initial orbit (determined by the initial yaw). The Earth sensors also maintain zero roll. The thrust vector is not inertially fixed, but sweeps out a cone about the negative orbit normal of the initial orbit. A diagram of the attitude appears in Figure 1.

The nominal transfer orbit provided by the launch vehicle is elliptic (eccentricity approximately 0.73) with apogee near geosynchronous radius (maximum dispersion about ± 100 km) at an inclination of approximately 27.5 degrees. The required final geosynchronous orbit has a near-zero inclination and a right ascension of the ascending node (Ω) near 270 degrees, which provides maximum stability to solar and lunar perturbations. Apogee will be placed on or near the line of relative nodes so that a simultaneous raising of perigee and reduction of inclination (coupled with the required change in Ω) can be accomplished optimally at each apogee motor firing. Perigee motor firings for fine adjustment of the apogee radius are small and purely in-plane. (An enhancement to include plane changes for the perigee maneuvers is under consideration for contingency planning.) Additional small maneuvers at either apsis are planned to achieve precise station acquisition. All maneuvers take place at designated apogees or perigees. Apogee maneuvers have either combined in-plane and out-of-plane parts or are purely in-plane.



(a) Yaw and pitch with respect to initial orbital coordinate system $(\hat{X}_o, \hat{Y}_o, \hat{Z}_o)$. \hat{Y}_o is parallel to the initial negative orbit normal, \hat{Z}_o is parallel to the nadir.



(b) Cross-sections of initial, postmaneuver, and final orbits for three apogee maneuvers. $\Delta\Omega$ is the desired nodal rotation

Figure 1. Maneuver Attitude (a) and Orbits (b) for the Station Acquisition Sequence

Maneuver durations of 45 to 60 minutes are anticipated for the first apogee motor firing, with shorter durations for the subsequent apogee motor firings. Apogee maneuvers with out-of-plane parts will be approximately centered about the line of relative nodes. In-plane maneuvers will be centered on an apsis.

3. SOFTWARE FOR DETERMINING IMPULSIVE DELTA-V VECTORS

Optimum, impulsive delta-V vectors are determined by the Modified Multiple Impulse Station Acquisition Maneuver Planning Program (SENARIO2). Postmaneuver orbital elements are computed for use in the maneuver targeting computation.

SENARIO2 was developed from SCENARIO (Reference 1) to compute impulsive delta-V vectors when maneuvers have an out-of-plane part. The solution is found in two stages. First, an optimum set of in-plane, impulsive delta-V vectors is determined in a two-body calculation to acquire station without regard to inclination or Ω (this is the original SCENARIO code). The user designates apogees and perigees for 3 to 10 maneuvers. Three maneuvers are solved for, placing the final apogee and perigee at geosynchronous radius with the last maneuver occurring at the desired longitude. For a two-maneuver sequence, the third maneuver is made negligibly small. To improve ground station coverage or in case of contingency, a nonoptimal set of in-plane delta-V vectors can be determined. Second, an optimum set of out-of-plane components to attach to the in-plane delta-V vectors of selected maneuvers is then determined using a standard minimization routine (a quasi-Newton algorithm available from the International Mathematics and Statistics Library (IMSL)). The optimization is described in detail in Reference 2. The result is achievement of the desired final inclination, ascending node, and in-plane goals. This simple procedure yields a rigorous optimization because apogee is very near geosynchronous radius and each perigee maneuver is purely in-plane. A more sophisticated optimization procedure might have been necessary otherwise.

Additional features of SENARIO2 include the following approximate calculations: short-term oblateness perturbations on semimajor axis and eccentricity up to the first apogee motor firing; maneuver attitude; azimuth, elevation, and range for up to 10 specified ground stations for a user-specified time interval surrounding each maneuver; spacecraft antenna aspect angle at each maneuver; and propellant usage according to the rocket equation. Premaneuver and postmaneuver orbital elements for use in the maneuver targeting and launch window computations are displayed.

4. SOFTWARE FOR MANEUVER TARGETING

The maneuver targeting computation in the General Maneuver (GMAN) Program determines the maneuver attitude, ignition time, and burn duration to achieve the postmaneuver orbits supplied by SENARIO2. GMAN uses these postmaneuver orbital elements to compute a coarse delta-V vector that sets an initial guess for the thrust direction and duration. An ignition time is either supplied by the user or calculated to result in a condition such as "maneuver center lies on the line of relative nodes." A thrust

simulation is then performed. The achieved orbit parameters are compared against the desired ones. A modified coarse delta-V vector is then computed, which attempts to compensate for the differences between the achieved and desired orbits. This process is iterated. Further details can be found in Reference 3.

The thrust direction for the GOES-1M spacecraft is not inertially fixed. It changes about 5 degrees during the first apogee maneuver. The orbit maneuver attitude control model was implemented in GMAN using an instantaneous orbital coordinate system. Because the orbit plane changes during an apogee maneuver, the attitude (defined in Section 2) is maintained by a recalculation of the spacecraft yaw in every time step. See Reference 4 for details of the calculation. In many cases convergence occurs despite the poor initial guess for thrust direction. In some cases convergence does not occur. References 5 and 6 supplement the discussion of convergence that follows.

Convergence can be physically impossible. Apogee maneuvers with little or no change in apogee radius are desired. If a maneuver is centered on apogee, it is physically impossible to prevent the apogee radius from increasing slightly (about 30 km on the first apogee maneuver). Figures 2 and 3 illustrate the apogee raising. This may be explained by comparison with the spin-stabilized attitude that keeps the thrust direction fixed while achieving a similar target orbit. The three-axis stabilized thrust vector follows the velocity vector more closely than the spin-stabilized one (i.e., the angle between the thrust vector and the spacecraft velocity vector is smaller for the three-axis stabilized attitude than for the spin-stabilized attitude). Apogee radius therefore increases more rapidly during the first half of a maneuver. Apogee radius decreases during the last half of a maneuver at about the same rate for both attitudes and the amount of the decrease is small because the spacecraft is near apogee. There is no net change in apogee radius for the spin-stabilized attitude, but a net increase in apogee radius does occur for the three-axis stabilized attitude.

To obtain an attitude that does not change apogee radius, it is necessary to off-center a maneuver about apogee. A tradeoff exists between convergence of the in-plane and out-of-plane parts for any amount of offcentering. A discrepancy between the desired and achieved ascending node of a few degrees can usually be tolerated on an early maneuver to permit in-plane convergence because the excess nodal rotation can be compensated for in a later maneuver with a minimal delta-V penalty.

A scan of initial yaw and pitch angles was made to find the minimum apogee rise for an apogee maneuver centered on the relative node at apogee. Pitch was varied arbitrarily, but yaw was determined to maintain an angle of 39.42 degrees between the thrust vector and the negative orbit normal of the initial orbit for the sake of out-of-plane convergence. The apogee radius increase could not be reduced below 25.2 km, and this occurred when the pitch was approximately 2.4 degrees. See Table 1 and Figure 2. The time dependence of the apogee radius is shown in Figure 3 for three of the cases in Table 1. Notice that the initial rise in apogee radius is large and it is followed by either a continued rise or a gentle lowering.

Failure to converge may also occur because the thrust direction changes. The GMAN fine targeting algorithm assumes that if the thrust vector initially points in the direction of the

Table 1. Change in Apogee Radius Versus Attitude

YAW (deg)	PITCH (deg)	APOGEE RADIUS CHANGE (km)
50.966135	6.0	40.5
50.796640	4.5	30.4
50.767960	4.2	28.9
50.734438	3.8	27.5
50.696518	3.3	26.1
50.652485	2.6	25.2
50.647054	2.5	25.2
50.641837	2.4	25.2
50.623107	2.0	25.4
50.591219	1.0	27.6
50.591219	-1.0	39.2
50.623107	-2.0	48.6
50.676357	-3.0	60.4
50.696518	-3.3	64.0
50.751121	-4.0	74.5
50.847619	-5.0	90.8
50.966135	-6.0	109.4

NOTE: Apogee on relative node, burn centered on apogee

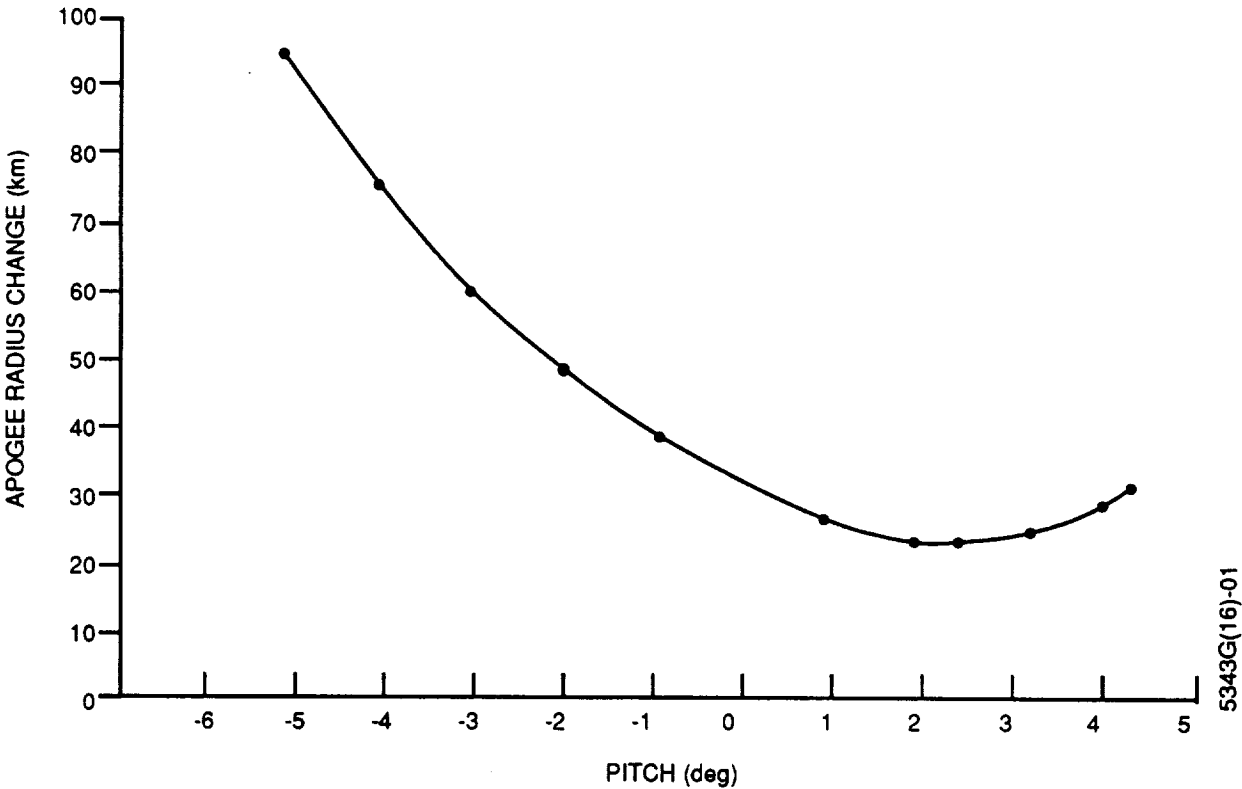


Figure 2. Apogee Radius Change Versus Pitch

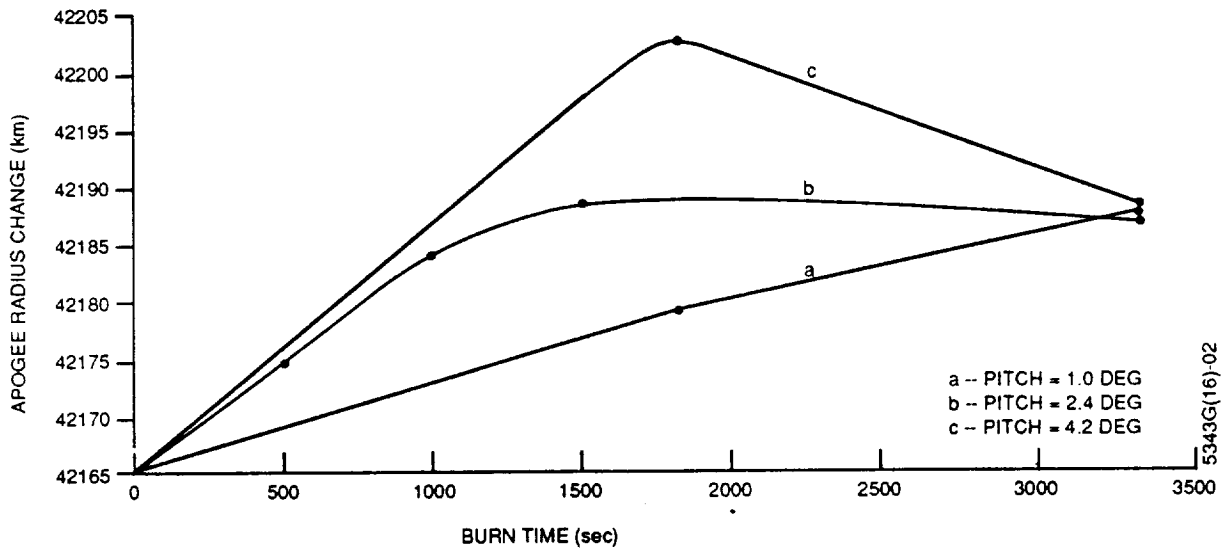


Figure 3. Apogee Radius Versus Burn Time

coarse delta-V vector, the resultant delta-V vector will be close to the coarse delta-V vector. The change in thrust direction obviates this assumption. To correct GMAN, a bias is applied to the initial Euler angles so that the resultant delta-V vector produced by the fine targeting module is close to the coarse delta-V vector (see Reference 4). This correction results in the attainment of convergence when an increase in apogee radius is desired, and produces a minimum apogee rise when no change in apogee radius is desired.

For a given set of initial and end thrust conditions, Table 2 shows the uncorrected yaw and pitch and associated in-plane errors (difference between achieved and desired values) on the third and subsequent iterations of GMAN targeting for the first apogee maneuver, and corrected yaw and pitch and associated in-plane errors on the fourth and subsequent iterations. Errors in the out-of-plane part are small and not shown.

The difference in direction between the uncorrected delta-V vector produced by fine targeting and the corrected delta-V vector is 0.78 degree.

Shift in Ignition Time To Improve In-Plane Convergence

When an unwanted apogee rise cannot be avoided because apogee lies near burn center, a shift of ignition time can enable apogee radius to remain unchanged. The amount of the shift is calculated by determining the location on the initial orbit where the position vector is lower than the original radius at burn center by an amount equal to the apogee radius rise. The difference in time corresponding to the difference in position is the amount of the shift. See Reference 4 for further details.

In Table 3, convergence for the first apogee maneuver is achieved for an ignition delay of 8 to 26 minutes or advancement by 11 to 28 minutes. The out-of-plane part fails to converge for larger shifts in ignition time. Notice that pitch exceeds 5 degrees in the cases

Table 2. In-Plane Errors for a GMAN Run

Δ apogee _{DESIRED} = 40.0 km	apogee _{INITIAL} = 42165.0 km		
Δ perigee _{DESIRED} = 9304.0 km	perigee _{INITIAL} = 6548.0 km		
i _{DESIRED} = 9.2104 deg	i _{INITIAL} = 27.0035 deg		
$\Delta\Omega$ _{DESIRED} = -0.4206 deg	Ω _{INITIAL} = 353.77 deg		
uncorrected yaw (deg) pitch (deg)	error in apo (km) per (km)	corrected yaw (deg) pitch (deg)	error in apo (km) per (km)
50.648 0.046	-10 9	50.601 -1.654	-0.7 0.7

Table 3. In-Plane Convergence Improvement Via Offcentering on the First Apogee Maneuver (Coincident Apogee and Relative Node)

INITIAL ORBITAL PARAMETERS AND GOALS								
	INITIAL VALUES		DESIRED VALUES		TOLERANCES		UNITS	
INCLINATION	27.0035		9.21035		0.05		deg	
Ω	353.8		353.4		7.0		deg	
APOGEE	42165.0		42165.0		5.0		km	
PERIGEE	6548.0		15852.0		30.0		km	
IGNITION DATE: 900401				RESULTS				
IGNITION TIME (HHMMSS)	INITIAL ATTITUDE		MANEUVER DURATION (sec)	ΔV (M/S)	ERRORS (ACHIEVED-DESIRED VALUES)			
	YAW (deg)	PITCH (deg)			INCLINATION (deg)	Δ RAAN (deg)	Δ APOGEE (km)	Δ PERIGEE (km)
142857	50.567	-3.770	3302	2977	0.088	6.53	0.29	-1.14
144557	50.644	-3.971	3293	2967	-0.018	2.37	3.23	-4.20
*145657	50.586	0.046	3285	2959	-0.0007	-0.34	29.8	26.70
150457	50.759	5.071	3293	2967	-0.012	-2.34	3.94	3.46
152257	50.999	5.195	3314	2989	-0.022	-6.96	0.88	-1.26

*MANEUVER CENTERED ON RELATIVE NODE.

of ignition delay. The maximum pitch available from the onboard control system is near this value.

Shift in Ignition Time To Improve Out-of-Plane Convergence

Errors affecting the out-of-plane convergence can similarly be compensated for by a shift in ignition time. Determine the achieved relative node and its distance from the desired relative node. The difference in time corresponding to the difference in position of the relative nodes is the amount of the shift. See Reference 4 for further details.

The following example for the second apogee maneuver demonstrates improved convergence with a burn center offset of 1 minute. The difference between achieved and desired inclination and Ω are shown as errors on the fourth iteration.

Table 4. Improved Out-of-Plane Convergence With a Time Shift

INITIAL ORBITAL ELEMENTS		GOALS	
$a = 29037.7$ km	$\Omega = 352.3$ deg	Δ apogee = 0.0 km	
$e = 0.4531738$	$\omega = 181.5$ deg	Δ perigee = 24556.7 km	
$i = 9.2$ deg	$M = 169.3$ deg	$i = 0.1$ deg	
	t_{ignition}	i_{ERROR} (deg)	Ω_{ERROR} (deg)
Centered	900403.214057	0.0300	-3.60
Offcentered	900403.213955	0.0002	-0.01

In addition to improving convergence, an a priori shift in ignition time may be a desirable, conservative measure to safeguard against hardware system problems or to balance the amount of apsidal motion between the prime and backup choices of apogee number for a maneuver.

Displacement of Apogee From the Relative Node

A slight shift in the argument of perigee displaces apogee from the relative node. A burn centered on the relative node could then be expected to have smaller in-plane errors. Table 5 compares an example of the second apogee maneuver with coincident apogee and relative node (item 1) against an identical one except for a displacement of 2 degrees between apogee and relative node (item 2). The change in apogee radius is 34.8 km when the burn is centered on the relative node with coincident apogee. When the apogee is 2 degrees from the relative node, the apogee radius change is -5.0 km. This result is within the convergence tolerance for the run.

Table 5. Comparison of Maneuver Goals Against Achieved Changes

I T E M	TIME HHMMSS	GOALS				ACHIEVED			
		INCLI- NATION (deg)	NODE CHANGE (deg)	APOGEE CHANGE (km)	PERIGEE CHANGE (km)	INCLI- NATION (deg)	NODE CHANGE (deg)	APOGEE CHANGE (km)	PERIGEE CHANGE (km)
1	213832	0.10000	-15.0000	0.0	24556.7	0.100	-34.47	34.8	24647.7
2	212740	0.10000	-15.0000	0.0	24556.7	0.099	-34.26	-5.0	24562.1

ITEM 1 -- AMF2 CENTERED ABOUT RELATIVE WITH APOGEE ON RELATIVE NODE.

ITEM 2 -- AMF2 CENTERED ABOUT RELATIVE NODE WITH APOGEE 2 DEGREES OFF THE RELATIVE NODE.

Apogee and relative node can be arranged to be noncoincident on the second apogee maneuver by adjusting ignition time on the first apogee maneuver. The amount of adjustment needed can be interpolated from the data in Table 6, which shows the angular displacement between relative node and apogee at the beginning and end of a maneuver for various ignition times. In this table the burns are not centered on the relative node.

Table 6. Angular Displacement Between Relative Node and Apogee for the First Apogee Maneuver Versus Ignition Time

IGNITION DATE: 900401 IGNITION TIME (HHMMSS)	INITIAL Ω (deg)	FINAL Ω (deg)	INITIAL Ω (deg)	FINAL Ω (deg)	INITIAL ARGUMENT OF PERIGEE (deg)	FINAL ARGUMENT OF PERIGEE (deg)	DISPLACEMENT OF RELATIVE NODE FROM APOGEE		CHANGE IN DISPLACEMENT OF RELATIVE NODE FROM APOGEE (deg)
							INITIAL ORBIT (deg)	FINAL ORBIT (deg)	
142857	27.5036006	9.2980758	353.76648	359.87827	180.21130	176.68929	3.00	-12.60	-15.60
143057	27.0036029	9.2840928	353.76648	359.39810	180.21128	176.91120	2.74	-11.70	-14.44
143657	27.0036083	9.2533123	353.76648	358.18352	180.21124	177.44410	2.09	-9.28	-11.37
144557	27.0036161	9.1926361	353.76648	355.71998	180.21117	177.72551	0.80	-5.24	-6.04
*145657	27.0036204	9.2096661	353.76648	353.00797	180.21109	180.40966	0.18	0.74	0.56
150657	27.0036206	9.1986236	353.76648	350.51139	180.21102	183.24896	-1.47	1.89	3.16
151057	27.0036198	9.2014617	353.76648	349.50238	180.21099	183.36782	-1.99	3.10	5.09
151457	27.0036182	9.1967485	353.76648	348.47664	180.21096	183.80722	-2.52	4.21	6.73
152157	27.0036143	9.1892858	353.76648	348.65480	180.21091	184.66892	-3.46	6.12	9.58

TOLERANCE ON APOGEE CHANGE = 5 km
(EXCEPT FOR THE CENTERED MANEUVER - SEE TABLE 3)

5343C(16)-00

If desired, both a change in the argument of perigee for the sake of a later maneuver and offcentering for the sake of convergence can be performed together on a maneuver.

5. SUMMARY

The SENARIO2 algorithm for the determination of optimum delta-V vectors for station acquisition, including combined in-plane/out-of-plane apogee maneuvers, was described. Associated computations of ground station coverage, coarse maneuver attitude, postmaneuver orbit elements, and approximate propellant usage enable the user to obtain a satisfactory station acquisition sequence for subsequent refinement.

The GOES-I/M maneuver attitude was implemented in GMAN. Convergence was ensured by modifying the targeting algorithm to bias the initial attitude to compensate for the change in thrust direction during a maneuver. An unavoidable rise in apogee radius occurs for maneuvers with apogee near the burn center. The rise can be avoided by shifting the ignition time or by changing the argument of perigee of the initial orbit so that apogee is displaced from the burn center.

Data from the spacecraft manufacturer on the INSAT-1D station acquisition are being studied for use in verifying the new software.

ACKNOWLEDGMENTS

We thank Mr. Roger Johnson of Computer Sciences Corporation for the close attention he paid this work.

REFERENCES

1. C. J. Petruzzo, W. C. Bryant Jr., K. G. Nickerson, *A Geostationary Longitude Acquisition Planning Algorithm*, AAS/AIAA Conference, Wyoming, September 1987
2. Computer Sciences Corporation, CSC/TM-87/6040, *Geostationary Operational Environmental Satellites (GOES) I/M Flight Dynamics Support System (FDSS) Mathematical Background*, V. Fernandes et al., September 1987
3. --, CSC/SD-82/6092UD3, *General Maneuver Program (GMAN) Mathematical Specifications*, Revision 1, J. Erickson, November 1987
4. D. Elkin, GMAN Specification Modifications No. 129, 3 January 1989, to Computer Sciences Corporation, CSC/TR-87/6002UD1, *Geostationary Operational Environmental Satellites (GOES) I/M Flight Dynamics Support System (FDSS) Requirements, Volume II: Functional Specifications, Update 1*, C. Audain et al., June 1988
5. D. Elkin, R. Johnson, SEAS QuickNote 468-89008, 3 January 1989
6. D. Elkin, SEAS Informational Memorandum - in preparation

GOES I-M IMAGE NAVIGATION AND REGISTRATION*

J. L. Fiorello, Jr., and I. H. Oh
Computer Sciences Corporation (CSC)

K. A. Kelly and L. Ranne
National Oceanic and Atmospheric Administration (NOAA)

ABSTRACT

Image Navigation and Registration (INR) is the system that will be used on future Geostationary Operational Environmental Satellite (GOES) missions to locate and register radiometric imagery data. It consists of a semiclosed loop system with a ground-based segment that generates coefficients to perform image motion compensation (IMC). The IMC coefficients are uplinked to the satellite-based segment, where they are used to adjust the displacement of the imagery data due to movement of the imaging instrument line-of-sight. This paper describes the flight dynamics aspects of the INR system in terms of the attitude and orbit determination, attitude pointing, and attitude and orbit control needed to perform INR. It discusses the modeling used in the determination of orbit and attitude, the method of on-orbit control used in the INR system, and various factors that affect stability. It also discusses potential error sources inherent in the INR system and the operational methods of compensating for these errors.

* This work was supported by the National Oceanic and Atmospheric Administration (NOAA), Suitland, Maryland, under Contract 50-DGNE-6-00003.

INTRODUCTION

The Geostationary Operational Environmental Satellites (GOES) I through M (I-M) will begin a new era in the monitoring of the Earth's meteorological environment by the National Oceanic and Atmospheric Administration (NOAA). This monitoring is done through the collection and distribution of environmental images and soundings of the Earth's surface and atmosphere. NOAA will use the Image Navigation and Registration (INR) System to navigate and register these images accurately. Image navigation is the process of determining the Earth latitude and longitude of each pixel in an image. Image registration is the process of maintaining the relative pixel-to-pixel pointing within an image and the relative pointing of a particular pixel from image to image. This paper introduces and describes the GOES I-M INR system and illustrates the intimate connections between the new concept of INR and concepts that are more familiar to flight dynamics specialists, namely, the concepts of orbit and attitude determination and control.

The images and soundings for GOES I-M are acquired by two instruments, the imager and the sounder, which are located on the Earth-pointing face of the spacecraft main body. Figure 1 shows these instruments and the other major components of the spacecraft. More detailed descriptions of the spacecraft are presented in the literature listed in the Bibliography.

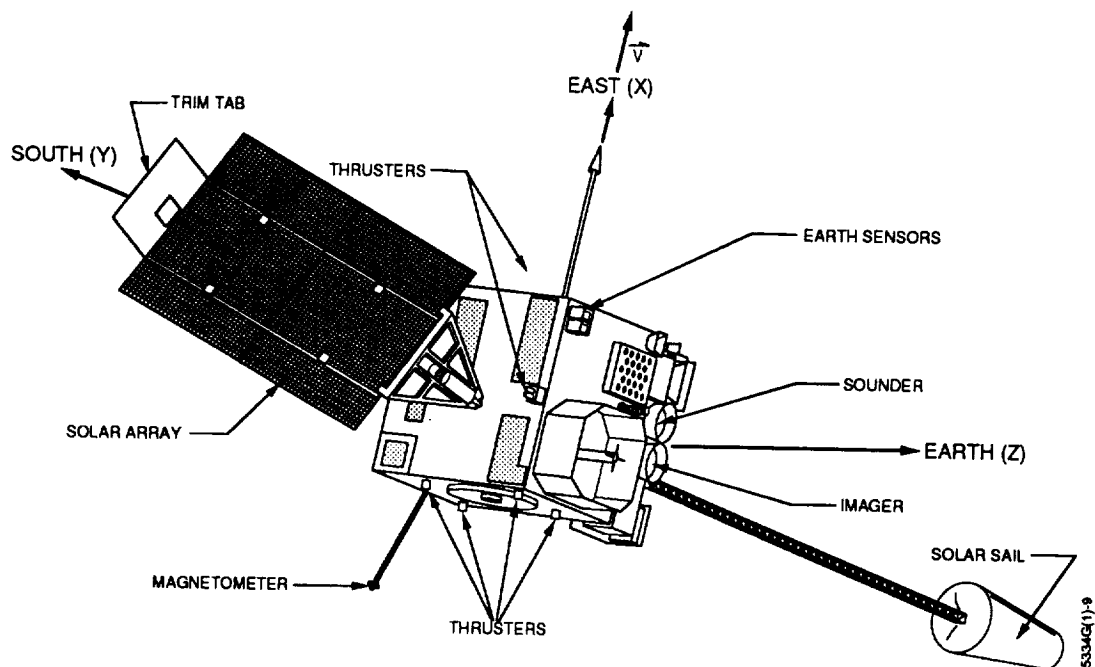


Figure 1. GOES I-M Spacecraft Configuration

To maintain proper positioning and pointing for the imager and sounder, two operational GOES I-M spacecraft will be positioned in geostationary orbits with a nominal attitude. These two operational spacecraft are located along the Equator at geostationary positions

of 75 and 135 degrees West longitude (Figure 2). At these locations, meteorological environmental images and soundings will be provided for much of the Western Hemisphere. Nonoperational spacecraft will be positioned in geostationary orbits at longitudinal locations safely away from the operational satellites. A nominal three-axis attitude is also sustained to provide proper pointing for the imager and sounder. This nominal attitude, shown in Figure 3, has the yaw axis pointing at nadir (the Earth), the pitch axis pointing along negative orbit normal, and the roll axis pointing along the velocity vector. Taken together, these geostationary locations and nominal attitude form the reference orbit and attitude for GOES-East and GOES-West, respectively.

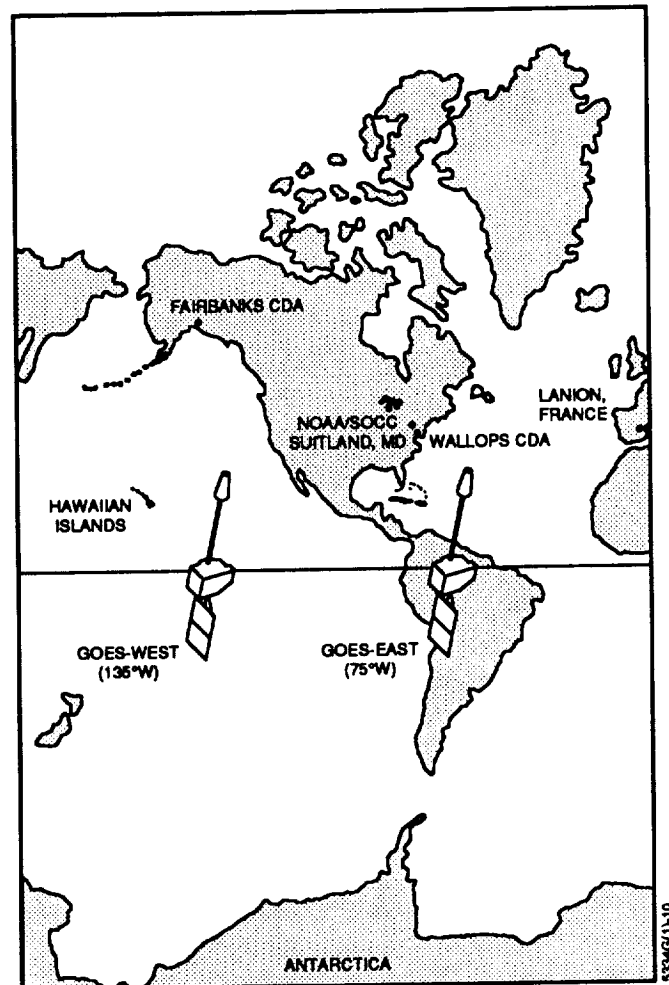


Figure 2. Nominal GOES Stations

Because they are fixed in an Earth-pointing direction, the imager and sounder use independent two-axis gimballed mirror scan systems to generate their respective images and soundings. Figures 4 and 5 show typical scan patterns for the imager and sounder detector arrays, respectively. The imager detector array consists of one visible and four IR channels, as shown in Figure 4. The sounder has 18 IR channels and 1 visible channel,

all of which are configured as shown in Figure 5. During a typical scan line, the mirror will continuously move along the scan line to a new position. At each new position, radiometric data are taken. At the end of a line, the mirror steps in the north/south direction to a new scan line. Both instruments act as their own star sensors, slewing away from the Earth to view stars.

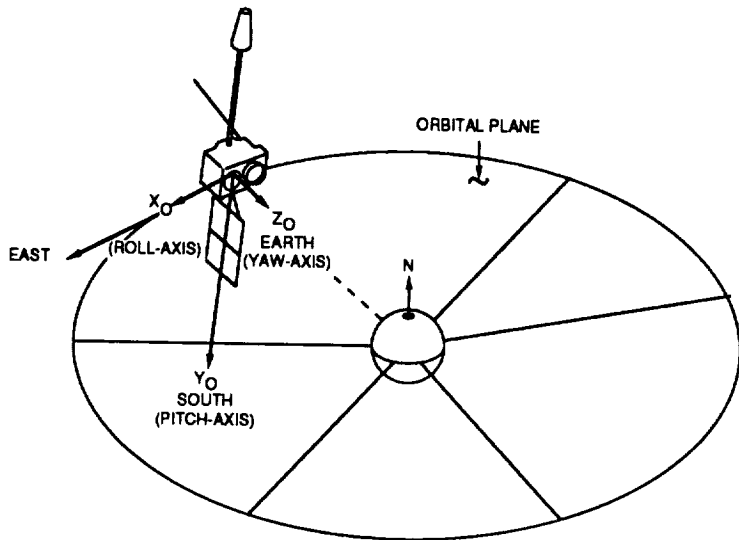
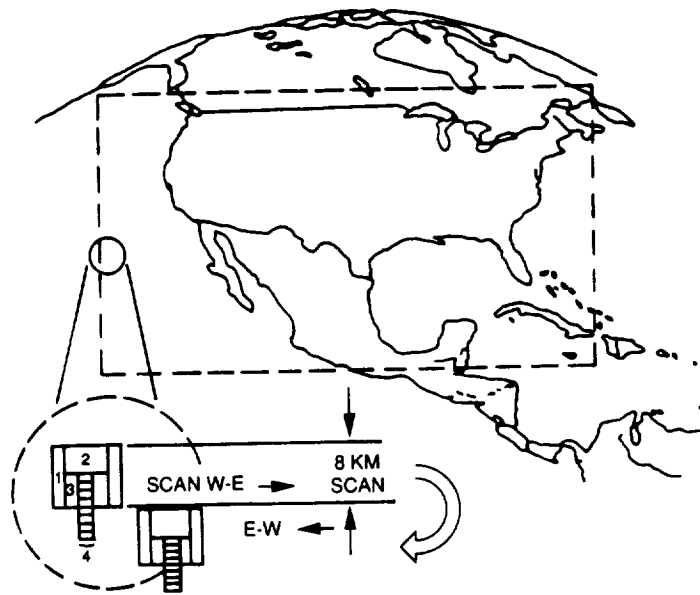


Figure 3. Nominal GOES I-M Orientation

The line-of-sight pointing for these instruments is not truly fixed. There are pointing errors that also move the line of sight. These errors are caused by orbit and attitude drifts, spacecraft thermal distortions, instrument servo errors, attitude control system noise, and dynamic interactions between the instruments and the spacecraft. The INR system is designed to remove or minimize these errors.

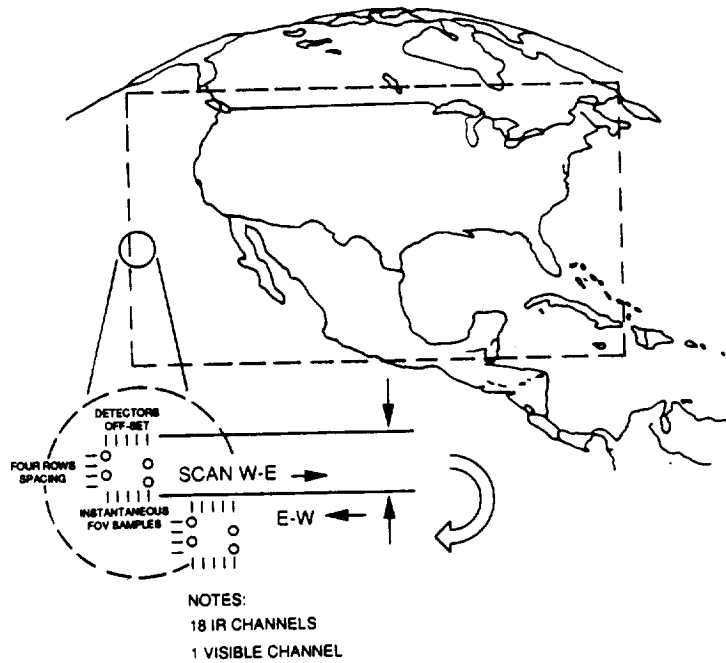
The GOES I-M INR system is a cyclical system, as represented in Figure 6. In this system, the imager and sounder gather star and landmark observations as part of their daily operations. These observations are sent to the Operations Ground Equipment (OGE), where they are used in conjunction with range data to perform orbit and attitude determination. Over the course of a day, an orbit and attitude profile is developed, from which a set of image motion compensation (IMC) coefficients are generated. These IMC coefficients are uplinked to the spacecraft, where they are used by the onboard computer to correct the pointing of each pixel for drifts caused by predicted, systematic errors such as orbit and attitude drifts and predictable thermal distortions. However, random errors also affect pixel pointing during the imaging period when these compensations are being made. These random errors are reflected in the new star and landmark observations that are taken and used for subsequent orbit and attitude determination. The goal of the INR system is to remove or minimize these errors to within acceptable values. Table 1 lists the specifications for these acceptable values. During orbit day, visible imagery data are used for INR; during orbit night, infrared imagery data are used.



NOTES:

- 1 = ONE 8-KM IR CHANNEL FOR 6.5- TO 7.00-MICROMETER WATER VAPOR
- 2, 3 = THREE 4-KM IR CHANNELS FOR 3.8- TO 4.00-MICROMETER NIGHT CLOUDS
10.2- TO 11.2-MICROMETER SURFACE TEMPERATURE
11.5- TO 12.5-MICROMETER SEA SURFACE TEMPERATURE
AND WATER VAPOR
- 4 = ONE 8-KM VISIBLE CHANNEL FOR 0.55- TO 0.75-MICROMETER CLOUD COVER

Figure 4. Typical Imager Scan Pattern



NOTES:

- 18 IR CHANNELS
- 1 VISIBLE CHANNEL

Figure 5. Typical Sounder Scan Pattern

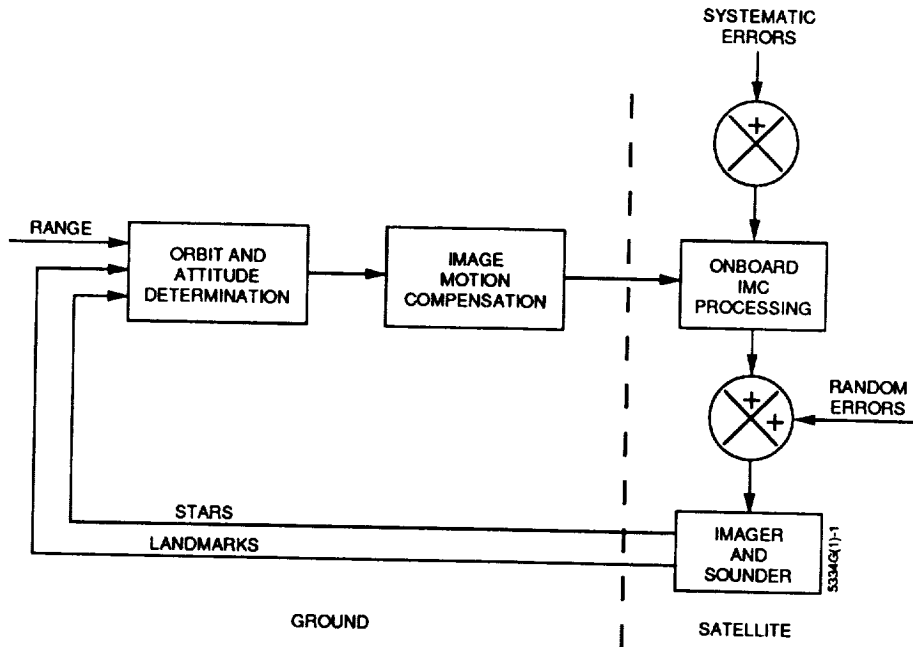


Figure 6. GOES I-M INR System

Table 1. INR Specifications

PARAMETER	ORBIT NOON ±8 HOURS		ORBIT MIDNIGHT ±4 HOURS	
	KILOMETERS*	MICRORADIANS	KILOMETERS*	MICRORADIANS
IMAGER				
IMAGE NAVIGATION (AT NADIR)	4	112	6	168
IMAGE REGISTRATION WITHIN A 25-MINUTE IMAGE	1.5	42	1.5	42
IMAGE REGISTRATION BETWEEN REPEATED IMAGES TAKEN WITHIN 90 MINUTES	3	84	3.75	105
IMAGE REGISTRATION BETWEEN REPEATED IMAGES TAKEN WITHIN 24 HOURS	6	168	6	168
SOUNDER				
IMAGE NAVIGATION (AT NADIR)	10	280	10	280
IMAGE REGISTRATION WITHIN A 120-MINUTE SOUNDING	3	84	4	112
IMAGE REGISTRATION BETWEEN SOUNDINGS TAKEN WITHIN 24 HOURS	10	280	10	280

*NOTE: AT GEOSYNCHRONOUS ALTITUDE, 28 MICRORADIANS SUBTENDS 1 KILOMETER ON THE GROUND.

5334G(1)-8

IMAGE NAVIGATION

Determining the location on the Earth at which a pixel is pointing requires a knowledge of the position and orientation of the pixel. This is equivalent to knowing the spacecraft orbit and the spacecraft and instrument attitudes. Consequently, orbit and attitude determination play a major role in image navigation.

Three types of observations are used in determining the orbit and attitude: range, landmark, and star data. Range data are normally acquired from NOAA's Command and Data Acquisition (CDA) station located at Wallops, Virginia. Occasionally, the NASA Deep Space Network (DSN) is also used. Landmark and star data are obtained by the imager and sounder. Landmarks are obtained during each instrument's normal imaging operation. Each operational satellite has a reference set of landmarks (Figure 7). The landmark is a well-defined land point, usually at a boundary between land and water. Figure 8 shows an example landmark for the GOES-West satellite. Visual landmarks are used during day, and infrared landmarks are used during night. Star observations are also obtained by the imager and sounder. After completion of an image, the scan mirror slews to a position just ahead of an expected star crossing. The mirror remains fixed while the normal orbital motion of the spacecraft allows the star to sweep across the mirror and be detected. The imager and sounder are capable of observing stars down to the sixth magnitude.

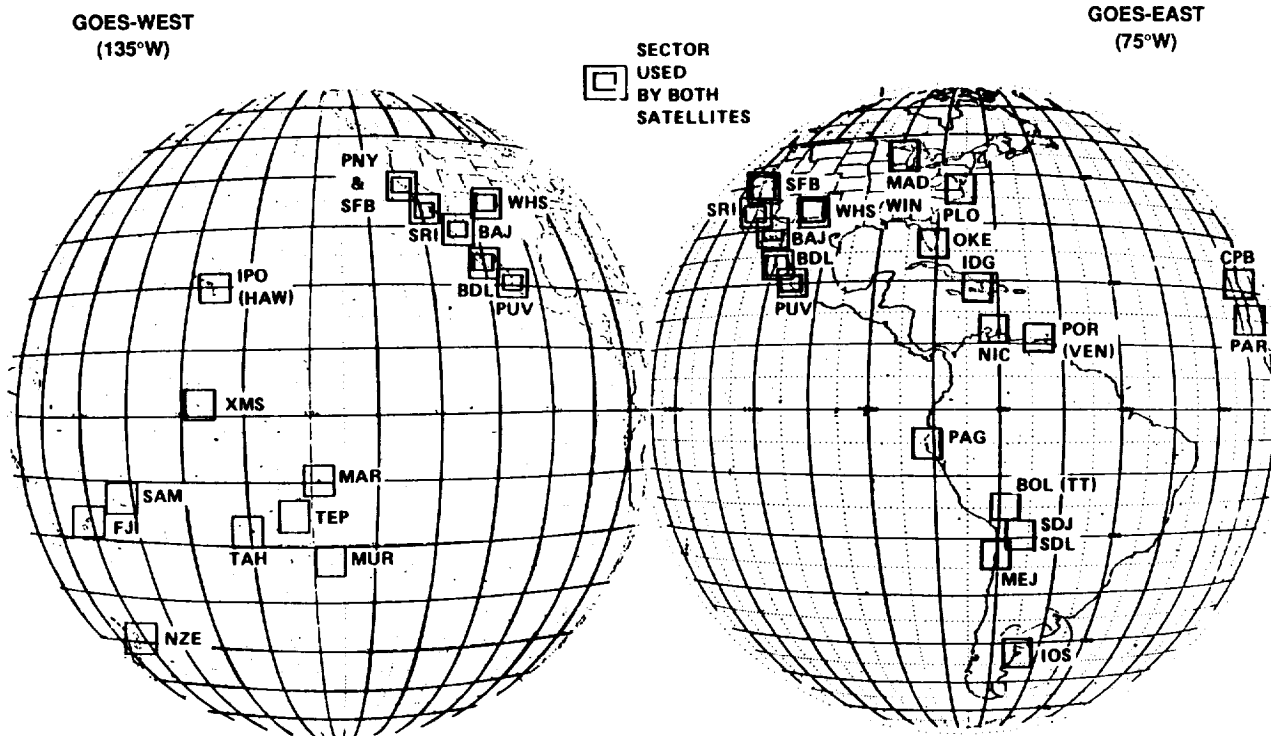


Figure 7. GOES Reference Landmark Locations

Once the observations are recorded, they are corrected for known physical effects and processed into observables. Range data are corrected for atmospheric refraction, polar

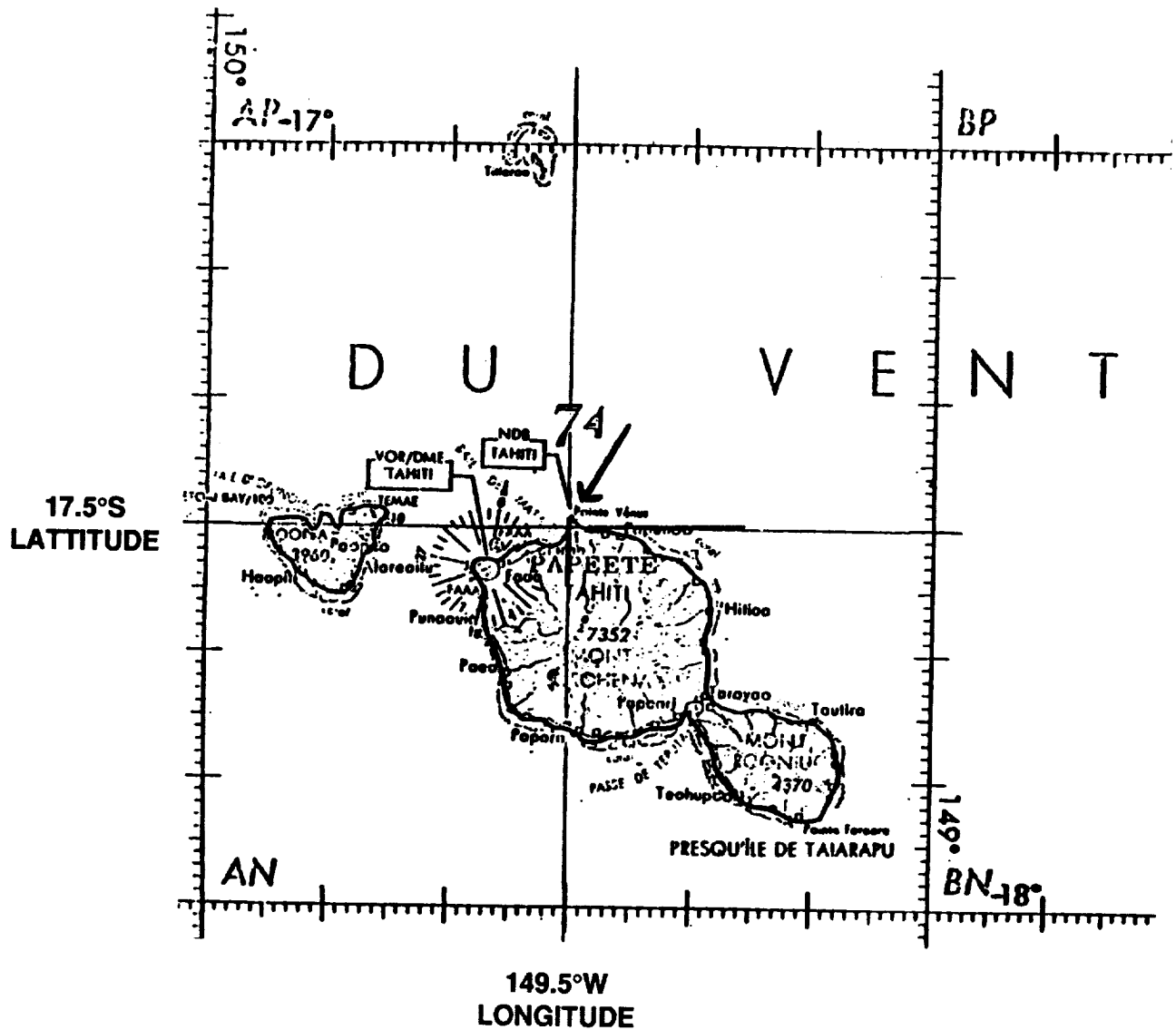
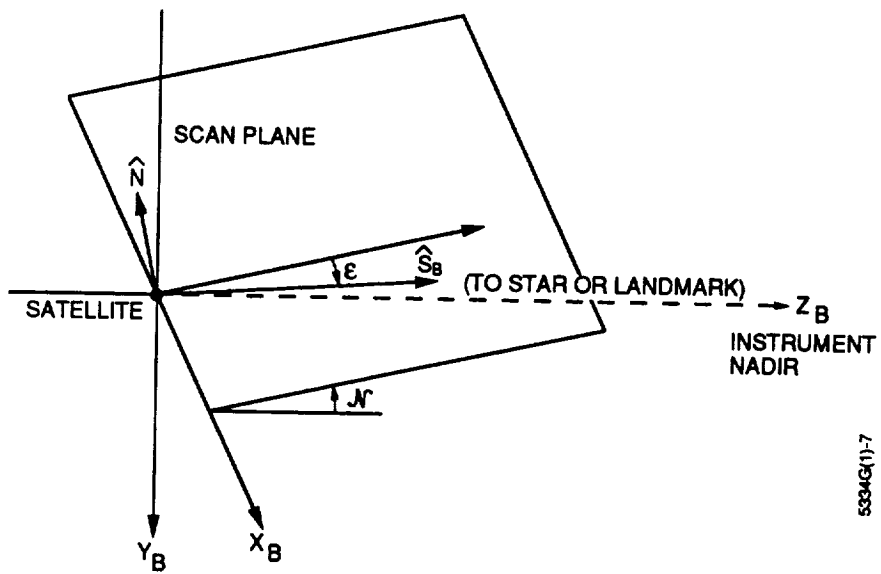


Figure 8. Example GOES Landmark—Tahiti

wander, and electronics delays. A predetermined station clock bias and range bias are then added to the range data to produce a slant range observable.

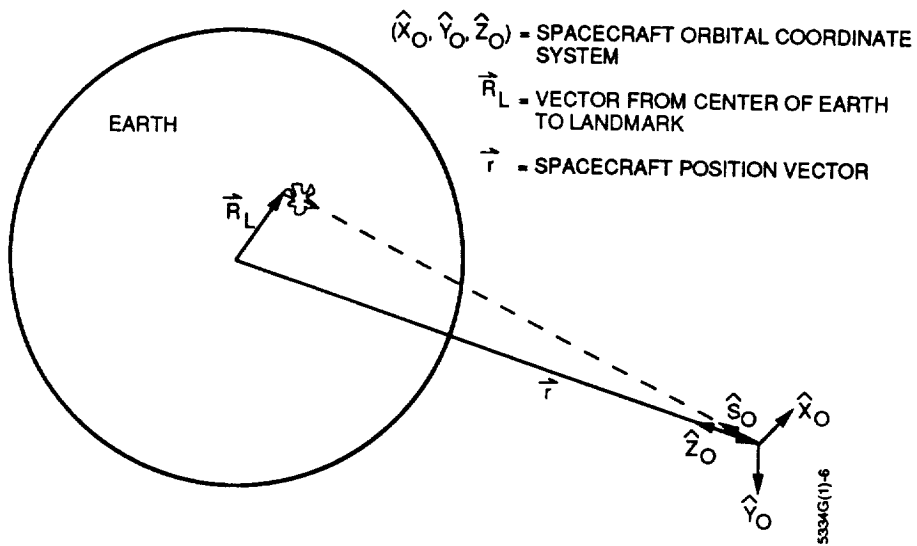
Star observations are corrected for proper motion, stellar aberration, and parallax; landmark observations are corrected for satellite orbital motion aberration. Additional corrections due to instrument characteristics such as image rotation and misalignments are also included in star and landmark observation corrections. Because of the orientation of the scan mirror with respect to the detector at a particular north/south scan angle, the projection of the image will be rotated as shown in Figure 9. This phenomena is known as image rotation. Mounting misalignments cause a constant systematic bias. Detector misalignment is caused by thermal distortions between other components of the spacecraft and the instrument. One additional correction is made on landmark observations. Because the onboard computer applies IMC shifts to pixels on the Earth, the landmark



5334G(1)-7

(X_B, Y_B, Z_B) = INSTRUMENT BODY COORDINATE SYSTEM

Figure 10. Scan Angle Observables in Instrument Body Coordinate System



5334G(1)-6

Figure 11. Scan Angle Measurement

orbit and attitude in terms of a state vector, generating partials of the measurement model with respect to the state vector, and estimating the orbit and attitude. Equations (1) and (2) form the basis for the first step—developing the measurement model for the scan angle observables—since these observables are components of \hat{S}_B in the instrument body coordinate system $(\hat{x}_B, \hat{y}_B, \hat{z}_B)$. The measurement model for the slant range, ρ , is illustrated geometrically in Figure 12 and mathematically by

$$\rho \text{ (slant range)} = |\vec{r} - \vec{R}_e| + \text{range bias} \quad (3)$$

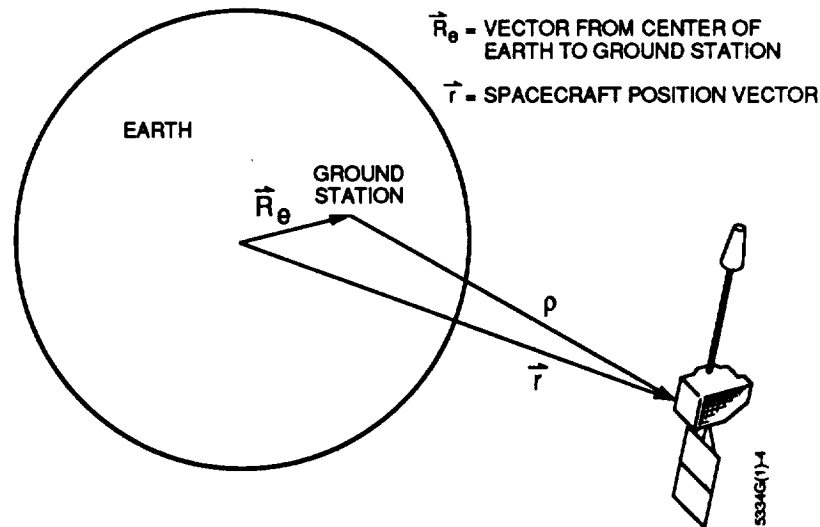


Figure 12. Range Measurement

The orbit model in the state vector is parameterized in terms of equinoctial elements that are used to avoid singularities for zero or near-zero inclination and zero or near-zero eccentricity orbits. The equinoctial elements are listed below in terms of the more familiar Keplerian elements.

<u>Equinoctial Elements</u>	<u>Keplerian Elements</u>
$a_f = e \cos (\Omega + \omega)$	$e = \text{eccentricity}$
$a_g = e \sin (\Omega + \omega)$	$\Omega = \text{right ascension of ascending node}$
$n = \left(\frac{\mu}{a^3} \right)^{1/2}$	$\omega = \text{argument of perigee}$
$(\mu = \text{gravitational constant})$	$a = \text{semimajor axis}$

Equinoctial Elements	Keplerian Elements
$L = \Omega + \omega + M$	$M = \text{mean anomaly}$
$\chi = \frac{\sin i \sin \Omega}{1 + \cos i}$	$i = \text{inclination}$
$\psi = \frac{\sin i \cos \Omega}{(1 + \cos i)}$	

The attitude model in the state vector is a linear combination of basis functions representing each of the five attitude angles: roll (ϕ), pitch (θ), yaw (ψ), roll misalignment (ϕ_{ma}), and pitch misalignment (θ_{ma}). The basis function consists of Fourier, exponential, and monomial sinusoid functions denoted by subscripts F, E, and MS, respectively:

$$\beta^i(t) = \beta_F^i(t) + \beta_E^i(t) + \beta_{MS}^i(t) \quad i = (1, \dots, 5) \text{ corresponding to } (\phi, \theta, \psi, \phi_{ma}, \theta_{ma}) \quad (4)$$

The attitude can be expressed by up to three basis function sets. A Fourier series

$$\beta_F^i(t) = \sum_{j=0}^n C_{1j}^i \cos(j\omega t + a_j^i) \quad (5)$$

is used to model the nominal daily attitude behavior. Exponential functions

$$\beta_E^i(t) = C_{E1}^i e^{-t/C_{E2}^i} \quad (6)$$

are included to model the deviations in attitude that usually occur around eclipse. Monomial sinusoid functions

$$\beta_{MS}^i(t) = \sum_{j=1}^4 C_{1j}^i (t - C_{3j}^i)^{D_j} \cos(O_j \omega t + C_{2j}^i) \quad (7)$$

are available to model attitude deviations that cannot be modeled by Fourier or exponential functions.

The solve-for parameters in the orbit model are the equinoctial elements at epoch, σ_0 ; in the attitude model, they are the coefficients (c_{ij}^k , a_j^i , D_j , and O_j) in the basis function set

modeling the attitude. Consequently, the partial matrix of the measurement model, \vec{M} , contains elements that are chain rule partial derivatives of these solve-for parameters:

$$\frac{\partial \vec{M}}{\partial \vec{\sigma}_0} = \frac{\partial \vec{M}}{\partial(\vec{r}, \vec{v})} \frac{\partial(\vec{r}, \vec{v})}{\partial \vec{\sigma}} \frac{\partial \vec{\sigma}}{\partial \vec{\sigma}_0} \quad (\text{orbit partials}) \quad (8)$$

$$\frac{\partial \vec{M}}{\partial \vec{c}} = \frac{\partial \vec{M}}{\partial \vec{\beta}} \frac{\partial \vec{\beta}}{\partial \vec{c}} \quad (\text{attitude partials}) \quad (9)$$

These partials are used in a linearized least-squares estimation to determine the orbit, attitude, and attitude misalignments.

IMAGE REGISTRATION

To maintain the relative pixel-to-pixel pointing within an image and between images, it is necessary to control the orbit and attitude of the spacecraft. For GOES I-M, orbit control is performed through manual ground commands, and attitude control is performed autonomously on the spacecraft.

To meet the INR requirements listed in Table 1, the geosynchronous GOES orbit must be controlled in both inclination (north/south excursion from the Equator) and longitude (east/west excursion from nominal longitude). The inclination is maintained to within 0.1 degree of the Equator, and the longitude is maintained to within 0.5 degree on either side of its nominal longitude.

Solar and lunar gravity are the primary perturbations that cause the inclination drift away from the Equator. This drift causes an inclination maneuver approximately every 2.8 months. The tesseral harmonic terms of the Earth's gravitational potential are the principle contributors to longitudinal drift. This drift causes a longitude maneuver approximately every 2.5 months.

Nominal attitude control is performed using a horizon sensor and a pair of momentum wheels. The momentum wheels nominally run with a constant pitch angular momentum to maintain Earth pointing. The horizon sensor senses pitch and roll. Pitch errors cause a speed modulation in both momentum wheels to control pitch. Roll errors cause a differential modulation of the momentum wheel speeds to induce momentum along the yaw axis. Roll and yaw are coupled due to the rotation of the roll/yaw plane around an orbit. Periodically, momentum is dumped using thrusters to avoid saturation of the momentum wheels.

The primary environmental torque at geosynchronous orbit is due to solar radiation pressure force, which causes an inertial roll torque. Coarse control of this torque is done using the rigid solar sail located on the north face of the spacecraft and the movable trim tab panel located on the base of the solar array (Figure 1). Fine control is done using the magnetic torquer coils.

The control system also performs corrections to the instrument servos, preventing image disturbances in one instrument caused by the independent motion of the scanning mirror in the other instrument. This autonomous correction, known as mirror motion compensation (MMC), causes the mirror drive electronics to adjust the inertial pointing of the mirror to compensate for attitude disturbances caused by motion of the other instrument's mirror.

Certain circumstances cause pointing disturbances in the control system and consequently affect INR. Cloud and radiance gradient excursions and solar or lunar intrusions into the horizon sensor field of view are such circumstances. Cloud and radiance gradient excursions result in a deviation in the detected infrared threshold that produces an anomalous pitch or roll error. Sun and Moon intrusions result in a deviation in the Earth horizon limb detection that also produces an anomalous pitch or roll error. Either of these conditions can be identified by observing the residual errors of star and landmark observations from their predicted locations. Special ground operations minimize their effects. In these special operations, intermediate IMC coefficient sets, based on the observation data affected by these conditions, are uplinked and used to navigate and register the image until normal conditions resume.

Orbit maneuvers also cause significant postmaneuver disturbances. During an orbit maneuver, the attitude is autonomously controlled using the horizon sensor, three mutually perpendicular gyros, and thrusters. An attitude error sensed by the sensor or the gyros causes an automatic thruster firing, compensating for the error. When the orbit maneuver is completed, attitude control is resumed by the horizon sensor and momentum wheels. The thruster firings during the maneuver cause significant disturbances that do not immediately die down after the maneuver. The yaw error from these disturbances is not immediately sensed. Special ground operations are used to reduce the yaw attitude error after the maneuver. These operations consist of determining the yaw error using star observations and manually performing short thruster firings to remove most of the yaw error. Any residual yaw error remaining is removed by the magnetic torquer coils.

IMAGE MOTION COMPENSATION

IMC is the main component of the INR system. It is the process used by the onboard computer to correct the azimuth and elevation pointing of each image pixel, in real time, for deviations caused by orbit drift, attitude drift, misalignments caused by spacecraft thermal distortions, and other systematic errors.

In effect, IMC corrects the true pointing of the pixels in an image to the ideal pointing of the pixels. The ideal pointing of the pixel is defined with respect to an ideal, or reference, orbit and attitude. The true pointing of the pixel deviates from this ideal pointing due to deviations of the orbit, attitude, and attitude misalignments from this reference orbit and attitude.

This is illustrated in Figure 13. In this figure, \vec{R}_R represents the ideal pointing of a pixel in the reference orbit and attitude coordinate system ($\hat{x}_R, \hat{y}_R, \hat{z}_R$). This system defines the ideal, or reference, orbit and attitude. The reference coordinate system is one in which the spacecraft orbit and attitude are as follows:

- The spacecraft is always located at its reference longitude (75°W for GOES-East or 135°W for GOES-West).
- The spacecraft is always along the Equator in a zero inclination orbit.
- The spacecraft attitude is referenced with roll = pitch = yaw = 0 in the orientation shown in Figure 3.

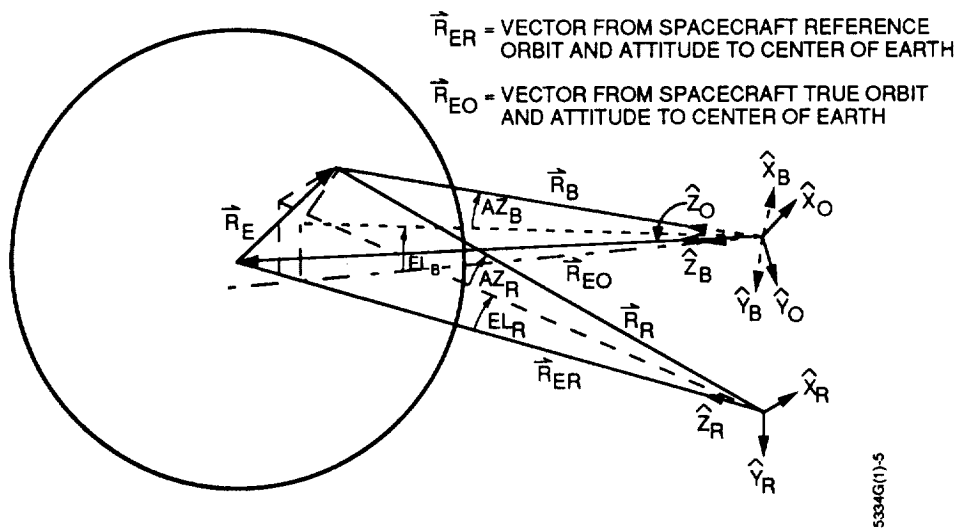


Figure 13. IMC Geometry

The true orbit deviation from the reference orbit is a function of the difference in longitude, λ_e , from the reference longitude; the nonzero inclination, i , of the true orbit; and the argument of latitude, u , of the spacecraft position in the nonzero inclination orbit. This is shown graphically in Figure 14. The 2-3-2 transformation, M_O , defines the relationship between the reference coordinate system, ($\hat{x}_R, \hat{y}_R, \hat{z}_R$), and the spacecraft orbital coordinate system, ($\hat{x}_O, \hat{y}_O, \hat{z}_O$). The geometries of these systems are shown in

The IMC system uses these transformations and misalignment offsets of the scan angles in the instrument body scan plane (Figures 9 and 10). Misalignment deviations are any roll and pitch misalignments, ϕ_{ma} and θ_{ma} , of the instrument with respect to the spacecraft. These misalignments affect the scan angle observables, ϵ and \mathcal{N} , through offsets, $\delta\epsilon$ and $\delta\mathcal{N}$, in the instrument body coordinate system (see Figure 9). These offsets are dependent upon the elevation angle, \mathcal{N} , of the scan plane in the instrument body coordinate system (see Figure 10):

$$\delta\epsilon = \theta_{ma} \cos \mathcal{N} + \phi_{ma} \sin \mathcal{N} \quad (13)$$

$$\delta\mathcal{N} = \theta_{ma} \sin \mathcal{N} - \phi_{ma} \cos \mathcal{N} \quad (14)$$

The coordinate transformations and misalignment offsets from Equations (12) through (14) are used to correct the azimuth and elevation angles that define the pointing of an image pixel. Referring to Figure 13, these angles in the instrument body coordinate system are AZ_B and EL_B . However, in the reference coordinate system, these angles are AZ_R and EL_R . IMC changes the true pointing of the pixel by applying the following compensations:

$$\delta AZ = AZ_R - AZ_B \quad (15)$$

$$\delta EL = EL_R - EL_B \quad (16)$$

This is done by using the ground-determined orbit and attitude states in the form of IMC coefficients. The corrections due to orbit deviations are used by expressing the ground-computed orbit in terms of the following parameters:

- ΔR —difference in radial distance from the ideal radial distance
- $\Delta \lambda$ —difference in subsatellite longitude from the ideal subsatellite longitude
- ΔL —difference in subsatellite latitude from the Equator
- $\Delta \psi$ —difference in yaw caused by the orbit's inclination

The corrections due to attitude are computed by determining the attitude angles from the solve-for coefficients of the attitude determination process. As many as 550 coefficients are uploaded daily to determine these orbit and attitude corrections.

During scanning of the Earth, the onboard computer continually computes these corrections. The onboard flight model approximates the exact computation to provide high-speed calculations for real-time pixel corrections. Because the mirror is continually scanning during these computations, the onboard computer performs extrapolations to account for this motion. It also models the curvature of the Earth at the limb to avoid erratic behavior at the scanner turnaround point.

SUMMARY

This paper introduced and described the new system of navigating and registering meteorological environmental images—Image Navigation and Registration—that will be used on the GOES I-M spacecraft. It also demonstrated the deep-rooted connection between INR and orbit and attitude determination and control.

Before the expected launch of the spacecraft in the early 1990s, NOAA is working to resolve several issues dealing with the operational performance of this system. As with any new spacecraft system, a thorough checkout of each component must be accomplished once in orbit before it begins operation. NOAA and NASA INR specialists are currently working together to ensure that every component of the INR system undergoes complete ground testing so that the in-orbit checkout will be successful.

During the operation of the system, anomalous or degraded INR performance could occur due to some unforeseen circumstance. Once again, NOAA is preparing for such circumstances by investigating potential anomalous behavior and preparing operational procedures for dealing with their occurrence. The special operational procedures previously discussed in the section on image registration are examples of NOAA's preparation.

ACKNOWLEDGMENTS

The authors wish to thank J. Rowe (Computer Sciences Corporation) for his thoughtful comments during preparation of this paper and the Technical Publications Department for their support in producing it.

BIBLIOGRAPHY

Computer Sciences Corporation, "Memo on INR Errors Outside of 60 Degrees Earth Central Angle," J. Fiorello (CSC) to L. Ranne (NOAA), to be published

Fiorello, J. (CSC), I. H. Oh (CSC), and L. Ranne (NOAA), "GOES-Next Navigation Operations," *NASA/GSFC Flight Mechanics/Estimation Theory Symposium*, May 11, 1988

Ford Aerospace and Communications Corporation, *GOES IJK/LM Image Navigation and Registration*, DRL 300-06, January 15, 1987

Ford Aerospace and Communications Corporation, *GOES IJK/LM Image Navigation and Registration Preliminary Design Review*, November 1987

Ford Aerospace Corporation, *GOES IJK/LM Dynamics and Controls Analysis Critical Design Review*, Book 2 of 3, March 1988

Ford Aerospace/Space Systems Division, *GOES IJK/LM Operations Ground Equipment (OGE) System Description, Analysis and Implementation Plan*, DRL 504-01, Vols. 3 and 7, October 24, 1988

International Telephone and Telegraph, *GOES Imager and Sounder NASA GSFC Code 300 Review*, December 8, 1987

Kelly, K. (NOAA), "GOES I-M Image Navigation and Registration and User Earth Location," *GOES I-M Operational Satellite Conference*, April 4, 1989

Shuttle Relative Navigation of a Tethered Satellite
Mission with Current On Board Software

Kevin A. Lee

McDonnell Douglas Space Systems Company
Engineering Services Division
16055 Space Center Blvd
Houston Texas, 77062

ABSTRACT

A Shuttle mission planned in 1991 will test the feasibility of tethers in space. This mission, a joint effort between Italy and the United States, will connect a satellite (built by the Italians) to the Shuttle with a 20 km long tether.

This mission poses unique navigation problems. The flight software on the Shuttle was never designed to account for the low level acceleration that is generated by the gravity gradient. IMUs on the Shuttle will sense the acceleration of the tether but it turns out that incorporating the continuous accelerometer noise also generates large error growth. Relative navigation is another important issue since the majority of the mission will be conducted while the satellite is out of the visual range of the crew. Some kind of feedback on the motion of the satellite will be desirable. Feedback of the satellite motion can be generated by using the rendezvous radar. To process the radar measurements, the flight software uses a 13 state Kalman Filter, but unfortunately with the filter currently tuned as it is, valid measurements tend to be ignored. This is due to the constraint of the tether on the satellite, which is an unmodeled force. Analysis shows that with proper tuning, relative navigation is possible.

PRECEDING PAGE BLANK NOT FILMED

1.0 INTRODUCTION

The first tether satellite mission (TSS1) is an attempt to fly the easiest profile that can be performed and yet provide us with valuable data to proceed with more complex tethered missions. Several questions and issues need to be resolved: Can the onboard flight software propagate the inertial state accurately enough? Can the ground software update the state? Can the Shuttle maintain a good target state? Additionally, there are numerous proximity issues that will also need to be answered. This paper will describe the analysis and answer the questions that pertain to the current onboard flight software, and in particular, to relative navigation issues.

The basic design of this mission is to fly the Shuttle at an altitude of 296 km. A satellite, built by Aeritalia, will be deployed away from the Earth (upward deploy) on a 20 km. long tether. The satellite is a 1.5 m diameter sphere containing various instrumentation. The tether consists of kevlar with a conducting wire passing through it. The mission does call for a 1 amp current to be passed along the tether.

Satellite thrusters will be used during the deploy until the gravity gradient between the Shuttle and the satellite is sufficient to continue deploying at the desired rate. During the deploy, the satellite will fall behind the z radial of the Shuttle and during the retrieval, it will be in front of the z radial. This can be seen pictorially in Figure 7.

There are two basic programs used to perform this analysis. The tether mission trajectories are generated using Shuttle Tethered Object Control Simulation (STOCS). STOCS is a high fidelity Shuttle simulation with a general purpose tether model attached. Reference 1 describes STOCS in greater detail. Onboard software is modeled in Shuttle Environment and Navigation Software for Onorbit and Rendezvous (SENSOR). Section 2.1 gives more explanation of the onboard software and Reference 2 gives a full description of SENSOR.

2.0 DISCUSSION

The satellite, a small object, will be out of visual range of the crew for the majority of the mission. Sensors mounted on the boom indicate, among other things, tether tension, tether angle and length of tether deployed, but this information does not give a lot of direct feedback on the satellite itself. More useful information could be obtained by using the rendezvous radar, which generates range, range rate and in and out of plane angles of the satellite. This radar data is also information that the crew has seen before and is familiar with.

The radar is self contained and handles tracking by itself so the simplest method of use would be to turn it on and watch the data. What happens if the radar breaks lock? Remember that the satellite is small and will be up to 20 km from the radar. Since the default search mode of the radar is to start the search with a shaft and trunnion angle of 0° and a range of 609 m, it is unlikely that the radar will be able to reacquire the target. An alternative would be to use the Relative Navigation (Rel Nav) function on the Shuttle. Using Rel Nav allows the flight software to maintain a target state. When the radar tries to acquire a target, the navigation software (Nav) will supply a target state vector. As will be seen later, there are also problems using the radar with Rel Nav.

2.1 FLIGHT SOFTWARE BASICS

There are two methods for incorporating accelerations into the state propagations. The first is by using modeled atmospheric drag and modeled vent and thrusting. An alternative method is by using the Inertial Measuring Unit (IMU) sensed acceleration output. The appropriate acceleration source is chosen by comparing the IMU sensed accelerations against the 1,000 μg threshold. If the sensed accelerations are less than this threshold, then the models are used, otherwise the IMU output is used. Sensed accelerations will also be used if the digital autopilot (DAP) jet flag is turned on during a given Nav cycle. The DAP jet flag is used to incorporate jet firing when it is known that the low level accelerations are due to the jet firing. Finally, a 4 x 4 gravity model is used for the state propagation which is performed by the Super G integrator.

Relative navigation data processing is done using a thirteen state Kalman Filter. The first three components of the state are the inertial position and velocity vectors. States seven through nine are the inertial unmodeled acceleration biases, which are used in the calculation of the vehicle accelerations. Finally, the last four states are the measurement biases. The flight software has a choice of filtering the Shuttle state or the target state.

2.2 PROCESSING A TETHER MISSION

The first step to onboard processing is to propagate the inertial position and velocity of the vehicles. For the Shuttle, the immediate consequence of having the tether attached is to impart a continuous low level acceleration. Unfortunately, the tether acceleration is below 1,000 μg . Setting the acceleration limit lower so that the state propagation could pick up the tether acceleration does not work since IMU errors are also incorporated. This leads to worse state propagation than when the tether is ignored. Ruling out flight software modifications, the inertial error growth will have to be accepted and handled through ground processing with state vector uplinks.

The next step to onboard processing is to address the relative navigation problem. Typically, the Shuttle state is the choice state for filtering. The reason is that normally the target has been tracked for months and it's orbit is well known. Also, the target will be essentially dead and therefore will not be venting or thrusting. Modeled accelerations are sufficiently accurate in propagating the target state for these types of rendezvous. The Shuttle, on the other hand, is conducting numerous venting and thrusting. Thus, the Shuttle state is better suited for filtering during a nominal rendezvous. For the tether mission, the Shuttle is still performing the venting and thrusting, but look at what the target is doing. It will be moving from an orbit at 296 km to an orbit at 316 km. Thus, the target state is better suited for filtering during the tether mission.

During the propagation/update process, the filter takes the measurements and adjusts the state by using the measurement residual and the Kalman gain. When the measurements are coming in, one would expect the filter to bring the state

closer to the truth. As shown in Figure 1, this does not happen.

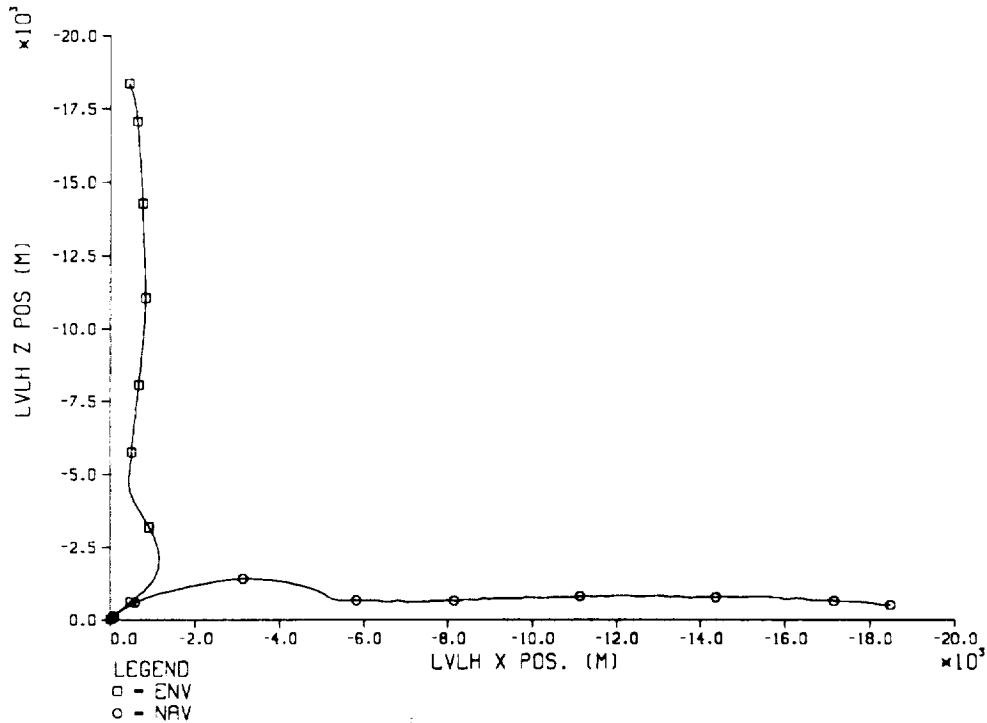


Figure 1 - RELATIVE MOTION FOR STVHO
USING STANDARD I-LOADS

If measurements were not being used, the satellite would follow a path shown in Figure 2, which depicts the natural motion of the satellite had the tether not been connected. This seems to indicate that Nav is using the dynamics in the state propagation and is ignoring the measurements. What is actually happening can be seen in Figure 3 and Figure 4. The measurements aren't being edited but rather the filter is adjusting the shaft bias by about 80° and the trunnion bias by 25°. Successful relative navigation now requires tuning the filter and giving the measurements more weight so that they are "believed" over the coded dynamics.

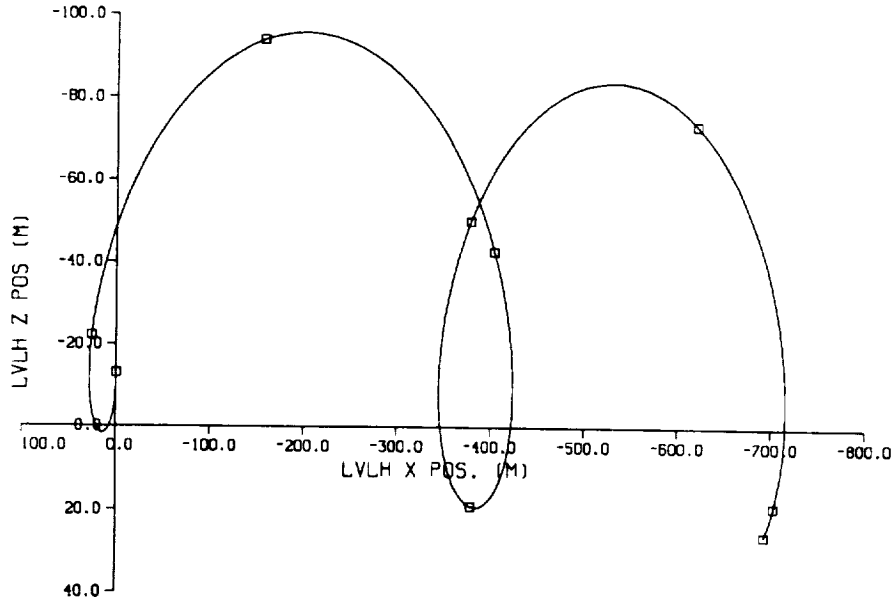


Figure 2 - RELATIVE MOTION OF SATELLITE
WITH OUT TETHER ATTACHED

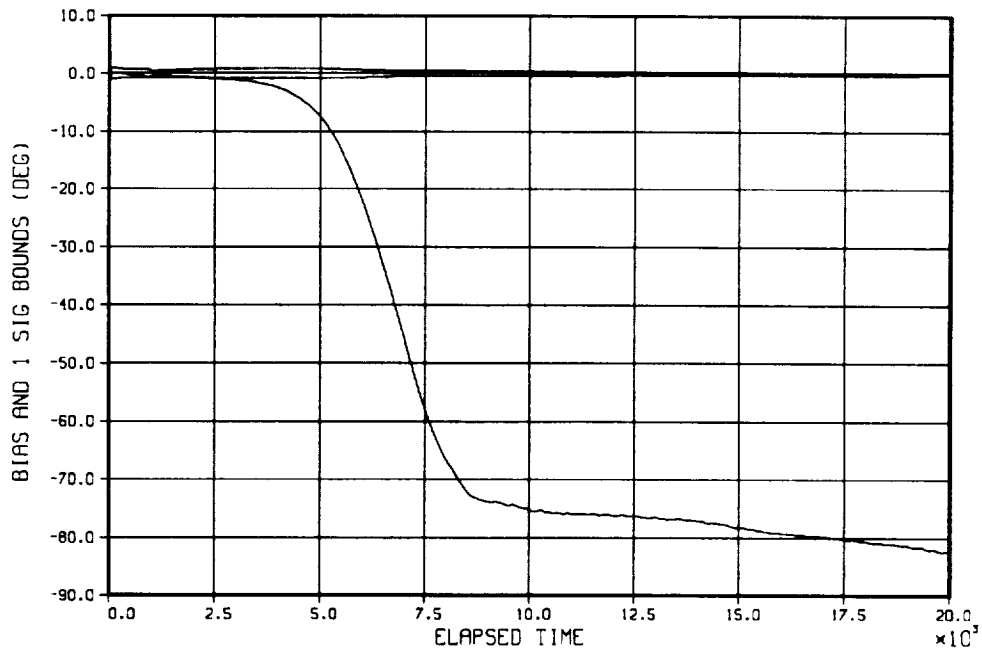


Figure 3 - RADAR SHAFT BIAS

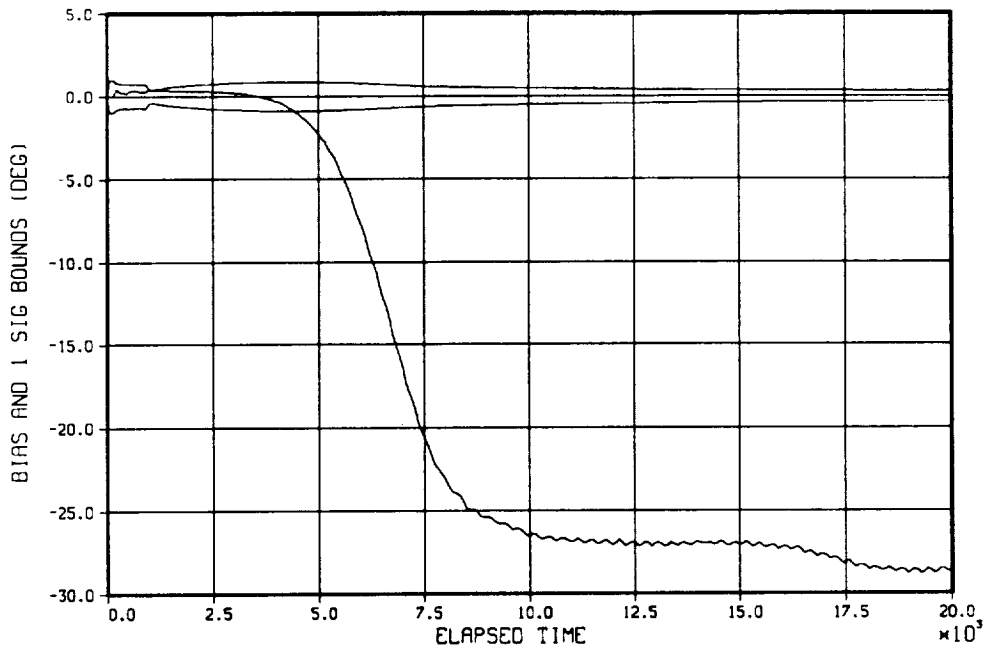


Figure 4 - RADAR TRUNNION BIAS

2.3 FILTER TUNING

The flight software is designed so that various parameters (called I-LOADs) can be changed without major recoding of the software. As an example, the choice of which vehicle state to filter is set by the I-LOAD Shuttle_filter_flag. Eight of these I-LOADs were found to require adjustments in order to properly tune the filter. The eight I-LOADs are shown in table 1.

TABLE 1 - I-LOADS USED TO TUNE THE FILTER

<u>I-LOAD NAME</u>	<u>DESCRIPTION</u>
UNMOD_ACC_BIAS_FLAG	Enable the filter to solve for unmodeled acceleration
SIG_UPDATE	change initial position and velocity σ to prox ops values
VAR_RRDOT	decrease initial range variance
VAR_RR_ANGLES	decrease initial radar angle variance
COV_U_A_COAST	increase initial unmodeled acceleration variance
BIAS_VAR_RRDOT	decrease range ecrv bias σ for state noise
BIAS_VAR_RR_ANGLES	decrease radar angle ecrv bias σ for state noise
VAR_U_A_COAST	increase unmodeled acceleration ecrv bias σ for state

SIG_UPDATE is used to initialize the covariance. Normally it is only used at the beginning of a rendezvous, but for the tether mission, uplinks are required which triggers a covariance reinitialization. COV_U_A_COAST will also be used at each uplink to reinitialize the unmodeled acceleration slots of the covariance matrix. Measurement variances are only used at rendezvous start up time and when an instrument is switched. The bias slots of the state (slots 7 - 13) are modeled as exponentially correlated random variables (ecrv). The last three parameters in table 1 control the ecrv state noise for the propagation.

2.4 RADAR BREAK-LOCK

A major impact to using relative Navigation during this mission will be if the radar loses the lock on the target. Having Rel Nav active will aid in the radar finding the target by telling the radar where to look, but in the period of time that no measurements are being processed, Nav is simply propagating the target state. The target state vector would then be following a path similar to that shown in Figure 2. Eventually Nav will be telling the radar

to point in the wrong direction. The question for the break-lock studies is how long will it take before Nav points the radar such that it can't locate the target? To answer this, some radar basics are needed.

When the radar is in GPC mode, it takes a state vector from Nav and points to that location. If a positive return signal is not received, a spiralling search within a designated cone is begun. The limit of the cone is determined by the expected distance to the target. For instance, a cone of $\pm 20^\circ$ is searched at 20 km and a cone of $\pm 30^\circ$ is searched at 13 km. A new search is begun every 20 seconds until the target is found.

This topic is studied from a navigation standpoint only. There are other concerns about the actual functioning of the radar hardware. One concern is that the radar may begin tracking the tether instead of the satellite. This can easily be checked real time by watching the radar data and comparing it to the timeline and the tether length output. If this phenomenon does happen, it will be during the portions of the mission when the satellite is towards the 20 km point and the tether begins to bow. At some point during the retrieval, the radar should be able to reacquire the satellite via Rel Nav and target state vector uplinks. Reacquiring the target during retrieval will still be a useful aid to the mission and crew by having some radar feedback as the satellite approaches the Shuttle.

3.0 MISSION ANALYSIS

Several different trajectories were generated and processed for the TSS1 mission. The purpose of having the different trajectories is to try to encompass the actual performance (a true unknown) within simulated data. To do this, various scenarios were generated by adjusting mission parameters. By doing this, the most difficult mission to navigate was found to be one that needed a lot of attitude controlling. This mission profile also required numerous uplinks to keep the Shuttle inertial state errors within procedural limits.

The particular trajectory used in this paper is named STVHO. The profile uses vernier jet control and there is a current flowing through the tether during the on-station phase of the mission. The Shuttle is held at a pitch of 25° nose up with 2° attitude dead bands. Six uplinks were required for this profile.

There is a concern as to what happens to a standard rendezvous when I-LOADs are changed. This could be a question if another rendezvous is scheduled for the same Shuttle mission or if an unplanned rendezvous would be desired. To look at this, I used a trajectory called OMP13, which is simulated data. A 30 cycle Monte Carlo run was performed on both STVHO and OMP13.

3.1 ANALYSIS OF STVHO

Figures 5 and 6 show the 30 cycle Monte Carlo output for STVHO. These two plots indicate good Rel Nav performance. The downtrack and cross track errors are both 320 m during the on-station phase and reducing to zero towards the end of the retrieval. The radial position error remains around 20 m throughout the whole mission. Velocity errors seen in Figure 6 also are acceptable. The spikes, which are more prominent in the velocity plot, are due to the state vector uplinks. When an uplink occurs, the covariance gets reset and it takes about 1,000 seconds for the filter to recover.

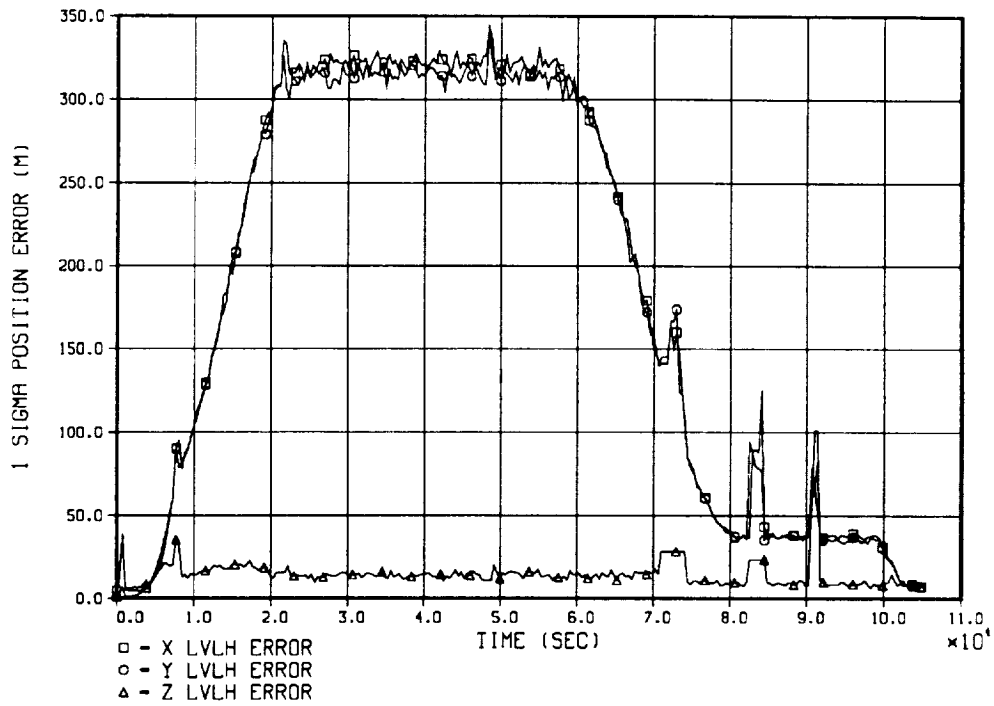


Figure 5 - RELATIVE POSITION ERROR FOR STVHO

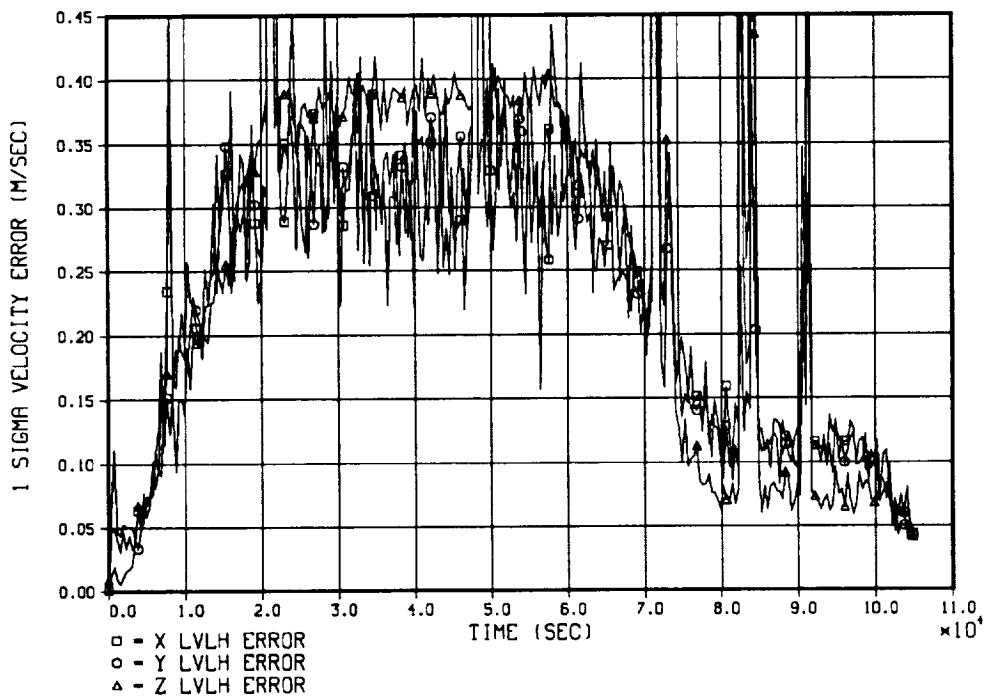


Figure 6 - RELATIVE VELOCITY ERROR FOR STVHO

Figure 7 shows the Shuttle centered relative motion plot for STVHO. Differences seen in the trace of the environment versus Nav is due to the measurement errors so the actual mission could vary depending on how well the measurement errors have been predicted. With the measurement errors used, the angle between the line of site error to the on-station points seen in Figure 7 is around 1.3°.

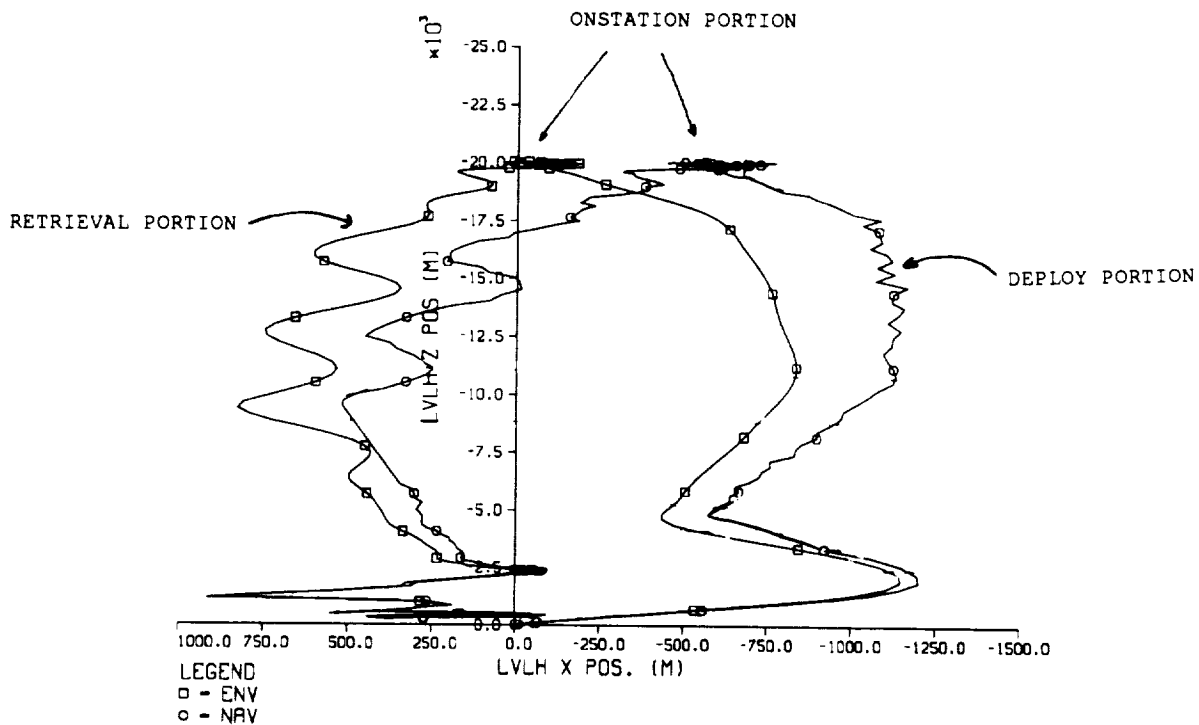


Figure 7 - RELATIVE MOTION PLOT FOR STVHO

3.2 ANALYSIS OF OMP13 USING THE NEW I-LOADS

Figures 8 and 9 show OMP13 using the standard filter I-LOADS. Star tracker measurements are taken during the first portion of the rendezvous. At 10,000 seconds the measurement source is switched to the rendezvous radar. These plots show typical performance. Figure 10 is the target centered relative motion plot. Figures 11, 12 and 13 are for OMP13 using the new I-LOAD set. Performance is the same up until 12,000 seconds. This is the point of the profile where the Terminal phase Initiation (TI) burn is executed.

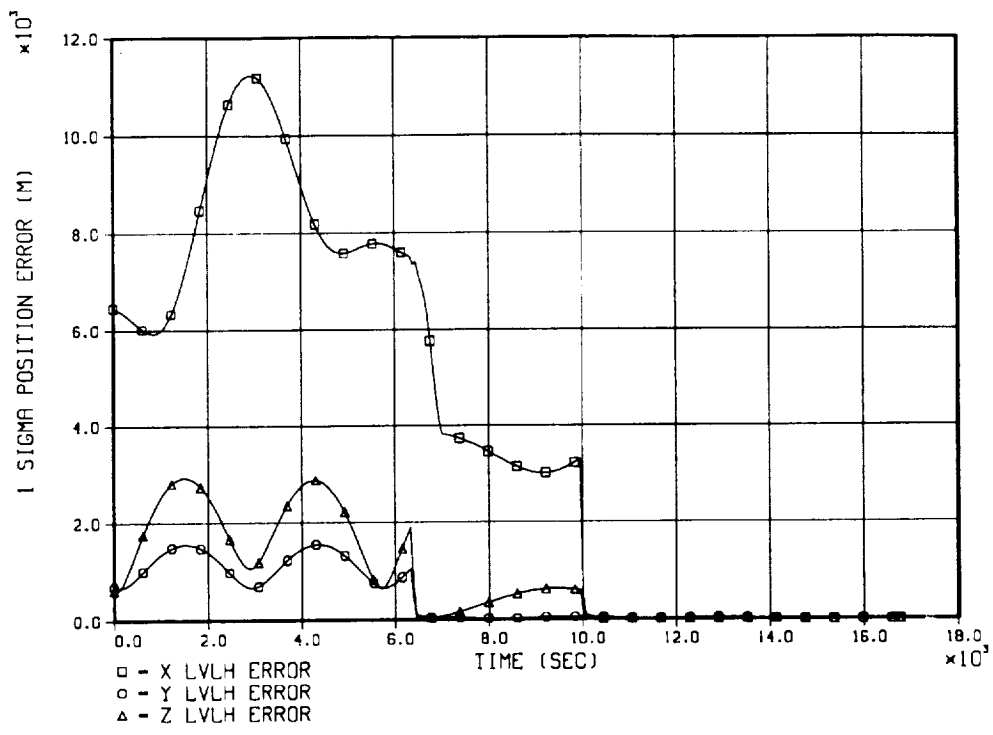


Figure 8 - RELATIVE POSITION ERROR FOR OMP13 WITH THE STANDARD I-LOADS

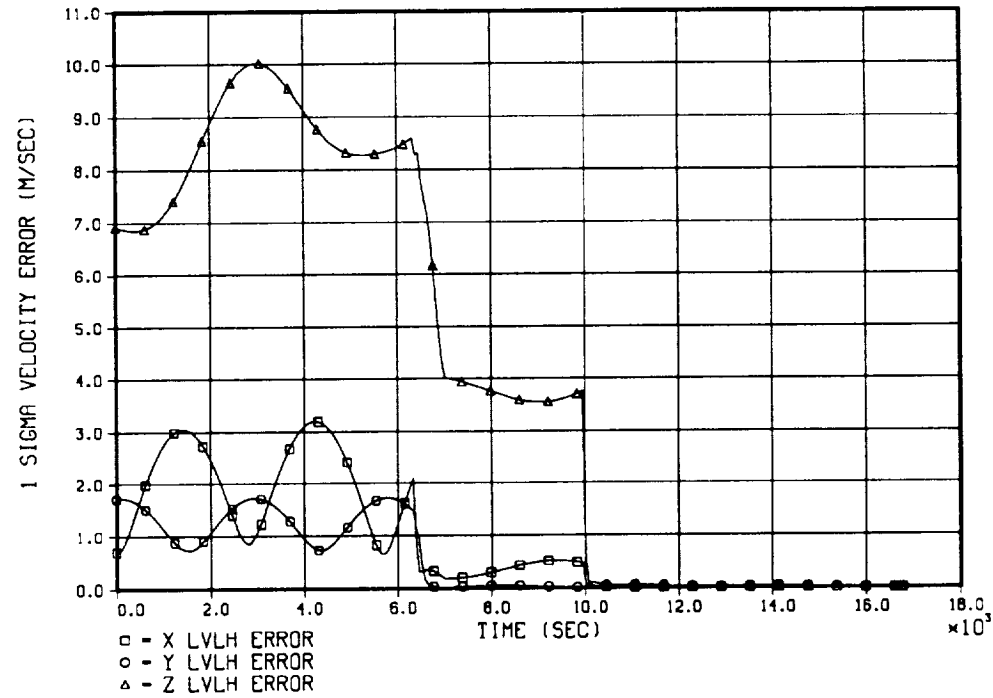


Figure 9 - RELATIVE VELOCITY ERROR FOR OMP13 WITH STANDARD I-LOADS

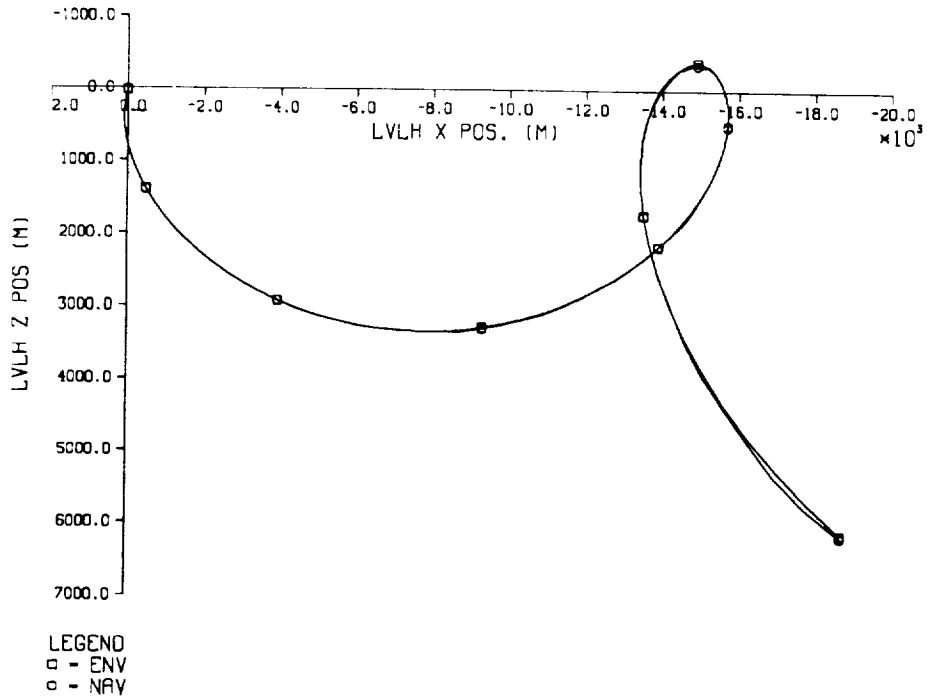


Figure 10 - RELATIVE MOTION PLOT FOR OMP13 WITH STANDARD I-LOADS

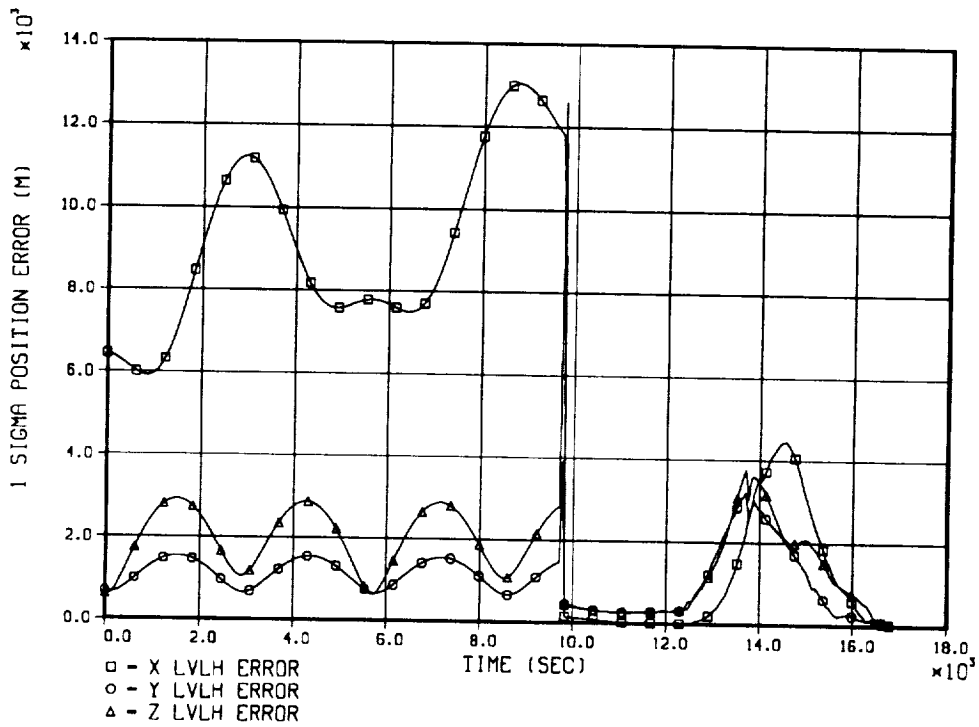


Figure 11 - RELATIVE POSITION ERROR FOR OMP13 WITH NEW I-LOADS

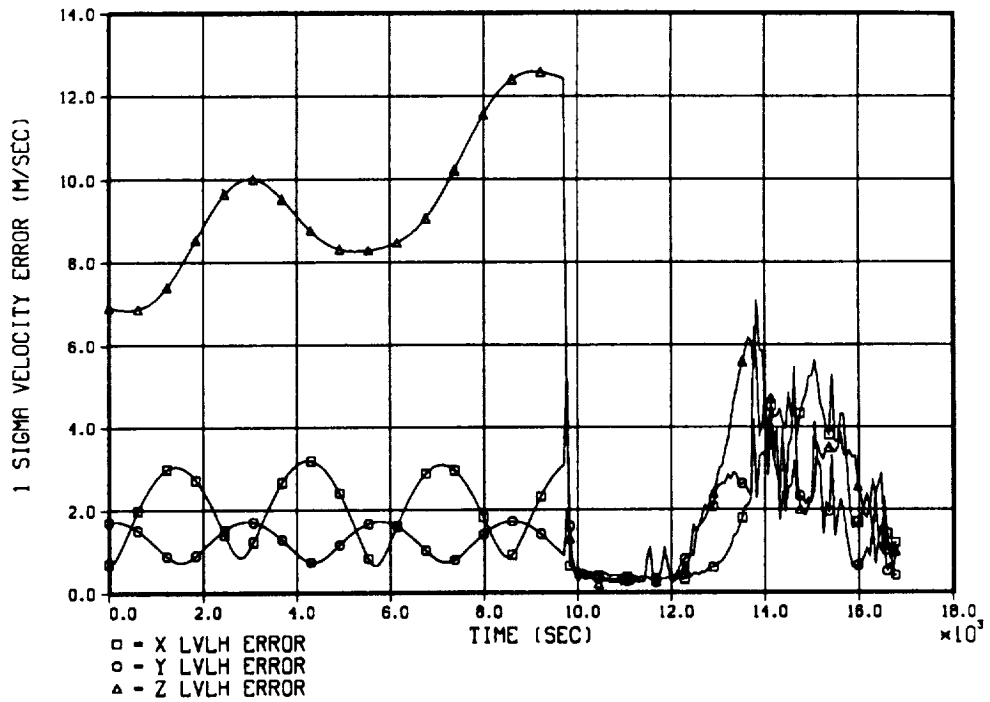


Figure 12 - RELATIVE VELOCITY ERROR FOR OMP13 WITH NEW I-LOADS

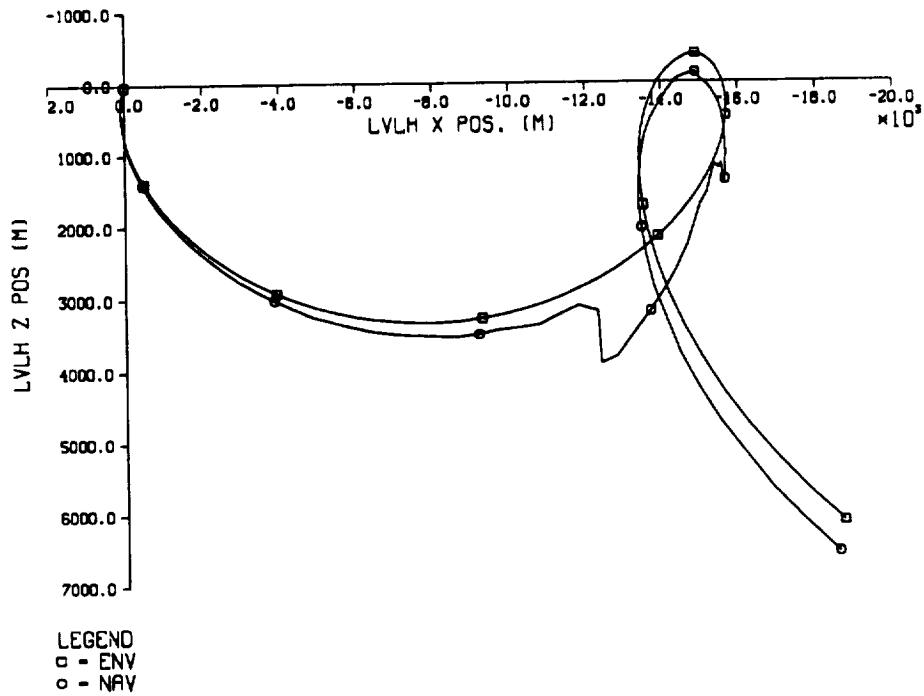


Figure 13 - RELATIVE MOTION PLOT FOR OMP13 WITH NEW I-LOADS

Another significant event during this time is angle measurements drop out from 12,000 seconds to 14,000 seconds. The relative motion data in Figure 13 does not reflect the state errors shown in Figure 11 because Figure 13 is from a single cycle run. The Monte Carlo analysis in SENSOR does not print the relative state for each cycle.

The performance of OMP13 with the new I-LOAD set is not good. The Root-Sum_Squared (RSS) position error at 14,000 seconds into the run is 7,000 m. The actual distance between the Shuttle and the target at this time is approximately 12,000 m. This portion of the rendezvous requires several midcourse maneuvers, which are normally targeted onboard. The plots show that the Nav state would not be accurate enough to do this.

3.3 RADAR BREAK-LOCK ANALYSIS

This analysis was performed by inhibiting measurements at a given time. This allowed Nav to propagate the target state using normal orbital dynamics. Figures 14, 15 and 16 show results at three different times: 1,000 seconds, 15,000 seconds and 45,000 seconds respectively. Relative times can be taken from the plots since there is 38.4 seconds between markers.

The objective is to see how long Nav can propagate the state before the state error is too large to help the radar point at the target. The lines shown on the plots indicate the point after which the target will not be within the search cone of a given Nav state. The work shown here attempts to answer the break-lock question from a navigation standpoint. The actual radar hardware could shorten the period of time for reacquisition.

Figure 14 shows an interesting propagation, which is due to the unusual motion of the satellite at the time the measurements are shut off. This plot indicates that it will take 800 seconds before the Nav state will point the radar in the correct direction to find the target. From this point, there is 700 seconds for which the Nav state will point the radar such that it can reacquire the target.

The next run, shown in Figure 15, behaves as expected. If the break-lock happens 15,000 seconds into the deploy, the radar has 450 seconds to reacquire

the target before Nav state errors become too large. This time is based only on the search cone. There is also a large range difference between the Nav state and the actual position of the target which could also limit the reacquisition time.

Figure 16 shows the final case analyzed. This break-lock is simulated at 45,000 seconds into the run, which is during the on-station phase of the mission. This plot indicates that about 400 seconds are available for Nav to help the radar find the target. Again, as previously mentioned, there is a large range difference between the environment and the Nav state.

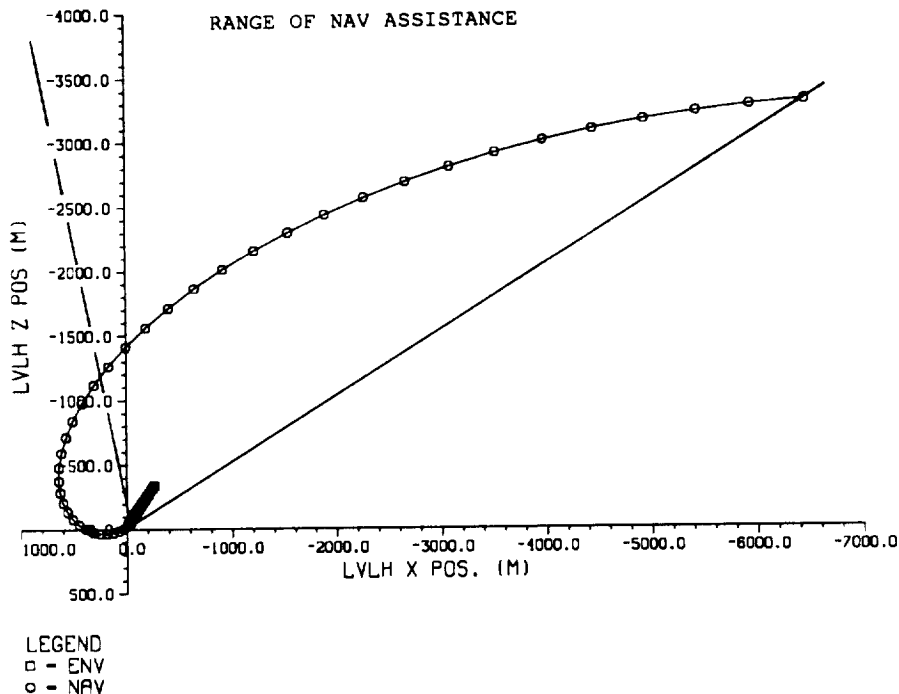


Figure 14 - RADAR BREAK-LOCK AT 1000 SECONDS

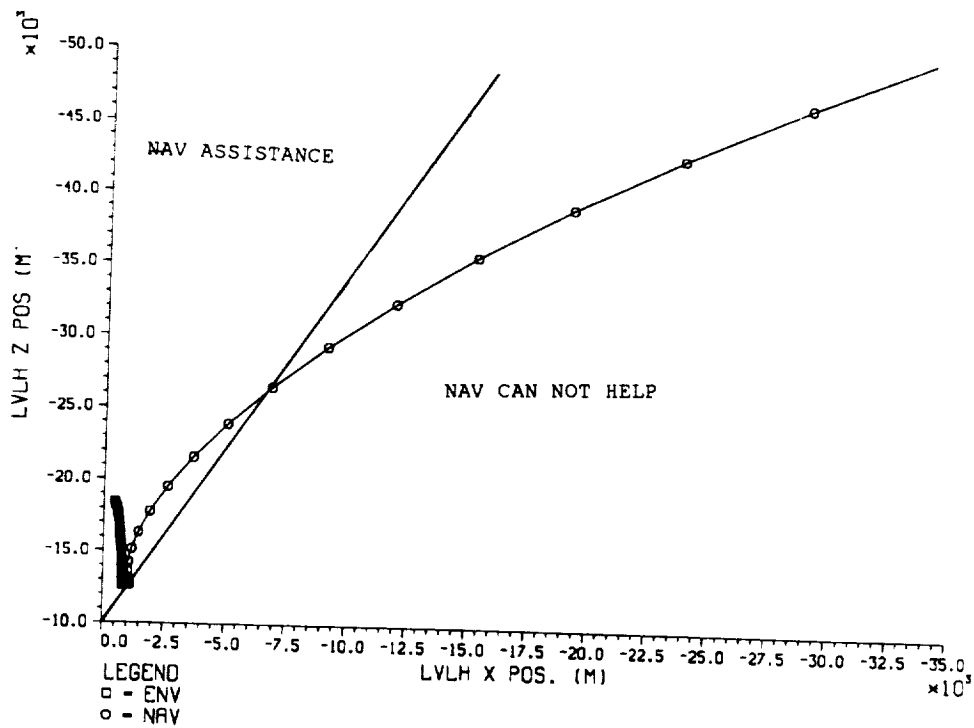


Figure 15 - RADAR BREAK-LOCK AT 15,000 SECONDS

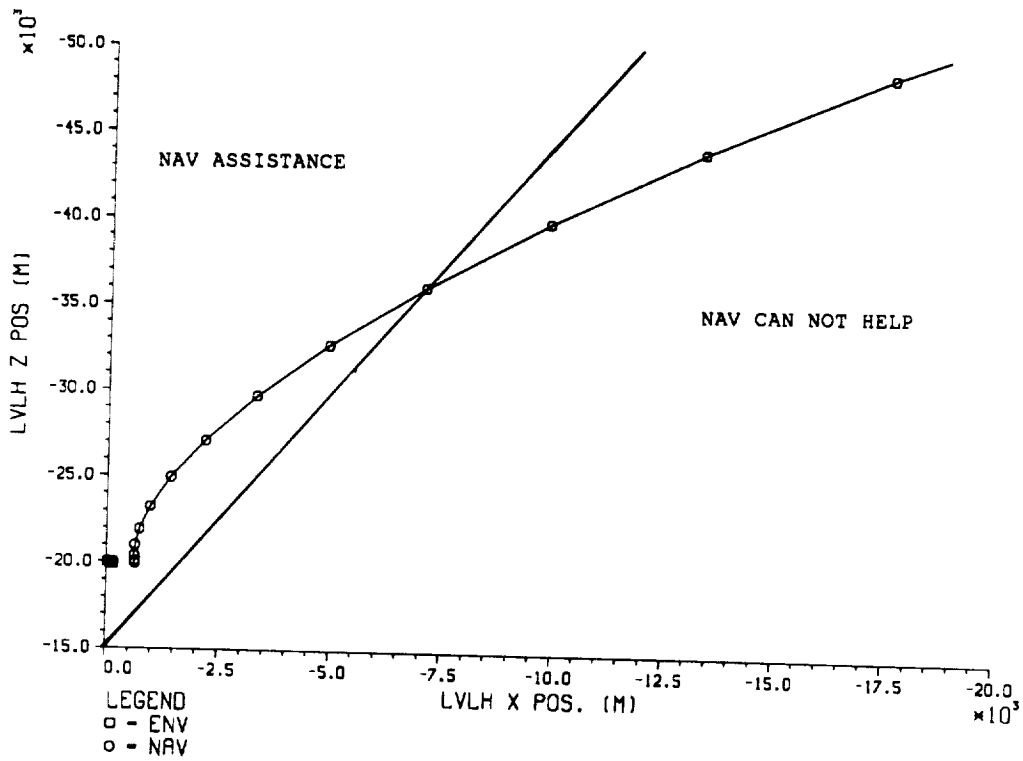


Figure 16 - RADAR BREAK-LOCK AT 45,000 SECONDS

4.0 CONCLUSIONS

Relative navigation performance is acceptable for the TSS1 mission. To do this requires 9 I-LOADs to be changed. This new I-LOAD set does work for the standard rendezvous trajectory that I have available, but shows poor performance during the final 14 km of the rendezvous. State vector uplinks around the time of the TI burn might be able to keep the state errors within acceptable limits. An alternative method of performing a standard rendezvous would be to target the midcourse maneuvers on the ground and then uplink them to the Shuttle. These ideas require more analysis.

The performance of the radar itself is a question that may not be completely answered until the mission. The satellite is small and will be difficult to track at 20 km. If tracking of the satellite is not possible at the extreme distances, Rel Nav and the radar, with the help of ground uplinks, should be able to acquire the target at some point during the retrieval.

5.0 REFERENCES

1. Wacker, R.A. and crew, "STOCS USER MANUAL", McDonnell Douglas Astronautics Co.-Houston Division, 1.1-TM-EH86020-06, 14 February 1986.
2. Alland, K.A. and Kralicek, T.L., "SENSOR6A USER'S GUIDE", McDonnell Douglas Technical Services Co.-Houston Astronautics Division, 1.2-TM-FM85018-219, 29 August 1985.

Impact of Tether Cutting on Onboard Navigation During the Tethered Satellite Mission -1

Dana M. Pirker
McDonnell Douglas Space Systems Company
Engineering Services Division
16055 Space Center Blvd, Houston, TX 77062
JSC Mail Code T5H
280-1500 x4074

Abstract

The first Tethered Satellite System mission (TSS-1) is manifested for Shuttle Flight STS-44 in January of 1991. The TSS mission presents a new challenge to engineers, requiring advanced guidance, navigation and control concepts. As an example, current navigational systems track the Orbiter exclusively and do not model the accelerations induced by the tether on the Shuttle. Due to the offset of the center of mass of the system from the that of the Shuttle, the navigational system assumes the tracking data are biased, and tracks the center of mass of the system. This offset can be quite large, to several hundreds of feet. As a result, determination of the navigational state of the Shuttle becomes more difficult and less certain.

Current NASA flight rules require that the navigational state of the Orbiter at deorbit burn be known to an accuracy of 20 nautical miles. Response of the Shuttle crew to this contingency may involve cutting the tether prior to a complete retrieval. This paper examines the degradation of the navigational state accuracy as modelled by Shuttle navigation systems.

Responses to the loss of communication scenario are proposed for two cases. The first case examines navigational performance during a "nominal" attitude profile. The second case is identical to the first, with the inclusion of modelled tether electrodynamic forces.

Comparisons of trajectories propagated from the onboard navigational state-vector and a reference ephemeris state-vector were performed, with the tether cut simulated at various points during the mission. Additionally, updates to the onboard navigational state via ground uplinks were provided prior to the assumed loss of communication. Through these comparisons, the onboard navigation state error was determined. Alternative responses result from efforts to minimize this error during the various phases of TSS-1 deployment. These results demonstrated existing NASA flight rules could be violated by cutting the tether, and suggests responses to a loss of communications contingency to maintain a more accurate navigational state.

Introduction

Perhaps the most exciting and challenging Shuttle mission ever flown is scheduled for STS 44, in late January, 1991. A satellite will be deployed in an nominally outward radial direction on a conducting tether during the first Tethered Satellite System mission (TSS-1). The satellite is designed by an Italian aerospace company, Aeritalia. Primary objectives for the mission are to demonstrate closed loop control of a tethered object, and to examine the behavior of a current carrying tether passing through the Earth's magnetic field.

The deployment of the satellite moves the center of mass of the system away from that of the Orbiter. For a twenty kilometer long tether, this separation can be as great as 100 meters. Additionally, the presence of the tether results in a tension force continually experienced by the Shuttle, a force unmodelled by current Shuttle ground-based navigational systems onboard Shuttle. Although the Inertial Measurement Units (IMUs) detect tether accelerations, these accelerations are within the noise thresholds. Therefore this data is not passed on to the navigational systems. These two facts make navigation difficult. When this force is suddenly removed, as in a cut or break of the tether, the Shuttle's orbit changes, and the system center of mass returns instantly to the Shuttle. The onboard navigation system is unaware of the removal of the tether, resulting in rapid navigational state degradation.

An accurate Shuttle state can be determined following a tether cut, given communications with ground based systems. The ground navigation systems are able to determine the new orbit of the Shuttle, then uplink an accurate state, resetting the onboard systems. Shuttle navigation proceeds as if the tether was never present. In a loss of communications contingency, however, an accurate updated state is unavailable to onboard systems.

This paper examines Shuttle navigational response to the removal of the tether. Additionally, responses are suggested to a loss of communications in an effort to minimize navigational error.

During a loss of communications, the onboard navigation systems perform unsatisfactorily, as no uplink can be provided. Efforts to minimize onboard navigational error growth result in responses to a loss of communications contingency. Navigation performance is improved to acceptable standards by reeling in the tether as much as possible prior to cutting.

Analysis tools used for the research of this paper include three simulations: The Shuttle Tethered Object Control Simulation (STOCS), a high fidelity engineering simulation of the TSS-1 mission (Reference 1); the Shuttle Environment Navigation Simulation for Orbit and Rendezvous (SENSOR), an onboard navigation simulation (Reference 2); and the Standalone Orbital Navigation (SONAV) program, a ground system emulator (Reference 3). An additional tool is the Houston Operations Predictor/Estimator (HOPE). HOPE was used primarily as a propagator of Shuttle state in the absence of tether accelerations (Reference 4).

Effect of Tether on Shuttle Navigation Systems and State

Current navigational systems track the Orbiter exclusively and do not model the accelerations imparted to the Shuttle by the tether. These accelerations include gravity gradients, and the aerodynamic and electrodynamic drag of the tether. The

gravity gradient accelerations are dominant of these three. Because the existing ground navigation systems do not incorporate these accelerations in their propagations, the combination of a propagation of the previous state and a weighted least-squares reduction of the observation data results in a state vector for that point in the TSS where the gravity gradient accelerations are zero. This point is approximately the center of mass of the system. Effectively, the ground navigation systems assume the observations are biased by the difference in position between the system center of mass and that of the Shuttle. As a result, the navigational accuracy of the shuttle deteriorates rapidly, particularly during reel-out, when these two points are moving apart. Reference 5 presents a further discussion of tether effects on inertial navigation.

To the onboard navigational systems, the presence of the tether goes completely unnoticed. Accelerations of the same magnitude as the tether tension appear as noise to the navigational systems. These forces are therefore not considered in the onboard state propagation.

The comparison of the ground ephemeris for the Shuttle and the simulated tethered trajectory in Figure 1 illustrates the effect of tethered operations on Shuttle navigation. During the initial phases of the mission (i.e. reel-out, see Figure 2 for a tether length profile), the navigational state error grows rapidly. Following the first uplink during the onstation portion of the mission, the ground system ephemeris matches the simulation quite closely. Navigation performance improves when the difference in the position vectors of the system center of mass and the Shuttle center of mass remains relatively constant, as it does during the onstation portion of the mission. The ground navigation systems predict the state of the Orbiter with greater accuracy, much more so than when the observation data biases are constantly changing.

Removal of the Tether

When a tether cut removes the TSS gravity gradient accelerations from the Shuttle, the ground navigation systems detect a displacement of the target's center of mass. Because the forces not modelled in the the ground system propagation are no longer present, the ground system no longer treats the observational data as biased, and once again generates state vectors for the center of mass of the Orbiter.

Just as the tether force went undetected while the tether was attached, the absence of the tether force also goes unnoticed. The onboard systems continue to propagate a state of the Shuttle determined with the tether attached, resulting in rapid navigational error growth. An uplink of a state-vector from the ground ephemeris resets the onboard state, however, and the onboard systems perform correctly.

At this point it is important to point out a limitation of the Shuttle navigational systems. The displacement of the center of mass following a tether cut can be thought of as an an acceleration being applied to the Shuttle. If the Shuttle experiences a large unmodelled force, ground navigation requires one full revolution of observation data to redefine the Orbiter's orbital energy. During this time, no uplink is provided to onboard systems. Consequently, the onboard navigation error becomes excessive (Figure 3).

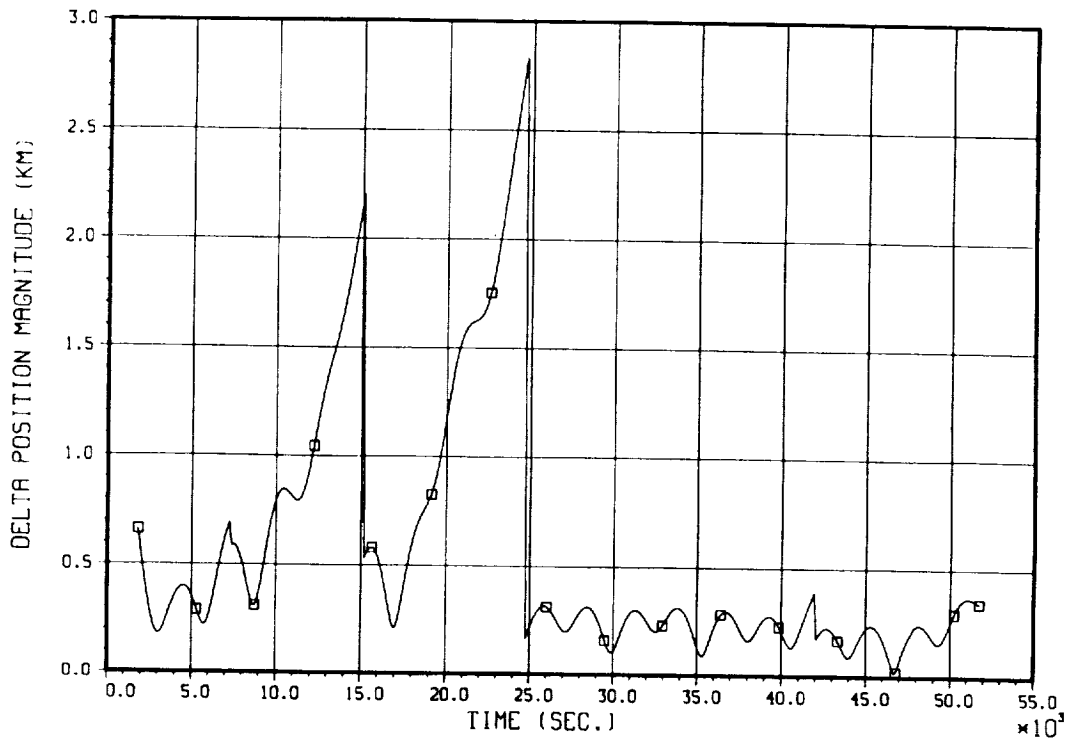


Figure 1: Comparison of Ground System vs. Simulated Trajectories

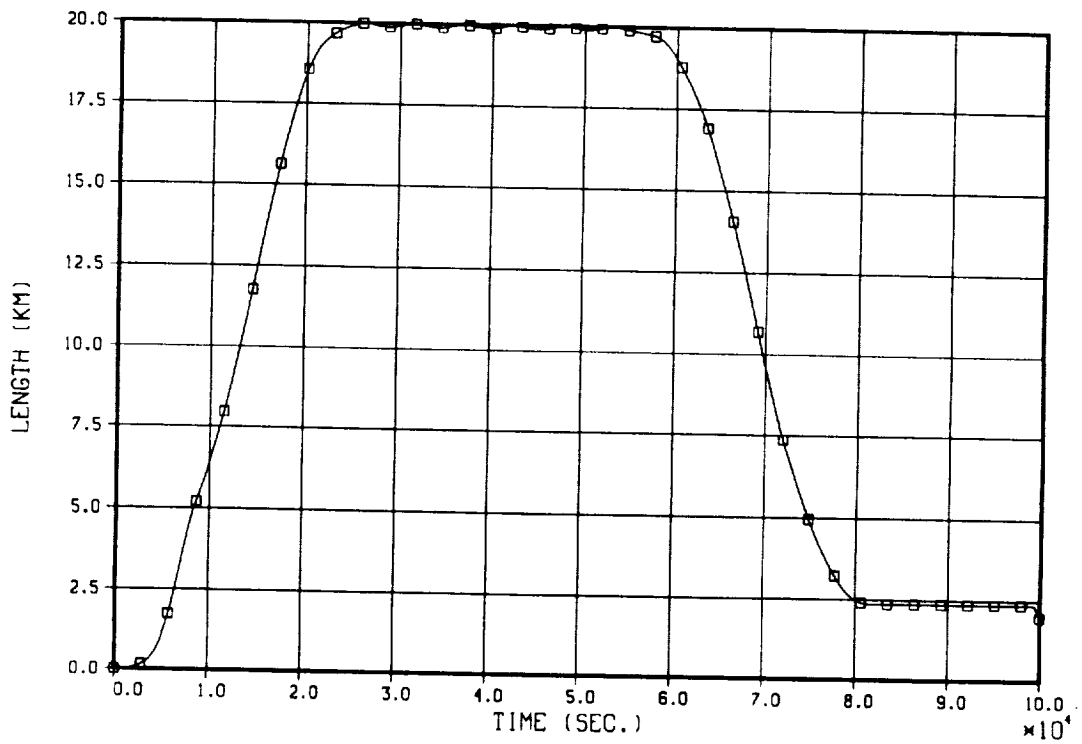


Figure 2: Tether Length Profile for Nominal and Electrodynamic Missions

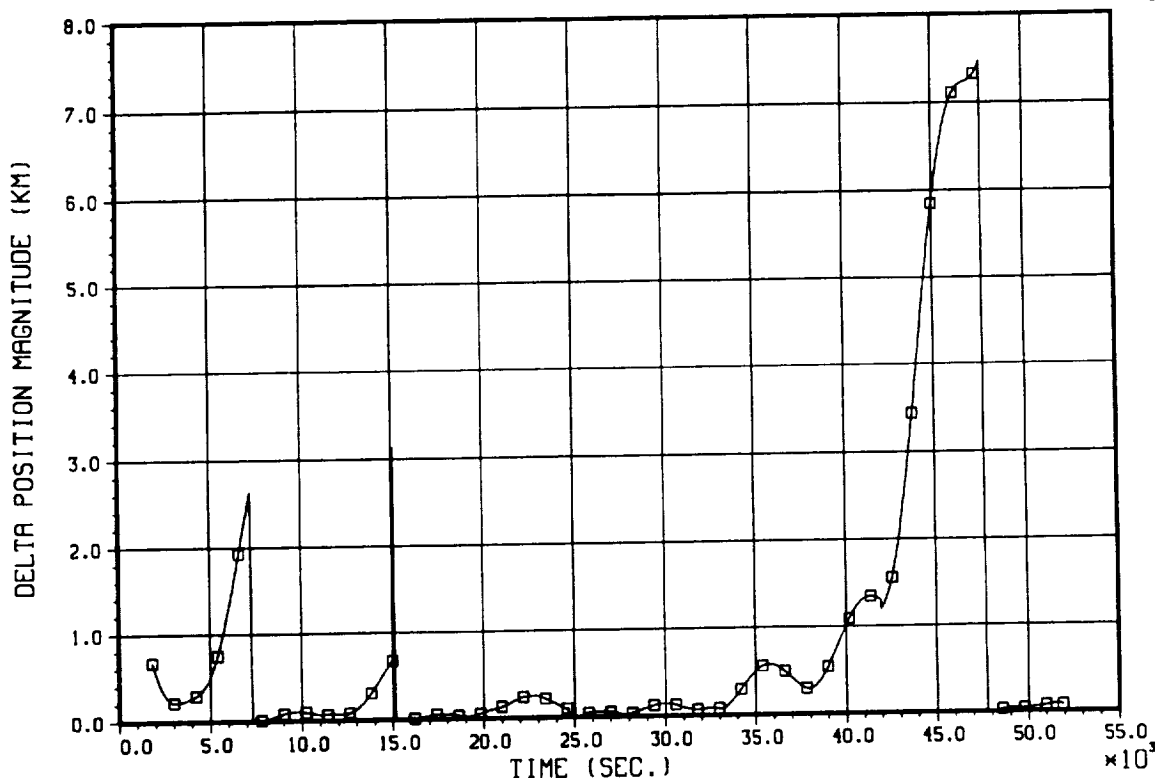


Figure 3: Comparison of Onboard vs. Simulated Trajectory

Simulation of a Cut Tether

Two mission profiles were considered in the study of an immediate cut and return response. The Shuttle was in an local vertical, local horizontal (LVLH¹) attitude hold for both profiles, with a constant pitch angle of 25 degrees, zero roll and yaw.

The first profile, considered a nominal case, assumes no current flows through the tether during any portion of the mission. The second is identical to the first, with the current turned on during the onstation portions of the mission.

A propagation of a Shuttle state-vector served as a simulation of Shuttle trajectory following a cut tether. The vector was propagated with gravitational and environmental accelerations, but without tether tension force. Assumptions validating this method of simulation begin with the assumption the cut is placed at the boom tip. By putting the cut at the boom tip, the dynamic behavior of recoiling tether need not be considered.

An additional assumption pertains to the change in energy of the Orbiter. If it is assumed a negligible amount of tether energy is imparted to the Orbiter as a result of cutting the tether, a propagation excluding tether related forces of the Shuttle state-vector is a valid simulation of a cut. Furthermore, in the STOCS generated trajectories

¹The LVLH coordinate system is a right-handed cartesian coordinate system with its Z axis pointed toward the center of mass of the Earth, and in the instantaneous orbital plane. The Y axis is formed by taking the cross product of the position and velocity vectors, in that order. The X axis is mutually orthogonal to the Y and Z axes.

presented here, a massless tether was used. This assumption neglects transmitted tether energy from sources such as wave transmission.

HOPE was used as the propagator for generation of post-cut trajectories. HOPE is a generic spacecraft trajectory navigation analysis tool, utilized to measure performance of new trajectory generation or navigation software. The HOPE propagator does not model tether-induced accelerations, but does have geopotential, atmospheric, and solar radiation models. Additionally, mass, attitude, and payload door timelines characteristic of TSS-1 mission can be included.

A complete TSS trajectory during which the tether has been cut can be formed by splicing the STOCS simulated trajectory and the propagation. These spliced trajectories were used for this study.

Responses to a Loss of Communication Contingency

With some insight into the systems navigating the Shuttle, examining a loss of communications scenario becomes possible. NASA flight rule 4-50 (Reference 6) sets a limit on the navigation uncertainty for a deorbit burn. It states the navigational state error at deorbit must not exceed 20 nautical miles (approximately 37.039 kilometers). Additionally, it states for the case of emergency deorbit with loss of communications, designers are to assume it will take four revolutions to find an appropriate landing site.

There are basically four responses to a loss of communications: immediate cut and return, a partial retrieval and return, a complete retrieval, or a tether length hold prior to cut and return.

At the time of writing this paper, simulation data for a complete retrieval from maximum tether length to the boom tip is not available, as the baseline tether retrieval includes a hold phase at a tether length of 2.4 kilometers (the reader is again referred to Figure 2). Therefore this option is not considered here.

Immediate Cut Response

Navigational error envelopes were generated for the four revolutions following the loss of communications. A cut was simulated by propagating the Shuttle state in the absence of tether accelerations, using a STOCS state-vector as the initial state of the Shuttle. The identical process was then performed using a state-vector determined by the onboard systems simulator, SENSOR. After the four revolution propagation, the resulting trajectories were compared. Any differences were recorded as the navigational state error of the onboard systems. The time of the tether cut was incremented in fifteen minute steps.

The navigational error of the onboard system during the nominal mission appears in Figure 4. The data shown represents the navigational error after the four orbital periods. The navigational error never exceeds 30 kilometers, and Flight Rule 4-50 is not violated. The maximum error occurs at the onset of the onstation portion, reflecting the effect of the system center of mass moving away from the Shuttle center of mass on Shuttle navigation. After the first uplink during the onstation portion, the navigation systems begin to maintain an accurate state when compared to the simulation. Navigational accuracy improves with constant measurement biases and small perturbative forces. Furthermore, note the decrease in error during

the first reel in of the retrieval phase of the mission (approximately 53,000 seconds to 80,000 seconds). Because the two centers of mass are approaching each other, navigational performance improves in the absence of perturbing accelerations.

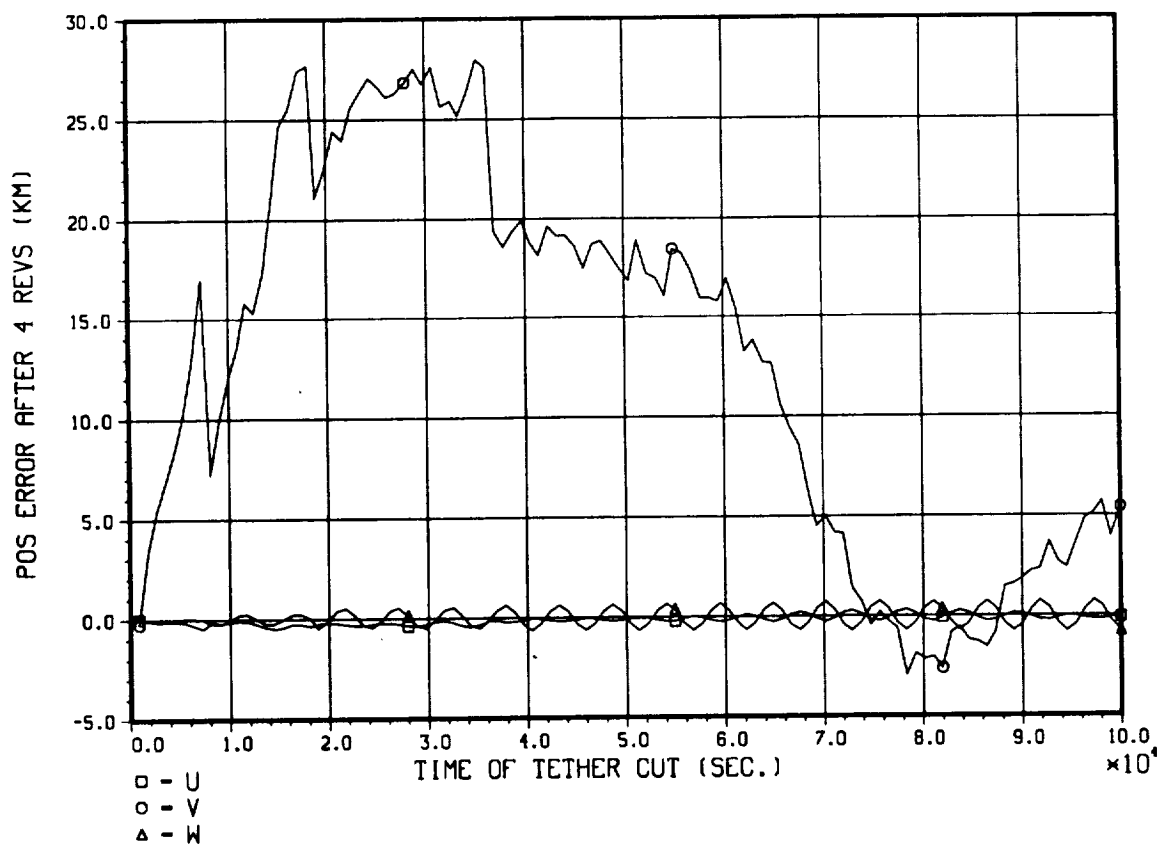


Figure 4: Nominal Mission Navigational Error After 4 Revolutions

Figure 5 shows the onboard navigational performance during a TSS mission with current flowing through the tether. The current is first turned on when the tether is fully deployed to a final length of 20 kilometers (at an approximate mission elapsed time of 20,000 seconds). The onboard state error approaches 37 kilometers at this time. After an uplink, providing the onboard systems with an accurate state and constant observational biases, the navigational state error four revolutions after the tether cut increases to within 160 meters of violating NASA flight rule 4-50. Because these data were generated following current navigational procedures, it is very likely this situation could occur during the course of the actual mission. An immediate cut and deorbit response is inappropriate for TSS-1.

The presence of perturbing accelerations induced by the tether cause the onboard state to quickly degrade. Similar to the nominal profile, note the initial improvement in onboard navigational performance during retrieval. Following an uplink in the middle of the onstation phase, however, the navigational error begins to grow, unlike the nominal case. Out-of-plane tether librations (see Figure 6) cause the Vernier Reaction Control System (VRCS) to hit roll and yaw deadbands, increasing the number of VRCS jet firings. These jet firings increase navigational degradation. Out-of-plane librations are the result of electrodynamic interactions of the tether and the Earth's magnetic field, begun during the onstation period. Because the

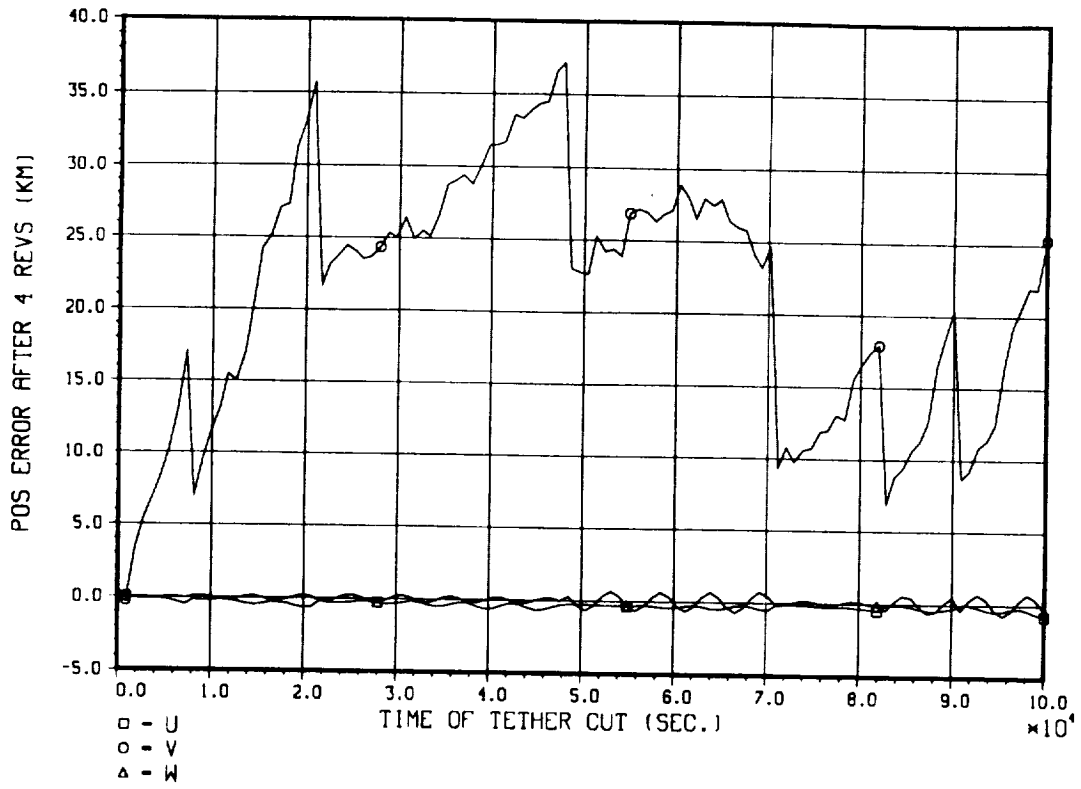


Figure 5: Electrodynamic Mission Navigational Error After 4 Revolutions

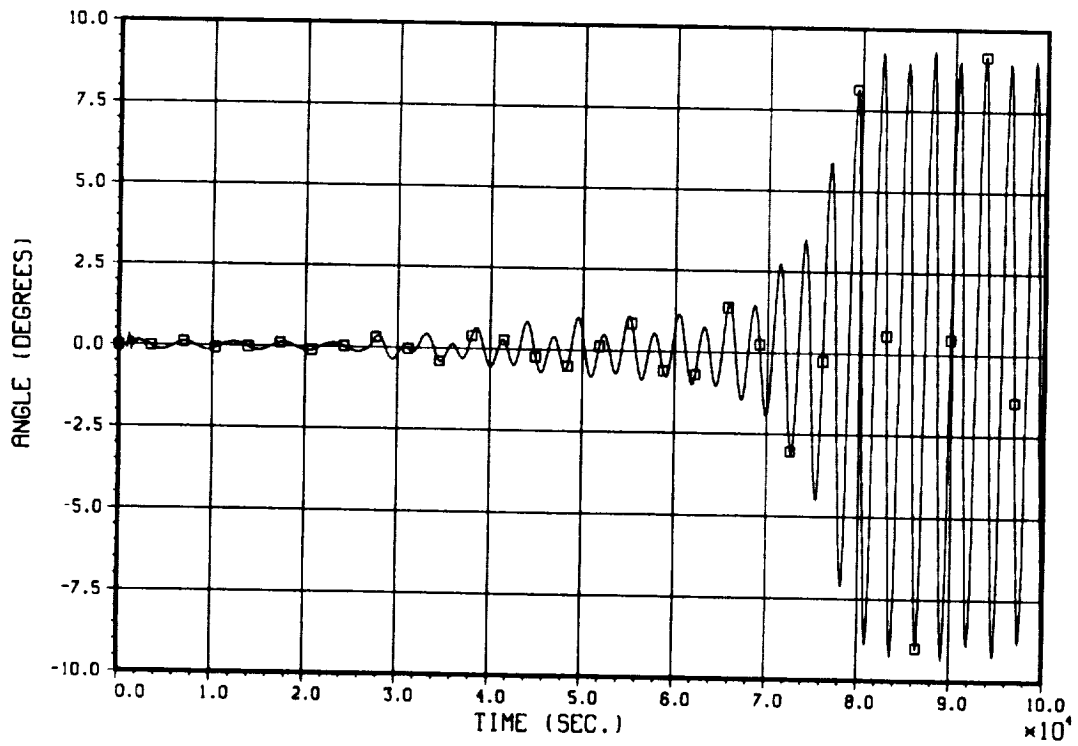


Figure 6: Electrodynamic Mission Out of Plane Librations (angle wrt local vertical)

Shuttle's trajectory is inclined with respect to the magnetic field lines, the tether electrodynamic force contains a component perpendicular to the Shuttle's orbital plane. At full deployment, the librations are relatively small and benign. As the tether length decreases, however, these librations increase in amplitude, resulting in more frequent RCS deadbanding.

Partial Retrieval and Cut

In a partial retrieval, followed by a tether cut, the tether is assumed to be reeled in following a nominal tether length profile to a given tether length and then cut. The loss of communications was assumed to occur just prior to an uplink, representing a worst case scenario. A electrodynamic mission profile was used, with the uplinks modified to place the missed uplink at the onset of retrieval. Onboard navigational errors were determined for a period of four revolutions after the beginning of retrieval.

In Figure 7, navigational error data show navigational performance improves in a loss of communications contingency if the tether is partially reeled in prior to cutting. A cut at 20 kilometers represents an immediate cut (in which the onboard navigational system performed unacceptably), demonstrating an error of 41 kilometers at the end of the four revolution period. Figure 8 compares the onboard navigational state to a simulated cut tether trajectory. The navigational state error grows linearly approximately 35 kilometers in four revolutions, or 8.75 kilometers per revolution.

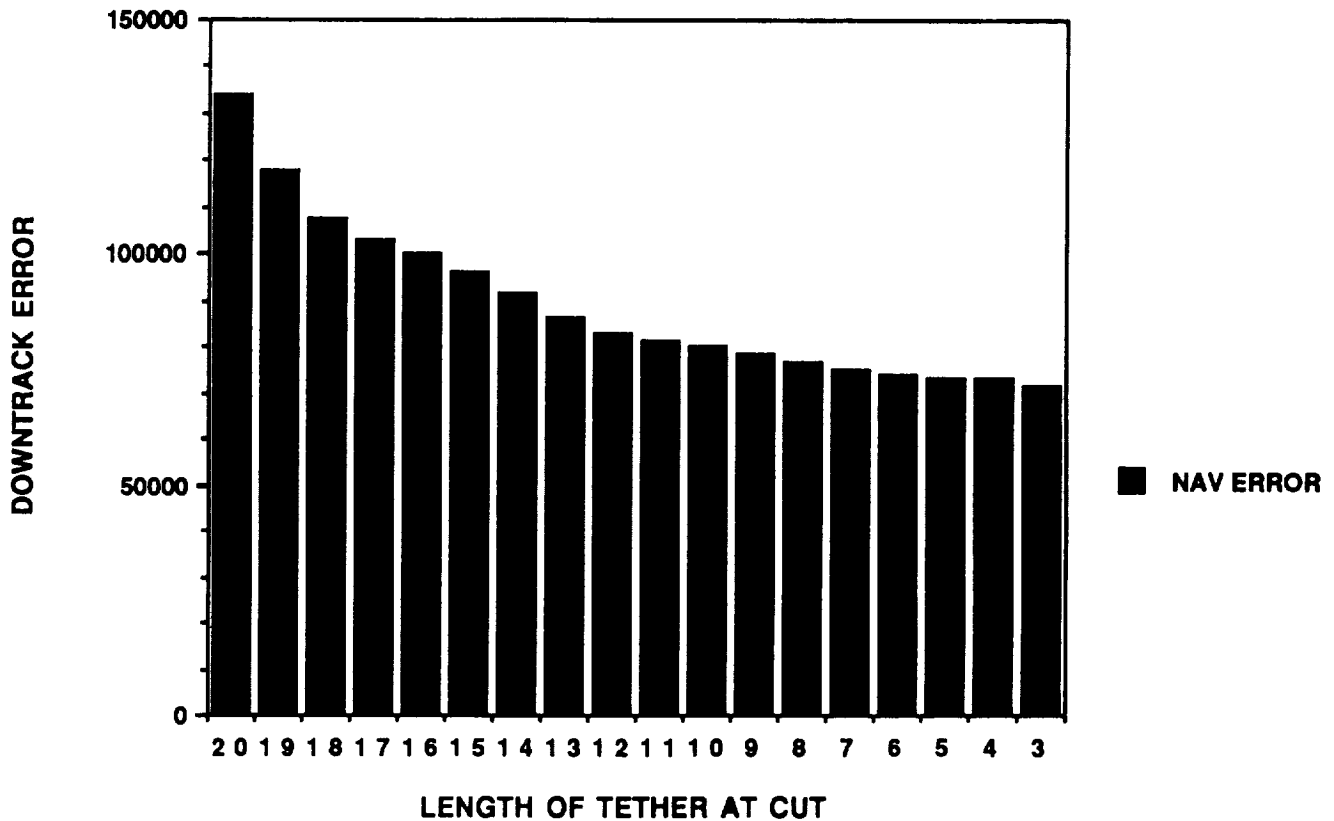


Figure 7: Accumulated Navigational Error After Partial Retrieval

As the tether is further shortened, navigational accuracy improves. The closer the satellite is reeled in, the better the navigational performance. At a tether length of 3 kilometers, the final navigation error is approximately 22 kilometers, well within the limits set by the NASA flight rule. A comparison similar to Figure 8 appears in Figure 9 for a partial retrieve to a final tether length of 3 kilometers. Note the navigational error growth rate after the tether cut is close to that of an immediate cut, approximately 8.75 kilometers per revolution. The increase in performance occurs during the retrieval portion of the response, due to the relatively slower navigational error growth rate.

Tether Length Hold Prior to Cut

The simplest operational response to a loss of communications contingency is to do nothing. In the TSS-1 mission, doing nothing means holding the tether length constant, and cutting the tether at the last possible moment before deorbit preparation must begin.

This response has a number of advantages. Because the Orbiter does not alter its orbit significantly until just prior to the deorbit burn, the onboard navigational systems propagate Shuttle state more accurately. Due to the operational simplicity of this response, a double failure is much less likely. The systems supporting the tether are used minimally, and it is less likely something else would go wrong.

The navigational error just prior to the deorbit burn for a 3 revolution hold followed by a tether cut appears in Figure 10. The loss of communications was assumed to occur just prior to an uplink in the middle of the onstation phase. The final error during this response is 23.5 kilometers, well within the limit set by the NASA flight rule.

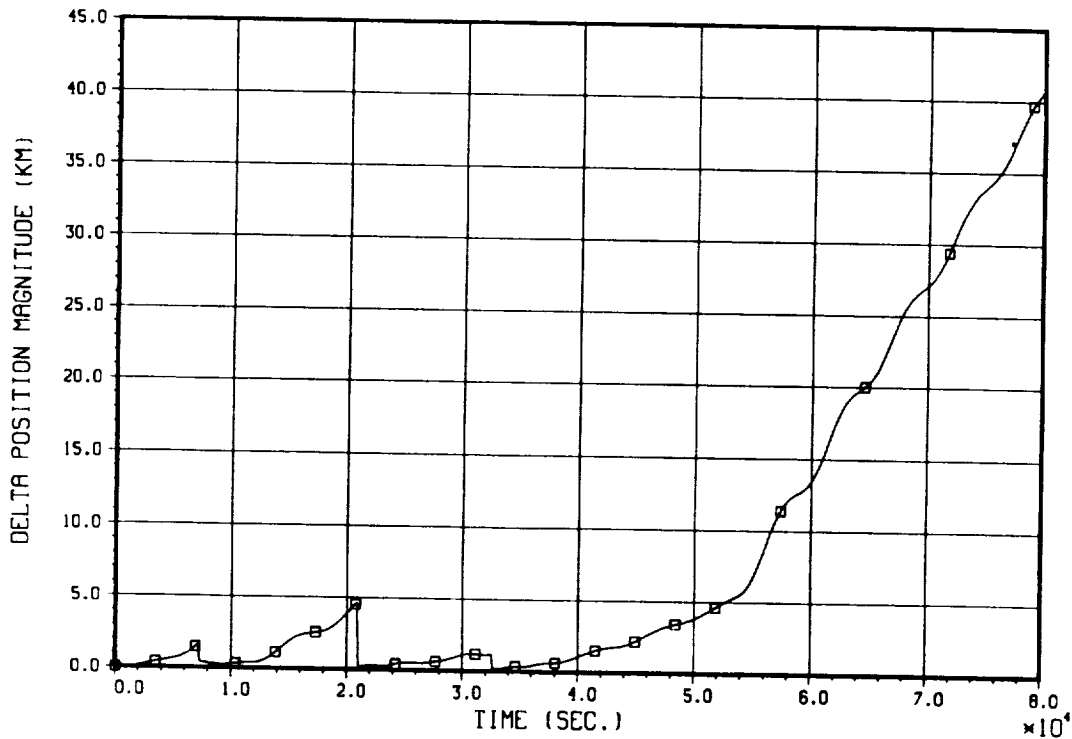


Figure 8: Electrodynamic Mission Navigational Error Growth - Cut at 20 km

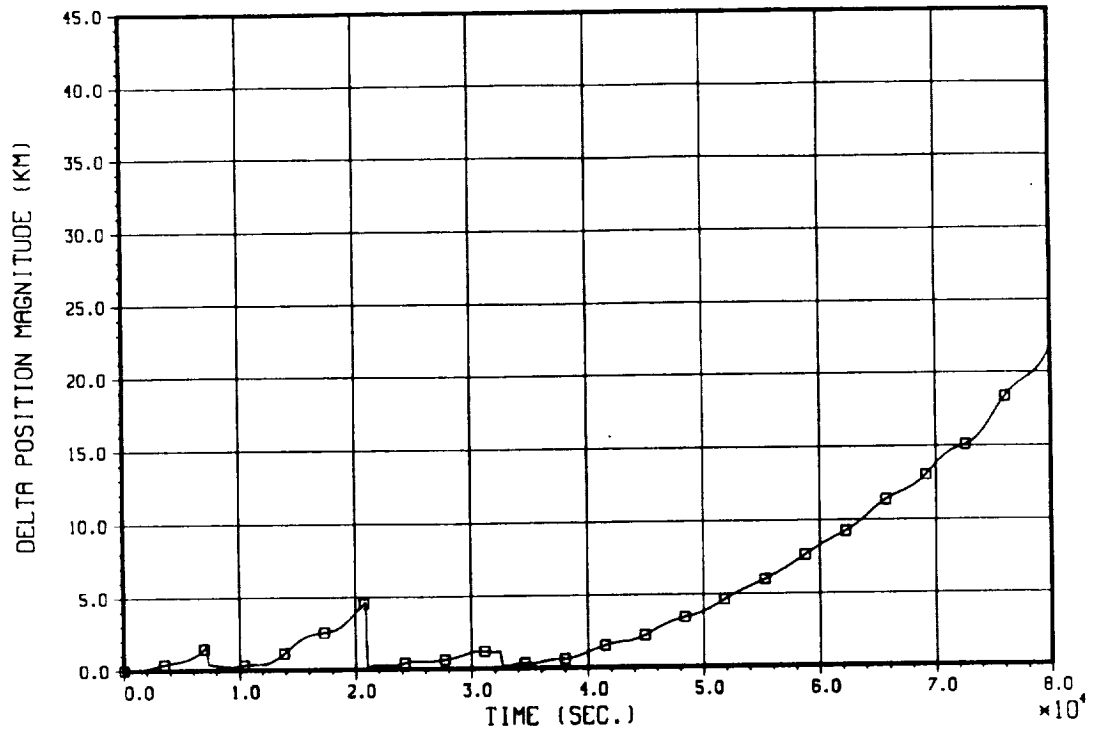


Figure 9: Electrodynamic Mission Navigational Error Growth - Cut at 3 km

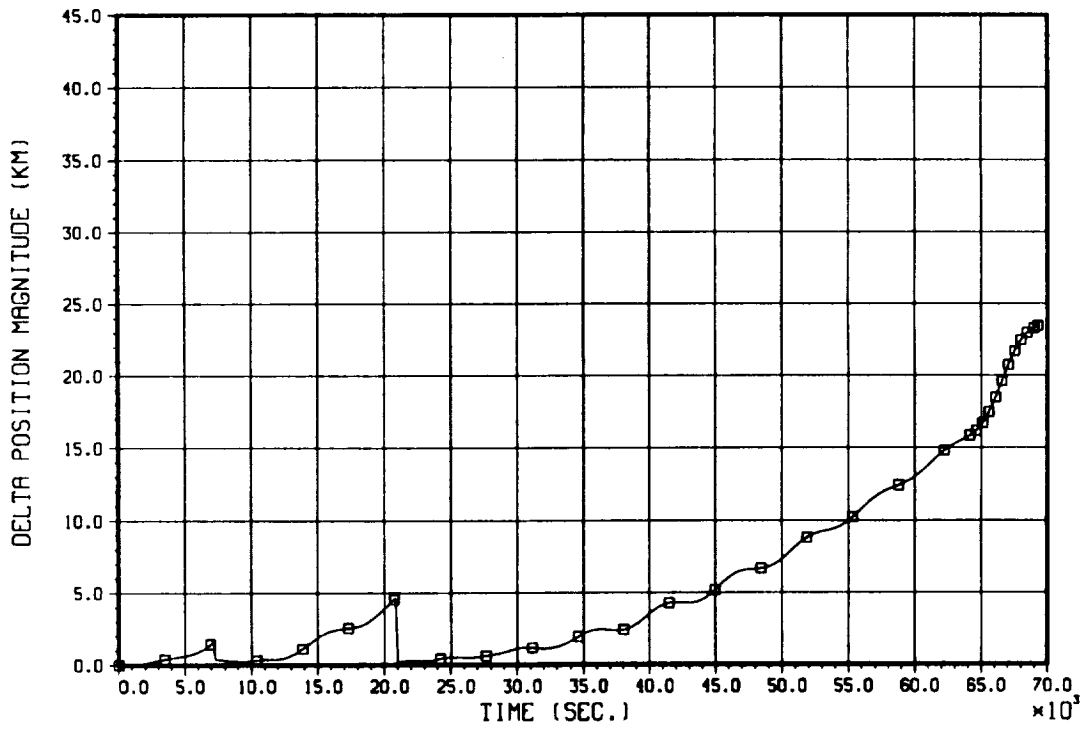


Figure 10: Comparison of Onboard vs. Simulated Trajectories - 3 Rev Hold and Cut

Conclusions

A cut tether contingency does not represent a threat to the a tethered system mission, provided the onboard navigation systems have contact with the ground. Although the onboard navigational error grows at an alarming rate immediately after a tether cut, the onboard systems can be reset with an uplink from the ground systems. Once reset, the onboard systems perform accurately.

During a loss of communications contingency, however, an incorrect action during the tether cut can threaten the mission, to the point of violation of NASA flight rules. Appropriate action requires not cutting the tether immediately after losing communications.

Tether retrieval, even partially, improves navigational performance. A tether hold offers an attractive alternative to retrieval, demonstrating comparable accuracy while remaining operationally simpler. The price for this simplicity, however, is loss of the satellite.

The benefits of retrieving the satellite outweigh reduced onboard navigational performance, provided existing flight rules are not violated. Therefore the best response to a loss of communications contingency would simply be to do nothing for as long as possible while attempting to reestablish contact with the ground systems. This response offers acceptable navigational accuracy, and is operationally simple. If contact can be reestablished, the satellite can be recovered.

References

1. Wacker, Roger, et. al.; "Shuttle Tethered Object Control Simulation (STOCS) Version 3 Users Guide," McDonnell Douglas Astronautics Company Design Note No. 1,1-DN-EH86020-01, 14 February, 1986.
2. Alland, K. A., and Kralicek, T. L.; "SENSOR6A User's Guide," McDonnell Douglas Astronautics Company -- Houston Astronautics Division Transmittal Memorandum 1.2-TM-FM85018-219, 29 August, 1985.
3. Morris, I., et. al., "SONAV User's Manual," McDonnell Douglas Technical Services Company -- Houston Astronautics Division Design Note 1.2-DN-FM85018-02, 28 February 1986
4. de Sulima, T. H., "Houston Operations Predictor/Estimator (HOPE) Engineering Manual, Revision 1, "TRW Note No. 70-FMT-792A, June 1970.
5. Lardas, M. N.; "Shuttle Tether Operations: The Effect on Orbital Trajectory and Inertial Navigation", McDonnell Douglas Space Systems Company, 17 April, 1989.
6. "STS Operational Flight Rules, All Flights," Mission Operations Directorate, NASA-JSC, JSC-12820, 20 January 1989, PCN-1 24 February 1989.

SHUTTLE TETHERED OPERATIONS: THE EFFECT ON ORBITAL TRAJECTORY AND INERTIAL NAVIGATION

Mark N. Lardas
Senior Engineer, Guidance & Control Mechanics
McDonnell Douglas Space Systems Company,
Engineering Services Division
16055 Space Center Blvd, Houston, TX 77062

1991 will see one of the most ambitious Shuttle missions ever planned -- the first full-scale test of a large tethered satellite system. The Orbiter will be linked to a 500 kg payload by a 20 km tether, an action with a profound effect on the trajectory of the Orbiter. For the first time in the history of the Shuttle program, the vehicle will conduct prolonged operations with the center of mass of the orbiting system a significant distance from the center of mass of the Space Shuttle Orbiter, a violation of a fundamental assumption made in both the Orbiter ground-based and onboard navigation software.

Inertial navigation of tethered operations with the Shuttle is further complicated by the presence of non-conservative forces in the system: RCS translational effects, atmospheric drag, and electro-magnetic dynamics. These can couple with the conservative tether dynamics effects, and degrade the navigation software performance.

This paper examines the primary effects of tether dynamics on the Orbiter's trajectory, coupling by conservative forces during tethered operations, and the impact of both on the ability to meet inertial navigation constraints. The impact of electro-dynamics, different RCS control modes, commanded attitudes, and attitude deadbands are presented. Operational guidelines which optimize successful mission navigation, and necessary navigation constraints are discussed.

INTRODUCTION:

In January, 1991, the Shuttle program will attempt one of its most ambitious missions to date -- the first full scale test of a large tethered satellite system. The Orbiter will be linked to a 500 kg payload by a 20 km tether, and tethered operations will occur over a 32-hour period. The Tethered Satellite System Mission 1 (TSS-1) has two major objectives: to attain a better understanding of the mechanics of tethered systems, and to investigate the feasibility of using conductive tethers to generate electricity. This mission will have the Shuttle Orbiter deploy the tethered satellite in an upward direction, with the Orbiter initially in a 28.5-degree inclination, 296 km (160 NMI), orbit.

TSS-1 poses unique challenges for Space Shuttle navigation. For the first time in the history of the Shuttle program, the vehicle will conduct prolonged operations with the center of mass of the orbiting system a significant distance from the center of mass of the Space Shuttle Orbiter, a violation of a fundamental assumption made in both the Orbiter ground-based and onboard navigation software. Inertial navigation of tethered operations with the Shuttle is further complicated by the presence of non-conservative forces in the system: Reaction Control System (RCS) translational effects, atmospheric drag, and electromagnetic dynamics. These couple with the conservative tether dynamics effects, degrading the navigation software performance.

The most significant sources of trajectory perturbations during TSS-1 tethered operations are due to tether-induced RCS attitude-control thruster firing. Direct tether effects, atmospheric drag on the tether, and electrodynamic drag during periods when current is flowing through the tether, have effects an order of magnitude smaller than these tether-induced thruster firings.

The results presented in this paper were obtained through analysis conducted on and with three simulations: The Shuttle Tethered Object Control Simulation (STOCS) -- a high fidelity engineering simulation of the TSS-1 mission (Reference 1); the Shuttle Environment Navigation Simulation for Orbit and Rendezvous (SENSOR) program, an onboard navigation system simulation (Reference 2); and the Standalone Orbital Navigation (SONAV) program, a Space Shuttle ground navigation system emulator (Reference 3).

SHUTTLE ONORBIT INERTIAL NAVIGATION:

The Space Shuttle uses two navigation systems: the onboard navigation system which provides the navigation state used by the Shuttle flight system and the Ground (more accurately Ground-based) navigation system which provides independent validation of the onboard navigation. The onboard navigation incorporates sensed and modelled accelerations to propagate an Orbiter state vector. The Ground navigation system uses radar observations of the Orbiter to

generate a new estimate of the state vector. When the onboard navigation state vector differs from the Ground-generated Orbiter ephemeris, the current ground ephemeris state vector is uplinked to onboard navigation system and replaces the onboard vector.

The onboard navigation propagates an initial state vector incorporating sensed accelerations and acceleration models into the equations of motion. The Orbiter's Inertial Measurement Units (IMUs) sense accelerations. When the acceleration are above a threshold (the standard onorbit acceleration threshold during non-powered flight is 1000 micro-gravities), then these accelerations are directly incorporated into the propagation. If the sensed acceleration is below the threshold, the sensed accelerations are replaced by an average model for RCS accelerations. The onboard navigation system also models geopotential effects and the effects of atmospheric drag on the Orbiter. A full description of the onboard navigation system can be found in Reference 4.

The onboard navigation accuracy degrades due to three reasons: initial state vector uncertainty, mismodelled or unsensed accelerations, and limitations of the environmental models. Any difference between the estimated state and the true state of the Orbiter increases linearly as it is propagated over time. The initial state vector is the best estimate of the Orbiter's position at that time. Even given optimal conditions, at least 50 meters of position uncertainty will exist in this estimate. Unsensed acceleration changes the true position of the Orbiter without being incorporated into the navigated state. A low-level acceleration present continuously over a period will produce a quadratic growth in in the navigation uncertainty. Finally, the environmental models used in the onboard navigation software are simplified models to save computation time and ease storage requirements. The onboard navigation uses a GEM10 4x4 geopotential model and a Babb-Muller drag model. These introduce an an error growth of 360 meters/rev into the navigation state.

These factors require the onboard navigation system to be periodically updated. Navigation solutions obtained by the Ground navigation system are used for this. The Ground navigation system takes an initial estimate of the Orbiter's state vector, propagate it using a more sophisticated set of environment models (GEM10 7x7 geopotential model and Jacchia-Lineberry atmosphere model). It performs a differential correction of the propagated trajectory through a weighted least-squares fit of tracking observations. Observation are taken from ground-based S-band and C-band tracking stations, and through Tracking and Data Relay System (TDRS) system S-band relay tracking. A new state vector is generated, until a convergent solution that minimizes tracking residuals -- the difference between the propagated state and the observed position at that time -- over the differential correction arc. Ground navigation can also model constant, Orbiter body-axis centered accelerations. A description of the Ground-based navigation systems can be found in Reference 5.

C-3

MECHANICS OF TETHERS:

Tethered operations are possible due to gradient effects of gravitational acceleration. The force of gravity attraction is proportional to the inverse of the distance between two bodies. Thus two bodies orbiting the Earth at different orbital radii have different gravitational acceleration -- the lower body has a greater acceleration acting on it than the higher body. If the difference in radius is small, then the difference in acceleration is also small. Two vehicles in low Earth orbit separated by 20 km difference in orbital radius experience a gravitational acceleration difference of approximately 0.05 m/sec².

Under normal circumstances the greater orbital velocity of the lower object would cause it to separate from the upper object. If the two objects are connected they cannot separate. Instead the connection, whether a rigid truss or a flexible tether, exerts a tension force on the endpoints, equal and opposite to the difference in gravitational acceleration vectors. If the tethered endpoints are aligned radially to the Earth's center of mass, the tether tension acceleration acts purely radially. Whenever the tether is not aligned radially, the tension has a downtrack component, reducing the velocity of the leading object, and increasing the velocity of the lagging object. If the tether length is constant, equilibrium is achieved when the two objects are aligned radially with the Earth's center of mass. (See Figure 1.) A full derivation of tethered equations of motion can be found in Reference 6.

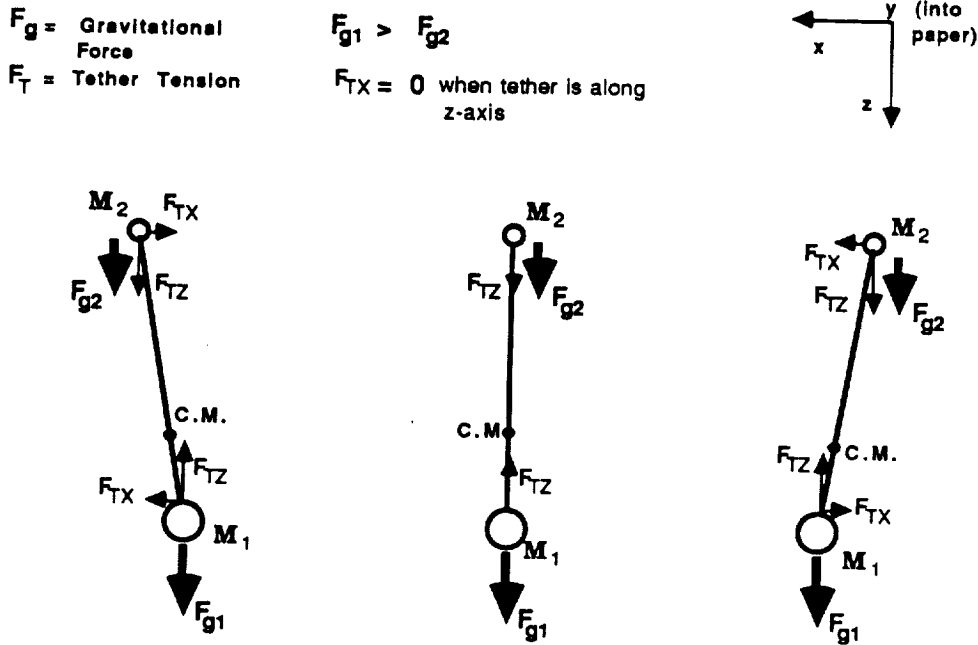


FIGURE 1: TETHER GRAVITY-GRADIENT STABILIZATION

Some interesting consequences result from this behavior. For tethers lengths of the order of interest of the TSS-1 mission (tether length is less than 1% of the orbital radius) the tethered system effectively orbits as if it were a point mass at the center of mass of the system. Changing the length of the tether changes the distance of the endpoints of the system from the system center of mass, without changing the orbital radius of the system C.M.

Tethers redistribute angular momentum, but do not create it. Changing the length of the tether, tether libration (rigid pendulous motion of the system), or spinning the endpoints are all means of redistributing angular momentum. Unless the tether is cut or broken, the energy transfer between endpoints of a tethered system is conservative.

Changing the length of the tether does change the orientation of the endpoints to each other. As the tether increases in length, the tension is reduced below the difference in gravitational force, and the lower endpoint begins to lead the upper endpoint. As the tether decreases in length, tether tension increase, and the upper endpoint begins to lead the lower endpoint. This behavior is illustrated in Figure 2, which shows relative motion between the Orbiter and the TSS-1 Object during tethered operations.

RELATIVE STATE: TSS-1 OBJECT - ORBITER

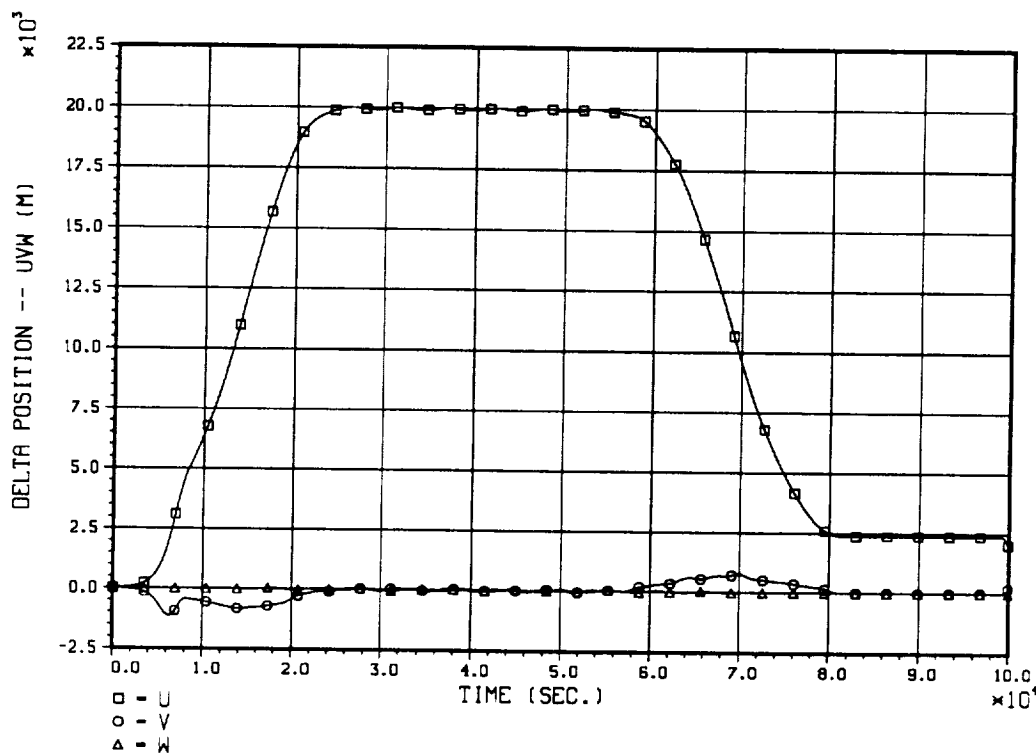


FIGURE 2: RELATIVE MOTION OF TETHERED ENDPOINTS (UVW FRAME)

TETHER LENGTH VS. TIME

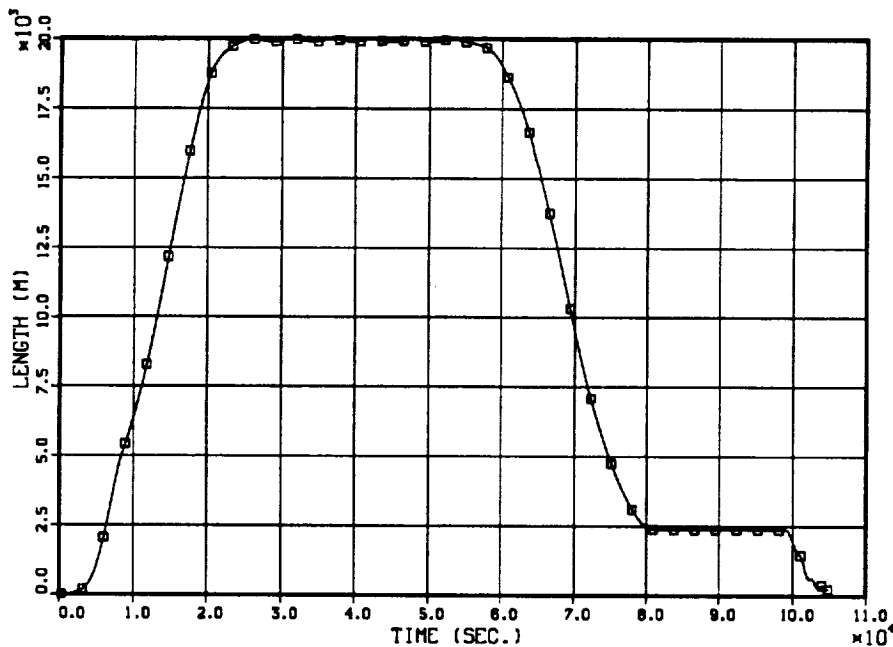


FIGURE 3: TSS-1 TETHER LENGTH PROFILE

Figure 3 illustrates the tether profile baselined for the TSS-1 mission. There are five phases in this profile. The tether deploy phase occurs over the first 24 000 seconds of tethered operations. The 20-km on-station phase runs from 24 000 seconds to 56 000 seconds. Retrieval to 2.4-km then begins and continues until 80 000 seconds. The 2.4 km on-station phase comprises the next 20 000 seconds, followed by retrieval to boom tip.

TETHER INTERACTION WITH THE ORBITER:

While tethered mechanics are conservative, the effect that they will have on the Orbiter's trajectory during the TSS-1 mission will not be. Two environmental sources -- atmospheric drag and electrodynamic drag introduce non-conservative energy perturbations to the system. Both these environmental perturbations and tethered mechanics, induce firing by the Orbiter's Reaction Control System (RCS) to maintain the Orbiter's commanded attitude. This thrusting adds or subtracts energy from the system as a function of the Orbiter's orientation. The attitudes and attitude control modes baselined for the TSS-1 mission will result in a net loss of energy.

Atmospheric drag on the tether and TSS-1 Object are minor, though constant perturbations. Drag is primarily a downtrack acceleration reducing net orbital energy. Less than 1% of the drag acceleration acts perpendicular to the orbital plane.

Electrodynamic drag results from using the tether to generate electricity. Electricity is generated by using the tether as a portion of a current loop, which is passing through the Earth's magnetic field. This generates a force normal to the Earth's magnetic field lines, proportional to the electrical power generated by the tether. (Note that "negative" electrical power -- pumping energy into the tether -- give a net gain in orbital energy.) Since the Earth's magnetic field is a tilted dipole, the magnetic field lines are rarely perpendicular to the Orbiter's velocity vector. A significant percentage of the electrodynamic perturbation will act out-of-plane. Electrodynamic force is functionally identical to atmospheric drag -- the in-plane component of force reduces the net orbital energy.

Tether tension does not directly affect the inertial trajectory of the system, but does have a significant induced effect. The tether applies a tension force on the endpoints. Unless the Orbiter's center of mass and the tether attach point are aligned with the tension vector, the tension will apply a torque, rotating the Orbiter until the attach point, Orbiter C.M. and tension vector are aligned. The planned attach point for the tether boom is ahead of the Orbiter C.M. The Orbiter will stabilize into a nose-forward, positive-pitch attitude (see Figure 4). The angle between the local vertical axis and Orbiter X-body axis that results is called the hang angle. Given the currently manifested tether attach point, and a stable tether of 20 km length, the Orbiter will settle into a +25 degree pitch attitude. Different attach points and tether lengths change this angle.

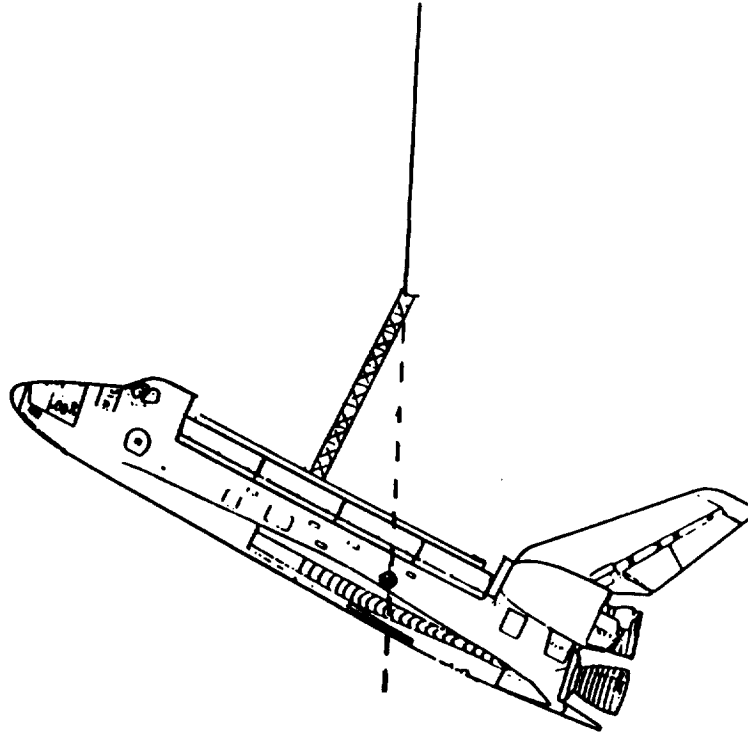
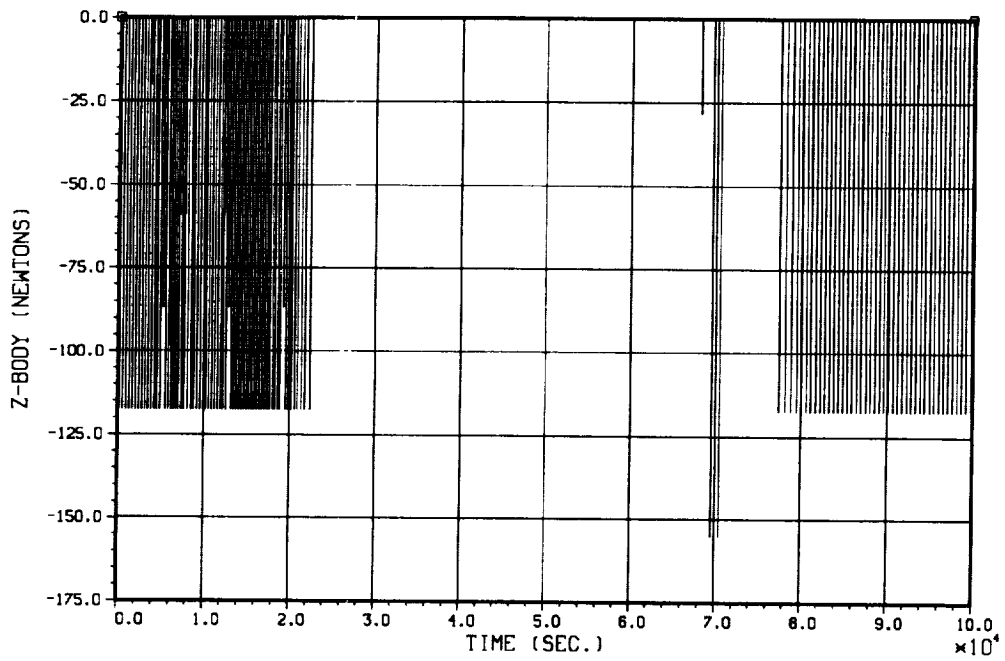


FIGURE 4: HANG-ANGLE INDUCED ORBITER ATTITUDE STABILIZATION

Z-BODY ORBITER CONTROL FORCE, PITCH - 25 DEG.



Z-BODY ORBITER CONTROL FORCE, PITCH - 30 DEG.

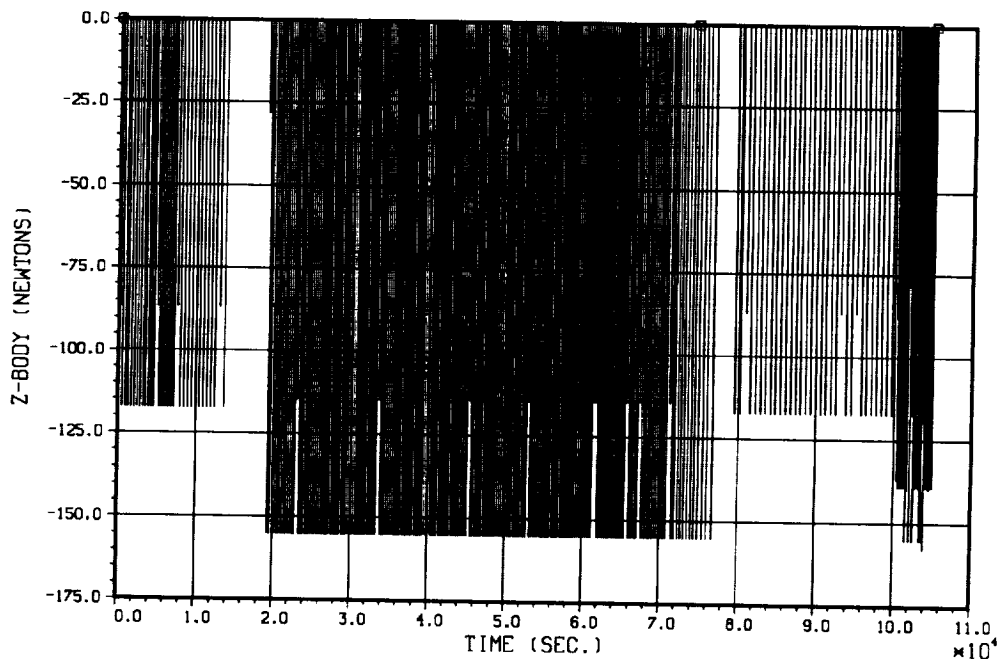


FIGURE 5: HANG-ANGLE INDUCED Z-BODY THRUSTER FIRING

Tether-induced hang-angle perturbations interacts with the Orbiter's RCS two ways. If the commanded pitch differs from the hang angle by less than the attitude angle deadband, then the tether will act to stabilize the Orbiter into its commanded attitude, much as a tail stabilizes a kite. If the difference between the commanded attitude and the hang angle exceeds the attitude deadband, high RCS thrusting results. The tether pulls the Orbiter towards the hang angle until the attitude deadband is reached. Then the RCS jets fire to restore the Orbiter to its commanded attitude.

Figure 5 illustrates these different behaviors. The upper graph presents the Z-body axis thruster firings in a simulation in which the Orbiter was commanded to hold a pitch of 25 degrees. The bottom graph presents Z-body axis firings in a simulation where the Orbiter had a commanded pitch of 30 degrees. In both cases, vernier control with a 2 degree attitude deadband was used, allowing the Orbiter to drift up to two degrees from the commanded attitude. During the period that the tether was in the 20 km on-station phase of the mission, the hang angle was 25-degrees. No RCS thrusting occurred over that time in the 25 degree commanded pitch case. The 30 degree pitch case exhibited high RCS activity over the same period.

Tether libration also induces attitude deadband firing. In-plane libration causes pitch deadbanding. Out-of-plane libration induces yaw and roll deadbanding. Figures 6 and 7 illustrate RCS thrusting present in a in-plane and out-of-plane libration simulation respectively. Both cases used a 5 degree tether libration. Libration-induced deadbanding can be caused by other tether perturbations. Electrodynamic drag produces both out-of-plane and in-plane force on the tether. The out-of-plane force induces out-of-plane libration, in turn, inducing yaw and roll deadbanding.

TETHER EFFECTS ON THE TRAJECTORY:

Tether interactions with the Orbiter perturbs the orbital trajectory of the system, directly or indirectly. Downtrack effects of continuous drag forces behave in a straightforward manner -- a continuous retrograde acceleration (shown in Table 1).

Tether-induced RCS firings produce more subtle effects. They could cause the dramatic effects shown in Table 1, if fired continuously while aligned in the downtrack axis. In reality, RCS jets are impulsive rather than continuous, and rarely aligned with the downtrack axis. Combinations of thrusters can either cancel or amplify translational effects. Despite the larger magnitude of the individual PRCS jets, these have a smaller translation effect when used for attitude control than the Vernier jets. The combinations of PRCS jets used for attitude control have much higher rotational coupling, and lower net translation.

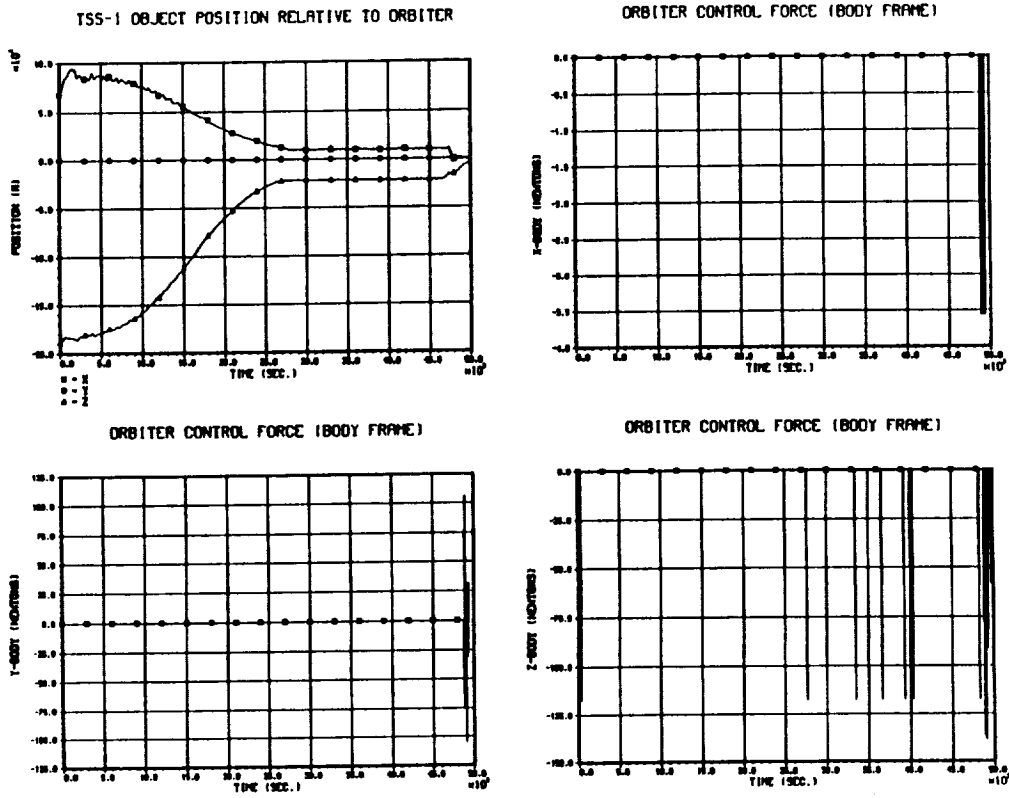


FIGURE 6: ORBITER THRUSTER FIRING -- IN-PLANE LIBRATION CASE

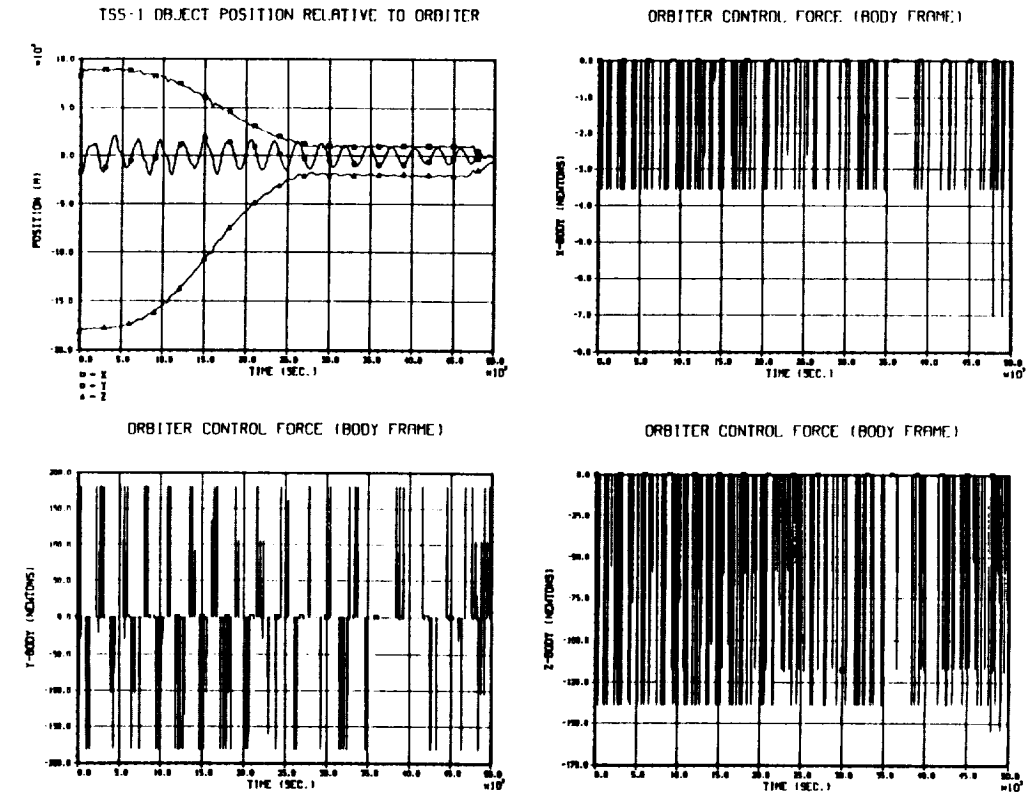


FIGURE 7: ORBITER THRUSTER FIRING -- OUT-OF-PLANE LIBRATION CASE

TABLE 1: PERTURBATION SOURCES AND TRAJECTORY EFFECT

PERTURBATION SOURCE	ACCELERATION (micro- Gravities)	NET CHANGE IN TRAJECTORY AFTER 5 REVS * (meters)
CONTINUOUS EFFECTS		
Atmospheric Drag on Tether (296 KM)	0.04	320
Electrodynamic Drag (1-Amp Current)	0.63	4 300
IMPULSIVE EFFECTS		
Vernier Attitude-Hold Thrusting (per Jet)	3.5	24 000
Primary RCS Attitude- Hold Thrusting (per Jet)	120	820 000
* Assumes perturbation is active over entire 5 revs -- for RCS jets this implies a thruster failed on. Shuttle fuel limitations would prevent this from occurring. This table is intended to show relative effects of these sources		

The Orbiter normally uses Vernier attitude control during on-orbit mission phases. This is baselined as the nominal control mode for the TSS-1 mission. The Orbiter has six Vernier thrusters. The vernier attitude-control firing patterns are shown in Figure 8. All six verniers are aligned in the Orbiter body frame Y-Z plane. Four of the jets thrust in the +Z-body direction, translating the Orbiter in the -Z direction. Any pitch or roll rotation yields a net -Z-axis translation of the Orbiter. When the Orbiter is in a +25 to +30 degree pitch relative to local horizon, significant downtrack perturbations occur. Table 2 gives the net downtrack acceleration that results from deadbanding when the Orbiter is in the nose-forward +25 degree pitch baselined for the 20-km on-station phase of the TSS-1 mission.

The total trajectory displacement induced by RCS attitude control thrusting is the product of the downtrack acceleration and the number of thruster firings. The best illustration of this behavior can be shown by comparing simulated trajectories of nominal deploy and the 5-degree high-pitch deploy (the cases which generated the

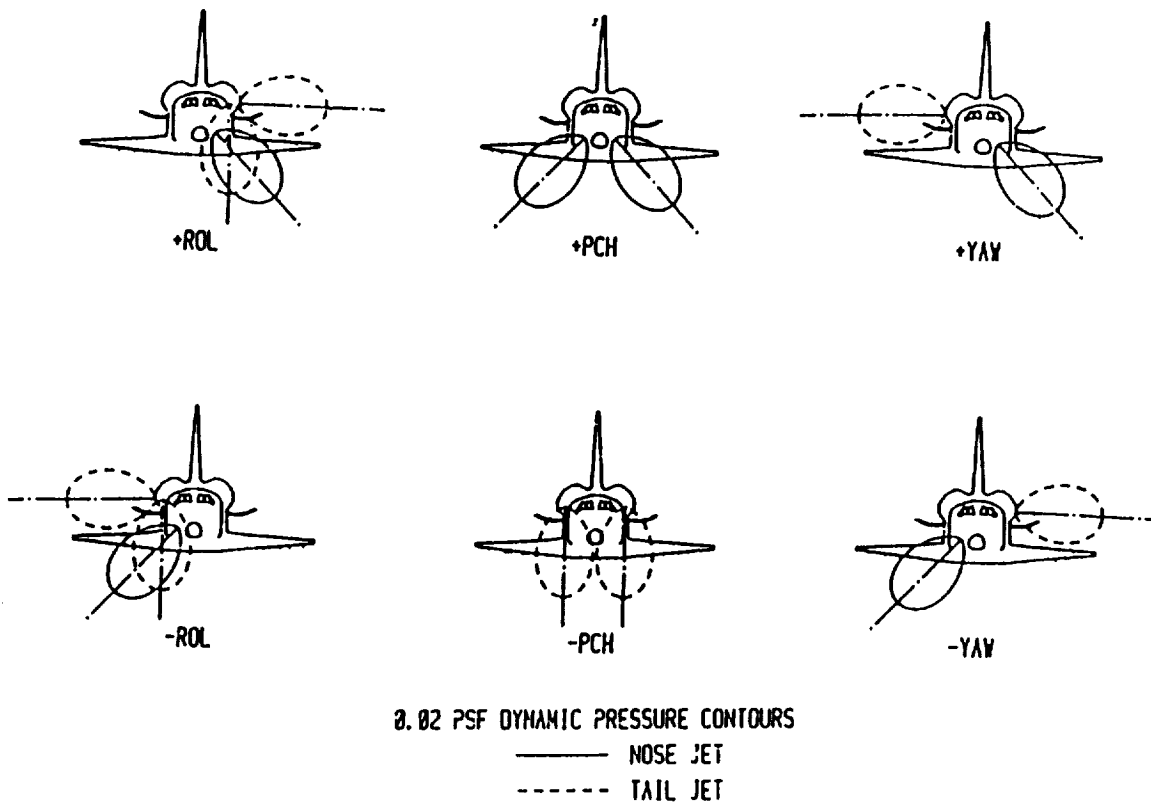


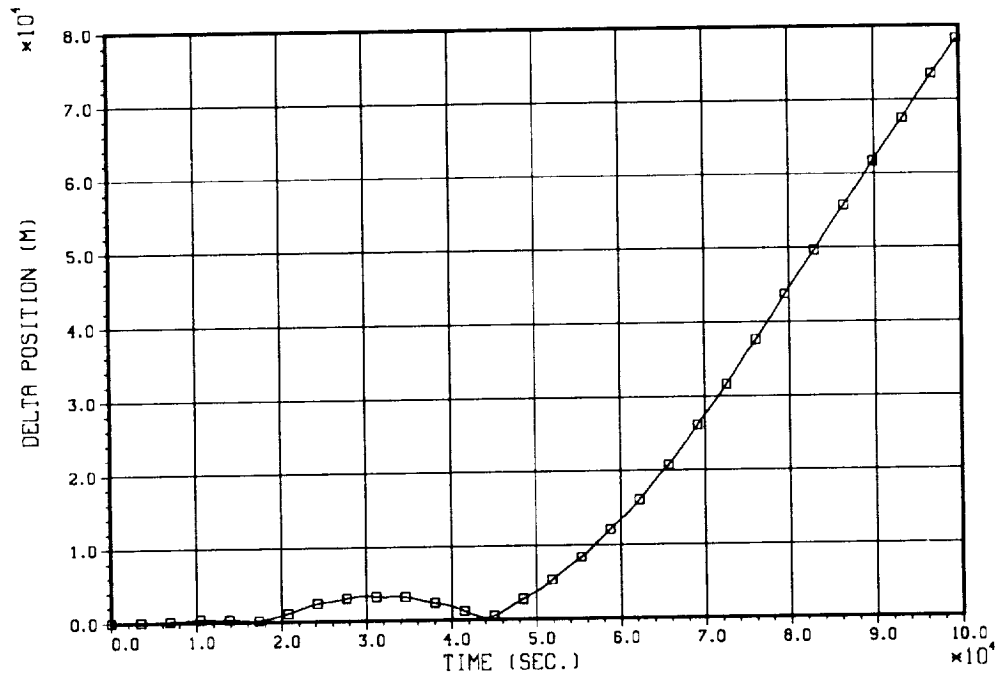
FIGURE 8: VERNIER ATTITUDE CONTROL -- JET-FIRING PATTERNS

jet-firing histories of Figure 5). Figure 9 presents both the difference in position and in the semi-major-axis between these cases. (Delta-SMA indicates total energy changes between two orbits.) The High-Pitch case lost energy relative to the Standard Deploy. Pitch-axis deadbanding was the primary cause of a trajectory position delta of nearly 80 000 meters, and an SMA change of -900 meters after 100 000 seconds of propagation.

TABLE 2: VERNIER-INDUCED DOWNTRACK ACCELERATION AT ORBITER ATTITUDE: PITCH = 25 deg; ROLL = 0 deg; YAW = 0 deg

Maneuver	Downtrack Accel (micro-G)
+PITCH	-0.38
-PITCH	-0.53
+ROLL	-0.45
+YAW	-0.19

POSITION DIFFERENCE



SEMI-MAJOR-AXIS DIFFERENCE

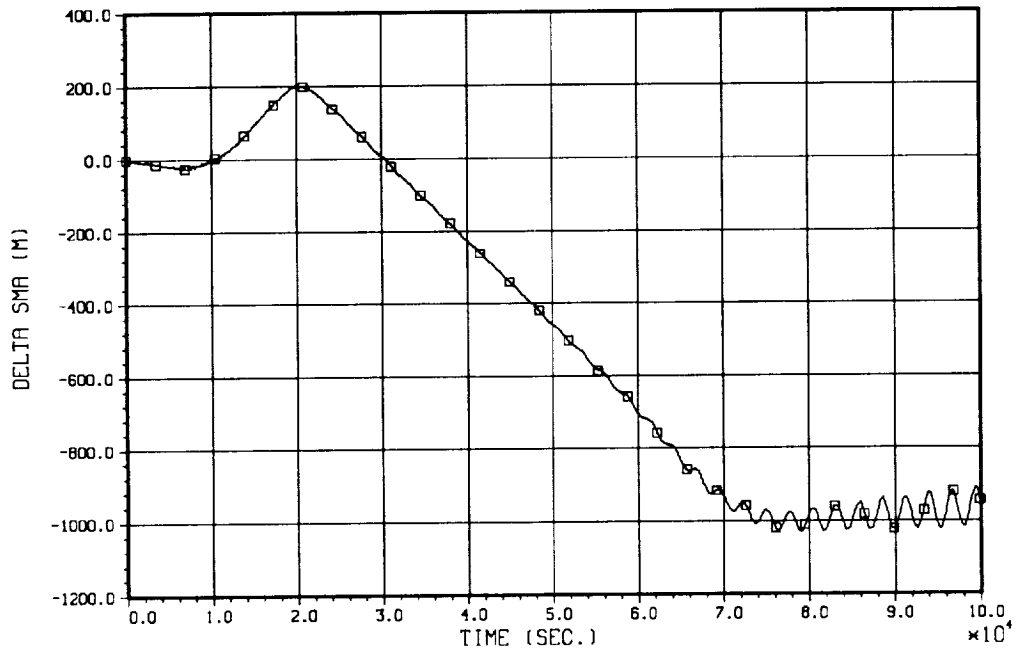


FIGURE 9: TRAJECTORY DELTAS -- STANDARD PROFILE VS. HIGH-PITCH CASE

One item of interest is the net gain in energy that the High-Pitch case demonstrates over the first 20 000 seconds of the profile. This is the period when the tether is being deployed, and the hang angle is +30 degrees pitch. Thus, the +30 degree commanded pitch of the High-Pitch case was closer to the tether-induced hang angle than the +25 commanded pitch of the Standard case over that phase of the mission. During the 20-km portion on-station of the mission through retrieval to the 2.4-km on-station period, the Standard case pitch was closer to the tether hang angle.

The net trajectory perturbation induced by tethered operations is a product of all tether-induced perturbation sources. Separating these effects is difficult due to coupling between them (e.g. electrodynamic drag exciting out-of-plane libration). Gross estimates of these effects can be developed by comparing trajectories with different perturbations present against a constant yardstick. Table 3 summarizes differences observed in six different simulated tether trajectories.

The Standard Profile used baselined TSS-1 mission tether profile with the following parameters: Commanded attitude: Nose-forward +25 degree pitch; Attitude deadbands of ± 2 degrees, Vernier attitude control, no tether electrodynamics, no tether libration. Each of the other five cases varied one of these parameters, but was otherwise identical.

TABLE 3: TRAJECTORY DIFFERENCES DUE TO TETHER-INDUCED PERTURBATIONS

COMPARED TRAJECTORIES	POSITION DELTA (Meters)	SMA DELTA (Meters)	SIM. TIME DELTA (Seconds)	PRIMARY PERTURB. SOURCES
Standard Profile vs. High-Pitch	79 200	-314	100 000	Pitch Deadbanding
Standard (Vernier) vs. PRCS Cntl	-106 700	1070	100 000	Vernier vs. PRCS Translation
Standard Profile vs. Science (Tether Electro-dynamics On)	56 400	-1280	100 000	Attitude Dead-banding, Out-of-Plane Libration, Electro-dynamics
Standard Profile vs. 5 deg In-Plane Libration	42 700	-60	55 000	Pitch Deadbanding
Standard Profile vs. 5 deg Out-of-Plane Libration	219 400	-4110	55 000	Yaw and Roll Axis Deadbanding

The High-Pitch case used a commanded pitch attitude of +30 degrees. The PRCS case used the Orbiter PRCS jets for attitude control. The Science case modelled the effects of a 1-ampere current flowing through the tether during the 20-km and 2.4-km on-station phases. The In-Plane and Out-of-Plane Libration cases began with a 5-degree libration in each of the respective axes. The High-Pitch, PRCS, and Science cases were each run over the entire tethered operation phase. The two libration cases began during the 20-km on-station phase, using the current Standard case parameters as their initial conditions, with a displaced TSS Object (to induce the libration). Comparisons in Table 3 are made against the Standard case. Negative SMA indicates that the compared case has less orbital energy at time of comparison than the Standard case.

TETHER EFFECTS ON INERTIAL NAVIGATION:

A tether separates the system center of mass from the tracked radar target (the Shuttle Orbiter) and induces acceleration which is not modelled by either the onboard or ground navigation systems and which is below the onboard navigation sensed-acceleration thresholds. Both acceleration mismodelling and C.M.-Tracking Target offset affect Shuttle navigation.

As the tether length increases, the Orbiter moves away from the system center of mass. The Ground-based radar observations track the Orbiter rather than the system C.M. When the tether is deployed to its full length (20 km), the radar observations are offset from the true center of mass of the system by 100 meters. A navigation solution minimizing the radar observation residuals of a single tracking pass produces a state vector which places the Orbiter in an orbit 100 meters below the actual semi-major-axis of the system. Propagating this vector yields a position difference from the actual trajectory of the Orbiter that grows by 4500 meters per revolution.

If several sets of radar observations, taken from different tracking stations and distributed over at least one orbital period are used a different solution occurs. Minimizing all tracking residuals over the period in question yields a state vector near the system's true C.M. The tracking residuals behave as if they were all biased by the offset difference. Reducing the residuals below that threshold at one station produces much larger residuals at the other stations.

Similar behavior is observed when single-station solutions are weighted with a covariance matrix. The covariance constrains the amount that the original input state vector can alter by changing the weighting placed on the observations in the least-squares regression. The result moves the solution's new state vector to the system C.M. rather than at the Orbiter. The C.M.-Tracking Target offset does not degrade navigation performance unless unconstrained single-station solutions are attempted.

The center of mass offset does not affect the onboard navigation system because this system does not use external inertial predic-

tions of the Orbiter's state. It propagates an initial state vector, assumed to be at the center of mass of the orbital system. This assumption is correct prior to the beginning of tethered operations. The Orbiter is at the system C.M. As tethered operations begin, and the Orbiter drops below the system C.M. the onboard navigation state vector remains at the system C.M. until it deviates due to environmental mismodelling and unsensed acceleration.

Tether-induced acceleration has more significant effects on Shuttle navigation. These accelerations are unmodelled by Ground Navigation and unsensed by the onboard navigation. With both systems, an accurate state vector propagates poorly over periods when the tether is inducing significant non-conservative acceleration. This has a greater impact on onboard navigation than on Ground navigation because the onboard navigation has no means of correcting for unincorporated accelerations, except by replacing the onboard navigation state with a new solution. The radar observations used in Ground navigation reset the Orbiter's state vector to the system C.M. with each set of radar data processed.

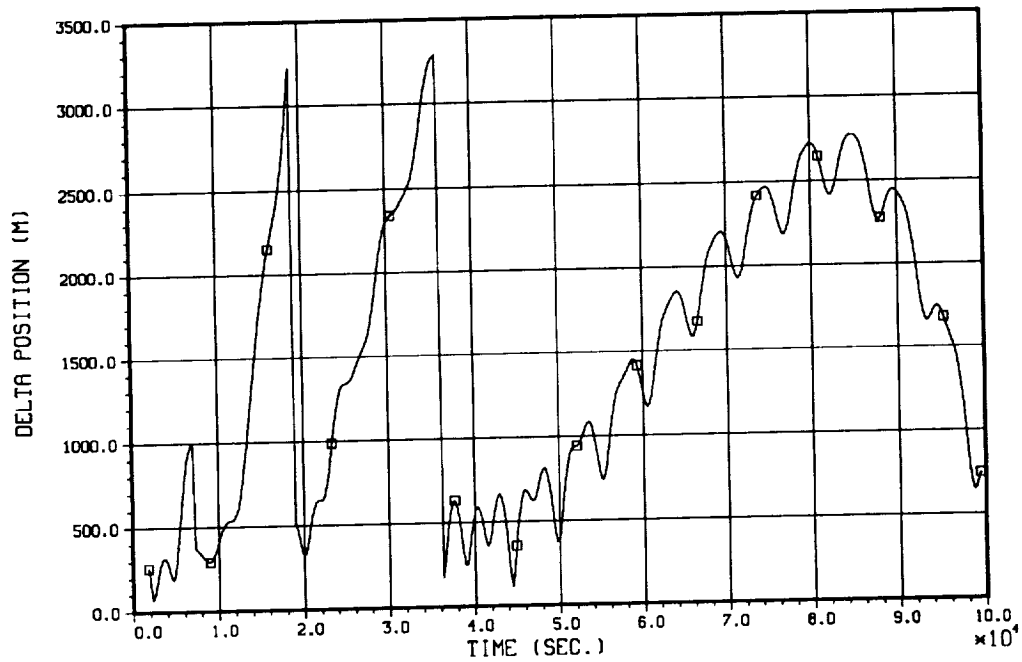
Figures 10 and 11 illustrate this behavior in the Standard and High-Pitch cases respectively. These illustrate navigation performance in quiet and active tether cases. The top graph shows the difference in position between the Ground ephemeris -- a propagation of a "best" constrained local solution -- with the STOCS-generated simulated trajectory. The lower graph displays the position difference between the Ground ephemeris and the onboard navigation state.

The Standard case had minimal tether-induced trajectory perturbation over the 20-km on-station portion of the mission. No RCS jet firings occurred, and the only mismodelled environmental perturbation present was atmospheric drag on the tether and TSS Object. The Ground ephemeris had to be updated three times, twice during the deploy phase and once during the on-station phase of the mission. Following the on-station update of the ground ephemeris, 36 000 seconds after the beginning of tethered operations, propagation of the ephemeris vector over the next 64 000 seconds yielded a maximum difference with the environment trajectory of less than 3700 meters.

The Onboard state deviated from the ground ephemeris by small amounts -- 900 meters maximum with differences smaller than 200 meters over the 20-km on-station phase. This is expected, as these differences represent the difference in propagation models in the two systems. Neither system propagates the unmodelled accelerations characteristic of tether-induced perturbations. The ground navigation system detects these as tracking passes subsequent to the pass from which the ground ephemeris was generated are processed, and correct the Orbiter's position. When these differences between the ground ephemeris and the local solutions exceed console guidelines ($20 * \Delta\text{SMA} + \Delta\text{downtrack position} > 6100$ meters), the ground ephemeris is replaced with a current good ground solution.

The High-Pitch case, with numerous RCS attitude firing throughout tethered operations, showed markedly different performance. The

TRAJ. COMPARISON: ENVIRON. VS. GROUND EPHEM



TRAJ. COMPARISON: ONBOARD VS. GROUND EPHEM

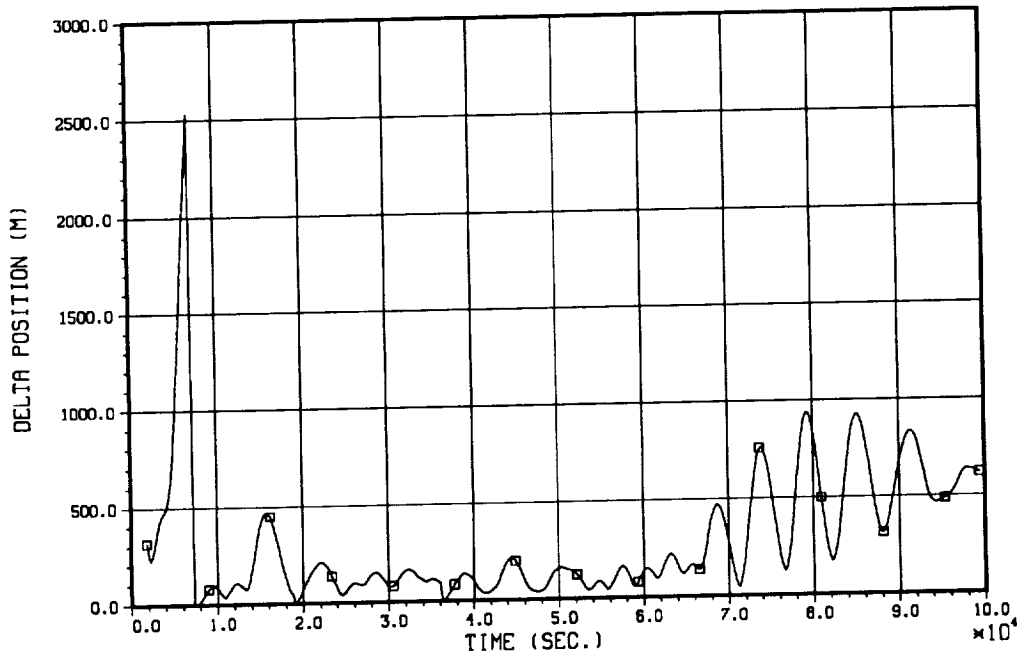
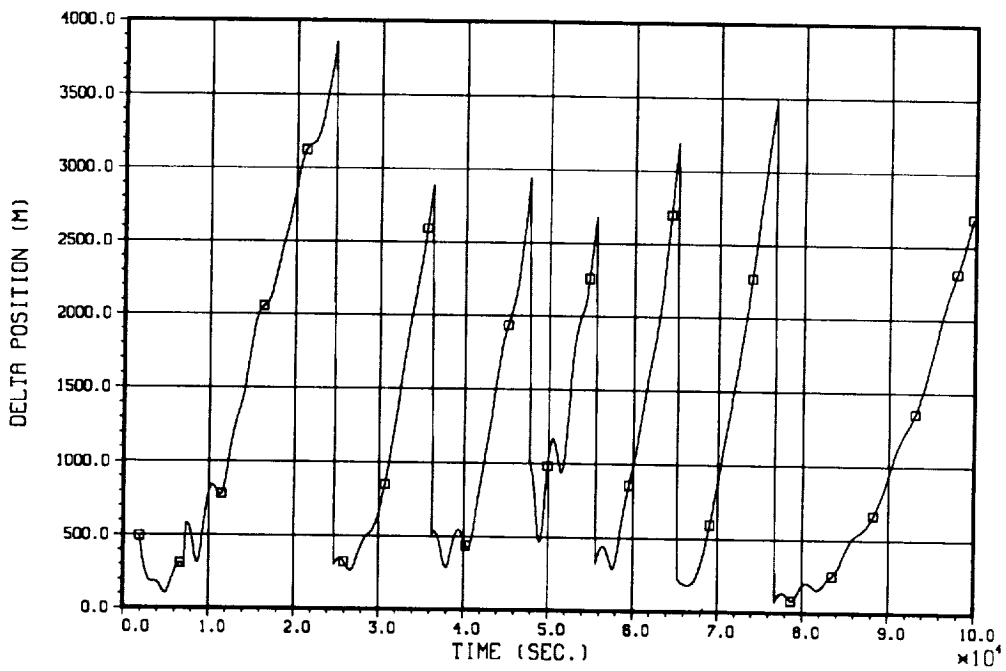


FIGURE 10: NAVIGATION PERFORMANCE -- STANDARD PROFILE

TRAJ. COMPARISON: ENVIRON. VS. GROUND EPHEM



TRAJ. COMPARISON: ONBOARD VS. GROUND EPHEM

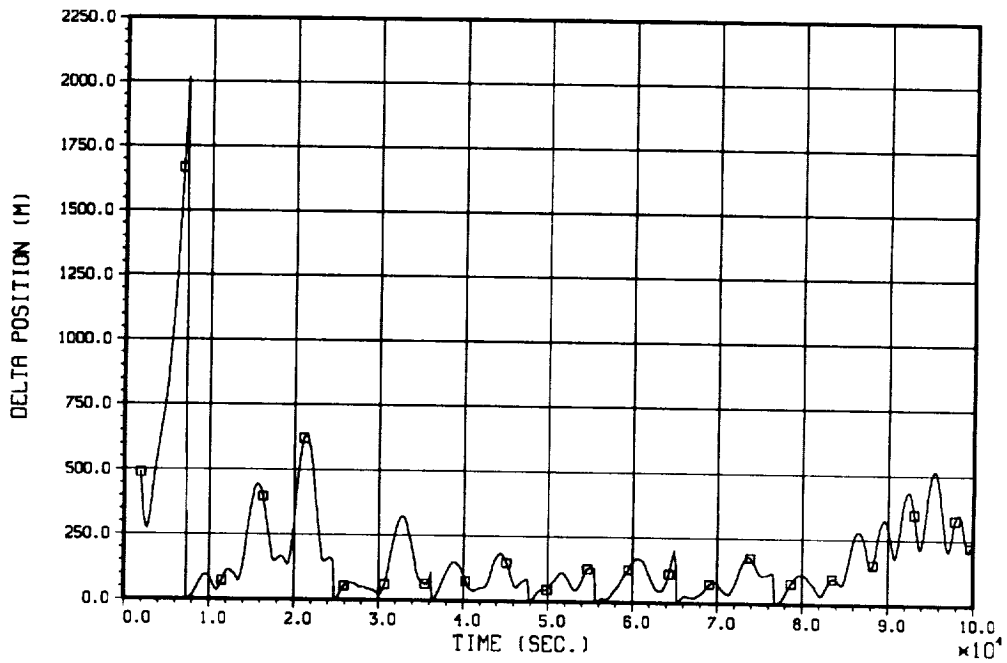


FIGURE 11: NAVIGATION PERFORMANCE -- HIGH-PITCH CASE

Ground ephemeris required frequent updating to correct the unmodelled acceleration introduced by the RCS system. Differences between Ground ephemeris and environment trajectory were much higher than those seen in the Standard case. Similarly degraded performance is demonstrated by the onboard navigation system.

CONCLUSION:

Tethered operations will have a significant effect on both the inertial trajectory of the TSS-1 mission and the navigation of that mission. Pure tether mechanics effects -- typified by the offset between the system center-of-mass and the Orbiter -- cause behavior that is interesting rather than damaging. Mission navigation is not adversely affected.

Tether-induced force does degrade navigation by causing low-level acceleration that are not directly incorporated into the propagation of the trajectory. These effect are cause major changes to the orbital trajectory over time. Even in this worse case, navigation performance using existing Mission Control Center software and processing guidelines did not degrade below acceptable limits. Tethered operations as exemplified by the TSS-1 mission will provide navigation challenges, but challenges that can be met.

REFERENCES:

1. Wacker, Roger, and others; "Shuttle Tethered Object Control Simulation (STOCS) Version 3 User Guide," McDonnell Douglas Astronautics Company Design Note No. 1.1-DN-EH86020-01, 14 February, 1986.
2. Alland, K.A. and Kralicek, T.L.; "SENSOR6A User's Guide," McDonnell Douglas Astronautics Company -- Houston Astronautics Division Transmittal Memorandum 1.2-TM-FM85018-219, 29 August, 1985.
3. de Sulima, T.H., "Houston Operations Predictor/Estimator (HOPE) Engineering Manual, Revision 1," TRW Note No. 70-FMT-792A, June 1970.
4. "Shuttle Operations Level C Navigation Requirements -- Onorbit," Mission Planning and Analysis Division, NASA-JSC, JSC-18368, September, 1982.
5. York, Will; "On-Orbit Ground Navigation Console Handbook," Mission Operations Directorate, Flight Design and Dynamics Division, NASA-JSC, JSC-20768, November 1, 1985.
6. Bond, Victor R., "The Development of the Equations of Motion for a Tethered Satellite System," McDonnell Douglas Technical Services Company Working Paper No. 1.2-WP-FM85011-01 NAS9-16715, 1985.

TEMPERATURE DEPENDENCE OF ATTITUDE SENSOR COALIGNMENTS ON THE SOLAR MAXIMUM MISSION (SMM)*

D. S. Pitone and A. H. Eudell, Computer Sciences Corporation (CSC)
F. S. Patt, Applied Research Corporation

ABSTRACT

This paper presents results on the temperature correlation of the relative coalignment between the fine-pointing Sun sensor (FPSS) and fixed-head star trackers (FHSTs) on the Solar Maximum Mission (SMM). This correlation can be caused by spacecraft electronic and mechanical effects.

Routine daily measurements reveal a time-dependent sensor coalignment variation. The magnitude of the alignment variation is on the order of 120 arc-seconds (arc-sec), which greatly exceeds the prelaunch thermal structural analysis estimate of 15 arc-sec. Differences between FPSS-only and FHST-only yaw solutions as a function of mission day are correlated with the relevant spacecraft temperature. If unaccounted for, the sensor misalignments due to thermal effects are a significant source of error in attitude determination accuracy. Prominent sources of temperature variation are identified and correlated with the temperature profile observed on the SMM.

It has been determined that even relatively small changes in spacecraft temperature can affect the coalignments between the attitude hardware on the SMM and the science instrument support plate and that frequent recalibration of sensor alignments is necessary to compensate for this effect. An alternative to frequent recalibration is to model the variation of alignments as a function of temperature and use this to maintain accurate ground or onboard alignment estimates. These flight data analysis results may be important considerations for prelaunch analysis of future missions.

* This work was supported by the National Aeronautics and Space Administration (NASA)/Goddard Space Flight Center (GSFC), Greenbelt, Maryland, under Contract NAS 5-31500.

1. INTRODUCTION

This paper presents the Solar Maximum Mission (SMM) flight system measurement of the correlation between the spacecraft structure temperature and the coalignment of the fine attitude sensors, composed of two Adcole fine-pointing Sun sensors (FPSSs) and two Ball Aerospace CT401 fixed-head star trackers (FHSTs). An overview of the SMM, including mission history and configuration, is presented. Possible causes of the variation in the coalignment, subsequently referred to as the misalignment, are discussed, and the conclusion is drawn that the spacecraft temperature is the predominant factor affecting the FPSS-FHST misalignment. Two methods of compensating for this misalignment, frequent in-flight calibration and misalignment function modeling, are compared with regard to accuracy and impact to science data collection. This work was done by the Flight Dynamics Division (FDD) attitude determination and control ground support team, working in the Flight Dynamics Facility (FDF) at Goddard Space Flight Center (GSFC).

1.1 MISSION HISTORY

The SMM was launched in February 1980 from the Eastern Test Range at Kennedy Space Center (KSC), into an approximately circular low-Earth orbit, with an inclination of nearly 28 degrees (deg) (Reference 1). The scientific objective of the mission was to study solar phenomena. The spacecraft attitude system provided three-axis stabilization and supported solar feature targeting. The spacecraft functioned normally until November 1980, when the standard reaction wheel (SRW) package that provides the controlling torques to the spacecraft began to fail. To preserve the mission, the SMM was put into a spin (≈ 1 deg per second) about the minor principal axis in which it remained until April 1984. With the spacecraft in the spin mode, only minimal solar observation was possible. During April 1984, the spacecraft was repaired in-orbit by the Space Transportation System (STS). The entire attitude control system was replaced, and the spacecraft was returned to the nominal scientific observing mode.

1.2 MISSION CONFIGURATION

The SMM was the first of the multimission modular spacecraft (MMS) series. The MMS were modular to facilitate mission repair and mission adaptation. The SMM basically consists of two parts as shown in Figure 1: the MMS itself and the experiment module. The modules that come with the MMS series are

- A Command and Data Handling (CD&H) system that handles all the communications between the ground and the spacecraft and includes the spacecraft on-board computer (OBC)
- A Modular Power System (MPS) that operates all the power systems, including the Solar Array System (SAS)
- A Modular Attitude Control System (MACS) that contains most of the sensors used in the attitude determination and control of the spacecraft. A High-Gain Antenna System (HGAS), for use in communicating with the Tracking and Data Relay Satellite System (TDRSS), is also attached to the end of the spacecraft.

ORIGINAL PAGE IS
OF POOR QUALITY

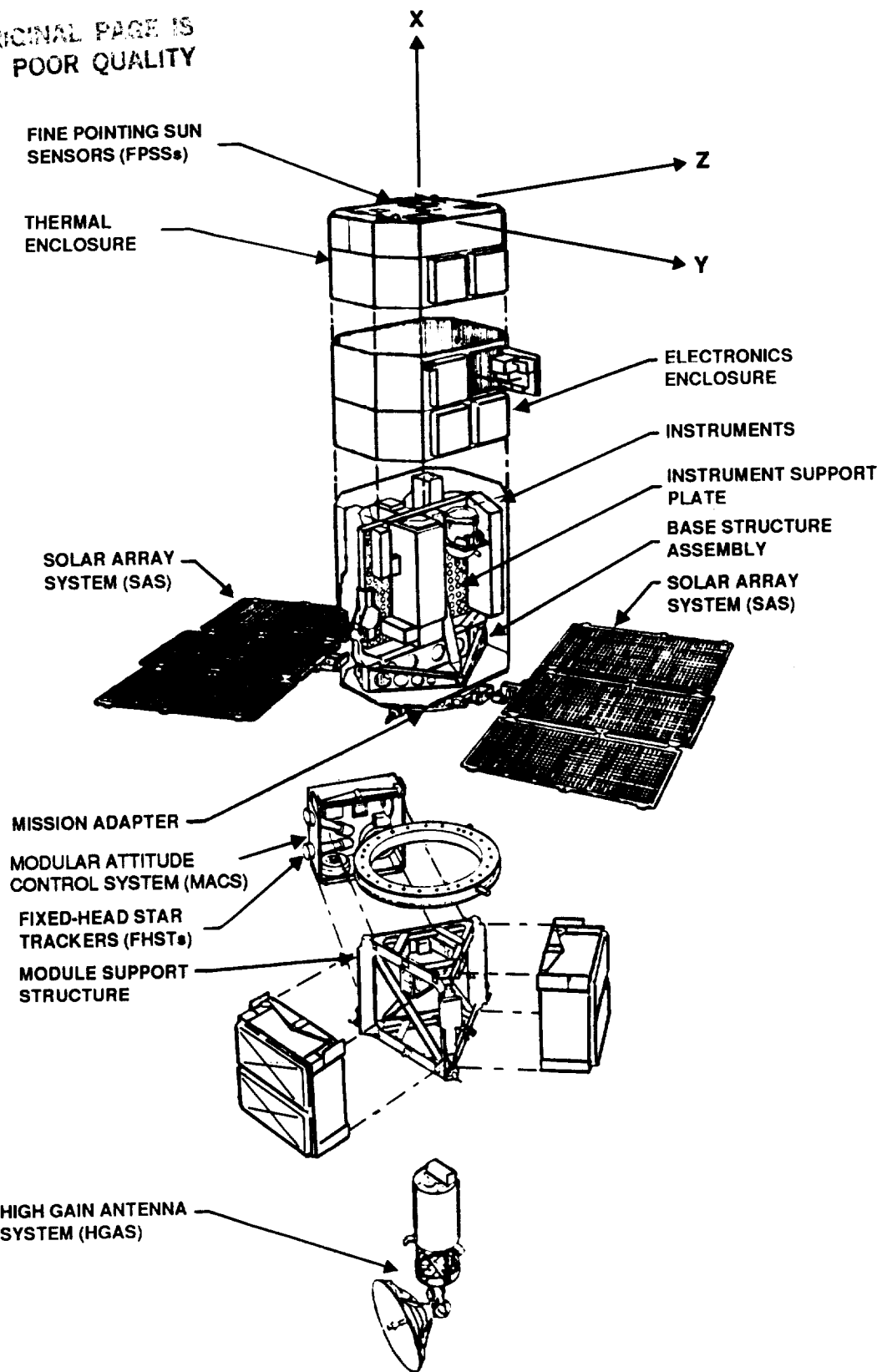


Figure 1. SMM/MMS Structure

The experiment module contains all the SMM mission-specific components. The two main types of components are the SMM scientific instruments and the mission-specific attitude sensors. The instruments comprising the scientific payload mainly study the emissions of the Sun on several different wavelengths, including x-ray, ultraviolet, and gamma ray. The mission-specific attitude sensors are the coarse Sun sensor (CSS) and the FPSSs. The FPSSs are the primary sources of solar pointing information in the normal mission mode, so their colocation with the scientific instruments makes sense. The two separate modules are connected by a mission adapter ring as shown in Figure 1.

The FPSS, a vector sensor, outputs rotations, α and β , about two sensor axes. It has a 2-deg-by-2-deg field-of-view (FOV). The specified accuracy of the FPSS is 5 arc-seconds (arc-sec) (3σ) within a 1-deg square FOV (Reference 2). The FPSS is mounted on the instrument support plate (ISP). The normal to the ISP is parallel to the y-axis of the spacecraft body frame, as shown in Figure 1.

The spacecraft body coordinate frame is defined by the orientation of the FPSS (Reference 2). The x-axis (roll) of the body frame is defined as parallel to the boresight of the FPSS. The y-axis (pitch) and z-axis (yaw) of the body frame are parallel to the FPSS axes. This definition of the body frame facilitates the calculation of the spacecraft pitch and yaw by the FPSS. The spacecraft pitch and yaw attitude may be read directly from the FPSS readings. Thus, at nominal (zero) roll, the spot on the Sun where the spacecraft is pointing may be easily obtained. However, because of this orientation, the FPSS provides no resolution on the roll attitude of the spacecraft. Also, since the FPSS nominally defines the body frame, no alignment calibration of the FPSS is necessary. The only calibration of the FPSS is for the electronic angular response curve of the sensor.

The FHSTs are also vector sensors. They are mounted in the MACS in the MMS section of the spacecraft. The FHSTs have a two-axis sensor coordinate system, with an 8-deg-by-8-deg FOV. Star positions are output in the telemetry as projected angles in the FHST coordinate frame. These values are then converted to a vector and transformed to the body frame by the FHST alignment matrix, S . Since the FPSS defines the body frame, S represents the relative alignment of the FHST and the FPSS, called the coalignment. The position accuracy of a single FHST measurement is 30 arc-sec (3σ) (Reference 2). This noise in the observation is mainly due to instrument temperature and the varying magnetic field of the Earth.

Since there are two well-separated FHSTs, a full three-axis attitude may be obtained solely from FHST data. However, in August 1987, FHST 2 experienced a loss of power and became inoperable. Hence, the quality of the FHST-only attitudes became significantly degraded. Since star observations in the sensor FOV are only separated by a maximum of 8 deg, poor attitude resolution about the FHST boresight axis resulted; thus, after the failure of FHST 2, FHST-only attitudes were of minimal use. Consequently, the analysis in this paper is concerned only with the FHST misalignment behavior before August 1987.

The FHSTs collect data by tracking stars in the FOV. A single star will be tracked for several (N) observations. These N observations are combined to form a track group,

which is the average position of the star in the FHST FOV. Thus, reduction in the uncertainty of the track group position can be averaged out by using

$$\sigma = 30/(N)^{1/2} \quad (1)$$

After a track group is formed, the FHST moves to another star and tracks the new star until another track group is formed. This process continues until the FHST becomes occulted.

The sampling rate of the star observations in telemetry and, therefore, the number of observations per track group, is set by the spacecraft telemetry mode. In science mode (the nominal operational mode) the number of observations that form a track group ranges from 6 to 20, while in engineering mode, 60 to 120 observations are available per track group. Engineering mode telemetry, however, does not contain experiment data. Thus, it is requested only for occasional calibration activities when the high FHST sampling rate can be justified. Because of this restriction, the accuracy of the attitude solutions computed from FHST data approximately ranges from 10 to 30 arc-sec (3σ), depending on the quality of the track groups and the degree to which the alignment matrix, S , is known.

Since, as stated previously, the FPSS is not able to determine the spacecraft roll, the FHSTs are the only source of fine roll determination. A coarse roll can be determined from magnetometer data; however, typical accuracies of the coarse-determined roll are between 1 and 2 deg, much larger than the specified roll accuracy of 0.1 deg. Thus, it is important to compute accurate coalignments of the FHSTs so that the computed roll is as accurate as possible. The nominal alignments of the FHSTs are the original design alignments. The calibrations are performed to calculate the misalignment from the nominal alignments.

The misalignment of the FHSTs has two components. The first component is the misalignment of the sensors with respect to the coordinate frame of the MACS. The second component is the misalignment of the MACS frame with respect to the body frame. Because of problems in observability of the orientation of the MACS frame, these components are combined into one set of values for the misalignment.

For the SMM, the misalignment matrices, M_i , represent the change in the alignment from the original design alignments, S_{oi} , where $i = 1$ or 2 , depending on which FHST is being calibrated. The alignment matrices, S_i , of the FHSTs can then be represented by

$$S_i = M_i S_{oi} \quad i = 1, 2 \quad (2)$$

Since the S_{oi} are known, the purpose of the FHST alignment calibrations is to compute the M_i . The calibrations are performed by taking observed vectors from the three sensors, one FPSS and two FHSTs, and comparing them to the respective reference vectors. The theoretical aspects of the SMM alignment calibrations have been presented in Reference 3 and will not be presented here. This alignment calibration scheme has typically yielded accuracies of 5 to 10 arc-sec in the relative alignment of the FHSTs if engineering mode telemetry is used in the calibration.

2. ANALYSIS

2.1 POSSIBLE CAUSES OF THE MISALIGNMENT VARIATION

Immediately after the SMM repair mission, the new FHST alignments were computed and used in the onboard and ground software. Thus, when pitch and yaw solutions were calculated by the FPSS and FHSTs separately, the resulting differences between the two solutions were initially very small, on the order of the position accuracy in the FHST. However, over the approximately 1-week period before the next alignment calibration was performed, a variation of the differences in yaw attitude, computed separately by the FHSTs and the FPSS, was exhibited that was clearly not random and was well in excess of the FHST solution accuracy (Reference 4). This initial variation is shown in Figure 2. Note that, as shown in Figure 3, the pitch differences show no such variation. Subsequently, to keep track of this variation, although the alignments were recalibrated, the original calibrated alignments were kept on hand and used to process a segment of data each day. The magnitude of the variation eventually reached 120 arc-sec, approximately 8 times greater than the original prerepair estimate for the alignment variation (Reference 5). Obviously, an unmodeled effect was causing this variation.

Several causes were proposed to account for the variation in misalignment:

- Spacecraft bending due to solar radiation pressure
- Electronic or mechanical changes in the sensors
- Uncertainty in the attitude solutions
- Mounting-plate expansion and contraction due to thermal effects

The first possible cause was eliminated because the effects would be too small to measure. Solar radiation pressure, while being a significant effect on spacecraft appendages, will not bend the body of a rigid spacecraft more than a fraction of an arc-second.

The next possibility is electronic or mechanical changes in the sensors themselves. Since the FPSS response was calibrated frequently and since the agreement between FHST readings did not exhibit measurable variations, the change in sensor response was ruled out. The FPSS response did show changes on the order of 1 to 2 arc-sec per month (Reference 4). This small change would not account for the 120-arc-sec differences being observed. An effect related to changes in the sensor, redefinition of the FPSS null, (zero pitch and yaw), occurred once in December 1984. Because of the manner of the FPSS angular response calibrations, the accuracy of the null of the FPSS is not determined directly. The null of the FPSS is defined as the output of the FPSS at the center of the Sun. Some of the experiments are capable of estimating the errors in their solar pointing. These readings have always been measured by the scientific personnel and communicated to the FDF personnel, who incorporated them into the FPSS response function. Because of changes in the electronic response of the FPSS, the null shows time-dependent shifts. Since scientists noticed a significant error in the FPSS null, it was redefined in December 1984 (Reference 4). This caused a significant (20 to 30 arc-sec) change in the

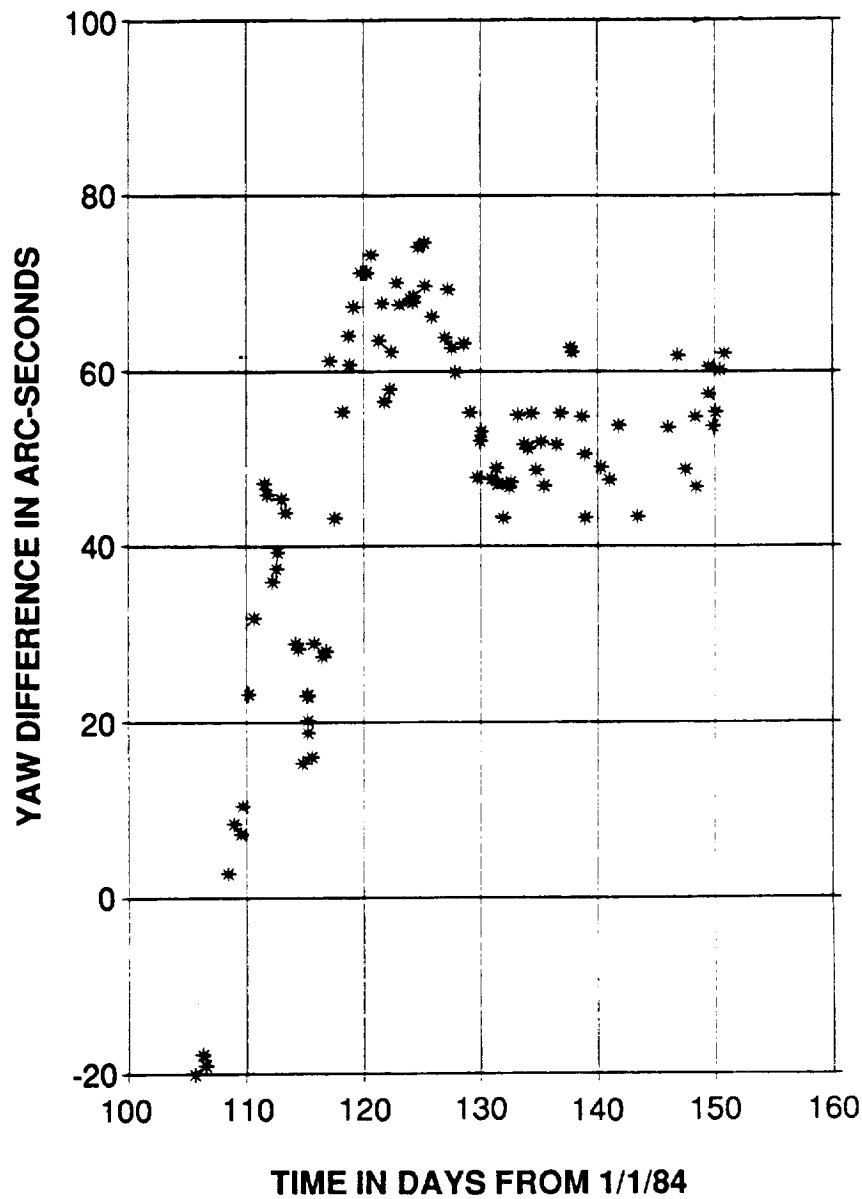


Figure 2. Initial Yaw Misalignment Variations

misalignment of the FHSTs. This shift in the FPSS null was most likely accumulated over the time since the repair mission. However, because of the manner in which the FPSS calibrations are performed, it could not be accounted for until the discrepancy was noticed by the scientific instruments. The effect of the null shift can be most clearly seen in the pitch misalignment data, shown in Figure 3. Note that the discontinuous drop at approximately day 350, which apparently reversed the accumulated drift from day 100. This same effect occurred in the yaw misalignment data; however, the discontinuous change was not significant enough to show clearly on the plot. This, however, serves the purpose to show that the effect would not be completely responsible for the misalignment variation.

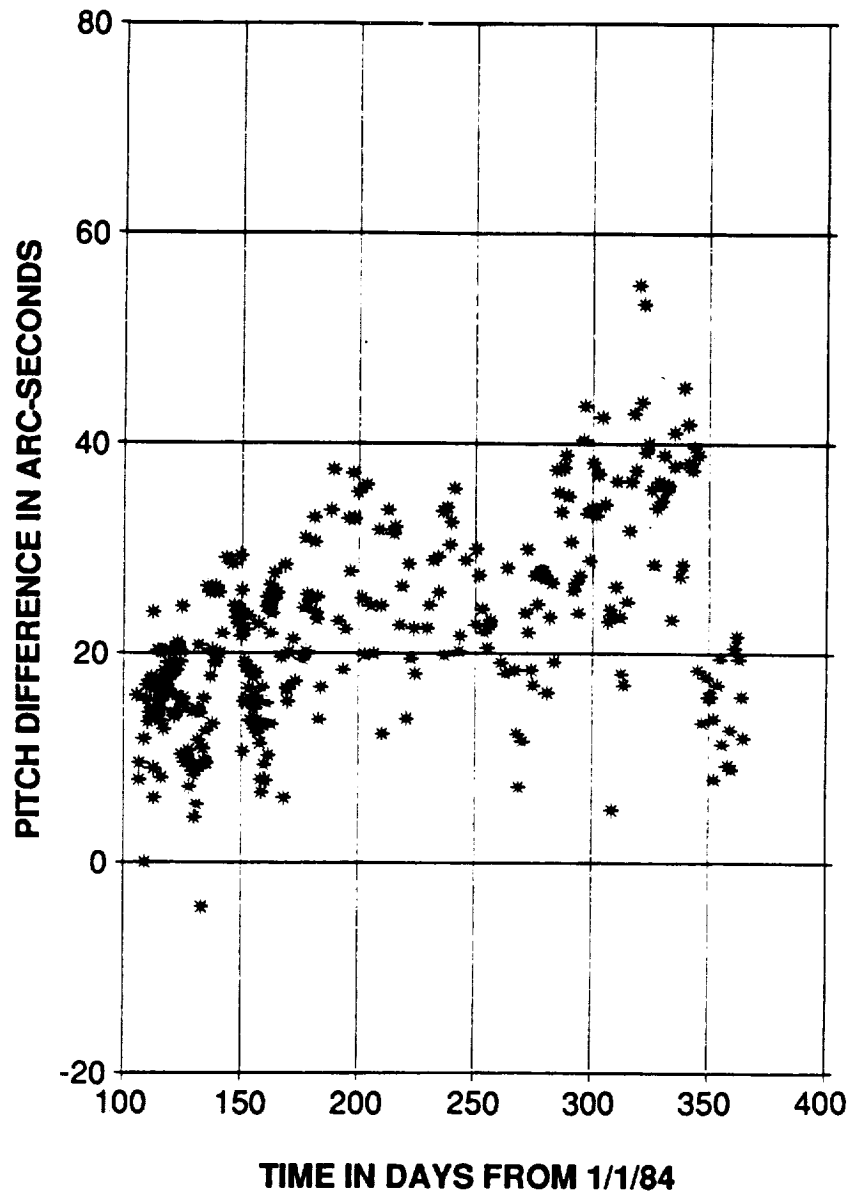


Figure 3. Pitch Misalignment Variation

The third possibility is the uncertainty in the attitude solutions. As mentioned previously, the misalignment variations were measured daily using FHST and FPSS attitudes computed during normal operations. This attitude comparison does not accurately determine the misalignments. More accurate results would have been obtained by performing frequent FHST calibrations; however, that approach was deemed unfeasible because of the resources required and the need to interrupt scientific observation to increase the FHST sampling rate during calibration. Hence, the less accurate but much quicker method of subtracting the computed attitudes was devised. The disadvantage is that a noise level is introduced that is equal in magnitude to the uncertainty of the less accurate attitude solution, which is the FHST attitude. Thus, a noise level of 20 to 30 arc-sec was expected

in the misalignment variation plot. However, this noise would not explain the observed variation because it is random, as compared to the observed patterned variation, and its magnitude is approximately one sixth of the magnitude of the observed variation. It is also worth noting that as full in-flight calibrations were performed, the results were completely consistent with the daily attitude calculations.

The effect of temperature variation on attitude sensor alignments has been seen on previous missions, most notably the Magnetic Field Explorer (Magsat) (Reference 6). Thus, the possibility of bending due to thermal effects was explored by checking various temperatures in the spacecraft. It was found that temperatures on the ISP and the mission adapter ring showed a variation over time that was similar to the variation seen in the yaw misalignment. Six temperatures were initially monitored; however, since all six showed the same basic variation, only one was used for graphing and statistical purposes. Since the temperatures were available in the spacecraft telemetry, they could easily be recorded from all real-time station contacts. The temperatures varied slowly over time, taking at least several orbits to change measurably. After this determination was made, data were collected for yaw misalignment and temperature only once per day. The variation of the temperature superimposed on a graph of the variation of the yaw misalignment is shown in Figure 4. The relative scales in the plot were chosen by performing a fit of yaw differences to temperature. The correlation is obvious. Figure 4 shows only 8 months of data to accentuate the correlation. However, all data taken between the SMM repair and the FHST 2 failure exhibited this trend.

The similarity of the two variations points to spacecraft thermal bending as the cause of the misalignment variation. Thus, the changing spacecraft temperatures cause a temperature gradient which, in turn, causes the spacecraft structure to bend. A temperature gradient requires two temperatures. However, because of a lack of thermocouples on the spacecraft, no other temperature, which when set up as a gradient with the ISP temperature resulted in a variation similar to the yaw misalignment. However, since the single temperature variation correlates so well with the yaw misalignment, it can be postulated that the second temperature remains basically constant (i.e., heat-sunk to the spacecraft chassis). In other words, the variation of the ISP temperature is equal to the variation of the temperature gradient.

The pitch misalignment never showed any significant patterned variation similar to the yaw misalignment variation. As shown in Figure 3, the variation seems to have a noise level of 20 to 30 arc-sec, a slow drift over several months, and a major shift at the point of the FPSS null redefinition. Thus, it seems the dominant effects in the pitch misalignment variation are the uncertainty of the FHST attitude solutions and the shift in the FPSS null.

The fact that the thermal profile variations seemingly do not affect the pitch misalignment can possibly be explained by the orientation of the ISP and the mounting of the FPSS on the ISP. As shown in Figure 5, the ISP is aligned along the z-axis (yaw). The FPSS is mounted in the middle of the ISP, right on the y-axis (pitch) and off-set from the z-axis. Thus, bending of the ISP translates directly into rotation of the FPSS about the yaw axis. Conversely, bending of the ISP will not cause any rotation about the pitch or roll axes.

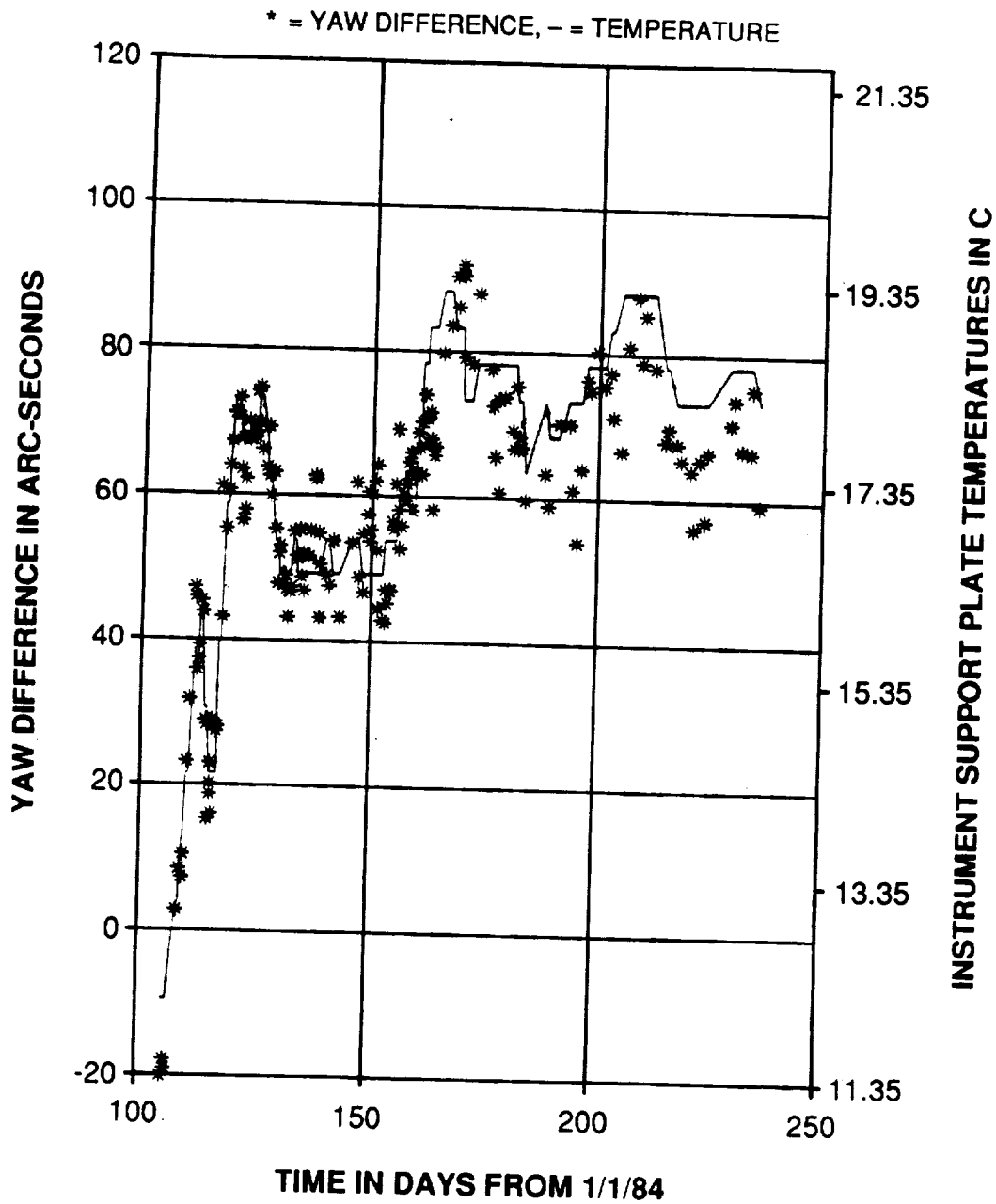


Figure 4. Yaw Attitude Differences and Instrument Support Plate Temperatures

Therefore, this analysis suggests that it is the FPSS that is actually moving. This causes a strange situation in that it is the movement of the FPSS that is causing the misalignment of the FHSTs. This peculiarity can be removed when it is realized that the FPSS defines the body-frame coordinates and, in fact, provides the most critical pointing information for the experiments. Thus, the movement of the FPSS causes the body frame to rotate, which, in turn, causes the FHST misalignment to change. Therefore, the FHSTs never really experience any significant motion with respect to the spacecraft chassis; it is the moving body frame that causes the alignment of the FHSTs to change. Presumably, the

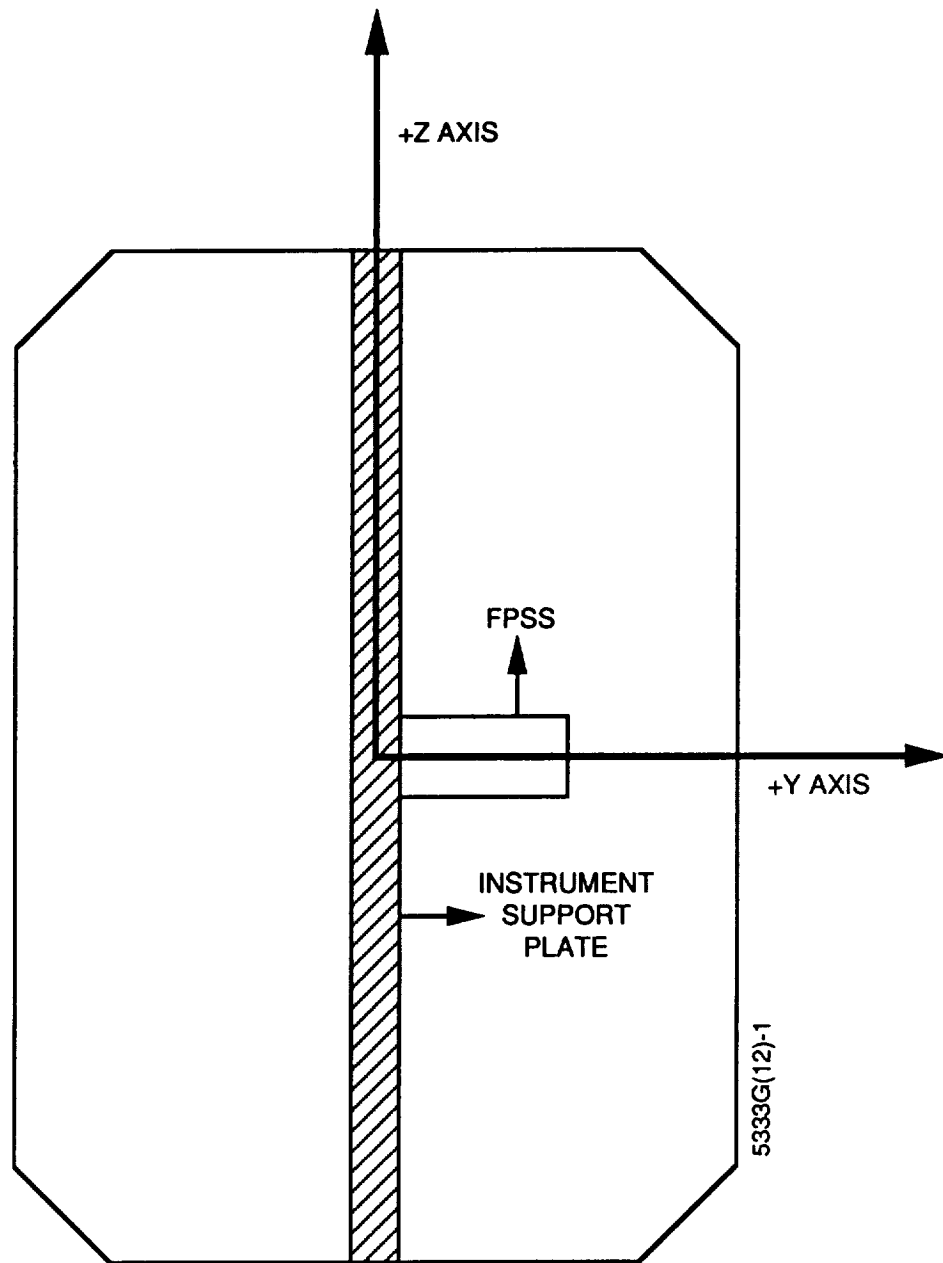


Figure 5. Orientation of Instrument Support Plate and FPSS

other attitude sensors on the spacecraft, such as the three-axis magnetometer, experience this same phenomena. However, because of the low accuracy of these instruments, this phenomena cannot be seen in their alignments. This analysis is a possible explanation of the misalignment variation. However, the full structure of the spacecraft would need to be analyzed before any explanations of the variation could be proved.

2.2 YAW MISALIGNMENT ESTIMATION FROM THE TEMPERATURE PROFILE

Since the dominating factor in the FHST misalignment variation about the yaw axis is the variation of the temperature, it would seem likely that the misalignment could be esti-

mated from the observed temperature, thus reducing the need for in-flight FHST alignment calibration. The first step was to set up a scatter plot of the yaw misalignment versus the temperature. This scatter plot, shown in Figure 6, shows a nearly linear

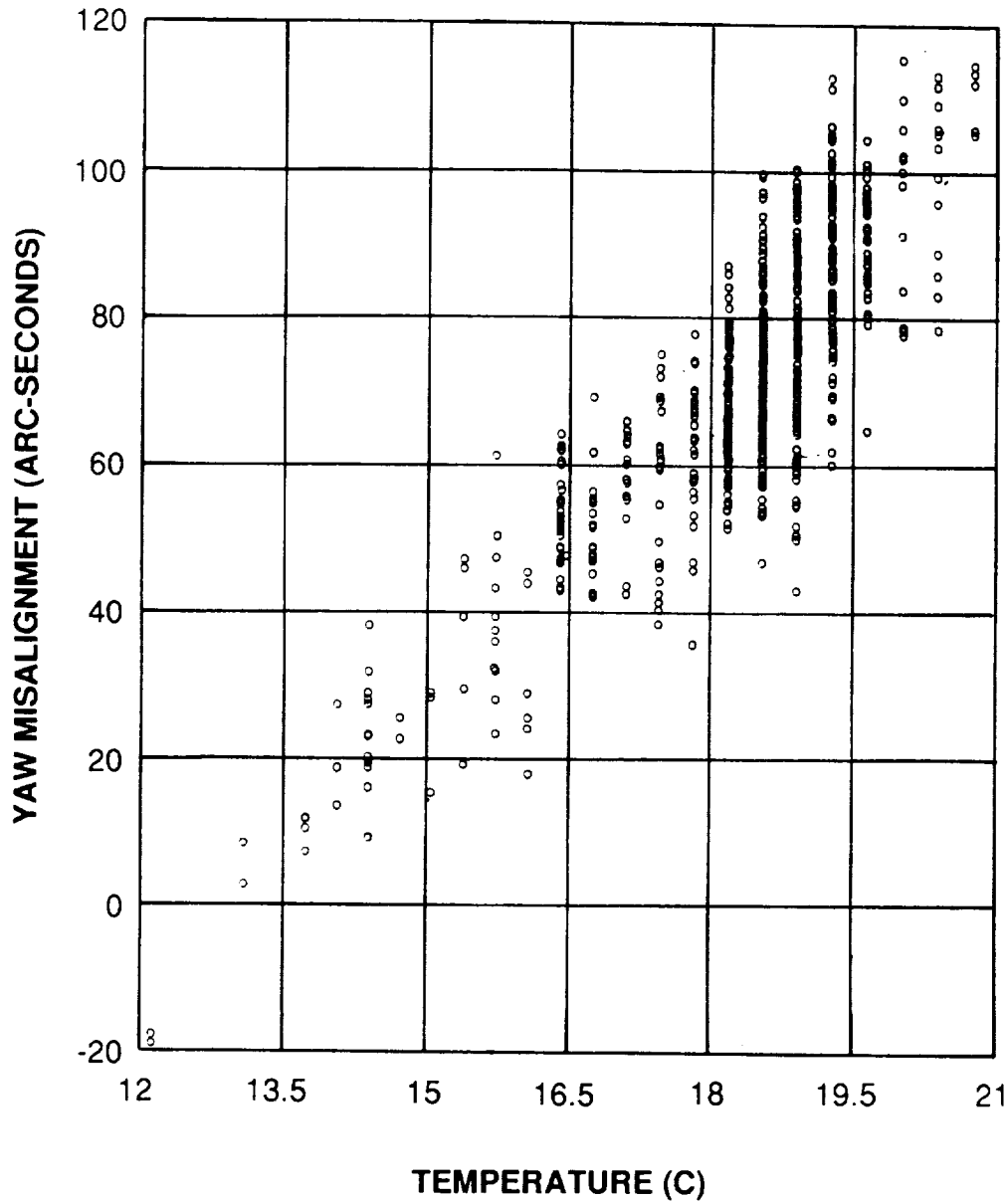


Figure 6. Yaw Misalignment Versus Temperature

relationship between the yaw misalignment and the temperature. A linear least-squares fit was performed on the data, and the resulting equation was

$$M = 13.410 * T - 173.790 \quad (3)$$

where M is the scalar yaw misalignment and T is the temperature. The root mean square (RMS) residual of the straight line fit was approximately 10.5 arc-sec, thus 99.7 percent

of the yaw misalignments calculated from the function in Equation (3) would be within 31.5 arc-sec (3σ). The error (1σ) in the slope is 0.3 arc-sec per deg celsius and the error (1σ) in the y-intercept is 5.6 arc-sec. This fit could be incorporated into the attitude determination system to estimate the misalignment matrix so that a more accurate attitude could be determined.

A more accurate fit may be determined if the effect due to the null shifts is taken into account. As shown in Figures 7 and 8, the data in Figure 6 can be broken down into two segments: data starting at the SMM repair mission and running until the date of the null shift in December 1984, and data starting at the null shift and running until the failure of FHST 2. Figures 7 and 8 show two different functions. Fits were done to the two functions and the equations were

$$M_1 = 10.801 * T - 130.029 \quad (4)$$

$$M_2 = 15.721 * T - 215.072 \quad (5)$$

The error (3σ) of the calculated misalignment in Equation (4) is 25.5 arc-sec, the uncertainty (1σ) in the slope is 0.3 arc-sec per deg, and the uncertainty (1σ) in the y-intercept is 5.9 arc-sec. The error (3σ) of the calculated misalignment in Equation (5) is 31.1 arc-sec, the uncertainty (1σ) in the slope is 0.5 arc-sec per deg, and the uncertainty (1σ) in the y-intercept is 7.6 arc-sec.

Equations (4) and (5) have different slopes, which poses an interesting question. Since the null shift is a change in the position of the boresight of the tracker, one would think this would be reflected as a change in the constant term of the misalignment function only. While a significant change in the constant term of these equations exists, the change in the slope indicates that the dependence of the misalignment on the temperature is changing. This would indicate that the equation for the estimate of the alignment would need to be calibrated. This would seem to undermine the estimate, since its prime use would be to replace FHST alignment calibration. However, since the variance improved by only about 2 arc-sec for the first segment, calibration of this equation would probably not exceed once per year.

2.3 SUGGESTIONS FOR SPACECRAFT OPERATIONS

It has been shown that as temperatures in the SMM structure vary; the yaw misalignments of the FHSTs vary similarly, thus degrading the accuracy of the attitude solutions. To compensate for this effect, two methods of solution are available: (1) frequent in-flight alignment calibration and (2) misalignment function modeling. Both methods have their advantages and disadvantages.

The advantage of frequent in-flight calibration is that immediately following the calibration, the resulting alignments are known to a high degree of accuracy, better than 15 arc-sec. However, this accuracy will degrade over a couple of weeks as the temperature varies. This problem can be overcome by recalibrating the alignments every 2 to 3 weeks. However, this points out the major disadvantage of this scheme: in-flight calibration of the

YAW MISALIGNMENT VS TEMPERATURE

840101 - 841211

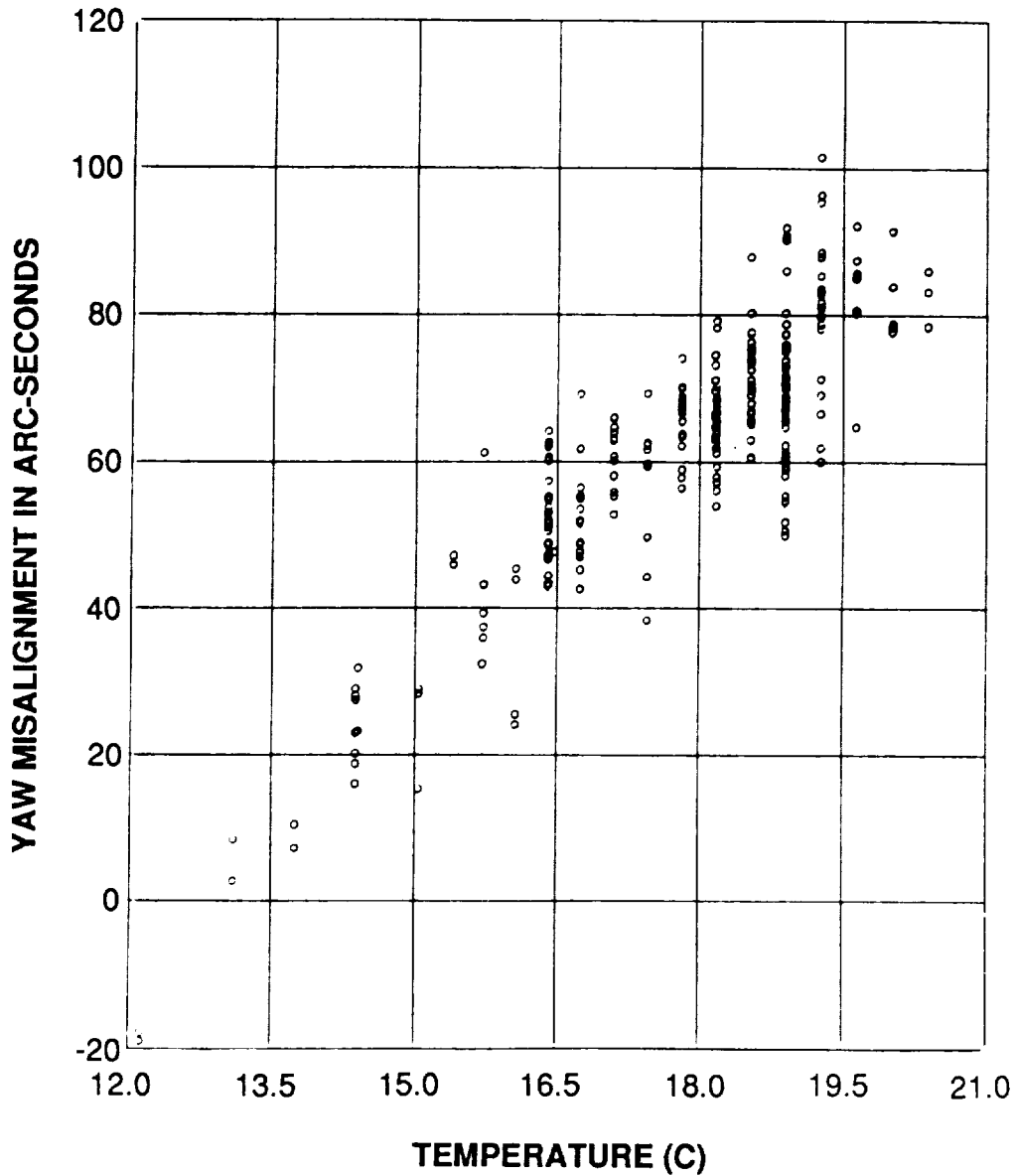


Figure 7. Yaw Misalignment Versus Temperature Before Null Redefinition

FHST misalignment requires operational time, typically three orbits, on the spacecraft and the ground and, in the case of the SMM, requires the use of engineering mode telemetry. Time spent calibrating the attitude sensors is lost to the scientists. Thus, ideally, these type of calibrations should be performed infrequently, perhaps no more often than every 2 months.

On the other hand, modeling of the misalignment function requires calibration of the function at most once a year. These calibrations of the function require no special operational time of the spacecraft; they can be completed during routine processing of the

YAW MISALIGNMENT VS TEMPERATURE

841212 - 861005

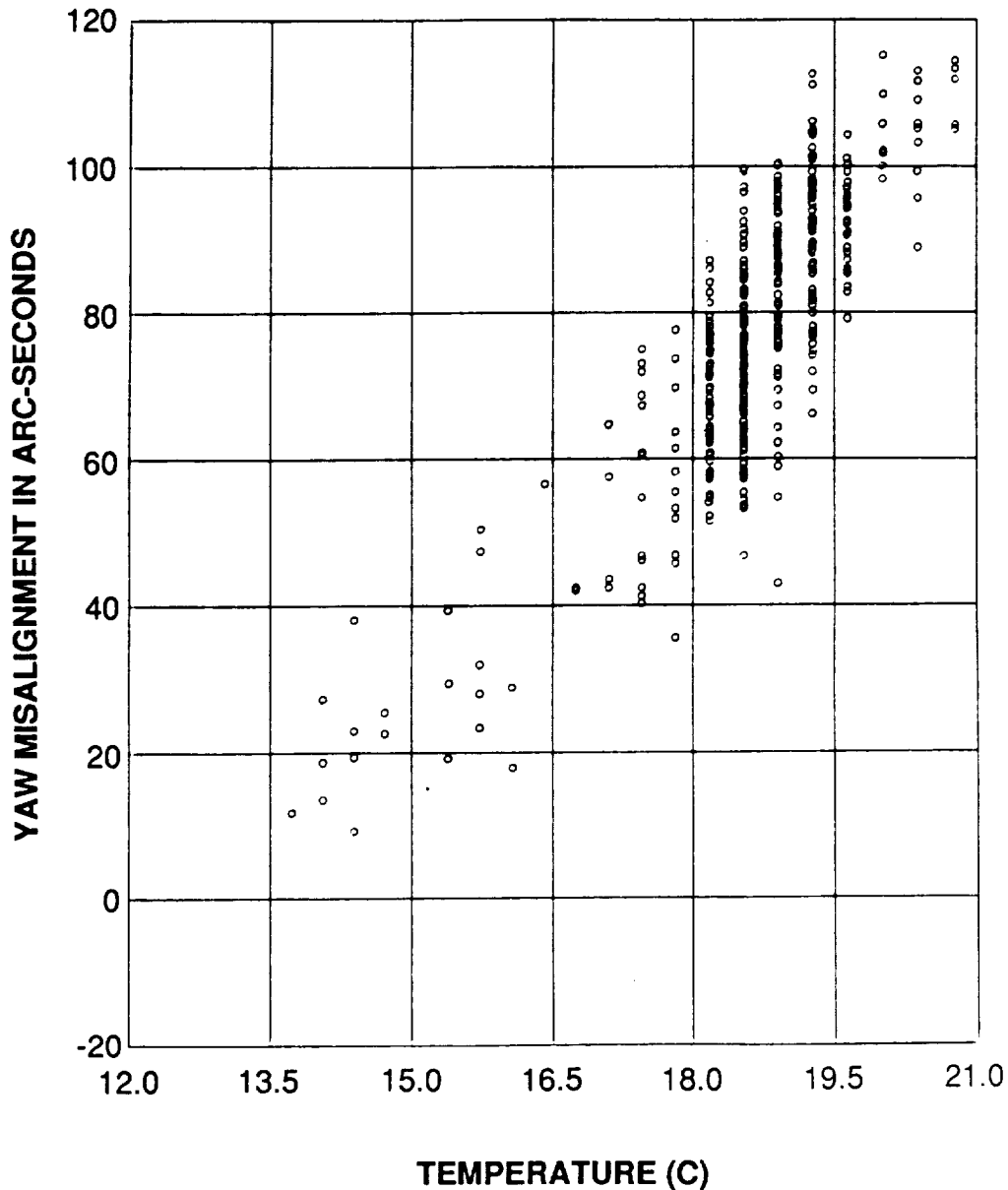


Figure 8. Yaw Misalignment Versus Temperature After Null Redefinition

attitude data. However, the disadvantage of using the misalignment function is slightly degraded knowledge of the misalignments, between 5 and 15 arc-sec less accuracy than the in-flight calibration.

For best results, it is suggested that a combination of the two methods be used. The in-flight calibrations should be used initially to determine an accurate estimate of the misalignment matrix, M , and the misalignment function should be used to monitor the changes in M . Then, every 6 months to 1 year, the alignment calibration should be re-done, using the in-flight method to maintain the most accurate estimate of M . This

scheme combines the advantages of both methods by using as little operational time as possible and maintaining a high degree of knowledge of the FHST alignment matrix.

For example, the SMM could use the following scheme. The postrepair FHST alignments could be calibrated using the in-flight method. Then, the yaw misalignment function could be used to maintain the yaw misalignment accuracy. The pitch and roll misalignment would not need to be maintained because their misalignments are not affected by the varying temperatures as stated previously. The changes in these misalignments due to the other factors are much smaller and could be maintained by the in-flight calibrations every 6 months.

2.4 MODELING THE TEMPERATURE DATA

The relevant temperatures on the SMM are received from the spacecraft telemetry; thus, the misalignment can be easily calculated from the simple models presented previously. However, for missions where the relevant temperature data are not available in the telemetry or where the configuration of the mission is substantially different from the SMM, the previously presented analysis needs to be supplemented by other sources of data.

For missions with a similar configuration to the SMM but for which temperatures are not available in the telemetry, an analysis of the temperature profile of the SMM shows that the profile can also be modeled simply. For the SMM, the temperatures on the ISP and the mission adapter ring are a function of instrument activity, distance from the Sun, and the length of the spacecraft day. The attitude of the spacecraft, of course, plays a large part in the profile. However, the SMM maintains nearly the same attitude relative to the Sun so that the temperature does not vary due to this effect. Therefore, this effect is not taken into account in this analysis. However, for missions with attitudes that are dynamic relative to the Sun, i.e., Earth-pointing or astronomical missions, this effect should also be modeled.

As seen in Figure 9, the dominating effect on the spacecraft temperature is payload instrument activity. Operating the scientific instruments generates a great deal of heat that is dissipated and radiated to other parts of the spacecraft. The temperature profile experiences major changes along with changes in instrument activity. At the repair of the SMM, approximately day 100 of 1984, all the payload instruments were off, and, as seen in Figure 9, the temperature was very low. As the mission started scientific activities, the payload instruments were turned on, and the temperature rose rapidly. Another example is seen later near day 250 when the spacecraft went into safehold mode and all the scientific instruments were powered off. For the SMM, safehold mode is the spacecraft's response to a perceived dangerous situation. The MACS safehold electronics takes attitude control from the OBC and holds the spacecraft in a Sun-oriented attitude until the problem is resolved. To conserve spacecraft power, most of the instruments are, consequently, powered off. Thus, the temperature of the spacecraft drops quickly.

Since the temperature changes in the case of powering on and off of the payload instruments occur relatively quickly, this effect can be modeled as a step function. The size of the step will vary with the number of instruments that are powered off. This component of the temperature profile is shown in Figure 9.

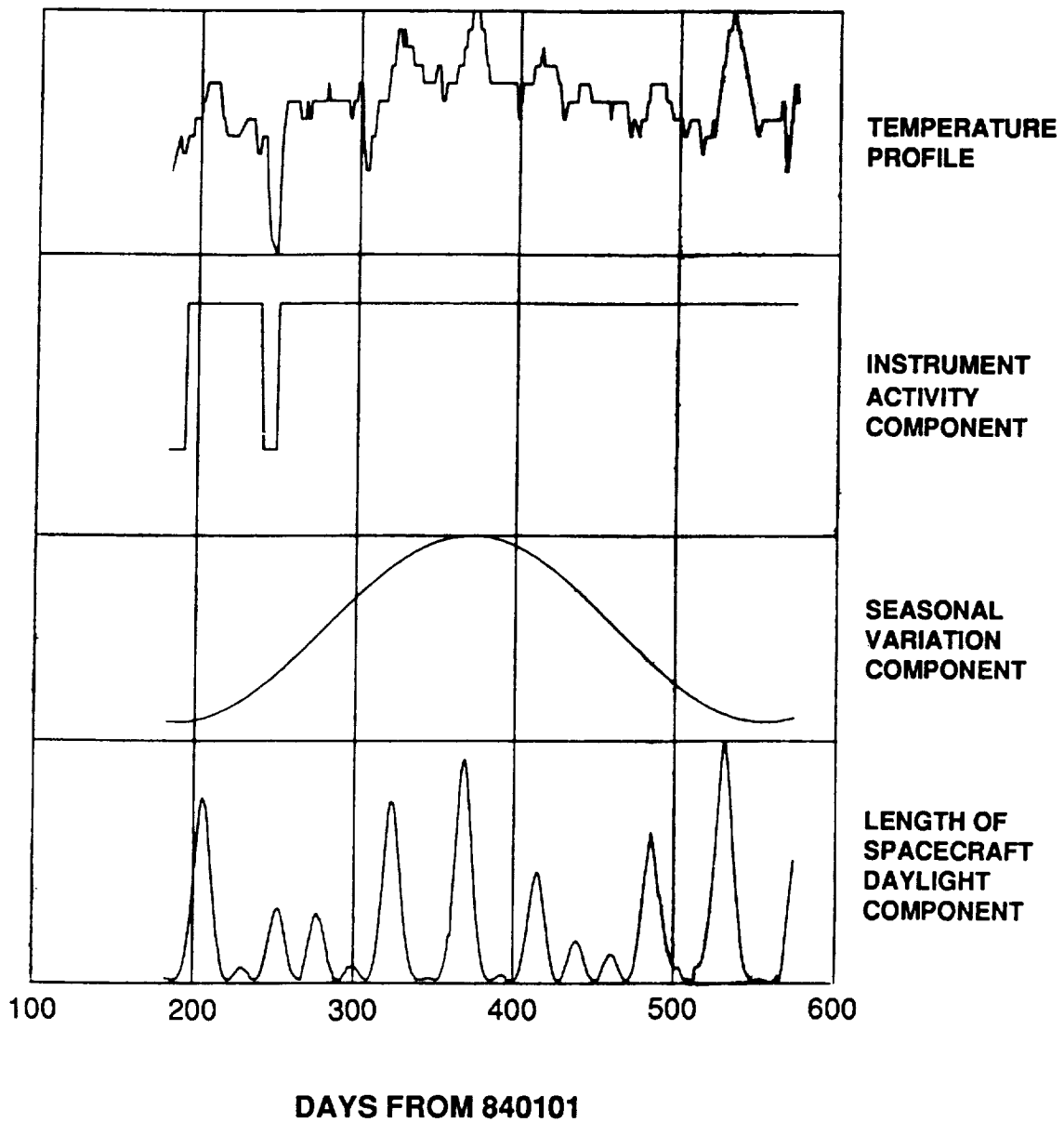


Figure 9. SMM Temperature Profile and Components

Another effect on the SMM temperature profile is the distance of the spacecraft from the Sun. This is a consequence of the Earth's orbit about the Sun. The Earth's orbit is not exactly circular, having an eccentricity of 0.016. Thus, the spacecraft is closer to the Sun in December at the Winter Solstice and farthest from the Sun in June at the Summer Solstice. This effect can be modeled by a sinusoidal pattern with a period of 1 year. The contribution of this effect on the SMM is shown in Figure 9.

The last effect on the temperature profile is the variation in the length of the spacecraft daylight period. The spacecraft daylight period is the amount of time per orbit that the

spacecraft is in view of the Sun. This varies due to the geometry of the orbit. Orbit dawn is defined as the beginning of the spacecraft daylight period, i.e., the time when the spacecraft becomes unblocked from the Sun by the Earth, and orbit dusk is defined as the end of the spacecraft daylight period. Then, orbit noon is the middle of the daylight period, the time exactly between orbit dawn and orbit dusk; orbit midnight is the time exactly between orbit dusk and orbit dawn. Due to geometrical considerations, the maximum time of the spacecraft daylight period is when the right ascension of the ascending node of the spacecraft is at orbit noon or midnight. This causes the declination of the spacecraft orbit to be a maximum near orbit dusk and dawn. The spacecraft crosses a shorter chord of the Earth at the higher declinations; thus, the effective amount of Earth that is blocking the Sun from the spacecraft is less. Consequently, orbit dawn occurs earlier and orbit dusk occurs later. The effect also has a seasonal component, being more pronounced near the solstices, as shown in Figure 9.

This effect is completely dependent on the orbit parameters and can be solved for exactly if the spacecraft ephemeris is known. If the mission is in the planning stages, the effect can be modeled from the preliminary knowledge of the orbital elements. This component of the temperature profile for the SMM is shown in Figure 9.

Once the effect of these parameters is taken into account, the total temperature profile can be formed. Then, after investigating the mission configuration and its response to temperature variation, an approximate function, analagous to Equations (3) through (5) can be determined. This function can be used in the premission attitude stability, determination, and control planning and the early mission operations. During the mission, data would be collected over a sufficiently long baseline to completely specify the model; if the SMM can be used as a guide, a minimum of 6 months would be required to account for the seasonal effects. Clearly, this approach requires substantially more intensive analysis than the use of direct temperature measurements.

3. SUMMARY AND CONCLUSION

In summary, flight data from the SMM mission attitude determination support demonstrates that spacecraft attitude sensor alignments vary with spacecraft temperature by up to 120 arc-sec over a 1-year period, with the majority of the variation occurring during the first few weeks as the temperatures stabilize. These levels are about eight times greater than were indicated in the currently available reports on the prelaunch thermal structural stability of the SMM. Methods have been proposed to incorporate flight measurement of the temperature-versus-alignment function and its variance to operational procedures with the benefit of reducing the spacecraft operations time required to support attitude sensor alignment calibration. Also, combining an approximate model of the temperature with the model of the alignment-versus-temperature could provide a significant reference for planning and analysis currently in progress for future missions. This prelaunch planning should also include incorporating the spacecraft structure temperatures in the attitude telemetry record.

ACKNOWLEDGMENTS

The authors wish to acknowledge the generous support of the following GSFC personnel: Mr. Frank Vaughn, Assistant Technical Representative, SMM Analytical Support Task; Mr. J. B. Joyce, Head, Mission and Network Support Section; and Mr. Gary Meyers, Head, Flight Dynamics Support Branch.

The authors also wish to thank Dr. Malcolm D. Shuster of the Johns Hopkins Applied Physics Laboratory for his technical advice and help in understanding and interpreting the data in this paper and Mr. Robert Shendock of the OAO Corporation for his help with the spacecraft hardware configurations. In addition, the authors would like to thank Dr. Milton Phenneger of Computer Sciences Corporation (CSC) for his help in preparing this work for publication. Acknowledgments for contributions to this paper are also extended to Mr. Bruce J. Twambly (CSC), Mr. Daniel R. Kulp (CSC), Ms. Deborah Roberts (CSC), Mr. Robert Feiertag (CSC), Mr. James R. Klein (CSC) and Mr. Joseph W. Dehen (CSC).

REFERENCES

1. Computer Sciences Corporation, CSC/TM-84/6131UD1, *Solar Maximum Mission Attitude Operations Handbook, Revision 4 - Update 1*, A. Eudell et al., July 1988
2. ---, CSC/SD-78/6082, *Solar Maximum Mission (SMM) Attitude System Functional Specifications and Requirements*, R. Byrne et al., September 1978
3. Shuster, M. D., D. M. Chitre, and D. P. Niebur, "In-flight Estimation of Spacecraft Attitude Sensor Accuracies and Alignments," *Journal of Guidance, Control, and Dynamics*, Vol. 5, No. 4, July-August 1982, pp. 339-343
4. Computer Sciences Corporation, CSC/TM-85/6714, *Analysis of the Solar Maximum Mission (SMM) Fine Pointing Sun Sensor (FPSS) Response Changes*, F. Patt, May 1985
5. Hewitt, D. R., *Multimission Modular Spacecraft (MMS) Thermal System Specification*, S-700-12, February 1977
6. Computer Sciences Corporation, CSC/TM-81/6036, *High Precision Attitude Determination for Magsat*, F. VanLandingham, April 1981



FLIGHT MECHANICS/ESTIMATION THEORY SYMPOSIUM

SESSION 3

PRECEDING PAGE BLANK NOT FILMED

TRUE COVARIANCE SIMULATION OF THE
EUVE UPDATE FILTER

by

I. Y. Bar-Itzhack* and R. R. Harman**
NASA - Goddard Space Flight Center
Greenbelt MD, 20771

Abstract

This paper presents a covariance analysis of the performance and sensitivity of the attitude determination Extended Kalman Filter (EKF) used by the On Board Computer (OBC) of the Extreme Ultra Violet Explorer (EUVE) spacecraft. The linearized dynamics and measurement equations of the error states are derived which constitute the "truth model" describing the real behavior of the systems involved. The "design model" used by the OBC EKF is then obtained by reducing the order of the truth model. The covariance matrix of the EKF which uses the reduced order model is not the correct covariance of the EKF estimation error. A "true covariance analysis" has to be carried out in order to evaluate the correct accuracy of the OBC generated estimates. The results of such analysis are presented which indicate both the performance and the sensitivity of the OBC EKF.

1.0 INTRODUCTION

The Extreme Ultraviolet Explorer (EUVE) is scheduled to be launched by a Delta launch vehicle in August 1990 into a 550 km orbit with a 28.5 degree inclination. The EUVE experiment will observe stellar objects emitting electromagnetic radiation with wavelengths of 100 to 1000 angstroms. The spacecraft design is called an Explorer Platform (EP). The EP is designed to be flexible enough to be used by many different experiments. The EP consists of three main modules: experiment, Platform Equipment Deck (PED), and the multimission modular spacecraft (MMS). The MMS contains the attitude control system, power system, and the command and data handling system. The EUVE mission is divided into two phases: all sky survey and spectroscopy. In the all sky survey, the spacecraft will be rotating at 3 revolutions per orbit (3 RPO about the roll axis) while instruments perpendicular to the roll axis scan the sky. Six months later, EUVE will be three axis stabilized at selected spectroscopic targets.

2.0 ALGORITHM

2.1 INTRODUCTION

The attitude of the Explorer Platform (EP) is determined by gyros which measure the angular rate vector of the EP, by two fixed-head star trackers (FHST), and by one fine sun sensor (FSS). The gyros yield three components of the angular rate vector of the EP rotation with respect to inertial space. The components measured by the gyros are the projections of the vector on the body axes, which are the axes of the attitude control system (ACS).

* NRC NASA Resident Research Associate. On Sabbatical leave from the Aerospace Engineering Dept., Technion - Israel Institute of Technology, Haifa 32000, Israel.

** Aerospace Engineer, Attitude Analysis Section, Flight Dynamics Analysis Branch.

If the exact orientation of the ACS with respect to inertial coordinates is known at some point, if the gyro outputs are perfect, and if no computation errors are introduced when solving the attitude propagation equations, then from that time on the EP attitude is known exactly. However, since the initial knowledge of the attitude is never perfect, since the gyro outputs include measurement and misalignment errors, and since the computation is not perfect either, the attitude of the EP is not perfectly known. Moreover, the attitude errors tend to diverge and consequently corrections of the computed attitude have to be performed. This is the reason for employing two FHSTs and one FSS in attitude determination.

Star tracker and Sun sensor measurements, when used correctly, check the attitude error growth. The information supplied by the FHSTs and by the FSS is blended with the attitude computed based on the gyro outputs and on the initial EP orientation. This blending is done by a Kalman filter (KF). The EP on board computer (OBC) software uses quaternions for attitude determination. The relationship between vector measurements, which are the outputs of the FHSTs and of the FSS, and the quaternion of rotation is non-linear. Therefore an Extended Kalman filter (EKF), rather than a KF, has to be employed.

For simplicity of implementation the EKF used by the OBC is actually a reduced order suboptimal filter which does not contain all the error sources in the gyros, in the FHSTs and in the FSS [1,2]. It is, therefore, necessary to investigate the predicted performance of the on board reduced order EKF. To evaluate the performance of the EKF, finer error models have to be used in describing the performance of the true hardware [3,4]. Such models are referred to in the literature as "truth models" [5]. In this paper we introduce a "truth model" which takes in account factors neglected in the OBC EKF model. These factors are gyro, FHST and FSS misalignments, gyro scale factor errors and the effect of the Sun not being captured in a narrow field of view about the boresight of the FSS.

A convenient analysis tool is the "true covariance" simulation [6]. This paper presents such analysis of the performance of the on board attitude determination EKF of the EUVE satellite. The "truth model" of the attitude determination problem is developed next. The "design model" is then listed in Section 2.3. Next the "true covariance" simulation algorithm is presented in Section 3. The analysis which was carried out and its results are presented in Section 4 and finally, the conclusions drawn from this analysis are presented in Section 5.

2.2 THE TRUTH MODEL

Error Propagation Model

Open-loop attitude determination

Consider Fig. 1 which describes a generic attitude control spacecraft (S/C). The input quaternion, q_1 , represents a command attitude and q_t is the quaternion which represents the actual attitude of the S/C. As shown in Fig. 1, gyros which are mounted on the S/C

measure its angular velocity. The readings of these gyros are used by the Attitude Determination algorithm to compute the quaternion q_c which represents the computed attitude. This configuration is called "open-loop" since here q_c is not fed back

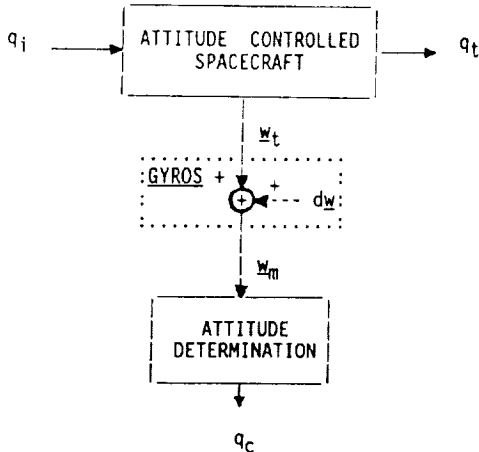


Fig. 1: Generic open-loop attitude determination configuration

into the attitude controlled S/C. Consequently in this configuration the gyro error, dw , of these gyros is not affecting the S/C attitude.

Let us denote by "i" the inertial coordinate system which is the reference coordinate system and by "a" the ACS coordinate system which we assume to be identical to the body system. The attitude determination problem is that of finding the quaternion which corresponds to the transformation matrix from "i" to "a" (or vice-versa). Since the gyros introduce measurement errors (dw) the computed attitude is erroneous. Therefore the computed transformation matrix which is supposed to transform vectors from the "i" to the "a" frame, actually transforms the vectors from the "i" frame to another erroneous coordinate system which we denote by "c". Thus we distinguish between three coordinate systems; namely, the "i", the "a" and the "c" systems. We assume that the error in computing the transformation matrix is small, consequently "a" and "c" are almost identical. In other words, a very small transformation takes us from

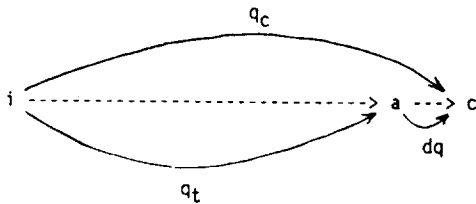


Fig. 2: Schematic description of the quaternion relations in the attitude determination problem

the "a" to the "c" system. To the transformations between the coordinates there correspond suitable

quaternions as depicted in Fig. 2. As indicated in this diagram

$$q_t = q_{i-to-a} \quad (1.a)$$

$$q_c = q_{i-to-c} \quad (1.b)$$

$$dq = q_{a-to-c} \quad (1.c)$$

The subscript "t" corresponds to the transformation to the true attitude of the vehicle whereas the subscript "c" denotes the transformation to the computed attitude. (Note that "c" corresponds to the subscripted notation 'measured' in refs. 2 and 3). When dealing with quaternion products, a special care has to be given to the question of what coordinate frame the quaternion is referred to. If each of the three quaternions defined is referred to the coordinate system from which it transforms vectors, then the following relation between them holds

$$q_{i-to-c}^j = q_{i-to-a}^j q_{a-to-c}^a \quad (2)$$

where the product on the right hand side of (2) is the quaternion product (defined in the Appendix) and the superscripts denote the frame to which each quaternion is referred. From (1.c) the rightmost quaternion in (2) is dq . Note that dq is the only quaternion referred to the body frame whereas the other two are referred to the inertial frame. Keeping this in mind we omit all superscripts and use the notations of (1) to write (2) as

$$q_c = q_t dq \quad (3)$$

Differentiation of (3) yields

$$\dot{q}_c = \dot{q}_t dq + q_t d\dot{q} \quad (4)$$

It is well known [7] that

$$\dot{q}_t = \frac{1}{2} q_t W \quad (5)$$

where W is a quaternion of angular velocities defined as follows

$$W = iw_x + jw_y + kw_z \quad (6)$$

The components w_x, w_y, w_z are the components of the true angular velocity vector at which the ACS coordinate frame rotates with respect to the inertial frame, coordinatized in the ACS frame. These components are measured by gyros which supply measured (and hence erroneous) data. In the lack of knowledge of the true rates, the gyro outputs are used in computing the quaternion, therefore the solution of (5) yields q_c rather than q_t ; that is, q_c is the solution of

$$\dot{q}_c = \frac{1}{2} q_c W_m \quad (7)$$

* Note that $q_{i-to-c}^j = q_{a-to-c}^i q_{i-to-a}^j$; that is, when all quaternions are referred to the inertial frame the order of the product is reversed.

where W_m is of the form of (6) only that the quaternion components are the measured rather than the exact angular rates.

When (5) and (7) are substituted into (4) we obtain

$$\frac{1}{2}q_t W_m = \frac{1}{2}q_t W dq + q_t d\dot{q} \quad (8)$$

Define a quaternion of angular-rate error as follows

$$dW = W_m - W$$

then

$$W = W_m - dW \quad (9)$$

Substituting (9) and (3) into (8) yields

$$\frac{1}{2}q_t dq W_m = \frac{1}{2}q_t (W_m - dW) dq + q_t d\dot{q}$$

which can be written as

$$q_t [d\dot{q} + \frac{1}{2}(W_m - dW) dq - \frac{1}{2}dq W_m] = 0$$

Since q_t is invertible, it is possible to pre-multiply both sides of the last equation by the inverse of q_t . This yields the result that the expression in the brackets is equal to zero and consequently

$$d\dot{q} = \frac{1}{2}dq W_m - \frac{1}{2}W_m dq + \frac{1}{2}dW dq \quad (10)$$

Let us express the quaternions appearing in (10) in a more explicit form by their vector and scalar parts. Accordingly

$$dq = \begin{bmatrix} d\dot{\phi} \\ \dots \\ d\phi \end{bmatrix} \quad W_m = \begin{bmatrix} W_m \\ \dots \\ 0 \end{bmatrix}$$

where $d\dot{\phi}$ is the vector part of the quaternion. When the quaternion product is carried out (see the Appendix for the rules of quaternion product), (10) reads as follows

$$\begin{bmatrix} d\dot{\phi} \\ \dots \\ d\phi \end{bmatrix} = \frac{1}{2} \begin{bmatrix} d\dot{\phi} \times W_m + d\phi W_m \\ \dots \\ -d\dot{\phi} \cdot W_m \end{bmatrix} - \frac{1}{2} \begin{bmatrix} W_m \times d\dot{\phi} + d\phi W_m \\ \dots \\ -W_m \cdot d\dot{\phi} \end{bmatrix} + \frac{1}{2} \begin{bmatrix} dW \times d\dot{\phi} + d\phi dW \\ \dots \\ -dW \cdot d\dot{\phi} \end{bmatrix}$$

The last quaternion equation is equivalent to two equations, one for the vector part of q and one for its scalar part. Using the following rules of vector product, $A \times B = -B \times A$ and $A \cdot B = B \cdot A$, the two equations can be written as

$$d\dot{\phi} = -W_m \times d\dot{\phi} + \frac{1}{2}d\phi dW + \frac{1}{2}dW \times d\dot{\phi} \quad (11.a)$$

$$d\phi = -dW \cdot d\dot{\phi} \quad (11.b)$$

When dq expresses a small rotation, its vector part, $d\dot{\phi}$, is small, therefore the last term on the right hand side of (11.a) is of second order and hence is negligible. The right hand side of (11.b) is negligible too and indeed, since the absolute value of any quaternion of rotation is equal to 1, the scalar part of dq satisfies the equation $d\phi = [1 - |d\dot{\phi}|^2]^{1/2}$ and since the vector part is small, $d\phi$ stays close to 1, hence its time derivative is nearly zero. Note that as $d\phi$ is nearly 1, the second term on the right hand side of (11.a) is not negligible. Consequently (11) yields

$$d\dot{\phi} \sim -W_m \times d\dot{\phi} + \frac{1}{2}dW \quad (12.a)$$

and as explained above

$$d\phi \sim 1 \quad (12.b)$$

The equation of interest is (12.a).

The transformation matrix T_c^a which corresponds to dq can be expressed in terms of small Euler angles. Define the angles as follows

ψ is the roll angle error defined about the body x-axis
 ϕ is the pitch angle error defined about the body y-axis
 χ is the yaw angle error defined about the body z-axis.

Note that for small rotations the order of rotation is irrelevant and we may refer all angles to the initial coordinate system which prevailed before the small rotations took place. Also note that these angles are referred to the body frame, "a", as is implied in (2) and (3). When the transformation matrix from the body to the computed frame is expressed as a function of the three Euler angles defined above and when the angles approach zero, the transformation matrix becomes

$$T_c^a = \begin{bmatrix} 1 & \psi & -\chi \\ -\psi & 1 & \phi \\ \chi & -\phi & 1 \end{bmatrix} \quad (13)$$

On the other hand, in terms of the components of dq , the upper right elements of T_c^a are [8]

$$t_{1,2} = 2dq_1 dq_2 + 2dq_3 dq_4 \quad (14.a)$$

$$t_{1,3} = 2dq_1 dq_3 - 2dq_2 dq_4 \quad (14.b)$$

$$t_{2,3} = 2dq_2 dq_3 + 2dq_1 dq_4 \quad (14.c)$$

The first term on the right hand side of each one of the above equations is of second order and hence is negligible. On the other hand, dq_4 appearing in the second term is the scalar part of dq which we denoted by $d\phi$. As noted earlier this component is nearly equal to one. For these reasons (14) can be approximated as follows

$$t_{1,2} = 2dq_3 \quad (15.a)$$

$$t_{1,3} = -2dq_2 \quad (15.b)$$

$$t_{2,3} = 2dq_1 \quad (15.c)$$

Comparing (15) to the corresponding elements in (13) yields

$$dq_1 = \frac{1}{2}\psi$$

$$dq_2 = \frac{1}{2}\chi$$

$$dq_3 = \frac{1}{2}\varphi$$

The above three components of q constitute the elements of $\underline{\hat{q}}$, thus

$$d\hat{q} = \frac{1}{2} \begin{bmatrix} \varphi \\ \chi \\ \psi \end{bmatrix} \quad (16)$$

and (12.a) can be written as

$$\begin{bmatrix} \dot{\varphi} \\ \dot{\chi} \\ \dot{\psi} \end{bmatrix} = \begin{bmatrix} 0 & \omega_z & -\omega_y \\ -\omega_z & 0 & \omega_x \\ \omega_y & -\omega_x & 0 \end{bmatrix} \begin{bmatrix} \varphi \\ \chi \\ \psi \end{bmatrix} + \begin{bmatrix} d\omega_x \\ d\omega_y \\ d\omega_z \end{bmatrix} \quad (17)$$

Closed-loop attitude determination

In the case of a closed-loop attitude determination, the S/C is maintained at a desired (possibly time-varying) attitude by a closed control loop which uses the gyro outputs to keep track of the S/C angular rate. This is shown in Fig. 3 in which a part of the control loop of a generic attitude control system of a S/C is presented. The purpose of this control loop is to force the S/C to follow a prescribed angular velocity vector, \underline{w}_i , and in particular to maintain a constant attitude when $\underline{w}_i=0$. (Normally the commanded rate \underline{w}_i is a function of the difference between a commanded quaternion and the computed quaternion, q_c). We note from Fig. 3 that

$$\underline{\bar{w}} = \underline{w}_i - \underline{w}_c \quad (18)$$

The control loop is designed to force $\underline{\bar{w}}$ to vanish, then

$$\underline{w}_c = \underline{w}_i \quad (19)$$

and since

$$\underline{w}_c = \underline{w} + d\underline{w} \quad (20)$$

therefore

$$\underline{w}_i = \underline{w} + d\underline{w}$$

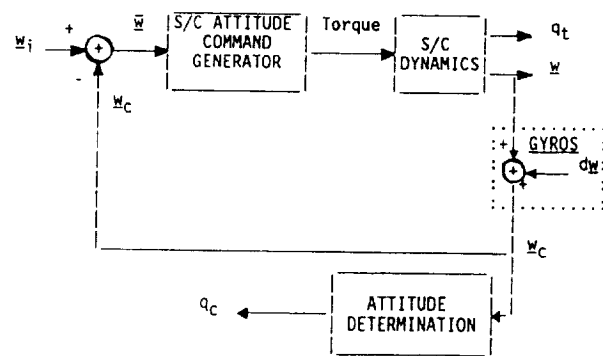


Fig. 3: Generic rate command control loop part of a spacecraft attitude control system

Consequently, \underline{w} , the actual angular rate of the S/C differs from the desired angular rate vector, \underline{w}_i , by the gyro drift rate vector, $d\underline{w}$; that is

$$\underline{w} = \underline{w}_i - d\underline{w} \quad (21)$$

and in particular when $\underline{w}_i = 0$; that is, when the S/C is required to maintain a constant attitude

$$\underline{w} = -d\underline{w} \quad (22)$$

that is; the S/C drifts at the drift rate of the gyros but in a direction opposite to the gyro drift. We conclude from this discussion that \underline{w} differs from the commanded rate by $d\underline{w}$. Consequently the attitude of the S/C differs from the commanded attitude by the attitude error angles $\varphi, \chi,$ and ψ . In this case therefore, the attitude errors develop according to the following equation rather than according to (17)

$$\begin{bmatrix} \dot{\varphi} \\ \dot{\chi} \\ \dot{\psi} \end{bmatrix} = \begin{bmatrix} 0 & \omega_z & -\omega_y \\ -\omega_z & 0 & \omega_x \\ \omega_y & -\omega_x & 0 \end{bmatrix} \begin{bmatrix} \varphi \\ \chi \\ \psi \end{bmatrix} - \begin{bmatrix} d\omega_x \\ d\omega_y \\ d\omega_z \end{bmatrix} \quad (23)$$

Indeed when the commanded angular rate is zero (23) yields

$$\dot{\varphi} = -d\omega_x, \quad \dot{\chi} = -d\omega_y \quad \text{and} \quad \dot{\psi} = -d\omega_z$$

The right most term in (23) is not a white noise vector, therefore this dynamic model, while correct, is not suitable for use in a KF algorithm. To solve this difficulty the standard procedure of "signal shaping" is applied. This is done by considering the non-white vector as an output of a linear system whose input is white [5]. This is accomplished as follows.

The elements $d\omega_x, d\omega_y, d\omega_z$ are the errors in measuring \underline{w} . In other words, they are the errors in the x,y and z gyros respectively. It is assumed that an accurate enough model of the gyro errors is a one where there are five contributions to $d\underline{w}$, which we denote by $\underline{u}_1, \underline{u}_2, d\underline{s}, \underline{w}_\beta$ and \underline{n}_1 ; that is,

$$d\underline{w} = \underline{u}_1 + \underline{u}_2 + d\underline{s} + \underline{w}_\beta + \underline{n}_1 \quad (24.a)$$

where \underline{u}_1 is a vector of constant drift rates of the gyros, \underline{u}_2 is a vector of random walk components of the gyros, $d\underline{s}$ is the vector of gyro scale factor errors and

w_g is the error due to gyro misalignments. Ω_1 is the white noise component of the gyros. Since μ_1 is constant

$$\dot{\mu}_1 = 0 \quad (24.b)$$

and since μ_2 is random walk then we can write

$$\dot{\mu}_2 = \Omega_2 \quad (24.c)$$

where Ω_2 is white noise. Note that despite the notation, Ω_2 does not have the units of angular velocity. Let us denote the vector of scale factor errors by k , then

$$k' = [k_x, k_y, k_z] \quad (24.d)$$

where ' denotes the transpose and k_x, k_y and k_z are the scale factor errors of the x, y and z gyros respectively. The expression for d_s is given by

$$d_s = \begin{bmatrix} w_x & 0 & 0 \\ 0 & w_y & 0 \\ 0 & 0 & w_z \end{bmatrix} k \quad (24.e)$$

Note that since k is a constant

$$\dot{k} = 0 \quad (24.f)$$

The gyro errors due to misalignments are generated by the projection on the gyro input axis of the angular velocity components which are nominally perpendicular to that axis. The misalignment angles are the angles by which the gyro sensitive axis is off from its nominal orthogonal direction towards the other two coordinate axes. Consequently we have

$$w_\beta = \begin{bmatrix} w_{\beta x} \\ w_{\beta y} \\ w_{\beta z} \end{bmatrix} = \begin{bmatrix} w_y & w_z & 0 & 0 & 0 & 0 \\ 0 & 0 & w_z & w_x & 0 & 0 \\ 0 & 0 & 0 & 0 & w_x & w_y \end{bmatrix} \begin{bmatrix} \beta_{xy} \\ \beta_{xz} \\ \beta_{yz} \\ \beta_{yx} \\ \beta_{zx} \\ \beta_{zy} \end{bmatrix} \quad (24.g)$$

where β_{ij} $i=a,y,z$ $j=x,y,z$ is the non-orthogonality angle between the i-th gyro and the j-th axis. Now since β_{ij} is constant we can write

$$\dot{\beta}_{ij} = 0 \quad \begin{matrix} i=x,y,z \\ j=x,y,z \end{matrix} \quad (24.h)$$

The next step in the derivation of the dynamics matrix is the augmentation of the system error model given in (23) with the gyro error model given in (24) [5]. Such an augmented model has, in our case, 27 states. Fortunately, we can eliminate 3 states by combining the constant drift rate components and the random walk components into one error. This will eliminate the possibility of distinguishing between them, but this is of no great consequence since even if we can estimate them separately, we subtract them both from the reading

of the gyro outputs in order to obtain more accurate gyro measurements, therefore the same result is achieved when we estimate their sum. When we combine μ_1 and μ_2 into one state denoted by μ , we may use (24.b) and (24.c) to write the dynamic model of μ

$$\dot{\mu} = \Omega_2 \quad (24.i)$$

In order to augment the models presented in (23) and (24) we define the following matrices

$$\Delta^* = \begin{bmatrix} \psi \\ z \\ \psi \\ u_x \\ u_y \\ u_z \end{bmatrix} \quad A^* = \begin{bmatrix} 0 & w_z & -w_y & -1 & 0 & 0 \\ -w_z & 0 & w_x & 0 & -1 & 0 \\ w_y & -w_x & 0 & 0 & 0 & -1 \\ 0 & 0 & 0 & 0 & 0 & 0 \\ 0 & 0 & 0 & 0 & 0 & 0 \\ 0 & 0 & 0 & 0 & 0 & 0 \end{bmatrix} \quad \dots (25)$$

$$-\Omega^* = \begin{bmatrix} n_{1x} \\ n_{1y} \\ n_{1z} \\ n_{2x} \\ n_{2y} \\ n_{2z} \end{bmatrix} \quad A^{**} = \begin{bmatrix} -w_x & 0 & 0 & -w_y & -w_z & 0 & 0 & 0 & 0 \\ 0 & -w_y & 0 & 0 & 0 & -w_z & -w_x & 0 & 0 \\ 0 & 0 & -w_z & 0 & 0 & 0 & 0 & -w_x & -w_y \\ 0 & 0 & 0 & 0 & 0 & 0 & 0 & 0 & 0 \\ 0 & 0 & 0 & 0 & 0 & 0 & 0 & 0 & 0 \\ 0 & 0 & 0 & 0 & 0 & 0 & 0 & 0 & 0 \end{bmatrix} \quad \dots (26)$$

$$g' = [\beta_{xy}, \beta_{xz}, \beta_{yz}, \beta_{yx}, \beta_{zx}, \beta_{zy}] \quad (27)$$

We may also want to consider the misalignment angles of the two FHSTs and of the FSS, therefore let us denote the vector of the three misalignment angles of the first FHST by 1g , that of the second FHST by 2g and the vector of the FSS misalignment angles by sg where

$$^1g' = [^1\beta_x, ^1\beta_y, ^1\beta_z] \quad (28.a)$$

$$^2g' = [^2\beta_x, ^2\beta_y, ^2\beta_z] \quad (28.b)$$

$$^sg' = [^s\beta_x, ^s\beta_y, ^s\beta_z] \quad (28.c)$$

Since all of these angles are constants we may write

$$^1\dot{g} = 0 \quad ^2\dot{g} = 0 \quad ^s\dot{g} = 0 \quad (29)$$

With the above information and notations we can now write the augmented dynamics equation of the "truth model". The augmented dynamics equation of the "truth model" is given in (30). The validity of (30) can be verified by examining (23) - (29).

$$\frac{d}{dt} \begin{bmatrix} \underline{x}^* \\ k \\ \underline{g} \\ 1g \\ 2g \\ sg \end{bmatrix} = \begin{bmatrix} A^* & A^{**} & 0 & 0 & 0 \\ 0 & 0 & 0 & 0 & 0 \\ 0 & 0 & 0 & 0 & 0 \\ 0 & 0 & 0 & 0 & 0 \\ 0 & 0 & 0 & 0 & 0 \\ 0 & 0 & 0 & 0 & 0 \end{bmatrix} \begin{bmatrix} \underline{x}^* \\ k \\ \underline{g} \\ 1g \\ 2g \\ sg \end{bmatrix} + \begin{bmatrix} n^* \\ 0 \\ 0 \\ 0 \\ 0 \\ 0 \end{bmatrix} \quad (30)$$

Measurement Model

Star tracker measurements

Define a star tracker coordinate system as shown in Fig. 4. The z axis points along the boresight of the star tracker. Consequently the x and y axes are in the image-plane of the star tracker. Denote by \underline{S} the vector in the direction of the star and whose length is the length of the light path from the image-plane to the optics. It is assumed that the light which is emitted from the star towards which the star tracker is pointing, hits the image-plane close to the boresight such that it can be assumed that the distance between the optics and the image plane is nearly equal to that of the light path from the optics to the image-plane, i.e. $h \approx |\underline{S}|$. The signals measured by the tracker are the projections of $-\underline{S}$ on the x and the y axes which, as mentioned, are in the image-plane. The OBC converts the two outputs of the star tracker to tangents of A and B. Obviously, the tangents of A and of B are, respectively, the projections of $-\underline{S}$ on the x and y axes of the tracker, where \underline{S} is a unit vector in the direction of the star. That is, if we denote these axes by \underline{x}_{st} and \underline{y}_{st} respectively, then

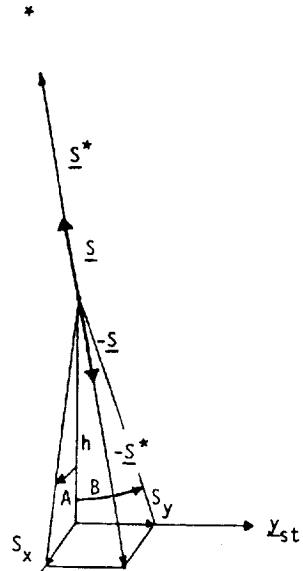


Fig. 4: Schematic diagram of the star tracker measurements

$$x_m = -\underline{S} \cdot \underline{x}_{st} + e_x \quad \dots (31.a)$$

$$y_m = -\underline{S} \cdot \underline{y}_{st} + e_y \quad \dots (31.b)$$

where x_m and y_m are the tangents of A and B, " \cdot " denotes the dot product of vectors and e_x and e_y are measurement noise signals which are assumed to be zero-mean white processes. (Actually, the OBC converts x_m and y_m into components of the unit vector \underline{S} . For small A and B these components are basically equal to the respective tangents). Let us now express the vector quantities of (31) in the EP body coordinate system

$$x_m = -\underline{S}_a \cdot (\underline{x}_{st})_a + e_x \quad (32.a)$$

$$y_m = -\underline{S}_a \cdot (\underline{y}_{st})_a + e_y \quad (32.b)$$

We use an under-bar and a subscript to denote a column matrix whose elements are the components of the vector in question when resolved in the coordinate system denoted by the subscript.

The observables (also known as effective measurements) which are processed by the EKF are the difference between measured and computed quantities. For star tracker measurements we feed the EKF with the difference between the measured components x and y given in (32) and the corresponding computed values which are obtained by transforming the star vector from inertial to body coordinates. The star vector coordinatized in the inertial frame, which we denote by \underline{S}_I , is precisely known from the almanac. We do not know, however, the exact value of T_a^I , the transformation matrix from inertial to body system. All we know is the computed transformation matrix T_c^I . The relationship between the two matrices is given by

$$T_c^I = T_a^I \Theta \quad (33)$$

where T_a^I is the error matrix given in (13). If we define the matrix Θ as follows

$$\Theta = \begin{bmatrix} 0 & \psi & -\psi \\ -\psi & 0 & \psi \\ \psi & -\psi & 0 \end{bmatrix} \quad (34)$$

then

$$T_c^I = I + \Theta \quad (35)$$

We also do not know the exact direction of \underline{x}_{st} and \underline{y}_{st} since the star tracker is misaligned. We only know $\underline{x}_{st,ass}$ and $\underline{y}_{st,ass}$ which are the vectors \underline{x}_{st} and \underline{y}_{st} in the assumed coordinate system of the FHST (that is, in the non misaligned FHST). Consequently, the computed values are calculated in correspondence with (32) as follows

$$x_c = -(T_c^I \underline{S}_I) \cdot (\underline{x}_{st,ass})_a \quad (36.a)$$

$$y_c = -(T_c^I \underline{S}_I) \cdot (\underline{y}_{st,ass})_a \quad (36.b)$$

Using (33) and (35) these two equations become

$$x_c = -[(I+\Theta)T_a^I \underline{S}_I] \cdot (\underline{x}_{st,ass})_a \quad (37.a)$$

$$y_c = -[(I+\Theta)T_a^I \underline{S}_I] \cdot (\underline{y}_{st,ass})_a \quad (37.b)$$

We note that

$$T_a^I \underline{S}_I = \underline{S}_a \quad (38)$$

therefore (37) can be written as

$$x_c = -[\underline{S}_a + \Theta \underline{S}_a] \cdot (\underline{x}_{st,ass})_a \quad (39.a)$$

$$y_c = -[\underline{S}_a + \Theta \underline{S}_a] \cdot (\underline{y}_{st,ass})_a \quad (39.b)$$

When we now difference (32) and (39) the following equations are obtained

$$z_1 = x_m - x_c = -\underline{S}_a \cdot (\underline{x}_{st})_a + e_x + [\underline{S}_a + \Theta \underline{S}_a] \cdot (\underline{x}_{st,ass})_a \quad \dots (40.a)$$

$$z_2 = y_m - y_c = -\underline{S}_a \cdot (\underline{y}_{st})_a + e_y + [\underline{S}_a + \Theta \underline{S}_a] \cdot (\underline{y}_{st,ass})_a \quad \dots (40.b)$$

We note that

$$\underline{x}_{st} = M_a^T, ass \underline{x}_{st, ass} \quad (41.a)$$

$$\underline{y}_{st} = M_a^T, ass \underline{y}_{st, ass} \quad (41.b)$$

where M_a^T, ass is the transformation matrix from the assumed FHST coordinate system to the actual one. In analogy to (35) it can also be shown that

$$M_a^T, ass = I - [\underline{\delta}x] \quad (42)$$

where

$$-[\underline{\delta}x] = \begin{bmatrix} 0 & \delta_z & -\delta_y \\ -\delta_z & 0 & \delta_x \\ \delta_y & -\delta_x & 0 \end{bmatrix} \quad (43)$$

The angles δ_i , $i=x,y,z$ are the misalignment angles of the actual FHST coordinates with respect to the assumed FHST coordinates. Note that because of the closeness of the two, the angles are the same in either coordinates. (See development leading to (56)). When we substitute (42) into (41) we obtain

$$\underline{x}_{st} = (I - [\underline{\delta}x]) \underline{x}_{st, ass} \quad (44.a)$$

$$\underline{y}_{st} = (I - [\underline{\delta}x]) \underline{y}_{st, ass} \quad (44.b)$$

hence

$$\underline{x}_{st} = \underline{x}_{st, ass} - \underline{\delta} \times \underline{x}_{st, ass} \quad (45.a)$$

$$\underline{y}_{st} = \underline{y}_{st, ass} - \underline{\delta} \times \underline{y}_{st, ass} \quad (45.b)$$

When (45) are substituted into (40) the following is obtained

$$z_1 = -\underline{S}_a \cdot (\underline{x}_{st, ass} - \underline{\delta} \times \underline{x}_{st, ass})_a + e_x + [\underline{S}_a + \theta \underline{S}_a] \cdot (\underline{x}_{st, ass})_a$$

$$z_2 = -\underline{S}_a \cdot (\underline{y}_{st, ass} - \underline{\delta} \times \underline{y}_{st, ass})_a + e_y + [\underline{S}_a + \theta \underline{S}_a] \cdot (\underline{y}_{st, ass})_a$$

which, after some multiplications and subtractions, yields

$$z_1 = \underline{S}_a \cdot (\underline{\delta} \times \underline{x}_{st, ass})_a + \theta \underline{S}_a \cdot (\underline{x}_{st, ass})_a + e_x \quad (46.a)$$

$$z_2 = \underline{S}_a \cdot (\underline{\delta} \times \underline{y}_{st, ass})_a + \theta \underline{S}_a \cdot (\underline{y}_{st, ass})_a + e_y \quad (46.b)$$

For (46) to be useful, we need to evaluate \underline{S}_a , $(\underline{x}_{st, ass})_a$ and $(\underline{y}_{st, ass})_a$. As mentioned earlier, \underline{S}_I is known from the almanac, therefore

$$\underline{S}_a = T_a^I \underline{S}_I \quad (47)$$

We do not know T_a^I but we do know T_c^I which, for small attitude errors, is quite close to T_a^I . The replacement of the true value by its estimate is one of the features of an EKF, so, we too, follow this practice, compute

$$\underline{S}_c = T_c^I \underline{S}_I \quad (48)$$

and use \underline{S}_c rather than \underline{S}_a in (46). Next we handle the computation of $(\underline{x}_{st, ass})_a$ and $(\underline{y}_{st, ass})_a$. It is clear that

$$(\underline{x}_{st, ass})_a = M_a^T, ass (\underline{x}_{st, ass})_T, ass \quad (49.a)$$

$$(\underline{y}_{st, ass})_a = M_a^T, ass (\underline{y}_{st, ass})_T, ass \quad (49.b)$$

where T denotes the star tracker coordinate system defined at the beginning of this section and M_a^T, ass

is the transformation matrix from the assumed tracker frame to the body frame. This matrix is known precisely. Let us write

$$M_a^T, ass = [m_1, m_2, m_3] \quad (50)$$

where m_1, m_2 and m_3 are the three columns of M_a^T, ass . It is clear that $(\underline{x}_{st, ass})_T$, the unit vector along the tracker assumed x axis expressed in tracker coordinates, is given by

$$(\underline{x}_{st, ass})_T = \begin{bmatrix} 1 \\ 0 \\ 0 \end{bmatrix} \quad (51.a)$$

and similarly

$$(\underline{y}_{st, ass})_T = \begin{bmatrix} 0 \\ 1 \\ 0 \end{bmatrix} \quad (51.b)$$

Therefore when (50) and (51) are substituted into (49), the following is obtained

$$(\underline{x}_{st, ass})_a = m_1 \quad (52.a)$$

$$(\underline{y}_{st, ass})_a = m_2 \quad (52.b)$$

When (52) is substituted into (46), and when \underline{S}_a is replaced in (46) by \underline{S}_c which is given in (48), the following is obtained

$$z_1 = \underline{S}_c \cdot [(\underline{\delta})_a \times m_1] + \theta \underline{S}_c \cdot m_1 + e_x \quad (53.a)$$

$$z_2 = \underline{S}_c \cdot [(\underline{\delta})_a \times m_2] + \theta \underline{S}_c \cdot m_2 + e_y \quad (53.b)$$

Noting that

$$\theta = -[\underline{Q}_a \times]$$

and using the vector identity

$$(\bar{A} \times \bar{B}) \cdot \bar{C} = (\bar{B} \times \bar{C}) \cdot \bar{A}$$

equations (53) can be written as

$$z_1 = (m_1 \times \underline{S}_c) \cdot \underline{\delta}_a + (m_1 \times \underline{S}_c) \cdot \underline{Q}_a + e_x \quad (54.a)$$

$$z_2 = (m_2 \times \underline{S}_c) \cdot \underline{\delta}_a + (m_2 \times \underline{S}_c) \cdot \underline{Q}_a + e_y \quad (54.b)$$

Expressed by its components $\underline{\delta}$ given as follows

$$\underline{\delta}_a = \begin{bmatrix} \delta_x \\ \delta_y \\ \delta_z \end{bmatrix} \quad (55)$$

however, the angles which constitute the components of $\underline{\delta}_a$ are defined in the FHST coordinate system. Therefore, to keep using the same angles we write $\underline{\delta}_a = M_a^T, ass \underline{\delta}$. But $M_a^T, ass = I - [\underline{\delta}x]$, therefore $M_a^T, ass \underline{\delta} = \underline{\delta} - [\underline{\delta}x]\underline{\delta} = \underline{\delta}$. Consequently,

$$\underline{\delta}_a = \underline{\delta} \quad (56)$$

When (56) is substituted into (54) we obtain

$$z_1 = (m_1 \times \underline{S}_c) \cdot \underline{\delta} + (m_1 \times \underline{S}_c) \cdot \underline{Q}_a + e_x \quad (57.a)$$

$$z_2 = (m_2 \times \underline{S}_c) \cdot \underline{\delta} + (m_2 \times \underline{S}_c) \cdot \underline{Q}_a + e_y \quad (57.b)$$

We can write (57) as follows

$$\begin{bmatrix} z_1 \\ z_2 \end{bmatrix} = \begin{bmatrix} (m_1 \times S_c)' \\ (m_2 \times S_c)' \end{bmatrix} \begin{bmatrix} \psi \\ \nu \\ -\psi \end{bmatrix} + \begin{bmatrix} (m_1 \times S_c)' \\ (m_2 \times S_c)' \end{bmatrix} \begin{bmatrix} \beta_x \\ \beta_y \\ \beta_z \end{bmatrix} + \begin{bmatrix} e_x \\ e_y \\ 0 \end{bmatrix} \quad \dots (58.a)$$

where ' denotes the transpose. This equation is the measurement model of a generic FHST. Each one of the two FHST has such a measurement equation. Writing (58) in terms of the state vector \underline{x} and thus forming the measurement matrix, H , is straight forward. The matrix which corresponds to this measurement equation for the first FHSS is

$${}^1H_F = \begin{bmatrix} (m_1 \times S_c)' \\ (m_2 \times S_c)' \end{bmatrix} \quad 0_{2 \times 12} \quad \begin{bmatrix} (m_1 \times S_c)' \\ (m_2 \times S_c)' \end{bmatrix} \quad 0_{2 \times 6} \quad \dots (58.b)$$

and the matrix for the second FHST is

$${}^2H_F = \begin{bmatrix} (m_1 \times S_c)' \\ (m_2 \times S_c)' \end{bmatrix} \quad 0_{2 \times 15} \quad \begin{bmatrix} (m_1 \times S_c)' \\ (m_2 \times S_c)' \end{bmatrix} \quad 0_{2 \times 3} \quad \dots (58.c)$$

FSS measurement model

The geometry of the FSS measurement is similar to that of the FHST presented in Fig. 4. Here, however, we cannot assume that the angles A and B are small; that is, the Sun vector is not nearly coincidental with the boresight line. Therefore all the developments that were based on this assumption are not valid in the development of the FSS error model. Consequently a different approach has to be taken. It is evident that \underline{s} shown in Fig.4, can be expressed in the FSS coordinates, s , as follows

$$\underline{s}'_s = [-\tan A, -\tan B, 1]d \quad (59.a)$$

$$d = [(\tan A)^2 + (\tan B)^2 + 1]^{-1/2} \quad (59.b)$$

Let $\underline{s}_{s,ass}$ denote a column matrix whose elements are the components of \underline{s} in the assumed (non-misaligned) FSS coordinates. The relationship between this vector and \underline{s}_s is given by

$$\underline{s}_s = G_{s,ass}^s \underline{s}_{s,ass} \quad (60)$$

where $G_{s,ass}^s$ is the transformation matrix from the assumed to the fine Sun sensor coordinates. In analogy to (42) we can write

$$G_{s,ass}^s = I - [{}^s\delta x] \quad (61)$$

where

$$- [{}^s\delta x] = \begin{bmatrix} 0 & s\beta_z & -s\beta_y \\ -s\beta_z & 0 & s\beta_x \\ s\beta_y & -s\beta_x & 0 \end{bmatrix} \quad (62)$$

Substitution of (61) into (60) yields

$$\underline{s}_s = \underline{s}_{s,ass} - [{}^s\delta x] \underline{s}_{s,ass} \quad (63)$$

From (63) we immediately realize that if instead of $\underline{s}_{s,ass}$ we use \underline{s}_s , we introduce an error due to the FSS misalignment. This error is $- [{}^s\delta x] \underline{s}_{s,ass}$.

The FSS outputs are really $(\tan A)_m$ and $(\tan B)_m$ where (see fig.4) $\tan A = S_x/h$ and $\tan B = S_y/h$. The subscript m denotes the measured $\tan A$ and $\tan B$. Define the following column matrix

$$\underline{s}'_{s,m} = [-(\tan A)_m, -(\tan B)_m, 1]d_m \quad (64.a)$$

$$d_m = [(\tan A)_m^2 + (\tan B)_m^2 + 1]^{-1/2} \quad (64.b)$$

Let $u_m = (\tan A)_m$ and $v_m = (\tan B)_m$, then (64) can be written as

$$\underline{s}'_{s,m} = [-u_m, -v_m, 1]d_m \quad (65.a)$$

$$d_m = [u_m^2 + v_m^2 + 1]^{-1/2} \quad (65.b)$$

Furthermore, using Taylor series expansion we can write [9]

$$\underline{s}'_{s,m} = \underline{s}'_s + d\underline{s}'_s \quad (66)$$

where

$$d\underline{s}'_s = \begin{bmatrix} W_{11} & W_{12} \\ W_{21} & W_{22} \\ W_{31} & W_{23} \end{bmatrix} \begin{bmatrix} e_x \\ e_y \end{bmatrix} = W\underline{e} \quad (67)$$

The matrix W is evaluated as follows [9]

$$\begin{aligned} W_{11} &= d_m - d_m^3 u_m^2 & W_{12} &= -d_m^3 u_m v_m \\ W_{21} &= W_{12} & W_{22} &= d_m - d_m^3 v_m^2 \\ W_{31} &= -d_m^3 & W_{32} &= -d_m^3 v_m \end{aligned} \quad (68)$$

and e_x and e_y are the additive measurement errors involved in measuring $\tan A$ and $\tan B$ respectively. From (66) and (67) we obtain

$$\underline{s}'_{s,m} = \underline{s}'_s + W\underline{e} \quad (69)$$

Substitution of (63) into (69) yields

$$\underline{s}'_{s,m} = \underline{s}'_{s,ass} - [{}^s\delta x] \underline{s}'_{s,ass} + W\underline{e} \quad (70)$$

Next we compute the estimate of \underline{s}'_s . We denote the computed value by $\underline{s}'_{s,c}$. The computation is carried out as follows

$$\underline{s}'_{s,c} = G_{s,ass}^a T_c^I \underline{s}'_I \quad (71)$$

In (71) we actually have to use the matrix T_a^I ; however, since this matrix is unknown to us we use T_c^I instead. \underline{s}'_I is taken from the ephemeris. From (33)-(35)

$$T_c^I = (I - [Qx])T_a^I$$

Thus (71) can be written as

$$\underline{s}'_{s,c} = G_{s,ass}^a (I - [Qx])T_a^I \underline{s}'_I$$

which can be written as

$$\underline{s}'_{s,c} = G_{s,ass}^a \underline{s}'_a - G_{s,ass}^a [Qx] \underline{s}'_a$$

where \underline{s}'_a is a column matrix whose elements are the components of \underline{s}'_I when the latter is resolved in the

body, a, coordinate system. Note that since $G_{S,ass}^a$ is orthogonal

$$-G_{S,ass}^a [\theta x] \underline{S}_a = -(G_{S,ass}^s \theta) \times G_{S,ass}^a \underline{S}_a = - (G_{S,ass}^a \theta) \times \underline{S}_{s,as}$$

Using the last equation, we can write the former as

$$\underline{S}_{s,c} = \underline{S}_{a,ass} - (G_{S,ass}^a \theta) \times \underline{S}_{s,ass} \quad (72)$$

Now define the first component of the effective measurement (which is to be processed by the EKF) as follows

$$z_1 = (\underline{S}_{s,m} - \underline{S}_{s,c})_x \quad (73)$$

where $()_x$ denotes the x component of the expression in the brackets. When (70) and (72) are substituted into (73), we obtain

$$z_1 = (\underline{S}_{s,ass} - [S_{\theta} x] \underline{S}_{s,ass} + W_{\theta} - \underline{S}_{a,ass} + (G_{S,ass}^a \theta) \times \underline{S}_{s,ass})_x$$

which yields

$$z_1 = (-[\underline{S}_{s,ass} x] G_{S,ass}^a \theta + \underline{S}_{s,ass} \times S_{\theta} + W_{\theta})_x \quad (74)$$

Following the rationale that led to (56), we can substitute $\underline{S}_{s,ass}$ in (74) by $\underline{S}_{s,m}$ with practically no loss of accuracy. In addition, we use the notation

$$G_{S,ass}^a = [g_1, g_2, g_3] \quad (75)$$

therefore (74) can be written as

$$z_1 = ([-\underline{S}_{s,m} x] [g_1, g_2, g_3] \theta + \underline{S}_{s,m} \times S_{\theta} + W_{\theta})_x \quad (76.a)$$

To compute z_2 we apply the foregoing development but now we use the y rather than the x component. This will yield a result similar to (76.a); namely,

$$z_2 = ([-\underline{S}_{s,m} x] [g_1, g_2, g_3] \theta + \underline{S}_{s,m} \times S_{\theta} + W_{\theta})_y \quad (76.b)$$

The last two equations can be put in the following form

$$\begin{bmatrix} z_1 \\ z_2 \end{bmatrix} = \begin{bmatrix} g_1 x \underline{S}_{s,m} & g_2 x \underline{S}_{s,m} & g_3 x \underline{S}_{s,m} \\ -2 & & \end{bmatrix} \begin{bmatrix} \varphi \\ \alpha \\ \psi \end{bmatrix} + \begin{bmatrix} S_{\theta} x \\ S_{\theta} y \\ S_{\theta} z \end{bmatrix} + W_2 \begin{bmatrix} e_x \\ e_y \\ 0 \end{bmatrix}$$

... (77.a)

where the subscript 2 denotes the first two rows of a matrix. The measurement matrix, H_s which corresponds to this measurement equation is given by

$$H_s = \begin{bmatrix} g_1 x \underline{S}_{s,m} & g_2 x \underline{S}_{s,m} & g_3 x \underline{S}_{s,m} & 0_{3 \times 24} & [S_{\theta} x] \\ -2 & & & & -2 \end{bmatrix} \quad (77.b)$$

Note that the 3rd row of the square matrices in (77) is omitted. This completes the development of the "truth model". To sum it up, the dynamics model is given by (30), the FHST measurement model is given by (58) and it fits either one of the two FHSTs, and finally, the measurement model of the FSS is given by (77).

2.3. THE DESIGN MODEL

Error Propagation Model

The "design model" is the simplified, reduced order model which is assumed to be the model of the system for the OBC filter design purposes. The following assumptions are made in the design of the EUVE Update Filter. The gyro scale factor errors and misalignments are negligible (or fully compensated for). The FHSTs and the FSS are perfectly aligned. With these assumptions the error propagation equation of the "truth model" reduces to

$$\begin{bmatrix} \dot{\varphi} \\ \dot{\alpha} \\ \dot{\psi} \\ \dot{u}_x \\ \dot{u}_y \\ \dot{u}_z \end{bmatrix} = \begin{bmatrix} 0 & w_z & -w_y & -1 & 0 & 0 \\ -w_z & 0 & w_x & 0 & -1 & 0 \\ w_y & -w_x & 0 & 0 & 0 & -1 \\ 0 & 0 & 0 & 0 & 0 & 0 \\ 0 & 0 & 0 & 0 & 0 & 0 \\ 0 & 0 & 0 & 0 & 0 & 0 \end{bmatrix} \begin{bmatrix} \varphi \\ \alpha \\ \psi \\ u_x \\ u_y \\ u_z \end{bmatrix} + \begin{bmatrix} w_{1x} \\ w_{1y} \\ w_{1z} \\ w_{2x} \\ w_{2y} \\ w_{2z} \end{bmatrix} \quad (78)$$

This model can be expressed as

$$\dot{\underline{x}}^* = A^* \underline{x}^* + \underline{n}^* \quad (79)$$

where \underline{x}^* , A^* and \underline{n}^* are defined in (25).

Measurement Model

Star tracker measurements

With the assumption mentioned before and corresponding to the "design model" of (78), The FHST measurement matrix of either star tracker reduces to

$$\begin{bmatrix} z_1 \\ z_2 \end{bmatrix} = \begin{bmatrix} (m_1 \times \underline{S}_c)^T \\ (m_2 \times \underline{S}_c)^T \end{bmatrix} \begin{bmatrix} \varphi \\ \alpha \\ \psi \end{bmatrix} + \begin{bmatrix} e_x \\ e_y \\ 0 \end{bmatrix} \quad (80.a)$$

This yields the following measurement matrix

$$H_F^* = \begin{bmatrix} (m_1 \times \underline{S}_c)^T \\ (m_2 \times \underline{S}_c)^T \end{bmatrix} \quad 0_{2 \times 3} \quad (80.b)$$

It is easily seen that this is the measurement matrix for either FHST.

Sun sensor measurements

Corresponding to the state vector of the "design model" the FSS measurement equation is reduced to

$$\begin{bmatrix} z_1 \\ z_2 \end{bmatrix} = \begin{bmatrix} g_1 \times S_{s,m} & g_2 \times S_{s,m} & g_3 \times S_{s,m} \\ \vdots & \vdots & \vdots \end{bmatrix}_2 \begin{bmatrix} \psi \\ \psi \\ \psi \end{bmatrix} + W_2 \begin{bmatrix} e_x \\ e_y \end{bmatrix}$$

... (81.a)

The corresponding measurement matrix is

$$H_s^* = \begin{bmatrix} g_1 \times S_{s,m} & g_2 \times S_{s,m} & g_3 \times S_{s,m} & 0_{3 \times 3} \end{bmatrix}_2 \quad (81.b)$$

3.0 TRUE COVARIANCE SIMULATION ALGORITHM

To present the so-called "true covariance" simulation algorithm whose development is introduced in [6], we have to define, D, the transformation matrix from the state vector of the "truth model" to that of the "design model". It is easy to see that in our case

$$D = [I_{6 \times 6} \quad 0_{6 \times 18}] \quad (82)$$

Using D we define the following matrices

$$dA = DA - A^*D \quad (83.a)$$

where A is the 24x24 matrix defined in (30). The matrixes A, A* and dA are then used to define A^C as follows

$$A^C = \begin{bmatrix} A & 0 \\ \dots & \dots \\ dA & A^* \end{bmatrix} \quad (83.b)$$

Next, we discretize the matrices A^C and Q* where the latter is the spectral density matrix of the white noise vector driving the dynamics part of the "design model" given in (78). The discretization algorithm is given in [5, pp. 296 - 299]. The discretization is denoted as follows

$$\begin{aligned} A^C &\text{---} \rightarrow \delta_k^C \\ Q^* &\text{---} \rightarrow Q_{k-1}^* \end{aligned}$$

With Q_{k-1}^{*} on hand, we compute Q_{k-1}^C as follows

$$Q_{k-1}^C = \begin{bmatrix} I \\ \dots \\ D \end{bmatrix} Q_{k-1}^* \begin{bmatrix} I & D^T \end{bmatrix} \quad (84)$$

In our case, all the preceding matrices are constant and need to be computed only once.

Between measurement updates we propagate the matrices C_k and P_k as follows

$$C_k(-) = \delta_{k-1}^C C_{k-1} \delta_{k-1}^{C'} + Q_{k-1}^C \quad (85.a)$$

$$P_k^*(-) = \delta_{k-1}^* P_{k-1}^*(+) \delta_{k-1}^{*'} + Q_{k-1}^* \quad (85.b)$$

where C_k is the second moment matrix of the augmented state vector whose entries are, from top to bottom, the state vector of the "truth model" given in (30), and a vector which is the difference between the state estimate generated by the OBC EKF and the correct value of this state. Note that the second vector, which has 6 components, is the correct estimation error vector. Therefore the last 6 elements on the main diagonal of C_k are the mean square errors of the filter estimation error and their evaluation is the goal of the "true covariance" analysis. In contrast to these 6 elements,

the 6 elements on the main diagonal of P_k^{*} are the apparent variances of the estimation error states. That is, if the "truth model" were identical to the "design model", these elements would have been the variances of the estimation error.

When a measurement is acquired, the following computations are carried out

$$K_k^* = P_k^*(-) H_k^{*'} [H_k^{*'} P_k^*(-) H_k^{*'} + R_k^*]^{-1} \quad (86.a)$$

$$P_k^*(+) = [I - K_k^* H_k^{*'}] P_k^*(-) [I - K_k^* H_k^{*'}]' + K_k^* R_k^* K_k^{*'} \quad (86.b)$$

$$dH_k = H_k - H_k^* D \quad (86.c)$$

$$B_k = \begin{bmatrix} I & 0 \\ \dots & \dots \\ -K_k^* dH_k & I - K_k^* H_k^{*'} \end{bmatrix} \quad (86.d)$$

$$C_k(+) = B_k C_k(-) B_k' + K_k^C R_k K_k^{C'} \quad (86.e)$$

4.0 CASE STUDY OBJECTIVES AND RESULTS

There were three primary objectives in the case studies. First, the performance of the EP filter was examined in the ideal situation when its model was equivalent to the truth model. Secondly, the expected onorbit behavior of the filter was examined. Lastly, a sensitivity analysis was performed. The cases studied were as follows:

- Case 1: No Errors
- Case 2: Expected Errors
- Case 3: Sensitivity Analysis
 - 3A: Gyro white noise about each axis
 - 3B: Gyro random walk about each axis
 - 3C: Gyro Misalignments about each axis
 - 3D: Gyro Scale factor errors about each axis
 - 3E: FHST noise
 - 3F: FHST # 2 misalignments about each axis
 - 3G: FSS noise
 - 3H: FSS misalignments about each axis

Each simulation was ten minutes. The attitude and gyro drift estimation errors were determined by the truth model and update filter. The results in sections 4.1, 4.2, and 4.3 represent the truth model determined estimation errors. The following is a listing of nominal simulation input values:

Initial State Variances

Initial Attitude Error: 1800 arcsec/axis
Initial Drift Rate Bias: 0.5 arcsec/sec/axis

Dynamic Noise Inputs

IRU White Noise drift (roll): (0.68936 arcsec/sec^{1/2})²
(pitch and yaw axes): (4.246E-2 arcsec/sec^{1/2})²
IRU Random Walk Drift: (4.4413E-5 arcsec/sec^{3/2})²/axis

Measurement Noise Input

FHST Measurement Noise Variances: (14 arcsec)²
FSS Measurement Noise Variances: (24.4131 arcsec)²

4.1 Case 1: No errors

The following case demonstrates the performance of the filter in the ideal case when the truth model was identical to the design model. The final attitude and gyro drift errors were as follows:

Attitude Estimation Errors (arcseconds)			3C	x	16.5005	19.1984	13.0119
Roll	Pitch	Yaw	3C	y	16.5005	19.1984	13.0119
4.8784	2.8321	2.5080	3C	z	16.5005	19.1984	13.0119
Gyro Drift Estimation Errors (arcseconds/second)			3D	x	16.5005	19.1984	13.0119
Roll	Pitch	Yaw	3D	y	16.5005	19.1984	13.0119
3.022E-2	0.9103E-2	8.313E-3	3D	z	16.5005	19.1984	13.0119
			3E		19.1600	25.7578	18.0298
			3F	x	27.2160	29.6328	15.9332
			3F	y	22.3209	25.5485	13.0534
			3F	z	17.3819	19.3448	21.7191
			3G		16.9075	18.9557	13.0284
			3H	x	16.7568	24.9939	13.1199
			3H	y	16.8615	19.8543	16.3459
			3H	z	16.5005	19.1984	13.0119

4.2 Case 2: Expected Errors

This case demonstrates the expected performance of the filter on orbit. The attitude is defined relative to one of the FHSTs (#1 in our simulations). Thus, the obtained attitude accuracy is on the order of the accuracy of the FHSTs which are the primary attitude sensor. The following are additional expected on orbit input errors:

- FHST #1 Misalignment: 0 arcseconds/axis
- FHST #2 Misalignment: 24 arcseconds/axis
- FSS Misalignment: 36 arcseconds/axis
- Gyro Scale Factor Error: 1000 ppm/axis
- Gyro Misalignment: 8 arcseconds/axis

The results are the following:

Attitude Estimation Errors (arcseconds)		
Roll	Pitch	Yaw
16.5005	19.1984	13.0119
Gyro Drift Estimation Errors (arcseconds/second)		
Roll	Pitch	Yaw
3.2513E-2	5.1160E-2	6.9354E-2

Comparing these values to the ideal case, one can see errors induced by only considering a subset of the true state vector in state estimation. The attitude estimation errors are off by several orders of magnitude and the gyro drift estimation errors are off almost an order of magnitude.

4.3 Case 3: Sensitivity Analysis

In the following simulations, the sensitivity of onboard filter to additional attitude sensor noises, misalignments, and scale factor errors was tested. These errors were applied separately to each sensor axis, and the resulting attitude and gyro drift estimation errors were observed. Sensitivity to the various error sources were determined in the following manner about each spacecraft axis (where applicable):

- Dynamic noise (white & random walk): 3x nominal/axis
- FHST #2 Misalignments: 2x nominal/axis
- FSS Misalignments: 2x nominal/axis
- Measurement noise (FHSTs & FSS): 2x nominal

The following tables and figures demonstrate the filter performance due to the increased errors.

Attitude Estimation Errors (arcseconds)				
Case	Axis	Roll	Pitch	Yaw
3A	x	18.6886	19.1984	13.0119
3A	y	16.5006	19.2332	13.0179
3A	z	16.5005	19.2065	13.0435
3B	x	16.5007	19.1984	13.0119
3B	y	16.5005	19.1994	13.0121
3B	z	16.5005	19.1987	13.0125

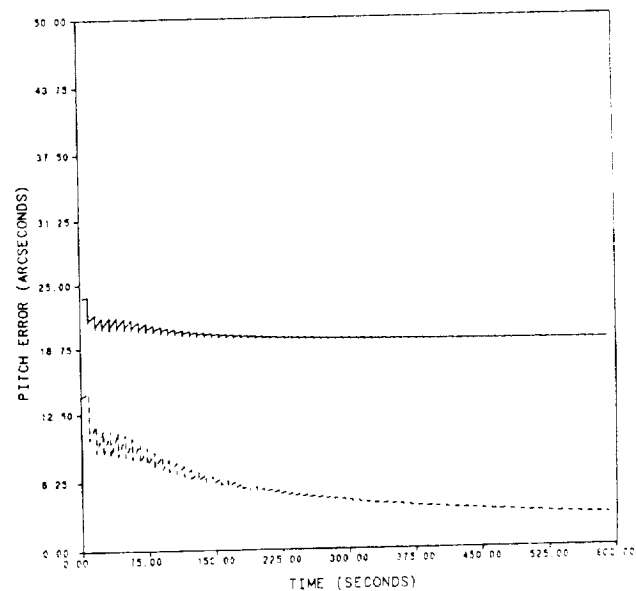


Fig. 5: The standard deviation of the pitch estimation error vs. time. (The solid line is that of the true error, and the dashed line is of the error predicted by the update filter covariance matrix.)

The time history of the standard deviations of the attitude and gyro drift estimation errors was plotted for Case 2 (expected onorbit errors). The results about each axis were found to be similar. A typical plot (pitch attitude error) is presented in Fig. 5.

Gyro Drift Estimation Errors (arcseconds/second)

Case	Axis	Roll	Pitch	Yaw
3A	x	8.7164E-2	5.1160E-2	6.9354E-2
3A	y	3.2513E-2	5.1451E-2	6.9364E-2
3A	z	3.2513E-2	5.1202E-2	6.9566E-2
3B	x	3.2564E-2	5.1160E-2	6.9354E-2
3B	y	3.2513E-2	5.1197E-2	6.9355E-2
3B	z	3.2513E-2	5.1161E-2	6.9378E-2

3C	x	3.2513E-2	5.1160E-2	6.9354E-2
3C	y	3.2513E-2	6.8993E-2	6.9354E-2
3C	z	3.2513E-2	5.1160E-2	8.3385E-2
3D	x	3.8577E-2	5.1160E-2	6.9354E-2
3D	y	3.2513E-2	5.1160E-2	6.9354E-2
3D	z	3.2513E-2	5.1160E-2	6.9354E-2
3E		3.5639E-2	6.5980E-2	8.9894E-2
3F	x	3.2513E-2	5.9675E-2	10.2473E-2
3F	y	3.2513E-2	5.1277E-2	8.9347E-2
3F	z	3.2513E-2	7.7423E-2	6.9809E-2

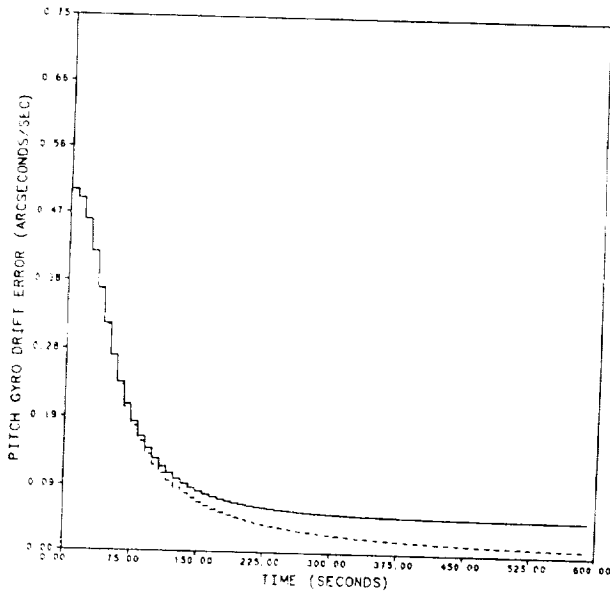


Fig. 6: The standard deviation of the pitch gyro drift estimation error vs. time. (The solid line is that of the true error, and the dashed is of the error predicted by the update filter covariance matrix.)

3G		3.2543E-2	5.1259E-2	6.8545E-2
3H	x	3.2513E-2	5.1467E-2	8.7576E-2
3H	y	3.2513E-2	6.0912E-2	7.1389E-2
3H	z	3.2513E-2	5.1160E-2	6.9354E-2

A typical plot for gyro drift error is presented in Fig. 6.

Of the gyro noises, the white noise component had the most effect on the filter performance. As expected, the effect was confined primarily to the axis being corrupted. When the X-axis gyro white noise was increased by 3x, the roll gyro drift estimation error jumped 5.0E-2 arcseconds/second, and the roll estimation errors jumped approximately 2 arcseconds. The effect of an increase in pitch and yaw gyro white noise had a very nominal effect on estimation errors. Since EUVE has a roll rate of 3 RPO, the roll gyro has to use less accurate gyro data as compared to the pitch and yaw axes which are approximately inertial. This inaccuracy in roll gyro data is modeled by an increase in the white noise component in the roll gyro data. Thus, an increase in the white noise about the roll axis affects the attitude much more significantly than an increase about the pitch and yaw axes. The gyro misalignments about the pitch and yaw axes corrupted

their respective drift estimates significantly due to their projections picking up the relatively high roll rate. The roll axis misalignments have no effect due to zero yaw and pitch rates. The gyro scale factors only showed up in the roll gyro drift estimation error due to the above mentioned high relative roll rate and 0 pitch and yaw rates. The FHST #2 misalignments were the largest contributor to attitude and gyro drift estimation errors as expected with the FHST X-axis misalignment causing roll and pitch errors of 27.2 and 29.6 arcseconds. The FHST Z-axis caused a yaw error of 21.7 arcseconds. The FSS misalignments affect on the attitude and gyro drift estimation errors were significant but not as significant as the FHSTs due to the larger sensor noise variance. The FSS X-axis misalignment translated into a pitch error of 24.9 arcseconds while a Y-axis misalignment caused roll and yaw attitude errors of 16.8 and 16.3 arcseconds respectively. The FHST measurement noise increases affected the attitude estimation errors almost as much as the FHST misalignments with roll, pitch, and yaw errors of 19.1, 25.7, and 18.0 arcseconds respectively. An increase in FSS measurement noise had a relatively small effect on estimation errors. The resulting roll, pitch, and yaw attitude errors were 16.9, 18.9, and 13.0 arcseconds respectively. The pitch attitude estimation error went down slightly as compared to the nominal simulation, and the roll and yaw attitude errors increased slightly. The reason the attitude estimation errors were affected so little as compared to the increased FHST noise simulation was due to the filter weighting the more accurate FHST measurements heavier than the less accurate FSS measurements.

5.0 CONCLUSIONS

Of all the errors, the FHST misalignments proved to cause the most significant attitude and gyro drift estimation errors. The roll and pitch estimation errors increased by approximately 10 arcseconds from the nominal estimation errors when the X-axis misalignment of FHST #2 was doubled to 48 arcseconds. Doubling the Z-axis misalignment of FHST #2 increased the yaw estimation errors by approximately 8 arcseconds. The pitch and yaw gyro drift estimation errors were affected most by Z and Y - axis misalignments of FHST #2. An increase in the white noise about the gyro X-axis was responsible for the largest roll gyro drift estimation error. The gyro drift estimation errors only affects the system when measurement update periods are large. EUVE should have a sufficient number of star measurement updates from the FHSTs. If not, the attitude estimation accuracy could degrade significantly. Overall, the results showed the EUVE update filter to be quite robust even though some significant errors were put into the system. This study demonstrated the six states modeled in the filter are the most significant states needed for onboard attitude estimation.

Appendix

Express the two quaternions q_1 and q_2 as follows

$$q_1 = \begin{bmatrix} r_1 \\ \dots \\ p_1 \end{bmatrix} \quad \text{and} \quad q_2 = \begin{bmatrix} r_2 \\ \dots \\ p_2 \end{bmatrix}$$

where r_1, r_2 are the vector parts of the respective quaternions and p_1, p_2 are their scalar parts. Then

$$q_1 q_2 = \begin{bmatrix} r_1 x r_2 + p_1 e_2 + p_2 e_1 \\ \dots\dots\dots \\ p_1 p_2 - r_1 e_2 \end{bmatrix}$$

The upper part of the column yields three components which are the components of the imaginary part of the quaternion product and the lower part yields the scalar part of the product.

References

1. K. Ha, "EP Update Filter Analysis", Fairchild Space Company, Inter-Office Communication, ACS:EP:035, August 17, 1987.
2. K. Ha, "EP Update Filter Development", Fairchild Space Company, Inter-Office Communication, ACS:EP:88:014, February 9, 1988.
3. M. Frieder, "Gyro Model for Kalman Filter Simulation", Fairchild Space Company, Inter - Office Communication, ACS:EP:87:019, June 11, 1987.
4. M. Frieder, "Star Tracker Model for Kalman Filter Simulation", Fairchild Space Company, Inter - Office Communication, ACS:EP:028, July 17, 1978.
5. A. Gelb, Applied Optimal Estimation, MIT Press, Cambridge MA, 1974.
6. I. Y. Bar-Itzhack, Seminar notes on True Covariance Analysis, Code 554, NASA-GSFC, Oct. 12, 88, p.29.
7. J. C. Wilcox, "A New Algorithm for Strapped-Down Inertial Navigation", IEEE Trans. on Aerosp. and Elect. Syst., Vol. AES-5, Sept. 67, pp.796-802.
8. J. R. Wertz (ed.) Spacecraft Attitude Determination and Control, D. Reidel Publishing Company, Boston, MA, 1978, p. 414.
9. J. Deutschmann and I.Y. Bar-Itzhack, "Extended Kalman Filter for Attitude Estimation of the Earth Radiation Budget Satellite," Flight Mechanics/Estimation Theory Symposium, NASA Goddard Space Flight Center, 23-24 May, 1989.

A GYROSCOPE CALIBRATION ANALYSIS FOR THE GAMMA RAY OBSERVATORY (GRO)*

Eleanor A. Ketchum
Goddard Space Flight Center (GSFC)

Michael H. Lee
Computer Sciences Corporation (CSC)

ABSTRACT

The attitude analysts of the Flight Dynamics Division (FDD) are responsible for calibrating, among other sensors, inertial reference units (IRU), a crucial activity for accurate attitude determination. The IRU calibration utility (IRUCAL) for the Gamma Ray Observatory (GRO) spacecraft, based on an algorithm developed by P. Davenport, includes user-specified weighting matrices for the measurements, for the a priori misalignments, and for the a priori biases. By assigning "large" values to the appropriate a priori weighting matrix elements, one can choose to adjust only the biases, only the misalignments, or some combination of the two. Different weight matrices produce vastly different biases and misalignments for the same measurement.

Current documentation and software do not adequately address the calculation and use of the optimal weight matrices involved in calibrating the IRU. This study investigates several facets of the GRO IRU calibration as it relates to the bias and misalignment weighting matrices. The physical meaning and use of the bias and misalignment weight matrices in IRU calibration are examined. The relation of the weighting and the final biases, misalignments, and their corrections are pursued.

Ultimately, methods for determining reliable, realistic weighting matrices to be used in the GRO IRUCAL utility are determined. Possible correlations among observation uncertainties are also explored. For the undetermined case where the maneuvers are insufficient to identify all calibration parameters, the weighting matrices allow as much information as possible to be extracted from the measurements. Finally, applicable simulated flight data are used, incorporating the appropriate calibration maneuvers, to test the weighting matrices in the IRUCAL utility, and examine correlation effects.

*This work was supported by the National Aeronautics and Space Administration (NASA)/Goddard Space Flight Center (GSFC), Greenbelt, Maryland, under Contract NAS 5-31500.

1. INTRODUCTION

The gyro calibration process contains many subtleties. Data can be used and interpreted several ways; identical data can be processed through the same software yet could achieve vastly different calibration results. A paper in the May 1988 Flight Mechanics and Estimation Theory Symposium (Reference 1) investigates the gyroscope calibration for the Hubble Space Telescope, using the same algorithm as the Gamma Ray Observatory (GRO) software. Last year's paper, by Davenport and Welter, examines the selection of the loss function weight matrix when more accurate attitude sensor information is available in pitch and yaw than roll; the study, however, ignores the use of a priori information, assigning a zero weight to that term in the loss equation. The GRO mission will not encounter such situations during normal operations but could benefit from incorporating a priori information into the gyro calibration effort. This paper examines the careful use of a priori gyro information and covariance in calibration for the GRO mission and also considers any implications for future missions.

The GRO mission will employ an inertial reference unit (IRU) consisting of three two-degree-of-freedom gyros built by Teledyne Systems Company. This National Aeronautics and Space Administration (NASA) standard IRU, DRIRU-II, has flown successfully on several missions, including the Solar Maximum Mission (SMM). Each gyro in the IRU contains two orthogonal sensing axes and are oriented to provide redundant sensing about each of these axes. References 2 and 3 contain a more detailed description of the IRU.

The general method that the Flight Dynamics Facility (FDF) will use to calibrate the IRU from the ground comes from the algorithm used by SMM. A period of fixed-inertial attitude will be followed by an attitude maneuver. A period of constant attitude will then follow the maneuver. An attitude solution will be determined using fixed-head star tracker (FHST) data for both periods of fixed attitude. Gyro data are collected and compared to the attitude solution generated by the FHSTs. Biases, misalignments, and scale factors can then be determined. The basic mathematics for gyro calibration is presented first as background for the reader. Further documentation is referenced for a more thorough discussion.

The search for a priori information begins with past missions. To anticipate the kinds of biases and misalignments GRO's IRU might experience during launch, past missions that used and calibrated the DRIRU-II in flight were examined. Unfortunately, Landsat did not fully calibrate its DRIRU-II because of the nature of the mission. SMM, however, used a calibration scheme similar to GRO's; the information from SMM's early mission could, therefore, be applied to the GRO effort. Unfortunately, some information is not available from the SMM calibration effort, so workarounds were developed where possible. A complete plan is, therefore, offered in Section 7 of this study so that all information will be available from GRO's early mission. These data can be analyzed for future launches to help establish appropriate a priori information to be incorporated into IRU calibration efforts for future missions.

During the GRO mission, flight dynamics analysts will be using the IRUCAL utility (part of the GRO Attitude Ground Support System (AGSS)) to process gyro data and calibrate

the IRU. In this utility, the user is given the option of including a priori information. The user is also allowed to weigh this information as he/she chooses. IRUCAL is sensitive to these weights, as identical information weighted differently results in dissimilar calibration results. Section 6 of this study explores this sensitivity by performing simulations. The dynamic simulator will create gyro data that will be processed through the AGSS. These processed data will then be put through simulations involving the IRUCAL, including different a priori estimates and weights. Different weighting schemes will be incorporated, noting the sensitivity of the results to weighting changes.

The final portion of this study presents conclusions and recommendations. Unfortunately, little is documented concerning past use of the DRIRU-II and in-flight calibration as far as actual early mission data. Some data could, however, be deduced and incorporated into the GRO IRU calibration effort. The study furnishes a detailed list and schedule of early calibration activities. During GRO's launch it will prove crucial to keep track of various information not only to test out new a priori weighting schemes but to provide critical information for missions still in the planning stages.

2. GRO GYRO CALIBRATION ALGORITHM

This discussion of the GRO gyro calibration algorithm closely follows Reference 1, and an alternate derivation can be found in Reference 4. The calibration algorithm for GRO assumes that a three-vector \mathbf{R} is output from the gyros, and the measured angular velocity is given by

$$\Omega_M = G_0 \mathbf{R} - \mathbf{D}_0 \quad (1)$$

where G_0 is the 3-by-3 scale factor/alignment matrix and \mathbf{D}_0 is the drift-rate bias. The algorithm determines a correction matrix \mathbf{M} to G_0 and a correction to the bias, \mathbf{d} . Ideally, the true angular rate Ω is found using the corrected alignment matrix \mathbf{G} and bias \mathbf{D} via the following equations:

$$\mathbf{G} = \mathbf{M} G_0 \quad (2a)$$

$$\mathbf{D} = \mathbf{M} \mathbf{D}_0 + \mathbf{d} \quad (2b)$$

$$\Omega = \mathbf{G} \mathbf{R} - \mathbf{D} = \mathbf{M} \Omega_M - \mathbf{d} \quad (2c)$$

Let $\mathbf{m} = \mathbf{M} - \mathbf{I}$, for \mathbf{I} the 3-by-3 identity matrix and define the difference between the measured and true angular rate ω by

$$\omega = \Omega_M - \Omega = -\mathbf{m} \Omega_M + \mathbf{d} \quad (3)$$

The elements of \mathbf{m} and \mathbf{d} are the parameters solved for in the calibration algorithm. These parameters can be related to attitude solutions as determined through data from sensors such as star trackers if gyro output data are available between attitude solutions.

Again following Reference 1, let attitude solutions at time t be denoted by $Q(t)$ in quaternion form. The quaternion time derivative is given by

$$Q'(t) = Q(t) q(\Omega/2) \quad (4)$$

where $q(\Omega/2)$ is a quaternion with vector component $\Omega/2$ and scalar component zero. Let Q be the quaternion representing the true rotation for a maneuver and Q_M be the quaternion representing the rotation as determined by the gyro output. The attitude error quaternion δQ expressing the rotation from the gyro-determined postmaneuver attitude to the true postmaneuver attitude is given by

$$\delta Q = Q_M (Q_M^{-1} Q) Q_M^{-1} = Q Q_M^{-1} \quad (5)$$

Applying the chain rule of differentiation to Equation (5) above gives

$$\delta Q' = Q q(\Omega/2) Q_M^{-1} + Q q^{-1}(\Omega_M/2) Q_M^{-1} \quad (6)$$

Noting that

$$q^{-1}(\Omega_M/2) = q(-\Omega_M/2)$$

and using Equation (3) results in

$$\delta Q' = Q q(-\omega/2) Q_M^{-1} \quad (7)$$

Integrating Equation (7) over the maneuver gives

$$\delta Q - 1 = \int Q q(-\omega/2) Q_M^{-1} dt \quad (8)$$

where 1 , the identity quaternion, is the constant of integration. Let Q_{R1} and Q_{R2} be the reference quaternions at the beginning and end of the maneuver (for GRO, these come from the Fine Attitude Determination System (FADS)) so that

$$Q = Q_{R1}^{-1} Q_{R2}$$

Similarly, define the gyro propagated quaternions Q_{G1} and Q_{G2} so that

$$Q_M = Q_{G1}^{-1} Q_{G2}$$

Equation (8) then becomes

$$(Q_{R1}^{-1} Q_{R2}) (Q_{G2}^{-1} Q_{G1}) - 1 = \int Q q(-\omega/2) Q_M^{-1} dt \quad (9)$$

The first order, Q can be replaced by Q_M in Equation (9). When this substitution is made, the integrand becomes the quaternion representation for the rotation of the vector $-\omega/2$ from the spacecraft coordinates at time t to the premaneuver spacecraft coordinates. Dropping the scalar portion of Equation (9) and substituting for Q gives

$$Z_i = \frac{1}{2} \int T_i \omega dt \quad (10)$$

where Z_i is the vector component of δQ , T_i is the (time-dependent) matrix transforming vectors to premaneuver spacecraft coordinates, and i is a subscript designating maneuver number. By dropping the scalar part of Equation (9), an approximation is made equating 1 to the cosine of the error rotation angle. Because of these approximations, the calibration algorithm is by nature an iterative process.

Least-squares techniques can be applied to Equation (10). Rewrite Equation (10) as

$$Z = H x \quad (11)$$

where Z is composed of the (assumed) n Z_i vectors for n maneuvers, and x is defined as shown below:

$$Z = \{Z_1^T, Z_2^T, \dots, Z_n^T\}^T \quad (12a)$$

$$x = \{m_{11}, m_{12}, m_{13}, m_{21}, m_{22}, m_{23}, m_{31}, m_{32}, m_{33}, d_1, d_2, d_3\} \quad (12b)$$

H is a $3n$ -by- 12 matrix of the form

$$H = \begin{bmatrix} U_1 & -Y_1 \\ \vdots & \vdots \\ U_n & -Y_n \end{bmatrix} \quad (13)$$

where each U_1 is a 3-by-9 matrix with components given by

$$(U_{j,k+3(i-1)})_1 = \frac{1}{2} \int (T_{jk})_1 (\Omega_M)_1 dt \quad (14)$$

and each Y_1 is a 3-by-3 matrix given by

$$(Y_{jk})_1 = \frac{1}{2} \int (T_{jk})_1 dt \quad (15)$$

An observed value for Z derived from combination of Q 's from the GRO FADS and the gyro's and is assumed to be of the form

$$Z_{obs} = H x_t + v \quad (16)$$

where \mathbf{x}_t contains the true bias and alignment parameters and \mathbf{v} is the measurement error in \mathbf{Z}_{obs} . The loss function J for the least-squares solution is chosen to be

$$J = \frac{1}{2} \{ \mathbf{E}^T \mathbf{W} \mathbf{E} + (\mathbf{x} - \mathbf{x}_a)^T \mathbf{S}_a (\mathbf{x} - \mathbf{x}_a) \} \quad (17)$$

where

$$\mathbf{E} = \mathbf{Z}_{\text{obs}} - \mathbf{H} \mathbf{x} \quad (18)$$

\mathbf{W} and \mathbf{S}_a are symmetric nonnegative definite weighting matrices, and \mathbf{x}_a is an a priori estimate of \mathbf{x} . \mathbf{x}^* , the least-squares solution for \mathbf{x} , is given by setting the derivative of the loss function with respect to \mathbf{x} equal to zero,

$$0 = \mathbf{H}^T \mathbf{W} [\mathbf{Z}_{\text{obs}} - \mathbf{H} \mathbf{x}^*] - \mathbf{S}_a [\mathbf{x}^* - \mathbf{x}_a] \quad (19)$$

or

$$\mathbf{x}^* = \{ \mathbf{H}^T \mathbf{W} \mathbf{H} + \mathbf{S}_a \}^{-1} [\mathbf{H}^T \mathbf{W} \mathbf{Z}_{\text{obs}} + \mathbf{S}_a \mathbf{x}_a] \quad (20)$$

Define

$$\delta \mathbf{x} = \mathbf{x}_t - \mathbf{x}^*$$

and substitute Equation (16) into Equation (19) to give

$$\delta \mathbf{x} = \{ \mathbf{H}^T \mathbf{W} \mathbf{H} + \mathbf{S}_a \}^{-1} [\mathbf{H}^T \mathbf{W} \mathbf{v} - \mathbf{S}_a (\mathbf{x}_t - \mathbf{x}_a)] \quad (21)$$

Let

$$\mathbf{N} = \{ \mathbf{H}^T \mathbf{W} \mathbf{H} + \mathbf{S}_a \}^{-1}$$

If the correlation between \mathbf{v} and $(\mathbf{x}_t - \mathbf{x}_a)$ is assumed to be zero, the covariance for $\delta \mathbf{x}$ can be written as

$$\langle \delta \mathbf{x} \delta \mathbf{x}^T \rangle = \mathbf{N} \{ \mathbf{H}^T \mathbf{W} \langle \mathbf{v} \mathbf{v}^T \rangle \mathbf{W} \mathbf{H} + \mathbf{S}_a \langle (\mathbf{x}_t - \mathbf{x}_a) (\mathbf{x}_t - \mathbf{x}_a)^T \rangle \mathbf{S}_a \} \mathbf{N} \quad (22)$$

If the optimal weightings,

$$\mathbf{W} = \langle \mathbf{v} \mathbf{v}^T \rangle^{-1} \quad (23a)$$

and

$$\mathbf{S}_a = \langle (\mathbf{x}_t - \mathbf{x}_a) (\mathbf{x}_t - \mathbf{x}_a)^T \rangle^{-1} \quad (23b)$$

are used, Equation (22) reduces to

$$\langle \delta x \delta x^T \rangle = N \quad (24)$$

3. CROSS-CORRELATION OF ERRORS

Equation (23a) above identifies the optimal weighting of the maneuvers for gyro calibration as the W matrix given by

$$W = \langle v v^T \rangle^{-1} \quad (25)$$

where v = measurement error in Z_{obs}

The GRO FADS computes the error for an attitude in a form appropriate for computing the error, v , for a maneuver. A maneuver, or calibration interval, is a time interval with gyro-rate information and accurate attitude solutions (available at the end points of the interval). The set of angles (measured in radians) of the small rotation carrying the true attitude matrix into the measured attitude matrix in the current spacecraft body frame defines the covariance of the error angle vector. The FADS computes this covariance for each attitude solution. Combining the attitude errors at each end of the maneuver comprises the total measurement error for the Z_{obs} corresponding to a single maneuver.

As long as the calibration interval is large enough so that the attitude solutions incorporate different star vectors, the attitude errors at the ends of the maneuver will be uncorrelated. The weight matrix is then given by

$$W = \{P_i + T_{if} P_f T_{if}^T\}^{-1} \quad (26)$$

where

- P_i = covariance of the initial error angle vector
- P_f = covariance of the final error angle vector
- T_{if} = transformation from spacecraft body frame at end of maneuver to body frame at start of maneuver

A difficulty arises for the more general case where Z_{obs} contains multiple intervals. When an attitude solution is used at both the end of one interval and the start of another, the covariance of v contains significant cross-correlation terms. GRO's IRU calibration algorithm neglects these cross-correlation terms.

In general, the effect of cross-correlations remains small as long as the algorithm is used efficiently. When given a time interval containing accurate attitude solutions (at the end points and inside the interval), those who calibrate the GRO IRU should choose their calibration interval with care. Only one calibration interval of maximum length should be formed; the original time interval should not be broken into two or more calibration intervals, thereby avoiding using one attitude solution for two calibration intervals.

4. INFORMATION FROM PAST MISSIONS

The IRU calibration algorithm for GRO is capable of including the weighting of the a priori estimates of the components of x . From Equation (23b), the optimal weighting matrix associated with this a priori information is

$$S_a = \langle (x_t - x_a) (x_t - x_a)^T \rangle^{-1} \quad (27)$$

Since the a priori values of x will always be zero, S_a reduces to the inverse of the covariance of x_t . The following two scenarios for estimating S_a are expected to occur during GRO's mission, the first of which is the focus of this section:

- GRO's gyros will first be calibrated on the ground. Therefore, when GRO is first deployed, the effects of the launch shock on the IRU will be the major contributor to the uncertainty in x_t .
- Following the first calibration of the gyros, the a priori information becomes simply the covariance of the δx from the previous calibration (propagated to a time appropriate for the current calibration effort).

Due to the lack of rigorous analysis on launch shock effects, only a rough estimate of the statistics of x_t after launch is considered. For this reason, several simplifications are incorporated. The first assumption is that the change in the alignment and bias for each gyro channel from the ground calibration values to the first in-flight calibration is assumed to be a normal random variable with zero mean.

The value of x_t depends on the error in the prelaunch calibration, the change due to launch shock, and all other effects occurring before the first calibration in orbit. Along with the space environment, launch shock is assumed to be the dominant effect. The best source of launch shock information should be past missions that also flew a DRIRU-II. Two missions have flown these IRUs: SMM and Landsat.

Unfortunately, because of the nature of its attitude during mission (constant 1 revolution per orbit (RPO)), Landsat did not calibrate the misalignments, as GRO's algorithm must, but depended solely on bias adjustments to meet accuracy requirements. Therefore, this study relies on SMM as the prime source of information on gyro performance during launch.

Following the development in Reference 5, gyro drift is neglected and an inertial frame is defined as the body frame at the start of the maneuver. The equation

$$\Omega_{\text{inertial}} = R M_o \Omega_M \quad (28)$$

where

R = matrix representing a rotation from the current body frame to the current inertial frame

M_0 = alignment correction matrix with perfect reference attitudes

expresses the transformation of the gyro-measured angular velocity into the inertial frame. During a commanded roll slew, the control system will try to rotate the spacecraft about the roll axis (as sensed by the gyros) at a constant rate. The following relations hold

$$\Omega_M = \left(\frac{d\phi}{dt}, 0, 0 \right)^T \quad (29)$$

$$R = \begin{bmatrix} 1 & 0 & 0 \\ 0 & \cos \phi & -\sin \phi \\ 0 & \sin \phi & \cos \phi \end{bmatrix} \quad (30)$$

where ϕ = roll slew angle at time t from start of maneuver

Integrating Equation (28) yields

$$\theta(M_1^0) = \int_0^t \Omega_{\text{inertial}} dt \quad (31)$$

$$= T(\phi) M_1^0 \quad (32)$$

or

$$\theta(M_1^0) = \begin{bmatrix} \phi M_{11}^0 \\ \sin(\phi) M_{21}^0 - (1 - \cos \phi) M_{31}^0 \\ (1 - \cos \phi) M_{21}^0 + \sin(\phi) M_{31}^0 \end{bmatrix} \quad (33)$$

where M_1^0 is the first column of M^0 and

$$T(\phi) = \int_0^\phi R d\phi = \begin{bmatrix} \phi & 0 & 0 \\ 0 & \sin \phi & -(1 - \cos \phi) \\ 0 & (1 - \cos \phi) & \sin \phi \end{bmatrix} \quad (34)$$

Let M be the calculated correction matrix containing errors and write

$$M_1 - M_1^0 = dM \quad (35)$$

The effect of errors in M_1 on gyro-measured attitude changes is given by

$$\epsilon = \left. \frac{d\theta(M_1^0)}{dM_1} \right|_{M_1 = M_1^0} \quad dM_1 = T(\phi) dM_1 \quad (36)$$

Solving Equation (34) for M_{11} , M_{21} , and M_{31} , yields

$$dM_{11} = \frac{\epsilon_1}{\phi} \quad (37a)$$

$$dM_{21} = \left(\frac{\epsilon_2}{2} \right) \left[\cot \left(\frac{\phi}{2} \right) + 1 \right] \quad (37b)$$

$$dM_{31} = \left(\frac{\epsilon_3}{2} \right) \left[\cot \left(\frac{\phi}{2} \right) - 1 \right] \quad (37c)$$

These equations can be used to give the roll gyro calibration uncertainty in M_{11} , M_{21} , and M_{31} due to the reference attitude uncertainties. For a pitch calibration slew through the angle ϕ_2 , the corresponding expressions are

$$dM_{12} = \left(\frac{1}{2} \right) \left[\epsilon_1 \cot \left(\frac{\phi_2}{2} \right) - \epsilon_2 \right] \quad (38a)$$

$$dM_{22} = \frac{\epsilon_2}{\phi_2} \quad (38b)$$

$$dM_{32} = \left(\frac{1}{2} \right) \left[\epsilon_2 \cot \left(\frac{\phi_2}{2} \right) + \epsilon_1 \right] \quad (38c)$$

Similarly for a yaw calibration maneuver of angle ϕ_3

$$dM_{13} = \left(\frac{1}{2} \right) \left[\epsilon_1 \cot \left(\frac{\phi_3}{2} \right) + \epsilon_2 \right] \quad (39a)$$

$$dM_{23} = \left(\frac{1}{2} \right) \left[\epsilon_2 \cot \left(\frac{\phi_3}{2} \right) - \epsilon_1 \right] \quad (39b)$$

$$dM_{33} = \frac{\epsilon_3}{\phi_3} \quad (39c)$$

The following results for the first two calibrations (in February and July 1980) of the SMM gyros are taken from Reference 6 and converted to their M and d forms. Each gyro has two channels. There exist, therefore, eight possible gyro configurations; A1B1C1, A2B1C1, etc. The configurations A1B1C1 and A2B2C2 together contain information from

all six gyro channels. Reference 3 quotes an accuracy of 0.005 deg (1σ) for the SMM FHST attitude solutions.

Equations (37) through (39) with all components of ϵ equal to $1.23E-4$ radians (0.005 deg spherical uncertainty at the start and end of the calibration interval) were used to compute the uncertainty in the calibration coefficients. Also, a roll slew of 90 deg, a pitch slew of 25 deg, and a yaw slew of 25 deg were assumed (Reference 6). The original calibration plan for SMM calibration plan called for a 55-minute (min) inertial period for the bias calibration (Reference 3), which results in a $2E-6$ deg/sec accuracy. Table 1 shows the calibration results and their approximate uncertainties.

Table 1. SMM Calibration Results

CALIBRATED VALUES	A1B1C1 (Feb)	A1B1C1 (Jul)	A2B2C2 (Feb)	A2B2C2 (Jul)	ACCURACY
VALUES x 10^{-4}					
M_{11}	22.0	21.0	1.9	4.0	0.8
M_{21}	10.9	9.8	7.1	6.0	0.6
M_{31}	2.9	4.0	3.3	5.4	0.6
M_{12}	-9.85	-9.11	-8.88	-7.85	0.6
M_{22}	-1.08	2.83	-7.67	-3.39	3.0
M_{32}	-47.4	-47.1	-39.9	-40.4	3.0
M_{13}	-9.67	-6.17	-7.58	-4.59	3.0
M_{23}	26.0	26.2	34.2	34.6	3.0
M_{33}	-10.1	-15.7	-3.34	-8.51	3.0
VALUES x 10^{-6} DEG/SEC					
d_1	-40.828	-39.292	-34.904	-34.493	2.0
d_2	107.80	107.94	-89.301	-87.852	2.0
d_3	-5.8081	-6.0539	-6.7913	-6.7340	2.0

For this study, the measurement uncertainty is sufficiently small to neglect its effect on any conclusions drawn. Several useful observations can be made from the SMM-tabulated calibration results.

The requirements for ground calibration indicate that the absolute alignment error be less than some relatively large tolerance. The GRO specification stipulates the absolute alignment errors be less than 300 arc-seconds (arc-sec) (Reference 2). GRO's prelaunch gyro alignment is, therefore, required to be within this tolerance of the nominal alignment.

A more stringent requirement exists on the measured ground alignment. For GRO, the orientation of the gyro axes to the system mounting interface is required to be known to within ± 10 arc-sec. The SMM calibration results assume the nominal alignment and no bias initially. Therefore, the results contain the corrections due to the large absolute

alignment errors. This correction can contain directional biases; the x-axis misalignment is likely to be similar for both configurations.

The calibration results show a 0.91 sample correction between the A1B1C1 and A2B2C2 misalignment terms (M_{ij}). The degree to which this effect is due to launch shock cannot be determined without the measured values for the prelaunch misalignments, and unfortunately, these results are no longer available. The sample mean and standard deviation are -1.8 and $21 (x 10^{-4})$, respectively, for the A1B1C1 configuration and -2.3 and $19 (x 10^{-4})$, respectively, for the A2B2C2 configuration. During the first calibration for the GRO DRIRU-II, the SMM results indicate that for the correction made to the nominal alignment matrix a zero mean can reasonably be assumed, and an uncertainty on the order of $20 (x 10^{-4})$ can be expected.

Although the M_{ij} terms contain scale factor and misalignment effects, this estimation treats the M_{ij} identically. For the current analysis, no further effort seems worthwhile; however, it should be noted that assuming that the M_{ij} terms are normal variables allows one to assign a confidence level of 90 percent to the assumption that the standard deviation of the M_{ij} for A1B1C1 is less than $34 (x 10^{-4})$.

When the initial estimate of the GRO alignment is taken from the more accurate measured prelaunch alignments, a substantially lower variance in the alignment results can be expected. Environmental testing performed on the DRIRU-II shows that the gyro uncertainties due to any environmental effects are small compared to the absolute alignment errors. The alignment shifts due to environmental tests of Reference 6 reflect a standard deviation of 17 arc-sec, with the absolute alignment errors producing a standard deviation of 111 arc-sec. A 17 arc-sec change in alignment (first order) corresponds to roughly a $0.8 (x 10^{-4})$ change in M_{ij} (i not equal to j for alignment effects). The GRO requirement (Reference 5) is for alignment stability to within 20 arc-sec.

Similarly, scale factor changes across the environmental testing were on the order of 120 parts per million (ppm) compared to absolute alignment errors on the order of 1300 ppm. The diagonal elements of M are roughly $1.2 (x 10^{-4})$ for a 120 ppm change in scale factor. Uncertainties comparable to this are on the order of the likely measurement errors for GRO calibration, 0.008 deg 1σ attitude solution uncertainty.

For the gyro biases, the environmental tests showed results similar to the alignment data. For the different test temperatures, the environmental change in the biases gave standard deviations ranging from 4 to 8 ($x 10^{-6}$ deg/sec). The standard deviation for the bias itself was on the order of 42 ($x 10^{-6}$ deg/sec). Again, the tested environmental stability was on the order of the attitude solution uncertainties, with the total bias correction an order of magnitude larger.

The following conclusions are drawn considering the a priori weighting matrix for the first in-flight calibration of GRO. For nominal initial calibration alignments and biases, large uncertainties (with respect to the expected measurement errors) should be assigned to the a priori estimates. The calibration algorithm will not be sensitive to the exact uncertainties used in this case; values commensurate with the SMM values are appropriate. If the

ground-measured alignments and biases are assumed to be the initial values, uncertainties that agree with the environmental stability requirements are probably appropriate. The a priori alignments and biases will then be weighted roughly equally to the in-flight measurements. Without access to the ground measured alignments and biases for SMM, assuming such small uncertainty due to launch shock, seems presumptuous. For GRO, however, maneuvers sufficient to determine the alignment/scale factor matrices and biases are planned. It is suggested that both approaches be implemented as well as a third approach using the ground-measured alignments and biases and applying large a priori uncertainties. The results for all three approaches should then be analyzed for consistency.

5. PROPAGATION OF COVARIANCE MATRIX

As noted previously, a method is needed to propagate the covariance matrix of the calibration solution x . After the first planned set of maneuvers for GRO, it is likely that only partial information will be available for subsequent calibration updates. In this situation, the GRO algorithm operates optimally if the a priori uncertainties are known.

Immediately after the first in-flight calibration, the covariance of the solved-for biases and misalignments can be computed. The uncertainty in the solved-for values then increases with time. The random walk acts as the standard model to describe the time variation of the estimated state vector (for gyro calibration, the 12 vector of the misalignment terms M_{ij} and the bias vector corrections).

For the DRIRU-II, random walk type modeling is used for the short term (roughly 6 hours). However, this type of modeling is not appropriate for the DRIRU-II's long-term behavior. The misalignment and bias corrections appear to be bounded in the long term as opposed to the unbounded behavior of the random walk processes. Reference 7 reports the ground measured 74-month stability value for the serial number 1001 DRIRU-II to be 7.9 arc-sec. The 74-month stability of its scale factor was 58-ppm (dropping the data for the "c" channel due to electronic module changes) and the 66-month stability for the serial number 1004 was 77 ppm. The absolute changes in the gyro biases for these two cases were 0.005 and 0.009 deg/hour, respectively.

Numbers commensurate with these can be used to give conservative estimates of the increase in the state vector corresponding to times of several months or more if the in-flight calibrations results support them. The noise processes leading to the increases in the state vector uncertainty are assumed to be independent. Therefore, only the diagonal terms of the covariance would increase.

The SMM values for misalignment angles can be approximated (in radians to first order) by the off-diagonal values of M . The scale factors (SF_1) resulting from the in-flight calibrations can be computed from the resultant alignment matrix and are displayed in Table 2.

The measurement accuracies are approximately 80 ppm for SF_1 and 300 ppm for SF_2 and SF_3 . The error propagation effects are on the order of the measurement noise so that

Table 2. SMM Scale Factors

SCALE FACTOR	A1B1C1 (Feb) (ppm)	A1B1C1 (Jul) (ppm)	A2B2C2 (Feb) (ppm)	A2B2C2 (Jul) (ppm)
SF ₁	-2195.6	-2096.1	189.84	399.9
SF ₂	-598.40	-727.45	404.31	212.3
SF ₃	1706.4	2008.5	683.8	964.5

these effects cannot be observed directly. However, as the derivation of Equations (35) through (42) demonstrates, the attitude solution errors effect on the calculation of M is linear in the attitude error vector ϵ . If, for example, M_{ij} for A1B1C1 in February is subtracted from the February value for A2B2C2, the error due to ϵ cancels, and the result becomes the difference in M_{ij} due to internal effects. If the two configurations are independent, the difference should have a variance given by the sum of the squares of the standard deviation for each configuration for M_{ij} .

The quantity of interest is the change in the difference from February to July. The computations are straightforward, and the sample standard deviation for the six off-diagonal elements of M is $0.38 (x 10^{-4})$ or equivalently a misalignment of approximately 7.8 arc-sec. The sample standard deviation for the three scale factors is 74 ppm. These results assume that the M_{ij} have zero means, and the two configurations are independent. A similar process can be applied to the biases, giving a sample standard deviation of $0.78 (x 10^{-6} \text{ deg/sec})$ or 0.003 deg/hour. All the values derived from SMM calibration results are consistent with the reported long-term test results.

The in-flight SMM calibration results support the ground test long-term outcome. Uncertainties based on the ground test results might be applicable to the GRO in-flight calibration effort. Once data are available for GRO, analysis similar to that accomplished in this study can be used to investigate the time propagation of uncertainty for GRO calibration.

6. SUGGESTED CALIBRATION PLAN

This section presents a suggested calibration plan that includes some accepted calibration practices (taken predominantly from the SMM and SM Repair Mission (SMRM), Reference 7) and several suggestions for faster, more accurate gyro calibration. Included also are certain components of calibration, times and initial bias values for example, which should be tracked for future analysis of both the GRO spacecraft and other missions using the same gyro package. Tracking the items could prove to be extremely enlightening for future missions for accurately deducing a priori calibration parameters and their weights. Valuable calibration information should be carefully saved for GRO and all subsequent DRIRU-II missions (particularly STS-launched missions); each case offers one more example of launch and deployment effects.

Basic Procedures

Initially, the gyro biases will be determined while GRO is in a fixed-inertial attitude at the very beginning of the mission. Ideally, at least 1/2 hour of data will be used, comparing the gyro-propagated attitude with a finer FHST solution. This early bias determination will help improve course attitude solutions during orbit night early in the mission.

Once the FHSTs have been calibrated to meet GRO attitude determination requirements, the acquisition of gyro misalignments and scale factors begins. A series of slews are performed. Ideally, six slews of 30 deg each will be performed, for example, beginning in a fixed-inertial attitude, +X axis as the velocity vector and the +Z axis as the orbit normal, then performing a +30-deg roll slew, then back to zero, then a -30-deg roll slew, back to zero and so forth for the other two directions. These are, at this writing, the planned attitude verification slews. The slews should be separated by a period (at least 10 minutes) of fixed-inertial attitude. An attitude solution is determined using the highly accurate FHST data, both before and after the maneuver; it is, therefore, important to plan the maneuvers to ensure star data during the inertial periods between slews. These fine FHST-determined attitude solutions are then compared with the gyro data throughout the maneuver. The IRUCAL utility in the GRO AGSS uses this information to determine the gyro misalignments and scale factors.

As mentioned in Section 3, correlation of errors should be considered during calibration. During a fixed-inertial attitude, it is beneficial to consider observations at the beginning and the end of the span and not to break the interval into two or more spans. Due to the algorithm currently used in the GRO operational software, which ignores the off-diagonal correlation terms, correlation at the shared end points of the smaller intervals discount any benefit from the increased information. To avoid any correlation problems encountered when performing slews, observations at a maneuver's end point should not be used as the beginning point for another maneuver. As long as the slews are separated by at least 10 minutes of fixed-inertial attitude, this should not be a problem.

The gyro calibration process is then complete. Calibration is, however, an iterative process. When the FHST calibration constants are improved, IRUCAL can be rerun using the new FHST information. Calculating the covariance of the gyro calibration solutions, a capability to soon be added to the current operational version of IRUCAL, would be extremely beneficial here. Using the previous results from gyro calibration as the a priori guess for the next iteration (\mathbf{x}_a in Equation (17)) and using the inverse of the propagated covariance to weight the guess (\mathbf{S}_a in Equation (17)) would expedite this iterative process.

Calibration Information to Preserve

Some information accumulated during these early calibration phases is not only crucial to GRO postlaunch gyro calibration analysis but also to future missions. As trends begin to emerge from calibration analysis of every mission using the DRIRU-II, accurate assumptions can be made about launch effects and gyro performance. These assumptions in turn can be used to infer a priori calibration coefficient information and weighting. Each launch, with careful documenting, supplies analysts with another case for comparison.

Although each launch and spacecraft is different, with a number of different launches, trends can still be established.

Specific items for consideration are listed below:

- A detailed record of the prelaunch, ground-measured alignments, biases and the times that the measurements were taken
- A detailed record of the first inflight calibration, including the attitude solutions and covariances, time-interval information (average rates, total angles, times), the calibration covariance, and information from all six channels
- A launch acceleration history as it relates to the gyro frame
- Calibration information (as detailed in first calibration above) for all subsequent calibration efforts, to aid in building a time model for the growth in error uncertainty

A series of simulations are planned using the GRO data simulators and operational attitude ground support software to be performed as soon as these tools are available. The GRO Software Simulator (GROSS), which simulates dynamic errors, in conjunction with the GRO telemetry simulator (GROSIM) will generate data for a series of attitude slews separated by inertially fixed intervals. The slews will mimic those planned for early attitude verification where possible (see above). The spacecraft x-axis will point at the Sun and the z-axis parallel to the orbit normal both for simplicity and validity. (During early mission, the GRO Flight Dynamics analysts would like to have the spacecraft x-axis pointing at the Sun to calibrate the Fine Sun Sensor (FSS) and for simplicity.) In this case, inertially fixed intervals (for FHST FADS solutions) will be planned for orbit night to ensure star data (when the FHSTs are viewing away from the Earth and are, therefore, not occulted.)

Data spans will be selected so that correlation effects are small; those with suspected high correlation may also be selected to analyze correlation effects on final calibration results. FADS solutions will be determined during the inertially fixed intervals, while gyroscope data accumulate during the maneuvers. Appropriate a priori calibration estimates will be determined. A series of a priori weights, both correct and with reasonable deviations, will be used with the a priori estimate in IRUCAL. Results from these simulations will be plotted to show sensitivity to a priori weighting changes.

7. CONCLUSIONS AND RECOMMENDATIONS

The current algorithm for GRO gyro calibration does not account for some important yet subtle areas of calibration, while some other useful features are traditionally ignored. The cross correlations of errors does not appear in the IRUCAL process; careful considerations of observation intervals can compensate.

The covariance of the errors in a calibration solution is not currently calculated in the GRO algorithm. This information could, however, prove useful in weighting the a priori

state calibration values. With proper, albeit simple, propagation over time, a previous calibration result can be used as an a priori estimate, weighted optimally by the inverse of covariance of the errors. This a priori information, though included in the algorithm (x_a in Equation (17)), has not generally been utilized in past calibration efforts.

Gyro calibration can be a very tricky process. When it is not carefully examined, important information is lost. Every mission using the DRIRU-II can learn about the expected launch effects and performance of their gyro from previous launches. The DRIRU-II gyro package is apparently quite accurate and stable; a priori knowledge could, consequently, be greatly beneficial. Therefore, the careful recording of calibration results of GRO in providing an initial a priori estimate improves the efficiency of the gyro calibration efforts of future missions, and that information for those missions that follow.

REFERENCES

1. P. B. Davenport and G. L. Welter, *Algorithm for In-Flight Gyroscope Calibration, Flight Mechanics/Estimation Theory Symposium*, May 1988
2. GRO Detailed Requirement Form (DRF) 3510-907 (provided by TRW)
3. Teledyne Systems Corporation, *DRIRU-II System Data Analysis*, April 1980
4. Computer Sciences Corporation, CSC/TM-77/6082, *Gyro Calibration Analysis for the High-Energy Astronomy Observatory-A (HEAO-A)*, J. E. Keat
5. --, CSC/TM-78/6342, *Analysis of Gyro Calibration for the Solar Maximum Mission (SMM)*, J. A. Garber and R. Byrne
6. --, CSC/TM-82/6004, *Solar Maximum Mission (SMM) Attitude Sensor Recalibration Analysis Report*, D. Levitt, F. Patt, and T. Gwynn
7. --, CSC/TM-83/6170, *Solar Maximum Repair Mission (SMRM) Calibration Support Plan*, F. Patt et al., November 1983

SPACECRAFT ATTITUDE DETERMINATION USING THE EARTH'S MAGNETIC FIELD

David G. Simpson

OAO Corporation, Greenbelt, Maryland 20770

A method is presented by which the attitude of a low-Earth orbiting spacecraft may be determined using a vector magnetometer, a digital Sun sensor, and a mathematical model of the Earth's magnetic field. The method is currently being implemented for the Solar Maximum Mission spacecraft (as a backup for the failing star trackers) as a way to determine roll gyro drift.

PRECEDING PAGE BLANK NOT FILMED

I. INTRODUCTION

For centuries sailors have used the Earth's magnetic field to guide their ships though the oceans of the world by means of the magnetic compass. Today it is possible for spacecraft to navigate themselves in much the same way, with the mariner's compass replaced by the modern magnetometer. In this paper I describe how a vector magnetometer, in conjunction with a digital Sun sensor, can be used to determine the attitude of a low-Earth orbiting spacecraft.

This work was motivated by the failure of one of the two star trackers on the Solar Maximum Mission (SMM) spacecraft in 1987. The complement of attitude sensors on SMM provides only gyroscopes, two star trackers, and vector magnetometers for determining the roll attitude. As currently written, the on-board computer flight software uses the gyros to determine the roll attitude of the spacecraft, with the star tracker used only to calculate the roll gyro drift. The magnetometers are not currently used for attitude determination on SMM.

Should the remaining star tracker fail, however, this would leave the magnetometers as the only means of determining an *absolute* roll attitude, since the gyros only measure changes in the attitude with respect to inertial space. The work described in this paper is a result of an effort to determine how SMM's magnetometers might be used as a replacement for the remaining star tracker in the event that it fails.

The approach here will be to find the components of two vectors (the geomagnetic induction and Sun vectors) in each of two coordinate frames (the spacecraft frame and a reference frame); we then solve for the rotation matrix between the two frames to determine the spacecraft attitude. These calculations will be performed by a computer on the ground using data telemetered from the spacecraft; the ground computer will calculate roll gyro drift coefficients which will be periodically uplinked to the on-board computer. Calculating the gyro drift coefficients on the ground will permit ground personnel to select data which was sampled while the geomagnetic field was relatively quiet, thus giving the most accurate results.

Section II of this paper describes how the Earth's magnetic field vector at the spacecraft position can be calculated from a mathematical model. Section III describes the calculation of the Sun vector, and Sections IV and V describe how these two vectors may be combined with sensor data to determine the spacecraft attitude. Section VI is a summary of the paper, and Section VII is a short discussion of associated Legendre functions.

II. MODELING THE GEOMAGNETIC FIELD

In order to determine the spacecraft attitude from the magnetometers, one must first generate an accurate mathematical model of the Earth's magnetic field. Ampere's law at the spacecraft position \vec{r} is (SI units):

$$\nabla \times \vec{H}(\vec{r}) = \vec{J}(\vec{r}) + \frac{\partial \vec{D}(\vec{r})}{\partial t} \quad (1)$$

where $\vec{H}(\vec{r})$ is the geomagnetic intensity at \vec{r} , $\vec{J}(\vec{r})$ is the electric current density, and $\partial \vec{D}(\vec{r})/\partial t$ is the displacement current. Since there is no current density at \vec{r} and the geomagnetic field is approximately static, we may take \vec{J} and $\partial \vec{D}/\partial t$ to both be zero. Eq. (1) then becomes

$$\nabla \times \vec{H}(\vec{r}) = \vec{0} \quad (2)$$

The constitutive relation for the magnetic induction \vec{B} is

$$\frac{1}{\mu_0} \vec{B}(\vec{r}) = \vec{H}(\vec{r}) + \vec{M}(\vec{r}) \quad (3)$$

where μ_0 is the permeability of free space ($4\pi \times 10^{-7} \text{ N A}^{-2}$), and \vec{M} is the magnetization, which is zero at \vec{r} . Eq. (3) then becomes

$$\frac{1}{\mu_0} \vec{B}(\vec{r}) = \vec{H}(\vec{r}) \quad (4)$$

Substituting Eq. (4) for \vec{H} into Eq. (2) we get

$$\nabla \times \frac{1}{\mu_0} \vec{B}(\vec{r}) = \vec{0} \quad (5)$$

since the curl of any gradient is zero, this means that \vec{B} can be written as the gradient of a magnetic scalar potential V :¹

$$\vec{B}(\vec{r}) = -\mu_0 \nabla V(\vec{r}) \quad (6)$$

It is conventional in geomagnetism to model the geomagnetic field by expanding the magnetic scalar potential $V(\vec{r})$ into a Laplace series of spherical harmonics with real eigenfunctions:²

$$V(r, \theta, \lambda) = \frac{a}{r} \sum_{n=1}^k \left(\frac{a}{r}\right)^{n+1} \sum_{m=0}^n [g^{nm} \cos m\lambda + h^{nm} \sin m\lambda] P^{nm}(\cos \theta) \quad (7)$$

where

- r is the distance of the spacecraft from the center of the Earth;
- θ is the co-elevation of the sub-satellite point (90° minus the north latitude);
- λ is the east longitude of the sub-satellite point;
- a is the radius of the Earth, taken to be 6371.2 km;
- $P^{nm}(\cos \theta)$ are the Gauss-normalized associated Legendre functions of the first kind;
- g^{nm} and h^{nm} are the Gauss-normalized coefficients of the expansion.

The $n=0$ terms in this expansion are absent because they would represent a magnetic monopole component of the field; the $n=1$ terms represent the dipole component, the $n=2$ terms represent the quadrupole component, etc.

The expansion coefficients g^{nm} and h^{nm} are found empirically; they are updated every five years and published along with their time derivatives (the *secular variation*) by the International Association of Geomagnetism and Aeronomy (IAGA). These published coefficients are Schmidt normalized and may be used to calculate the geomagnetic scalar potential $V(\vec{r})$ using Eq. (7) if the Schmidt-normalized associated Legendre functions P_n^m are substituted for the Gauss-normalized functions P^{nm} . Using Gauss normalization will save about 7% in computer time, however,³ so for convenience in computer work, Gauss normalization will be used throughout this paper.

Table I shows the Gauss-normalized coefficients g^{nm} and h^{nm} for the International Geomagnetic Reference Field (IGRF) 1985. These were calculated from the Schmidt-normalized coefficients published by the IAGA and can safely be extended to 1990 with the secular variation coefficients in the last two columns.

TABLE I. International Geomagnetic Reference Field, IGRF 1985.
Coefficients are Gauss-normalized.

n	m	g_{nm} (nT)	h_{nm} (nT)	\dot{g}_{nm} (nT/yr)	\dot{h}_{nm} (nT/yr)
1	0	-29877		23.2	
1	1	-1903	5497	10.0	-24.5
2	0	-3110		-20.6	
2	1	5274	-3795	5.9	-19.9
2	2	1464	-268	6.1	-17.5
3	0	3250		12.8	
3	1	-6761	-955	-14.1	16.2
3	2	2409	550	-1.2	4.5
3	3	660	-234	0.1	-8.5
4	0	4099		0.4	
4	1	4317	1289	-3.3	21.0
4	2	1420	-978	-30.5	8.6
4	3	-891	142	-2.9	5.2
4	4	125	-220	-5.0	0.7
5	0	-1693		10.2	
5	1	3619	478	1.0	1.0
5	2	1944	1137	-11.5	-1.5
5	3	-442	-729	-15.1	-0.5
5	4	-357	-166	0.2	1.3
5	5	-34	67	-0.1	0.0
6	0	751		20.2	
6	1	1229	-302	-5.7	-7.6
6	2	747	1345	25.4	-16.4
6	3	-1853	687	6.0	-8.0
6	4	22	-273	0.0	-12.6
6	5	40	-9	2.1	-1.2
6	6	-69	13	0.8	-0.1
7	0	2011		5.4	
7	1	-2164	-2909	-21.3	7.1
7	2	58	-753	-14.5	29.0
7	3	491	-20	16.4	22.5
7	4	-74	284	12.3	23.5
7	5	25	105	2.5	1.9
7	6	22	-51	-1.2	0.5
7	7	0	-4	-0.1	0.6
8	0	1056		35.2	
8	1	402	469	0.0	6.7
8	2	0	-1178	16.8	-56.1
8	3	-456	207	16.6	4.1
8	4	-241	-668	-8.0	-21.4
8	5	30	163	-4.4	3.0
8	6	27	82	0.7	-5.5
8	7	10	-40	-1.3	-0.3
8	8	-4	-6	-0.5	0.8

TABLE I (cont.)

<u>n</u>	<u>m</u>	$\underline{g^{nm}}$ (nT)	$\underline{h^{nm}}$ (nT)	$\underline{\dot{g}^{nm}}$ (nT/yr)	$\underline{\dot{h}^{nm}}$ (nT/yr)
9	0	475			
9	1	1274	-2675		
9	2	109	1738		
9	3	-996	747		
9	4	507	-282		
9	5	-101	-202		
9	6	-17	157		
9	7	53	75		
9	8	5	-16		
9	9	-3	1		
10	0	-722			
10	1	-973	243		
10	2	421	0		
10	3	-826	496		
10	4	-234	701		
10	5	370	-296		
10	6	124	0		
10	7	20	-20		
10	8	16	33		
10	9	8	0		
10	10	0	-4		

When the coefficients in Table I are substituted into Eq. (7), we get the geomagnetic scalar potential $V(\vec{r})$; substituting this $V(\vec{r})$ into Eq. (6) yields the geomagnetic induction vector $\vec{B}(\vec{r})$ in a reference frame fixed in the Earth (which will be referred to as the EB (Earth-based) frame). The EB frame has its origin at the center of the Earth, its x axis pointing out of the intersection of the equator with the prime meridian, its z axis pointing out of the Earth's geographic north pole, and its y axis in the $\hat{x} \times \hat{z}$ direction.

If we calculate the gradient in Eq. (6) in spherical polar coordinates,

$$\nabla\psi = \frac{\partial\psi}{\partial r} \hat{e}_r + \frac{1}{r} \frac{\partial\psi}{\partial\theta} \hat{e}_\theta + \frac{1}{r \sin\theta} \frac{\partial\psi}{\partial\lambda} \hat{e}_\lambda \quad (8)$$

the resulting spherical components of \vec{B} may be used to easily calculate the standard geomagnetic elements:²

X	$= -B_\theta$	(Northward component)
Y	$= B_\lambda$	(Eastward component)
Z	$= -B_r$	(Downward component)
H	$= (X^2 + Y^2)^{\frac{1}{2}}$	(Horizontal intensity)
V	$= Z $	(Vertical intensity)
F	$= (X^2 + Y^2 + Z^2)^{\frac{1}{2}}$	(Total intensity)
D	$= \arctan(Y/X)$	(Magnetic declination)
I	$= \arctan(Z/H)$	(Magnetic inclination)

A computer program which calculates $\vec{B}(\vec{r})$ can then be checked by comparing the geomagnetic elements it calculates with the elements found in charts and tables in the literature.⁵

For spacecraft attitude determination, we will need to know the components of the modeled geomagnetic induction vector $\vec{B}(\vec{r})$ in the *geocentric inertial* (GCI) reference frame rather than the EB frame. The GCI frame is fixed with respect to the stars and has its origin at the Earth's center, its x axis toward the vernal equinox, its z axis out of the Earth's geographic north pole, and its y axis in the $\hat{z} \times \hat{x}$ direction.

The GCI frame differs from the EB frame only by a rotation about their common z axis. Specifically, in cartesian coordinates

$$\vec{B}_{GCI} = R \vec{B}_{EB} \quad (9)$$

where the rotation matrix R is given by

$$R = \begin{bmatrix} \cos \gamma & \sin \gamma & 0 \\ -\sin \gamma & \cos \gamma & 0 \\ 0 & 0 & 1 \end{bmatrix} \quad (10)$$

and where γ is the Greenwich hour angle of the vernal equinox, which is equal to the sidereal time at Greenwich (GST) and is given by⁶

$$\gamma = \text{LST} - (\lambda/15^\circ) \quad (11)$$

where LST is the local sidereal time and λ the east longitude of any convenient point on the Earth's surface. An expression for γ which is often more convenient is⁶

$$\gamma = 99^\circ.6910 + 36000^\circ.7689T + 0^\circ.0004T^2 + \text{UTC} \quad (12)$$

where T is the time (in Julian centuries of 36525 days) since 1900 and UTC is Coordinated Universal Time expressed in *degrees*.

Alternatively, if we work in spherical polar coordinates, Eqs. (9) and (10) may be replaced with

$$\begin{aligned} B_{r\text{GCI}} &= B_{r\text{EB}} \\ B_{\theta\text{GCI}} &= B_{\theta\text{EB}} \\ B_{\lambda\text{GCI}} &= B_{\lambda\text{EB}} - \gamma \end{aligned} \quad (13)$$

III. SUN VECTOR CALCULATION

The geomagnetic induction vector $\vec{B}(\vec{r})$ modeled in Section II is by itself insufficient to determine the spacecraft attitude, since if the spacecraft is rotated about the \vec{B} vector it will still yield the same components of \vec{B} in a reference frame fixed in the spacecraft; hence one degree of freedom is left unspecified.⁷ It is therefore necessary to know the components of one more vector (not parallel to $\vec{B}(\vec{r})$) in order to specify the spacecraft attitude completely. For this discussion we choose the Earth-to-Sun vector (or simply the "Sun vector") \hat{S} , and in this section I discuss how to calculate the components of \hat{S} in the GCI frame. (The cartesian GCI components of \hat{S} will be used along with the cartesian GCI components of \vec{B} from Section II to determine the spacecraft attitude in Sections IV and V.) The Sun unit vector \hat{S} is given in cartesian GCI coordinates approximately by (ignoring the small corrections for parallax and light aberration)⁸

$$\hat{S}(t) = \begin{bmatrix} \cos L \\ \sin L \cos \epsilon \\ \sin L \sin \epsilon \end{bmatrix} \quad (14)$$

where $L(t)$ is the mean longitude of the Sun and ϵ is the mean inclination of the ecliptic from the Earth's equatorial plane.

The mean longitude of the Sun $L(t)$ may be calculated from⁸

$$L(t) = L(t_0) + M(t) + 2e \sin M(t) + \beta t \quad (15)$$

where t_0 is a reference time, e is the eccentricity of the Earth's orbit ($e = 0.016722$), $M(t)$ is the mean anomaly of the Sun, and β is defined by

$$\beta = \frac{360^\circ}{\tau_{sy}} - \frac{360^\circ}{\tau_{ay}} \quad (16)$$

where τ_{sy} is the length of the sidereal year (3.1558149548×10^7 seconds) and τ_{ay} is the length of the anomalistic year (3.1558433×10^7 seconds).

The mean anomaly of the Sun $M(t)$ is given by⁸

$$M(t) = M(t_0) + \frac{360^\circ}{\tau_{ay}} (t - \sigma) \quad (17)$$

where σ is the time it takes light to travel from the Sun to the Earth, about 499 seconds.

Finally, the mean inclination of the ecliptic ϵ is given by⁸

$$\epsilon = 23^{\circ}27'8.26'' - 46.845'' T \quad (18)$$

where T is the time in Julian centuries since 1900.

IV. GENERAL ATTITUDE DETERMINATION

Knowing the cartesian components of the geomagnetic induction unit vector \vec{B} and the Sun unit vector \hat{S} in the GCI reference frame (as described in Sections II and III), we can now determine the spacecraft attitude if we also know the components of these two vectors in the *spacecraft* (SC) reference frame (i.e. along the roll (x), pitch (y), and yaw (z) axes). The essence of the problem of determining the spacecraft attitude is then this: we are given the components of two vectors in each of these two reference frames which have a common origin, and we must solve for the rotation matrix between the two frames. There are several ways of doing this; I will describe here one of the simplest methods, known as the *algebraic method*.⁹ Let $\vec{\xi}$ be some vector whose components we wish to transform from the GCI reference frame to the SC frame. The two sets of components are related by

$$\vec{\xi}_{SC} = A \vec{\xi}_{GCI} \quad (19)$$

where $\vec{\xi}_{SC}$ and $\vec{\xi}_{GCI}$ are column vectors containing the SC and GCI components, respectively, and A is the rotation matrix we wish to solve for. *Formally*, we could solve this equation for A by post-multiplying both sides by the inverse of the matrix $\vec{\xi}_{GCI}$:

$$A = \vec{\xi}_{SC} \vec{\xi}_{GCI}^{-1}$$

Unfortunately, $\vec{\xi}_{GCI}$ is not a square matrix, so we cannot take its inverse directly (without a somewhat messy diversion into pseudo-inverses).

In the algebraic method, we use the two known vectors \hat{B} and \hat{S} to *construct* an orthogonal triad of vectors (\hat{a} , \hat{b} , and \hat{c}) in each reference frame (SC and GCI). (This will work only if \hat{B} and \hat{S} are not parallel.) We then define a matrix M for each frame which has the vectors \hat{a} , \hat{b} , and \hat{c} as its columns; the columns of this matrix will transform from GCI to SC coordinates just like the vector $\vec{\xi}$ above, *and* we will be able to take its inverse (since it will be a square matrix), thus allowing us to solve for the rotation matrix A.

Specifically, let us define the vectors \hat{a} , \hat{b} , and \hat{c} in the GCI and SC reference frames as follows:

$$\begin{array}{rcl}
 & \text{GCI Frame} & \text{SC Frame} \\
 \hat{a}_{\text{GCI}} & = \hat{S}_{\text{GCI}} & \hat{a}_{\text{SC}} = \hat{S}_{\text{SC}} \\
 \hat{b}_{\text{GCI}} & = \frac{\hat{S}_{\text{GCI}} \times \hat{B}_{\text{GCI}}}{|\hat{S}_{\text{GCI}} \times \hat{B}_{\text{GCI}}|} & \hat{b}_{\text{SC}} = \frac{\hat{S}_{\text{SC}} \times \hat{B}_{\text{SC}}}{|\hat{S}_{\text{SC}} \times \hat{B}_{\text{SC}}|} \\
 \hat{c}_{\text{GCI}} & = \hat{a}_{\text{GCI}} \times \hat{b}_{\text{GCI}} & \hat{c}_{\text{SC}} = \hat{a}_{\text{SC}} \times \hat{b}_{\text{SC}}
 \end{array} \quad (20)$$

where:

\hat{B}_{GCI} is the geomagnetic induction unit vector in GCI cartesian coordinates, calculated as in Section II.

\hat{S}_{GCI} is the Sun unit vector in GCI cartesian coordinates, calculated as in Section III.

\hat{B}_{SC} is the geomagnetic induction unit vector in SC cartesian coordinates, from the spacecraft magnetometers.

\hat{S}_{SC} is the Sun unit vector in SC cartesian coordinates, from the spacecraft digital Sun sensor.

We now construct two 3x3 square matrices M_{GCI} and M_{SC} whose columns are the cartesian components of \hat{a} , \hat{b} , and \hat{c} :

$$\begin{aligned} M_{GCI} &= \left[\hat{a}_{GCI} \mid \hat{b}_{GCI} \mid \hat{c}_{GCI} \right] \\ M_{SC} &= \left[\hat{a}_{SC} \mid \hat{b}_{SC} \mid \hat{c}_{SC} \right] \end{aligned} \quad (21)$$

Since the rotation matrix A rotates column vectors from the GCI to the SC reference frame, it will also rotate each column of M_{GCI} into the corresponding column of M_{SC} :

$$M_{SC} = A M_{GCI}$$

Since M_{GCI} is a square matrix, we can now solve for the rotation matrix A by post-multiplying both sides by the inverse of M_{GCI} :

$$A = M_{SC} M_{GCI}^{-1}$$

Furthermore, since M_{GCI} was defined to be an orthogonal matrix, its inverse is equal to its transpose and so

$$A = M_{SC} M_{GCI}^T \quad (22)$$

The matrix A given by Eq. (22) rotates any vector from the GCI to the spacecraft reference frame and thus determines the spacecraft attitude.

V. SMM ROLL ATTITUDE DETERMINATION

On SMM, the roll, pitch, and yaw angles are measured with respect to the somewhat whimsically named "SUN" reference frame, defined by the three orthonormal vectors \hat{S} , \hat{U} , and \hat{N} :

\hat{S} is the Sun unit vector, calculated as in Section III.

$$\hat{U} = \frac{\hat{P} \times \hat{S}}{|\hat{P} \times \hat{S}|} \quad (\hat{U} \text{ points out of the east limb of the Sun, } (23) \\ \text{along the solar equator.})$$

$$\hat{N} = \hat{S} \times \hat{U} \quad (\hat{N} \text{ is } \hat{P} \text{ projected onto the plane normal to the } \\ \text{line of sight.})$$

where \hat{P} is the solar spin axis unit vector. In order to determine the spacecraft attitude from the magnetometers and the Fine Pointing Sun Sensor (FPSS), we will need to know the components of the vectors \hat{S} , \hat{U} , and \hat{N} in the GCI reference frame.

We first need to calculate the cartesian components of the solar spin axis unit vector \hat{P} in the GCI frame. We begin by working in the *ecliptic* (ECL) frame, defined by the unit vectors x_{ECL} , y_{ECL} , and z_{ECL} :

- x_{ECL} points in the direction of the vernal equinox;
- y_{ECL} points in the direction of $\hat{z}_{ECL} \times \hat{x}_{ECL}$;
- z_{ECL} points toward the ecliptic north pole.

The vector \hat{P} in the ecliptic frame has cartesian components⁸

$$\hat{P}_{ECL} = \begin{bmatrix} \sin \Omega & \sin i \\ -\cos \Omega & \sin i \\ \cos i \end{bmatrix} \quad (24)$$

where Ω is the longitude of the ascending node of the solar equator on the ecliptic, given by⁸

$$\Omega = 73^\circ 40' + 50^\circ 25' \Lambda \quad (25)$$

where Λ is the time in years since 1850; i is the inclination of the solar equator to the ecliptic:

$$i = 7^{\circ} 15' \quad (26)$$

The ecliptic and GCI reference frames differ only by a rotation of magnitude $-\epsilon$ about their common x axis, where ϵ is the inclination of the ecliptic (Eq. (18)). Hence the GCI cartesian components of \hat{P} are

$$\hat{P}_{\text{GCI}} = \begin{bmatrix} 1 & 0 & 0 \\ 0 & \cos \epsilon & -\sin \epsilon \\ 0 & \sin \epsilon & \cos \epsilon \end{bmatrix} \hat{P}_{\text{ECL}} \quad (27)$$

Having found the cartesian components of the solar spin axis unit vector \hat{P} in the GCI frame, and knowing the components of \hat{S} from section III, we may now use Eq. (23) to determine the cartesian components of the \hat{U} and \hat{N} vectors in the GCI frame; these will be used in Eq. (29) below to determine the SMM roll attitude.

It is especially convenient to determine SMM's roll angle ρ when the spacecraft's FPSS is pointed at Sun center (so that the pitch and yaw angles are zero). In this case the x axis of the spacecraft reference frame (the roll axis) will coincide with the \hat{S} vector of the SUN frame. The two reference frames will then differ only by a rotation about their common x - \hat{S} axis (Fig. 1). The roll angle ρ is then given by⁸

$$\rho = \phi_1 - \phi_2 \quad (28)$$

where ϕ_1 is calculated from the magnetic field model and solar ephemeris (Sections II-V):

$$\phi_1 = \tan^{-1} \frac{-\hat{B}_{\text{GCI}} \cdot \hat{U}_{\text{GCI}}}{\hat{B}_{\text{GCI}} \cdot \hat{N}_{\text{GCI}}} \quad (29)$$

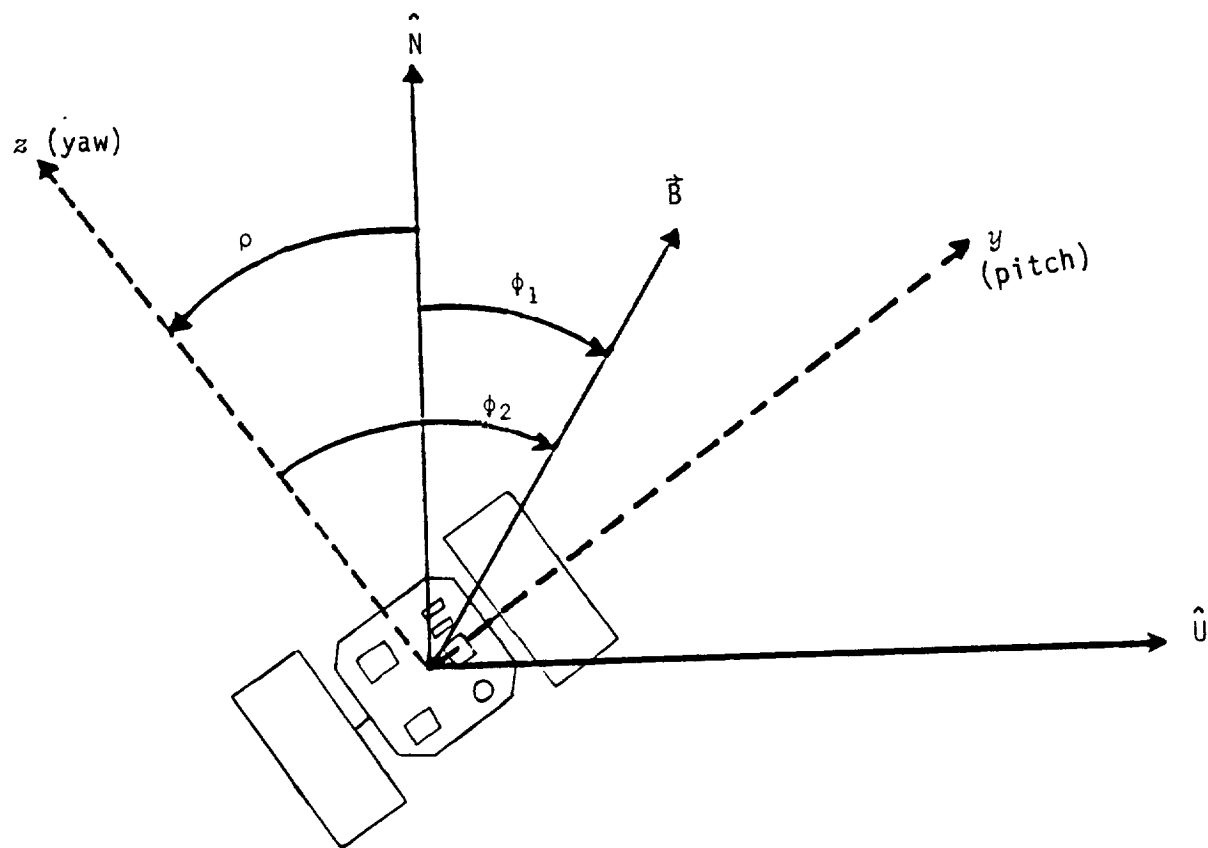


Fig. 1. Determination of SMM roll attitude. This view is looking from the Sun down onto the SMM top face plate. (After [8].)

and ϕ_2 is found from magnetometer data:

$$\phi_2 = \tan^{-1} \frac{-\vec{B}_{\text{mag pitch}}}{\vec{B}_{\text{mag yaw}}} \quad (30)$$

Substituting Eqs. (29) and (30) into Eq. (28) then determines the SMM roll attitude. Note that we do not require any FPSS data in this case; the Sun vector \hat{S}_{SC} was tacitly assumed to lie along the \hat{S} axis of the SUN frame since the FPSS is pointed at Sun center.

VI. SUMMARY

Two methods for spacecraft attitude determination using the Earth's magnetic field have been presented: the *algebraic method* for spacecraft in general (Section IV), and a simpler method specific to SMM (Section V). Both methods compare the Earth's magnetic field as calculated by a mathematical model (Eq. (7)) with magnetometer measurements; in addition, the Sun vector calculated by Eq. (14) and measured with a digital Sun sensor is used to completely specify the spacecraft attitude.

VII. APPENDIX: ASSOCIATED LEGENDRE FUNCTIONS

The associated Legendre functions of the first kind form a complete orthogonal set of functions over the interval $\theta = [0, \pi]$; it is this property which makes them a useful basis in which to expand the geomagnetic scalar potential $V(\vec{r})$.

Although a variety of normalization conventions for the associated Legendre functions are in common use, the three most common are the so-called Neumann, Schmidt, and Gauss normalization conventions. Neumann normalization is the convention most often found in mathematics textbooks¹⁰⁻¹². The geomagnetic coefficients g and h given in the literature are usually defined for the Schmidt-normalized associated Legendre functions; Schmidt normalization has the advantage that the normalization constants are independent of m (for $m \neq 0$) for any given n , so the relative strengths of the different terms can be easily judged. Gauss normalization is useful because it saves about 7% in computation time on a computer³; the g and h coefficients in this paper have been converted to Gauss normalization for ready use in computer work.

The various normalization conventions are defined as follows:

Neumann normalization (P_{nm}):

$$\int_0^\pi P_{nm}(\cos \theta) P_{\ell m}(\cos \theta) \sin \theta \, d\theta = \frac{2}{2n+1} \frac{(n+m)!}{(n-m)!} \delta_{n\ell}$$

Schmidt normalization (P_n^m):

$$\int_0^\pi P_n^m(\cos \theta) P_\ell^m(\cos \theta) \sin \theta \, d\theta = \frac{2(2 - \delta_{m0})}{2n+1} \delta_{n\ell}$$

Gauss normalization (P^{nm}):

$$\int_0^\pi P^{nm}(\cos \theta) P^{\ell m}(\cos \theta) \sin \theta \, d\theta = \frac{2(n-m)!(n+m)!}{(2n+1)[(2n-1)!!]^2} \delta_{n\ell}$$

One may easily calculate the conversion factors for converting between Schmidt and Gauss normalizations by simply taking the square root of the quotient of the respective normalization constants. In particular, if the conversion factors S_{nm} are defined by¹³

$$p_n^m = S_{nm} p^{nm}$$

then

$$S_{nm} = \left[\frac{\frac{2(2-\delta_{m0})}{2n+1} \delta_{n\ell}}{\frac{2(n-m)! (n+m)!}{(2n+1) [(2n-1)!!]^2} \delta_{n\ell}} \right]^{\frac{1}{2}}$$

or

$$S_{nm} = \left[\frac{(2-\delta_{m0}) (n-m)!}{(n+m)!} \right]^{\frac{1}{2}} \frac{(2n-1)!!}{(n-m)!}$$

Table II lists the explicit values of these conversion factors up to $n=12$. To convert a table of Schmidt-normalized coefficients g_n^m and h_n^m (such as those usually found in the literature) from Schmidt to Gauss normalization, use

$$g^{nm} = S_{nm} g_n^m$$

$$h^{nm} = S_{nm} h_n^m$$

and analogous expressions for the secular variation coefficients.

TABLE II. Conversion factors S_{nm} between Schmidt- and Gauss- normalized associated Legendre functions of the first kind.

<u>n</u>	<u>m</u>	<u>S_{nm}</u>	<u>n</u>	<u>m</u>	<u>S_{nm}</u>
1	0	1	9	0	12155/128
1	1	1	9	1	(7293/128) $\sqrt{5}$
2	0	3/2	9	2	(663/64) $\sqrt{110}$
2	1	$\sqrt{3}$	9	3	(221/128) $\sqrt{2310}$
2	2	(1/2) $\sqrt{3}$	9	4	(51/64) $\sqrt{5005}$
3	0	5/2	9	5	(255/128) $\sqrt{286}$
3	1	(5/4) $\sqrt{6}$	9	6	(17/64) $\sqrt{4290}$
3	2	(1/2) $\sqrt{15}$	9	7	(51/256) $\sqrt{1430}$
3	3	(1/4) $\sqrt{10}$	9	8	(3/128) $\sqrt{12155}$
4	0	35/8	9	9	(1/256) $\sqrt{24310}$
4	1	(7/4) $\sqrt{10}$	10	0	46189/256
4	2	(7/4) $\sqrt{5}$	10	1	(4199/128) $\sqrt{55}$
4	3	(1/4) $\sqrt{70}$	10	2	(4199/256) $\sqrt{165}$
4	4	(1/8) $\sqrt{35}$	10	3	(323/128) $\sqrt{4290}$
5	0	63/8	10	4	(323/128) $\sqrt{2145}$
5	1	(21/8) $\sqrt{15}$	10	5	(323/128) $\sqrt{858}$
5	2	(3/4) $\sqrt{105}$	10	6	(323/512) $\sqrt{4290}$
5	3	(9/16) $\sqrt{70}$	10	7	(19/256) $\sqrt{72930}$
5	4	(3/8) $\sqrt{35}$	10	8	(19/256) $\sqrt{12155}$
5	5	(3/16) $\sqrt{14}$	10	9	(1/256) $\sqrt{461890}$
6	0	231/16	10	10	(1/512) $\sqrt{92378}$
6	1	(33/8) $\sqrt{21}$	11	0	88179/256
6	2	(33/32) $\sqrt{210}$	11	1	(29393/512) $\sqrt{66}$
6	3	(11/16) $\sqrt{210}$	11	2	(2261/256) $\sqrt{2145}$
6	4	(33/16) $\sqrt{7}$	11	3	(969/512) $\sqrt{30030}$
6	5	(3/16) $\sqrt{154}$	11	4	(969/128) $\sqrt{1001}$
6	6	(1/32) $\sqrt{462}$	11	5	(6783/512) $\sqrt{143}$
7	0	429/16	11	6	(399/512) $\sqrt{14586}$
7	1	(429/32) $\sqrt{7}$	11	7	(133/512) $\sqrt{36465}$
7	2	(143/32) $\sqrt{42}$	11	8	(7/256) $\sqrt{692835}$
7	3	(143/32) $\sqrt{21}$	11	9	(21/512) $\sqrt{46189}$
7	4	(13/16) $\sqrt{231}$	11	10	(1/512) $\sqrt{1939938}$
7	5	(13/32) $\sqrt{231}$	11	11	(1/512) $\sqrt{88179}$
7	6	(1/32) $\sqrt{6006}$	12	0	676039/1024
7	7	(1/32) $\sqrt{429}$	12	1	(52003/512) $\sqrt{78}$
8	0	6435/128	12	2	(7429/512) $\sqrt{3003}$
8	1	2145/32	12	3	(7429/512) $\sqrt{2002}$
8	2	(429/64) $\sqrt{70}$	12	4	(22287/2048) $\sqrt{2002}$
8	3	(39/32) $\sqrt{1155}$	12	5	(1311/512) $\sqrt{17017}$
8	4	(195/64) $\sqrt{77}$	12	6	(3059/1024) $\sqrt{4862}$
8	5	(15/32) $\sqrt{1001}$	12	7	(161/512) $\sqrt{138567}$
8	6	(15/64) $\sqrt{858}$	12	8	(161/1024) $\sqrt{138567}$
8	7	(3/32) $\sqrt{715}$	12	9	(23/512) $\sqrt{323323}$
8	8	(3/128) $\sqrt{715}$	12	10	(23/1024) $\sqrt{176358}$
			12	11	(1/512) $\sqrt{2028117}$
			12	12	(1/2048) $\sqrt{1352078}$

ACKNOWLEDGEMENTS

Thanks are due to J. D'Agostino, G. Snyder, and S. Fry for their help in preparing this paper. This work was supported by the NASA Goddard Space Flight Center under Contract No. NAS 5-29320.

REFERENCES

- ¹ J.D. Jackson, *Classical Electrodynamics*, 2nd ed. (Wiley, New York, 1975).
- ² S. Chapman and J. Bartels, *Geomagnetism*. (Oxford University Press, New York, 1940).
- ³ B. T. Trombka and J. C. Cain, *Computation of the IGRF I. Spherical Expansions*, NASA Document No. X-922-74-303, GSFC (August 1974).
- ⁴ IAGA Division I, Working Group 1, "International Geomagnetic Reference Field Revision 1985", *EOS Trans. AGU*, 67, 523 (1986).
- ⁵ D. R. Barraclough and D. J. Kerridge, *International Geomagnetic Reference Field 1985: Grid-point Values and Charts* (IAGA Bulletin No. 52, July 1986).
- ⁶ C. R. Sturch, "Time Measurement Systems", in *Spacecraft Attitude Determination and Control*, edited by James R. Wertz (D. Reidel, Dordrecht, 1985).
- ⁷ F. F. Mobley, "Spacecraft Attitude Determination and Attitude Control", Johns Hopkins University Applied Physics Laboratory (unpublished).
- ⁸ Computer Sciences Corporation, *Solar Maximum Mission Attitude Determination and Control Software Description*, Document No. CSC/SD-79/6081 (June 1979).
- ⁹ G. M. Lerner, "Three-Axis Attitude Determination", in *Spacecraft Attitude Determination and Control*, edited by James R. Wertz (D. Reidel, Dordrecht, 1985).
- ¹⁰ G. Arfken, *Mathematical Methods for Physicists*, 3rd ed. (Academic, Orlando, 1985).
- ¹¹ J. Mathews and R. L. Walker, *Mathematical Methods of Physics*, 2nd ed. (Benjamin-Cummings, Menlo Park CA, 1970).
- ¹² P. M. Morse and H. Feshbach, *Methods of Theoretical Physics*. (McGraw-Hill, New York, 1953).
- ¹³ M. Plett, "Magnetic Field Models", in *Spacecraft Attitude Determination and Control*, edited by James R. Wertz (D. Reidel, Dordrecht, 1985).

BILINEAR MODELING AND NONLINEAR ESTIMATION *

Thomas A.W.Dwyer III Fakhreddine Karray
Department of Aeronautical and Astronautical Engineering
University of Illinois ,Urbana,IL 61801
and
William H. Bennett
Techno-Sciences,Inc. 7833 Walker Drive,Greenbelt,MD 20770

Abstract: In This paper we illustrate new methods of online nonlinear estimation applied to the lateral deflection of an elastic beam from on board measurements of angular rates and angular accelerations. We contrast the development of the filter equations, together with practical issues of their numerical solution as developed from global linearization by nonlinear output injection with the usual method of the the extended Kalman filter(EKF). We show how nonlinear estimation due to gyroscopic coupling can be implemented as an adaptive covariance filter using off-the-shelf Kalman filter algorithms. The effect of the global linearization by nonlinear output injection is to introduce a change of coordinates in which only the process noise covariance is to be updated in online implementation. This is in contrast to the computational approach which arises in EKF methods arising by local linearization with respect to the current conditional mean. We also highlight processing refinements for nonlinear estimation based on optimal ,nonlinear interpolation between observations. In these methods the extrapolation of the process dynamics between measurement updates is obtained by replacing a transition matrix with an operator spline that is optimized off-line from responses to selected test inputs .

*Supported in part by SDIO/IST and managed by AFSOR under contract F49620-87-C-0103, and by NASA grant NAG-1-613

1 Introduction

In this paper, a new nonlinear, nonparametric method is proposed for off-line modeling and on-line estimation of nonlinear dynamic systems. For illustration, it is applied to the estimation of the deformation of an elastic structure, undergoing rapid rotational maneuvers.

In these circumstances, the structural stiffness and damping coefficients depend on the angular acceleration $\dot{\omega}$, the angular rate ω and the square of the angular rate. In the single axis case, the excitation of the structure is represented by the vector $u^T = (\dot{\omega}, \omega^2, 2\omega)$, to which the structural dynamics responds as a "bilinear" (i.e., parametrically excited) system. A similar technique for multiaxial rotations yields a bilinear model with respect to matrix valued excitations.

Two methods of estimation and modeling are combined to achieve deformation state determination:

- A method based on a feedback linearized procedure which gives an estimate by a filter constructed from the equivalent linear dynamics, which is faster than the extended Kalman filter.
- The modeling of the deformation state of the structure by means of a Volterra series interpolator.

2 Simplified Model of a Deformable Structure and Equations of Motion

For purposes of illustration of the principles involved, the structure will consist of a primary mirror, attached to a spacecraft (containing the hardware of the slewing controller), and a secondary mirror attached to the central one in the shape of a Cassegrain telescope by means of massless links. The primary mirror structure will also be regarded as attached to the spacecraft by means of a massless link. Equivalently the same model can be thought to represent a laser beam expander, as in Figure 1. More realistic models, such as in [1] or [2], exhibit the same form of interaction between the rotational and vibrational dynamics. The simplified telescope part of the structure can itself be modeled as a system of two masses attached together by a single "equivalent" link, with "equivalent" stiffness and damping coefficients, so that the same restoring and dissipation forces at the secondary are obtained as if with more than one link. The modeling of such a deformable body is

summarized in Figure 2 .

If one takes now only the vibrational equation of motion ,and set the rotation around a single axis \vec{b}^3 ,i.e, $\vec{\omega} = \dot{\theta}\vec{b}^3$,and if the translational acceleration term is substituted from the translational equation, then one finds:

$$M\ddot{\mathbf{y}} + (C + 2\dot{\theta}\bar{J}M)\dot{\mathbf{y}} + (K + (\ddot{\theta} + \bar{J}\dot{\theta}^2)\bar{J}M)\mathbf{y} + (\ddot{\theta} + \dot{\theta}^2\bar{J})\bar{J}M\rho = \mathbf{f} \quad (1)$$

where \bar{J} is not an inertia term, but rather an augmented symplectic matrix, made of blocks $\begin{pmatrix} 0 & -1 \\ 1 & 0 \end{pmatrix}$ while M is a modified structure mass matrix to account for contributions due to translation, and ρ is the $2n \times 1$ matrix components of the vectors ρ_i from the undeformed appendage mass centers. Here \mathbf{y} denotes the $(2n \times 1)$ (for planar motion or $(3n \times 1)$ for out of plane motion) matrix of deflection coordinates of the center of mass of n appendages from their undeformed positions, $n = 2$ in the case of the secondary mirror and the spacecraft platform regarded as appendages of the primary.

\mathbf{f} is the $(2n \times 1)$ (say, 4×1 here) matrix of body coordinates of external forces acting on the centers of mass of the n appendages.

All other notations used are found in [12],[13].

Let now η be a new variable such that

$$\eta = M(\mathbf{y} + \rho) \quad (2)$$

and let

$$\tilde{C} = CM^{-1} \quad (3)$$

$$\tilde{K} = KM^{-1} \quad (4)$$

as well as

$$\mathbf{u}^T = (\dot{\omega}, \omega^2, 2\omega) \quad (5)$$

Then the vibrational equation of motion becomes:

$$\ddot{\eta} + (\tilde{C} + u_3\bar{J})\dot{\eta} + (\tilde{K} + u_1\bar{J} + u_3\bar{J}^2)\eta = \mathbf{f} + K\rho \quad (6)$$

This transformed equation can also be written in the bilinear form ,which will be used frequently in the following sections,

$$\dot{\mathbf{X}} = A\mathbf{X} + B(\mathbf{X})\mathbf{u} + \mathbf{b} \quad (7)$$

where:

$$A = \begin{pmatrix} [0] & [I] \\ [-\tilde{K}] & [-\tilde{C}] \end{pmatrix} \quad (8)$$

$$B(\mathbf{X}) = \begin{pmatrix} [0] & [0] & [0] \\ \bar{J}\mathbf{X}_1 & \bar{J}^2\mathbf{X}_1 & \bar{J}\mathbf{X}_2 \end{pmatrix} \quad (9)$$

and

$$\mathbf{b} = \begin{pmatrix} [0] \\ \mathbf{f} + K\rho \end{pmatrix} \quad (10)$$

while \mathbf{X}_1 and \mathbf{X}_2 are the vector components of the state vector $\mathbf{X} = (\eta^T, \dot{\eta}^T)^T$.

This simplified model, insofar as the links are regarded to be mass-less, exhibits all the coupling effects between slewing motion and vibrational motion. A distributed model under the assumption of symmetry about the mass center also yields product terms between $\dot{\theta}^2$ and structural deformations, and can be found in Chapter 9 of the book by Junkins and Turner[3]. That model of a symmetric four appendage spacecraft can also be used to illustrate the procedures being developed in this study, if desired, although damping must be present, so that the matrix A above will be stable. A slewing Timoshenko beam model likewise exhibits this gyroscopic coupling effect, and also accounts for damping, so that A becomes stable, as found in [4].

3 Estimation of the state by means of observers

This part of the estimation technique will deal mainly with updating the state from sensor data.

3.1 Extended Kalman filter formulation

Usually, when one deals with a nonlinear system of which the state variables cannot all be observed (or are corrupted with noise), then the most commonly used method of filtering or smoothing is the extended Kalman filter formulation [5]. Let the dynamical system be modeled as shown,

$$\begin{cases} \dot{x} = f(x) + G(x)u^* + G(x)\xi \\ y = h(x + \nu) \end{cases} \quad (11)$$

where u^* is the deterministic (mean) part of the input, ξ is a zero mean input noise, and h is defined in our case as $h = (h_1^T, h_2^T)^T$, where

$$\begin{cases} h_1(\cdot) = M^{-1}(\cdot - \mathbf{n}) \\ h_2(\cdot) = M^{-1}(\cdot) \end{cases} \quad (12)$$

Let $R_i\delta(t - \tau) = E[\nu_i(t)\nu_i(\tau)^T]$ be the covariance matrix of the sensor noise vectors ν_i , with $R = \text{diag}(R_1, R_2)$ and let $Q\delta(t - \tau) = E[\xi(t)\xi(\tau)^T]$ be

the covariance matrix of the actuator noise with ν_i and ξ presumed to be uncorrelated for simplicity.

The propagation error matrix is defined by P , which satisfies the following Riccati differential equation along the estimated state trajectory \hat{x} :

$$\begin{aligned} \dot{P} = & \left[\frac{\partial f}{\partial x} \right]_{\hat{x}} P + P \left[\frac{\partial f}{\partial x} \right]_{\hat{x}}^T + G(\hat{x}) Q G(\hat{x})^T - \\ & P \left[\frac{\partial h}{\partial x} \right]_{\hat{x}}^T R^{-1} \left[\frac{\partial h}{\partial x} \right]_{\hat{x}} P \end{aligned} \quad (13)$$

\hat{x} can be expressed as an observer,

$$\begin{cases} \dot{\hat{x}} = f(\hat{x}) + G(\hat{x})u^* + K(y - \hat{y}) \\ \hat{y} = h(\hat{x}) \end{cases} \quad (14)$$

where K is the extended Kalman gain, and is defined as follows:

$$K = P \left[\frac{\partial h}{\partial x} \right]_{\hat{x}}^T R^{-1} \quad (15)$$

A procedure [6] based on a change of variables, in preliminary studies gave a faster computation time. This procedure is outlined next.

3.2 Feedback linearized procedure:

The idea is to change the state configuration of the original system, which has the particular form below:

$$\begin{cases} \dot{x}_1 = F_1(x_1)x_2 \\ \dot{x}_2 = F_2(x)(u^* + \xi) + f_2(x) \end{cases} \quad (16)$$

$$\begin{cases} y_1 = h_1(x_1 + \nu_1) \\ y_2 = h_2(x_2 + \nu_2) \end{cases} \quad (17)$$

By using the change of variables $x'_1 = x_1$, $x'_2 = F_1(x_1)x_2$, $u' = \dot{x}_1 = F_2(x)u^* + f_2(x)$ and $y'_1 = h_1^{-1}(y_1)$, $y'_2 = h_2^{-1}(y_2)$ one gets

$$\begin{cases} \dot{x}'_1 = x'_2 \\ \dot{x}'_2 = u'^* + \xi' \end{cases} \quad (18)$$

where $\xi' = F_1 F_2 \xi$ and $\nu'_i = F_1 \nu_i$, so that the covariance of ξ' is approximated by

$$Q' = F_1(\hat{x}_1) F_2(\hat{x}) Q F_2(\hat{x})^T F_1(\hat{x}_1)^T \quad (19)$$

while that for ν'_i is approximated by

$$R'_i = F_1(\hat{x}_1)R_i F_1(\hat{x}_1)^T \quad (20)$$

Then the new error covariance matrix propagation is derived from the following Riccati differential equation:

$$\begin{aligned} \dot{P}' = & \begin{pmatrix} [0] & [I] \\ [0] & [0] \end{pmatrix} P' + P' \begin{pmatrix} [0] & [0] \\ [I] & [0] \end{pmatrix} + \\ & \begin{pmatrix} [0] \\ [I] \end{pmatrix} Q' \begin{pmatrix} [0] & [I] \end{pmatrix} - \\ & P' \begin{pmatrix} [I] & [0] \\ [0] & [I] \end{pmatrix} R'^{-1} \begin{pmatrix} [I] & [0] \\ [0] & [I] \end{pmatrix} P' \end{aligned} \quad (21)$$

The observed deformation state is also propagated in the usual manner:

$$\begin{aligned} \dot{\hat{x}}'(t) = & \left\{ \begin{pmatrix} [0] & [I] \\ [0] & [0] \end{pmatrix} - K' \begin{pmatrix} [I] & [0] \\ [0] & [I] \end{pmatrix} \right\} \hat{x}'(t) + \\ & \begin{pmatrix} [0] \\ [I] \end{pmatrix} u' + P'(t, t_0) R'(t)^{-1} \begin{pmatrix} h_1^{-1}(\cdot) & [0] \\ [0] & F_1 h_2^{-1}(\cdot) \end{pmatrix} y(t) \end{aligned} \quad (22)$$

where the innovation process gain is now given as follows:

$$K' = P'(t, t_0) R'(t)^{-1} \quad (23)$$

For the case of single axis slew-induced structural deformation estimation one has $F_1 = I$ and $F_2 =$ lower half of $B(X)$ defined by equation (2). In particular, one finds $R'_i = R_i$, so that, in contrast to the extended Kalman filter, only the P' -independent forcing term of the equation (21) given by Q' has to be updated, all coefficients being now constants. In dealing with this procedure a 25% increase in speed, with comparable accuracy has been found in preliminary simulations discussed below. The problem in using either one of those two estimation techniques (even the faster one) in more realistic models than the example used here, is the high dimensionality of the filter then required, which may not be accommodated by the on-board data processing rate, causing estimation delays.

C-4

3.3 Estimation Examples:

A simplified model of a beam expander was represented by a primary mirror mass elastically linked to a secondary mirror mass according to the simplified model outlined in Section 2. Restoring forces and dissipative forces proportional to relative secondary mirror motion were modeled at the secondary. The structural parameters are found in the companion example in Subsection 5.1. A piecewise constant angular acceleration was commanded, representing the acceleration-deceleration profile of a minimum time retargeting maneuver. The commanded angular acceleration profile was:

$$\dot{\omega}(t) = \begin{cases} 0.3 \text{rad.s}^{-2} & \text{if } 0 \leq t \leq .5(s); \\ -0.3 \text{rad.s}^{-2} & \text{if } .5(s) \leq t \leq 1(s); \end{cases}$$

Presumed angular accelerometer and gyro noise covariances were transformed into equivalent process noise for the feedback-linearized filter, with the additional simplification of neglecting a square noise term corresponding to the second entry $u_2 = \omega^2$ of the equivalent input u . Presumed strain gauge sensor noises were taken from the literature. The sensor noise covariance matrix was modeled as a diagonal matrix with all diagonal elements equal to 0.00018. Likewise the input covariance for u_1 was 0.000005 and for u_3 was 0.00001. The input covariance related to the input u_2 was supposed to be negligible with respect to the other two. Two simulations were made, each one of them to illustrate the two methods of estimation described above. The first simulation was made without active bias suppression, i.e. $\mathbf{f} = \mathbf{0}$ in equation (10), the results being shown in Figures 3, 4. The second simulation was made with the use of bias suppression making $\mathbf{b} = \mathbf{0}$ in equation (7) by letting $\mathbf{f} = -\mathbf{K}\rho$, the results being shown in Figures 5, 6.

4 Off Line Modeling

In this section the method of Optimal Bilinear System Interpolation is used. In this technique the dynamical system is represented in bilinear form (by active suppression, if needed, of the bias term \mathbf{b}),

$$\begin{cases} \dot{\mathbf{X}} &= \mathbf{A}\mathbf{X} + \mathbf{B}(\mathbf{X})\mathbf{u} \\ \mathbf{y} &= \mathbf{c}^T\mathbf{X} \end{cases} \quad (24)$$

where $\mathbf{B}(\mathbf{X}) = [\mathbf{B}_1\mathbf{X} \mid \mathbf{B}_2\mathbf{X} \mid \dots]$. This also means:

- The (I/ O) behavior is highly nonlinear.
- The model is high dimensional if arising from Carleman linearization.
- There is no clean ARMA model for system identification.

Then, by using optimal interpolation one finds:

- A closed form, circuit-implementable, reduced order, decoupled model which is also bilinear: cf. Figure 7.
- (I/ O)-based system identification can be used to tune the model to known responses to designer-selected typical excitations.
- The dimension of the new system model is equal to the number of test signals.

In the present application, the model is "a priori" bilinear by the choice made for the inputs, so that the dimension is that of the structural model, here given by the number of mass points. For more realistic structural models, the filter dimension would nevertheless be high. Rather than tolerate the time delay found in the previous techniques of estimation, the method of operator spline interpolation can be used, to find the deflection amount between observations. The input-output (I/O) operator V ,

$$V : u \rightarrow y \quad (25)$$

from the excitation vector u to an output vector y (such as ν given by equation (2)) is imbedded in a Hilbert space of (I/O) operators of candidate bilinear systems, equipped with a reproducing kernel, see equation (31)

$$K_t(u, v) = \exp \int_{t_0}^t u^T(s) R^{-1} v(s) ds \quad (26)$$

where the weight matrix R is determined by eigenvalues of A in equation (24), which in the context of the present application corresponds to bounds on the structural frequencies. An interpolator of the form

$$\hat{V}_i(u) = \sum_i c_i(t) K_i(u, u^i) \quad (27)$$

is constructed, tuned so that the structural responses to preselected test inputs u^i are recorded, and optimally interpolating at system level the responses to other excitations in the signal class.

If the recorded system responses y^i to the test input u^i are reliably known, the 'tuned' coefficients c_i are obtained by solving the matrix equation

$$G(t)c(t) = \bar{y}(t) \quad (28)$$

where $c(t) = \text{col}\{c_i\}$, $\bar{y}(t) = \text{col}\{y^i(t)\}$ and $G(t) = \{K_i(u^i, u^j)\}_{i,j}$. A more complex matrix equation yields the c_i for uncertain y^i : cf. [7], [8], [9]. The optimization leading to the functional interpolator \hat{V}_i is formulated as a minimization of the maximum distance between the interpolating operator and any candidate operator that matches the experimental input-output signals. If the system data are not accurate, a weighted minimization that does not require exact matching of system responses can also be used. This minimization is carried out in a Hilbert space of input-output operators equipped with a weighted "Fock space" scalar product which is the Hilbert sum of the causal (i.e., with lower triangular domains of integration) L^2 scalar products of the kernels of the Volterra series of the operators in question, for which K_i is the reproducing kernel. The general method is discussed in [9], although causality was differently implemented there, since symmetric kernels were used.

The Hilbert space structure for m inputs (here $m = 3$) is defined as follows: let

$$\begin{aligned} h_{n,i_1,\dots,i_n}(t, t_1, \dots, t_n) &= c^T \exp\{(t - t_1)A\} B_{i_1} \dots \\ &\dots \exp\{(t_{n-1} - t_n)A\} B_{i_n} \exp(t_n A) X(0) \end{aligned} \quad (29)$$

where $B(X) = [B_1(X) | B_2(X) | \dots]$ and $i_1, \dots, i_n \in \{1, \dots, m\}$.

These are the Volterra kernels for $u_{i_1}(t_1), \dots, u_{i_n}(t_n)$ so long as triangular integration is used as in equation (30). Then the inner product is given as shown ,

$$\langle V_i, V_l \rangle = \sum_n \sum_{i_1} \dots \sum_{i_n} r_{i_1} \dots r_{i_n} \int_0^t \int_0^{t_1} \dots$$

$$\int_0^{t_n} h_{n,i_1,\dots,i_n}(t, t_1, \dots, t_n) h_{n,i_1,\dots,i_n}(t, t_1, \dots, t_n) dt_n \dots dt_1 \quad (30)$$

with designer-selected weights $r_i > 0$ corresponding to $R = \text{diag}\{r_i\}$, which yields the reproducing property:

$$\langle V_t, K_t(u, \cdot) \rangle = V_t(u) \quad (31)$$

The Volterra series for a bilinear system will yield a bounded norm $\langle V_t, V_t \rangle$ provided the weights r_j are chosen so that

$$\sum_i r_i \|B_i\|^2 \leq \frac{2a}{N} \quad (32)$$

where $N = \text{dim}X$ and " a " is a bound on the real parts of the eigenvalues of A , so that $\| \exp(At) \|^2 \leq N \exp(-2at)$. The bound (32) is obtained after cancellation of intermediate exponents in the factors $\exp\{-2a(t_{i-1} - t_i)\}$, which can be interchanged when computing L^2 bounds of $|h_{n,i_1,\dots,i_n}(t, t_1, \dots, t_n)|$, to guarantee negativity of the remaining exponential coefficients. The same bound is sufficient for having $|\hat{y}(t)| = |\hat{V}_t(u)| \rightarrow 0$ as $t \rightarrow \infty$ when u is L^2 (Square integrable), as is found by use of the reproducing property (31) (Lower bounds are also needed when the inputs are not L^2 , but are bounded almost everywhere: Dwyer, [7]). The advantages of such modeling are:

- The model dimension is equal to the number of test inputs.
- The modeling error is distributed throughout the chosen input signal class (i.e by frequency or amplitude), rather than depending on nearness to a single reference input.
- The interpolated signal(response) can be proven to converge asymptotically to the true system response for any (unknown) excitation in the chosen signal class.

In this technique of modeling, the real data $\eta^{(i)}$, $\dot{\eta}^{(i)}$ can be recorded by exciting the real system with (constant or nonconstant) test inputs to construct the interpolator. The test inputs can be chosen to approximate the expected excitations of the system. Thus, the real system time responses are used for model matching, rather than responses synthesized from the mathematical

model.

The problem with this technique, however, lies in the fact that storage of curves is required in order to compute the c_i 's. The number of stored curves is equal to $m \times k \times I^N$, where m is the number of test inputs, k is the dimension of the output vector \mathbf{y} , N the dimension of the state to be modeled and I is the number of possible initial values of each component. This difficulty does not allow the system to run in real time: e.g., for the case of n point masses linked by massless but elastic connections one has $N = 2n$ and $k = n$ when measuring deflections or $k = N = 2n$ if full state information is required in the planar motion case.

5 Interpolator-Based Estimation:

In this section, the two last techniques are combined to create a more effective one by making use of the transition matrix spline of the bilinear system of the model:

$$\hat{\eta}(t) = \hat{\Phi}(t, t_k) \hat{\eta}(t, t_k) \quad (33)$$

In fact, the matrix-valued operator spline $\hat{\Phi}$ interpolates the transition matrices Φ_i corresponding to the bilinear system model excited by constant or piecewise constant test inputs $u^{(i)}$. This permits the construction of the response of the real time system in piecewise closed form, thereby replacing response curve storage by an analytic transition matrix generator, rather than the construction of the coefficients interpolator c_i from the output test signals $\mathbf{y}^T = (y^1, y^2, \dots, y^m)$.

One gets each entry c_i^{pq} of the matrix valued spline coefficients c_i by letting $\bar{y}^i = \Phi_i^{pq}$ in equation (28) where Φ_i^{pq} is the (p, q) -entry in the transition matrix with constant $u^{(i)}$:

$$\Phi_i = \exp\left\{(A + \sum_j B_j u_j^{(i)})t\right\} \quad (34)$$

The interpolated transition matrix is then used to update between observations the structural state estimates obtained from an adaptive covariance filter based on a globally feedback-linearized transformation (seen in Section 3.2) of the bilinear structural model.

This last technique has the following features:

- $\hat{\Phi}$ is open loop, with $\hat{\eta}$ made to match the real system at discrete

intervals by re-initializing:

$$\begin{pmatrix} \hat{\eta}(t) \\ \dot{\hat{\eta}}(t) \end{pmatrix} = \hat{\Phi}(t, t_k) \begin{pmatrix} \hat{\eta}(t_k) \\ \dot{\hat{\eta}}(t_k) \end{pmatrix} \quad (35)$$

In contrast, the direct modeling of the I/O operator

$$\hat{\eta} = \sum_i c_i(t) \exp \int^t u^T R^{-1} u^i dt \quad (36)$$

continuously tracks the true system time responses $\eta^i(t)$, but in this case $c_i(t)$ cannot be generated analytically and must be computed off-line.

- The presence of an additive input does not give rise to a steady state tracking error observed in the earlier literature when additive as well as multiplicative inputs are present, as is the case for rapidly slewing structures. Indeed, a convolution correction based on $\hat{\Phi}$ can be added, eliminating the need for active suppression of the bias term \mathbf{b} in equation (7).

- The number of curves to be generated is only $m \times N^2$ instead of $m \times k \times I^N$, (where again $N = 2n$ for the example of a structure composed of point masses connected by elastic appendages and in plane motion).

- The possibly high dimensional recursive filter can run at a slower sampling rate chosen to be consistent with on board CPU capabilities.

5.1 Interpolation Example

An interpolator was designed for the same two bodies beam expander model previously described: The interpolator was optimized for input vectors $u^T = (u_1, u_2, u_3)$ of the form $(constant, 0, 0)$, $(0, constant, 0)$ and $(0, 0, constant)$, chosen with a positive constant during the first half of a 1 second nominal minimum time rotation, and negative during the second half, for the first test input vector. The same positive constant was chosen throughout the 1 second re-pointing for the second and third test input vectors, this qualitatively correspond to the nominal angular motion where $\dot{\omega}$ is a square wave beginning at $+0.3$ and reversing, which yields positive (though not constant) values for ω_2 and 2ω : cf. Eq.(5). The constants were selected for boundedness of the interpolator according to [7],[8]. For the sake of convergence of the interpolator to the actual output of the system, and in the case of applying test inputs which are not square integrable, the matrix R described above in the reproducing kernel analytical form should have diagonal elements satisfying the following condition:

$$a/m - \sqrt{(a/m)^2 - \|B_i\|^2 N \lambda_i^2} \leq$$

$$r_i N \|B_i\|^2 \leq a/m + \sqrt{(a/m)^2 - \|B_i\|^2 N \lambda_i^2} \quad (37)$$

If A is $N \times N$, $\|B_i\|^2 = \sum_{pq} b_{i,pq}^2$ where $b_{i,pq}$ is the (p, q) element of B_i , then λ_i , which is the upper limit of the i -th test input component, must be chosen to satisfy the bounds below,

$$0 < \lambda_i < a/m\sqrt{N}\|B_i\| \quad (38)$$

where a is an upper bound on the real parts of the eigenvalues of the matrix A , and m is the number of test inputs applied to the interpolator. Indeed, the bound (41) allows selecting positive r_i 's in the inequality (37), which itself occurs in obtaining bounds on $\hat{y}(t) = V_t(u)$ from equation (34), to guarantee $\hat{y}(t) \rightarrow 0$:cf.[6]

In case the applied test inputs are square integrable, as will be chosen on the example, one needs only a simpler form of bounds for r_i described as follows, which implies the inequality (32) if all r_i are the same,

$$0 \leq r_i N \|B_i\|^2 \leq 2a/m \quad (39)$$

The data used to drive this example are very near to those of a space based laser model:

$$J_0 = 20,556 \text{ kg.m}^2, m^0 = 10,720 \text{ kg}, m^1 = 152 \text{ kg}, \rho^1 = (0, 14.421 \text{ m})^T$$

$$K = \begin{pmatrix} 1642 & 121.6 \\ 121.6 & 1355.8 \end{pmatrix}, C = \begin{pmatrix} 162 & 120 \\ 120 & 1357 \end{pmatrix}$$

The nondiagonal form of the above matrices K and C is due to the fact that the two links that hold the small mirror in the top can be regarded as an equivalent link with equivalent stiffness and damping matrices, as shown in [13].

Now by applying those data to the system and by the choice of *constant* = .3 in the test inputs, one finds $0 \leq r_i \leq 1/12$ where $r_i = r$ for all i , giving $R = \text{diag}(r_i) = r[I]_{m \times m}$. Two series of simulations were made. In each one of them two alternatives, namely, bias elimination, i.e., $\mathbf{b} = \mathbf{0}$ or no external tip forces, i.e., $\mathbf{f} = \mathbf{0}$ are considered. In the first series of simulations the interpolator was used over the entire minimum time 1second maneuver and thereafter. The results for the case of lateral deflection of the appendage are shown in Figures 8,9. It is important to notice here that in case of bias presence, a numerical convolution product was used with the original

transition matrix $\Phi(t, t_k)$ as well as with the interpolated transition matrix $\hat{\Phi}(t, t_k)$ for the sake of error comparisons. "Original" in the plots means the numerical solution of Eq.(1), "discrete" means the numerical computation of $\Phi_u(t, 0)x(0) + \Phi_u(t, \cdot) * b$. One last numerical difficulty was observed, in addition to care needed in generating the contribution from b by convolution (at least in this unusual beam expander example). That was the singularity of Eq.(28) at $t=0$ as already discussed in [9], which caused numerical unreliability during the first 0.25 seconds of this motion. Thus "transient error" is consistent with the "adaptive" nature of the interpolator which must "learn" from the system response to alleviate this numerical difficulty, in the other series the state estimated in the example of section 3.3 was used to re-initialize the interpolator each .5s. The results are shown in Figures 10,11. The re-initialization from the estimated state at given moments yielded better results than when using the same interpolator throughout.

6 Concluding Remarks

Filter algorithms combine the propagation of measurements "between" observations with updating of measurements "across" observations. Such updating to account for new observations has been shown here to be obtainable from an estimator based on a globally feedback-linearized model of a nonlinear process.

In case nonlinear transformation of the observed part of the process state is required, it was shown that the associated matrix Riccati differential equation for the propagation of the estimation error covariance needs to be updated only in its "driving" term, given by the process noise covariance. In contrast, all the coefficients of the Riccati equation for the corresponding extended Kalman filter must be updated, so that considerable CPU time is saved by pre-linearization, although the filter dimension is the same. Dimension reduction between measurements is therefore still desirable, motivating the next part of this work, which is reviewed below. If the process dynamics is "parametrically excited", e.g. by gyroscopic coupling, it was then shown how the process state can be propagated between observations by interpolation of the input-output operator that maps the process excitation to the (time-varying) state transition matrix. This interpolator was shown to be simultaneously optimized to match the measured system response to a set of pre-selected "test inputs", which if chosen piecewise constant can also be encoded analytically in closed form. Since the interpolator dimension is determined by the dimension of the pro-

cess state ,it is therefore faster to periodically re-start the interpolator at the rate the feedback linearized filter(or any other) can process full state information, rather than be tied down to the full order filter processing rate. New results were then given on the application of the method to the on-line estimation of transverse deflections of a rapidly slewing, gyroscopically slew-coupled beam expander,previously reported in [12]. Applications to line of sight disturbance error bound estimation in sliding control following [10] are also outlined in [11]. the interpolation technique may also be used to update observations for multi-axis motion of multibody systems , but this latter work is still undeveloped.

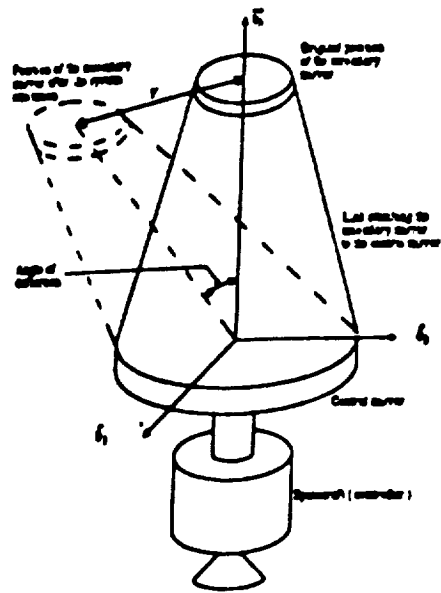
REFERENCES

1. T.R Kane, R.R.Ryan and A.K.Banerjee,"Dynamics of a Cantilever Beam Attached to a Moving Base." *J. of Guidance, Control and Dynamics*,v.10,No.2(Mar-Apr. 1987),pp.139-151.
2. J. Baillieul,"Linearized Model For The Control Of Rotating Beams",*Proc IEEE CDC*, (Austin, Tx, Dec 7-9,1988),v.3,pp. 1726-1731.
3. J.L.Junkins and J.D.Turner, "Optimal Spacecraft Rotational Maneuvers" , Elsevier, 1986.
4. H.Bennett, H.G.Kwaty and G.L.Blankenship,"Nonlinear Dynamics and Control Issues for Space-Based Directed Energy Weapons",*Proc. 27th IEEE Conf on Decision and Control*,(Austin,Tx, Dec.7-9,1988).
5. A.Gelb,Ed ,"Applied Optimal Estimation", MIT Press,1974. break
6. M.S.Fadali, S.Gardner and T.A.W. Dwyer III , "Nonlinear Decoupling And Control Of Manipulators With Sensor And Actuator Noise.", *Proc. 2nd IASTED Internat Conf, on Applied Control and Idcntification* (Los An-

geles, CA, Dec.10 -12, 1986),Acta Press, Calgary, 1987.

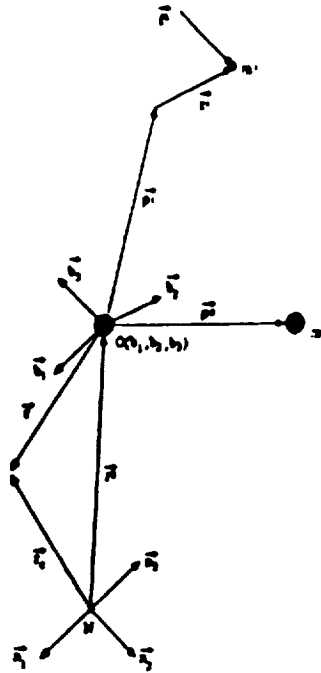
7. T.A.W. Dwyer III , "Operator Spline Methods in the Design of Non-linear Equalizers",*Proc.IEEE ISCAS* (San jose,CA,May 5-7,1986), v.2 ,pp. 701-703.
8. T.A.W. Dwyer III , "Optimal Interpolation and Smoothing Of Bilinear Systems",*Proc. ACC*(Seattle,WA, June 18-20, 1986), v. 1, pp 394-397.
9. R.J.P. de Figueiredo and T.A.W DwyerIII,"A Best Approximation Framework and Implementation for Simulation of Large-Scale Nonlinear Systems", *IEEE trans. on Circuits and Systems*,v.CAS-27, No.11 (Nov.1980), pp. 1005-1014.
10. J.J. E.Slotine, "Sliding Controller Design for Non-linear Systems", *int.J.of Control*,v.40, No.2(1984), pp.421-434.
11. T.A.W. Dwyer III and F. Karray,"Nonlinear Robust Variable Structure Control of Pointing and Tracking with Operator Spline Estimation",*Proc. IEEE International Symposium on Circuits and Systems*(Corvalis,Oregon, May 9-11,1989) Paper # SSP 15-5.
12. T.A.W. Dwyer III and F. Karray,"Nonlinear Modeling Identification and Estimation of Slew Induced Structural Deformations",*Proc. Model Determination for Large Space Systems Workshops*(Pasadena,CA, March22-24,1988) ,JPL D-5574,V3,pp860-876.
13. T.A.W. Dwyer III and F. Karray,"Bilinear Modeling and Estimation of Slew Induced Deformations", Submitted to *J. of Astronautical Sciences*.

ORIGINAL PAGE IS
OF POOR QUALITY



Simplified Design of The Space Laser Telescope Structure.

Figure 1.



Vectorial Configuration of a Deformable Discrete Structure

Figure 2.

ORIGINAL PAGE IS
OF POOR QUALITY

Extended Kalman Filter Method

Case where no forces are applied ($f=0$)

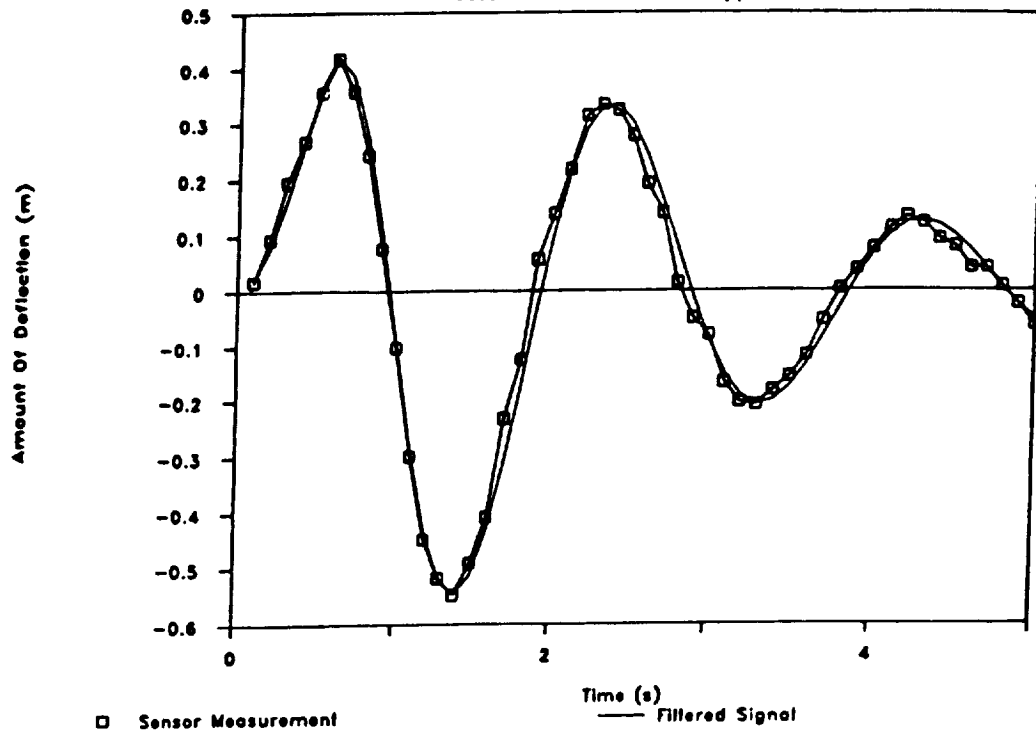


Figure 3.

Extended Kalman Filter Method

Case where no bias is present ($b=0$)

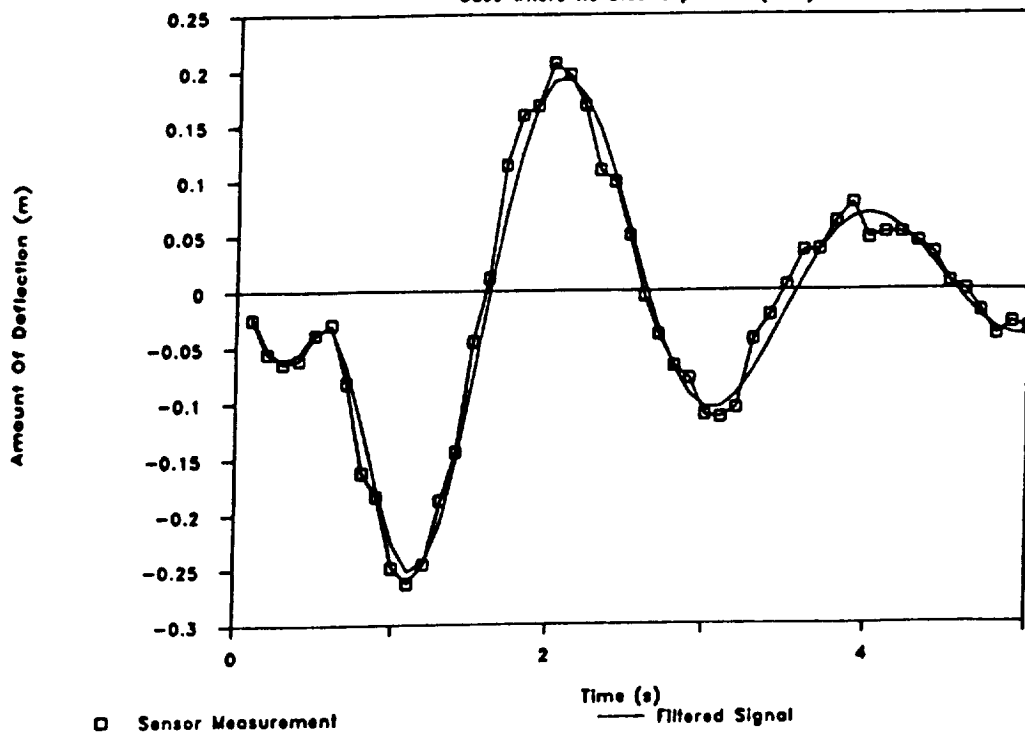


Figure 4.

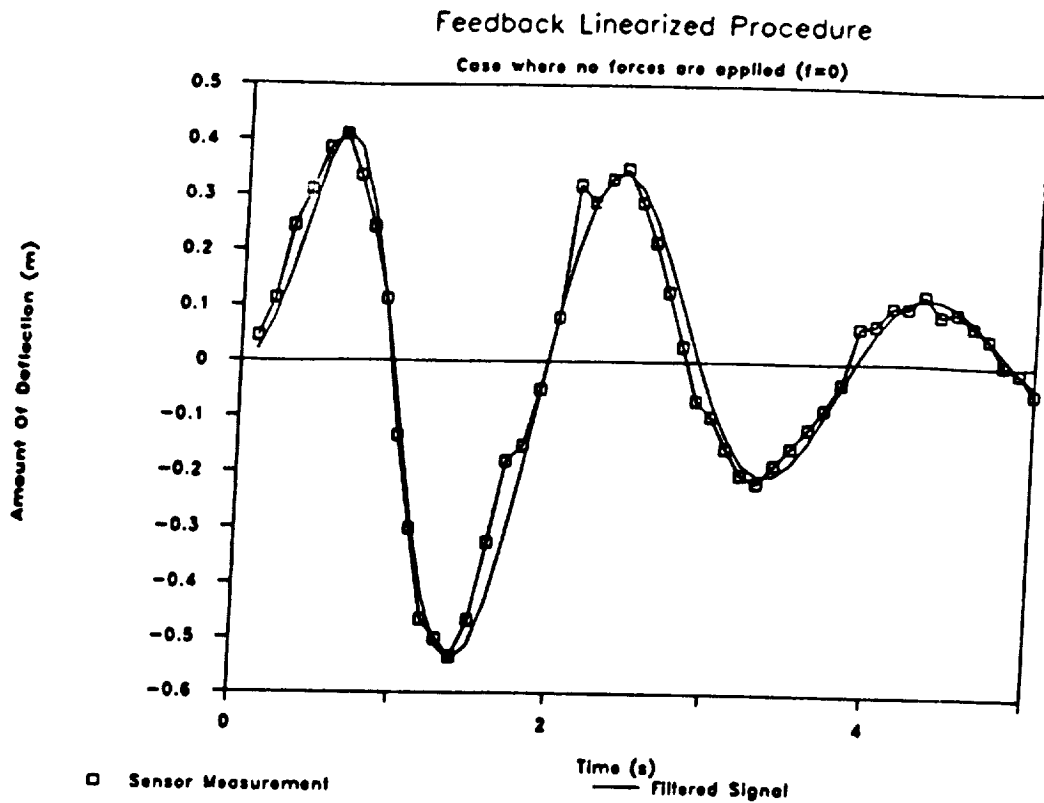


Figure 5.

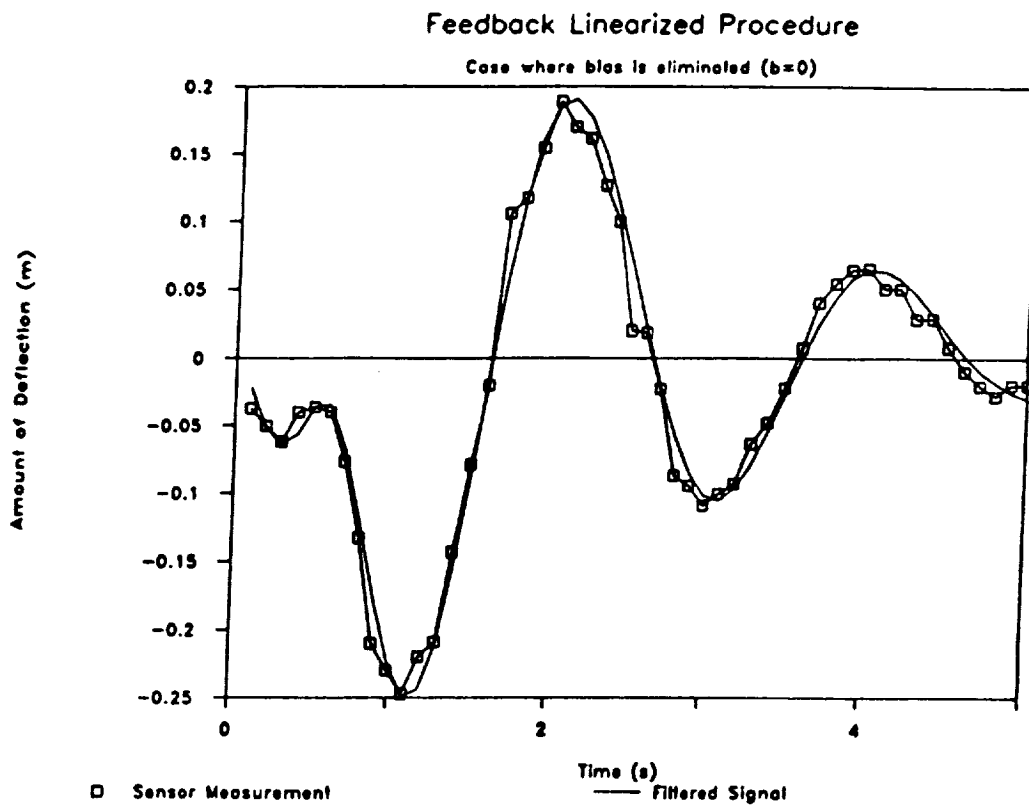
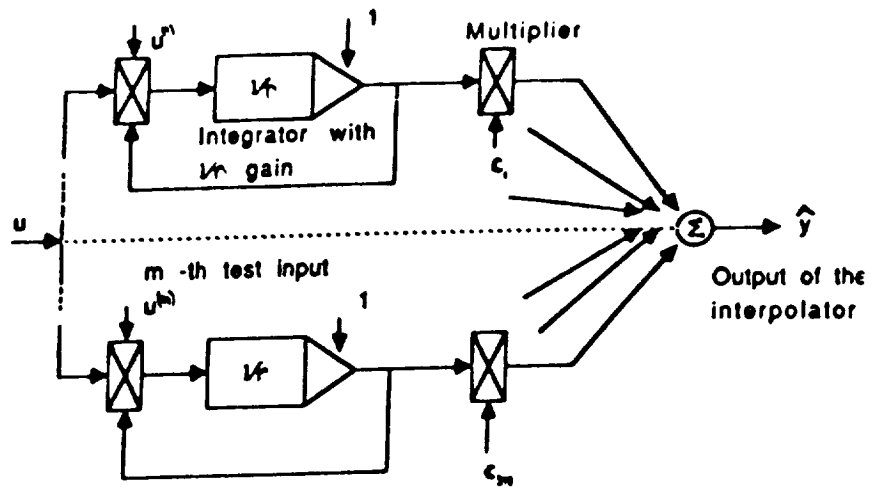


Figure 6.



Optimal Interpolator For Bilinear System

Figure 7.

Optimal Interpolation In case $b=0$

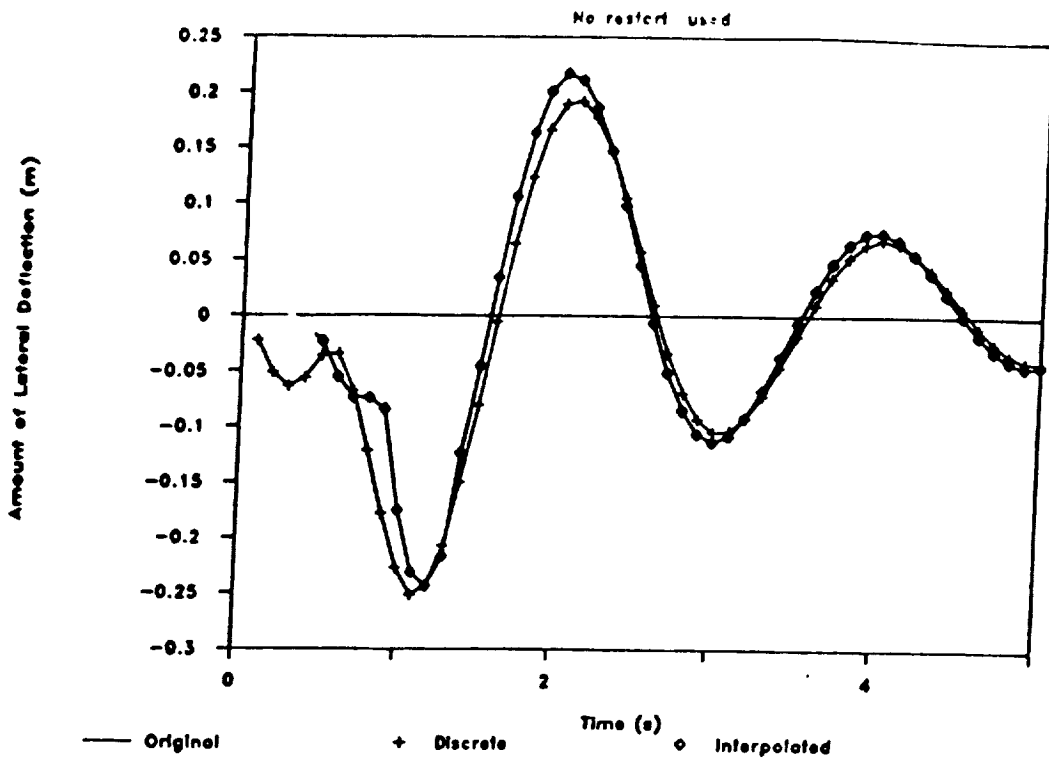


Figure 9.

Optimal Interpolation In case $f=0$

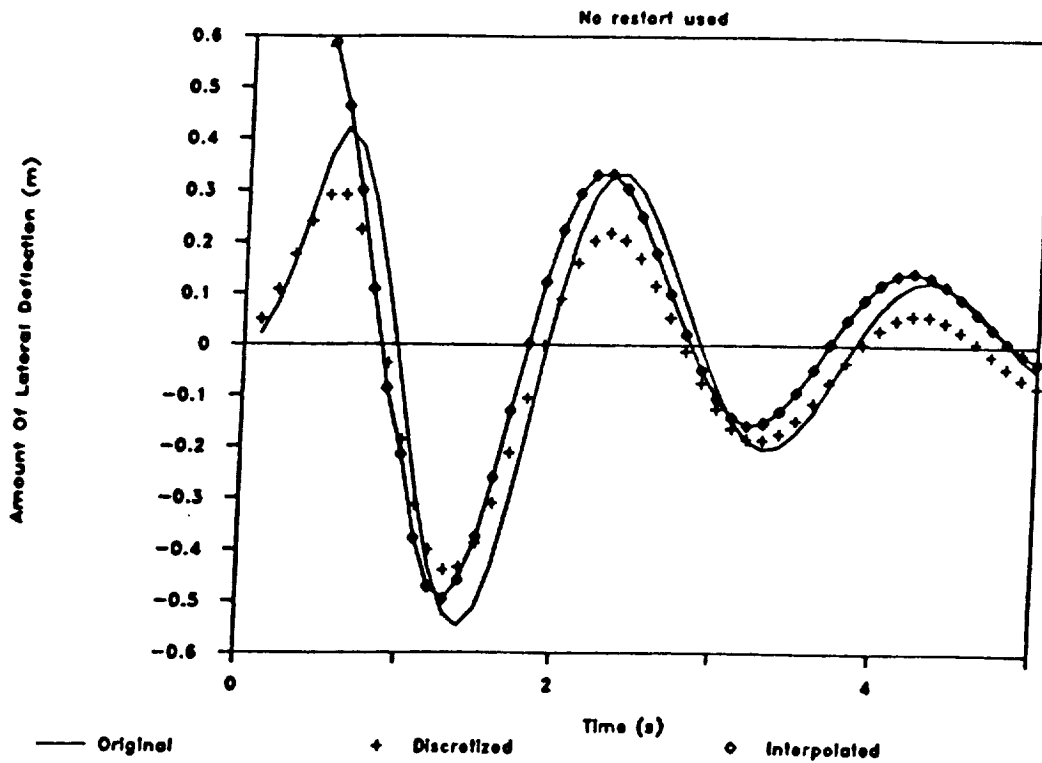


Figure 8.

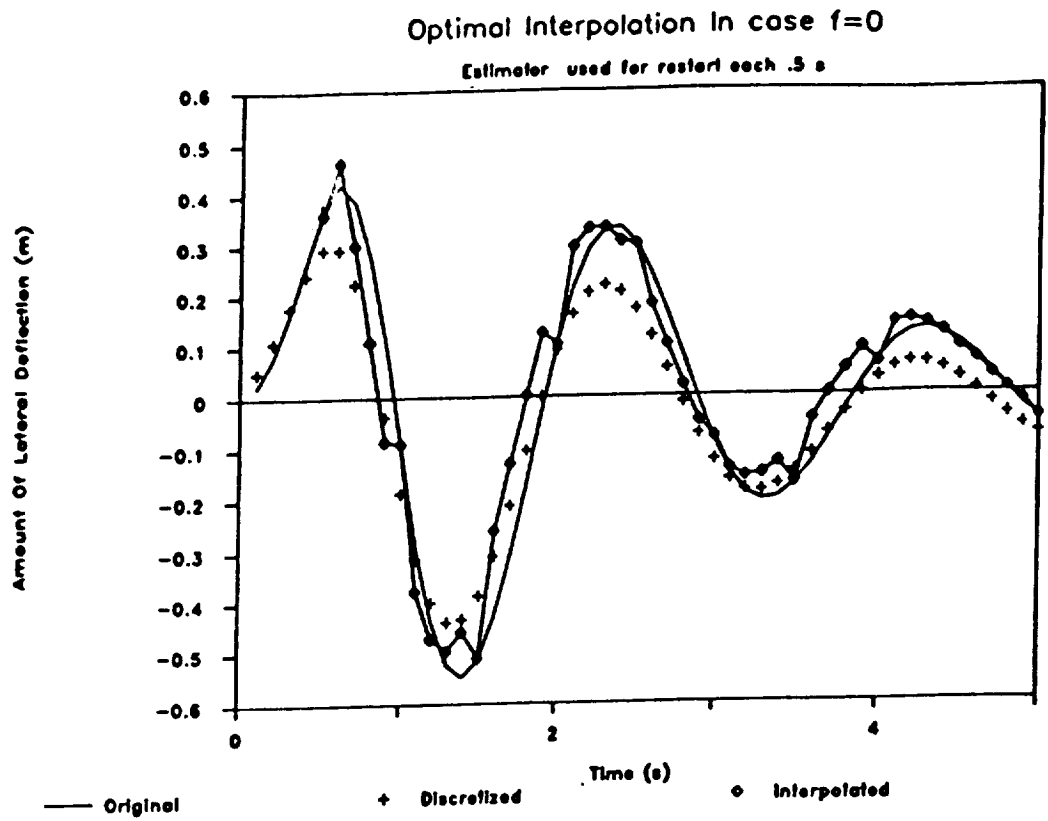


Figure 10.

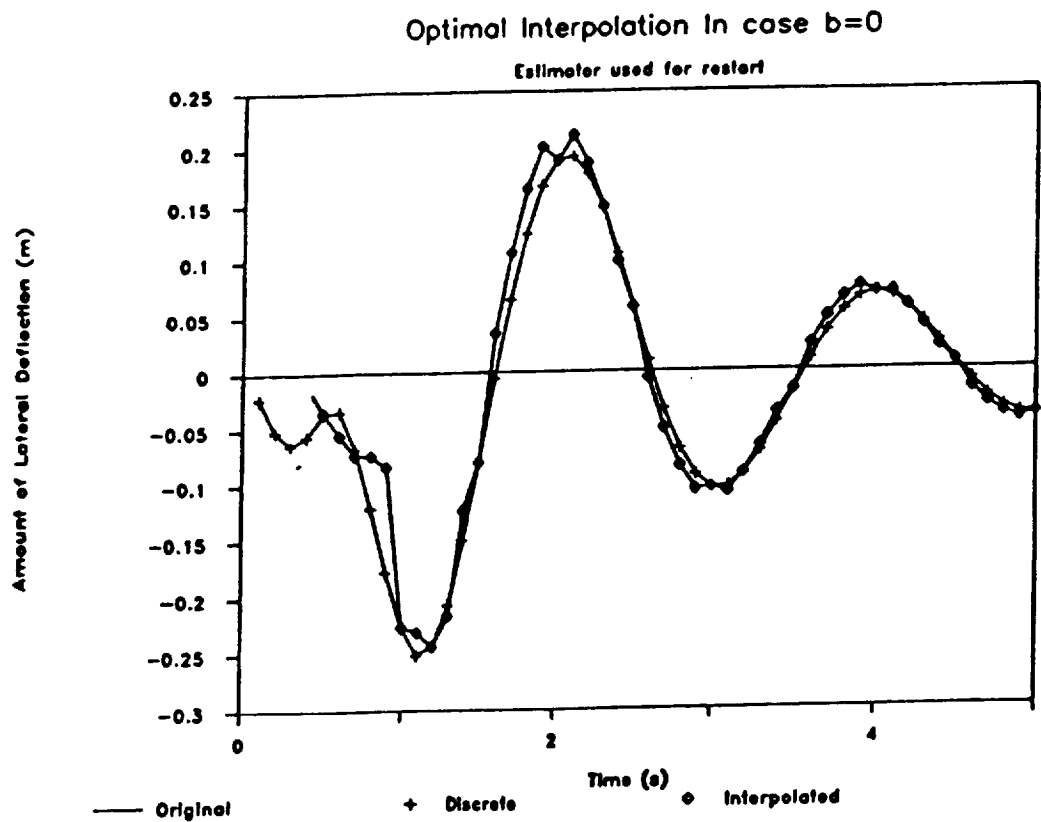


Figure 11.

EXTENSION OF EULER'S THEOREM
TO n-DIMENSIONAL SPACES

by

Itzhack Y. Bar-Itzhack*

NASA - Goddard Space Flight Center
Greenbelt, MD 20771Abstract

Euler's theorem states that any sequence of finite rotations of a rigid body can be described as a single rotation of the body about a fixed axis in three dimensional Euclidean space. The usual statement of the theorem in the literature cannot be extended to Euclidean spaces of other dimensions. Equivalent formulations of the theorem are given in this paper and proven in a way which does not limit them to the three dimensional Euclidean space. Thus, the equivalent theorems hold in other dimensions. The proof of one formulation presents an algorithm which shows how to compute an angular-difference matrix that represents a single rotation which is equivalent to the sequence of rotations that have generated the final n-D orientation. This algorithm results also in a constant angular-velocity which, when applied to the initial orientation, yields eventually the final orientation regardless of what angular velocity generated the latter. Finally, the extension of the theorem is demonstrated in a four dimensional numerical example.

* National Research Council - NASA Resident Research Associate, Flight Dynamics Analysis Branch. On Sabbatical leave from the Aeronautical Engineering Department, Technion-Israel Institute of Technology, Haifa 32000, Israel.

I. EULER'S THEOREM

In 1775 Euler published a paper on the rotation of rigid bodies [1]. In that paper, which was written in Latin, he

Theorema.

Quomodocunque sphaera circa centrum suum conuertatur, semper assignari potest diameter, cuius directio in situ translato conueniat cum situ initiali.

Fig.1: Euler's theorem on the rotation of a rigid body as it appeared in the 1775 publication.

presented the theorem whose photograph is shown in fig. 1. The theorem states the following:

In whatever way a sphere is rotated about its center, it is always possible to reckon a diameter about which a rotation brings the sphere into coincidence with its original location.

A modern formulation of this theorem states [2]:

A body set of axes at any time t can always be obtained by a single rotation of the initial set of axes.

We prefer to formulate this theorem as follows:

Regardless of the way a coordinate system is rotated from its original orientation, it is always possible to find a fixed axis in space about which a single rotation of the initial coordinates ends at the final orientation.

Euler's theorem serves as a cornerstone in attitude determination [3-9] and tracking [7,9,10]. In particular, if \hat{n} is a unit vector along the axis of rotation and θ is the angle by which the initial coordinate system has to be rotated in order to coincide with the final one, then $D(\hat{n},\theta)$, the transformation matrix from the initial to the final coordinate system, is given by [7-10]

$$D(\hat{n},\theta) = I\cos\theta + (1-\cos\theta)\hat{n}\hat{n}^T - \sin\theta[\hat{n}\times] \quad (1)$$

where I denotes the identity matrix, T denotes the matrix transpose and $[\hat{n}\times]$ denotes the cross product matrix of \hat{n} . The relationship formulated in (1) can also be expressed as follows

$$D(\hat{n},\theta) = e^{-[\underline{\theta}\times]} \quad (2)$$

where $\underline{\theta} = \hat{n}\theta$. The rate of change of the vector quantity $\underline{\theta}$ as a function of \underline{w} , the angular velocity at which the coordinate system rotates, is given by [9,10]

$$\dot{\underline{\theta}}(t) = \underline{w}(t) + \frac{1}{2}\underline{\theta}(t)\times\underline{w}(t) + \frac{2-\theta(t)\cot[\theta(t)/2]}{2\theta(t)^2} \underline{\theta}(t)\times[\underline{\theta}(t)\times\underline{w}(t)] \quad (3)$$

II. ALTERNATE FORMULATIONS OF EULER'S THEOREM

Angular-matrix (discrete) formulation

Denote the skew-symmetric matrix $[\underline{\theta}\times]$ by $\underline{\theta}$; that is,

$$\underline{\theta} = [\underline{\theta}\times] \quad (4)$$

where the explicit expression for θ is:

$$\theta = \begin{bmatrix} 0 & -\theta_3 & \theta_2 \\ \theta_3 & 0 & -\theta_1 \\ -\theta_2 & \theta_1 & 0 \end{bmatrix} \quad (5)$$

Equation (2) can be written as

$$D(\hat{n}, \theta) = e^{-\theta} \quad (6)$$

Let the initial orientation of a certain coordinate system with respect to some reference system be expressed by the attitude matrix D_0 . Suppose now that this coordinate system is rotated from its initial orientation by the sequence of rotations $\theta_1, \theta_2, \dots, \theta_k$. Denote the cross product matrices which correspond to $\theta_1, \theta_2, \dots, \theta_k$ by $\underline{\theta}_1, \underline{\theta}_2, \dots, \underline{\theta}_k$ respectively. Then, in view of (6), the attitude matrix that transforms the reference coordinate system to the final one, and which expresses the orientation of that system, is given by

$$D_f = e^{-\theta_k} \dots e^{-\theta_2} e^{-\theta_1} D_0 \quad (7)$$

On the other hand

$$D_f = e^{-\theta_f} D_0 \quad (8)$$

However

$$\theta_f \neq \theta_k + \dots + \theta_2 + \theta_1 \quad (9)$$

We realize that the equivalence between (7) and (8) is another expression of Euler's theorem. We can, then, formulate Euler's

theorem also as follows:

Regardless of the way a coordinate system is rotated from its original orientation, it is always possible to express the final orientation of the system by the attitude matrix D_f where

$$D_f = e^{-\theta_f} D_0$$

and θ_f is a skew-symmetric matrix.

We call this formulation discrete because the rotation expressed by θ_f is equivalent to the discrete k rotations expressed by the individual θ_i ($i=1,2, \dots, k$) matrices.

Angular-rate (continuous) formulation

Euler's theorem gave rise to (1) and (3) which indicate how to find the orientation of a coordinate system, at any given time t_f , with respect to its initial orientation at time t_0 if $\underline{w}(t)$, the history of its rate of rotation, is known for $t_0 < t < t_f$; namely, $\underline{w}(t)$ is used in (3) to solve for $\underline{\theta}(t)$ and then, that solution is used in (1) to obtain the required orientation specified by $D(t_f)$. The attitude matrix $D(t_f)$ can be computed in yet another way, since the rate of change of $D(t)$ as a function of $\underline{w}(t)$ is given by the well known matrix differential equation

$$\dot{D}(t) = - [\underline{w}(t) \times] D(t) \quad (10)$$

The matrix $[\underline{w}(t) \times]$ is defined on the components of $\underline{w}(t)$ when the latter is resolved in the changing (final) coordinate system. We also denote this matrix by $W(t)$; that is,

$$W(t) = [\underline{w}(t)x] \quad (11)$$

Hence (10) can be written also as

$$\dot{D}(t) = -W(t)D(t) \quad (12)$$

The explicit expression for $W(t)$ (or $[\underline{w}(t)x]$) is given by the skew-symmetric matrix:

$$W(t) = \begin{bmatrix} 0 & -w_3(t) & w_2(t) \\ w_3(t) & 0 & -w_1(t) \\ -w_2(t) & w_1(t) & 0 \end{bmatrix} \quad (13)$$

There is, then, an equivalence between the pair (1) and (3) on the one hand, and (12) on the other hand.

Euler's theorem states, basically, that there always exists a vector $\underline{\theta}(t_f)$ which specifies the orientation regardless of which $\underline{w}(t)$ generated that $\underline{\theta}(t_f)$. Consequently, any $\underline{w}(t)$ which satisfies the following two conditions, rotates the initial coordinate system into the same orientation

$$\frac{\underline{w}(t)}{w(t)} = \hat{n} \quad (14.a)$$

$$\int_{t_0}^{t_f} \underline{w}(t) dt = \underline{\theta}(t_f) \quad (14.b)$$

While the truth of the last proposition is self evident, it can also be easily verified by solving (3) for any angular rate $\underline{w}(t)$ which satisfies conditions (14). Since any $\underline{w}(t)$ which satisfies (14) rotates the initial coordinates into the same orientation,

then certainly the constant angular rate vector specified by

$$\underline{w} = \frac{\underline{\theta}(t_f)}{t_f - t_0} \quad (15)$$

rotates the initial coordinates into the same orientation and since according to Euler's theorem such $\underline{\theta}(t_f)$ always exists, then such constant \underline{w} exists too. Finally, since such a constant \underline{w} exists then, following (4) and (11), there also exists a corresponding constant matrix, W ,

$$W = \frac{1}{t_f - t_0} \theta_f \quad (16)$$

which when used in solving (12), yields the $D(t_f)$ that corresponds to $\underline{\theta}(t_f)$. Therefore, in view of the equivalence between the pair (1) and (3) on the one hand, and (12) on the other hand, we can phrase an equivalent formulation of Euler's theorem as follows:

Regardless of what matrix $W(t)$ generated $D(t_f)$, it is always possible to find a constant matrix W which generates the same $D(t_f)$.

We call this formulation continuous because it relates to the continuous change of the orientation as a result of the existence of an angular rate at which the orientation changes.

III. REPRESENTATION OF ROTATIONS IN n-D

Denote the dimension of an Euclidean space by n . The rotation matrix in n -D, being a square matrix, consists of n^2 elements.

However, the orthogonality of the matrix imposes $(n+1)n/2$ constraints on it. Consequently a rotation matrix in n-D has only $m=(n-1)n/2$ independent parameters. That is, a rotation matrix in n-D is defined by exactly $m=(n-1)n/2$ parameters. Consider now the 3-D rotation. As indicated by (1) and indeed as stated by Euler [1,11] the vector $\underline{\theta}(t_f)$ in its three components contains the necessary and sufficient information for specifying the 3-D rotation. Similarly the orthogonal rotation matrix $D(t_f)$ contains three independent parameters although it has nine elements. So the 3-D case is unique in that $n=m$ and the rotation can be described by either a vector or a matrix. In all other dimensions, though, $n \neq m$ and since m parameters are needed to define the rotation, a vector with its n elements cannot specify a rotation. Rotation matrices though, with their m independent parameters, do specify the rotation. As a consequence of this discussion, it is concluded that the original version of Euler's theorem or any of its variants presented in Section I are not extendible to n-D while the alternate formulation of Euler's theorem given in the preceding section may be extended to n-D.

IV. EULER'S THEOREM IN n-D

In view of the conclusion drawn in the last section, the general formulations of Euler's theorem in n-D are that given in Section II. Let us first address the angular-matrix (discrete) formulation and rephrase it in a more general frame by the following theorem:

Theorem 1: Given the arbitrary unitary matrices $D_0=D(t_0)$ and $D_f=D(t_f)$, then D_f can always be expressed in the form:

$$D_f = e^{-\theta} D_0 \quad (17)$$

where θ is a skew Hermitian-matrix.

Since the rotation matrix is orthogonal, the angular-matrix formulation of Euler's theorem is a special case of this theorem. Although the theorem is not new [see e.g. exercise 4 on p. 346 of ref. 12], for the sake of completeness, we present here a proof of the theorem.

Proof: Define the unitary matrix

$$D = D_f D_0^+ \quad (18)$$

where + denotes the conjugate transpose of a matrix. Since D is unitary, it is also normal and as such it has n orthogonal eigenvectors (see theorem A1 in the Appendix). Define a matrix V whose columns are the eigenvectors of D. Then V is unitary. Since the eigenvectors of D form an orthonormal set, then

$$D = V G V^+ \quad (19)$$

where G is the diagonal matrix of the eigenvalues of D (see A2). Now since D is unitary, its n eigenvalues g_1, g_2, \dots, g_n lie on the unit circle of the complex plane (see A3); that is,

$$g_i = e^{j\phi_i} \quad i=1,2, \dots, n$$

where $j=(-1)^{1/2}$ and ϕ_i is the phase of the i^{th} eigenvalue. Let us form a diagonal matrix $\bar{\delta}$

$$\bar{\theta} = \text{diag}(-\phi_1, -\phi_2, \dots, -\phi_n) \quad (20)$$

Then, obviously,

$$G = e^{-j\bar{\theta}} \quad (21)$$

Next we define a constant matrix θ as

$$\theta = V j\bar{\theta} V^+ \quad (22)$$

then (see A4)

$$e^{-\theta} = e^{-V j\bar{\theta} V^+} = V e^{-j\bar{\theta}} V^+ \quad (23)$$

Substituting (21) into (23) we obtain

$$e^{-\theta} = V G V^+ \quad (24)$$

A comparison between (24) and (19) yields

$$D = e^{-\theta} \quad (25)$$

Then from (18) and (25) we obtain

$$D_f = e^{-\theta} D_o$$

To complete the proof we still have to show that θ is skew-Hermitian. From (25)

$$D^+ = e^{-\theta^+} \quad (26)$$

Also (see A5)

$$D^{-1} = e^{\theta} \quad (27)$$

but, since D is unitary

$$D^+ = D^{-1}$$

therefore the right hand side of (26) is equal to that of (27), consequently

$$e^+ = -e$$

This completes the proof.

With Theorem 1 on-hand we are ready now to address the angular-rate (continuous) formulation of Euler's theorem. Here too we rephrase the latter in a more general frame as follows:

Theorem 2: Given the arbitrary unitary matrices $D_0 = D(t_0)$ and $D_f = D(t_f)$, then D_f can always be obtained as a solution of (12) with the initial condition D_0 where W is a constant skew-Hermitian matrix.

Note that due to the orthogonality of the rotation matrix, the angular-rate formulation of Euler's theorem constitutes a special case of the last theorem. The following proof of the latter is based on the former theorem.

Proof: From Theorem 1

$$D_f = e^{-\theta} D_0$$

On the other hand, the solution (12) when W is constant is

$$D_f = e^{-W(t_0 - t_f)} D_0$$

the equality of these yields

$$W = \frac{1}{t_f - t_0} \theta \quad (28)$$

that is; no matter what $W(t)$ generated D_f , we can always find a

constant W according to (28) for which the solution of (12) with the initial condition D_0 yields D_f at t_f . Since θ is skew-Hermitian then, from (28), W is skew-Hermitian too. This concludes the proof.

While we can consider W as an average velocity computed by (28), we note however that W is not the average of $W(t)$; that is,

$$W \neq \frac{1}{t_f - t_0} \int_{t_0}^{t_f} \dot{W}(t) dt \quad (29)$$

This inequality is known in 3-D as **non-commutativity**. (Another expression for the non-commutativity of rotations is the inequality expressed in (9)).

The above theorems extend Euler's theorem in two ways. First they deal with the general n -D rather than the 3-D case and secondly they extend Euler's theorem to the unitary (complex) transformation. Euler's original formulation is, then, a special case of the above theorems.

V. NUMERICAL EXAMPLE

To demonstrate the facts pointed out in the preceding section we bring a fourth order example in which we show how D_f which is obtained as a result of the solution of (5) for a certain time varying angular velocity matrix, $W(t)$, can be obtained by the solution of (5) with a constant angular velocity matrix, W .

For simplicity we deal with a special unitary matrix; namely, with an orthogonal one. Also for simplicity and with no loss of

generality, we choose $D_0=I$. We first use the following time varying $W(t)$ to solve (12) from $t_0=0$ to $t_f=0.5$ sec

$$W(t) = \begin{bmatrix} 0. & 1.5t & 1.5t^2 & 0.8t^3 \\ -1.5t & 0. & -0.9\sin(6.28t) & -0.95/(1.-t) \\ -1.5t^2 & 0.9\sin(6.28t) & 0. & 0.75 \\ -0.8t^3 & 0.95/(1.-t) & -0.75 & 0. \end{bmatrix} \quad (30)$$

this yields the following solution at t_f :

$$D_f = \begin{bmatrix} 0.98130682 & -0.15805594 & -0.08266215 & -0.07226489 \\ 0.18388549 & 0.76180341 & 0.21777062 & 0.58173674 \\ 0.04691911 & -0.10221727 & 0.96379421 & -0.24176631 \\ -0.03196326 & -0.61985926 & 0.12978307 & 0.77324588 \end{bmatrix}$$

The following eigenvector matrix of D_f is obtained using the EIGZF routine of the IMSL library:

$$V = \begin{bmatrix} -0.038+j0.161 & -0.038-j0.161 & 0.687+j0. & 0.687+j0. \\ 0.683+j0. & 0.683+j0. & 0.037-j0.177 & 0.037+j0.177 \\ -0.170+j0.184 & -0.170-j0.184 & -0.052-j0.659 & -0.052+j0.659 \\ -0.056+j0.664 & 0.056-j0.664 & -0.151+j0.181 & -0.151-j0.181 \end{bmatrix}$$

The same routine also yields the following eigenvalues of D_f :

$$g_1 = 0.7452+j0.6668 = e^{j0.7300}$$

$$g_2 = 0.7452-j0.6668 = e^{-j0.7300}$$

$$g_3 = 0.9949+j0.1012 = e^{j0.1013}$$

$$g_4 = 0.9949-j0.1012 = e^{-j0.1013}$$

The diagonal matrix $j\bar{\omega}$ is computed according to (20) and used in (22) and (28) to compute the following constant angular velocity matrix:

$$W = \begin{bmatrix} 0.00000000 & 0.37147707 & 0.12387442 & 0.04981448 \\ -0.37147707 & 0.00000000 & -0.35388342 & -1.31771209 \\ -0.12387442 & 0.35388342 & 0.00000000 & 0.40459905 \\ -0.04981448 & 1.31771209 & -0.40459905 & 0.00000000 \end{bmatrix} \quad (31)$$

When now (12) is solved with the initial condition $D_0=I$ starting at $t_0=0$. then, as expected, D_f is the solution obtained at time $t=0.5$. Finally, to demonstrate the inequality presented in (29) we average $W(t)$ given in (30). The resulting average is:

$$\frac{1}{t_f - t_0} \int_{t_0}^{t_f} W(t) dt = \begin{bmatrix} 0. & 0.375 & 0.125 & 0.025 \\ -0.375 & 0. & -0.573 & -1.317 \\ -0.125 & 0.573 & 0. & 0.750 \\ -0.025 & 1.317 & -0.750 & 0. \end{bmatrix}$$

Obviously the latter matrix differs from the constant angular matrix, W , given in (31).

V. CONCLUSIONS

Euler's fundamental theorem on the ability to describe any orientation of a rigid body as a single rotation and the various known versions of this theorem cannot be directly extended to other dimensions because all known formulations hinge on the concept of axis of rotation which does not exist in dimensions other than three. Nevertheless, when it is recognized that the general n-D rotation is characterized not by an axis of rotation but rather by an angular-difference matrix or by an angular velocity matrix, Euler's theorem can be reformulated in 3-D in ways which are equivalent to the other known formulations and then the new formulations can be extended to n-D. In this work we presented the new formulations in 3-D and then we proved that

they hold for any dimension. One of the new formulations states that no matter what was the sequence of rotations that resulted in the final orientation, it is always possible to express the rotation matrix as an exponential function of a skew-symmetric angular-difference matrix. The other new formulation of Euler's theorem states that no matter how the angular velocity matrix changes as a function of time, we can always find a constant angular-velocity matrix which will result in identical orientation change over the same time interval.

The proof of the theorems supplied the algorithm needed to compute the angular-difference matrix and the equivalent constant angular-velocity matrix once the initial and the final attitudes as well as the time interval are given. To demonstrate the new formulations of the theorem and their extendibility to dimensions other than 3 we used the algorithm to solve a 4-D example. The example clearly demonstrates the ability to reach the same final orientation using a constant angular velocity matrix.

Appendix

This appendix lists some known theorems which are used in the proof of the theorem on the extended Euler theorem.

- A1: A set of n orthonormal eigenvectors can be found for an $n \times n$ normal matrix. [See p. 76 of Ref. 13].
- A2: A matrix can be reduced to a diagonal matrix by a similarity transformation if and only if a set of n linearly

independent eigenvectors can be found. [See p. 72 of Ref. 13].

A3: The eigenvalues of a unitary matrix have absolute value 1. [See p. 129 in Ref. 14].

A4: If $A = TJT^{-1}$, then $f(A) = Tf(J)T^{-1}$. [See p. 80 of Ref. 13].

A5: If $A = e^B$ then $A^{-1} = e^{-B}$.

Proof: Since B and $-B$ commute, then $e^B e^{-B} = e^{B-B} = I$

hence

$$Ae^{-B}=I$$

thus

$$A^{-1}=e^{-B}$$

Acknowledgment

The author wishes to express his thanks to Dr. F. Landis Markley for reviewing this paper and for many constructive discussions and suggestions. The author also wishes thank Dr. R.J. Rowland, Jr. of the Department of Classics of the University of Maryland for his help in translating Euler's theorem from the Latin.

REFERENCES

- [1] L. Euler, "Formulae Generales pro Trandlatione Quacunqve Corporum Rigidorum," Novi Acad. Sci. Petrop., Vol. 20, 1775, pp. 189-207.
- [2] H. Goldstein, *Classical Mechanics*, 2nd edition, Addison-Wesley, Reading Mass, 1980, p.118.

- [3] M. O. Rodrigues, "Des Lois Géométriques Qui Régissent les Déplacement d'un Système Solide dans L'espace, et de la Variation des Coordonnées Provenant de ces Déplacements Considérés Independamment des Causes qui Peuvent les Produire," **J. de Mathématiques Pures et Appliquées**, (Liouville), Vol. 5, 1840, pp. 380-440.
- [4] A. Cayley, "On the Motion of Rotation of a Solid Body," **Cambridge Mathematical Journal**, Vol. III, 1843, pp. 224-232, also in **The Collected Mathematical Papers of Arthur Cayley**, Vol. I, The Cambridge University Press, 1889. Johnson Reprint Corp. New York, 1963, pp.28-35.
- [5] A. Cayley, "On certain Results Relating to Quaternions," **Cambridge Mathematical Journal**, Vol. III, 1843, pp. 141-145, also in **The Collected Mathematical Papers of Arthur Cayley**, Vol. I, The Cambridge University Press, 1889. Johnson Reprint Corp. New York, 1963, pp.123-126.
- [6] J. W. Gibbs **Scientific Papers**, Vol. II, Dover Publication Inc., New-York, 1961, p. 65.
- [7] T. F. Wiener, "Theoretical Analysis of Gimballess Inertial Reference Equipment Using Delta-Modulated Instruments," Doctoral Dissertation, M.I.T. Cambridge Mass, 1962.
- [8] J. R. Wertz (ed.), **Spacecraft Attitude Determination and Control**, D. Reidel, Dordrecht Holland, 1978.
- [9] M. D. Shuster, **Fundamentals of Spacecraft Attitude Determination**, in preparation.
- [10] J. E. Bortz, "A New Mathematical Formulation for Strapdown Inertial Navigation," **IEEE Trans. on Aerosp. Elect. Sys.**, Vol. AES-7, Jan. 1971, pp. 61-66.
- [11] P. L. Pio, "Euler Angle Transformations," **IEEE Transactions on Automatic Control**, Vol.-11, No. 5, October 1960, pp. 707-715.
- [12] P. Lancaster and M. Tismenetsky, **The Theory of Matrices**, 2nd edition, Academic Press, Orlando FL, 1985.
- [13] D. M. Wiberg, **State Space and Linear Systems**, Schaum's Outline Series, McGraw Hill, New-York, 1971.
- [14] J. R. Westlake, **A Handbook of Numerical Matrix Inversion and Solution of Linear Equations**, John Wiley and Sons, New-York, 1968.

ANALYSIS OF THE FLIGHT DYNAMICS OF THE SOLAR MAXIMUM MISSION (SMM) OFF-SUN SCIENTIFIC POINTING*

D. S. Pitone and J. R. Klein
Computer Sciences Corporation (CSC)

ABSTRACT

This paper presents the algorithms created and implemented by the Goddard Space Flight Center's (GSFC's) Solar Maximum Mission (SMM) attitude operations team to support large-angle spacecraft pointing at scientific objectives. The mission objective of the post-repair SMM satellite was to study solar phenomena. However, because the scientific instruments, such as the Coronagraph/Polarimeter (CP) and the Hard X-ray Burst Spectrometer (HXRBS), were able to view objects other than the Sun, attitude operations support for attitude pointing at large angles from the nominal solar-pointing attitudes has been required. Subsequently, attitude support for SMM has been provided for scientific objectives such as Comet Halley, Supernova 1987A, Cygnus X-1, and the Crab Nebula. In addition, the analysis has been extended to include the reverse problem, computing the right ascension and declination of a body given the off-Sun angles. This analysis has led to the computation of the orbits of seven new solar comets seen in the field-of-view (FOV) of the CP. The activities necessary to meet these large-angle attitude-pointing sequences, such as slew sequence planning, viewing-period prediction, and tracking-bias computation are described. Analysis is presented for the computation of maneuvers and pointing parameters relative to the SMM-unique, Sun-centered reference frame. Finally, science data and independent attitude solutions are used to evaluate the large-angle pointing performance.

*This work was supported by the National Aeronautics and Space Administration (NASA)/Goddard Space Flight Center (GSFC), Greenbelt, Maryland, under Contract NAS 5-31500.

1. INTRODUCTION

This paper presents

- Algorithms used in support of large-angle attitude pointing maneuvers by the Solar Maximum Mission (SMM) spacecraft to nonsolar scientific objectives
- A brief history of the mission and its primary scientific objectives
- Background of the problem of pointing at celestial objects, especially as pertains to the SMM

The algorithms used to compute the necessary parameters for the observations are derived and results are presented that show the algorithms worked correctly, with accuracy significantly better than that specified by the SMM project. This work was performed by the Flight Dynamics Division (FDD) attitude determination and control analysts in the Flight Dynamics Facility (FDF) at Goddard Space Flight Center (GSFC).

1.1 MISSION HISTORY

The SMM spacecraft was launched in February 1980 from the Eastern Test Range into an approximately circular low-Earth orbit, with an inclination of nearly 28 degrees (deg) (Reference 1). The spacecraft functioned normally until November 1980 when the standard reaction wheel (SRW) package that controls the spacecraft attitude failed. To preserve the mission, the spacecraft was put into a spin, approximately 1 deg per second (sec), about the minor principal axis. While the spacecraft was in this spin mode, very little scientific work was accomplished. In April 1984, the spacecraft was repaired in-orbit by astronauts aboard the Space Transportation System (STS) orbiter. The entire modular attitude control system (MACS) was replaced, and the spacecraft returned to normal operations.

Some time before the repair mission, scientists at the GSFC Laboratory for Astronomy and Solar Physics proposed that the SMM be used to observe Comet Halley for approximately 1 month before and after perihelion of the comet's orbit (February 9, 1986). During this time, the comet, as seen from the Earth, would be between 7 and 45 deg from the Sun, and very little useful ground-based observation was anticipated.

1.2 SMM SCIENTIFIC OBJECTIVES AND PAYLOAD

The original scientific objective of the SMM was to study solar phenomena, especially the solar maximum of 1981. The mission was planned to be three-axis stabilized to keep the scientific payload pointed at the Sun. However, because of the SRW failure, most of the scientific instruments missed the solar maximum. Since the repair of the spacecraft, a tremendous amount of solar radiation data at a variety of wavelengths has been amassed. In addition, beginning with the Comet Halley observations, several interesting nonsolar targets have been and are being studied.

A Coronagraph/Polarimeter (CP), designed to study the solar corona in the visible spectrum, was used to observe Comet Halley and the Moon. In addition, seven solar grazing

comets have been discovered during routine operation of the CP. A Hard X-Ray Burst Spectrometer (HXRBS) was pointed at Cygnus X-1 (a suspected black hole) and the Crab Nebula. The Gamma Ray Spectrometer (GRS) was used to study gamma ray output from Supernova 1987A and the Ultra-Violet Spectrometer (UVSP) observed a transit of the Sun by Mercury. All of these observations required attitude excursions from the primary solar objective and provided valuable data for the scientific community on a wide range of celestial objectives.

1.3 MANEUVER REQUIREMENTS

The goal of this analysis is to provide algorithms for attitude control of the SMM so that the scientific payload points at the desired celestial body and tracks it, even if it is moving relatively fast, to keep the body in the instrument field of view (FOV). In addition, the periods during which the celestial body is visible to the spacecraft (i.e., not occulted by the Earth) must be determined.

Requirements for attitude support of the large-angle attitude pointing maneuvers were not defined until several years after the spacecraft had been launched. For this reason, mathematical algorithms were developed for each nonsolar objective, as needed. The algorithms were later combined to form one software system that could efficiently plan the large-angle off-solar pointing maneuvers for any celestial body. The software was designed to plan the maneuver sequence, compute the viewing periods available, and determine the tracking parameters. Once computed, these data are uplinked to the spacecraft.

The constraints imposed by the SMM experimenters were few and were concerned with getting the best observations possible. To accomplish normal pointing, an accuracy of a tenth of a degree was desired. Another consideration was the determination accuracy in the viewing periods. Because of uncertainties in the spacecraft ephemeris, pointing accuracy, and spacecraft gyro drift, accuracy in computing the start and stop times of the viewing periods was estimated to be 10 sec (3σ).

Consideration for spacecraft safety placed other constraints on the maneuvers. The most important constraint was that the spacecraft had to remain in a power-positive mode to ensure survival of the spacecraft following any observation period contingency. This effectively meant that the body-fixed Solar Panel Array would always need to be absorbing at least as much energy as the spacecraft was using. During nominal operation, the solar panels are approximately perpendicular to the spacecraft-to-Sun vector. As a result of the analysis by the power engineers, the maximum off-Sun pointing angle was set at 65 deg.

2. PROBLEM ANALYSIS

2.1 THE SMM REFERENCE FRAMES

The SMM spacecraft attitude is represented in a solar reference frame, referred to as the SUN frame. The X-axis of the SUN frame is defined by the apparent spacecraft-to-Sun unit vector, \underline{V}_{ss} . The Y-axis is the unitized cross-product of the Sun's North Pole vector,

\underline{S}_{np} , and \underline{V}_{ss} . The Z-axis completes the right-handed coordinate system. The equations for the unit vectors along the Sun frame axes are (Reference 2)

$$\underline{X} = \underline{V}_{ss} \tag{1}$$

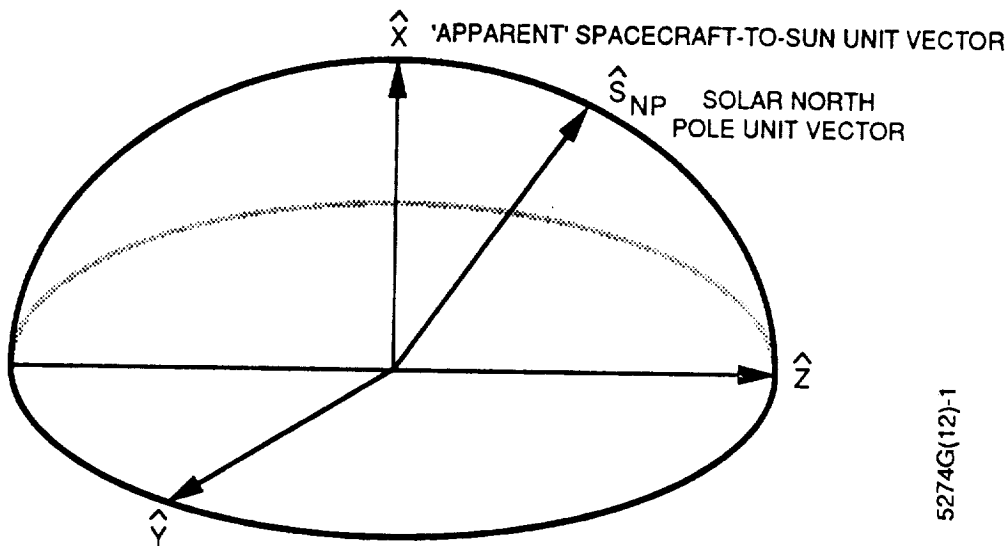
$$\underline{Y} = a (\underline{S}_{np} \times \underline{X}) \tag{2}$$

$$\underline{Z} = a (\underline{S}_{np} - (\underline{S}_{np} \cdot \underline{X}) \underline{X}) \tag{3}$$

where

$$a = [1 - (\underline{S}_{np} \cdot \underline{X})^2]^{-1/2} \tag{4}$$

Figure 1 illustrates the SUN coordinate system.



5274G(12)-1

Figure 1. Solar Coordinate System

The transform, A, from geocentric inertial (GCI) coordinates to the SUN frame, is computed from the actual spacecraft and Sun positions with consideration for the Earth and spacecraft velocities and the speed of light to correct for aberration. Thus, for attitude determination, reference vectors must be transformed using A to get the reference vectors in the SUN frame. Due to the spacecraft's orbit about the Earth and the Earth's orbit about the Sun, the SUN frame is constantly changing. Thus, each time the attitude of the

spacecraft is computed by the spacecraft's onboard computer (OBC) or the ground system, the SUN frame has to be recomputed.

The SMM spacecraft attitude is represented as the transformation from the SUN frame to the SMM body frame. As shown in Figure 2, the fine-pointing Sun sensor (FPSS) and the scientific instruments are at one end of the spacecraft. During normal operations, the attitude control system is designed to point this end of the spacecraft at small areas of the Sun. The X-axis (roll) of the spacecraft body frame is defined to coincide with the direction of the FPSS boresight. Two orthogonal axes perpendicular to the FPSS boresight and corresponding to the FPSS outputs are defined as the Y- (pitch) and Z- (yaw) axes of the body frame. This alignment is advantageous because the spacecraft pitch and yaw rotations are read directly from the output of the FPSS when the Sun is in the FOV of the FPSS, which is 4-square deg. Thus, during normal operations, the spacecraft is observing the Sun, and the attitude accuracy in pitch and yaw is 5 arc-sec (3σ). The roll is determined by the fixed-head star trackers (FHSTs) to an accuracy of approximately 30 arc-sec (3σ). During periods of solar occultation or spacecraft pitch or yaw offpoint, the Sun is not in the FPSS FOV, and the attitude of all three axes is determined by the FHSTs to an accuracy of approximately 30 arc-sec (3σ). Most of the scientific instrument boresights are parallel to the boresight of the FPSS; thus, the output from the FPSS can be used directly to determine where the instruments are pointing to within 5 arc-sec when the Sun is being observed.

The SMM attitude matrix, B, is the matrix that transforms a vector from the SUN frame to the SMM body frame. If the roll angle is ϕ , the pitch angle θ , and the yaw angle β , the matrix B is (Reference 2)

$$B = T_3(\beta) T_2(\theta) T_1(\phi) \quad (5)$$

where T_i are the individual matrices for each Euler rotation on the intermediate axes. Thus,

$$B = \begin{bmatrix} \cos \beta \cos \theta & | & \cos \beta \sin \theta \sin \phi + \sin \beta \cos \phi & | & -\cos \beta \sin \theta \cos \phi + \sin \beta \sin \phi \\ -\sin \beta \cos \theta & | & -\sin \beta \sin \theta \sin \phi + \cos \beta \cos \phi & | & \sin \beta \sin \theta \cos \phi + \cos \beta \sin \phi \\ \sin \theta & | & -\cos \theta \sin \phi & | & \cos \theta \cos \phi \end{bmatrix} \quad (6)$$

2.2 CALCULATION OF POINTING MANEUVERS

Pointing at a celestial object involves rotating the SMM to align its X-axis with the spacecraft-to-target vector. In general, pointing from an initial target to any other target on the celestial sphere can be accomplished by consecutive rotations about any two orthogonal axes (Reference 3). Thus, any pair of rotations of roll, pitch, or yaw will suffice. For convenience, the first maneuver is chosen to be a roll. After this, the four choices for the second maneuver are positive or negative pitch or yaw. The magnitude of any of these second maneuvers is simply the angular distance from the Sun to the target

objective. For this algorithm, the roll corresponding to each choice of second rotations is computed, and the smallest roll is chosen.

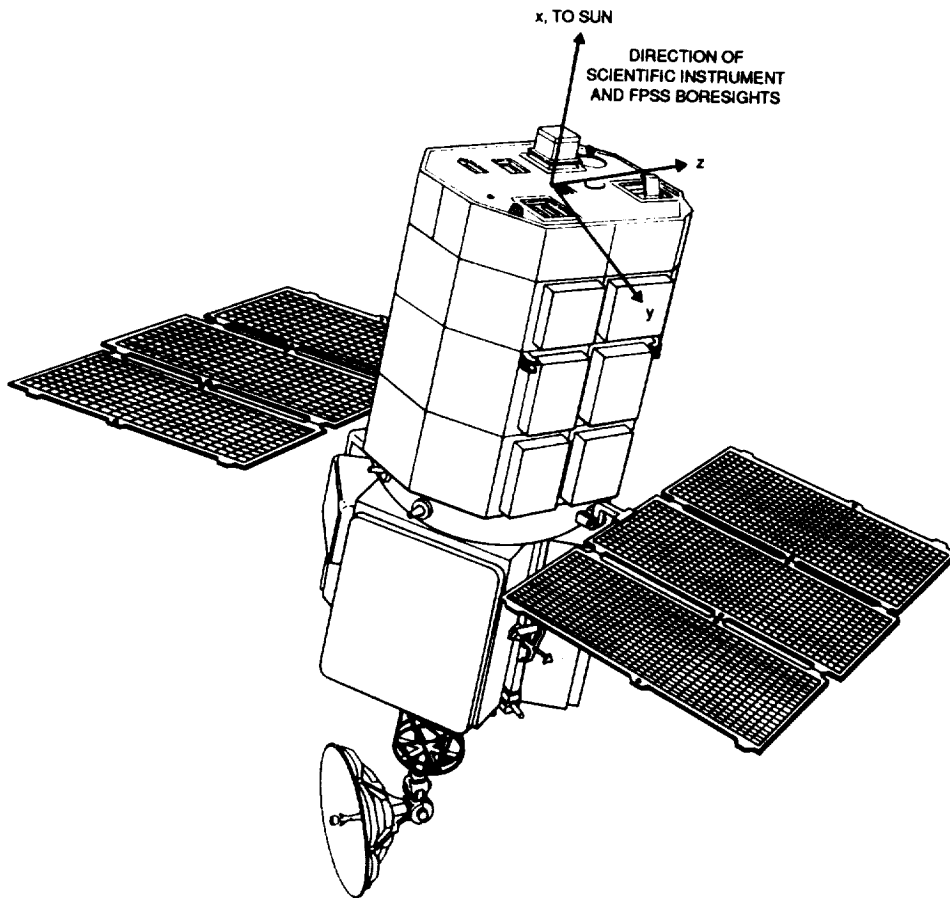


Figure 2. Scientific and FPSS Boresight Directions

To compute the maneuvers, the roll-yaw combination is computed first. The attitude matrix, B , for this case is $T_3(\beta) T_1(\phi)$ or

$$B = \begin{bmatrix} \cos \beta & | & \sin \beta \cos \phi & | & \sin \beta \sin \phi \\ -\sin \beta & | & \cos \beta \cos \phi & | & \cos \beta \sin \phi \\ 0 & | & -\sin \phi & | & \cos \phi \end{bmatrix} \quad (7)$$

This transforms vectors from the SUN frame to the body frame after the maneuvers have been completed.

Since the scientific instrument boresights are parallel to the X-axis, the representation of the celestial target vector in the body frame after the maneuver is desired to be

$$\underline{V}_{scb} = \begin{bmatrix} 1 \\ 0 \\ 0 \end{bmatrix} \quad (8)$$

The GCI coordinate representation of the celestial target vector, unchanged by the maneuver is

$$\underline{V}_{gci} = \begin{bmatrix} V_{gci1} \\ V_{gci2} \\ V_{gci3} \end{bmatrix} \quad (9)$$

To represent the celestial target vector in the SUN frame, the matrix A is calculated for the time of the maneuvers. The representation of the celestial target vector, \underline{V}_s , in the Sun frame is

$$\underline{V}_s = A \underline{V}_{gci} \quad (10)$$

while \underline{V}_{scb} is related to \underline{V}_s as follows:

$$\underline{V}_s = B^T \underline{V}_{scb} \quad (11)$$

or

$$\begin{bmatrix} V_{s1} \\ V_{s2} \\ V_{s3} \end{bmatrix} = \begin{bmatrix} \cos \beta & | & -\sin \beta & | & 0 \\ \sin \beta \cos \phi & | & \cos \beta \cos \phi & | & -\sin \phi \\ \sin \beta \sin \phi & | & \cos \beta \sin \phi & | & \cos \phi \end{bmatrix} \begin{bmatrix} 1 \\ 0 \\ 0 \end{bmatrix} \quad (12)$$

Thus, \underline{V}_s can be computed from Equation (10) and substituted into the left-hand side of Equation (12). The unknowns in Equation (12) are then the maneuver angles β and ϕ . Further reduction of this equation leads to

$$V_{s1} = \cos \beta \quad (13)$$

$$V_{s2} = \sin \beta \cos \phi \quad (14)$$

$$V_{s3} = \sin \beta \sin \phi \quad (15)$$

Dividing Equation (15) by Equation (14)

$$V_{s3}/V_{s2} = \tan \phi \quad (16)$$

Thus, the equations for the roll-yaw maneuvers are

$$\text{Yaw} = \beta = \cos^{-1} (V_{s1}) \quad (17)$$

$$\text{Roll} = \phi = \tan^{-1} (V_{s3}/V_{s2}) \quad (18)$$

The sign of the roll is resolved by using the function DATAN2 to compute the inverse tangent. The roll-pitch sequences are calculated from the above roll-yaw results by adding and subtracting 90 deg from the roll and selecting the sign of the pitch accordingly. As stated earlier, the maneuver sequence requiring the smallest roll rotation is the favored sequence. For targets that are further than 65 deg from the Sun, the maneuver to the attitude closest to the celestial body is computed. In this case the angular distance from the target to the planned closest attitude is also computed and delivered to the experimenters.

2.3 COMET POSITION DETERMINATION

To date, seven Sun-grazing comets have been discovered in the CP FOV during normal observations of the solar corona. The CP uses an occulting disk on its sensor FOV to block out the main part of the Sun, enabling it to observe the solar corona. These comets could not have been observed without this special instrumentation of the CP. Several observations of each comet in CP instrument coordinates have been reported. In support of these observations, it is desired to transform the CP comet coordinate positions to GCI coordinates to determine the orbits of the comets.

The determination of the comet positions in GCI coordinates is the inverse of the maneuver planning. It is assumed that the CP boresight is parallel to the X-axis of the spacecraft. The comet position in CP coordinates is transformed to an equivalent spacecraft roll-pitch maneuver sequence that would point the spacecraft directly at the comet. The spacecraft, however, is never actually maneuvered; the maneuver is only computed so that the maneuver planning procedure can be reversed, and the comet position computed. The position vector in the Sun frame is then determined from the roll-pitch angles. The comet position vector in GCI coordinates is computed by multiplying the comet position vector in the Sun frame by the transpose of A at the time of the observation.

The CP uses a two-dimensional polar coordinate system. The first coordinate is the counterclockwise rotation about the X-axis (roll) from the positive Z-axis (yaw). Thus, this is the negative roll necessary to align the positive Z-axis (yaw) with the Sun-to-comet vector. The second coordinate is the angular separation between the center of the Sun and the comet, along the positive Z-axis (yaw). This corresponds to a negative pitch angle. The result is the roll-pitch angle pair that would be required to maneuver the spacecraft and align the boresight with the spacecraft-to-comet vector.

If the matrix, B' , for a roll (ϕ)-pitch (θ) maneuver from a null attitude in the Sun frame to the comet is

$$B' = \begin{bmatrix} \cos \theta & | & \sin \theta \sin \phi & | & -\sin \theta \cos \phi \\ 0 & | & \cos \phi & | & \sin \phi \\ \sin \theta & | & -\cos \theta \sin \phi & | & \cos \theta \cos \phi \end{bmatrix} \quad (19)$$

then the position vector, \underline{V}_c , of the comet in the Sun frame is simply

$$\underline{V}_c = B'^T \begin{bmatrix} 1 \\ 0 \\ 0 \end{bmatrix} \quad (20)$$

or

$$\underline{V}_c = \begin{bmatrix} \cos \theta & | & 0 & | & \sin \theta \\ \sin \theta \sin \phi & | & \cos \phi & | & -\cos \theta \sin \phi \\ -\sin \theta \cos \phi & | & \sin \phi & | & \cos \theta \cos \phi \end{bmatrix} \begin{bmatrix} 1 \\ 0 \\ 0 \end{bmatrix} \quad (21)$$

This assumes that the spacecraft attitude is zero roll, pitch, and yaw so that the SUN frame is aligned to the body frame. If the spacecraft is at a non-nominal attitude, the matrix B must be recomputed, taking into account the spacecraft attitude at the time of the observation. The comet position in GCI coordinates, \underline{V}_{cgci} , is then

$$\underline{V}_{cgci} = A^T \underline{V}_c \quad (22)$$

The vector, \underline{V}_{cgci} , is then reduced to right ascension and declination (mean of 1950) and delivered to the International Astronomical Union (IAU), where it is used for orbit computations.

2.4 CELESTIAL BODY VIEWING PERIOD PREDICTION

Because of the geometry of the SMM orbit, every point in the celestial sphere of the spacecraft is occulted by the Earth at some time in one revolution of the ascending node of the spacecraft's orbit. Thus, a list of periods when the celestial target can be viewed by the spacecraft is necessary for all times that observations of nonsolar targets are being planned. The computation of these periods is done by comparing the relevant angles in the geometry of the spacecraft, Earth, and the target objective.

The unit vector, \underline{W}_{sce} , from the center of the Earth to the spacecraft, is constantly changing as the spacecraft orbits the Earth and is known from the spacecraft ephemeris. The vector from the Earth to the target body, \underline{W}_{eb} , is normally computed from the right ascension and declination of the target body in the Earth's celestial sphere. To compute the viewing periods, the spacecraft-to-target vector, \underline{W}_{sb} is needed. Since the distance to the viewing target in most cases has not been relevant, the Earth-to-target vector is

represented as a unit vector. Thus, vector addition of the Earth-to-target vector and the Earth-to-spacecraft vector does not give the spacecraft-to-target vector. Instead, it is assumed that the parallax of the target body's position due to the spacecraft's orbit around the Earth is negligible, and, therefore,

$$\underline{W}_{eb} \approx \underline{W}_{sb} \quad (23)$$

For objects out of the solar system and the outer planets, this approximation will yield results that are well within the constraints. For the inner planets and comets, this approximation leads to an error in the vector of between 1 arc-sec and 20 arc-sec. This will translate to an error of less than 1 sec in the occultation times, which can be considered negligible compared to the 10-sec constraint on the accuracy. If observations of the Moon are planned, the position error caused by the above assumption can reach 1 deg. This will translate to approximately a 15-sec error in the occultation times, which is greater than the maximum error allowed. To resolve this, the Earth-to-Moon vector obtained from lunar ephemerides is used to calculate \underline{W}_{sb} directly by vector addition.

Once \underline{W}_{sb} and \underline{W}_{sce} are known, the angle, Φ , between the vectors is computed by taking the inverse cosine of the dot product of the two vectors as

$$\Phi = \cos^{-1} (\underline{W}_{sb} \cdot \underline{W}_{sce}) \quad (24)$$

This geometry is illustrated in Figure 3.

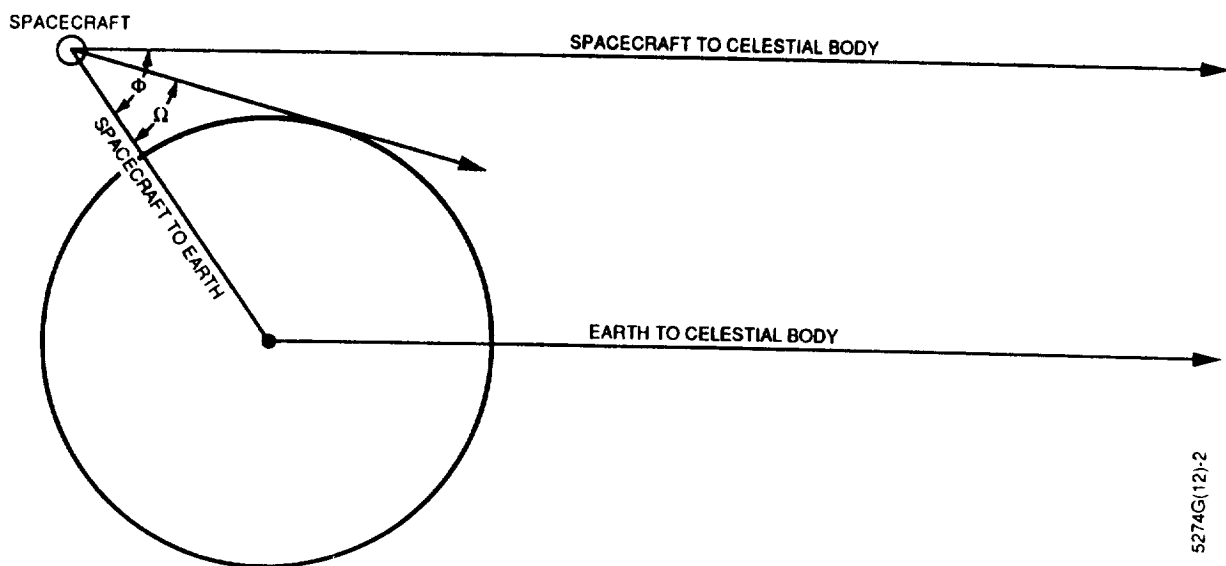


Figure 3. Occultation Geometry

To compute whether the celestial target is blocked by the Earth, Φ is compared to the subtended Earth half angle, Ω . The computation of Ω assumes a perfectly circular

Earth, with a radius equal to the equatorial radius. This translates to a maximum of 8 sec for celestial objects with declinations near positive or negative 90 deg. However, nearly all of the celestial targets observed by the SMM have had declinations close to the Sun's. Thus, the typical error induced by the Earth's oblateness is typically near 3 or 4 sec.

The half angle subtended by the Earth is given by

$$\Omega = \sin^{-1} (R/D) \quad (25)$$

where R is the equatorial radius of the Earth and D is the magnitude of the Earth-to-spacecraft vector obtained from the spacecraft ephemeris file. The relationship of the computed angles is also shown in Figure 3. The only variable on the right-hand side of Equation (25) is D. This varies with the orbital eccentricity and more slowly with the rate of decay of the spacecraft's altitude above the Earth. Thus, for SMM, Ω changes very slowly and is approximately 69 deg. The celestial object is considered to be occulted by the Earth from the spacecraft if Ω is larger than Φ . Conversely, if Φ is larger than Ω , the celestial object is considered in view of the spacecraft. This makes sense intuitively, since at times the spacecraft is between the Earth and the celestial object, Φ will be obtuse, while if the Earth is between the spacecraft and the celestial object, Φ will be acute.

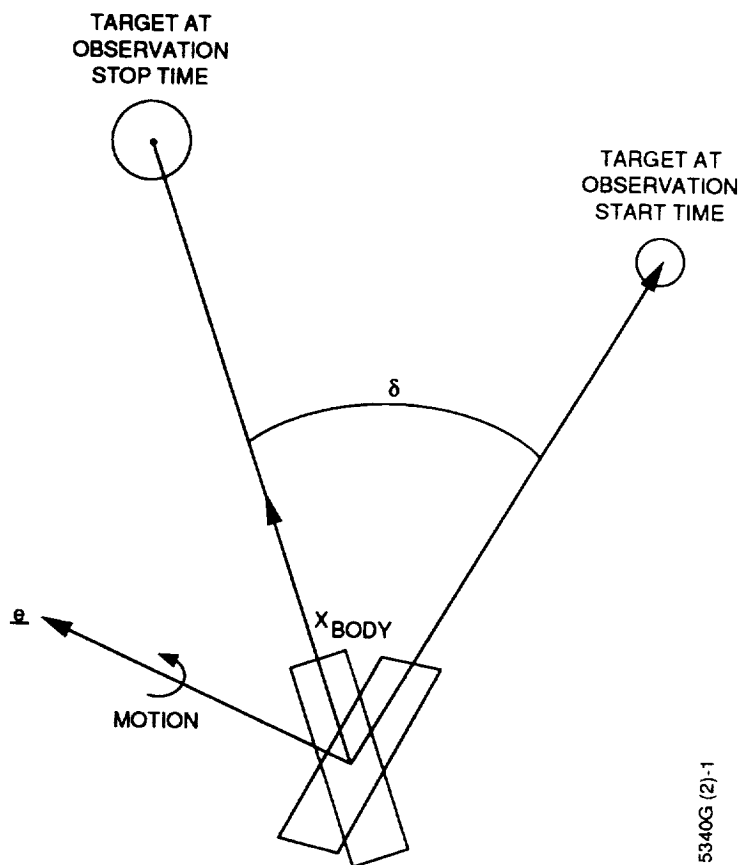
Earth occultation computations are performed every 4 minutes (min) for the period of interest. When a change occurs, a binary search is used to narrow the change time to the nearest second, which will typically have a maximum error (3σ) of less than 10 sec (Reference 4).

2.5 TRACKING PARAMETER COMPUTATION

Targets not in the solar system, such as distant stars, do not move significantly relative to the SMM due to the spacecraft's orbit about the Earth or the Earth's motion about the Sun. Thus, during observations of very distant objects, provisions need not be made to track motion of the celestial target due to parallax and proper motion. However, bodies in heliocentric (planets or comets) or geocentric (the Moon) orbits will move through an angle δ , which can be represented as a rotation about a unit vector, \underline{e} , in the spacecraft inertial reference unit (IRU) coordinate frame as illustrated in Figure 4. This motion is due to the spacecraft's motion about the Earth, the Earth's motion about the Sun, and the target objects motion in its orbit about the Sun or Earth. During an observation period at a constant attitude, this motion will cause the celestial target to move through, and eventually out of, the scientific sensor FOV. To compensate, the spacecraft is rotated about the axis \underline{e} by the angle δ from the beginning to the end of the observation period. This motion is called tracking.

Tracking by the spacecraft is accomplished by computing the angle, δ , and axis of rotation, \underline{e} , of the target body in the IRU sensor frame of reference and combining δ and \underline{e} with the observation time Δt to form a command gyro rate bias vector (historically called BGDT) which is uplinked to the spacecraft. These BGDTs cause the gyros to show motion opposite to the way the target is moving. This apparent (in that the spacecraft is not

actually moving) motion causes the SRWs to counteract the apparent motion and move the spacecraft in the direction of the celestial objective. Thus, tracking is accomplished. To compute the BGDs, the transformation matrix, H, between the SMM body-frame attitude at the start of the observation period and the attitude at the end of the observation period is computed and used to determine average rates about the three IRU axes.



5340G (2)-1

Figure 4. Tracking Geometry

To compute H, the maneuvers to point the spacecraft at the target are computed by the methods described earlier at the observation start and stop times. The maneuvers are assumed to be relative to an attitude of roll, pitch, and yaw equal to zero. Thus, using Equation (6), the SUN-frame-to-body-frame matrices, B_1 and B_2 , at the start and stop times are computed. However, the coordinate frame that B is referenced to at all times on the SMM mission is the SUN frame, which, as stated above, is not inertial. The attitude motion for target tracking must be referenced to an inertial frame. For this, the GCI-to-SUN frame matrix, A, is used. In addition, because the BGDs are for the IRUs, they must be represented in the IRU sensor frame. Defining G_1 and G_2 to be the GCI-to-IRU transformation matrices at the start and stop times, respectively, and M to be the IRU-to-body transformation matrix, then

$$G_1 = M^T B_1 A_1 \quad (26)$$

$$G_2 = M^T B_2 A_2 \quad (27)$$

and

$$G_2 = H G_1 \quad (28)$$

Solving for H yields

$$\begin{aligned} H &= G_2 G_1^T = M^T B_2 A_2 (M^T B_1 A_1)^T \\ &= M^T B_2 A_2 A_1^T B_1^T M \end{aligned} \quad (29)$$

If the Sun frame were an inertial frame, A_1 would be equal to A_2 , and Equation (29) would be simplified. Now that H has been found, δ and \underline{e} can be computed from H, and the BGDs can be computed.

To compute δ and \underline{e} , H is written as an Euler rotation with unit vector \underline{e} in the IRU frame and rotation angle δ . Thus, using the Euler convention for a general rotation, H is (Reference 4)

$$H = \cos(\delta) I + (1 - \cos(\delta)) \underline{e} \underline{e}^T - \sin(\delta) [[\underline{e}]] \quad (30)$$

where $[[\underline{e}]]$ is the skew symmetric matrix representation of a vector. The general form for a three-component vector is

$$[[\underline{x}]] = \begin{bmatrix} 0 & -x_3 & x_2 \\ x_3 & 0 & -x_1 \\ -x_2 & x_1 & 0 \end{bmatrix} \quad (31)$$

Thus, it is desired to manipulate Equation (30) to solve for \underline{e} and δ . Defining the parameter k^2 as

$$k^2 = (H_{23} - H_{32})^2 + (H_{31} - H_{13})^2 + (H_{12} - H_{21})^2 \quad (32)$$

substitution from Equation (30) leads to

$$\begin{aligned} k^2 &= [e_2 e_3 (1 - \cos \delta) + e_1 \sin \delta - e_2 e_3 (1 - \cos \delta) + e_1 \sin \delta]^2 \\ &+ [e_1 e_3 (1 - \cos \delta) + e_2 \sin \delta - e_1 e_3 (1 - \cos \delta) + e_2 \sin \delta]^2 \quad (33) \\ &+ [e_1 e_2 (1 - \cos \delta) + e_3 \sin \delta - e_1 e_2 (1 - \cos \delta) + e_3 \sin \delta]^2 \end{aligned}$$

Some simple algebra leads to

$$\begin{aligned} k^2 &= 4e_1^2 \sin^2 \delta + 4e_2^2 \sin^2 \delta + 4e_3^2 \sin^2 \delta \\ &= 4 * \sin^2 \delta * (e_1^2 + e_2^2 + e_3^2) \end{aligned} \quad (34)$$

Since \underline{e} is a unit vector, the last quantity on the right-hand side of Equation (34) is equal to 1. Therefore,

$$k^2 = 4 * \sin^2 \delta \quad (35)$$

or taking the square root of both sides and solving for δ

$$\delta = \sin^{-1} (k/2) \quad (36)$$

where k is defined by Equation (32).

To solve for \underline{e} , the off-diagonal terms in Equation (30) are used. To demonstrate this using e_1 ,

$$\begin{aligned} H_{23} - H_{32} &= e_2 e_3 (1 - \cos \delta) + e_1 \sin \delta - e_2 e_3 (1 - \cos \delta) + e_1 \sin \delta \\ &= 2 * e_1 * \sin \delta \end{aligned} \quad (37)$$

Solving for e_1

$$e_1 = (H_{23} - H_{32}) / (2 * \sin \delta) \quad (38)$$

Similarly,

$$e_2 = (H_{31} - H_{13}) / (2 * \sin \delta) \quad (39)$$

$$e_3 = (H_{12} - H_{21}) / (2 * \sin \delta) \quad (40)$$

To compute the BGDs, the angle of rotation in the IRU coordinate frame is divided by the observation time. The rate about each of the IRU axes is then

$$x' = e_1 * (\delta/\Delta t) \quad (41)$$

$$y' = e_2 * (\delta/\Delta t) \quad (42)$$

$$z' = e_3 * (\delta/\Delta t) \quad (43)$$

where Δt is the observation time. These rates are converted to the units of the SMM IRU, radians per 0.512 sec, and uplinked to the spacecraft for use in the control loop.

3. RESULTS AND CONCLUSIONS

3.1 RESULTS

To date, these algorithms have been used to support all the SMM scientific off-Sun maneuvers. Since the computed parameters are designed to support pointing to celestial objects other than the Sun, the performance of the algorithms is ultimately measured by the quality of these observations. Thus far, the science observations have been completed without incident and have yielded excellent results each time. Images obtained from the SMM scientific instruments have always had the target object in the sensor FOV and at the correct times. In addition, for the heliocentric and geocentric objectives, the tracking system has continuously kept the object in view.

As an independent check, attitude determination solutions during the observations have indicated the spacecraft pointing accuracy is within 180 arc-sec. The accuracy of the solutions was approximately 30 arc-sec (3σ). The bulk of the pointing error was due to uncertainty in the IRU bias. During the observations, the spacecraft was inertially stabilized by the IRU package. However, spacecraft attitude drift occurred because of uncertainty in the knowledge of the IRU bias. This bias was calibrated periodically, and the error in the pointing did not exceed 120 arc-sec due to the error in the bias.

Most of the remaining error in the pointing accuracy was due to uncontrollable timing problems with the maneuvers. Since the geometry of the spacecraft, Earth, Sun, and target-body system was constantly changing, the required maneuvers were constantly changing. The algorithm derived above assumes the maneuvers were instantaneous. However, the SMM maneuvered at approximately 5 deg per min; consequently, pointing errors were incurred. In addition, the start time of the maneuvers was calculated at 5-sec intervals. Thus, if the maneuvers did not start at these times, greater error was incurred. The pointing errors due to the timing errors did not exceed 50 arc-sec. Other potential error sources include uncertainties in the position of the target body, the initial spacecraft attitude from which the maneuvers were performed, and the IRU scale factors which controlled the magnitude of a commanded maneuver.

3.2 CONCLUSIONS

Algorithms to support off-Sun maneuvers of the SMM have been presented. These algorithms compute parameters for maneuver planning, viewing period start and stop times, and target tracking rate. All of these items are necessary to maneuver the spacecraft to observe and track the celestial target objective. Because the Sun reference frame is non-inertial, the equations differ from ones normally seen. This work can be adapted to spacecraft that are controlled relative to the inertial frame; however, the primary application is to missions with non-inertial reference frames, such as Earth-pointing (1 revolution per orbit) missions.

ACKNOWLEDGMENTS

The authors wish to acknowledge the generous support of the following GSFC personnel: Mr. Frank Vaughn, Assistant Technical Representative, SMM Analytical Task;

Mr J. B. Joyce, Head, Mission and Network Support Section; and Mr. Gary Meyers, Head, Flight Dynamics Support Branch.

The authors also wish to thank Dr. Milton Phenneger of Computer Sciences Corporation (CSC) for his help in preparing this work for publication. In addition, the authors wish to thank Mr. Bruce Twambly for his proofreading of the technical work in this paper and his work on software that was developed as a result of this analysis. Acknowledgement for contributions to this paper are also extended to Mr. Daniel R. Kulp (CSC), Mr. Arnold Eudell (CSC), Ms. Deborah Roberts (CSC), and Mr. Robert Feiertag (CSC).

REFERENCES

1. Computer Sciences Corporation, CSC/TM-84/6131UD1, *Solar Maximum Mission Attitude Operations Handbook, Revision 4*, A. Eudell et al., July 1988
2. --, CSC/SD-78/6082, *Solar Maximum Mission (SMM) Attitude System Functional Specifications and Requirements*, R. Byrne et al., September 1978
3. Wertz, J. R., editor, *Spacecraft Attitude Determination and Control*, CSC/PR-76/6001, Dordrecht - Holland: D. Reidel
4. Computer Sciences Corporation, CSC/SD-88/6138, *Solar Maximum Mission (SMM) Celestial Body Pointing and Occultation Prediction Program (CBPOPP) User's Guide*, D. S. Pitone, November 1988

EXTENDED KALMAN FILTER FOR ATTITUDE ESTIMATION OF THE EARTH RADIATION BUDGET SATELLITE

by

Julie Deutschmann* and Itzhack Y. Bar-Itzhack**
NASA - Goddard Space Flight Center
Greenbelt, MD 20771

Abstract

This paper describes the design and testing of an Extended Kalman Filter (EKF) for ground attitude determination, misalignment estimation and sensor calibration of the Earth Radiation Budget Satellite (ERBS). Attitude is represented by the quaternion of rotation and the attitude estimation error is defined as an additive error. Quaternion normalization is used for increasing the convergence rate and for minimizing the need for filter tuning. The paper presents the development of the filter dynamic model, the gyro error model and the measurement models of the Sun sensors, the IR horizon scanner and the magnetometers which are used to generate vector measurements. The filter is applied to real data transmitted by ERBS sensors. Results are presented and analyzed and the EKF advantages as well as sensitivities are discussed. On the whole the filter meets the expected synergism, accuracy and robustness.

attitude determination. The EKF designed for ERBS allows for all of the calibration to be performed along with the attitude determination.

The use of the extended Kalman filter (EKF) for spacecraft attitude determination has been dealt with quite extensively in the past. Kau et al. [1] as well as Farrell [2], for example, used an ad-hoc solution to the problem of estimating the Euler angles directly from vector measurements. A more general approach to this problem was presented in [3]. The problem of estimating the direction cosine matrix directly from vector measurements was discussed in [4]. The filter which was required there was a linear one with some adaptation. A general analytic exposition of the use of the EKF for spacecraft attitude determination was given by Lefferts, Markley and Shuster [5]. Reference [6] dealt with the problem of estimating the attitude quaternion from vector measurements. Basically, the estimated quantity was the difference between the best known value of the quaternion and its true value. This difference was defined as a four component additive quantity. Because of this definition the estimate of the quaternion is not necessarily normal unless it converges to the correct quaternion. It was found that normalization of the estimated quaternion during the filtering process speeds up convergence and eliminates the need for filter tuning. In other references, e.g. [5], [7] and for on board attitude determination software which is used in LANDSAT 4 and is planned to be used in the GRO and EP spacecraft a multiplicative quaternion difference is used. Since it is assumed that this difference quaternion is small and as for small rotations the scalar part of the quaternion is close to 1, those algorithms are estimating only three attitude - error components. Obviously, estimation of an additive quaternion error of four parameters plus the induced normality constraint is equivalent to estimating three parameters. Because of our good experience with the additive quaternion error approach [6] we chose to implement this approach in the present EKF algorithm.

I. INTRODUCTION

An important part of spacecraft ground support is attitude determination, sensor alignment, and sensor calibration. In the past, at Goddard Space Flight Center (GSFC) in the Flight Dynamics Division (FDD) each task was performed separately, usually using a relatively small state. The use of more sophisticated algorithms has been suggested in the literature, but they have not yet been tested with real spacecraft data for ground processing in Flight Dynamics.

The purpose of this study was to design and test an Extended Kalman Filter (EKF). The filter was designed for the Earth Radiation Budget Satellite (ERBS). ERBS is equipped with the following sensors which are used for attitude determination: 2 redundant Inertial Reference Units (IRUs) each containing 3 single-axis gyroscopes, 2 digital fine Sun sensors (FSSs), 2 infrared (IR) horizon scanners, and 1 three-axis magnetometer. The state estimated by the filter consists of the attitude parameters (quaternion), sensor misalignments for the Sun sensor, magnetometer and gyros, biases for the Sun sensor, horizon scanner, magnetometer, and gyros, and scale factor corrections

for the Sun sensor, magnetometer, and gyros. The filter was tested using real spacecraft data transmitted to Earth by ERBS.

Kalman filters have not been used for ground attitude processing in the FDD at GSFC. The current ground support software implements single frame and batch estimators and, as mentioned before, much of the calibration effort is performed separately from the

In the next section we introduce the algorithms developed for the ERBS EKF.

II. THE EXTENDED KALMAN FILTER ALGORITHM

The EKF algorithm is based on the following assumed models: System model:

$$\dot{X} = f(X(t), t) + w(t) \quad (2.1)$$

Measurement Model:

$$z_k = h_k(X(t_k)) + y_k \quad (2.2)$$

where:

$$\begin{aligned} X(t) &= \text{state vector.} \\ w(t) &= \text{zero mean white process.} \\ y_k &= \text{zero mean white sequence.} \end{aligned}$$

The EKF algorithm is as follows [8]. The measurement update of the state estimate and of the estimation error covariance are performed as follows:

* Aerospace Engineer, Attitude Analysis Section, Flight Dynamic Analysis Branch.

** Professor, on leave from the Aerospace Department of Technion -Israel Institute of Technology. Member, Technion Space Research Institute, Haifa 32000, Israel.

State Estimation Update:

$$\hat{\Delta}_k(+) = \hat{\Delta}_k(-) + K_k [Z_k - h_k(\hat{\Delta}_k(-))] \quad (2.3)$$

where the Gain Matrix is evaluated as follows:

$$K_k = P_k(-) H_k^T (\hat{\Delta}_k(-)) [H_k(\hat{\Delta}_k(-)) P_k(-) H_k^T (\hat{\Delta}_k(-)) + R_k]^{-1} \quad \dots (2.4)$$

Error Covariance Update:

$$P_k(+) = [I - K_k H_k] P_k(-) [I - K_k H_k]^T + K_k R_k K_k^T \quad (2.5)$$

The propagation of the state estimate and the error covariance are accomplished using:

State Estimation Propagation:

$$\dot{\hat{\Delta}}(t) = f(\hat{\Delta}(t), t) \quad (2.6)$$

Error Covariance Propagation:

$$\dot{P}(t) = F(\hat{\Delta}(t), t) P(t) + P(t) F^T(\hat{\Delta}(t), t) + Q(t) \quad (2.7)$$

where

$$F(\Delta(t), t) = \left. \begin{array}{l} \frac{\partial f(\Delta(t), t)}{\partial \Delta(t)} \end{array} \right|_{\Delta(t) = \hat{\Delta}(t)} \quad (2.8a)$$

$$H(\Delta(-)) = \left. \begin{array}{l} \frac{\partial h(\Delta(t))}{\partial \Delta(t)} \end{array} \right|_{\Delta(t) = \hat{\Delta}(t)} \quad (2.8b)$$

R_k = covariance matrix of white sequence.
 Q = spectral density matrix of $\underline{x}(t)$.

The EKF rather than the linear KF algorithm must be used because the measurement vectors obtained from the sensors are non-linear functions of the state vector. The state vector was selected to be:

$\underline{x} =$	\underline{q}	4 quaternion components	(2.9)
	\underline{s}_g	3 gyro scale factor errors	
	\underline{q}_g	6 gyro misalignment angles	
	\underline{b}_g	3 gyro biases	
	\underline{q}_s	3 FSS misalignment angles	
	\underline{c}_s	2 FSS scale factor errors	
	\underline{b}_s	2 FSS biases	
	\underline{d}_h	2 IR horizon scanner biases	
	\underline{s}_m	3 magnetometer scale factors	
	\underline{q}_m	6 magnetometer misalignments	
\underline{b}_m	3 magnetometer biases		

Following the tradition of the NASA Goddard's Flight Dynamics Division we used vector measurements to update the EKF. (It should be noted that this is not a must but rather a choice). The effective measurements which are used to update the filter are defined as follows

$$\underline{y} = M_{AT} W_{T', meas} - A(\hat{q}) \underline{y}_I \quad (2.10)$$

where:

- \underline{y} = effective measurements.
- M_{AT} = transformation matrix from the nominal (non-misaligned) sensor to body coordinates.
- $W_{T', meas}$ = unit vector as measured by the sensor in the sensor misaligned coordinates.
- $A(\hat{q})$ = transformation matrix from the inertial to the body coordinates as a function of the estimated quaternion.
- \underline{y}_I = the measured unit vector as known in the inertial coordinates.

While the traditional EKF algorithm updates the state estimate according to (2.3), we use \underline{y} (as computed in (2.10)) to update the state estimate as follows

$$\hat{\Delta}_k(+) = \hat{\Delta}_k(-) + K_k \underline{y}_k \quad (2.11)$$

To reconcile this apparent deviation from the ordinary EKF algorithm, define dZ_k as follows

$$dZ_k = Z_k - h_k(\hat{\Delta}_k(-)) \quad (2.12)$$

then (2.3), the state update equation in the ordinary EKF algorithm, reads

$$\hat{\Delta}_k(+) = \hat{\Delta}_k(-) + K_k dZ_k \quad (2.13)$$

Next define $\underline{x}(t_k)$ as

$$\underline{x}(t_k) = \hat{\Delta}_k(-) + \underline{x}(t_k) \quad (2.14)$$

expand (2.2) in a Taylor series expansion about $\hat{\Delta}_k(-)$ and omit terms of second and higher order of $\underline{x}(t_k)$. This yields

$$Z_k = h_k(\hat{\Delta}_k(-)) + H_k \underline{x}(t_k) + \underline{y}_k \quad (2.15)$$

where H_k is as defined in (2.8b). When Z_k from (2.15) is substituted into (2.12) we obtain

$$dZ_k = H_k \underline{x}(t_k) + \underline{y}_k \quad (2.16)$$

that is, dZ_k is linearly related to $\underline{x}(t_k)$. An inspection of (2.13) reveals that the EKF estimates $\underline{x}(t_k)$, which according to (2.16) is linearly related to the effective measurement dZ_k , and then adds the estimate, $\underline{x}(t_k)$, to $\hat{\Delta}_k(-)$, the best estimate of $\hat{\Delta}(t_k)$. As will be seen in the ensuing, also our use of \underline{y} , as defined in (2.10), in the state update equation, (2.11), amounts to estimating $\underline{x}(t_k)$, which is linearly related to \underline{y} , and adding the estimate to $\hat{\Delta}_k(-)$. In fact, to show the latter we only have to show that $\underline{x}(t_k)$ is linearly related to \underline{y} . This will indeed be shown in Section IV.

III. THE DYNAMICS MODEL

The states which vary in time are the attitude parameters and bias states which are modeled as Markov rather than as bias states. (The reason for this modeling will be discussed later). The scale factors and misalignments are assumed to be constant in time.

The attitude matrix is given in terms of the quaternion, q , as follows

$$A = \begin{bmatrix} q_1^2 - q_2^2 - q_3^2 + q_4^2 & 2(q_1 q_2 + q_3 q_4) & 2(q_1 q_3 - q_2 q_4) \\ 2(q_1 q_2 - q_3 q_4) & -q_1^2 + q_2^2 - q_3^2 + q_4^2 & 2(q_2 q_3 + q_1 q_4) \\ 2(q_1 q_3 + q_2 q_4) & 2(q_2 q_3 - q_1 q_4) & -q_1^2 - q_2^2 + q_3^2 + q_4^2 \end{bmatrix} \quad (3.1)$$

The quaternion changes in time according to [8, pp. 511, 512]

$$\dot{\hat{q}} = \hat{Q}q \quad (3.2)$$

where:

$$\hat{Q} = \frac{1}{2} \begin{bmatrix} 0 & w_z & -w_y & w_x \\ -w_z & 0 & w_x & w_y \\ w_y & -w_x & 0 & w_z \\ -w_x & -w_y & -w_z & 0 \end{bmatrix} \quad (3.3)$$

and where w_x, w_y, w_z are the components of the spacecraft angular velocity vector resolved in the spacecraft coordinates. The true quaternion of the spacecraft propagates in time according to (3.2). We cannot compute q precisely since we do not know precisely the initial quaternion nor do we know w precisely as it is a measured vector and the measurement contains errors. The measured angular velocity can be written as

$$\bar{w} = w + dw \quad (3.4)$$

where

\bar{w} = gyro reading.
 w = true angular velocity.
 dw = vector of gyro errors.

Since the true quaternion propagates according to (3.2) we propagate the estimated quaternion in a similar manner; that is, we propagate it according to

$$\dot{\hat{q}} = \hat{Q}\hat{q} \quad (3.5)$$

where \hat{Q} has the form of (3.3) but its elements are the elements of the measured angular rate \bar{w} . Now a matrix $d\hat{Q}$ can be defined as follows

$$\hat{Q} = \bar{Q} - d\hat{Q} \quad (3.6)$$

Substitution of (3.6) into (3.2) results in

$$\dot{\hat{q}} = \bar{Q}\hat{q} - d\hat{Q}\hat{q} \quad (3.7)$$

When (3.5) is subtracted from (3.7) we obtain

$$\dot{\hat{q}} - \hat{Q}\hat{q} = \bar{Q}(\hat{q} - \hat{q}) - d\hat{Q}\hat{q} \quad (3.8)$$

As discussed in the introduction, we define an additive quaternion error as follows

$$dq = q - \hat{q} \quad (3.9)$$

Then (3.8) can be written as

$$d\dot{q} = \bar{Q}dq - d\hat{Q}q \quad (3.10)$$

A matrix, B , can be defined as follows

$$B = \frac{1}{2} \begin{bmatrix} -q_4 & q_3 & q_2 \\ -q_3 & -q_4 & q_1 \\ q_2 & -q_1 & -q_4 \\ q_1 & q_2 & q_3 \end{bmatrix} \quad (3.11)$$

and used in (3.10). However, since q itself is not known, we use its estimate, \hat{q} to compute (3.11). When this is done, we can write (3.10) as follows

$$d\dot{q} = \bar{Q}dq + \hat{B}dw \quad (3.12)$$

where \hat{B} is computed as in (3.11) using \hat{q} rather than q . Equation (3.12) is the dynamics equation of the additive quaternion error.

Equation (3.12) cannot be used as a dynamics model in an EKF since the vector of gyro errors, dw , is not a white noise vector. It could be modeled though as a linear system excited by a white noise. Consequently this linear model can be augmented with the dynamics model of (3.12). The augmented model is linear and is driven by a white noise vector hence the model can legitimately be used by the EKF [8]. To accomplish that we use the following standard gyro error model.

$$\begin{bmatrix} \bar{dw}_x \\ \bar{dw}_y \\ \bar{dw}_z \end{bmatrix} = \begin{bmatrix} S_{gx} & 0 & 0 \\ 0 & S_{gy} & 0 \\ 0 & 0 & S_{gz} \end{bmatrix} \begin{bmatrix} \bar{w}_x \\ \bar{w}_y \\ \bar{w}_z \end{bmatrix} + \begin{bmatrix} \theta_{gxy} & \theta_{gxz} \\ \theta_{gyx} & \theta_{gyz} \\ \theta_{gzx} & \theta_{gzy} \end{bmatrix} \begin{bmatrix} \bar{w}_x \\ \bar{w}_y \\ \bar{w}_z \end{bmatrix} + \begin{bmatrix} b_{gx} \\ b_{gy} \\ b_{gz} \end{bmatrix} + \begin{bmatrix} n_{glx} \\ n_{gly} \\ n_{glz} \end{bmatrix} \quad (3.13)$$

where

$$S_g^T = [S_{gx}, S_{gy}, S_{gz}] \quad (3.14a)$$

$$\theta_g^T = [\theta_{gxy}, \theta_{gxz}, \theta_{gyx}, \theta_{gyz}, \theta_{gzx}, \theta_{gzy}] \quad (3.14b)$$

$$b_g^T = [b_{gx}, b_{gy}, b_{gz}] \quad (3.14c)$$

$$n_g^T = [n_{glx}, n_{gly}, n_{glz}] \quad (3.14d)$$

and T denotes the transpose, S_g , θ_g and b_g are as explained in (2.9) and n_g is a white noise vector. We can write (3.13) as follows

$$\begin{bmatrix} \bar{dw}_x \\ \bar{dw}_y \\ \bar{dw}_z \end{bmatrix} = \begin{bmatrix} \bar{w}_x & 0 & 0 & \bar{w}_y & \bar{w}_z & 0 & 0 & 0 & 0 & 1 & 0 & 0 \\ 0 & \bar{w}_y & 0 & 0 & 0 & \bar{w}_x & \bar{w}_z & 0 & 0 & 0 & 1 & 0 \\ 0 & 0 & \bar{w}_z & 0 & 0 & 0 & 0 & \bar{w}_x & \bar{w}_y & 0 & 0 & 1 \end{bmatrix} \bar{x}^* + \begin{bmatrix} n_{glx} \\ n_{gly} \\ n_{glz} \end{bmatrix} \quad \dots \quad (3.15)$$

where

$$\bar{x}^{*T} = [S_g^T, \theta_g^T, b_g^T] \quad (3.16)$$

Define the following matrices

$$U = \begin{bmatrix} \bar{w}_x & 0 & 0 \\ 0 & \bar{w}_y & 0 \\ 0 & 0 & \bar{w}_z \end{bmatrix} \quad W = \begin{bmatrix} \bar{w}_y & \bar{w}_z & 0 & 0 & 0 & 0 \\ 0 & 0 & \bar{w}_x & \bar{w}_z & 0 & 0 \\ 0 & 0 & 0 & 0 & \bar{w}_x & \bar{w}_y \end{bmatrix} \quad \dots \quad (3.17a) \quad \dots \quad (3.17b)$$

then (3.15) can be written as

$$d\bar{w} = [U|W|I]\bar{x}^* + n_g \quad (3.18)$$

The vectors S_g and θ_g contained in \bar{x}^* are constants, therefore

$$G_3 = \begin{bmatrix} -\hat{q}_3 & \hat{q}_4 & \hat{q}_1 \\ -\hat{q}_4 & -\hat{q}_3 & \hat{q}_2 \\ -\hat{q}_1 & \hat{q}_2 & \hat{q}_3 \end{bmatrix} \quad G_4 = \begin{bmatrix} -\hat{q}_4 & \hat{q}_3 & -\hat{q}_2 \\ -\hat{q}_3 & \hat{q}_4 & \hat{q}_1 \\ -\hat{q}_2 & -\hat{q}_1 & \hat{q}_4 \end{bmatrix} \quad \dots \quad (4.16c) \quad \dots \quad (4.16e)$$

Further define

$$h_i = G_i v_i \quad (4.17)$$

Then (4.14) can be written as

$$v_A = A(q)v_I - [h_1 | h_2 | h_3 | h_4] \begin{bmatrix} dq_1 \\ dq_2 \\ dq_3 \\ dq_4 \end{bmatrix} \quad (4.18)$$

Finally, define

$$H_q = [h_1 | h_2 | h_3 | h_4] \quad (4.19)$$

then (4.18) can be written as

$$v_A = A(q)v_I - H_q dq \quad (4.20)$$

Now recall the definition of v_A and v_I as shown in (4.3). From these definitions it is obvious that we may substitute (4.11) and (4.20) into (4.1). When this is done and in view of (4.2), we obtain

$$y = H_q dq + M_{AT} \theta w_T + M_{AT} d w_T \quad (4.21)$$

Note from (4.8) that

$$\theta = -[ex] \quad (4.22)$$

therefore (4.21) can be written as

$$y = H_q dq - M_{AT} [ex] w_T + M_{AT} d w_T \quad (4.23)$$

The matrix M_{AT} is not known to us; however, we do know M_{AT} . It is easy to see that using the latter rather than the former does not affect the accuracy to any meaningful degree. For identical reasoning we use w_T rather than w_T . When these changes are made and the order of the cross product is changed in (4.23), we obtain

$$y = H_q dq + M_{AT} [w_T, meas \times] e + M_{AT} d w_T \quad (4.24)$$

While (4.1) indicates how to generate the effective measurement y which updates the estimate, (4.24) indicates the linear relationship between y , the attitude errors, the misalignment errors of the sensor whose measurements are being used and $d w_T$, the total error generated by the sensor. The derivation of (4.24) is the first stage in finding the measurement matrix, H , (defined in (2.8b)) for each of the sensors used onboard ERBS. In order to conclude the development which will yield those H matrices, we have to express $d w_T$ in terms of the error states of each sensor which constitute a part of x shown in (2.9). This is done next.

Fine Sun Sensor (FSS) Measurement Model

The Sun sensor measures the tangents of the two angles of the vector from the spacecraft to the sun.

These two angles are A and B . Using the measured quantities $(\tan A)_m$ and $(\tan B)_m$, the unit vector measured by the sensor is computed as follows

$$w_T, meas = [1 + (\tan A)_m^2 + (\tan B)_m^2]^{-1/2} \begin{bmatrix} (\tan A)_m \\ (\tan B)_m \\ 1 \end{bmatrix} \quad (4.25)$$

Let $u_m = (\tan A)_m$ and $v_m = (\tan B)_m$ then (4.25) becomes

$$w_T, meas = (1 + u_m^2 + v_m^2)^{-1/2} \begin{bmatrix} u_m \\ v_m \\ 1 \end{bmatrix} \quad (4.26)$$

Perturbation of (4.26) yields the following vector of errors for the measured sun vector.

$$d w_T = (1 + u_m^2 + v_m^2)^{-1/2} \begin{bmatrix} du \\ dv \\ 0 \end{bmatrix} - (1 + u_m^2 + v_m^2)^{-3/2} \begin{bmatrix} u_m^2 du + u_m v_m d v \\ u_m v_m du + v_m^2 dv \\ -u_m du + v_m dv \end{bmatrix} \quad (4.27)$$

Let

$$Q = (1 + u_m^2 + v_m^2)^{-1/2} \quad W_{11} = Q - Q^3 u_m^2 \quad W_{12} = -Q^3 u_m v_m \quad W_{21} = -Q^3 u_m v_m \quad W_{22} = Q - Q^3 v_m^2 \quad W_{31} = -Q^3 u_m \quad W_{32} = -Q^3 v_m \quad (4.28)$$

Then (4.27) can be written as

$$d w_T = \begin{bmatrix} W_{11} & W_{12} \\ W_{21} & W_{22} \\ -W_{31} & -W_{32} \end{bmatrix} \begin{bmatrix} du \\ dv \end{bmatrix} = W_s \begin{bmatrix} du \\ dv \end{bmatrix} \quad (4.29)$$

The measured quantities $(\tan A)_m$ and $(\tan B)_m$ can be written as

$$(\tan A)_m = \tan A + C_A \tan A + b_A + n_A \quad (4.30a)$$

$$(\tan B)_m = \tan B + C_B \tan B + b_B + n_B \quad (4.30b)$$

where

- C_A, C_B = scale factor errors
- b_A, b_B = biases modeled as Markov states in (3.25a)
- n_A, n_B = white noise

From (4.30) and the definition of u_m and v_m we realize that

$$du = C_A \tan A + b_A + n_A \quad (4.31a)$$

$$dv = C_B \tan B + b_B + n_B \quad (4.31b)$$

When (4.31) is substituted into (4.29) the following is obtained

$$d\mathbb{W}_T' = W_s \begin{bmatrix} C_A \tan A \\ C_B \tan B \end{bmatrix} + W_s \begin{bmatrix} b_A \\ b_B \end{bmatrix} + W_s \begin{bmatrix} n_A \\ n_B \end{bmatrix} \quad (4.32)$$

which can be written as

$$d\mathbb{W}_T' = \begin{bmatrix} W_s \begin{bmatrix} \tan A & 0 \\ 0 & \tan B \end{bmatrix} \\ W_s \begin{bmatrix} C_A \\ C_B \\ b_A \\ b_B \end{bmatrix} \\ + W_s \begin{bmatrix} n_A \\ n_B \end{bmatrix} \end{bmatrix} \quad (4.33)$$

This is then substituted into (4.24) resulting in

$$y = \begin{bmatrix} H_q & \begin{bmatrix} 0 & \dots & 0 \\ 0 & \dots & 0 \\ 0 & \dots & 0 \end{bmatrix} & M_{AT} \begin{bmatrix} W_T', \text{meas} \end{bmatrix} \end{bmatrix} \\ M_{AT} W_s \begin{bmatrix} \tan A & 0 \\ 0 & \tan B \end{bmatrix} & M_{AT} W_s \begin{bmatrix} 0 & \dots & 0 \\ 0 & \dots & 0 \\ 0 & \dots & 0 \end{bmatrix} & x \\ + M_{AT} W_s \begin{bmatrix} n_A \\ n_B \end{bmatrix} \end{bmatrix} \quad (4.34)$$

Equation (4.34) gives the measurement matrix, H, for the FSS which is used in computing the gain matrix and updating the covariance matrix. Since $\tan A$ and $\tan B$ are not available to us, we use, respectively, $(\tan A)_m$ and $(\tan B)_m$ instead. Since the measured and the true quantities are close, this change practically introduces no error.

IR Horizon Scanner Measurement Model

The horizon scanner measures the roll and pitch of the spacecraft with respect to the geodetic coordinate system (GDS), i.e. it measures the direction of the nadir vector. The horizon scanner misalignment errors are assumed to be small with respect to roll and pitch errors, to be additive to roll and pitch and indistinguishable from them. The unit vector in the direction of the nadir in the GDS is given as

$$z_{GDS}^T = [0, 0, 1] \quad (4.35)$$

In body coordinates this vector is given as

$$z_{body} = \begin{bmatrix} -\cos(r)\sin(p) \\ \sin(r) \\ -\cos(r)\cos(p) \end{bmatrix} \quad (4.36)$$

where r is the roll angle and p is the pitch angle. As mentioned, this is the measured vector; that is

$$\mathbb{W}_T', \text{meas} = \begin{bmatrix} -\cos(r)\sin(p) \\ \sin(r) \\ -\cos(r)\cos(p) \end{bmatrix}_{\text{meas}} \quad (4.37)$$

which is equal to the true vector plus error. The error vector is obtained by perturbing (4.36). The perturbation yields

$$d\mathbb{W}_T' = \begin{bmatrix} \sin(r)\sin(p)dr - \cos(r)\cos(p)dp \\ \cos(r)dr \\ -\sin(r)\cos(p)dr - \cos(r)\sin(p)dp \end{bmatrix} \quad (4.38)$$

Let

$$W_h = \begin{bmatrix} \sin(r)\sin(p) & -\cos(r)\cos(p) \\ \cos(r) & 0 \\ -\sin(r)\cos(p) & -\cos(r)\sin(p) \end{bmatrix} \quad (4.39)$$

then (4.38) can be written as

$$d\mathbb{W}_T' = W_h \begin{bmatrix} dr^* \\ dp^* \end{bmatrix} \quad (4.40)$$

We characterize the horizon scanner errors as bias (modeled as Markov process in (3.25b)) plus white noise; that is,

$$dr^* = d_r + n_{hr} \quad (4.41a)$$

$$dp^* = d_p + n_{hp} \quad (4.41b)$$

where d_r and d_p are the roll and pitch biases and n_{hr} and n_{hp} are the roll and pitch white measurement noise components. When (4.41) are substituted into (4.40), the following is obtained

$$d\mathbb{W}_T', \text{meas} = W_h b_h + W_h n_h \quad (4.42)$$

where b_h is as defined in (3.26) and $n_h^T = [n_{hr}, n_{hp}]$. Since z_{body} is already in body coordinates, M_{AT} given in (4.1) and in (4.24) is the identity matrix. Since the horizon scanner was assumed not to have misalignment error the term containing misalignment angles in (4.24) is not needed. The model for the horizon scanner is given in (4.43) below. Again y is computed using (4.1).

$$y = \begin{bmatrix} H_q & \begin{bmatrix} 0 & \dots & 0 \\ 0 & \dots & 0 \\ 0 & \dots & 0 \end{bmatrix} & W_h \begin{bmatrix} 0 & \dots & 0 \\ 0 & \dots & 0 \\ 0 & \dots & 0 \end{bmatrix} & x + W_h n_h \end{bmatrix} \quad (4.43)$$

Equation (4.43) yields the H matrix to be used with IR horizon scanner measurements. Similarly to the evaluation of the Sun sensor H matrix, we use the measured roll and pitch to evaluate W_h in (4.43).

Magnetometer Measurement Model

The three magnetometers mounted orthogonally to one another measure the Earth's magnetic field components along each of their axes. This arrangement of sensors is identical to the three gyro arrangement which measure the spacecraft's angular rate. The magnetometer error sources are also identical to the gyro error sources which are: scale factor errors, misalignments, bias (modeled as Markov process) and white measurement noise. Therefore the magnetometer errors can be represented by the same model as for the gyros. Therefore, in analogy to (3.13), we write the following expression for the errors introduced by the magnetometers

$$\begin{bmatrix} dB_x \\ dB_y \\ dB_z \end{bmatrix} = \begin{bmatrix} S_{mx} & 0 & 0 \\ 0 & S_{my} & 0 \\ 0 & 0 & S_{mz} \end{bmatrix} \begin{bmatrix} B_x \\ B_y \\ B_z \end{bmatrix} + \begin{bmatrix} 0 & \theta_{mxy} & \theta_{mxz} \\ \theta_{myx} & 0 & \theta_{myz} \\ \theta_{mzx} & \theta_{mzy} & 0 \end{bmatrix} \begin{bmatrix} B_x \\ B_y \\ B_z \end{bmatrix} + \begin{bmatrix} b_{mx} \\ b_{my} \\ b_{mz} \end{bmatrix} + \begin{bmatrix} n_{mx} \\ n_{my} \\ n_{mz} \end{bmatrix} \quad (4.44)$$

where B_x , B_y and B_z are the magnetometer measurements and

$$S_m^T = [S_{mx}, S_{my}, S_{mz}] \quad (4.45a)$$

$$\theta_m^T = [\theta_{mxy}, \theta_{mxz}, \theta_{myx}, \theta_{myz}, \theta_{mzx}, \theta_{mzy}] \quad (4.45b)$$

$$b_m^T = [b_{mx}, b_{my}, b_{mz}] \quad (4.45c)$$

$$n_m^T = [n_{mx}, n_{my}, n_{mz}] \quad (4.45d)$$

S_m , θ_m and b_m are the vectors of magnetometer scale factors, misalignments and biases, and n_m is the white measurement noise vector. The magnetometer output vector B_{meas} can be written as

$$B_{T,meas} = B_T + dB \quad (4.46)$$

where B_T is the true magnetic field vector in the assumed magnetometer coordinates (note the difference between these sensors and the FSS and IR horizon scanner). We can write (4.44) as follows

$$\begin{bmatrix} dB_x \\ dB_y \\ dB_z \end{bmatrix} = \begin{bmatrix} B_x & 0 & 0 & B_y & B_z & 0 & 0 & 0 & 0 & 1 & 0 & 0 \\ 0 & B_y & 0 & 0 & 0 & B_x & B_z & 0 & 0 & 0 & 1 & 0 \\ 0 & 0 & B_z & 0 & 0 & 0 & 0 & B_x & B_y & 0 & 0 & 1 \end{bmatrix} x^+ + \begin{bmatrix} n_{mx} \\ n_{my} \\ n_{mz} \end{bmatrix} \quad (4.47)$$

where

$$x^{+T} = [S_m^T, \theta_m^T, b_m^T] \quad (4.48)$$

Define the matrix B' as follows

$$B' = \begin{bmatrix} B_x & 0 & 0 & B_y & B_z & 0 & 0 & 0 & 0 & 1 & 0 & 0 \\ 0 & B_y & 0 & 0 & 0 & B_x & B_z & 0 & 0 & 0 & 1 & 0 \\ 0 & 0 & B_z & 0 & 0 & 0 & 0 & B_x & B_y & 0 & 0 & 1 \end{bmatrix} \quad (4.49)$$

We may write then (4.47) as

$$dB = B' x^+ + n_m \quad (4.50)$$

Note that dB is not identical to dB_T , the way the latter is defined in (4.4) since dB contains the magnetometer misalignment errors whereas dB_T does not. For this reason dB cannot be substituted for dB_T in (4.24). We have, then, to use the basic definition of y as applied to the magnetometer readings in order to formulate the linear relationship between y and the magnetometer errors which constitute x^+ . For magnetometer measurements we formulate our effective measurement, y , as follows

$$y = M_{AT} B_{T,meas} - A(\hat{Q}) y_I \quad (4.51)$$

Substitute (4.46) into (4.51) and in view of (4.3b) also substitute (4.20) into (4.51). This results in

$$y = M_{AT} B_T + M_{AT} dB - A(\hat{Q}) y_I + H_Q dq \quad (4.59)$$

Note that the first and third terms on the right-hand side of (4.59) cancel one another. Then when (4.50) is substituted into (4.59) we obtain the desired result

$$y = H_Q dq + M_{AT} B' x^+ + M_{AT} n_m \quad (4.60)$$

or more explicitly

$$y = \begin{bmatrix} H_Q & 0 & \dots & 0 \\ 0 & \dots & \dots & 0 \\ 0 & \dots & \dots & 0 \end{bmatrix} M_{AT} B' + M_{AT} n_m \quad (4.61)$$

Equation (4.61) yields the H matrix to be used with the magnetometer measurement updates. As for the previous sensors, we use the measured magnetometer data to evaluate B' . Finally, note again that the effective magnetometer measurements which have to be processed by the EKF are computed using (4.51) and not (4.1).

Measurement Error

The main component in the magnetometer noise vector, n_m , is the quantization error. Its nature and characterization is explained as follows. The output of the magnetometers is received in the telemetry stream as

$$N^T = [N_x, N_y, N_z] \quad (4.62)$$

with N in counts. The i th component of N ($i=x,y,z$) is obtained from the actual measured components as [9]

$$N_i = \text{INT}(B_{i,meas}/K_i) \quad (4.63)$$

where INT means "the integer part of". Obviously, a certain part of the measured value is lost due to the INT operation: that is

$$\text{INT}(B_{i,meas}/K_i) + n_i = B_{i,meas}/K_i \quad (4.64)$$

The nature of the INT operation is such that n_i can vary between 0 to 1. Moreover, the distribution of the chopped off value is uniform over the range 0 to 1. It is then easy to show that

$$E(n_i) = 0.5 \quad (4.65a) \quad \text{Var}(n_i) = 1/12 \quad (4.65b)$$

Substituting (4.63) into (4.64) yields

$$N_i = B_{i,meas}/K_i - n_i \quad (4.66)$$

It is easy to see why in order to calculate the magnetometer readings on the ground the following computation is performed

$$B_{i,comp} = K_i [N_i + 0.5] \quad (4.67)$$

Substituting (4.66) into (4.67) yields

$$B_{i,comp} = K_i [B_{i,meas}/K_i - n_i + 0.5] \quad (4.68)$$

Define the measurement noise of magnetometer i as

$$n_{m,i} = K_i (0.5 - n_i) \quad (4.69)$$

then, in view of (4.65),

$$E(n_{m,i}) = 0 \quad (4.70a) \quad \text{Var}(n_{m,i}) = K_i^2/12 \quad (4.70b)$$

where E denotes the expected value and Var denotes the variance. From (4.48) and (4.69)

$$B_{i,comp} = B_{i,meas} + n_{m,i} \quad (4.71)$$

and in vector form

$$\underline{B}_{comp} = \underline{B}_{meas} + \underline{n}_m \quad (4.72)$$

From (4.46), (4.47), (4.61) and (4.72) it is obvious that the noise vector to be used in (4.61) is the vector \underline{n}_m as defined in (4.69) whose expected value and variance are defined in (4.70)

V. QUATERNION NORMALIZATION

The quaternion which represents attitude is a normal one. It was found [6] that forcing normalization on the estimated quaternion is advantageous since it speeds up convergence and eliminates the need for filter tuning. It was found in the present work too that normalization has these benefits. As shown in [6], normalization of the quaternion is equivalent to removing a portion of the estimate. This part that is removed must be accounted for in the next stage of the filtration. The handling of the normalization in this work is not identical to the one in [6] since here the covariance and state are propagated by solving their respective differential equations and not by using the state transition matrix as is the case in [6]. There the part of the estimate which is removed by normalization is propagated using the state transition matrix and is considered at the next measurement update of the state estimate. Here though the normalization is done in between measurements. After the state estimate update by the horizon scanner measurement, the quaternion is normalized as follows

$$\hat{q}_{IR}^*(+) = \hat{q}_{IR}(+) / |\hat{q}_{IR}(+)| \quad (5.1)$$

where the subscript IR denotes the fact that the quaternion estimate being dealt with is at the time point where the IR horizon scanner measurement are considered, (+) denotes the a-posteriori estimate and the superscript * denotes the resultant normal quaternion. It can be shown [6] that the normalization

removes the following part from $\hat{q}_{IR}(+)$

$$d\hat{q}_N = \hat{q}_{IR}(+) \hat{q}_{IR}^T(+) d\hat{q}_{IR} \quad (5.2)$$

where $d\hat{q}_{IR} = K_{IR} \underline{y}_{IR}$ is the estimate of $d\hat{q}$ which is computed using the kalman gain and the effective measurement of the scanner. Now when the FSS measurements are processed next, the estimate of the quaternion is updated as follows

$$d\hat{q}_{FSS}(+) = d\hat{q}_N + K_{FSS} [\underline{y}_{FSS} - H_{FSS} d\hat{q}_N] \quad (5.3a)$$

$$\hat{q}_{FSS}(+) = \hat{q}_{IR}^*(+) + d\hat{q}_{FSS}(+) \quad (5.3b)$$

where $\hat{q}_{FSS}(+)$ is the quaternion estimate after its update by the FSS measurements. If no normalization is

performed, $\hat{q}_{IR}^*(+) = \hat{q}_{IR}(+)$, $d\hat{q} = 0$ and (5.3) change

accordingly. In any event, the quaternion, $\hat{q}_{FSS}(+)$, is used as the a priori estimate of \hat{q} for the magnetometer update, if available, or else is propagated to the next time point.

VI. COMPENSATION

When propagating the state estimate and the covariance, we use the measured angular velocity. We know, however, that the propagated values are not accurate since the gyro outputs contain errors. As we estimate those errors, we can do better if we correct the gyro outputs for estimated errors. This operation is known as calibration.

We also want to compensate the measurements obtained from the FSS, the IR horizon scanner, and the magnetometers which are all orientation measuring devices whose outputs are used to update the filter. The reason we want to compensate these sensors' outputs is different in nature than the reason for compensating the gyro outputs. Rewrite (4.1) and (2.11)

$$\underline{y} = M_{AT} \underline{W}_T, meas - A(\hat{q}) \underline{v}_I \quad (6.1)$$

$$\hat{\underline{x}}_k(+) = \hat{\underline{x}}_k(-) + K_k \underline{y}_k \quad (6.2)$$

The term $K_k \underline{y}_k$ is nothing but the estimate of \underline{x} defined in (2.14) as

$$\underline{x}(t_k) = \hat{\underline{x}}(-) + \underline{x}(t_k) \quad (6.3)$$

That is, in (2.11) we estimate the difference between the true value of \underline{x} and its latest estimate, and add the estimate of the difference to the latest estimate of \underline{x} to form its updated estimate. Now let us consider an error term in one of the sensor measurements, say a bias. This bias is a part of $\underline{W}_T, meas$ and thus, as indicated in (6.1), bears its signature on \underline{y} . Consequently, if certain observability conditions are met, it is estimated and added to the state estimate as indicated in (6.3). If no compensation takes place, the next time the measurements of this sensor will be processed the bias will again be estimated and added to the previous estimate of this bias, thus creating a too large and hence wrong estimate. The correct way, then, to handle this case is to eliminate the estimate of the bias from $\underline{W}_T, meas$. This way only residual bias which has not been estimated yet will be present in \underline{y} as shown in (6.1). Only the estimate of this residual will, then, be added to the existing estimate of the

bias, which is a part of $\hat{\underline{x}}$, yielding a correction to the previous estimate. This logic holds for the other error states too. The way we carried out the compensation is outlined in the ensuing.

Gyro Compensation

From (3.4)

$$\underline{w} = \underline{\bar{w}} - d\underline{w} \quad (6.4a)$$

$$\text{therefore} \quad \hat{\underline{w}} = \underline{\bar{w}} - d\hat{\underline{w}} \quad (6.4b)$$

Rewrite (3.18)

$$d\underline{w} = [U|W|I] \begin{bmatrix} -\hat{s}_g \\ \hat{\theta}_g \\ \hat{b}_g \\ \dots \end{bmatrix} + \underline{n}_{g1} \quad (6.5)$$

Since U and W are functions of \underline{w} , and since the noise vector is of zero mean, a good estimate of $d\underline{w}$ is obtained from (6.5) as

$$d\hat{\underline{w}} = [U(\hat{\underline{w}})|W(\hat{\underline{w}})|I] \begin{bmatrix} -\hat{s}_g \\ \hat{\theta}_g \\ \hat{b}_g \\ \dots \end{bmatrix} \quad (6.6)$$

This estimate can then be used in (6.4b) to yield an estimate of \underline{w} which is then used in the propagation algorithm instead of the raw gyro outputs.

FSS Compensation

Consider

$$\underline{y} = M_{AT} \underline{w}_{T',meas} - A(\hat{q}) \underline{v}_I \quad (6.7)$$

and recall (4.3)

$$\underline{w}_A = M_{AT} \underline{w}_{T',meas} \quad (6.8a) \quad \underline{v}_A = A(\hat{q}) \underline{v}_I \quad (6.8b)$$

As explained earlier, \underline{y} is a linear function of \underline{x} which is the difference between $\hat{\underline{x}}$ and \underline{x} . We want \underline{x} to go to zero when $\hat{\underline{x}}$ approaches \underline{x} . Indeed, when $\hat{\underline{x}}$ approaches \underline{x} , \hat{q} approaches q and \underline{v}_A computed in (6.8b) really yields the components of the unit vector in the Sun's direction when resolved in body coordinates. However,

even when $\hat{\underline{x}}$ is equal to \underline{x} , $\underline{w}_{T',meas}$ will not be equal to \underline{w}_T and therefore \underline{w}_A computed in (6.8a) will not be equal to \underline{v}_A and thus \underline{y} will not be zero. (This fact shouldn't be confused with the fact that \underline{y} goes to zero when the errors themselves go to zero). Only when

$\underline{w}_{T',meas}$ goes to \underline{w}_T as $\hat{\underline{x}}$ goes to \underline{x} , will \underline{y} go to zero as it should. To achieve this use (4.4) to note that

$$\underline{w}_T = M_{TT'} (\underline{w}_{T',meas} - d\underline{w}_{T'}) \quad (6.9)$$

As shown in (4.7), for small FSS misalignment angles

$$M_{TT'} = I + \theta \quad (6.10)$$

Transposing (6.10) we obtain

$$M_{T'T} = I - \theta \quad (6.11)$$

which when substituted into (6.9) yields

$$\underline{w}_T = (I - \theta) (\underline{w}_{T',meas} - d\underline{w}_{T'}) \quad (6.12)$$

Therefore a reasonable estimate of \underline{w}_T is

$$\hat{\underline{w}}_T = (I - \hat{\theta}) (\underline{w}_{T',meas} - d\hat{\underline{w}}_{T'}) \quad (6.13)$$

Replacing $\underline{w}_{T',meas}$ in (6.7) by $\hat{\underline{w}}_T$ yields the desired result

$$\underline{y} = M_{AT} (I - \hat{\theta}) (\underline{w}_{T',meas} - d\hat{\underline{w}}_{T'}) - A(\hat{q}) \underline{v}_I \quad (6.14)$$

where, in view of (4.32), $d\hat{\underline{w}}_{T'}$ is computed as follows

$$d\hat{\underline{w}}_{T'} = W_s \begin{bmatrix} -\hat{c}_A(\tan A)_m \\ -\hat{c}_B(\tan B)_m \end{bmatrix} + W_s \begin{bmatrix} -\hat{b}_A \\ -\hat{b}_B \end{bmatrix} \quad (6.15)$$

Note that initially when our estimate of \underline{x} is zero, (6.14) is reduced to (6.1).

IR Horizon Scanner Compensation

The arguments made in outlining the FSS compensation are also valid for the horizon scanner only that here $d\underline{w}_{T'}$ is different and there are no sensor misalignments (they are considered to be a part of the bias errors). Following (4.42), we compute for the horizon scanner

$$d\hat{\underline{w}}_{T'} = \hat{w}_h \hat{b}_h \quad (6.16a)$$

and

$$\hat{\theta} = 0 \quad (6.16b)$$

and substitute them into (6.14). The result is then the compensated effective measurement of the IR horizon sensor.

Magnetometer Compensation

As shown in (4.51) which is rewritten below, \underline{y} is computed differently for the magnetometer measurements; namely

$$\underline{y} = M_{AT} \underline{B}_T \text{meas} - A(\hat{q}) \underline{v}_I \quad (6.17)$$

where

$$\underline{B}_T \text{meas} = \underline{B}_T + d\underline{B} \quad (6.18a)$$

and

$$d\underline{B} = B' \underline{x}^+ + \underline{n}_m \quad (6.18b)$$

$$\underline{x}^{+T} = [\underline{s}_m^T, \underline{q}_m^T, \underline{b}_m^T] \quad (6.18c)$$

Following the rationale behind the FSS and IR horizon scanner and in view of (6.18), we compensate the magnetometer readings as follows. Compute

$$\hat{\underline{x}}^{+T} = [\hat{\underline{s}}_m^T, \hat{\underline{q}}_m^T, \hat{\underline{b}}_m^T] \quad (6.19a)$$

$$d\hat{\underline{B}} = B' \hat{\underline{x}}^+ \quad (6.19b)$$

where B' is computed according to (4.49) using the uncompensated outputs of the magnetometers. Next compute the compensated magnetometer measurements

$$\hat{\underline{B}}_T = \underline{B}_T \text{meas} - d\hat{\underline{B}} \quad (6.19c)$$

which are used to compute the effective measurement as follows

$$\hat{\underline{y}} = M_{AT} \hat{\underline{B}}_T - A(\hat{q}) \underline{v}_I \quad (6.19d)$$

VII. THE COMPLETE ERBS EKF ALGORITHM

The models developed in the previous section were implemented into a program written in Fortran. The data used in the program is actual spacecraft data transmitted to Earth by ERBS.

MEASUREMENT UPDATES

The program is set up to compute an update initially and then propagate. The updates are performed for each sensor individually, the horizon scanner update is performed first, followed by the sun sensor, and the magnetometer. If any sensor data are not available the program bypasses that sensor and goes on to the next. In between each sensor update, the updated state and covariance are set to the a-priori values going into the next sensor update. If no sensor data are available, the a-posteriori state and covariance are set equal to the a-priori and are propagated to the next time point.

Below is a summary of the algorithm and how it is applied to each update and to the propagation.

IR Update

Compute H:

$$H = \begin{bmatrix} \bar{H}_q & | & 0 \dots 0 & | & \bar{w}_h & | & 0 \dots 0 \\ \hline & & 0 \dots 0 & & & & 0 \dots 0 \\ \hline & & 0 \dots 0 & & & & 0 \dots 0 \end{bmatrix} \quad (7.1)$$

Compute $\underline{w}_{T',meas}$:

$$\underline{w}_{T',meas} = \begin{bmatrix} -\cos(r)\sin(p) \\ \sin(r) \\ -\cos(r)\cos(p) \end{bmatrix}_{\text{meas}} \quad (7.2)$$

Compensate \hat{W}_T', meas :

$$\hat{Q}_T = \hat{W}_T', \text{meas} - \hat{Q}_h \hat{Q}_h \quad (7.3)$$

Compute residual and uncertainty of residual:

$$y = \hat{Q}_T - A(\hat{Q}) \underline{V}_{I,ir} \quad (7.4)$$

$$(u_{ir})_j = ([HP(-)H^T + R_{ir}])_j^{1/2} \quad (7.5)$$

where the subscript *ir* denotes quantities pertinent to the horizon scanner, $\underline{V}_{I,ir}$ is the spacecraft-to-earth unit vector obtained from the ephemeris and *j* denotes the *j*th element on the main diagonal of the residual covariance matrix.

State and Covariance Update

Compute K:

$$K_k = P_k(-) H_k^T [H_k P_k(-) H_k^T + R_k]^{-1} \quad (7.6)$$

Update \hat{X} :

$$\hat{X}_k(+) = \hat{X}_k(-) + K_k y_k \quad (7.7)$$

Update P:

$$P_k(+) = (I - K_k H_k) P_k(-) (I - K_k H_k)^T + K_k R_k K_k^T \quad (7.8)$$

Sun Sensor Update

Compute H:

$$H = \begin{bmatrix} 0 & \dots & 0 \\ H_q & 0 & \dots & 0 \\ 0 & \dots & 0 & \dots & 0 \\ 0 & \dots & 0 & \dots & 0 \end{bmatrix} M_{AT} [\hat{W}_T', \text{meas}^X] \begin{bmatrix} \tan A & 0 \\ 0 & \tan B \end{bmatrix} \begin{bmatrix} M_{AT} W_s & 0 & \dots & 0 \\ 0 & \dots & 0 & \dots & 0 \\ 0 & \dots & 0 & \dots & 0 \end{bmatrix} \quad (7.9)$$

Compute \hat{W}_T', meas :

$$\hat{W}_T', \text{meas} = (1 + (\tan A)_m^2 + (\tan B)_m^2)^{-1/2} \begin{bmatrix} (\tan A)_m \\ (\tan B)_m \\ 1 \end{bmatrix} \dots \quad (7.10)$$

Compensate \hat{W}_T', meas :

$$\hat{Q}_T = (I - \hat{Q}) (\hat{W}_T', \text{meas} - W_s \begin{bmatrix} \hat{C}_A(\tan A)_m \\ \hat{C}_B(\tan B)_m \end{bmatrix} - W_s \begin{bmatrix} \hat{G}_A \\ \hat{G}_B \end{bmatrix}) \dots \quad (7.11)$$

Compute residual and uncertainty of residual:

$$y = \hat{Q}_T - A(\hat{Q}) \underline{V}_{I,fss} \quad (7.13)$$

$$(u_{fss})_j = ([HP(-)H^T + R_{fss}])_j^{1/2} \quad (7.14)$$

where the subscript *fss* denotes quantities pertinent to the fine Sun sensor, $\underline{V}_{I,fss}$ is the spacecraft-to-Sun unit vector obtained from a Solar-Lunar-Planetary file and *j* denotes the *j*th element on the main diagonal of the residual covariance matrix. The state and covariance are then updated as in (7.6) through (7.8).

Magnetometer Update

Compute H:

$$H = \begin{bmatrix} 0 & \dots & 0 \\ H_q & 0 & \dots & 0 \\ 0 & \dots & 0 & \dots & 0 \end{bmatrix} M_{AT} B' \quad (7.15)$$

Compute \hat{B}_T', meas :

$$\hat{B}_T', \text{meas} = \begin{bmatrix} \hat{B}_x \\ \hat{B}_y \\ \hat{B}_z \end{bmatrix} \quad (7.16)$$

Compensate \hat{B}_T', meas :

$$\hat{Q}_T = \hat{B}_T', \text{meas} - \hat{B}' \begin{bmatrix} \hat{S}_m \\ \hat{Q}_m \\ \hat{G}_m \end{bmatrix} \quad (7.17)$$

Compute residual and uncertainty of residual:

$$y = \hat{Q}_T - A(\hat{Q}) \underline{V}_{I,mag} \quad (7.18)$$

$$(u_{mag})_j = ([HP(-)H^T + R_{mag}])_j^{1/2} \quad (7.19)$$

where the subscript *mag* denotes quantities pertinent to the magnetometers, $\underline{V}_{I,mag}$ is a unit vector in the direction of the magnetic field obtained from a 1980 International Geomagnetic Reference Field model available in a Fortran subroutine and *j* denotes the *j*th element on the main diagonal of the residual covariance matrix. The state and covariance are then updated as in (7.6) through (7.8).

STATE AND COVARIANCE PROPAGATION

After all the sensor updates are performed, the state and covariance are propagated using a fourth order Runge-Kutta routine. The state and covariance are propagated ahead using the gyro data at the time of the update and the gyro data one second (nominally) ahead. Before propagating, though, the gyro data is compensated as follows.

$$\hat{W} = \underline{W} - [U|W|I] \begin{bmatrix} \hat{S}_g \\ \hat{Q}_g \\ \hat{G}_g \end{bmatrix} \quad (7.20)$$

State Propagation

$$\dot{\hat{X}}(t) = f(\hat{X}(t), t) \quad (7.21)$$

Covariance Propagation

$$\dot{P}(t) = F(\hat{X}(t), t) P(t) + P(t) F^T(\hat{X}(t), t) + Q(t) \quad (7.22)$$

VIII. RESULTS

Reference Solution

The reference we used for comparison was the attitude solution obtained from the batch estimator used on the ground for operational attitude determination for ERBS. Table 8.1 shows the attitude solutions in the GDS and uncertainties for three different conditions (cases). Case 1 used sensor standard deviations of: FSS = 0.002 deg, IR = 0.2 deg,

MAG = 0.5 (unit vector). An orbit's worth of data was used to compute the solution. Case 2 used the same amount of data as the first but the sensor standard deviations were: FSS = 0.1 deg, IR = 0.5 deg, MAG = 0.5 (unit vector). Case 3 had the same sensor standard deviations as the second but only 30 seconds of data were used. Obviously, the reference solution is not unique although the real solution is.

Table 8.1 Final Attitude Solutions and Uncertainties (deg.)

	Case 1		Case 2		Case 3	
	Attitude	Unc.	Attitude	Unc.	Attitude	Unc.
Yaw	-0.294	0.0135	-0.262	0.004	-0.731	0.012
Roll	0.400	0.0118	0.421	0.005	0.316	0.070
Pitch	0.650	0.173	0.420	0.004	0.384	0.007

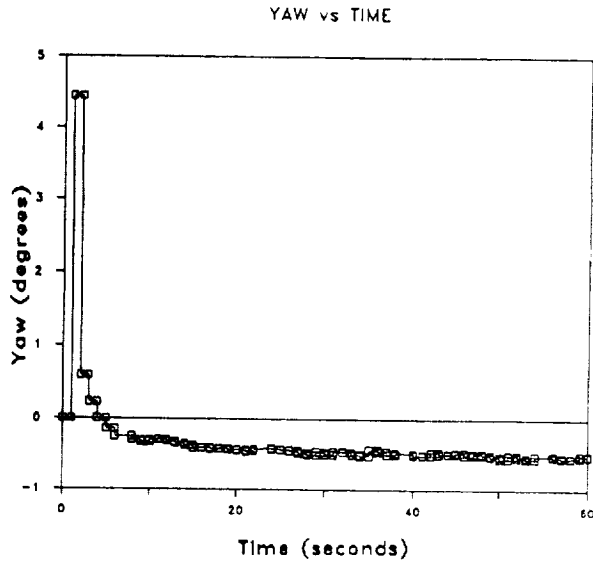


Figure 2: YAW vs. TIME Full State

Filter Solution

Since ERBS is not inertially fixed, it is not very enlightening to see the variation in the quaternion. Therefore, in order to compare the filter solution to the batch solution, the estimated quaternion was converted to roll, pitch, and yaw in the GDS. We used the filter first to estimate attitude only. Figure 1 shows the yaw solution in the GDS and is a typical example of the behavior when estimating attitude only.

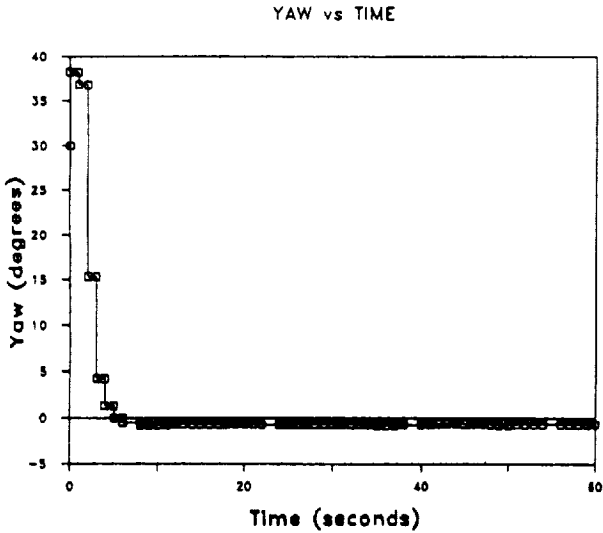


Figure 1: YAW vs. TIME No Calibration States

The filter was then run with the full state starting at an a-priori attitude of zero degrees yaw, roll, and pitch. Figures 2 and 3 show the behavior of the yaw and pitch. Roll is similar to pitch. Figure 4 shows the estimation of the Z component of the gyro bias and Figure 5 shows an example of the residual behavior.

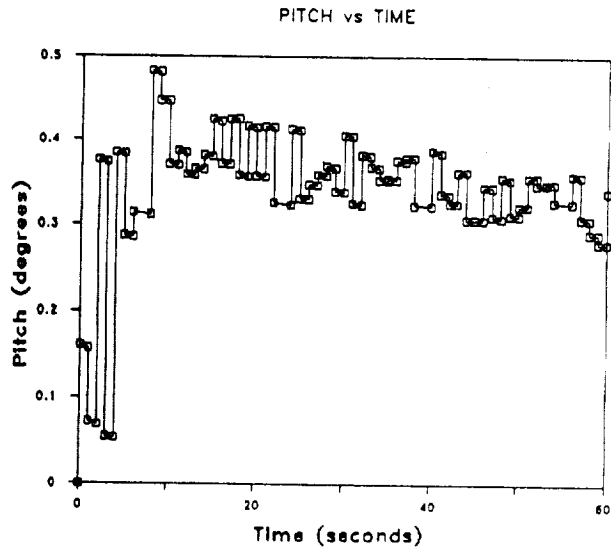


Figure 3: PITCH vs. TIME Full State

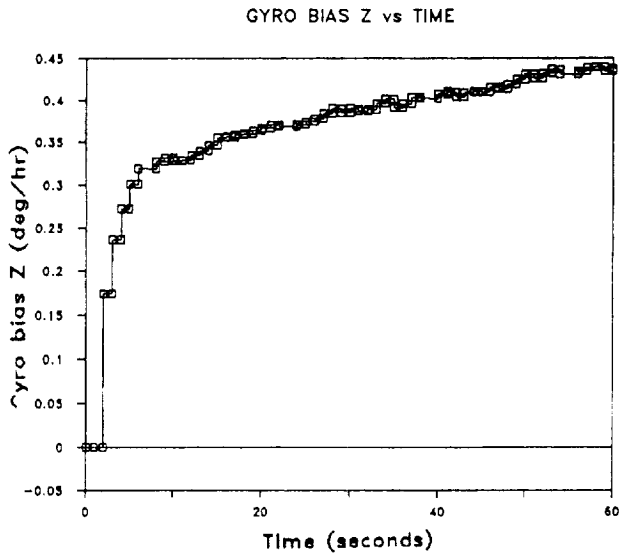


Figure 4: GYRO BIAS Z vs. TIME
Full State

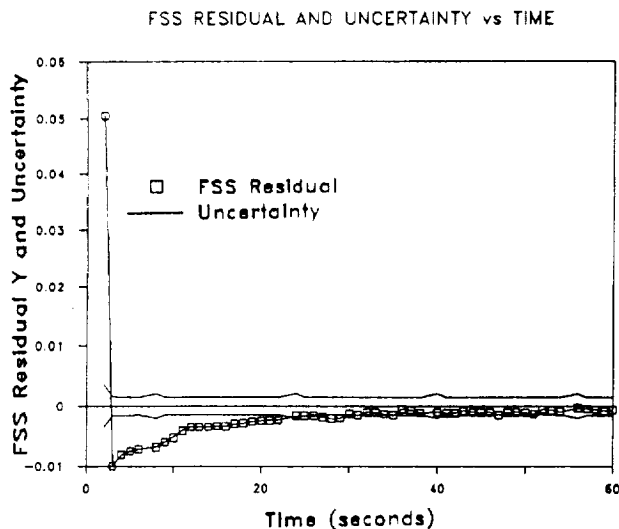


Figure 5: FSS RESIDUALS Y vs. TIME
Full State

Table 8.2 gives the final attitude solutions and the various calibration states (after 60 sec of data) for 2 different sets of initial conditions (which actually differ only in the FSS and IR bias uncertainty).

Table 8.2: Attitude and Calibration States for Varying Initial Conditions

	Case 1		Case 2	
Yaw	-0.512		-0.676	
Roll	0.354		0.406	
Pitch	0.339		0.253	
	<u>Value</u>	<u>Unc.</u>	<u>Value</u>	<u>Unc.</u>
GYRO				
SF	0.194E-4	0.01	0.360E-5	0.01
	-0.598E-4	0.00998	3.898E-5	0.00998
	-0.786E-4	0.01	-4.384E-5	0.01
θ (deg)	0.62E-4	0.057	3.2E-4	0.057
	0.34E-4	0.057	0.50E-4	0.057
	0.028E-4	0.057	0.013E-4	0.057
	0.15E-4	0.057	0.046E-4	0.057
	-0.070E-4	0.057	0.052E-4	0.057
	-14.6E-4	0.057	-10.2E-4	0.057
Bias (Deg/hr)	-0.0211	1.995	-0.0984	1.995
	0.0094	1.995	-0.0096	1.995
	0.4381	1.995	0.3037	1.995
FSS				
θ (Deg)	0.0648	0.050	0.0017	0.056
	0.0466	0.054	0.0114	0.056
	0.0896	0.057	0.0140	0.057
SF	-0.0235	0.00607	-0.00557	0.009
	-0.0177	0.00830	0.00044	0.00954
Bias (Deg)	0.1732	0.086	0.077	0.151
	0.0812	0.058	-0.0468	0.0709
IR				
Bias (Deg)	0.2115	0.032	0.0340	0.0472
	-0.2377	0.033	-0.0840	0.046
MAG				
Bias (mg)	-0.499	0.699	-0.597	0.698
	-1.479	0.816	-1.237	0.816
	0.289	0.911	0.223	0.911
(other magnetometer states are negligible)				

Initial Uncertainties:

Gyro

- SF = 3*0.01
- θ = 6*0.057 deg
- bias = 2.0*3 deg/hr

FSS

$\theta = 3 \times 0.057$ deg,
SF = 2×0.01
Bias = 2×0.1 in case 1,
 2×0.316 in case 2

IR

--

Bias = 2×0.1 in case 1,
 2×0.316 in case 2

MAG

Bias = 3×1 mGauss

IX. CONCLUSIONS

The ERBS EKF shows good, quick convergence properties when estimating only attitude. The filter is robust in that it can overcome initial attitude errors of up to 30 degrees (it may even go higher but 30 degrees was the limit of our testing). When the remaining calibration states are added, and the sensor measurements are compensated for their calibration states the filter is not very robust. Starting the filter with a large initial attitude error would be outside of the linear region and the filter is not expected to give good behavior in those conditions.

The attitude solutions estimated by the filter show some oscillation. Since the results presented are from real spacecraft data the filter would be expected to follow more closely the oscillations in the data whereas a batch solution would have these oscillations averaged out.

We found, when estimating the entire state, that the results were dependent on the initial uncertainties due to a lack of observability. The batch solution which was used as our basis of comparison also was dependent on initial conditions. It could not be used as a true reference.

The ability of the filter to quickly converge to an attitude solution from a large initial error demonstrates the feasibility of using an EKF for ground attitude processing in FDD, particularly in a real-time situation. Since all the states cannot be estimated simultaneously due to a lack of observability, more investigation into the a-priori uncertainties is necessary in order to achieve a desired accuracy in the final calibration states.

X. FUTURE WORK

In this work, the batch solution served only as a basis for comparison. It cannot be treated as a true reference. Simulated data will be used in the future, which will provide a true reference. From there further studies of the different calibration states and the ability of the filter to estimate them can be determined. At the time of this writing, the runs using simulated data were still being debugged.

A further enhancement of the filter state will need to be made to include more than one sensor of a single type. Currently the filter only estimates calibration parameters for the sensors with coverage; no switching is done when the coverage changes over to another sensor of the same type.

As mentioned previously, the ability to overcome large initial attitude errors makes the filter attractive for real-time operations. A real-time EKF will be developed which estimates attitude and possibly gyro calibration states only.

References

1. Kau, S., Kumar, K.S.P. and Granley, G.B., "Attitude Determination Via Nonlinear Filtering," IEEE Transactions on Aerospace and Electronic Systems, Vol. AES-5, Nov. 1969, pp. 906 - 911.
2. Farrell, J.L., "Attitude Determination by Kalman Filtering," Automatica, Vol. 6, 1970, pp. 419 - 430.
3. Bar-Itzhack, I.Y. and Idan, M., "Recursive Attitude Determination from Vector Observations: Euler Angle Estimation," Journal of Guidance, Control, and Dynamics, Vol. 10, March - April 1987, pp. 152-157.
4. Bar - Itzhack, I.Y. and Reiner, J., "Recursive Attitude Determination from Vector Observations: DCM Identification," Journal of Guidance, Control, and Dynamics, Vol. 7, Jan. - Feb. 1984, pp. 51 - 56.
5. Lefferts, E.J., Markley, F.L., and Shuster, M.D., "Kalman Filtering for Spacecraft Attitude Estimation," Journal of Guidance, Control, and Dynamics, Vol. 5, Sept. - Oct. 1982, pp. 417 - 429.
6. Bar - Itzhack, I.Y. and Oshman, Y., "Recursive Attitude Determination from Vector Observation: Quaternion Estimation," IEEE Transactions on Aerospace and Electronic Systems, Vol. AES-21, Jan. 1985, pp. 128 - 136.
7. Murrell, J.W., "Precision Attitude Determination for Multimission Spacecraft," Paper No. 78-1248, AIAA Guidance and Control Conference, Palo-Alto, CA., August 7-9, 1978.
8. Gelb, A., (ed.), Applied Optimal Estimation, M.I.T. Press, Cambridge MA, 1988.
9. Wertz J. R., Spacecraft Attitude Determination and Control, D. Reidel Publishing Company, Dordrecht Holland, 1978.

FLIGHT MECHANICS/ESTIMATION THEORY SYMPOSIUM

SESSION 4

**AUTOMATION OF ORBIT DETERMINATION FUNCTIONS
FOR NATIONAL AERONAUTICS AND SPACE
ADMINISTRATION (NASA)-SUPPORTED SATELLITE
MISSIONS***

**H. Mardirossian, K. Heuerman, A. Beri, and M. Samii
Computer Sciences Corporation (CSC)**

**C. E. Doll
Goddard Space Flight Center (GSFC)**

ABSTRACT

The Flight Dynamics Facility (FDF) at Goddard Space Flight Center (GSFC) provides spacecraft trajectory determination for a wide variety of National Aeronautics and Space Administration (NASA)-supported satellite missions, using the Tracking Data Relay Satellite System (TDRSS) and Ground Spaceflight and Tracking Data Network (GSTDN). To take advantage of computerized decisionmaking processes that can be used in spacecraft navigation, the Orbit Determination Automation System (ODAS) was designed, developed, and implemented as a prototype system to automate orbit determination (OD) and orbit quality assurance (QA) functions performed by orbit operations. Based on a machine-resident generic schedule and predetermined mission-dependent QA criteria, ODAS autonomously activates an interface with the existing trajectory determination system using a batch least-squares differential correction algorithm to perform the basic OD functions. The computational parameters determined during the OD are processed to make computerized decisions regarding QA, and a controlled recovery process is activated when the criteria are not satisfied. The complete cycle is autonomous and continuous.

ODAS has been extensively tested for performance under conditions resembling actual operational conditions and found to be effective and reliable for extended autonomous OD. Details of the system structure and function are discussed, and test results are presented.

*This work was supported by the National Aeronautics and Space Administration (NASA)/Goddard Space Flight Center (GSFC), Greenbelt, Maryland, under Contract NAS 5-31500.

1. INTRODUCTION

Operational orbit support for many current National Aeronautics and Space Administration (NASA) missions involves a well-defined sequence of activities leading up to the generation and transmission of estimated dynamic states and definitive and predictive ephemerides for supported spacecraft. These activities can be separated into three stages: tracking data preprocessing (TDP), orbit determination (OD), and orbit product generation and transmission (OPGT). Figure 1 provides an overview of this type of orbit support at the Goddard Space Flight Center (GSFC). Only the OD stage is described in detail. The TDP and OPGT stages are included to show their relationships with the OD stage. This paper presents the Orbit Determination Automation System (ODAS), which is designed to automate activities involved in the OD stage (References 1 and 2). Automation is achieved in ODAS through replacement of functions that are normally performed by an analyst. A brief description of the functions involved in OD is useful in understanding the nature of the automation processes in ODAS and is provided below.

Current trajectory determination systems process tracking measurements and use them in conjunction with parameterized dynamic models to update the estimate of the dynamic states of supported spacecraft (References 3 and 4). As a specific example, the Goddard Trajectory Determination System (GTDS), employed regularly at GSFC, employs a differential correction (DC) algorithm to fit the tracking measurements to the models and estimate a solution state for the spacecraft orbit. The estimated solution state is used to generate trajectories and other orbit-related products. In Figure 1, the orbit maintenance schedule serves to provide information about when spacecraft are due for OD; the tracking data base represents the collection of tracking measurements, a subset of which is used for OD. The operational OD at GSFC involves the following steps, some of which require intervention by the analyst:

Step I. The analyst scans the orbit maintenance schedule at regular intervals to determine if an orbit update is scheduled for a spacecraft at a time close to the time of the scan.

Step II. The analyst appraises the tracking measurements for the particular spacecraft in the tracking data base to establish sufficiency in quantity and distribution.

Step III. The analyst determines initial parameters to be supplied to the trajectory determination system as control and data information and incorporates the values into OD control/input data sets (CIDS), which the analyst retrieves from the control and input parameters data base.

Step IV. The resulting set of OD processing commands sets up the trajectory determination system in a specific processing mode. The analyst initiates orbit estimation in this processing mode.

Steps V and VI. If the estimation process converges, a solution state for the spacecraft is generated by the computational system. The analyst examines the computed results, including state vectors, other estimated parameters, and ephemerides.

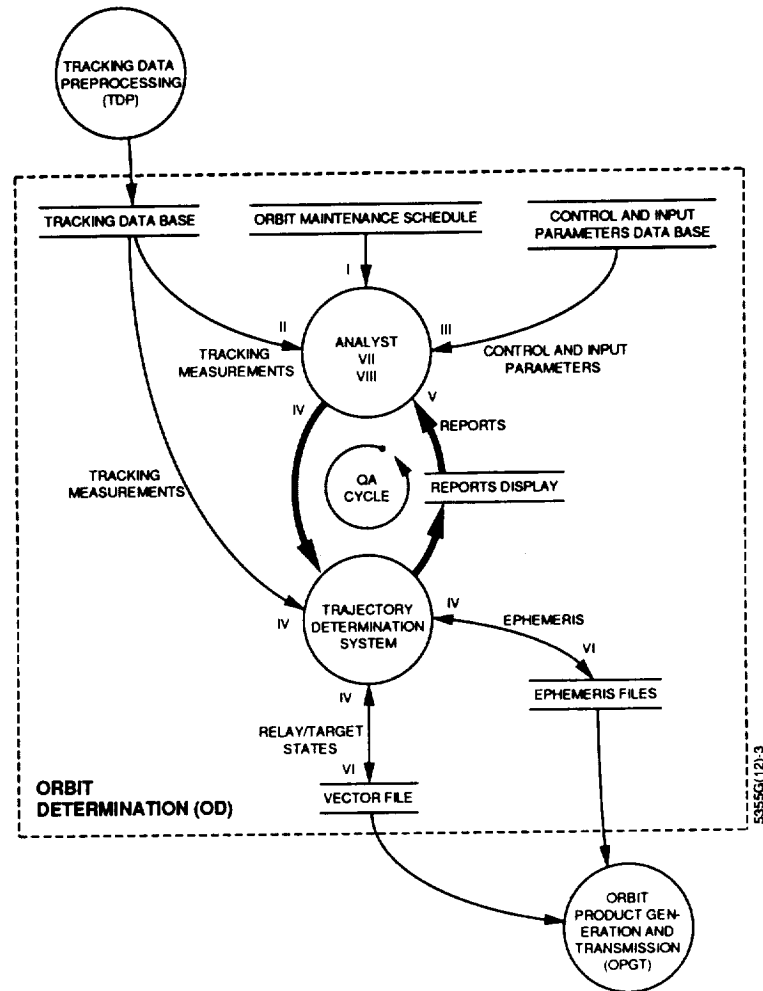


Figure 1. Orbit Determination Activities

Step VII. The analyst determines the pass/fail condition of the estimation result on the basis of a comparison of specific quality assurance (QA) parameters available from reports generated by the trajectory determination system with mission-dependent QA criteria. This is the QA failure detection process.

Step VIII. In case of QA failure, the analyst determines specific changes in processing modes that might lead to improved orbit estimation. This is the QA failure recovery initiation process.

The analyst modifies the processing modes in which the trajectory determination system is set up and repeats the OD and QA operations described in steps II through VIII as often as necessary to generate a satisfactory solution. This represents OD QA through a cyclical recovery process represented by the bold circle in Figure 1.

Since automation of the OD process potentially provides benefits—such as reduced analyst intervention, reduced demand on system resources, improved operational

flexibility, improved reliability, automatic accumulation of historical experience, and a ready source of operational and analytical training—ODAS was developed to create an autonomous analog of the processing environment depicted in Figure 1. Some of the OD steps have been previously automated by systems such as the Orbit Production Automation System (OPAS), which incorporates aspects of steps I, III, and IV (Reference 5), and the Automatic Orbit Determination IV (AOD-IV) system (Reference 6), which specializes in applications of step III. However, these systems require analyst intervention for all other phases of the OD process. The ability of ODAS to sustain autonomous operation of the entire OD process indefinitely without any analyst intervention is the system's primary distinguishing feature.

The remainder of this paper concerns the functional and structural aspects of ODAS. The specific prototype described in this paper was developed within the GTDS environment. In Section 2, primary functions of ODAS that provide autonomous analogs of the steps in Figure 1 are discussed. In Section 3, the structural configuration and coordination of the primary ODAS functions in performing the overall OD process is described. In Section 4, selected system tests are described and the test results presented to illustrate some of the operational aspects of the system. In Section 5, the significant conclusions resulting from this prototyping study are summarized, and directions for future enhancements are discussed.

2. ODAS FUNCTIONS

The functional objective of ODAS is to provide an autonomous analog of the overall OD process represented by the boxed area in Figure 1. The eight-step OD process has been described in Section 1. The functional design of ODAS consists of logical functions that accomplish tasks corresponding to each of the eight steps in the proper sequence without any analyst intervention. Additional logical functions in ODAS provide the capability to perform this autonomous OD continuously for an indefinite period. These functions are discussed in the remainder of this section.

Table 1 lists all the primary ODAS functions and establishes a mapping between each ODAS function and an operational step. Each ODAS function is briefly described.

OD Update Scheduling. This function schedules spacecraft for OD. ODAS makes periodic queries of a generic scheduling data (GSD) file for information related to the update frequency and processing parameters. OD updates are then performed according to these specifications.

Tracking Data Sufficiency Checking. The DC process of GTDS operates on tracking measurements from a chosen period denoted as the "data arc" (step IV of Figure 1). Typically in step II, the analyst considers the number of distinct trackers, the number of tracking data batches, and the presence and disposition of large periods containing no measurements (gaps) in qualifying the measurement set as sufficient or insufficient for achieving a reliable OD solution. In case of insufficiency, the analyst can extend the data arc further back in time (arc retrocession) to access more data or "better" data. In ODAS, the data arc is specified generically in the GSD file and is converted into a specific data arc.

Automated data tracking sufficiency checking and arc retrocession capabilities analogous to step II are present in ODAS.

Table 1. ODAS Functions and Corresponding Routine Operational Orbit Determination Steps

ODAS FUNCTION	ROUTINE OD OPERATION*
OD UPDATE SCHEDULING	I
TRACKING DATA SUFFICIENCY CHECKING	II
CIDS CREATION	III
CIDS SUBMISSION	IV
DC/STATISTICAL OUTPUT REPORT (SOR) EXTRACTION	V
DC FAILURE DETECTION	VII
DC FAILURE RECOVERY	VIII, III, IV, V
EPHEMERIS QA	VI
TIME CONTROL	NR
PROCESSING SUSPENSION/RESUMPTION	NR
SYSTEM STATUS REPORTING	NR

*NR: NOT REPRESENTED IN FIGURE 1.

CIDS Creation. In close analogy to step III, the CIDS creation function of ODAS retrieves a skeleton CIDS, which represents a specific GTDS processing mode from the CIDS file and incorporates processing information from the GSD file into the data set.

CIDS Submission. This function submits the CIDS to the processing queue of a host computer system to initiate the corresponding DC process. The CIDS submission step is the automated version of step IV.

DC/SOR Extraction. This function extracts certain parameters, which includes the parameters specified in Table 2, from the DC/SOR output reports for analysis. For several of the GSFC-supported spacecraft, acceptable limits are specified for these parameters (Reference 7). In ODAS, several additional quantities are included in the DC/SOR subset because of their potential values in DC recovery in case of DC failure. The DC/SOR extraction is analogous to step V.

DC Failure Detection. This function determines whether DC was successful or failed established QA criteria. The QA parameters are retrieved from the DC/SOR subset and are compared with predetermined limits/tolerances from a user-defined QA criteria file. The current design of ODAS recognizes a fixed set of seven DC failures listed in Table 2. This function of ODAS corresponds to step VII in Figure 1.

DC Failure Recovery. The last step in the overall OD process is step VIII, for which the analyst decides whether to repeat the estimation under different processing conditions if a DC failure is detected. The analyst may implement one or more recovery procedures,

Table 2. ODAS DC Failures

ODAS NAME	DC FAILURE TYPE
F1	NONCONVERGENT DC
F2	FINAL WEIGHTED ROOT MEAN SQUARE (WRMS) OF OBSERVATION RESIDUALS EXCEEDS CRITERION
F3	ESTIMATED ATMOSPHERIC DRAG SCALING PARAMETER (q_1) OUTSIDE NOMINAL RANGE
F4	ESTIMATED SOLAR RADIATION PRESSURE SCALING PARAMETER (C_R) OUTSIDE NOMINAL RANGE
F5	STANDARD DEVIATION OF RANGE OBSERVATION RESIDUALS (σ_R) EXCEEDS CRITERION
F6	STANDARD DEVIATION OF RANGE-RATE/DOPPLER OBSERVATION RESIDUALS ($\sigma_{R/D}$) EXCEEDS CRITERION
F7	ESTIMATED ABSOLUTE POSITION ERROR IN A PRIORI STATE (ΔR) EXCEEDS CRITERION

involving repeating the estimation under different processing conditions. Typical examples of recovery procedures are using a different selection of batches of tracking data, a different range of values for the atmospheric density, or a different convergence criterion. The choice is dictated by the type of DC failure detected. The overall failure recovery process may involve more than one recovery procedure. This process is automated in ODAS by the DC Failure Recovery function. Currently, ODAS provides five distinct recovery procedures, which are listed in Table 3. In general, each recovery procedure can generate a different set of failed criteria and different magnitudes of departures from the criteria. ODAS computes a weighted sum of the magnitudes to use as an average indicator of the overall degree of failure and implements recommended recovery procedures in an attempt to reduce this indicator to zero. In addition, the overall recovery process is controlled through limits on the maximum number of recovery attempts and the minimum relative improvement in the indicator.

Table 3. Procedures Employed in ODAS to Attempt Recovery From DC QA Failure

ODAS NAME	RECOVERY PROCEDURE
P1	CHANGE HARRIS-PRIESTER DENSITY TABLE
P2	EXTEND DATA ARC BACKWARD
P3	ELIMINATE BIASED OR NOISY BATCHES
P4	INCREASE INITIAL WRMS
P5	USE FINAL ELEMENTS AS INPUT

Ephemeris QA. Operationally, OD consistency is measured through a point-by-point comparison of adjacent overlapping ephemerides. The magnitude of the maximum difference, $|\Delta R_{\text{ephem}}|$, relative to a tolerance specified in Reference 7 provides the required measure of OD consistency. This function is included in step V of Figure 1 and is performed in ODAS using an algorithm that involves extraction of the ephemeris comparison results from the GTDS reports and the tolerances from the criteria file.

Time Control. The time control function of ODAS is a device for biasing and scaling the time variable, with respect to actual clock time, to allow the autonomous operations of ODAS to be performed for arbitrary times (past and present) and to proceed at accelerated schedules. This function is not a replication of any single step in Figure 1 because routine operational OD is performed in real time.

Processing Suspension/Resumption. To provide continuous operation for indefinite periods of time, portions of ODAS must be active continuously. The current operational OD support, on the other hand, involves periods (for tracking measurement accumulation, the TDP stage of Figure 1) during which OD is not actively performed. A capability is devised to detect the onset and duration of such a processing mode, suspend activities for the required period, release resources, and resume processing automatically at the end of the suspension period. A short suspension mode is also provided to handle lull periods during a series of clustered OD updates.

System Status Reporting. ODAS generates status reports both for transmitting results between ODAS components and for informing the analyst who monitors the automated OD operation. The chronological progress reports data and archival capabilities can be utilized to support operational analysis.

The functions described above represent the primary building blocks of an OD automation system. The ODAS prototype discussed in this paper is constructed with the specific requirements of the GSFC FDF environment in mind, such as compatibility with the global trajectory computation and orbital products support system. The construction is embodied in a particular configuration of the functions as components of larger units, namely subsystems of ODAS, and of the sequential and hierarchical relationships among the subsystems. This specific configuration of ODAS is the subject of Section 3.

3. ODAS CONFIGURATION

The primary ODAS functions described in Section 2 can be designed in several ways, depending on the host computational system and operational/development requirements. At GSFC, operational orbit support is based on background batch processing with programs that are available in GTDS. "Batch" here is the computational term describing a noninteractive processing of complete, predefined jobs and must be distinguished from the batch estimation technique in OD, referred to in Sections 1 and 2. The requirement for prototype development that greatly influenced the design of the primary ODAS functions in the current version of ODAS was the use of GTDS components as black boxes: no modifications were made to the GTDS programs. The resulting configuration, shown in Figure 2, incorporates the DC, Ephemeris Generation (EPHEM), and Ephemeris

Comparison (COMPARE) programs of GTDS without modifications. One of the prominent features of ODAS, namely the presence of numerous interface input/output (I/O) files, is a direct consequence of this requirement.

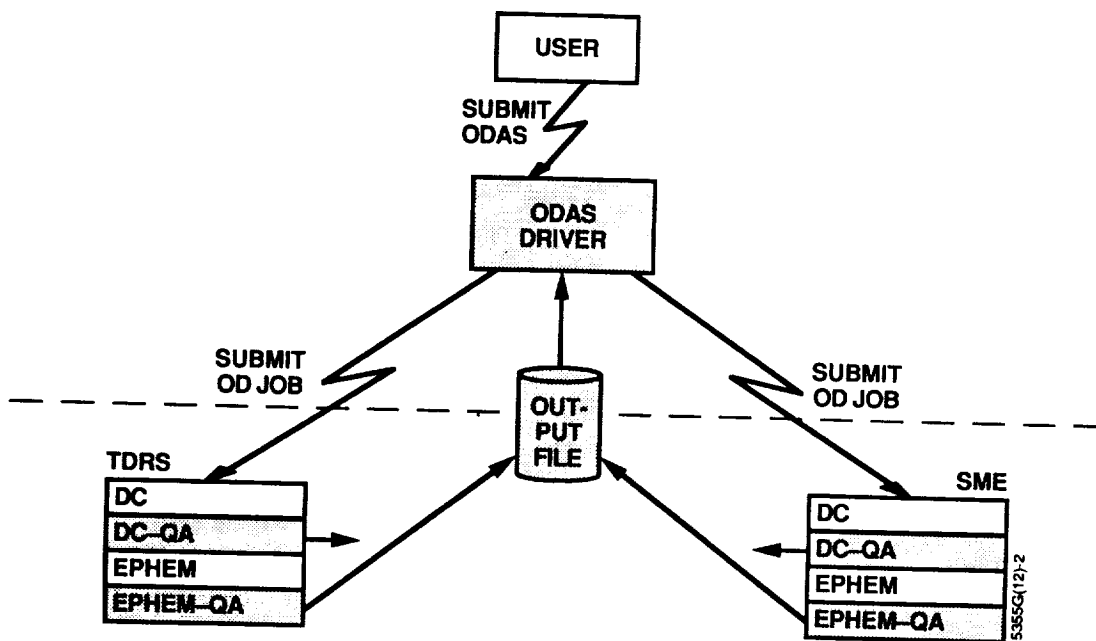


Figure 2. ODAS Configuration

The design of the ODAS prototype consists of the following five coordinated subsystems and the interfaces between the subsystems as defined in Figure 2:

- The ODAS Driver subsystem
- The DC subsystem
- The DC QA subsystem
- The EPHEM subsystem
- The EPHEM QA subsystem

The user initiates ODAS by submitting the ODAS Driver subsystem, which executes indefinitely until terminated by the user. The ODAS Driver periodically submits a series of OD jobs, each consisting of the other four subsystems, for all spacecraft scheduled for OD update. Figure 2 represents a typical situation in which the ODAS Driver has submitted two OD jobs, one for the Tracking and Data Relay Satellite (TDRS) and another for the Solar Mesospheric Explorer (SME). The DC QA subsystem analyzes the DC results and, in the case of OD failures, communicates the result to the interface output file and terminates execution. In the case of successful DC, the EPHEM and EPHEM QA subsystems are executed, and the result is communicated to the interface output file. The ODAS

Driver monitors the output file to determine the status of the OD process and make decisions affecting subsequent processing. The remainder of this section describes the logical functions being performed within each subsystem.

ODAS Driver Subsystem. The ODAS Driver is responsible for the overall initiation and control of the computational functions within ODAS. It resides permanently on the host system and is designed to be in perpetual execution, monitoring all automation functions, and effectively synchronizing tasks. The ODAS Driver is functionally separated into five major components:

- The scheduler component
- The tracking data sufficiency checking component
- The job submission component
- The timer component
- The suspension/resumption component

After scheduling spacecraft for OD for the day, the Driver suspends its activities, resuming at scheduled OD times for each spacecraft. It then checks the tracking data for sufficiency; if the data do not meet the user-defined criteria for sufficiency, the Driver extends the data arc backward in time to obtain additional data. If arc extension still does not meet the criteria, the Driver stops processing that spacecraft for that day. If the sufficiency checking passes, the Driver then prepares CIDS for that spacecraft and submits jobs involving the four ODAS subsystems for OD and QA processing. After submission of OD jobs, the Driver periodically checks the output file for the results of OD. If the OD results indicate a DC failure and a directive to reexecute the DC to recover from the failure, the Driver prepares new CIDS and resubmits the four ODAS subsystems for another round of OD processing.

DC QA Subsystem. The DC QA subsystem performs quality assurance of DC results and consists of four components. The DC/SOR subset extraction component extracts subsets of parameters from the DC reports and the SOR analysis. The failure detection component diagnoses specific DC failures, based on computational parameters generated by the DC processing in the SOR. It determines whether a DC solution has met the spacecraft acceptance criteria determined by the user. In the absence of DC failure, the DC QA subsystem terminates and initiates processing of the EPHEM subsystem. In the presence of DC failure, the DC QA subsystem activates the recovery component. For a specific DC failure, the recovery component invokes a corresponding recovery procedure, which translates into system control modifications that have been prescribed by expert analysts. The results transmission component transmits the decisionmaking information from the DC QA subsystem to the ODAS Driver subsystem.

EPHEM QA Subsystem. The EPHEM QA subsystem performs QA on the results from the EPHEM subsystem by comparing the maximum difference between the previous definitive ephemeris and the currently computed definitive ephemeris. The EPHEM QA subsystem consists of three components. The compare extraction component takes the

computational parameters for a spectrum of different solutions between two sequential ephemerides and provides the data to the EPHEM QA subsystem for further analysis. The failure detection component determines if ephemeris comparison results meet specific mission-dependent requirements. The results transmission component transmits the decisionmaking information from the EPHEM QA subsystem to the ODAS Driver subsystem.

Certain characteristics of the configuration are crucial to reliable, continual operation of ODAS. The logical separation of the individual OD jobs from the Driver, for example, ensures that problems arising during the DC and post-DC processing will not affect any ODAS Driver functions, thereby enabling processing of the remainder of the OD jobs to proceed normally. The maintenance of a single interface (see Output File in Figure 2) between the ODAS Driver and all OD jobs allows efficient monitoring, coordinating, and scheduling by the ODAS Driver. Of great significance is the generic table-driven nature of the DC failure detection and recovery components, which allows convenient modification of the actual choices of recovery algorithms to be associated with particular DC failures. In this area, ODAS requires continuous evolutionary enhancements, as indeed does any mode of operational processing requiring complex decisionmaking regarding options for improving OD.

4. TEST RESULTS AND DISCUSSION

The presence of scheduling, time scaling, and suspension/resumption functions in ODAS allows extensive system and performance testing in a relatively short time (Reference 8). All tests involve the automated analog of the OD process of Figure 1. Many tests address additional ODAS-unique functions, such as extraction of a preselected set of parameters from the DC/SOR characterizing the measurements and the measurement residuals. The tests were performed using an ODAS prototype implemented in VS FORTRAN on an IBM-compatible host computer.

Test results presented in this section are grouped by individual ODAS functions. Only selected tests that typify test categories are presented in this section. Eight spacecraft were used in testing ODAS:

- TDRS-E
- SME
- Solar Maximum Mission (SMM)
- Landsat-4
- Landsat-5
- Meteorological Observation Satellite (NIMBUS-7)
- Earth Radiation Budget Satellite (ERBS)
- Dynamics Explorer (DE)-A

One or more tests were performed in the course of OD for each of the spacecraft, as shown in test case matrix entries for each function. Test result summaries are presented in the remainder of this section.

Initiation. The objective of testing the initiation function was to check the validity of ODAS response with respect to different system start parameters (see Table 4). The tests consisted of initiating ODAS as a cold start (first initiation of ODAS), terminating its processing, and reinitiating it as a warm start (subsequent initiations of ODAS within the same day) and varying speed ratio as compared to clock time.

Table 4. Test Matrix for the Initiation Function of ODAS

INITIATION SUBFUNCTIONS	TDRS	SME	SMM	Landsat-4	Landsat-5	NIMBUS-7	ERBS	DE-A
COLD START ODAS	•	•	•	•	•	•	•	•
WARM START ODAS	•	•	•	•	•	•	•	•
SPEED RATIO	•	•	•	•	•	•	•	•

ODAS was initiated as a cold start with all eight spacecraft scheduled for OD. After performing OD for TDRS, execution was halted by the user for a short period and then reinitiated as a warm start. ODAS resumed processing activities that were continuations of those interrupted at the time its operation was halted. ODAS was also initiated using a speed ratio of six (six times faster than normal clock time), where a 24-hour cycle was compressed into 4 hours of real clock time. All tests were successful.

Scheduler. The goal of testing of the scheduler function was to confirm the ODAS scheduling ability under various conditions (see Table 5). This included transforming the generic schedule of spacecraft provided by the user through the GSD to a specific schedule for a given day of ODAS operation.

Using a generic schedule for all spacecraft, ODAS created a specific schedule for the current test day (September 11, 1987) and the next day for all spacecraft. Additionally, OD for DE-A was rescheduled for September 11, 1987, at 02 hours according to the GSD entry. ODAS successfully scheduled DE-A for 2 a.m. on the current test day. The timer component accurately kept track of the ODAS time, and the suspension/resumption component suspended ODAS activities and resumed at scheduled spacecraft OD times. All tests were successfully performed.

Tracking Data Sufficiency Checking. The goal of testing the tracking data sufficiency checking function of ODAS was to verify that ODAS would only perform OD when sufficient tracking data were in the 60-byte metric tracking data base for a given data arc. As shown

Table 5. Test Matrix for the Scheduler Function of ODAS

SCHEDULER SUBFUNCTIONS	TDRS	SME	SMM	Landsat-4	Landsat-5	NIMBUS-7	ERBS	DE-A
SCHEDULE SPACE-CRAFT	•	•	•	•	•	•	•	•
RESCHEDULE SPACE-CRAFT								•
TIMER COMPONENT	•	•	•	•	•	•	•	•
SUSPEND/RESUME ODAS	•	•	•	•	•	•	•	•

in Table 6, seven subfunctions were tested, based on the specific parameters defining sufficiency. The parameters are

- Number of distinct trackers
- Total number of tracking data batches
- The largest gap in data
- The total number of observations

Table 6. Test Matrix for the Tracking Data Sufficiency Checking Function of ODAS

TRACKING DATA SUFFICIENCY CHECKING SUBFUNCTIONS	TDRS	SME	SMM	Landsat-4	Landsat-5	NIMBUS-7	ERBS	DE-A
SUFFICIENCY CHECK PASSED	•	•	•	•	•	•	•	•
INSUFFICIENT TRACKERS					•			
INSUFFICIENT BATCHES				•				
DATA GAP TOO LARGE	•			•				
INSUFFICIENT OBSERVATIONS					•			
ARC RETROCESSION FAILURE			•					
NO TRACKING DATA							•	•

In addition, the case of an unsuccessful attempt at tracking data improvement using arc retrocession was also tested.

To test the case of insufficient trackers, the criterion for minimum number of distinct trackers for Landsat-5 was set to four. The tracking data contained only three distinct trackers, which did not satisfy the criterion. ODAS extended the data arc back to obtain an extra distinct tracker to meet the criterion, then continued with the processing of OD for Landsat-5. To test the case of insufficient batches, the criterion for the minimum acceptable number of batches was set to 14 for Landsat-4. The data contained only 13 batches for the given arc. ODAS extended the data arc back to obtain an extra batch to meet the criterion. To test the case of no tracking data, a 60-byte metric tracking data base that contained no tracking data for ERBS and DE-A spacecraft was chosen. The sufficiency tracking function detected this, generated warning messages, and aborted OD processing for DE-A and ERBS.

Job Submission. The goal of testing the job submission function was to verify that ODAS did possess the ability to set up and submit GTDS DC, EPHEM, and their associated QA subsystems. Testing the job submission function of ODAS involved checking the accuracy of job control language (JCL) and input for all the jobs submitted (see Table 7).

Table 7. Test Matrix for the Job Submission Function of ODAS

JOB SUBMISSION SUBFUNCTIONS	TDRS	SME	SMM	Landsat-4	Landsat-5	NIMBUS-7	ERBS	DE-A
CIDS MODIFICATION	•	•	•	•	•	•	•	•
JOB SUBMISSION	•	•	•	•	•	•	•	•

Using the skeleton CIDS files set up by the user for all spacecraft, ODAS created updated CIDS files for the specific test day and submitted them for all spacecraft. All tests were successful.

DC Failure Detection. The goal of testing the DC failure detection function was to verify the ODAS capability to detect and respond to DC failures (see Table 8). The tests were performed by setting the failure criteria to unreasonable numbers to guarantee the failures of certain desired parameters. In Table 5, the subfunctions listed represent all of the single-failure cases.

ODAS was executed using sufficient data for all spacecraft to test the case of DC convergence. The case of nonconvergent DC was generated by using a small data arc and an extremely stringent convergence criterion. Divergence of the DC was detected, and a recovery attempt was initiated. The remaining subfunctions in the table refer to individual DC failures, all of which were successfully detected.

DC Failure Recovery. The goal of these tests are twofold. The tests described here are designed to verify whether the recommended recovery procedure would be initiated when a particular DC failure was detected. However, other tests within this category have a performance aspect to them for which the ultimate effectiveness of the specific recovery procedure in resolving that specific failure is to be verified. This aspect of testing relies

Table 8. Test Matrix for the DC Failure Detection Function of ODAS

DC FAILURE DETECTION SUBFUNCTIONS	TDRS	SME	SMM	Landsat-4	Landsat-5	NIMBUS-7	ERBS	DE-A
CONVERGED DC	•	•	•	•	•	•	•	•
NONCONVERGENCE		•						
FINAL WRMS TOO LARGE	•	•		•	•			
ρ_1 OUT OF RANGE		•	•					
C_R OUT OF RANGE	•							
σ_R TOO LARGE			•	•	•			
$\sigma_{R/D}$ TOO LARGE				•		•		
ΔR TOO LARGE						•		

most heavily on complete decisionmaking processes reliant on qualitative human experience, requirements which are difficult to emulate in the ODAS-type development environment. This area properly belongs in the realm of basic research and is not addressed here. Testing the DC failure recovery component of the DC QA subsystem involved a complicated set of tests to check the performance of the five ODAS recovery procedures. It involved creating DC failures and verifying attempts at using the proper recovery procedure(s) to recover from the failure(s) (see Table 9).

Table 9. Test Matrix for the DC Failure Recovery Function of ODAS

DC FAILURE RECOVERY SUBFUNCTIONS	TDRS	SME	SMM	Landsat-4	Landsat-5	NIMBUS-7	ERBS	DE-A
MODIFY H-P DENSITY TABLE NUMBER		•						•
EXTEND DATA ARC BACKWARD		•						
DELETE BIASED/NOISY BATCHES	•		•	•				
INCREASE INITIAL WRMS VALUE					•			
USE FINAL ELEMENTS AS INPUT						•		
UNRECOVERABLE		•						

Testing the recovery procedure to modify the H-P density table number involved the case of ϱ_1 failures. ODAS successfully computed a new density table number to meet the QA criterion and recover from the failures. For example, performing DC for SME spacecraft produced a solution with $\varrho_1 = -0.724$, using H-P density table number 8. This failed the QA criterion set at an acceptable range of -0.7 to 0.7 . ODAS computed a new H-P density table number 7, reexecuted DC, and obtained a solution with $\varrho_1 = -0.645$, which passed the QA criterion.

Testing the recovery procedure to extend the data arc backward involved using TDRS with a data arc of 34 hours. ODAS successfully extended the data arc backward by half an arc length (17 hours).

Testing the recovery procedure to eliminate biased or noisy batches involved using TDRS, SMM, and Landsat-4. For example, a WRMS value of 2.47 was obtained for TDRS, where the QA criterion was set at 1.45. ODAS used the recovery procedure to eliminate biased or noisy batches and identified a set of batches that need to be deleted. This successfully brought the WRMS value to 1.43, which passed the QA test.

Ephemeris QA. The goal of testing the Ephemeris QA function of ODAS was to verify the successful comparison of ΔR_{ephem} with the criterion for maximum EPHEM overlap difference (see Table 10).

Table 10. Test Matrix for the Ephemeris QA Function of ODAS

EPHEMERIS QA SUBFUNCTIONS	TDRS	SME	SMM	Landsat-4	Landsat-5	NIMBUS-7	ERBS	DE-A
PASS COMPARE CRITERIA	•							
FAIL COMPARE CRITERIA	•	•			•		•	

For the case of TDRS spacecraft, the ΔR_{ephem} value met the QA criterion. The criterion was changed, and ODAS reported an EPHEM QA failure. For the initial day of ODAS execution, all EPHEM QA failed since no previous overlap data arcs were available for comparison.

ODAS Reporting. The goal of testing the reporting function of ODAS was to verify that proper information was sent to the designated files, and the ODAS activities could be monitored (see Table 11). This involved executing ODAS and monitoring the output files.

ODAS successfully processed its output files. The log files contained different levels of detailed reporting on ODAS activities. The DC/SOR output files contained summaries of DC results for few executions for each spacecraft.

Miscellaneous Functions. The goal of testing the miscellaneous functions of ODAS was to validate other embedded functions. These are defined in Table 12.

Table 11. Test Matrix for the Reporting Function of ODAS

REPORTING SUBFUNCTIONS	TDRS	SME	SMM	Landsat-4	Landsat-5	NIMBUS-7	ERBS	DE-A
ODAS LOG FILES	•	•	•	•	•	•	•	•
DC/SOR SUBSET FILES	•	•	•	•	•	•	•	•
OTHER OUTPUT FILES	•	•	•	•	•	•	•	•

Table 12. Test Matrix for Miscellaneous Functions of ODAS

MISCELLANEOUS SUBFUNCTIONS	TDRS	SME	SMM	Landsat-4	Landsat-5	NIMBUS-7	ERBS	DE-A
DC/SOR OUTPUT EXTRACTION	•	•	•	•	•	•	•	•
DIFFERENT DATA TYPES	•					•		
CONTINUOUS EXECUTION	•	•	•	•	•	•	•	•

The DC/SOR output extraction function successfully extracted all required output parameters from the DC/SOR output file for all spacecraft. This involved searching through the output files, locating the required parameters, and extracting them. ODAS successfully processed different data types, e.g., TDRS System (TDRSS) data with TDRS spacecraft, and only Spaceflight and Tracking Data Network (STDN) Ranging Equipment (SRE) data for NIMBUS-7 spacecraft. ODAS was also executed on a continuous basis for 3 days without any problems to check the durability of the system for long periods on uninterrupted execution. All tests were successful.

The test results summarized above demonstrate the viability of autonomous routine OD operation for extended periods of time without analyst intervention. Several types of situations, e.g., host system failure and unacceptable DC solution (DC failure unrecoverable by the ODAS DC QA subsystem), will require analyst intervention. It is possible to enhance ODAS to extend the range of situations that may be handled autonomously. Feasibility studies of several enhancements are in progress.

5. SUMMARY

The development and testing of a working prototype ODAS has established the feasibility of reliable continuous autonomous routine operational OD, especially for situations where successful DC solutions are obtained in the first attempt, representing the major fraction

of operational situations. In addition, the inclusion of a generic subsystem capable of accepting direct instructions on specific recovery procedures from an analyst allows ODAS to stay abreast of current levels of expertise, while providing an archival function for past expertise on operational OD techniques. As described in Section 4, preliminary tests of the performance of particular recovery options applied to certain types of DC failure have already been successfully demonstrated in an ODAS testbed. Continued refinement in this area is in progress and represents a definite future direction for ODAS. Associated with this concept is the application of artificial intelligence methodologies to the quality assurance component to exploit the efficient learning algorithms of the latter (Reference 9). Future concepts also include applications to onboard navigation, particularly of refined recovery procedures to provide improved solution reliability for onboard processor-based OD.

APPENDIX

This appendix contains brief descriptions of the five ODAS recovery procedures. Detailed descriptions are available in Reference 2.

Recovery Procedure P1 (Change H-P Density Table). Recovery procedure P1 provides a new modified H-P atmospheric density table corresponding to a different $F_{10.7}$ solar flux. The H-P atmospheric density model currently used in GTDS consists of 10 numerical tables specifying minimum and maximum densities as a function of spacecraft height. Each table corresponds to a specific 10.7-centimeter (cm) solar flux. The recovery procedure uses the estimated value of Q_1 , an atmospheric density scaling parameter used during DC to compute a more appropriate H-P atmospheric density table. The QA criterion for Q_1 is a range, i.e.,

$$Q_{1,\min} < Q_1 < Q_{1,\max}$$

The P1 algorithm employs an analytical representation of the tabulations to determine a higher flux table if Q_1 is larger than $Q_{1,\max}$ and a lower flux table if Q_1 is smaller than $Q_{1,\min}$.

Recovery Procedure P2 (Extend Data Arc Backward). Recovery procedure P2 extends the data arc backward in time by one half the current arc length to obtain additional tracking data.

Recovery Procedure P3 (Eliminate Biased or Noisy Batches). Recovery procedure P3 detects biased or noisy batches in the tracking data and creates directives to delete these batches when performing OD. P3 is used to modify the set of observations that is accepted for input to GTDS DC and uses statistics for the observation residuals from the SOR. Since the SOR editor has editing criteria that are different than those used in the DC process, the SOR data are supplemented by additional statistical data. The procedure is based on a modeled range of acceptable means and standard deviations for individual batches of tracking measurements and eliminating any that fall outside this range in a subsequent DC.

Recovery Procedure P4 (Increase Initial WRMS). P4 modifies the initial WRMS specification to accept additional observations during DC. During the DC process, a number of iterations are performed that correct a least-squares fit of the observation residuals. Elimination of observations that correspond to a residual in the first DC iteration that lies outside a user-specified range (proportional to a user-specified initial WRMS) is a mechanism used to eliminate certain measurements for DC. P4 operates on the premise that the user-specified WRMS may have been inappropriately small and computes an increment based on the fraction of accepted measurements and a simple model for the initial statistical distribution of the observation residuals.

Recovery Procedure P5 (Use Final Elements as Input). Recovery procedure P5 is a means for performing further DC iterations in an attempt to achieve better convergence characteristics. The procedure detects the behavior of the WRMS of residuals as a function of DC iterations to determine if the direction is toward convergence or divergence. If the DC process is convergent, this procedure recommends additional iterations, starting with the elements from the last iteration of the earlier DC.

REFERENCES

1. Computer Sciences Corporation, CSC/SD-86/6714, *System Definition and Requirements Analysis of the Orbit Determination Automation System*, June 1986
2. ---, CSC/SD-89/6013, *System Description for the Orbit Determination Automation System (ODAS), Revision 1*, H. Mardirossian, K. Heuerman, and A. Anderson, March 1989
3. Goddard Space Flight Center, X-582-76-77, *Mathematical Theory of the Goddard Trajectory Determination System*, J. O. Cappellari, Jr., C. E. Velez, and A. J. Fuchs, April 1976
4. Computer Sciences Corporation, CSC/SD-85/6738, *Goddard Trajectory Determination System (GTDS) User's Guide, Revision 2*, D. Squier and K. Byers, December 1987
5. ---, CSC/TM-87/6706, *Orbit Operations Section CLIST System Description and User's Guide*, A. Drew and J. P. Amenabar, November 1987
6. ---, CSC/SD-84/6854, *Automated Orbit Determination-IV (AOD-IV) System Description and User's Guide*, W. L. Steger, III and M. V. Samii, July 1984
7. ---, CSC/SD-86/6001, *Operational Orbit Determination Procedures and Quality Assurance Manual*, November 1986
8. ---, SEAS (550)/IM-88/-26/(58-472), *Orbit Determination Automation System (ODAS) System Test Results Report*, H. Mardirossian and F. Anzola, May 1988
9. ---, CSC/TM-88/6096, *Orbit Determination Automation System (ODAS) Future Development Concepts*, H. Mardirossian, October 1988

**CALCULATION OF DOUBLE-LUNAR SWINGBY
TRAJECTORIES: I. KEPLERIAN FORMULATION***

Stephen Stalos
Computer Sciences Corporation (CSC)

ABSTRACT

Scientific satellites may require translunar orbits aligned with the Sun-Earth line, with most of the period spent in either the sunward or antisunward direction. To maintain alignment, the orbit's line of apsides must rotate at a rate equal to mean angular motion of the Earth about the Sun. To maintain this rotation of the line of apsides by use of fuel onboard the spacecraft is prohibitively expensive. Farquhar and Dunham (Reference 1) proposed a method for maintaining the desired alignment by gaining momentum at the expense of the Moon during a close approach—a lunar swingby—as the spacecraft passes beyond lunar orbit, then returning the momentum at the second lunar swingby as the spacecraft returns within the lunar orbit. The cycle of double-lunar swingbys may then be repeated. Dunham (Reference 2) presented the orbit parameters necessary to achieve double-lunar swingby orbits which will maintain Sun-Earth line alignment. The details of the Keplerian approach to calculation of these parameters are presented. Methods for solution of the necessary equations for these parameters are presented.

* This work was supported by the National Aeronautics and Space Administration (NASA)/Goddard Space Flight Center (GSFC), Greenbelt, Maryland, under Contract NAS 5-31500.

1. DEFINITION OF A DOUBLE-LUNAR SWINGBY CYCLE

Consider a Keplerian orbit about the Earth with its line of apsides pointing toward the Sun. After 3 months, ignoring perturbations, the line of apsides would be perpendicular to a line drawn from the Sun to the Earth; to maintain its Sun-pointing line of apsides, this line must rotate about the Earth at a rate equal to the mean angular motion of the Earth about the Sun. Farquhar and Dunham (Reference 1) described a method to achieve such an apsidal rotation rate for translunar orbits. The method requires two close lunar encounters, swingbys, per cycle. The first swingby occurs as the spacecraft, moving away from the Earth, crosses the lunar orbit with the Moon to its left. This "trailing edge" swingby increases the energy of the spacecraft's orbit and hence increases the semimajor axis. We call the orbit with the larger semimajor axis the outer-segment loop or simply "outer loop," and the original orbit the inner-segment loop or simply "inner loop." The spacecraft's outer loop orbit period is such that more than one lunar month passes following the first lunar swingby before the spacecraft again crosses the Moon's orbit, this time moving toward the Earth. The second swingby occurs at this crossing, again with the Moon to the left of the spacecraft. Thus a "leading edge" swingby occurs, removing energy from the spacecraft's orbit and reducing its semimajor axis to its original length—the length before the first lunar swingby. Next, slightly less than one lunar month passes, the spacecraft is now ready for another outward crossing of the Moon's orbit, and the Moon and spacecraft are at the same relative position as for the first lunar swingby. This defines one complete "double-lunar swingby" cycle. Note that at the first swingby the Moon's pull rotated the line of apsides counterclockwise. The second swingby, occurring as the spacecraft moved toward the Earth, also resulted in a counterclockwise rotation of the line of apsides. If, then, the sum of these two rotations divided by the time for one complete cycle equals the mean angular motion of the Sun, the spacecraft's line of apsides will continue its sunward alignment.

Figure 1 shows one complete double-lunar swingby cycle. The Moon's positions at the first, second, and third (first) swingbys are shown as S_1 , S_2 , and S_3 . The true anomaly of the spacecraft at the time of the first swingby is shown as f_1 for the inner loop orbit and f_0 for the outer loop orbit. Thus the apsidal rotation is $2(f_1 - f_0)$, and occurs in a time equal to the time from S_1 to S_3 . We can then write the first necessary condition for a lunar swingby as

$$\Delta \dot{\omega} \equiv \frac{2(f_1 - f_0)}{2t_a + t_s} - \frac{2\pi}{T_E} = 0 \tag{1}$$

↑

rate of rotation
of line of apsides
for one double-
lunar swingby
cycle

↑

mean angular
motion of Earth
about the Sun

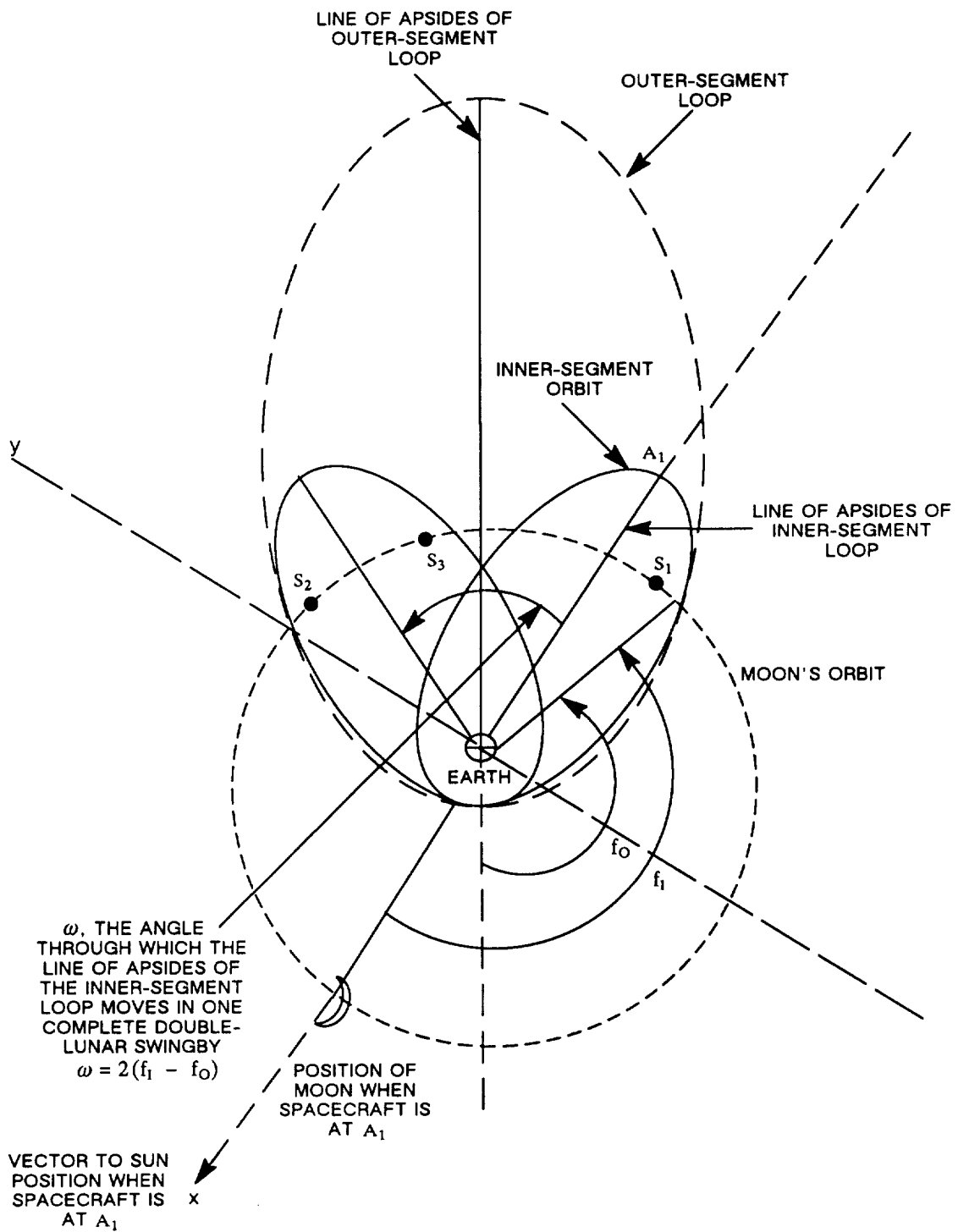


Figure 1. A Double-Lunar Swingby Trajectory

where

T_E = Earth's orbital period

$2t_a$ = time spent in outer loop from S_1 to S_2

t_s = twice the time from perigee of inner loop to S_1 , plus one complete inner loop period

Two more conditions relate the spacecraft's orbital parameters to the Moon's motion:

$$\Delta\theta_1 \equiv \left\{ 2(f_1 - f_O) + 2\left(\pi - f_1 - \frac{r_m}{A_m}\right) \right\} - \frac{2\pi}{T_m} (2t_a) = 0 \quad (2)$$

↑
angle traveled by Moon from S_1 to S_2 expressed in inner and outer loop true anomalies

↑
angle traveled by Moon (mod 2π) between S_1 and S_2 expressed in outer loop time, $2t_a$, from S_1 to S_2

$$\Delta\theta_2 \equiv \left\{ 2\left(\pi - f_1 - \frac{r_m}{A_m}\right) \right\} - \left\{ 2\pi - \frac{2\pi}{T_m} t_s \right\} = 0 \quad (3)$$

↑
angle traveled by Moon from S_2 to S_3 expressed in inner loop true anomaly

↑
angle traveled by Moon from S_2 to S_3 expressed in terms of inner loop period

where

A_m = radius of Moon's orbit

r_m = swingby distance of spacecraft from Moon

T_m = Moon's orbital period

These three equations specify the geometry constraints for a complete double-lunar swingby cycle.

2. REFORMULATION OF THE NECESSARY EQUATIONS

In this Keplerian formulation, the transfer from the inner orbit segment to the outer orbit segment is assumed to occur instantaneously when the spacecraft crosses the lunar orbit. We also assume a circular lunar orbit.

The three equations may be expressed solely in terms of three variables; a_i , P_i , and α , where

$\alpha \equiv$ bend angle; angle through which velocity of spacecraft is changed at S_1

$a_i \equiv$ apogee distance of inner loop

$P_i \equiv$ perigee distance of inner loop

The three nonlinear equations may then be solved numerically to determine these three unknowns. A description of the solution process is given in Section 3. We now show all the relations which allow Equations (1), (2), and (3) to be expressed in terms of α , a_i , and P_i .

For Equation (1), we require expressions for f_I , f_O , t_a , and t_s in terms of α , a_i , and P_i .

$\mu_E =$ gravitational parameter for Earth

$a_i = \frac{1}{2} (a_i + P_i) =$ semimajor axis of inner loop

$e_i = \frac{(a_i - P_i)}{a_i} =$ eccentricity of inner loop

$\cos f_I = \frac{\left\{ \frac{a_i}{A_m} (1 - e_i^2) - 1 \right\}}{e_i}$

$f_I = \tan^{-1} \left\{ \frac{\sin f_I}{\cos f_I} \right\} =$ true anomaly of inner loop at S_1

$v_s = \left\{ \mu_E \left(\frac{2}{A_m} - \frac{1}{a_i} \right) \right\}^{1/2}$, spacecraft speed at S_1 , in inner loop

$v_m = \frac{2\pi A_m}{T_m}$, velocity of Moon in its orbit

$\left. \begin{array}{l} v_{xm} = -v_m \sin f_I \\ v_{ym} = +v_m \cos f_I \end{array} \right\}$ x and y components of Moon's velocity

$$v_x = -\sin f_I$$

$$v_y = e_I + \cos f_I$$

$$v_{xs} = v_s \left\{ \frac{v_x}{(v_x^2 + v_y^2)^{1/2}} \right\}$$

$$v_{ys} = v_s \left\{ \frac{v_y}{(v_x^2 + v_y^2)^{1/2}} \right\}$$

$$\left. \begin{aligned} v_{xO} &= v_{xm} + (v_{xs} - v_{xm}) \cos \alpha - (v_{ys} - v_{ym}) \sin \alpha \\ v_{yO} &= v_{ym} + (v_{ys} - v_{ym}) \cos \alpha + (v_{xs} - v_{xm}) \sin \alpha \end{aligned} \right\} \begin{array}{l} \text{rotation of spacecraft} \\ \text{velocity vector with} \\ \text{respect to Moon by} \\ \text{an angle } \alpha \end{array}$$

$$v_O = (v_{xO}^2 + v_{yO}^2)^{1/2}, \text{ spacecraft speed, at } S_1, \text{ in outer loop}$$

$$a_O = \left(\frac{2}{A_m} - \frac{v_O^2}{\mu_E} \right)^{-1}, \text{ semimajor axis of outer loop}$$

$$E_I = 2 \tan^{-1} \left\{ \left(\frac{1 - e_I}{1 + e_I} \right)^{1/2} \tan \frac{f_I}{2} \right\}, \text{ eccentric anomaly of inner loop at } S_1$$

$$r_x = A_m \cos f_I$$

$$r_y = A_m \sin f_I$$

$$h = r_x v_{yO} - r_y v_{xO}, \text{ angular momentum of outer loop orbit}$$

$$f_O = \tan^{-1} \left\{ \frac{h(r_x v_{xO} + r_y v_{yO})}{h^2 - \mu_E A_m} \right\}, \text{ true anomaly of outer loop, at } S_1$$

$$e_O = \left\{ 1 - \frac{h^2}{\mu_E a_O} \right\}^{1/2}, \text{ eccentricity of outer loop}$$

$$E_O = 2 \tan^{-1} \left\{ \left(\frac{1 - e_O}{1 + e_O} \right)^{1/2} \tan \frac{f_O}{2} \right\}, \text{ eccentric anomaly of outer loop, at } S_1$$

$$T_O = \frac{2\pi}{\sqrt{\mu_E}} a_O^{3/2}, \text{ period of outer loop}$$

$$T_I = \frac{2\pi}{\sqrt{\mu_E}} a_I^{3/2}, \text{ period of inner loop}$$

$$t_a = \frac{1}{2} T_O - \frac{E_O - e_O \sin E_O}{2\pi/T_O}, \text{ time from } S_1 \text{ to apogee of outer loop}$$

$$t_s = 2 \left\{ \frac{E_I - e_I \sin E_I}{2\pi/T_I} \right\} + T_I, \text{ one inner loop period plus twice the time from perigee of inner loop to } S_1$$

For Equation (2), we express r_m in terms of previously defined quantities.

μ_m = gravitational parameter for Moon

$$v_\infty = \{(v_{xs} - v_{xm})^2 + (v_{ys} - v_{ym})^2\}^{1/2}$$

$$r_m = \frac{\mu_m}{v_\infty^2} \left(\frac{1}{\sin \frac{\alpha}{2}} - 1 \right)$$

For Equation (3), all variables have been related previously to α , a_i , and P_i .

3. SOLUTION OF THE EQUATIONS

Writing the equations as

$$\Delta \dot{\omega} = f_1(\alpha, a_i, P_i) = 0$$

$$\Delta \theta_1 = f_2(\alpha, a_i, P_i) = 0$$

$$\Delta \theta_2 = f_3(\alpha, a_i, P_i) = 0$$

or

$$\vec{F}(\vec{x}) = \begin{Bmatrix} f_1(\vec{x}) \\ f_2(\vec{x}) \\ f_3(\vec{x}) \end{Bmatrix} = 0, \quad \vec{x} \equiv \begin{Bmatrix} \alpha \\ a_i \\ P_i \end{Bmatrix}$$

we use the Newton-Raphson method to find the required solution vector, \vec{x} .

The method is to guess a new iterate, \bar{x}^{N+1} , from the previous iterate, \bar{x}^N , by

$$\bar{x}^{N+1} = \bar{x}^N - \frac{\vec{F}(\bar{x}^N)}{J(\bar{x}^N)}$$

where $J(\bar{x})$ is the Jacobian matrix

$$J(\bar{x}) = \left\{ \begin{array}{ccc} \frac{\partial f_1}{\partial x_1} & \frac{\partial f_1}{\partial x_2} & \frac{\partial f_1}{\partial x_3} \\ \frac{\partial f_2}{\partial x_1} & \frac{\partial f_2}{\partial x_2} & \frac{\partial f_2}{\partial x_3} \\ \frac{\partial f_3}{\partial x_1} & \frac{\partial f_3}{\partial x_2} & \frac{\partial f_3}{\partial x_3} \end{array} \right\}$$

In fact, we define

$$\vec{Z}^{N+1} \equiv -(\bar{x}^{N+1} - \bar{x}^N)$$

and write

$$J(\bar{x}^N) \vec{Z}^{N+1} = \vec{F}(\bar{x}^N)$$

This linear system can be solved for \vec{Z}^{N+1} once J and \vec{F} are evaluated at \bar{x}^N . Then \bar{x}^{N+1} is found from

$$\bar{x}^{N+1} = -\vec{Z}^{N+1} + \bar{x}^N$$

The partial derivatives are estimated numerically via central differences

$$\frac{\partial f_i}{\partial x_j} = \frac{f_i(x_j + h_{ij}) - f_i(x_j - h_{ij})}{2h_{ij}}$$

The step size h_{ij} is chosen such that

$$|h_{ij}| \left| \frac{\partial f_i}{\partial x_j} \right| \approx \sqrt{\epsilon} |f_i|$$

where ϵ is a machine constant. For IBM double precision, $\epsilon = 2.2 \times 10^{-16}$. For IBM single precision, $\epsilon = 9.5 \times 10^{-7}$.

4. SAMPLE CALCULATION

Computer output for a sample solution of a double-lunar swingby orbit is shown in the appendix. First, the initial guess values for the three independent variables are shown.

$$\alpha = 0.2 \text{ radians} = 11.46 \text{ degrees}$$

$$a_i = 700,000 \text{ km}$$

$$P_i = 40,000 \text{ km}$$

Next, values for h , used to calculate partial derivatives, are displayed. Then the results of each iteration are shown in the form

$$J(\vec{x}) \vec{Z}(\vec{x}) = \vec{F}(\vec{x})$$

After seven iterations, the final values of the independent variables are shown: $\alpha = 19.4205$ degrees, $a_i = 549,888$ km, and $P_i = 37,432$ km. These results agree with those given on page 2-2 of Reference 2.

C. 5

APPENDIX — SAMPLE DOUBLE-LUNAR SWINGBY CALCULATION

The following shows details for a solution of a double-lunar swingby orbit.

```

PERIOD OF SATELLITE:      27.3217 DAYS,
PERIOD OF PLANET:       365.2500 DAYS,
PLANET GRAV. PARAMETER: 3.986E+05 KM**3/SEC**2,
SATELLITE GRAV. PARAMETER: ( 3.986E+05 /      81.3700 ) KM**3/SEC**2
SATELLITE ORBITAL RADIUS: 384399. KM
    
```

INITIAL VALUES FOR X :

```

2.00000E-01  7.00000E+05  4.00000E+04
    
```

ERROR TOLERANCES FOR SUCCESSIVE ITERATES :

```

1.00000E-06  1.00000E-06  1.00000E-06
    
```

FROM HSET, H VALUES ARE:

```

2.00000E-06  3.50000E+00  2.02500E+00
5.00000E-07  4.37500E-01  2.02500E+00
6.75000E-06  8.75000E-01  4.00000E-01
    
```

***** ITERATION NUMBER 1 *****

THE SOLUTION TO THE FOLLOWING MATRIX EQUATION,

$$\begin{vmatrix} 3.02452E-07 & -2.30101E-13 & 2.28045E-13 \\ -4.53911E+01 & -4.36530E-05 & 5.97961E-06 \\ 1.13706E+00 & 1.24872E-05 & 2.72502E-05 \end{vmatrix}
 \begin{vmatrix} Z(1) \\ Z(2) \\ Z(3) \end{vmatrix}
 =
 \begin{vmatrix} -9.61618E-08 \\ -2.51620E+00 \\ 1.74578E+00 \end{vmatrix}$$

IS Z : -1.44445E-01 2.04596E+05 -2.36627E+04

ITERATION 1, X : 3.44445E-01 4.95404E+05 6.36627E+04
 F-NORM = 2.62326E+00

***** ITERATION NUMBER 2 *****

THE SOLUTION TO THE FOLLOWING MATRIX EQUATION,

$$\begin{vmatrix} 5.51903E-07 & -3.29366E-13 & 3.67081E-13 \\ -1.15460E+01 & -3.90971E-05 & 2.20171E-06 \\ 7.55482E-01 & 1.17588E-05 & 2.18728E-05 \end{vmatrix}
 \begin{vmatrix} Z(1) \\ Z(2) \\ Z(3) \end{vmatrix}
 =
 \begin{vmatrix} 4.00435E-08 \\ 2.61698E+00 \\ -6.28797E-03 \end{vmatrix}$$

IS Z : 8.56683E-03 -6.74558E+04 3.56809E+04

ITERATION 2, X : 3.35878E-01 5.62860E+05 2.79819E+04
 F-NORM = 8.89039E-01

***** ITERATION NUMBER 3 *****

THE SOLUTION TO THE FOLLOWING MATRIX EQUATION,

$$\begin{bmatrix} 2.35513E-07 & -5.67579E-13 & 6.72816E-13 \\ -3.32048E+01 & -6.23036E-05 & 1.39124E-05 \\ 4.51755E-01 & 1.10362E-05 & 2.66817E-05 \end{bmatrix} \begin{bmatrix} Z(1) \\ Z(2) \\ Z(3) \end{bmatrix} = \begin{bmatrix} -1.38927E-08 \\ -7.87616E-01 \\ -1.01423E-01 \end{bmatrix}$$

IS Z : -3.44420E-03 1.24880E+04 -8.90822E+03

ITERATION 3, X : 3.39323E-01 5.50372E+05 3.68901E+04
F-NORM = 5.10358E-02

***** ITERATION NUMBER 4 *****

THE SOLUTION TO THE FOLLOWING MATRIX EQUATION,

$$\begin{bmatrix} 2.90579E-07 & -5.71015E-13 & 5.48010E-13 \\ -2.78361E+01 & -5.74992E-05 & 9.34668E-06 \\ 5.00948E-01 & 1.11918E-05 & 2.51765E-05 \end{bmatrix} \begin{bmatrix} Z(1) \\ Z(2) \\ Z(3) \end{bmatrix} = \begin{bmatrix} -4.62181E-10 \\ -4.30255E-02 \\ -8.01032E-03 \end{bmatrix}$$

IS Z : 3.71385E-04 4.80824E+02 -5.39298E+02

ITERATION 4, X : 3.38951E-01 5.49891E+05 3.74294E+04
F-NORM = 2.36043E-04

***** ITERATION NUMBER 5 *****

THE SOLUTION TO THE FOLLOWING MATRIX EQUATION,

$$\begin{bmatrix} 2.94573E-07 & -5.68936E-13 & 5.40713E-13 \\ -2.75352E+01 & -5.71133E-05 & 9.10926E-06 \\ 5.05424E-01 & 1.12043E-05 & 2.51065E-05 \end{bmatrix} \begin{bmatrix} Z(1) \\ Z(2) \\ Z(3) \end{bmatrix} = \begin{bmatrix} -3.21530E-12 \\ -2.13269E-04 \\ -2.27742E-05 \end{bmatrix}$$

IS Z : -1.49764E-08 3.35773E+00 -2.40526E+00

ITERATION 5, X : 3.38951E-01 5.49888E+05 3.74318E+04
F-NORM = 4.30244E-09

***** ITERATION NUMBER 6 *****

THE SOLUTION TO THE FOLLOWING MATRIX EQUATION,

$$\begin{bmatrix} 2.94591E-07 & -5.68930E-13 & 5.40685E-13 \\ -2.75337E+01 & -5.71117E-05 & 9.10824E-06 \\ 5.05440E-01 & 1.12043E-05 & 2.51062E-05 \end{bmatrix} \begin{bmatrix} Z(1) \\ Z(2) \\ Z(3) \end{bmatrix} = \begin{bmatrix} -4.24080E-17 \\ -3.82426E-09 \\ -4.78174E-10 \end{bmatrix}$$

IS Z : 2.49561E-11 4.83695E-05 -4.11348E-05

ITERATION 6, X : 3.38951E-01 5.49888E+05 3.74318E+04
F-NORM = 1.01585E-14

***** ITERATION NUMBER 7 *****

THE SOLUTION TO THE FOLLOWING MATRIX EQUATION,

$$\begin{bmatrix} 2.94591E-07 & -5.68930E-13 & 5.40685E-13 \\ -2.75337E+01 & -5.71117E-05 & 9.10824E-06 \\ 5.05440E-01 & 1.12043E-05 & 2.51062E-05 \end{bmatrix} \begin{bmatrix} Z(1) \\ Z(2) \\ Z(3) \end{bmatrix} = \begin{bmatrix} -1.05879E-22 \\ -8.21565E-15 \\ -1.94289E-15 \end{bmatrix}$$

IS Z : 5.44511E-17 9.81024E-11 -1.22264E-10

ITERATION 7, X : 3.38951E-01 5.49888E+05 3.74318E+04
F-NORM = 5.16254E-15

SOLUTION CONVERGED IN 7 ITERATIONS.

X : 3.38951E-01 5.49888E+05 3.74318E+04
Z : 5.44511E-17 9.81024E-11 -1.22264E-10
F : 2.64698E-23 3.99680E-15 1.16573E-15

ALPHA, BEND ANGLE = 19.4205 DEGREES,
APOGEE OF INNER ORBIT = 5.4988764E+05 KM,
PERIGEE OF INNER ORBIT = 3.7431801E+04 KM,
ECCENTRICITY OF INNER ORBIT = 0.8725334,
APOGEE OF OUTER ORBIT = 8.9892445E+05 KM,
PERIGEE OF OUTER ORBIT = 1.0420415E+05 KM,
ECCENTRICITY OF OUTER ORBIT = 0.7922417,
SWINGBY DISTANCE = 2.7638929E+04 KM.

REFERENCES

1. R. W. Farquhar and D. W. Dunham, "A New Trajectory Concept for Exploring the Earth's Geomagnetic Tail," *Journal of Guidance and Control* 4, 1981, pp. 192-196
2. D. W. Dunham and S. A. Davis, *Catalog of Double-Lunar Swingby Orbits for Exploring the Earth's Geomagnetic Tail*, Computer Sciences Corporation, CSC/TM-80/6322, October 1980

ACTIVE RENDEZVOUS BETWEEN A LOW-EARTH ORBIT USER SPACECRAFT AND THE SPACE TRANSPORTATION SYSTEM (STS) SHUTTLE*

H. L. Hooper and J. R. Herrnstein
Computer Sciences Corporation (CSC)

ABSTRACT

This study considers active rendezvous of an unmanned spacecraft with the Space Transportation System (STS) Shuttle. The paper first discusses the various operational constraints facing both the maneuvering spacecraft and the Shuttle during such a rendezvous sequence. Specifically, the actively rendezvousing user spacecraft must arrive in the generic Shuttle control box at a specified time after Shuttle launch. In so doing it must at no point violate Shuttle separation requirements. In addition, the spacecraft must be able to initiate the transfer sequence from any point in its orbit.

The paper then discusses the four-burn rendezvous sequence incorporating two Hohmann transfers and an intermediate phasing orbit as a low-energy solution satisfying the above requirements. The general characteristics of the four-burn sequence are discussed, with emphasis placed on phase orbit altitude and delta-velocity (ΔV) requirements. The report then considers the planning and execution of such a sequence in the operational environment. Factors crucial in maintaining the safety of both spacecraft, such as spacecraft separation and contingency analysis, are considered in detail.

*This work was supported by the National Aeronautics and Space Administration (NASA)/Goddard Space Flight Center (GSFC), Greenbelt, Maryland, under Contract NAS 5-31500.

1. INTRODUCTION

This report presents the results of an investigation into analysis and mission planning techniques for unmanned user spacecraft involved in active rendezvous with the Space Transportation System (STS) Shuttle. During the investigation, a rendezvous computation program that incorporates these techniques was developed. This software was used to generate the results presented in the report.

Section 2 presents background information on Shuttle standard rendezvous policies. These requirements coupled with a desire to minimize fuel expenditures make a rendezvous sequence consisting of a series of Hohmann transfers a desirable technique. The general characteristics of such a rendezvous sequence are discussed in detail in Section 3. Special attention is given to the cost in terms of Delta-V (ΔV) of such a maneuver sequence.

Section 4 discusses several operational issues confronting unmanned spacecraft rendezvousing with the Shuttle. The issues include safety of the Shuttle during the maneuver sequences, tracking coverage, lighting coverage, and maneuver contingencies. Section 5 presents a summary of the conclusions reached in the report.

2. BACKGROUND — STS SHUTTLE RENDEZVOUS REQUIREMENTS

This section presents the requirements imposed by the Shuttle on an actively rendezvousing user spacecraft. These requirements were derived from References 1 through 5. Because many of these policies are still formulative, all the referenced reports are preliminaries.

The rendezvous sequence is initiated when the "Go for descent" declaration is issued by mission controllers at Johnson Space Center (JSC). This is done after the Shuttle has achieved orbit and a systems check has determined that the rendezvous sequence may proceed. Nominally, this occurs at 5 hours mission-elapsed time (MET), or 5 hours after launch.

Upon receiving the "Go for descent" declaration, the unmanned user spacecraft (chase spacecraft) must complete its rendezvous with the Shuttle (target spacecraft) at a predetermined time, currently given as 53 hours MET. This rendezvous completion time is referred to by JSC as the Control Box Start Time (CBST). The rendezvous is considered complete when the maneuvering spacecraft has achieved the Shuttle control box (Figure 1) and has ceased all translational maneuvering. As illustrated, the control box is a region above and ahead of the Shuttle with its origin at the Shuttle. The horizontal component measures angular separation along the Shuttle orbit, while the vertical component measures radial distance from the Shuttle.

Upon achieving the CBST at the completion of the rendezvous, the user spacecraft must satisfy a semimajor axis and eccentricity requirement limiting the difference in apogee and perigee altitudes to 14.8 kilometers (km). In addition, a maximum angular separation

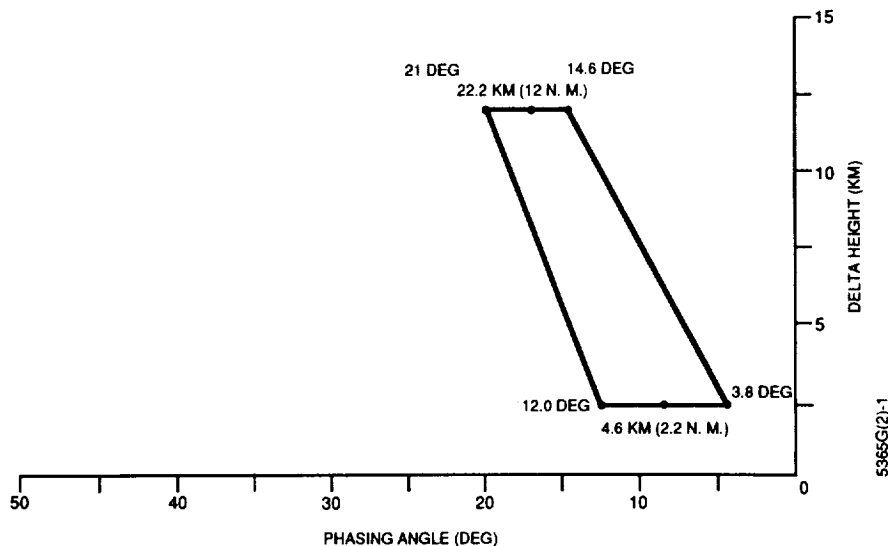


Figure 1. STS Shuttle Generic Control Box; Orbit Normal Out of Page

of 0.03 degree (deg) in the orbital planes of the spacecraft is required. The user spacecraft must be capable of absorbing up to approximately 0.1 deg of launch dispersion errors in the orbit plane of the Shuttle. Finally, the user spacecraft must be capable of handling Shuttle launch slips of up to 1 hour. This, combined with the possibility of 24-hour Shuttle launch delays, requires that the user spacecraft be capable of completing rendezvous with the Shuttle from any initial orientation (or phasing) with the Shuttle. Stated differently, the user spacecraft must possess a 360-deg phasing capability with the Shuttle.

3. USER SPACECRAFT/STS SHUTTLE RENDEZVOUS SEQUENCE

This section describes a rendezvous sequence that is well-suited to the operational environment and that satisfies all the requirements presented in the previous section while minimizing ΔV requirements. The section begins with a discussion of the characteristics of the Hohmann transfer and proceeds to describe a rendezvous sequence consisting of a series of Hohmann transfers with intermediate phasing orbits. The rendezvous technique does not require any specific initial orbital conditions. However, to simplify the current discussion, it is assumed that the user spacecraft begins in a higher orbit than the Shuttle.

3.1 THE HOHMANN TRANSFER

A Hohmann transfer is well-known as the optimum maneuver sequence for transferring between two circular coplanar orbits. The first burn of such a maneuver places the chase spacecraft in an elliptic transfer orbit with perigee at the same altitude as the target orbit. The second burn occurs 180 deg after the first and circularizes the transfer orbit, leaving the chase spacecraft in the same orbit as the target vehicle.

If the chase and target orbits are not coplanar, a plane change must be done at some point in the maneuver sequence. This could be accomplished by executing all the plane change in either the initial or the final orbit, independently of the altitude change to be performed. However, the transfer ΔV is optimized by simultaneous execution of the plane-change and orbital-change maneuvers. Efficiency is further improved by distributing the plane changes between the two burns. Figure 2 shows the significant ΔV savings associated with linking plane and altitude changes by distributing the plane changes between the two burns of the Hohmann transfer.

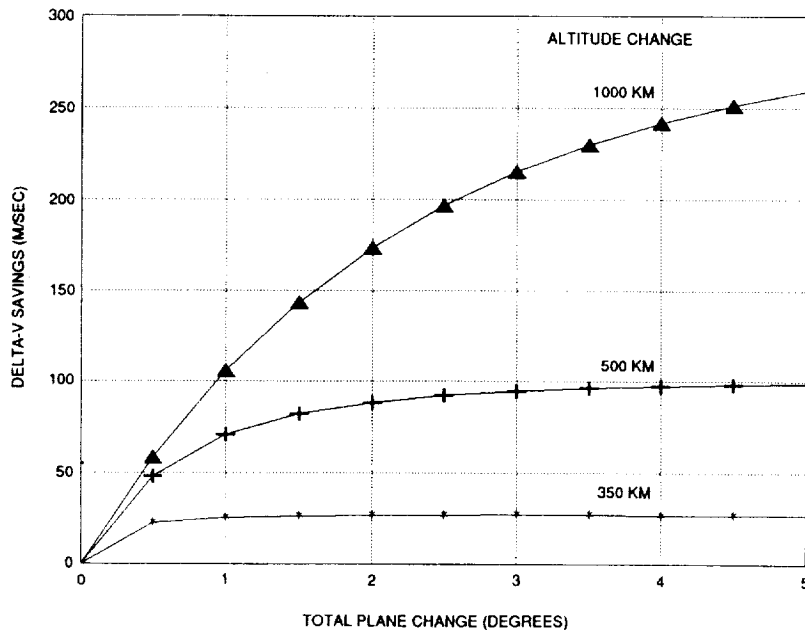


Figure 2. Delta-V Savings by Coupling Altitude and Plane Changes

3.2 MULTIPLE BURN TRANSFERS

If two spacecraft are to rendezvous using a Hohmann transfer, the correct angular separation, or phasing, must exist between the spacecraft at the initiation of the transfer. This angle is referred to as the Hohmann phase angle (HPA). The relative periods of the two orbits determine the value of the HPA.

The synodic period represents the length of time required for spacecraft in different orbits to return to the same orientation with respect to each other. This is the time between successive occurrences of the HPA. If the synodic period is greater than the amount of time allotted for a particular rendezvous scenario, the required HPA may not be achievable for all initial orientations. For a 2-day rendezvous, the synodic period is longer than the rendezvous duration if the initial user spacecraft altitude is less than 145 km above the nominal Shuttle altitude of 315 km. For a spacecraft such as the Gamma Ray Observatory (GRO), which is nominally only 35 km above the Shuttle at the start of the rendezvous sequence, additional measures must be taken.

The required 360-deg phasing capability can be achieved while maintaining the ΔV advantages inherent in the Hohmann transfer by employing a sequence consisting of a series of Hohmann transfers. Such a sequence, the four-burn rendezvous sequence, is illustrated in Figure 3. The four-burn sequence consists of two Hohmann transfers. The first transfer places the chase spacecraft in an intermediate orbit called the phase orbit. The second transfer maneuvers the chase vehicle to the target spacecraft. The phase orbit is computed such that the HPA between the phase and target orbits is achieved at the time of the final transfer. By varying the altitude of the phase orbit, the user spacecraft is capable of achieving rendezvous with the Shuttle from any initial relative orientation.

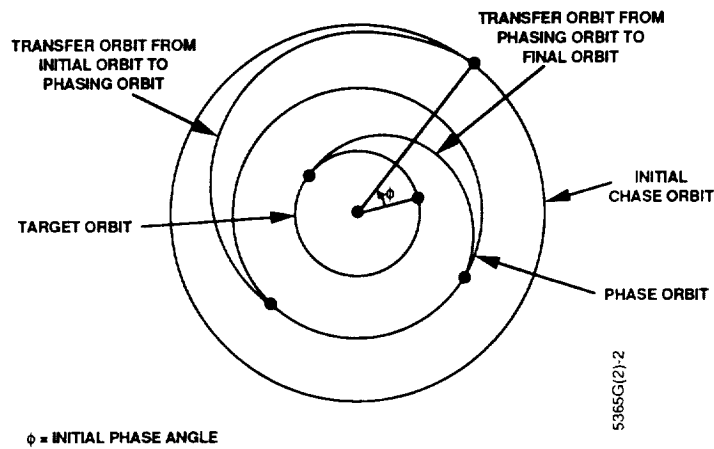


Figure 3. Four-Burn Transfer Scenario

The concept of linking in- and out-of-plane corrections to save ΔV is as applicable to the four-burn scenario as it is to the case of a direct Hohmann transfer. To combine plane changes and altitude changes, each of the four burns must occur along the relative node defined by the intersection of the user spacecraft and Shuttle orbit planes at the termination of the rendezvous sequence.

3.2.1 PHASE ORBIT ALTITUDE

To apply the four-burn sequence, it is necessary to accurately compute the semimajor axis of the phase orbit, given a set of initial conditions. This is done using the following equation:

$$0 = \left[\left(\frac{\mu}{a_i^3} \right)^{1/2} - \left(\frac{\mu}{a_p^3} \right)^{1/2} \right] T - \phi - 2\pi - \frac{\pi}{\sqrt{8}} \left[\left(\frac{a_p + a_c}{a_p} \right)^{3/2} + \left(\frac{a_p + a_t}{a_p} \right)^{3/2} \right] \quad (3-1)$$

where

- μ = Earth's gravitational constant (398600.64 (km³/sec²))
- a_t = target spacecraft semimajor axis
- a_c = chase spacecraft semimajor axis
- a_p = phase orbit semimajor axis
- ϕ = initial phase angle
- T = total rendezvous duration

Equation (3-1) is solved iteratively until a value for a_p is found which makes the right-hand side of the equation arbitrarily close to zero.

Figure 4 shows phase orbit altitude as a function of phase angle, ϕ , for a 3-day transfer from 350 to 315 km. The figure demonstrates that two phase orbit solutions exist for each initial phase angle: one above the target spacecraft and the other below. The solid portions of the curves show the phase orbit solutions having the lower ΔV requirement for each specific initial phase angle. The crossover point from the upper to the lower solution occurs when the solutions require equivalent ΔV expenditure.

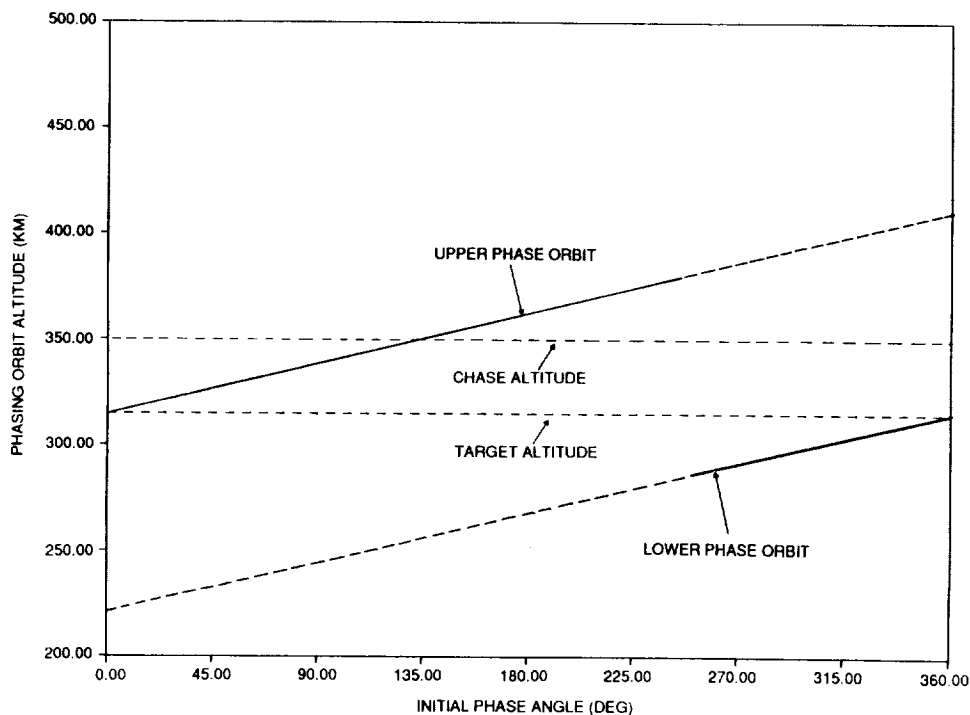


Figure 4. Phase Orbit Altitude as a Function of Initial Spacecraft Phase Angle for a 3-Day, 350- to 315-km Scenario

Further examination of variations in phase orbit altitude with rendezvous time and initial spacecraft altitudes suggests several noteworthy trends. The phase orbit semimajor axis is

essentially a linear function of phase angle, with the upper and lower solutions being nearly parallel. Furthermore, the y-intercept of the upper phase orbit altitude/phase angle function is the target spacecraft semimajor axis and its slope varies inversely with T, the rendezvous duration. With these relationships in mind, it is possible to write three analytical equations that accurately predict the phase orbit altitudes and the crossover point over the ranges of Shuttle altitudes (300 to 350 km), user spacecraft altitudes (300 to 500 km), and rendezvous durations (2 to 5 days) under consideration:

$$a_{pu}(\phi) = \frac{k_u}{T} \phi + a_t \quad (3-2)$$

$$a_{pl}(\phi) = \frac{k_l}{T} \phi + \left[a_t - 2\pi \frac{k_l}{T} \right] \quad (3-3)$$

$$\phi_c = \frac{T}{k_l + k_u} \left[a_c - a_t + \frac{2\pi k_l}{T} \right] \quad (3-4)$$

where

- a_{pu} = semimajor axis of the upper phase orbit
- a_{pl} = semimajor axis of the lower phase orbit
- ϕ_c = phase angle at which crossover occurs

and

$$k_l = \frac{2}{3} \left[\frac{\mu}{\left[\sqrt{\frac{\mu}{a_t^3} + \frac{\pi}{T}} \right]^5} \right]^{1/3} \quad (3-5)$$

$$k_u = \frac{2}{3} \left[\frac{\mu}{\left[\sqrt{\frac{\mu}{a_t^3} - \frac{\pi}{T}} \right]^5} \right]^{1/3} \quad (3-6)$$

The expressions for k_u and k_l were derived by taking a Taylor series expansion of an expression for phase orbit altitude based on spacecraft angular rates and assuming only the linear terms to be significant. Numerical analysis can be performed to demonstrate that, in agreement with the initial simplifying assumption of a linear relationship between phase orbit altitude and ϕ , k_u and k_l do remain essentially constant over the ranges under consideration. The derivation of k_l and k_u and the associated numerical analysis can be found in Reference 6.

Equations (3-2) through (3-6) predict phase orbit altitudes to within several kilometers of the more accurate solutions computed iteratively by Equation (3-1). They can, therefore, be used to compute quick approximations to the phase orbit altitude.

3.2.2 DELTA-V CONSIDERATIONS

Figure 5 shows the ΔV associated with the upper and lower phase orbit solutions for a 3-day, coplanar transfer from 350 to 315 km. Figure 6 presents the cost of the less expensive phase orbit solutions for the same transfer with rendezvous durations of 2, 3, and 4 days. The ΔV saved by crossing over from the upper to the lower phase orbit solution for phase angles approaching 360 deg is clear. As expected, the maximum ΔV occurs at the crossover point. This maximum ΔV value is critical in rendezvous scenarios with the Shuttle since a 360-deg phasing capability is required. This means that it is necessary to budget enough fuel to be able to handle the maximum possible ΔV .

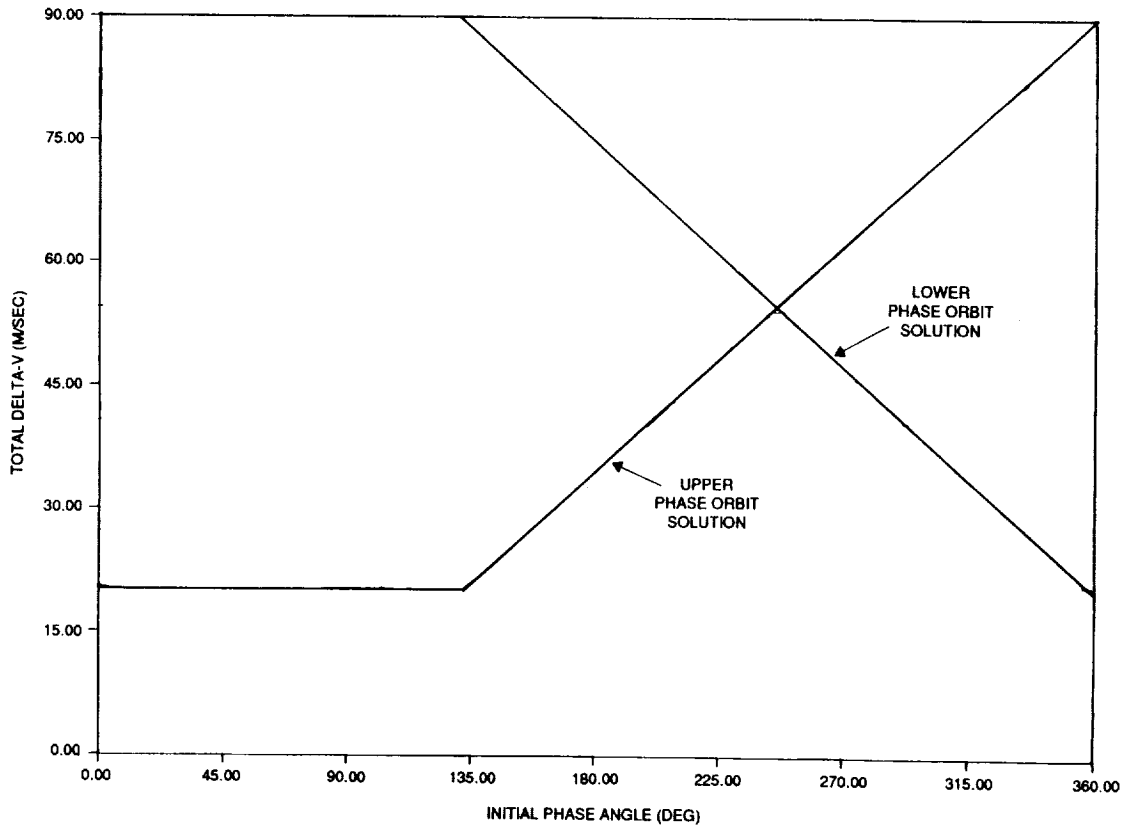


Figure 5. Delta-V Versus Phase Angle for 3-Day Rendezvous; Upper and Lower Phase Orbit Solutions

The magnitude of the maximum ΔV can be determined without solving the rendezvous problem by computing the orbit with which the target orbit has a synodic period equal to the rendezvous duration. This orbit can be called the synodic orbit. The cost of a direct Hohmann transfer from this orbit to the target orbit is equal to the maximum four-burn

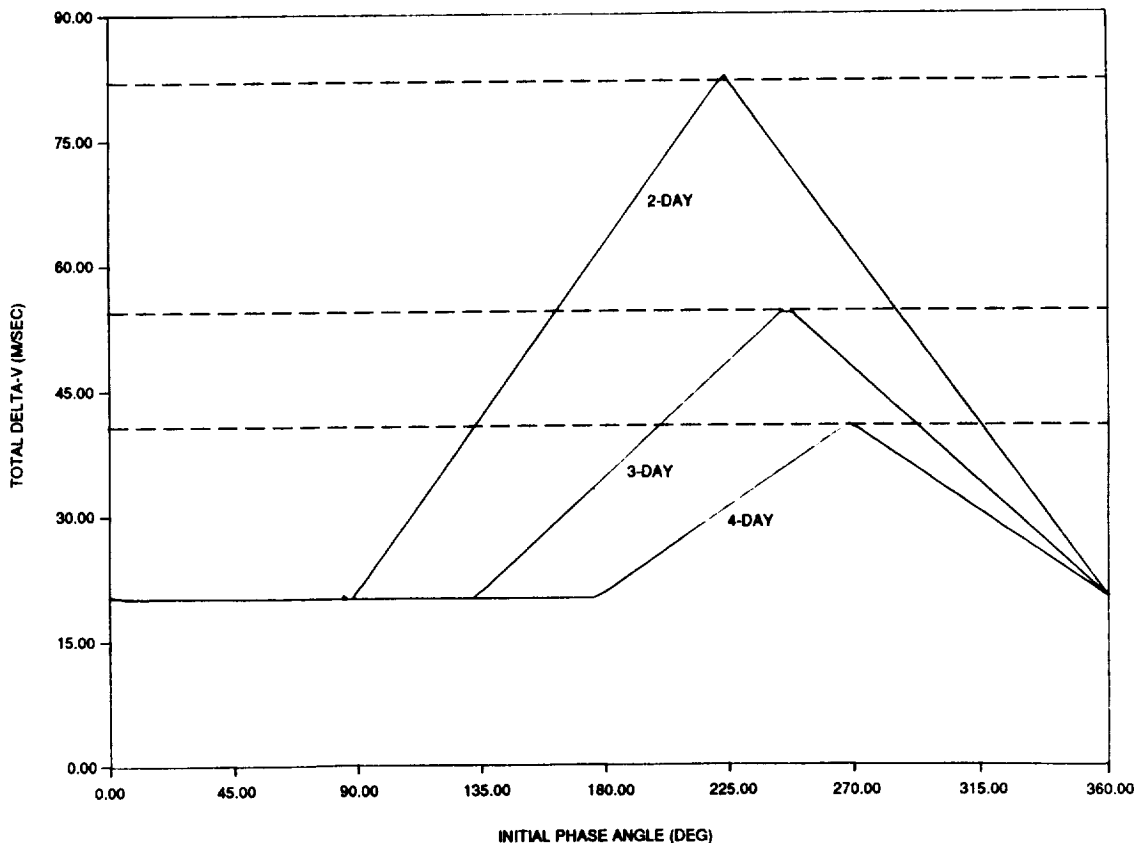


Figure 6. Delta-V Versus Phase Angle for 2-, 3-, and 4-Day Rendezvous; Low-Energy Solutions

solution ΔV . These synodic orbit ΔV s are represented in Figure 6 as dashed horizontal lines. As anticipated, each of the lines is tangent to the peak of the appropriate four-burn sequence ΔV curve.

Figure 6 leads to the intuitive result that as the rendezvous time goes down, the cost of the most expensive solution goes up. A corollary of this is the conclusion that increasing the initial altitude of the chase spacecraft has no effect on the maximum ΔV until the altitude of the synodic orbit is passed. This is graphically shown in Figure 7. The ΔV is shown as a function of phase angle for five different user spacecraft initial altitudes for a 2-day rendezvous sequence. When the initial altitude is equal to the synodic altitude of 459 km, the ΔV becomes constant at the maximum ΔV value. Raising the initial altitude beyond this increases the ΔV to a still higher value.

Figure 8 demonstrates another important characteristic of ΔV costs in the four-burn sequence. The figure illustrates the standard ΔV versus ϕ curve for a 3-day rendezvous from 350 to 315 km. In addition, Figure 8 includes the ΔV when an initial coast period of 12 hours is executed before the initiation of the rendezvous sequence while maintaining the time of rendezvous completion. Figure 8 indicates that the strategy of coasting to a

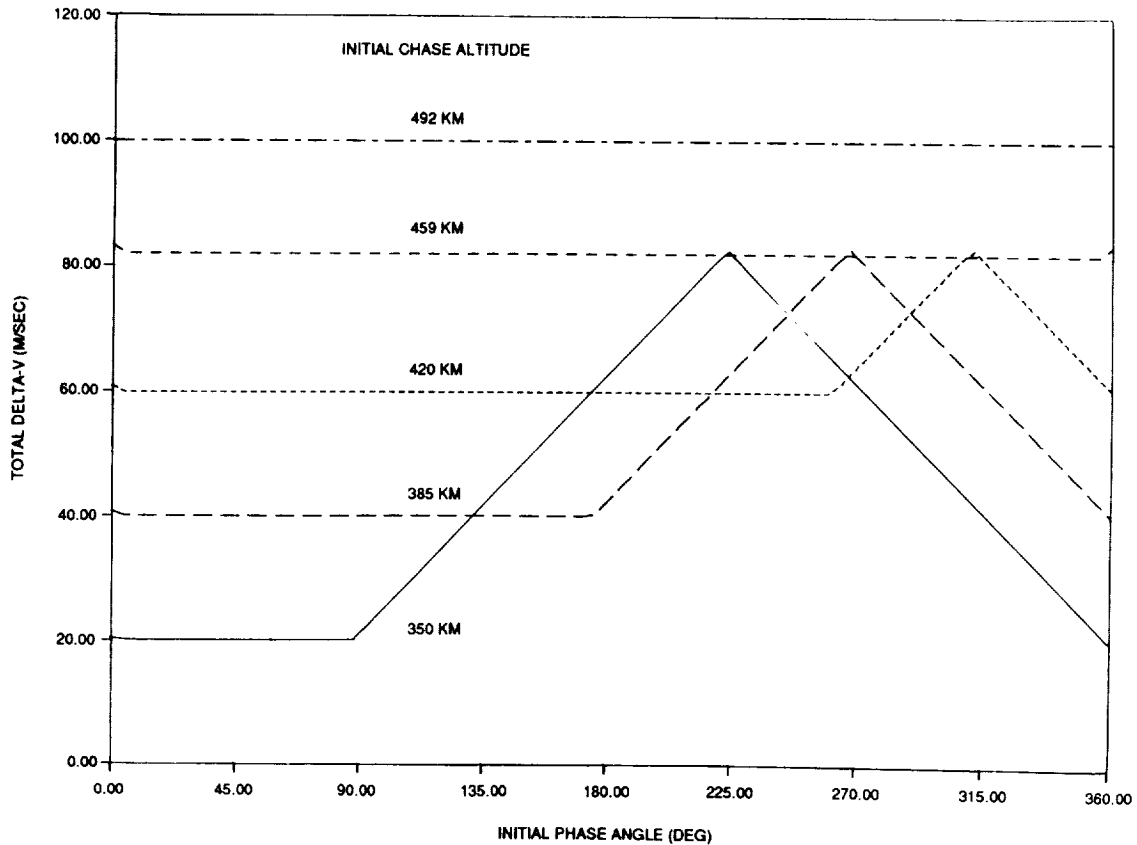


Figure 7. Delta-V Versus Phase Angle for a 2-Day Rendezvous From Five Initial Altitudes

more optimal phasing before initiating the rendezvous sequence never saves any ΔV and, in fact, raises the maximum ΔV value. The explanation for this occurrence is that the benefits of the more optimal phasing are more than countered by the increased cost associated with a shorter rendezvous duration.

The effect of plane changes on ΔV is demonstrated in Figure 9. A transfer from 350 to 315 km in 2 days for a coplanar case and for plane changes of 0.1 and 0.2 deg is shown. As previously described, the four-burn solution minimizes the impact of plane changes by combining in- and out-of-plane corrections. Because of this, the effect of plane changes on ΔV diminishes as the amount of altitude change required increases. Specifically, Figure 9 shows that the increase in the maximum ΔV is approximately 3 meters/second (m/sec) for the 0.1-deg plane change. If plane changes were not combined with the orbit maneuvers, the increase would be about 14 m/sec.

Each of the curves in Figure 9 possesses a discontinuity at a phase angle of 180 deg, which results from the requirement that each of the burns occurs at the appropriate relative node. In generating the curves shown in Figure 9, the phase angle was varied by moving the initial location of the chase spacecraft around its orbit while keeping the target position fixed. For each solution, the chase spacecraft coasts forward to the nearest

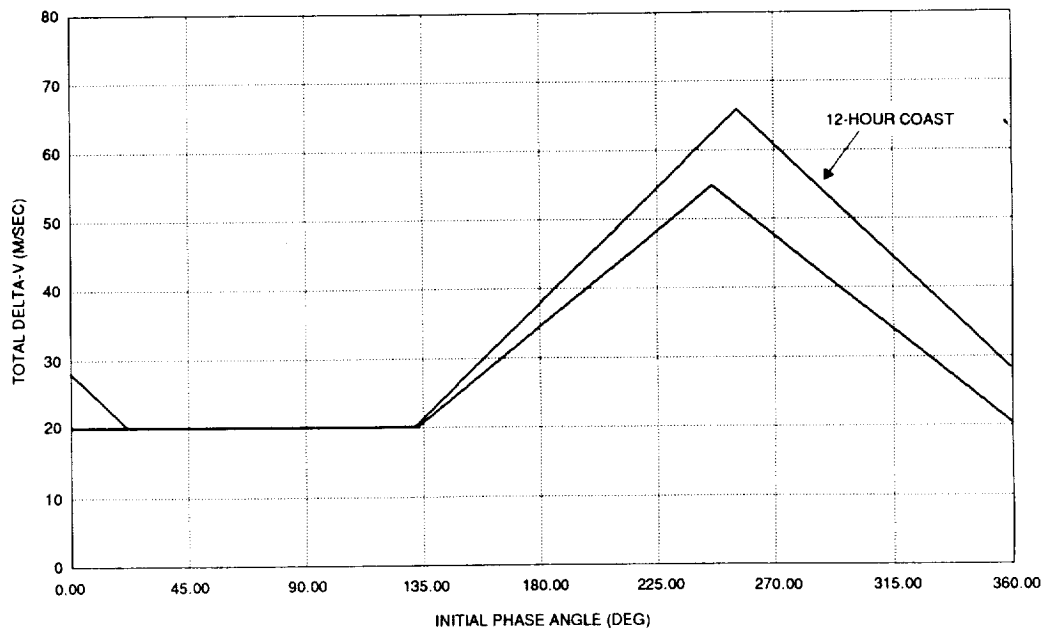


Figure 8. Total Delta-V Versus Initial Phase Angle for a 3-Day Rendezvous With a 12-Hour Initial Coast

relative node before executing the first transfer and a portion of the plane change. This coast distance monotonically decreases until the initial position of the chase spacecraft reaches the first node at a phase angle of 180 deg. At this point, no coast time is required. The change in coast time is gradual until this point and is thus not discernible. However, for the next solution, the chase spacecraft starts beyond the first relative node and must coast a full 180 deg to achieve the next node. This jump in the initial coast distance from 0 to 180 deg noticeably changes the remaining rendezvous sequence and is, therefore, discernible in the ΔV curves as a discontinuity.

4. OPERATIONAL CONSIDERATIONS

This section discusses the actual application of the four-burn sequence to user spacecraft/Shuttle rendezvous scenarios. The section describes several important considerations relevant to both the permission analysis phase and the actual maneuver-planning phase in which specific maneuvers are computed.

4.1 PREMISSION ANALYSIS

The maneuver-planning phase of rendezvous with the Shuttle requires the capability to compute exact solutions that satisfy Shuttle tolerances. To achieve adequate accuracy, it is necessary to use an integrator that includes detailed perturbation models. This process can be time consuming since the rendezvous solutions are developed through an iterative scheme. This lengthy computation time may not be acceptable during the permission analysis phase of rendezvous with the Shuttle, during which many cases must be considered and large numbers of solutions computed.

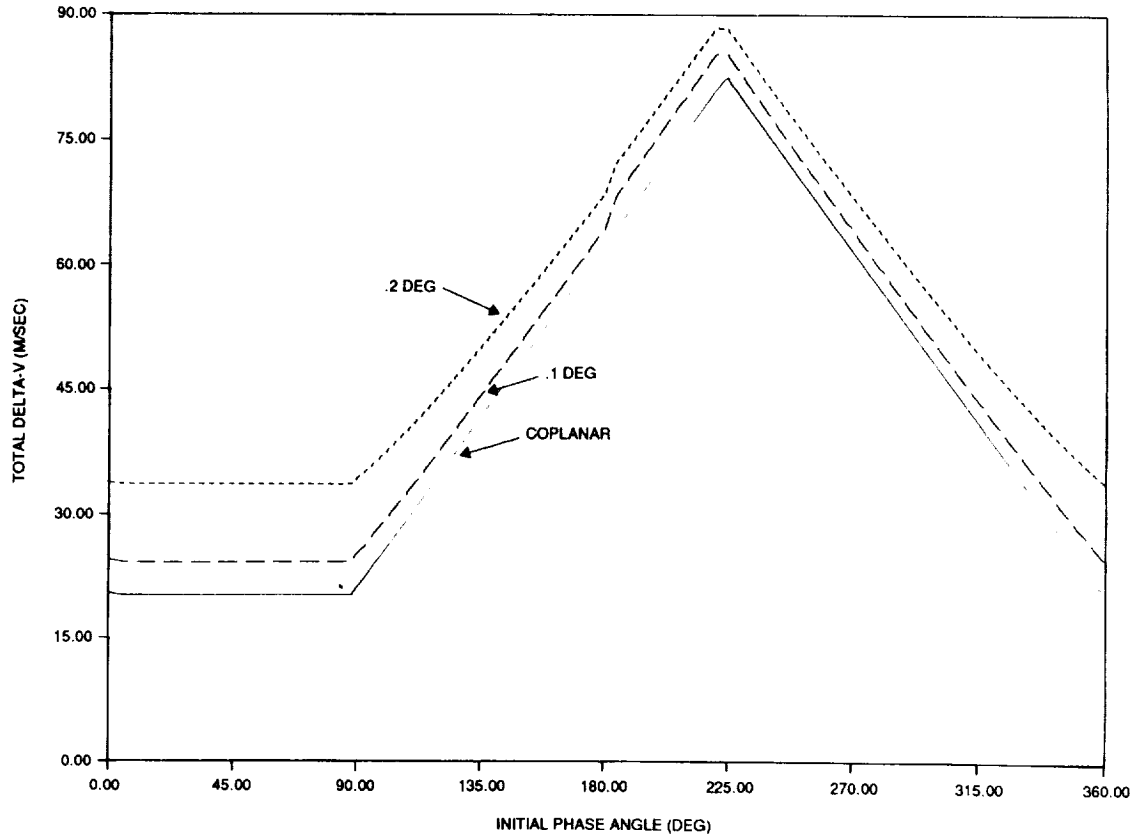


Figure 9. Delta-V Versus Phase Angle for Coplanar and Non-Coplanar Transfers

Thus, to expedite the analysis process, it is necessary to be able to quickly compute large numbers of acceptably accurate analytic solutions. However, the computation of analytic results is complicated by the various perturbations confronting spacecraft. Figure 10 illustrates the types of along-track, radial, and out-of-plane errors encountered in the final positions of the user spacecraft and Shuttle when analytic rendezvous solutions that neglect the nonspherical shape of the Earth and the effects of drag are input into an integrator that includes these perturbations. Figure 10 demonstrates that along-track errors of up to 13 deg, semimajor axis errors of 4.5 km, and ascending node errors of as much as 0.6 deg are generated when these perturbations are ignored.

These errors are dramatically reduced by incorporating into the rendezvous computation scheme analytic models describing the perturbative forces. Drag is modeled by assuming a linear relationship between altitude and density, and by employing a series of Harris-Priester atmospheric density tables that describe density conditions for a range of solar-flux values. Approximating the effects of the nonspherical shape of the Earth requires considering both the short period and secular terms of the spherical harmonic expansion describing the Earth's geopotential field. Specifically, the short-period terms affect semimajor axis, inclination, and eccentricity, while the secular terms affect ascending node, argument of perigee, and mean motion.

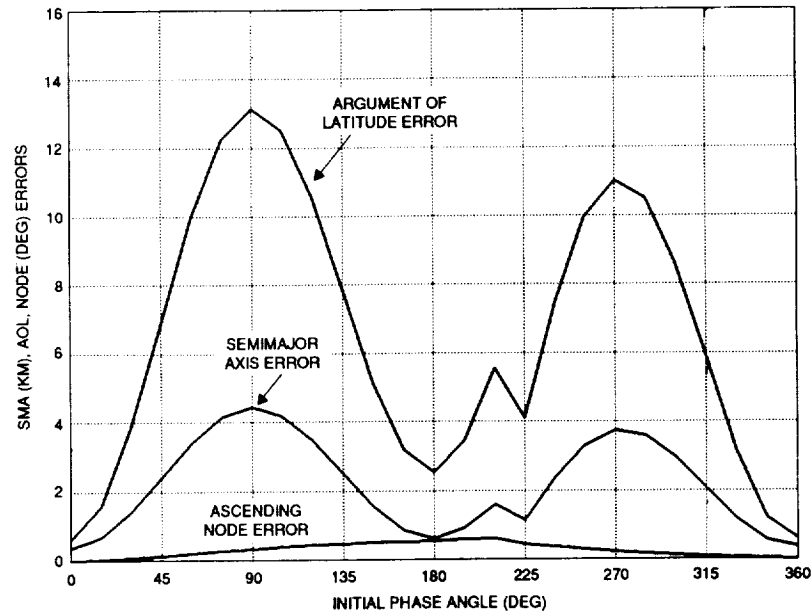


Figure 10. Errors in Analytic Solutions When No Perturbations Are Included

Figure 11 shows along-track, radial, and out-of-plane errors when these perturbation models are included in the analytic rendezvous computations. Comparison of Figure 11 with Figure 10 illustrates the significant improvement in result accuracy. The improved analytic results are accurate enough for most analysis applications and can be computed approximately 100 times faster than the integrated solutions. In addition, by using these high-quality analytic results as first-guess solutions, the speed with which exact integrated solutions can be computed for maneuver-planning purposes is greatly increased.

4.2 SPACECRAFT SEPARATION

Ensuring that the user spacecraft maintains adequate separation from the Shuttle during the entire rendezvous sequence is a crucial element of the rendezvous sequence. Any initial phase angles that could cause difficulties in this regard must be determined before the mission and handled appropriately. Of particular concern are phase angles that result in phase orbits below the Shuttle because for these cases the user spacecraft passes through the Shuttle altitude twice during the rendezvous sequence. This discussion considers separation issues relevant to both transfer orbits.

It is possible for the user spacecraft and the Shuttle to collide during the first transfer down to the phase orbit if the final rendezvous point is in the Shuttle control box and the initial phase angle is sufficiently small. For example, a phase angle of approximately 0.7 deg (chase leading target) for a 350 to 315 km, 3-day rendezvous to the center of the control box results in the two spacecraft passing within a few hundred meters of each other. This situation is shown schematically in Figure 12.

One method of avoiding the dangers associated with small initial phase angles is to coast to a larger phase angle before beginning the rendezvous sequence. As Figure 13 shows

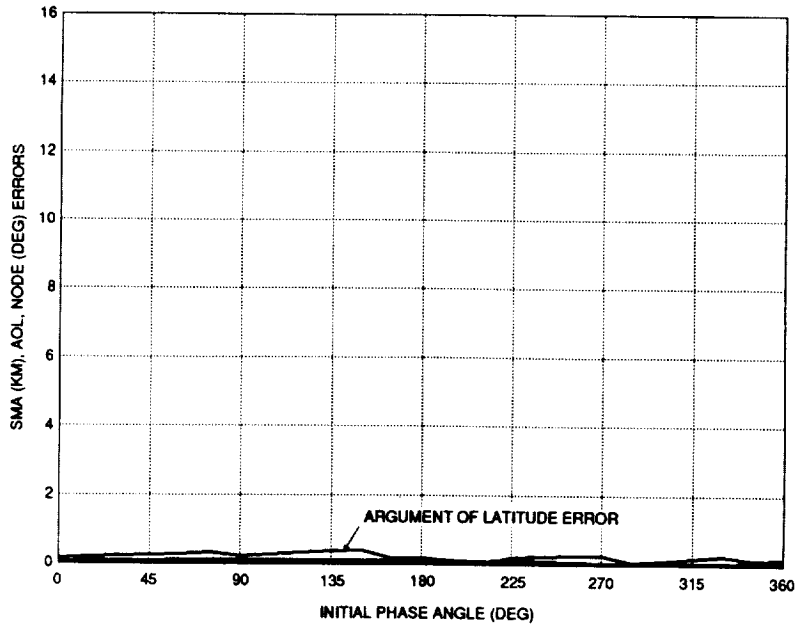


Figure 11. Errors in Analytic Solutions When Drag and J2 Are Included

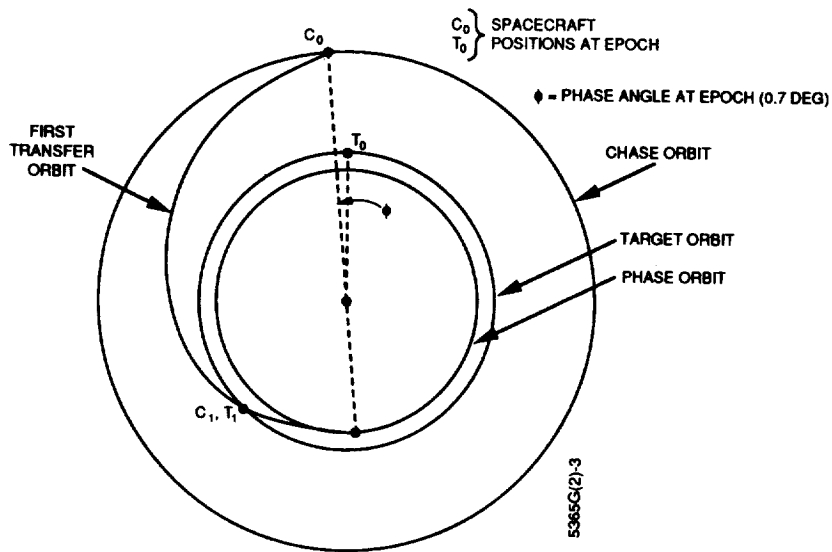


Figure 12. First Transfer Orbit for a 0.7-Deg Phasing

schematically, this initial coast increases the initial phase angle to a value that presents no danger of contact even if the second burn cannot be performed and extra revolutions are required in the transfer orbit. For the specific case involving the 0.7-deg phasing described above, a coast period of 6 hours increases the minimum separation of the

spacecraft to approximately 1500 km. Such a coast would not increase the maximum ΔV of the rendezvous sequence since it would only be performed for phasings near 0 deg.

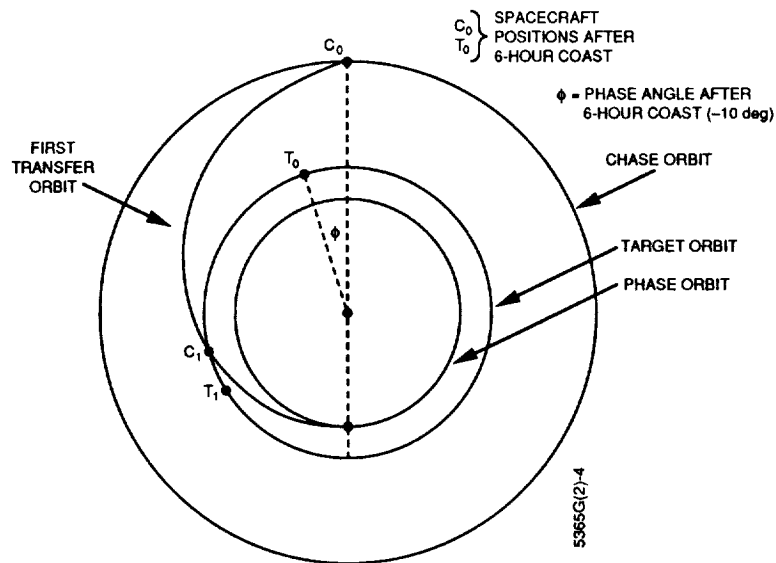


Figure 13. First Transfer Orbit After an Initial 6-Hour Coast

Separation problems are less severe for the second transfer from the phase orbit up to the Shuttle control box. It can be demonstrated that, irrespective of the altitude of the phase orbit, the angular separation when the user spacecraft passes through the Shuttle altitude will always be essentially the same as the final angular separation. This phenomena, shown schematically in Figure 14, implies that adequate separation during the final transfer can be ensured by simply adjusting the final rendezvous point in the Shuttle control box.

While the final transfer presents little difficulties under nominal conditions, under certain off-nominal circumstances, separation problems can arise. Specifically, if unplanned extra revolutions are necessary in the second transfer orbit, the user spacecraft and Shuttle may drift closer together. This will occur if the phase orbit is sufficiently close to the Shuttle orbit such that the period of the transfer orbit is greater than that of the Shuttle. This will cause the Shuttle to catch up with the user spacecraft during the unplanned extra revolutions and introduce the possibility of contact. All dangers associated with extra revolutions in the second transfer orbit are removed by positioning the phase orbit further below the Shuttle than the final rendezvous point is above. This can be achieved using the initial coast option described previously.

4.3 BIASING

J2 nodal precession due to the nonspherical shape of the Earth causes initially coplanar orbits of differing altitudes to become noncoplanar over time. For rendezvousing spacecraft, it is possible to compute an offset angle that when applied to the initial plane of one spacecraft causes the orbits to precess into the same plane by the termination of the

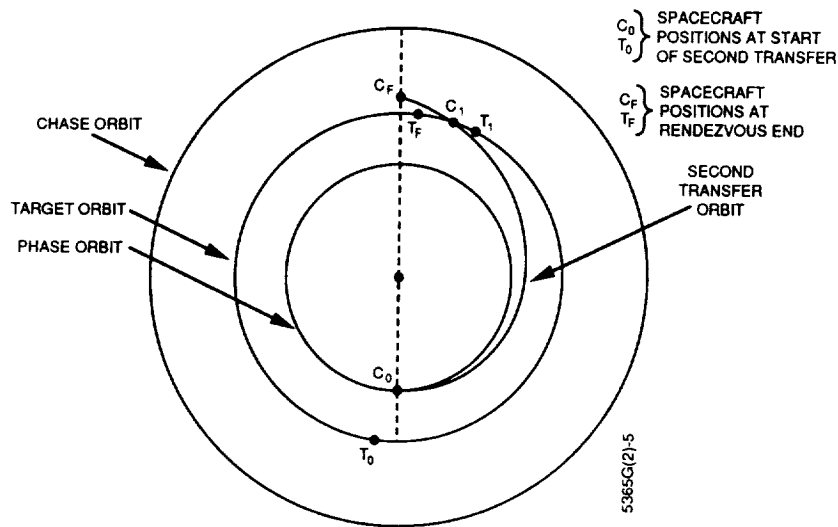


Figure 14. Final Transfer Orbit for Rendezvous to the Control Box

sequence. This bias angle can be used to avoid the plane changes that J2 would otherwise generate. Computation of this bias angle is a critical element in the interface between the user spacecraft and the Shuttle. Shuttle mission planners will use the computed bias angle to define the orbit plane into which the Shuttle is to be launched.

Since the nodal precession rate is affected by spacecraft altitude, the bias angle will be a function of the phase orbit altitude, and, therefore, a function of the initial conditions of the rendezvous. Figure 15 shows the bias angle for the upper and lower phase orbit solutions for six different sequences in which user spacecraft altitude, Shuttle altitude, and rendezvous duration were all varied. Figure 15 demonstrates that while the bias angle is a function of the initial phase angle, ϕ , it is essentially independent of spacecraft altitudes and rendezvous duration.

The following equations describing this linear relationship between bias angle, $\Delta\Omega$, and the phase angle can be derived from the analytic equations for phase orbit altitude (Equations (3-2) and (3-3)):

$$\Delta\Omega_u = -\frac{\partial \dot{\Omega}}{\partial a} k_u \phi \quad (4-1)$$

$$\Delta\Omega_\ell = -\frac{\partial \dot{\Omega}}{\partial a} k_\ell \phi + 2\pi \frac{\partial \dot{\Omega}}{\partial a} k_\ell \quad (4-2)$$

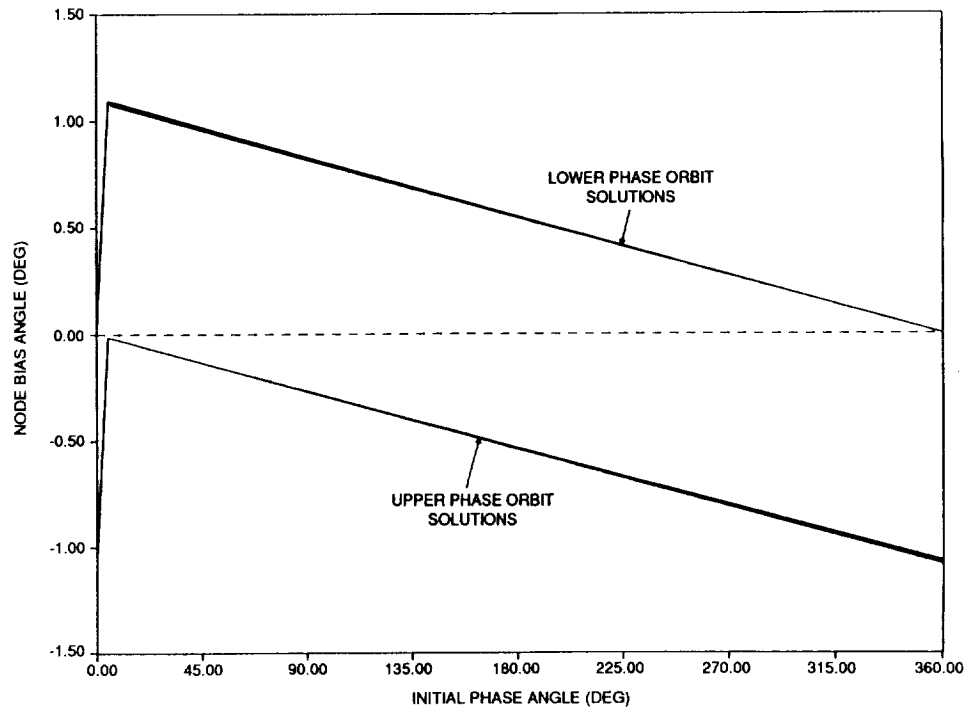


Figure 15. Bias Angle as a Function of Initial Phase Angle for Various Initial Conditions

where

$\Delta\Omega_\ell$ = bias angle corresponding to the lower phase orbit

$\Delta\Omega_u$ = bias angle corresponding to the upper phase orbit

$\dot{\Omega}$ = nodal precession rate

a = user spacecraft semimajor axis during rendezvous sequence

Numerical analysis demonstrates that the partial derivative of the nodal precession rate with respect to semimajor axis is essentially a constant over the range of altitudes under consideration (300 to 500 km). This is in agreement with the observed linearity of the bias angle/ ϕ function.

Equations (4-1) and (4-2) predict the bias angle to within several hundredths of a degree and thus can be used for quick approximations.

4.4 TRACKING COVERAGE AND LIGHTING CONSTRAINTS

A probable requirement of rendezvous with the Shuttle is the capability to position each of the burns to satisfy various lighting and tracking coverage constraints. Specifically, Shuttle lighting requirements may specify that both spacecraft must be in the light at the termination of the rendezvous sequence. In addition, user spacecraft power and attitude sensor requirements may demand specific lighting conditions. Finally, Tracking Data and

Relay Satellite (TDRS) coverage will probably be necessary at each burn. Satisfying each of these requirements simultaneously can be achieved by adjusting the launch window of the Shuttle and the times of each of the burns.

It is anticipated that these constraints can be satisfied by using existing software to determine lighting and coverage characteristics during the proposed time for the rendezvous sequence. The proper conditions can be met by varying the time and therefore the location of rendezvous and by adjusting the coast period before the first burn and the time spent in the transfer orbits.

4.5 THRUSTER CALIBRATION AND CONTINGENCY PLANNING

An essential element of rendezvous between user spacecraft and the Shuttle involves contingency analysis. The sequences developed must allow for orbit determination and thruster calibration and techniques for recovering from off-nominal burns.

Thruster performance and spacecraft attitude errors in any maneuver must be compensated for in subsequent maneuvers to avoid unacceptably large errors. For example, if the first maneuver is 10 percent hot and the subsequent maneuvers are not retargeted, the resulting final along-track errors can be as large as 1300 km for a 3-day rendezvous from 350 to 315 km. Similarly, firing 10 percent hot in the final two burns of an otherwise nominal sequence can introduce final semimajor axis errors as large as 6.5 km.

Rendezvous sequences with the Shuttle must include techniques for determining and correcting for such errors. One possible technique for error determination and correction is simply to allow the first two burns to proceed, and then, upon achieving the phase orbit, to perform orbit determination and thruster calibration, and to recompute a new solution if necessary.

While straightforward, such a strategy is not desirable because it allows for the possible execution of two consecutive off-nominal burns with no thruster calibration between them. This could result in a phase orbit that is off-nominal to the extent that communications through TDRS will be jeopardized. For example, if burns 1 and 2 are both 10 percent hot, the phase orbit can be as much as 6.5 km below the nominal altitude for a 350 to 315 km scenario. Figure 16 illustrates that this altitude error will result in Doppler errors in excess of typical user spacecraft maximums (dashed horizontal lines) after only 1.5 revolutions. The maximums shown in this figure are for GRO. In addition, execution of burns 3 and 4 with no orbit determination between them removes the ability to fine tune the final transfer orbit.

An operationally better strategy is to incorporate a coasting period in each of the transfer orbits to provide time for orbit determination, thruster calibration, and any necessary retargeting. One advantage of such a sequence is that performing corrections after one instead of two burns lessens the likelihood of errors accumulating and is therefore likely to reduce Doppler errors. Figure 17 demonstrates that a 10 percent error in the first burn of a 350 to 315 km 3-day transfer results in more than 5 hours of TDRS coverage in the off-nominal transfer orbit before Doppler errors exceed the GRO maximums. In addition, this technique provides the capability to make corrections in the final transfer orbit after an off-nominal third burn.

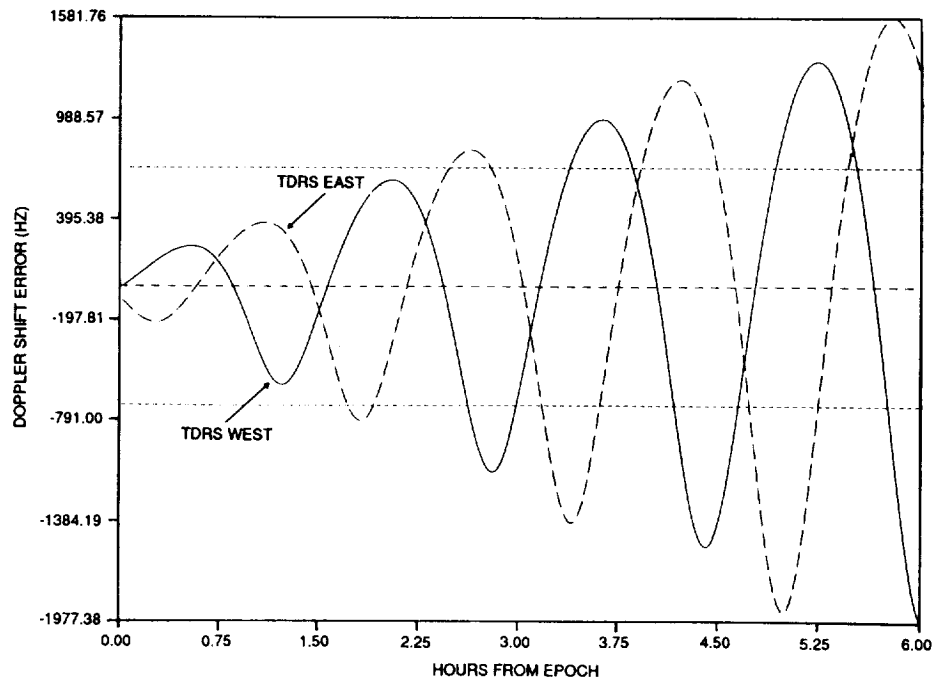


Figure 16. Doppler Shift Error in Phase Orbit After Two Off-Nominal Burns

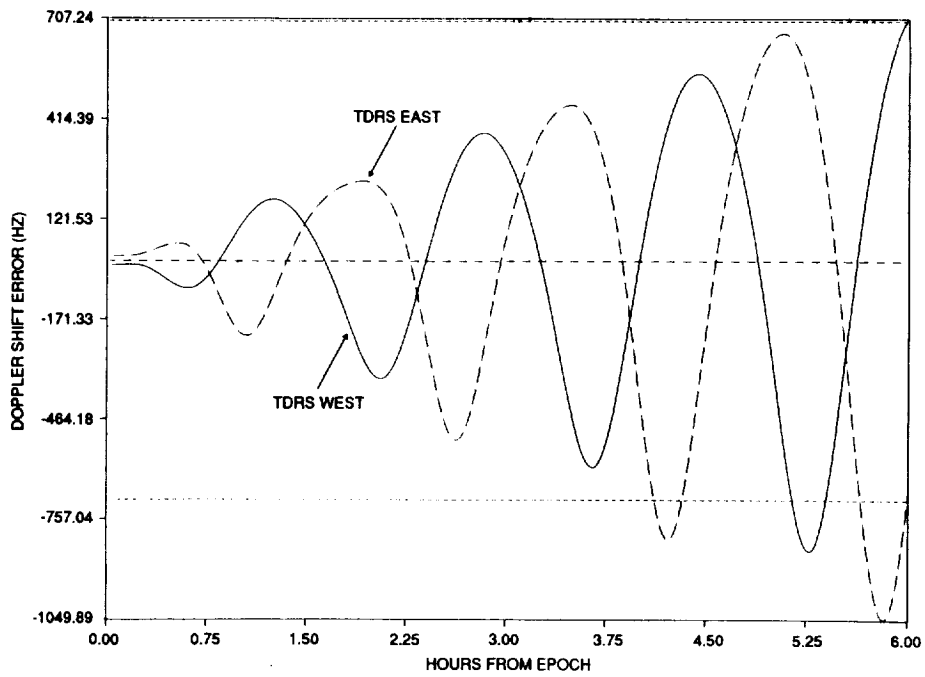


Figure 17. Doppler Shift Error in Transfer Orbit After One Off-Nominal Burn

Assuming this second type of rendezvous sequence is utilized, a typical recovery sequence would proceed as follows. Orbit determination would occur immediately after the first burn during the planned coast in the first transfer orbit. The user spacecraft thrusters would be calibrated using the newly determined orbits. If the actual transfer orbit is not within predetermined tolerances, a new rendezvous solution would be computed and executed. Figure 18, which illustrates such a recovery sequence, shows the off-nominal first burn (burn 0), the planned three-revolution coast period in the first transfer orbit, and the new four-burn solution from this off-nominal orbit.

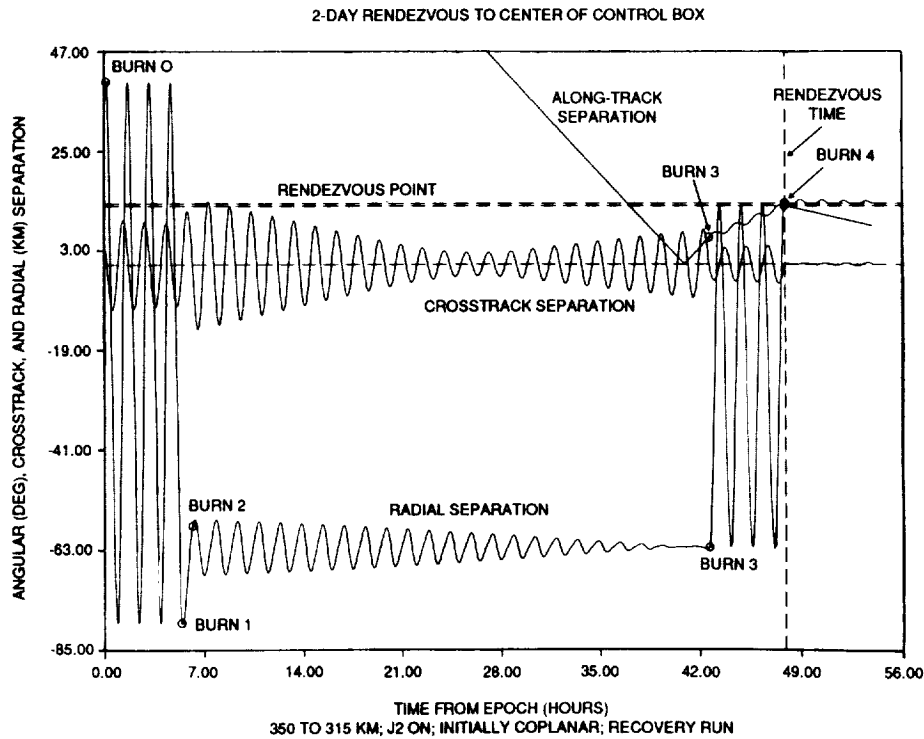


Figure 18. Two-Day Rendezvous to Center of Control Box

5. CONCLUSIONS

This paper has considered active rendezvous between a low-Earth orbit user spacecraft and the STS Shuttle. It demonstrates that rendezvous with the Shuttle requires that user spacecraft be able to execute coplanar or noncoplanar transfers in a specified amount of time from any initial orientation with the Shuttle. This general requirement, together with safety considerations and the desire to minimize ΔV expenditures, makes a rendezvous sequence consisting of a series of Hohmann transfers a desirable technique.

The general characteristics of such a rendezvous sequence are described. Specifically, relationships between phase orbit altitude and ΔV and the initial conditions of the sequence are explored in detail. Phase-orbit altitude is demonstrated to be essentially a linear function of the phase angle, with slope inversely related to the time of the

rendezvous. The ΔV of such a sequence is demonstrated to be a function of the phase angle, with the maximum value being determined by the duration of the sequence and the altitude of the user spacecraft.

The final portion of the document considers relevant issues associated with the application of such a sequence in the operational environment. Rendezvous solutions that satisfy Shuttle tolerances are demonstrated. Techniques for ensuring that adequate spacecraft separations are maintained at all times are discussed. Bias angles for minimizing the number of necessary plane changes and strategies for guaranteeing proper lighting and coverage characteristics are considered. Finally, two methods for recovering from off-nominal burns are presented.

REFERENCES

1. Lyndon B. Johnson Space Center (JSC) Missions Operations Directorate, *Rendezvous Options*, D. J. Pearson, April 1987
2. --, *Rendezvous Techniques Options*, D. J. Pearson, February 1987
3. NASA, S-84-05028, *Spacecraft Standard Retrieval Policy*
4. Rockwell STSOC, *The Rendezvous Control Box*, C. G. M. de Bont, May 1987
5. NSTS 07700, *System Description and Data Design - Payload Deployment and Retrieval System*, Volume XIV, Appendix 6, May 1988 (Draft)
6. Computer Sciences Corporation, CSC/TM-87/6013, *Noncoplanar Rendezvous and the Biasing Technique*, J. R. Herrnstein and J. P. Carrico, April 1989

Optimum Data Weighting and Error Calibration for Estimation of
Gravitational Parameters

Francis J. Lerch
Geodynamics Branch, GSFC
Greenbelt, MD 20771

ABSTRACT

A new technique has been developed for the weighting of data from satellite tracking systems in order to obtain an optimum least-squares solution and an error calibration for the solution parameters. Data sets from optical, electronic, and laser systems on 17 satellites in GEM-T1 (Goddard Earth Model, 36x36 spherical harmonic field) have been employed toward application of this technique for gravity field parameters. Also GEM-T2 (31 satellites) was recently computed as a direct application of the method and is summarized here. The method employs subset solutions of the data associated with the complete solution and uses an algorithm to adjust the data weights by requiring the differences of parameters between solutions to agree with their error estimates. With the adjusted weights the process provides for an automatic calibration of the error estimates for the solution parameters. The data weights derived are generally much smaller than corresponding weights obtained from nominal values of observation accuracy or residuals. Independent tests show significant improvement for solutions with optimal weighting as compared to the nominal weighting. The technique is general and may be applied to orbit parameters, station coordinates, or other parameters than the gravity model.

PRECEDING PAGE BLANK NOT FILMED

1. INTRODUCTION

The method of data weighting has been an outgrowth of a calibration process for the error estimation of gravitational models that have been derived from satellite data, Lerch et al. (1985 and 1988) and Wagner and Lerch (1978). The principle of the new technique is to estimate the weighting of the data so as to produce realistic error estimates of the solution parameters from subset solutions of least squares normal equations. Application has generally been with use of a large set of satellites with inhomogeneous data from tracking systems of laser, electronic, and camera (optical) data. The gravity model of GEM-T1 (Marsh et al., 1988) using some 17 satellites has been tested with the new technique and the GEM-T2 (Marsh et al., 1989) solution with some 31 satellites has been derived with the new process of optimum weighting of the satellite data sets.

The accuracy estimation of the gravity model is particularly important for the TOPEX Project (1992 launch) for ocean application of its altimetry. It requires that the radial orbit error be accurate to better than 10 cm due to the uncertainty of the gravity field. Hence the estimation process for the errors, which are based upon the weights assigned to the data, must be reliable. The accuracy of the solutions, particularly the low degree field, is also important for the Lageos orbit. Accuracy is needed for the estimation of baseline motion of laser tracking sites at the centimeter per year level as part of the NASA Crustal Dynamics Project.

2. OBSERVATION WEIGHTING AND DATA CHARACTERISTICS

Observations obtained from geodetic satellite tracking systems generally have precision levels, particularly laser systems, much better than the observation residuals obtained from satellite orbital arcs in post fit analyses using the best models. This is true even though the orbital models employed were derived from the same satellite data and with the same arc lengths of several days. The problem here is that there are unmodeled systematic errors (biases) which need to be accounted for in the weighting system of the solution (Brown, 1988).

In Figure 1 an example of the characteristics of the residuals is shown for a pass of data from a typical laser tracking site. The precision error (σ_0) of the laser data is generally small (centimeter level) as compared to the rms (σ_t) of the residuals for a satellite data set t . Values of σ_t are given in Tables 1A and 1B (GEM-T1 and T2 data sets) for different satellite data types and for laser systems σ_t varies from 10 cm for Lageos orbits to over 50 cm on GEOS-1 orbital data in 1978.

Note in Figure 1 that the residuals of a tracking pass with noise removed fit very closely to a straight line as a function of a bias offset (b_0) and a timing error. The bias offset is the dominant part of the residuals. If the residuals were random with rms equal to σ_t the weight per observation point should be

$$w_t = 1/\sigma_t^2 ,$$

but with a constant offset (b_0), say for $N=50$ points in a pass, the weight should be degraded by

$$w_t = 1/N\sigma_t^2 = .02/\sigma_t^2 .$$

The latter case is characteristic of our situation particularly for the high precision laser data. The bias effects per pass tend to fluctuate randomly from pass to pass.

In general for a given satellite data type t we have

$$w_t = f_t / \sigma_t^2$$

where σ_t is the rms of residuals for the satellite data set and f_t is a downweighting factor to account for the bias effects and the correlated effects of the residuals particularly within the pass. The weighting technique will obtain w_t directly. Note from Table 1A (and 1B), $\hat{\sigma}_t^2$ as well as σ_t is given for each data type where

$$w_t = 1 / \hat{\sigma}_t^2$$

hence

$$f_t = (\sigma_t / \hat{\sigma}_t)^2$$

which is approximately a constant

$$f_t \approx .01$$

for the satellites with the laser data. In Table 1B for the Starlette ('86) and AJISAI laser data, $f_t \approx .002$ where the data weight rates were 5 times faster (1 per second as compared to 1 per 5 seconds). Note also for the optical where systems with passive (non-flashing lamps) camera data, the degradation (factor) is much less, namely

$$f_t \approx .20$$

which may be expected since the number of points per pass are fewer and the ratio of noise to bias is relatively more significant than with the laser data.

3. LEAST SQUARES MINIMIZATION

The method of solution is a modified least squares process which minimizes the sum (Q) of signal and noise as follows:

$$Q = \sum_{\ell, m} \frac{C_{\ell, m}^2 + S_{\ell, m}^2}{\sigma_{\ell}^2} + f \sum_t \sum_{\text{obs } i} \frac{r_{it}^2}{\sigma_t^2} f_t \quad (1)$$

- where the signal is given by

$C_{\ell, m}, S_{\ell, m}$: spherical harmonics comprising the solution coefficients; and

σ_{ℓ} : $\frac{1}{\sqrt{2}} \times \frac{10^{-5}}{\ell^2}$ is rms of the coefficients of degree ℓ (a priori rule) and is introduced to permit larger solutions to degree and order 36x36. This law, based upon Kaula's rule, has been obtained independently from studies of the spectra of the Earth's gravity field and is used here to represent the observed power within the geopotential.

- and the noise by

r_{it} : observation residual (observed-computed) for the i th observation of satellite tracking data set (type) t ; and

σ_t : RMS of observation residuals (generally significantly greater than a priori data precision)

f_t : downweighting factor to compensate for unmodeled error effects for each data type t (ideally $f=1$ for pure noise)

The optimum weighting method estimates the combined weight directly, namely

$$w_t = f_t / \sigma_t^2 .$$

When minimizing Q above using the least squares method, the normal matrix equation and error covariance is obtained as follows:

$$N_x = R$$

are the normal equations, where x is the solution, R is the vector of residuals, and

$$V_{zz} = N^{-1}$$

is the approximate form for the variance-covariance error matrix which must be calibrated by adjusting the weighting.

The process of minimizing both signal (Kaula constraints) plus noise in (1) is also known as collocation by Moritz (1978). With the normal least squares approach (noise-only minimization) there is a problem of separability due to the strong correlation between many of the high degree coefficients. The absence of collocation (GEM-T1 without the Kaula constraint) results in excessively large power in the adjustment of the potential coefficients. Figure 2 illustrates the instability of the least-squares solution when collocation is not used. A satellite-derived gravity solution has been solved without collocation which is evaluated using a global set of independent gravity anomalies. An unrestricted high degree field performs poorly due to excessively large adjustment in the coefficients which is normally circumvented in the standard least-squares method by solving for a smaller sized field. Unfortunately, by restricting the size of the field, one also is requiring the higher degree terms above the field limits to be constrained absolutely to zero. Figure 2 also shows the disadvantage of this approach where the smaller sized field (PGS-3067) contains aliasing in its coefficients and does not perform well. (The abbreviation PGS stands for Preliminary Gravity Solution.) The aliasing signal sensed in the data above the field limits is absorbed into the adjustment of the lower degree coefficients. The best approach is seen with the least squares collocation (or constrained) solution, GEM-T1, with a complete solution of a 36x36 field in harmonics.

4. LEAST SQUARES NORMAL EQUATIONS

In matrix form the observation equation is given by, assuming linearity,

$$\begin{aligned} O - C &= r = r_0 - Ax \\ x &= X - X_R \end{aligned} \tag{3}$$

where

$r = O - C$ --- residual, observation (O) minus computed value (C) from solution

$x = X - X_R$ --- adjustment of solution (X) from reference value (X_R) (for error analysis $X_R \equiv X(\text{true})$)

A --- matrix of partials evaluated at $X = X_R$

r_0 --- residuals based upon a priori value X_R .

For the gravity field, the linearity of perturbations may be seen for the spectrum of harmonics in Kaula (1966). The weighted normal equations are where W is a diagonal weight matrix (Lawson and Hanson, 1974)

$$A^T W r = 0$$

then from (1)

$$A^T W A x = A^T W r_0 \tag{4}$$

For error analysis it is convenient to let the reference value

$$X_R = X(\text{true})$$

then from (3) x is the error in the solution X , namely

$$x = X - X(\text{true})$$

Hence (4) becomes

$$A^T W A x = A^T W e \tag{5}$$

where

$$\begin{aligned} e &\equiv r_o = 0 - C_R \\ &= 0 - C(\text{true}) \end{aligned}$$

represents the errors due to all unmodeled systematic effects including random noise but excluding errors in the adjusted parameters. Instead these are the errors in x given by the solution to (5). Our solutions will be represented by the form (5) as we are interested in the difference between two solutions, x and \hat{x} , namely

$$\begin{aligned} x - \hat{x} &= [X - X(\text{true})] - [\hat{X} - X(\text{true})] \\ &= X - \hat{X} \end{aligned} \tag{6}$$

The normal matrices for (5) are written compactly as

$$N x = R$$

where

$$\begin{aligned}
 N &= A^T W A \\
 R &= A^T W e
 \end{aligned}
 \tag{7}$$

The normal matrices for each data subset t will be given as

$$\begin{aligned}
 w_t N_t &= w_t A_t^T A_t \\
 w_t R_t &= w_t A_t^T e_t
 \end{aligned}
 \tag{8}$$

where $t=0$ is a special case which corresponds to the signal constraints where the weight is fixed.

5. METHOD OF ESTIMATION OF WEIGHTS

The technique for estimating w_t for each data set t is based upon a complete solution (S) with all the data and a subset solution (S_t) where data set t is removed. Let the normal equations for the complete solution x and the subset solution x_t be given as in (7) namely

$$Nx = R \quad (9)$$

$$\bar{N} x_t = \bar{R}$$

where from (7)

$$\bar{N} = \sum_{j \neq t} w_j N_j \quad \bar{R} = \sum_{j \neq t} w_j R_j \quad (10)$$

$$N = \bar{N} + w_t N_t \quad R = \bar{R} + w_t R_t$$

The covariance (variance-covariance) matrices (V) for the errors x and x_t are obtained as

$$V(x) = N^{-1} \equiv E(xx^T) \quad (11)$$

$$V(x_t) = \bar{N}^{-1} \equiv E(x_t x_t^T)$$

As in (6)

$$\begin{aligned} x_t - x &= [X_t - X(\text{true})] - [X - X(\text{true})] \\ &= X_t - X \end{aligned} \quad (12)$$

The covariance of the difference between the solutions is

$$\begin{aligned}
V(x_t - x) &= E(x_t - x)(x_t - x)^T \\
&= V(x_t) - 2 E(x_t x^T) - V(x) \\
&= V(x_t) - V(x)
\end{aligned} \tag{13}$$

where as shown below

$$E(x_t x^T) = V(x) \tag{14}$$

From (9)

$$E(x_t x^T) = \bar{N}^{-1} E(\bar{R} R^T) \bar{N}^{-1} \tag{15}$$

From (10) and (11)

$$\begin{aligned}
E(\bar{R} R^T) &= E[\bar{R}(\bar{R} + w_t R_t)^T] \\
&= E(\bar{R} \bar{R}^T) = \bar{N} V(x_t) \bar{N} \\
&= \bar{N}
\end{aligned} \tag{16}$$

since

$$E(\bar{R} R_t^T) = 0$$

The latter result is true as from (10) the data set t is excluded from the subset solution, making \bar{R} and R_t independent. Hence (14) results by substituting (16) into (15) and using (11).

5.1 WEIGHTING ALGORITHM

Using just the gravity parameters in $(X_t - X)$ the weighting algorithm is given by the calibration factor k_t obtained from

$$(X_t - X)^T (X_t - X) = (x_t - x)^T (x_t - x) = k_t \text{ TR } V(x_t - x) \quad (17)$$

where TR denotes the trace of the matrix and where from (9) through (13)

$$x_t - x = \bar{N}^{-1} R - N^{-1} R = X_t - X \quad (18)$$

$$\bar{N} = \sum_{j \neq t} w_j N_j \quad (19)$$

$$N = \bar{N} + w_t N_t$$

$$\bar{R} = \sum_{j \neq t} w_j R_j \quad (20)$$

$$R = \bar{R} + w_t R_t$$

$$V(x_t - x) = \bar{N}^{-1} - N^{-1} = V(x_t) - V(x) \quad (21)$$

Since k_t scales the error variances it will be inversely proportional for scaling the weight w_t to obtain the adjusted weight w'_t , namely

$$w'_t = w_t / k_t \quad (22)$$

This latter result will be derived more directly below. By iterating on the solutions x_t for each data set t and the complete solution x for all data sets until

$$k_t = 1$$

for each t , the weights by (22) will then converge and the error estimates will automatically be calibrated from (17).

Results are given below to show how the weights and associated calibration factors converge. Because of the extensive computations for a large number of data sets a reasonable set of a priori values for the weights should be available for their refinement in the optimization process.

The gravity parameters of spherical harmonic coefficients are calibrated as a set by (17). Calibrations (k_t) are also given by subsets of spectral components from the harmonics of degree l and order m . For all satellite data sets t (Lerch et al., 1988) relatively little variation is seen in the spectral calibrations.

5.1.1 Weighting Adjustment

The relation (18) for the weighting adjustment

$$w_t' = w_t/k_t$$

is derived from use of (17) through (21). It is assumed that the data set t does not significantly change the solutions x and x_t beyond first order effects as follows:

$$\begin{aligned} V(x_t - x) &= \bar{N}^{-1} - N^{-1} = \bar{N}^{-1} - (\bar{N} + w_t N_t)^{-1} & (23) \\ &= \bar{N}^{-1} - (I + w_t N_t)^{-1} \bar{N}^{-1} \\ &\approx w_t \bar{N}^{-1} N_t \bar{N}^{-1} \end{aligned}$$

To the same approximation

$$x_t - x = w_t \bar{N}^{-1} R_t$$

$$E(x_t - x)(x_t - x)^T = w_t^2 \bar{N}^{-1} E(R_t R_t^T) \bar{N}^{-1} \quad (24)$$

From (8)

$$E(R_t R_t^T) = A_t^T E(e_t e_t^T) A_t \quad (25)$$

$$= \hat{\sigma}_t^2 N_t$$

$$= N_t / w_t^c$$

where $\hat{\sigma}_t$ accounts for the unmodeled systematic effects in e_t and the corresponding weighting effect is given as

$$w_t^c = \frac{1}{\hat{\sigma}_t^2} = f_t / \sigma_t^2$$

Using (23) and (25) then (24) becomes

$$E(x_t - x)(x_t - x)^T = \frac{w_t}{w_t^c} V(x_t - x) \quad (26)$$

From (26) and (17)

$$k_t = w_t / w_t^c$$

which gives the result (22).

6. TESTS AND RESULTS FOR OPTIMUM WEIGHTING TECHNIQUE

Sample tests of the weighting algorithm (22) were made using GEM-T1 plus additional data sets for several satellite data types of laser, optical, and electronic data. Results are given in Table 2 which show that the algorithm nearly converges in one step from the a priori starting weights. Plots of w_t vs k_t from (17) show a strong linear relationship from the origin ($w_t = k_t = 0$). Hence

$$\frac{w'}{k'} = \frac{w}{k}$$

and by setting $k' = 1$ for calibration the adjusted weight w' should nearly converge from (22).

The above tests were made in preparing the weights for additional data sets to GEM-T1 that were combined for the GEM-T2 model. The convergence of these weights for GEM-T2 is shown in Table 3. In addition to the optimum weights the technique provides an automatic calibration of the error estimates based upon the satellite data types t since each of the k_t from (17) is required to converge to 1.

The data weights in GEM-T1 were derived primarily by requiring the weight for each data type t to give the best overall agreement with independent mean gravity anomalies (Rapp, 1986) and with the satellite observation residuals on selected test arcs. The calibration factors ($k_t^{1/2}$) for several of the major data types (Lerch et al., 1988) are given in Table 4 which show that the weights converge ($k_t = 1$) except for the Lageos laser data. However, several additional tests were made in Table 4 for the calibration factor using independent data from Seasat altimetry (Rapp, 1986) and surface gravity data (Pavlis, 1988). All of the latter tests show good calibration of the error estimates, indicating optimum weighting was closely achieved. The last test deliberately increased the weighting for a subset of laser data by a

factor of 10 giving a value $k_t=(2.75)^2$. From (22) the adjusted weight should be reduced by a factor of $1/k_t$ which would nearly recover the original weight in one step of the iteration process. The gravity model with the increased weight naturally gives smaller error estimates but it also gave significantly worse agreement with independent surface gravity anomalies.

7. SUMMARY

The optimum weighting technique was shown to be important in the weighting of satellite data, particularly precise laser data where unmodeled systematic effects require a significant downweighting factor as shown in Table 1. The method of weighting was shown in Section 6.0 to provide realistic error estimates for GEM-T1 and T2. These models were calibrated using subset solutions based not only on data employed in their solutions but also upon independent data from altimetry and gravimetry. Because of the important application of the gravity model to ocean altimetry in the Topex Project, the gravity model errors were projected on the radial component of the TOPEX orbit and the result gave 10 cm for GEM-T2 which nearly meets the goal of the gravity model.

It was also shown in Section 6.0 that the model with the increased weight on the data over the optimum weighting gave much poorer agreement with independent surface gravity anomalies. The optimum weighting technique based upon the mathematical formulae is general and may be applied to other than gravitational parameters such as station coordinates and in particular orbit parameters where knowledge of accuracy estimation and refined solutions are needed.

ACKNOWLEDGMENTS

I wish to express my sincere thanks to Girish Patel of STX Corporation for his analysis and computation of the GEM-T1 and T2 data weights and calibrations of this report.

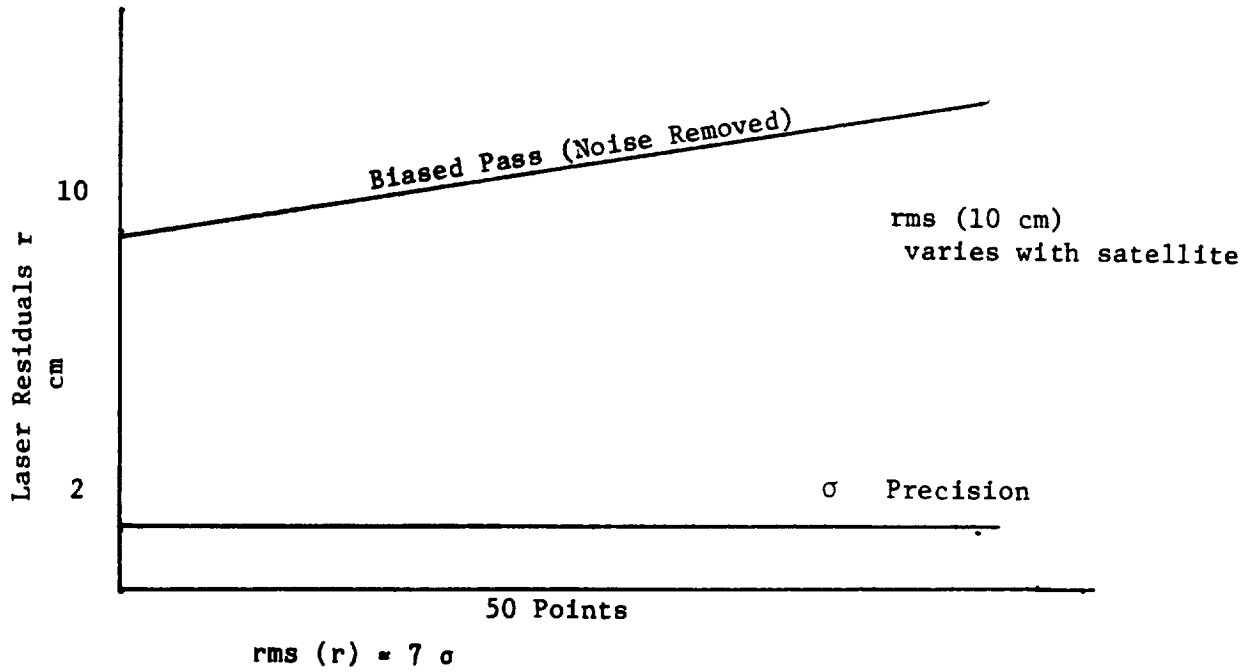
REFERENCES

- Brown, R.D., Characterization of the GEOS-1 Laser Ranging Residuals (1976-1980), STX Contract Report 8801, Oct. 1988.
- Kaula, W.M., Theory of Satellite Geodesy, Blaisdell Press, Waltham, Mass., 1966.
- Lawson, C.L. and R.J. Hanson, Solving Least Squares Problems, Prentice-Hall, Englewood Cliffs, New Jersey, 1974.
- Lerch, F.J., Klosko, S.M., Wagner, C.A. and Patel, G.B., "On the Accuracy of Recent Goddard Gravity Models," J. Geophys. Res., 90, (B11), pp. 9312-9334, 1985.
- Lerch, F.J., J.G. Marsh, S.M. Klosko, E.C. Pavlis, G.B. Patel, D.S. Chinn and C.A. Wagner, "An Improved Error Assessment for the GEM-T1 Gravitational Model," NASA TM 100713, 1988.
- Marsh, J.G., F.J. Lerch, B.H. Putney, D.C. Christodoulidis, D.E. Smith, T.L. Felsentreger, B.V. Sanchez, S.M. Klosko, E.C. Pavlis, T.V. Martin, J.W. Robbins, R.G. Williamson, O.L. Colombo, D.D. Rowlands, W.F. Eddy, N.L. Chandler, K.E. Rachlin, G.B. Patel, S. Bhati, and D.S. Chinn, "A New Gravitational Model for the Earth from Satellite Tracking Data: GEM-T1," J. of Geophys. Res., 93, 6169-6215, 1988.
- Marsh, J.G., F.J. Lerch, B.H. Putney, D.E. Smith, T.L. Felsentreger, B.V. Sanchez, S.M. Klosko, E.C. Pavlis, T.V. Martin, J.W. Robbins, R.G. Williamson, O.L. Colombo, D.D. Rowlands, W.F. Eddy, N.L. Chandler, K.E. Rachlin, G.B. Patel, S. Bhati, and D.S. Chinn, "A New Gravitational Model for the Earth from Satellite Tracking Data: GEM-T2," in Print, 1989.

- Moritz, H., "Least Squares Collocation," Rev. Geophys., 16, 421-430, 1978.
- Pavlis, N.K., "Modeling and Estimation of a Low Degree Geopotential Model from Terrestrial Gravity Data," Report No. 386, Department of Geodetic Science, OSU, March 1988.
- Rapp, R.H., "Gravity Anomalies and Sea Surface Heights Derived from a Combined GEOS-3/SEASAT Altimeter Data Set," J. Geophys. Res. 91, E5, 4867-4876, 1986.
- Wagner, C.A. and Lerch, F.J., "The Accuracy of Geopotential Models," Planet. Space Sci., Vol. 26, pp. 1081-1140, 1978.

Figure 1.

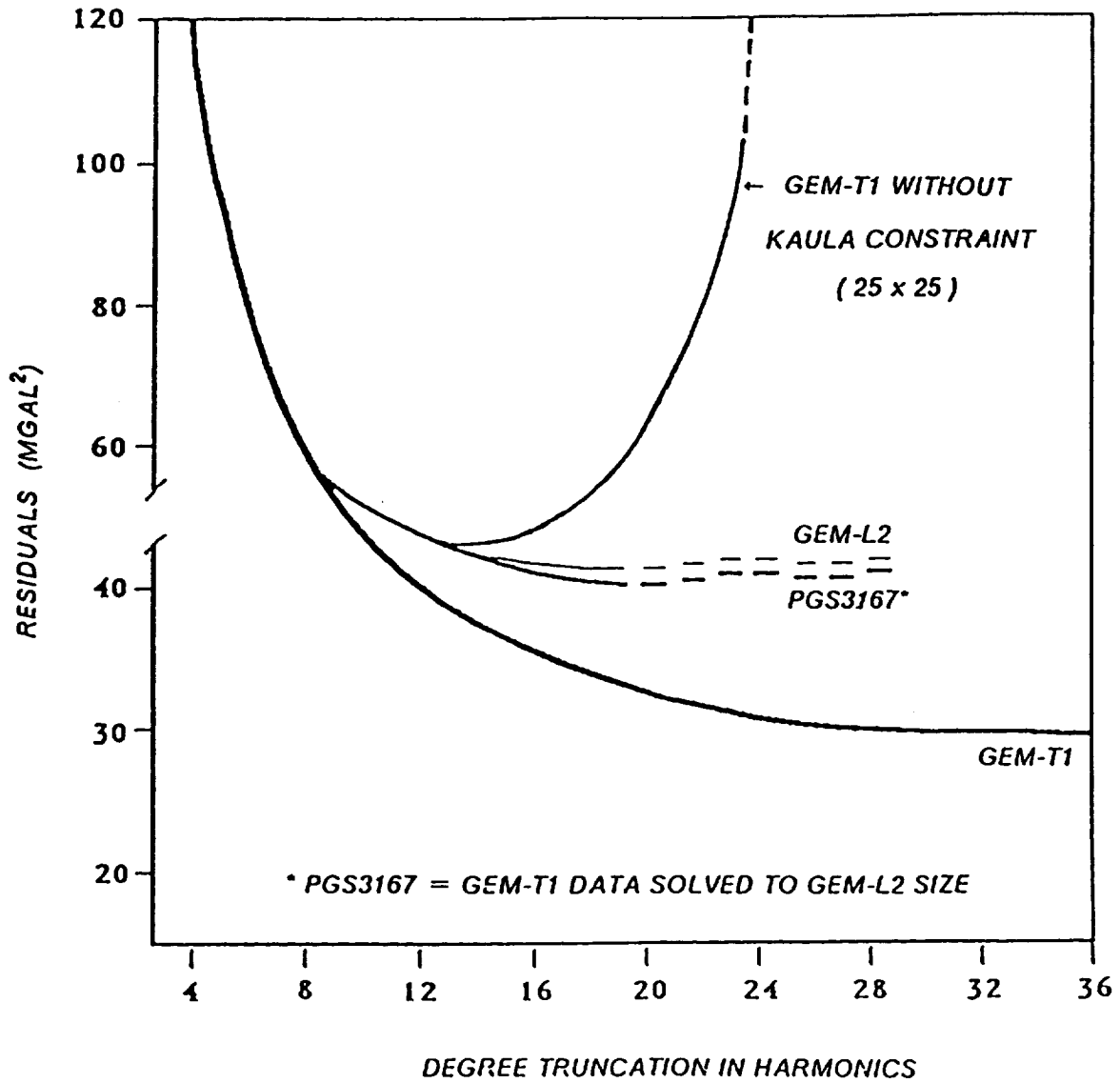
Characteristics of a Pass of Orbital Laser Residuals
at a Tracking Site in Post Fit Analysis



$$\begin{aligned}
 \text{WEIGHT PER POINT} &= \frac{1}{50} \frac{1}{(rms)^2} \\
 &= \frac{.02}{(rms)^2} \\
 &= \frac{.003}{\sigma^2}
 \end{aligned}$$

Figure 2

GRAVITY MODEL COMPARISON WITH 1114
5° X 5° SEASAT GRAVITY ANOMALIES



Models show three modes of solution. The 25 x 25 field solves GEM-T1 tracking data without the Kaula constraint showing misclosure for high degree terms. PGS-3167 solves GEM-T1 data (with Kaula constraint) to the GEM-L2 size field (20 x 20), showing no improvement over our previous model. GEM-T1 uses the Kaula constraint with a high degree field (36 x 36) and is free of the above problems.

TABLE 1A
SATELLITE DATA IN GEM-T1

SATELLITE	SEMI MAJOR AXIS (km.)	ECC	INCL DEG	DATA TYPE	# OF ARCS	# OF OBS	RMS RESID. σ_t	SIGMA* WEIGHTS $\hat{\sigma}_t$
1 LAGEOS	12273.	.0038	109.85	LASER	57	144527	10cm.	112cm.
2 STARLETTE	7331.	.0204	49.80	LASER	46	57356	20cm.	224cm.
3 GEOS-3	7226.	.0008	114.98	LASER	36	42407	70cm.	816cm.
4 PEOPLE	7006.	.0164	15.01	LASER	6	4113	90cm.	816cm.
5 BE-C	7507.	.0257	41.19	LASER	39	64240	50cm.	577cm.
				CAMERA	50	7501	2 arcsec	5.6 arcsec
6 GEOS-1	8075.	.0719	59.39	LASER	48	71287	70cm.	667cm.
				CAMERA	43	60750	1 arcsec	8.9 arcsec
7 GEOS-2	7711.	.0330	105.79	LASER	28	26613	80cm.	816cm.
				CAMERA	46	61403	1 arcsec	8.9 arcsec
8 DI-C	7341.	.0532	39.97	LASER	4	7455	150cm.	816cm.
				CAMERA	10	2712	2 arcsec	7.3 arcsec
9 DI-D	7622.	.0848	39.46	LASER	6	11487	100cm.	816cm.
				CAMERA	9	6111	2 arcsec	8.9 arcsec
10 SEASAT	7170.	.0021	108.02	LASER	14	14923	70cm.	707cm.
				DOPPLER	14	138042	.5cm/sec	7cm/sec
11 OSCAR-14	7440.	.0029	89.27	DOPPLER	13	63098	1cm/sec	8cm/sec
12 ANNA-1B	7501.	.0082	50.12	CAMERA	30	4463	2 arcsec	4.5 arcsec
13 BE-B	7354.	.0135	79.69	CAMERA	20	1739	2 arcsec	4.5 arcsec
14 COURIER-1B	7469.	.0161	28.31	CAMERA	10	2476	2 arcsec	4.5 arcsec
15 TELSTAR-1	9669.	.2429	44.79	CAMERA	30	3962	2 arcsec	4.5 arcsec
16 VANGUARD-2RB	8496.	.1832	32.92	CAMERA	10	686	2 arcsec	4.5 arcsec
17 VANGUARD-2	8298.	.1641	32.89	CAMERA	10	1299	2 arcsec	4.5 arcsec

$$* \text{SIGMA} (\hat{\sigma}) = \left(\frac{1}{w}\right)^{\frac{1}{2}}$$

TABLE 1B

NEW SATELLITE DATA IN GEM-T2 IN ADDITION TO GEM-T1

SATELLITE	SEMI MAJOR AXIS (km.)	ECC	INCL DEG	DATA TYPE	# OF ARCS	# OF OBS.	σ_t RMS RESID.	$\hat{\sigma}_t$ SIGMA* WEIGHTS
LAGEOS '84,'85,'86,'87	12273	.0038	109.85	LASER	29	134093	10cm.	112cm.
STARLETTE '83,'84	7331	.024	49.80	LASER	38	40041	20cm.	224cm.
STARLETTE '86				LASER	73	411102	20cm.	500cm
AJISAI	1500	.0006	50.0	LASER	36	156021	16cm.	316cm.
GEOS-1 '80	8075	.0719	59.39	LASER	30	54129	32cm.	258cm.
GEOS-3 '80	7226	.0008	114.98	LASER	50	54526	25cm.	224cm.
GEOS-3				LASER	26	17027	70cm.	816cm.
GEOS-3:ATS '75,'76				SST	9	19074	.4cm/sec	7.1cm/sec
GEOS-3:ATS '77,'78,'79				SST	17	8326	.2cm/sec	3.2cm/sec
NOVA	1170	.0011	89.96	DOPPLER	16	73238	.4cm/sec	2.6cm/sec
LANDSAT-1	900	.0012	99.12	DOPPLER	10	26426	1.5cm/sec	10.5cm/sec
GEOSAT	800	.0008	108.0	DOPPLER	13	549141	1.3cm/sec	4.5cm/sec
OVI-2	8317	.0184	144.27	CAMERA	4	973	2 arcsec	5.8 arcsec
ECHO-1RB	7966	.0118	47.21	CAMERA	32	4482	2 arcsec	8.2 arcsec
SECOR-5	8151	.0793	69.22	CAMERA	13	726	2 arcsec	5.8 arcsec
INJUN-1	7316	.0079	66.82	CAMERA	44	3310	2 arcsec	8.2 arcsec
TRANSIT-4A	7322	.0076	66.82	CAMERA	50	3832	2 arcsec	8.2 arcsec
5BN-2	7462	.0058	89.95	CAMERA	17	820	2 arcsec	8.2 arcsec
OGO-2	7341	.0752	87.37	CAMERA	16	1207	2 arcsec	8.2 arcsec
OSCAR-7	7411	.0224	89.70	CAMERA	4	1862	2 arcsec	5.8 arcsec
MIDAS-4	9995	.0112	95.83	CAMERA	50	31779	2 arcsec	8.2 arcsec

TABLE 2
 TEST FOR OPTIMUM WEIGHTING TECHNIQUE
 WITH GEM-T1 AS SUBSET SOLUTION
 (TWO ITERATIONS)

$$w'_t = \frac{w_t}{k_t}$$

<u>GEM-T1 +</u>	<u>k_t</u>	<u>w_t</u>	<u>w'_t</u>
1980 GEOS-1 LASER (30 ARCS)	.49 .88	.05 .10	.10 .11
STARLETTE LASER (73 1986 ARCS)	.46 .78	.020 .043	.043 .055
NOVA DOPPLER (16 ARCS)	1.60 1.02	.1 .062	.062 .061
9 NEW OPTICAL SATS. (230 ARCS)	3.2 .97	.2 .063	.063 .065
LANDSAT S-BAND (10 ARCS)	.60 .98	.0025 .0042	.0042 .0043

TABLE 3

DATA WEIGHTS AND CALIBRATION OF GEM-T2

SUBSET SOLUTION DATASET	PGS3429		PGS3454		PGS3480		GEM-T2 ⁽²⁾	
	FACTORS	WEIGHTS	WEIGHTS	FACTORS	WEIGHTS	FACTORS	WEIGHTS	FACTORS
AJISAI	1.28	.4	<u>.3</u> ⁽¹⁾	1.21	<u>.2</u>	1.29	<u>.1</u>	.79
LAGEOS	1.29	.8	.8	1.00	.8	1.11	.8	.87
STARLETTE	1.04	.2,.2,.04	.2,.2,.04	1.01	.2,.2,.04	.96	.2,.2,.04	.96
4-LASER*	1.02	.015	.015	1.00	.015	.96	.015	1.01
GEOSAT	.59	.01	<u>.015</u>	.66	<u>.035</u>	.75	<u>.05</u>	.81
GEOS-3:ATS LASER,SST	.68	.015,.1,.02	.015, <u>.05</u> .02	.73	.015, <u>.1</u> .02	.66	.015,.1,.02	.66 ⁽³⁾
NOVA	.82	.07	<u>.075</u>	.83	<u>.1</u>	.83	<u>.15</u>	.90
LANDSAT	.90	.0075	.0075	.90	<u>.009</u>	.92	.009	.92
1980 GEOS-3 LASER	.86	.1	<u>.15</u>	.91	<u>.2</u>	.97	.2	.96
1980 GEOS-1 LASER	.87	.1	<u>.15</u>	.97	.15	.99	.15	1.05
OPTICAL*	.95	.05,.06	.05,.06	.95	.05,.06	.94	.05,.06	.92
SEASAT		.02	.02	1.02	.02	.97	.02	.94
OSCAR		.015	.015	1.47	<u>.007</u>	.95	.007	1.13
3-LASER*		.015	.015	.82	.015	.83	<u>.02</u>	.87

1. UNDERLINED WEIGHTS ARE THE ADJUSTED ONES IN THE ITERATED SOLUTIONS
2. CALIBRATION FACTORS ARE CONSERVATIVE BUT SUFFICIENTLY CONVERGED
3. ATS SST WEIGHT DELIBERATELY UNDERWEIGHTED BASED UPON COMPARISON WITH SEASAT ALTIMETER ANOMALIES

* 4-LASER dataset is laser data from GEOS-1 , GEOS-2 , GEOS-3 and BE-C satellites
 3-LASER dataset is laser data from DI-C , DI-D , and PEOPLE satellites
 OPTICAL dataset is the camera data from 20 satellites shown in TABLE 1A and 1B

TABLE 4

SUMMARY OF RESULTS FOR ERROR CALIBRATION

	CALIBRATION FACTOR
GEM-T1 vs. GEM-T1 minus DATA SUBSET	
4-LASERS (GEOS 1,2,3, BE-C)	1.06
STARLETTE LASER	1.10
OSGAR + SEASAT DOPPLER	1.09
OPTICAL (11 SATS)	0.84
LAGEOS LASER	1.45
 GEM-T1 vs. GEM-T1 + SURFACE GRAVITY	 0.95
 GEM-T1 vs. GEM-T1 + SURFACE GRAVITY + SEASAT ALTIMETER	 0.94
 GEM-T1 vs. SURFACE GRAVITY + SEASAT ALTIMETER	 0.99
 GEM-T1 minus LAGEOS vs. LAGEOS + SURFACE GRAVITY + SEASAT ALTIMETER	 0.95
 Weighting Factor $f=0.2$ 10 TIMES DATA WEIGHT OF GEM-T1 GEM-T1 vs. GEM-T1 minus 4-LASERS	 2.75

**The Controllability of the Aeroassist Flight Experiment
Atmospheric Skip Trajectory**

by

R. Wood-Engineer/AFE, Mail Code T5L, Phone 280-1500
McDonnell Douglas Space Systems Co.-Engineering Services Division
Houston, Texas

The Aeroassist Flight Experiment (AFE) will be the first vehicle to simulate a return from geosynchronous orbit, deplete energy during an aerobraking maneuver, and navigate back out of the atmosphere to a low earth orbit. It will gather scientific data necessary for future Aeroassisted Orbital Transfer Vehicles (AOTV's). Critical to mission success is the ability of the atmospheric guidance to accurately attain a targeted post-aeropass orbital apogee while nulling inclination errors and compensating for dispersions in state, aerodynamic, and atmospheric parameters. In trying to satisfy mission constraints, atmospheric entry-interface (EI) conditions, guidance gains, and Earth-atmosphere modeling were investigated for effects on the trajectory. This paper presents the results of the investigation; emphasizing the adverse effects of dispersed atmospheres on trajectory controllability.

THE CONTROLLABILITY OF THE AEROASSIST FLIGHT EXPERIMENT ATMOSPHERIC SKIP TRAJECTORY

1.0 OBJECTIVES

The Aeroassist Flight Experiment (AFE) will be the first vehicle to simulate a return from geosynchronous orbit (GEO), deplete energy during an aerobraking maneuver, and navigate back out of the atmosphere to a low earth orbit (LEO). The objective of this study was to evaluate the controllability of the atmospheric skip trajectory and investigate the relative contributions of the factors detrimental to that control.

2.0 BACKGROUND

2.1 Mission Purpose & Definition

The AFE is to serve as the precursor for future missions involving Aeroassisted Orbital Transfer Vehicles (AOTV's). AOTV's will someday be the combination wrecker/taxi that will transport people and machines back and forth between LEO and higher orbits, and will eventually be used for lunar and mars journeys. Aerobraking is advantageous when decelerating from a high energy state (such as a geosynchronous or lunar-to-earth transfer orbit) to a low energy state (such as a LEO). The deceleration can be performed in either of two ways. The first way is to fire engines, but large amounts of fuel are needed for this type of maneuver. The other way to decelerate is to plunge through a planetary atmosphere and let the aerodynamic drag do the work. This technique is to be used with the AFE.

The AFE mission will consist of many phases (Ref. 1). First, the vehicle will be transported to LEO by the Space Shuttle in the mid 1990's. Once deployed, the AFE will ignite a solid rocket motor (SRM) and accelerate to a state that simulates a craft returning from GEO. The SRM casing will then be discarded and allowed to re-enter. The AFE vehicle will perform trim burns to properly position itself for atmospheric entry (approximately 400kft, called "entry interface" or "EI"). The atmospheric guidance will then assume control and guide the vehicle through the atmosphere while targeting a pre-selected exit orbit. During the aeropass, onboard experiments and instruments will sample the flow and record measurements. This data will be later used to verify computational fluid dynamics (CFD) codes. After exiting the atmosphere, and reaching apogee, orbital maneuvers will be performed to correct for errors and circularize the orbit for subsequent rendezvous and retrieval by the Shuttle. Figure 2.1-1 illustrates the basic mission profile.

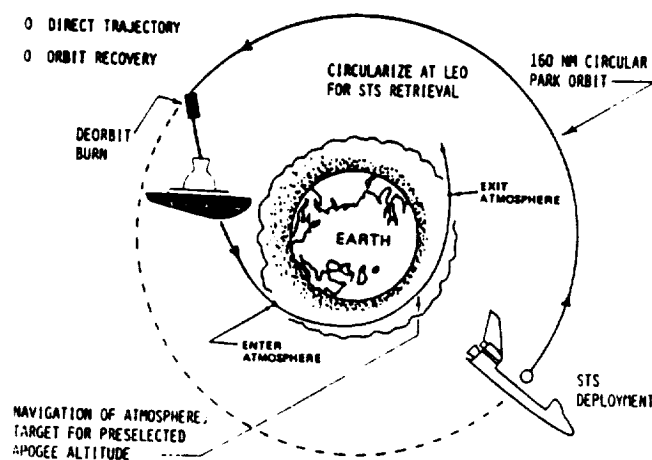


Figure 2.1-1 - Basic AFE Mission Profile

2.2 Vehicle Configuration & Characteristics

The basic design of the AFE vehicle consists of three components: the aerobrake, the carrier vehicle, and the main propulsion unit. Figure 2.2-1 shows a schematic of the AFE flight article.

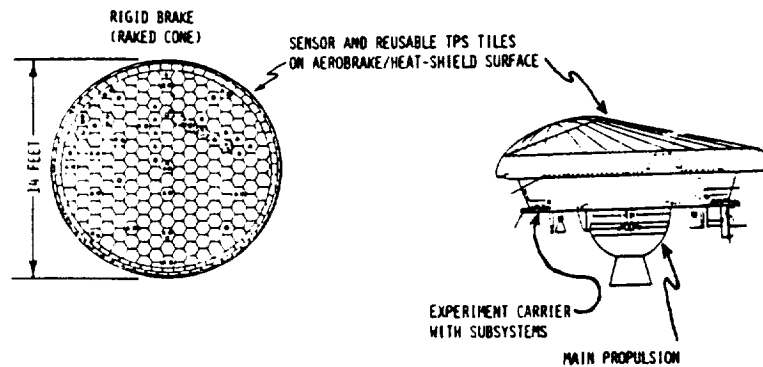


Figure 2.2-1 - AFE Schematic

The aerobrake is a raked cone which provides an aerodynamic component of lift during the aeropass (nominal L/D is 0.28) which can rotate about the velocity vector via reaction control system (RCS) jets. By rotating the lift vector, the vertical (or "in-plane") component of lift can be adjusted in flight so that the pre-selected exit apogee is attained. The position of the lift vector is measured in terms of the bank angle. The horizontal (or "out-of-plane") component of lift is constantly causing the orbital plane to change. The difference between the desired and actual orbital planes is called the "wedge angle." The wedge angle is controlled by periodically reversing the side of the vertical plane on which the bank angle is being modulated. This is done by simply changing the sign of the bank angle and is called a "roll-reversal." The brake is a fixed-geometry structure covered by thermal protection system (TPS) tiles like those on the Shuttle. Data-gathering sensors are positioned in the tiles to support the onboard experiments.

The primary structure of the system is the carrier vehicle. It is the link between the aerobrake and the propulsion system. It will house the computer systems as well as many experiment packages. The carrier vehicle will also contain a strapdown inertial measurement unit (IMU) for navigation.

The remaining component is the main propulsion system. It consists of a SRM that will deliver the vehicle to its simulated return-from-GEO conditions. The SRM is jettisoned prior to EI by way of a large spring system between the SRM casing and the carrier vehicle.

The atmospheric guidance to use for the mission is still undecided. Currently, several algorithms are undergoing testing. For this study, C. J. Cerimele's HYPAS guidance routine (Ref. 2) was used. The HYPAS guidance separates the aeropass into two phases: the equilibrium glide phase and the exit phase. During the first phase, the logic attempts to gradually null the altitude acceleration while controlling the loads the vehicle is experiencing and ensuring sufficient capture. Once a particular deceleration has occurred, control is transferred to the exit phase logic. The exit phase uses an analytic prediction/correction technique to attain a targeted exit apogee altitude.

3.0 TRAJECTORY SIMULATION TOOLS

The three degree-of-freedom (DOF) Descent Design System (DDS) simulation program, originally developed for the Space Shuttle program, was modified to simulate the AFE trajectories. A fourth DOF was added to model the balancing of the pitching moment. DDS is fast and efficient for performing nominal trajectory simulations.

For dispersion analyses, the 3-DOF shuttle-based LAND monte-carlo program was upgraded to 4-DOF and renamed the Aerobraking Monte-carlo Analysis Program (AMAP) (Ref. 3). AMAP models dispersions in state, aerodynamic, atmospheric, and navigational parameters. Finally, dispersed atmosphere profiles (for use in AMAP) were created using the stand-alone version of the 1986 Global Reference Atmosphere Model (GRAM86) program (Ref. 4).

4.0 INVESTIGATION METHOD & RESULTS

McDonnell Douglas Space Systems Company (MDSSC) supports the Mission Planning & Analysis Division (MPAD) of NASA at the Johnson Space Center. MPAD directed MDSSC to optimize the AFE trajectory. The key parameters in the optimization were: (1) the peak heat rate experienced during the aeropass, and (2) the post-aeropass change in velocity (ΔV) required to circularize the orbit. In effect, the ability to control and manipulate the trajectory was examined (Ref. 5). The current constraints were that the mean (average) peak heat rate be under 40.3 Btu/ft² s and, if possible, the mean plus 3-sigma peak heat rate to be under 40.3 Btu/ft² s. Also, the mean plus 3-sigma post-aeropass ΔV had to be less than 400 fps.

4.1 Transfer Orbit Perigee and Guidance Gain Variation

The first step in the study was to vary guidance gains and the transfer orbit perigee. The gains altered were the equilibrium glide phase altitude rate and dynamic pressure terms: GHDOT and GQ respectively. Varying the gains simply alters the reaction of the guidance algorithm to different situations. For instance, increasing GHDOT increases the sensitivity of the guidance to altitude-rate variations. Varying the transfer orbit perigee translates into entering the atmosphere at a varied flight path angle (Γ). Aside from perigee and gain variations, all other conditions were held constant and 100-case monte-carlo trajectories flown using AMAP. This meant that the guidance was subjected to 100 sets of dispersion combinations for each gain and perigee adjustment. The statistical results were tabulated in terms of the mean and the mean plus 3-sigma values. Figures 4.2-1 and 4.2-2 show plots of the statistical results of the mean peak heat rates and the mean plus 3-sigma post-aeropass ΔV 's for the gain and gamma combinations.

As expected, the region of mean plus 3-sigma ΔV of less than 400 fps (mission constraint) has a generally higher peak heat rate than do the regions of larger ΔV 's. The figures show the nominal heat rate for lift-vector-up trajectories (i.e. the best possible heat rates) when ΔV constraints are ignored. The AFE heat rate constraint of 40.3 is also shown. It is clear that the mean heat rate constraint of 40.3 is possible to meet while maintaining a ΔV of less than 400 fps. However, meeting a mean plus 3-sigma of 40.3 was not possible for perigee and gain variation alone.

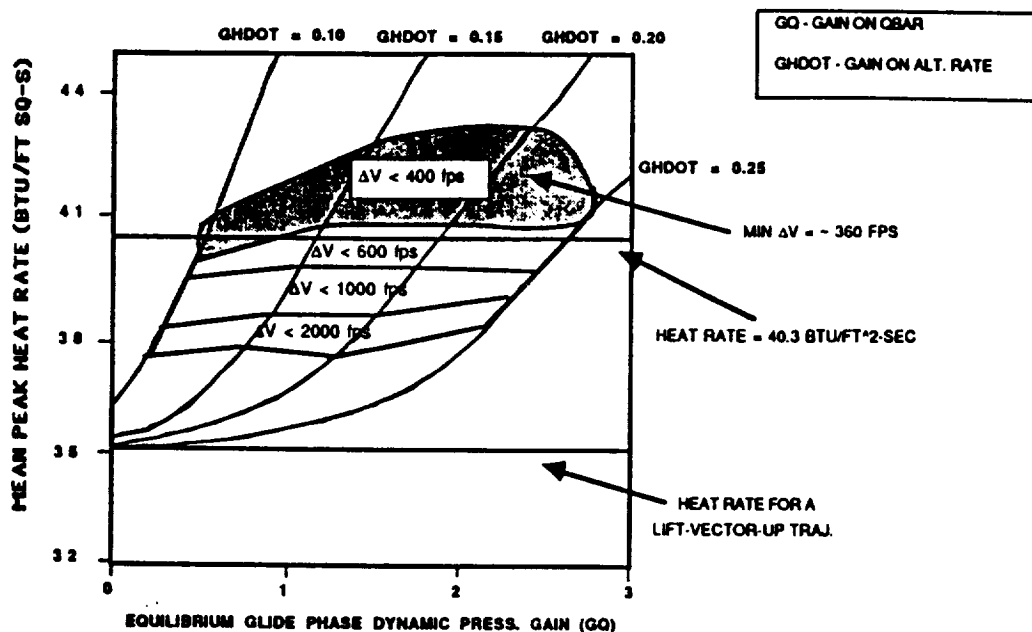


Figure 4.2-1 - Effects of Gain Variation on Mean Peak Heat Rate & ΔV for Gamma = -4.4 Degrees

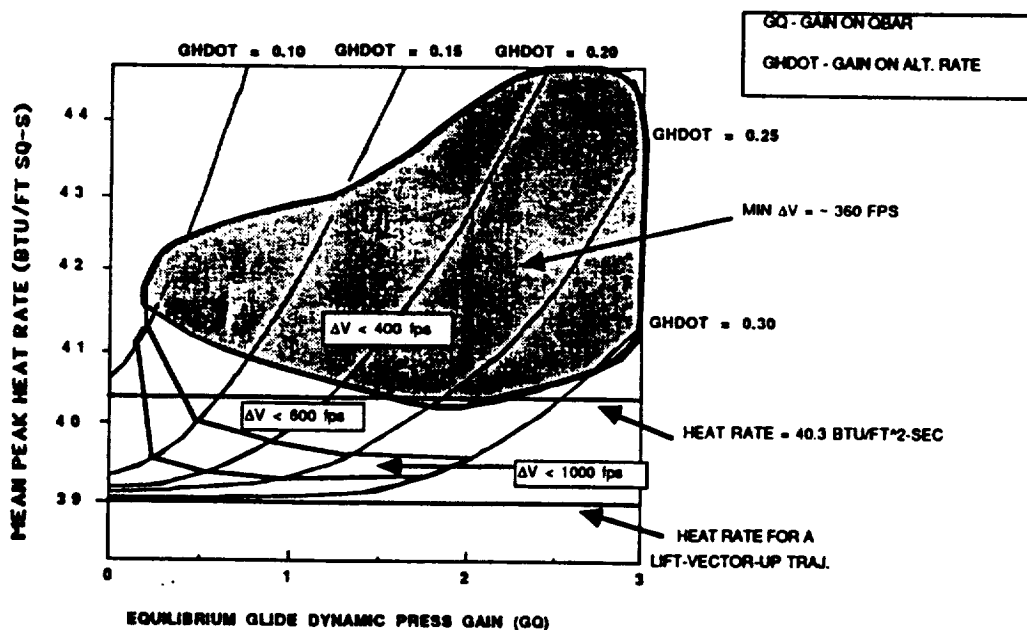


Figure 4.2-2 - Effects of Gain Variation on Mean Peak Heat Rate & ΔV for Gamma = -4.5 Degrees

Figures 4.2-3 and 4.2-4 show that gamma variation outside the -4.4 to -4.5 range results in increased peak heat rates and/or ΔV 's.

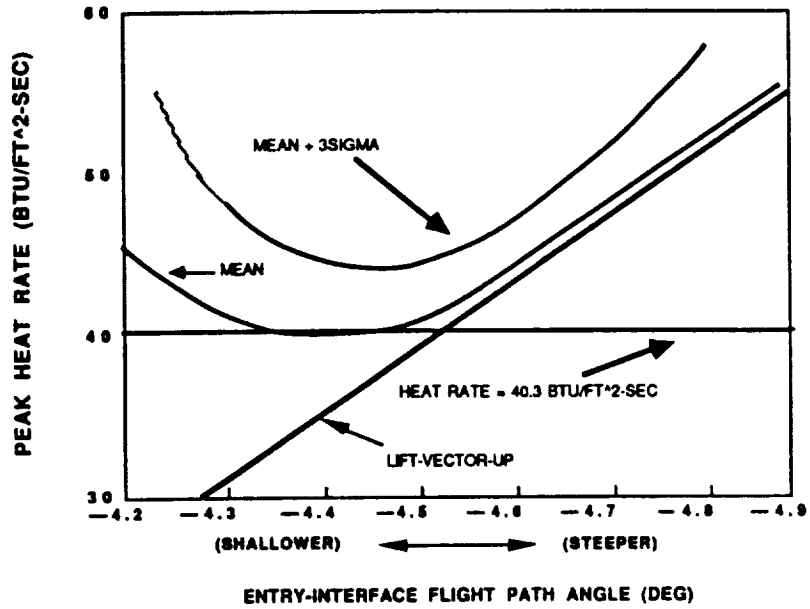


Figure 4.2-3 - Peak Heat Rate Vs. Gamma

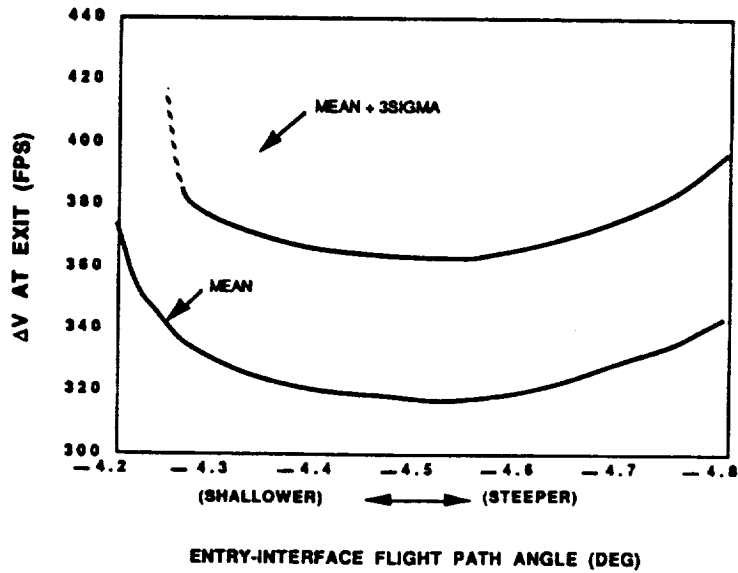


Figure 4.2-4 - Mean + 3-Sigma ΔV Vs. Gamma

4.2 Transfer Orbit Apogee Variation

The next step in the study was to vary the transfer orbit apogee to try to attain a mean plus 3sigma heat rate of less than 40.3 Btu/ft² s. The transfer orbit apogee was added to the list of parameters to be varied. This translates into altering the inertial velocity at EI. Of course, altering this parameter means deviating from the overall mission objective of simulating a GEO-return. For instance, lowering the transfer orbit apogee (i.e. lowering EI velocity) signifies returning from a lower-than-GEO. The optimal gains for each flight path angle (found from the previous section) were used while the transfer orbit apogee was scanned. Figures 4.3-1 and 4.3-2 show the results.

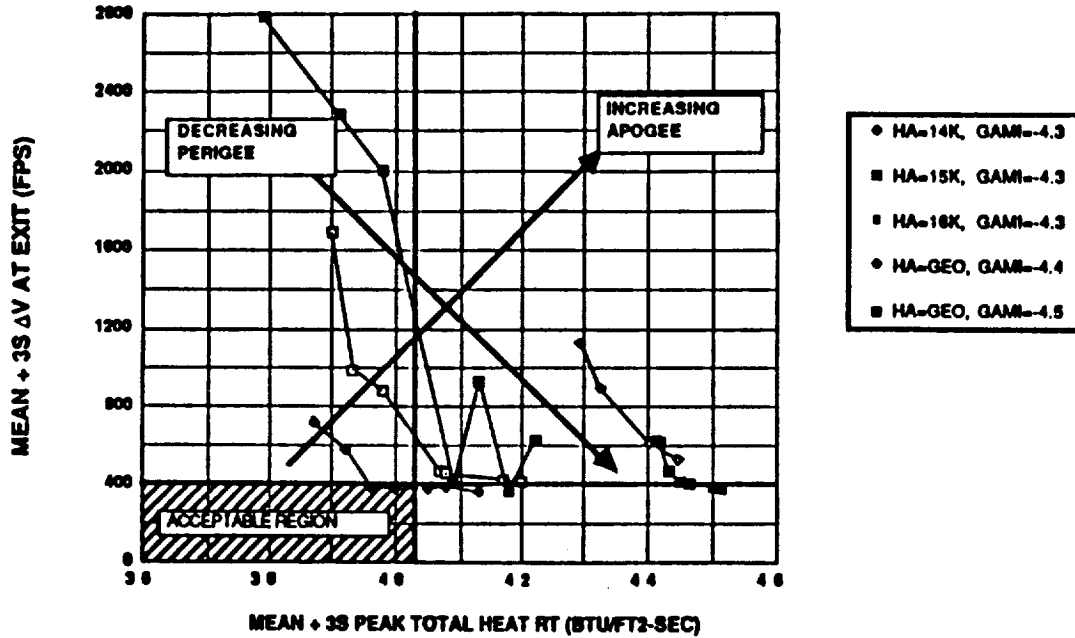


Figure 4.3-1 Heating Vs. ΔV for Varying Transfer Orbit Apogee & Perigee

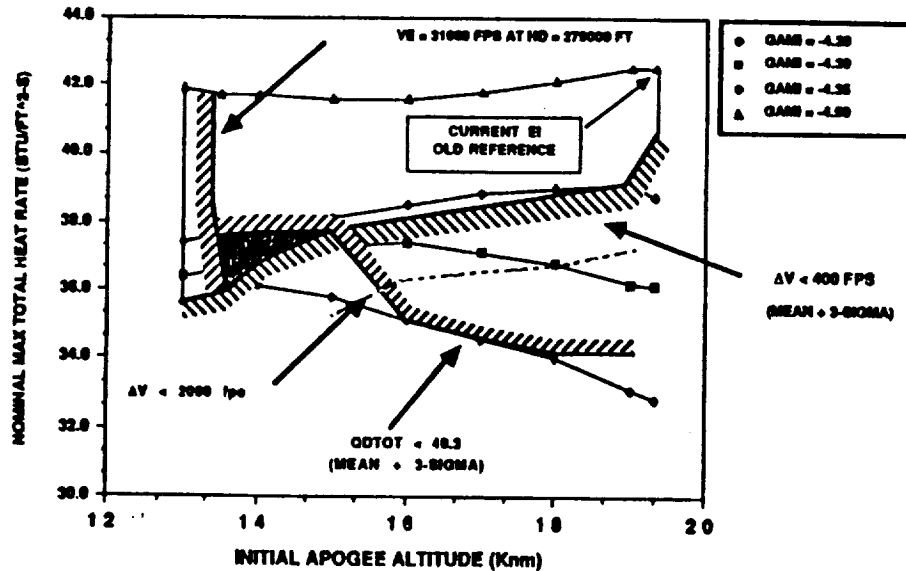


Figure 4.3-2 Heating Vs. Transfer Orbit Apogee Altitude

Both figures show that, in order to satisfy the ΔV and heat rate constraints, both the transfer orbit apogee and perigee had to be significantly altered. Also, when a constraint was added to satisfy the conditions necessary for the flow conditions to be sampled (relative velocity at 279000 ft > 31660 fps), Figure 4.3-2 revealed only a very small region of acceptability (shaded area).

4.4 Relative Contributions of Individual Dispersion Sources

Knowing that lowering the transfer orbit apogee is highly undesirable, the next step in the study was to investigate the relative contributions of the individual dispersion sources in order to define which ones (if any) were dominating the controllability of the trajectory. Dispersion sources were all deactivated and only a single source re-activated. This was done for each dispersion source in turn so that the effects of a single source could be statistically analyzed. Figures 4.4-1 and 4.4-2 show the effects of the single dispersion sources on the 3-sigma peak total heat rate and post-aeropass ΔV .

In both figures, it is clear that the dominating factor influencing the peak heat rate and post-aeropass ΔV is the dispersed atmosphere set. When compared to the other dispersion sources, the effect of the atmospheres is completely dominant.

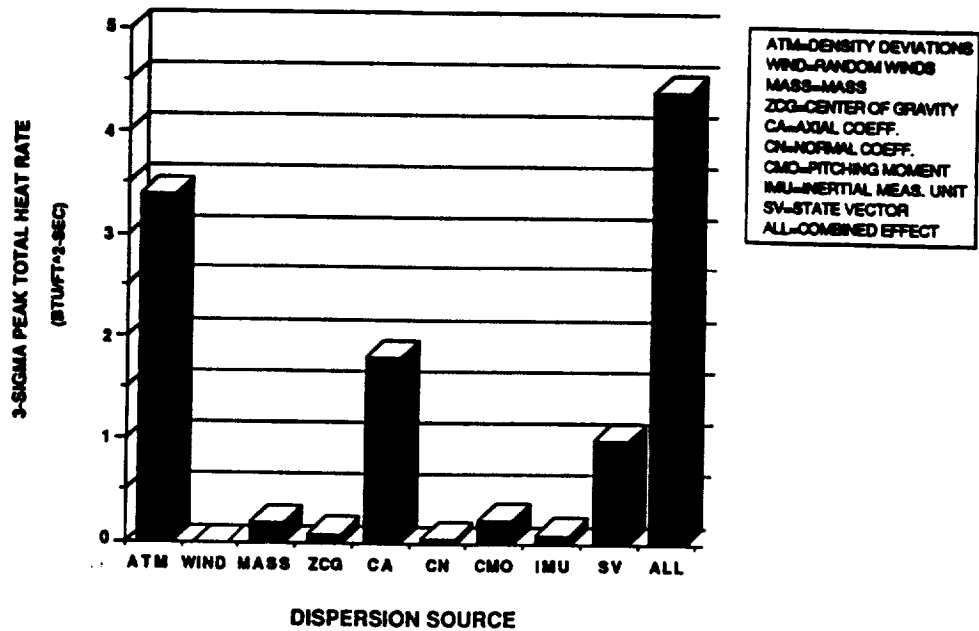


Figure 4.4-1 - Effects of Single Dispersion Sources on Peak Heat Rate

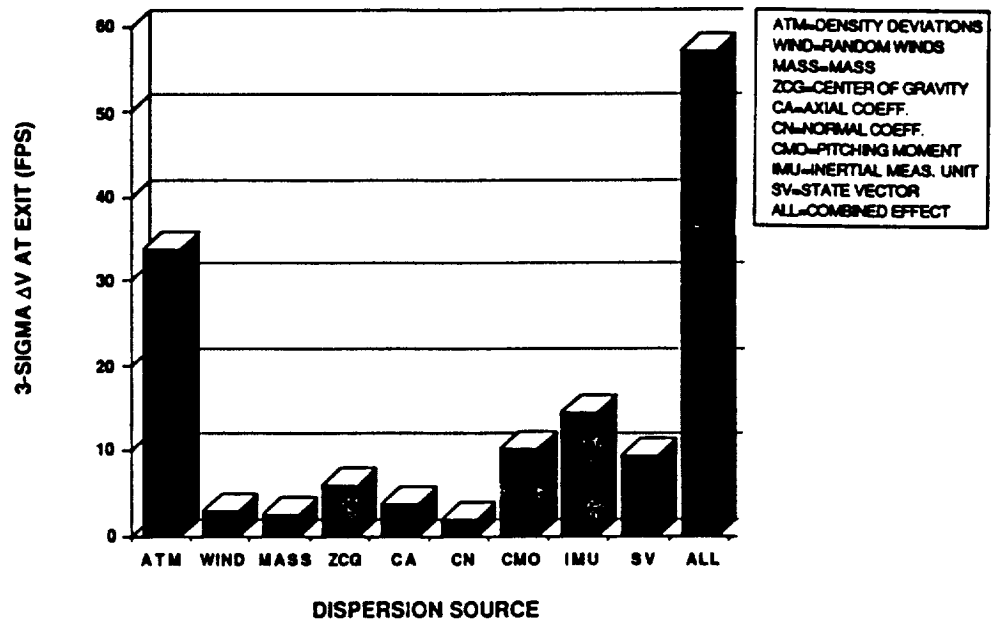


Figure 4.4-2 - Effects of Single Dispersion Sources on Post-Aeropass ΔV

The GRAM mean monthly atmosphere, as well as the plus/minus 3-sigma boundaries, is shown in Figure 4.4-3. The 0% horizontal line on the plot indicates no deviation from the '76 standard atmosphere. A density above the 0% line indicates a thicker atmosphere (at a certain altitude) than the '76 standard, while below the line indicates a thinner atmosphere than the '76 standard. It is clear that the GRAM mean and the '76 standard atmosphere profiles are not significantly different over the altitudes that the AFE vehicle will traverse (236kft to 400kft).

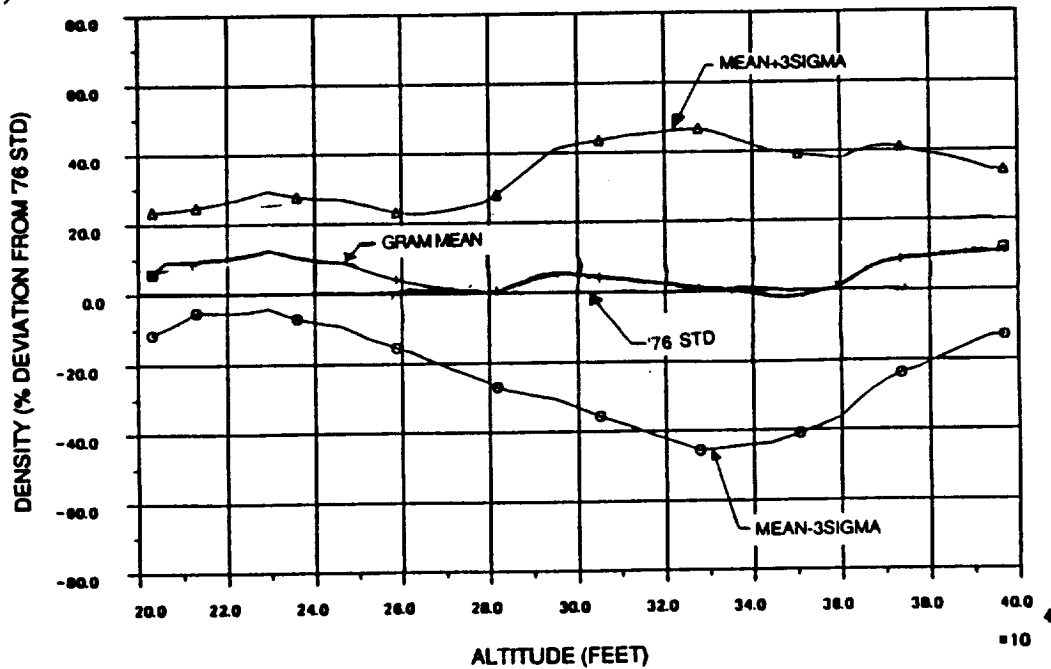


Figure 4.4-3 - GRAM Mean Atmosphere & +/- 3sigma Boundaries

In the AMAP monte-carlo simulations however, the vehicle does not experience the mean atmosphere. Instead, the vehicle is subjected to GRAM-supplied deviations to the mean as a function of altitude. The deviations model density shears as well as overall thick and thin atmospheres. A sample dispersed atmosphere profile is shown in Figure 4.4-4.

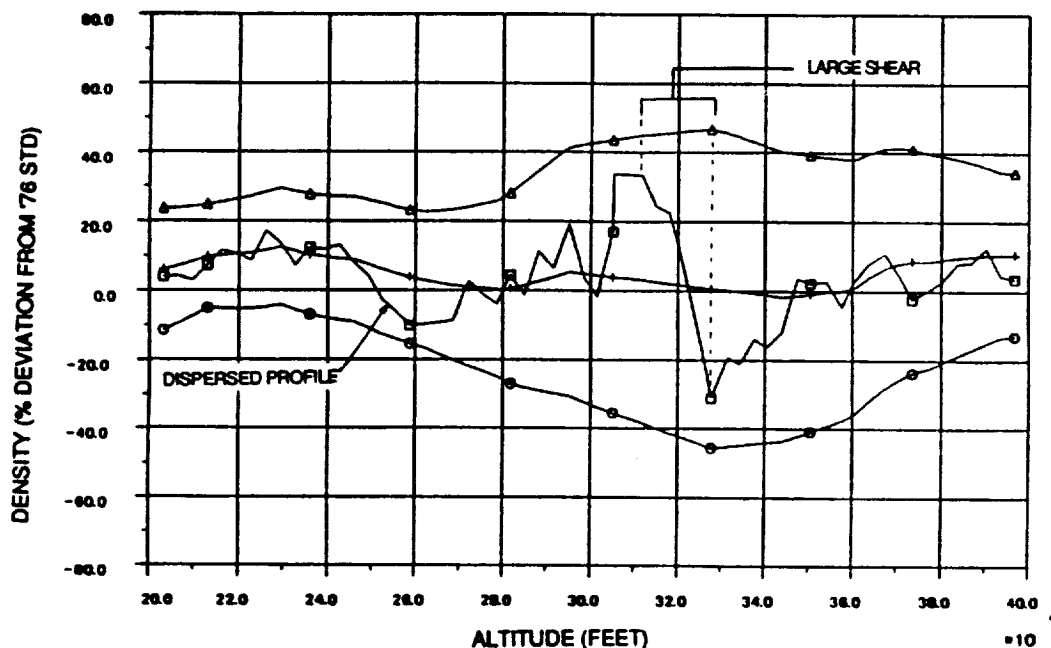


Figure 4.4-4 - Sample Dispersed Density Profile

The extremely jagged profile indicates the necessity of the guidance to react to density dispersions. It is important to realize that guidance has no way of predicting the atmospheric conditions it will encounter. In other words, the atmosphere is an "unknown" dispersion. Attempts are made during the flight to estimate the actual density (derived from navigation-supplied parameters such as drag acceleration and relative velocity), but the estimated density can be inaccurate. In addition, although knowing the current density is beneficial, it is not nearly as advantageous as knowing the upcoming density. In other words, guidance would like to prepare for a density shear or a completely thick or thin atmosphere prior to encountering it. Since guidance has no such knowledge, the effects of the corrections it does command (i.e. changes in bank angle) lag behind the actual density changes.

Currently, the guidance always predicts that the upcoming atmosphere it encounters will be the '76 standard. Indeed, if the density shears are short-period and relatively symmetric about the 0% line (See Fig. 4.4-5), then guidance's '76 standard model of the atmosphere will approximate the average of the dispersed profile and satisfactory trajectory performance is likely.

On the other hand, if the shears are long-period or the overall atmosphere is generally thick or thin, guidance's model becomes inaccurate and poor performance often results. It is especially critical that the guidance model is accurate during the region encompassing minimum altitude. In this region, the vehicle is transitioning from a negative altitude rate to a positive one. This means that a pseudo-constant altitude is being held for a relatively long period of time (See Figure 4.4-6). Also, this phase of constant altitude is the most critical region for control. Since the dispersed density is a function of altitude only, the vehicle may experience a thicker or

thinner-than-expected density for a long period of time and in the critical portion of the trajectory. Of course, inaccurate modeling of the atmosphere by guidance during this time often results in poor performance. An example of an atmosphere possessing a large density deviation (from '76 standard) during minimum altitude is shown in Figure 4.4-7. During testing, it has consistently caused significant difficulties for the guidance routine.

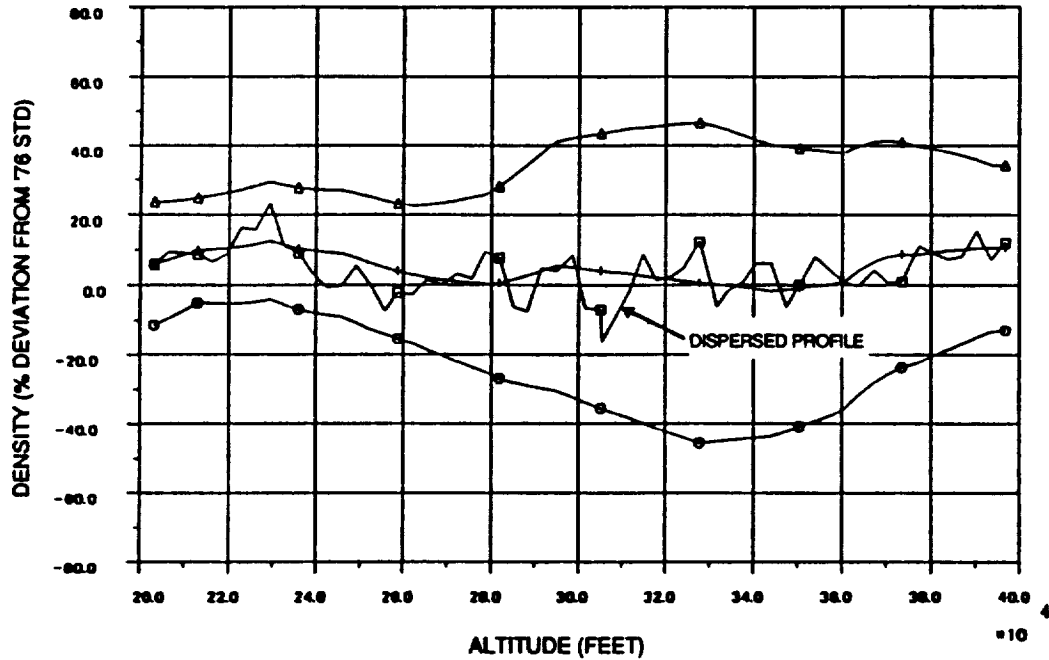


Figure 4.4-5 - "Mild-Case" Atmosphere Profile

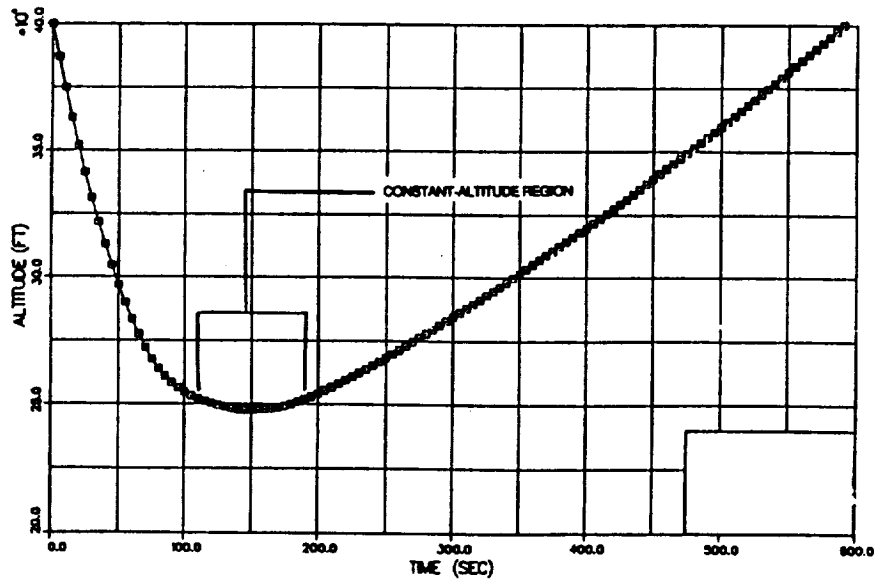


Figure 4.4-6 - Altitude Vs. Time for a Typical AFE Trajectory

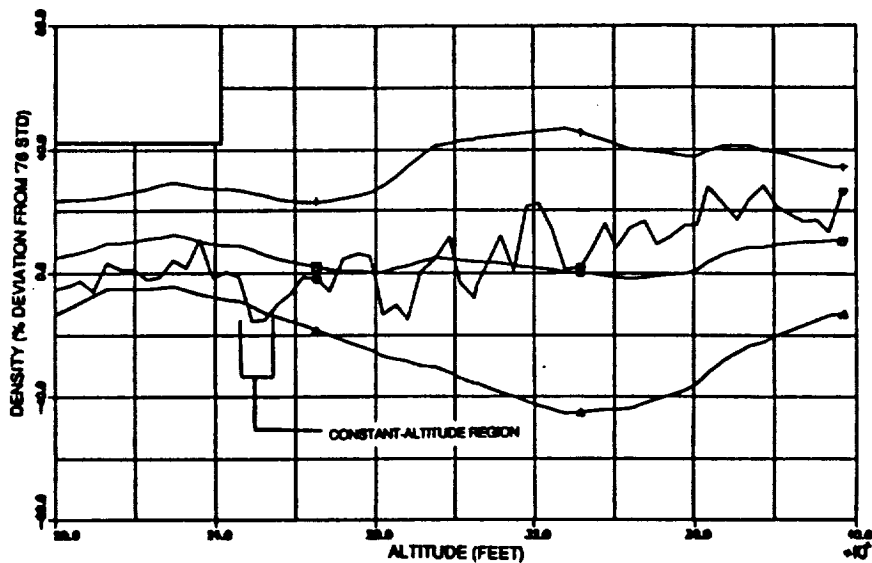


Figure 4.4-7 - "Bad-Case" Atmosphere Profile

5.0 CONCLUSIONS

Under the conditions of this study, the results indicate that mission constraints of a mean peak heat rate of 40.3 Btu/ft²sec and a mean + 3sigma post-aeropass ΔV of less than 400 fps can be satisfied if the guidance gains and transfer orbit perigee are chosen properly. However, due to the sensitivity of the trajectory parameters to gain and perigee changes, the regions of constraint satisfaction are very small.

Attempting to further minimize the peak heating and attain a mean plus 3sigma peak total heat rate of 40.3 Btu/ft²sec proved successful but only through large decreases in transfer orbit apogee. But, varying the transfer orbit apogee from GEO is inconsistent with mission objectives and is highly undesirable.

Investigation of the relative contribution of factors detrimental to control revealed the domination of the dispersed atmospheres in determining the regions of controllability (i.e. constraint satisfaction). Although decreasing the magnitude of other dispersion sources should improve performance, without advanced knowledge of the actual density profile or an accurate model of it, guidance has great difficulty compensating in real-time for atmospheric dispersions. These dispersions, especially during the constant-altitude phase, can be sufficiently deviated from guidance's atmosphere model that large errors result in the post-aeropass orbit. In general, a trade must be made between post-aeropass ΔV and the peak heat rate. To minimize the atmospheric dispersion effects on ΔV , the vehicle must "dig deeper" into the atmosphere. Doing this, however, results in an increased heat rate.

6.0 REFERENCES

1. **Aeroassist Flight Experiment Preliminary Design Document. Marshall Space Flight Center, Alabama, May 1986.**
2. **Cerimele, C.J. and Gamble, J.D.: A Simplified Guidance Algorithm for Lifting Aeroassist Orbital Transfer Vehicles. AIAA 23rd Aerospace Sciences Meeting, Reno, Nevada. AIAA Paper 85-0348, January 1985.**
3. **Neal, S.D.: Aerobraking Montecarlo Analysis Program (AMAP) Revision II Update, McDonnell Douglas Space Systems Company - Engineering Services Division, Houston, Texas. MDSSC-ES TM-FM9-GA-06, January 1989.**
4. **Justus, C.G.; Fletcher, G.R.; Gramling, F.E.; & Pace, W.B.: The NASA/MSFC Global Reference Atmosphere Model - MOD 3 (With Spherical Harmonic Wind Model), NASA Contract Report 3256, March 1980.**
5. **Crull, T.J.; Neal, S.D.; Wood, R.L.: AFE Trajectory Heating Analysis (Presentation to NASA-MPAD), McDonnell Douglas Space Systems Company - Engineering Services Division, Houston, Texas. September 1989.**

7.0 ACKNOWLEDGEMENTS

The author wishes to acknowledge MDSSC personnel S.D. Neal and T.J. Crull for their significant contributions to the technical content and style of this paper. Their assistance is greatly appreciated.

ATMOSPHERIC DRAG MODEL CALIBRATIONS FOR SPACECRAFT LIFETIME PREDICTION*

A. L. Binebrink, M. S. Radomski, and M. V. Samli
Computer Sciences Corporation (CSC)

ABSTRACT

Although solar activity prediction uncertainty normally dominates decay prediction error budgets for near-Earth spacecraft, the effect of drag force modeling errors for given levels of solar activity needs to be considered. This paper reports an analysis of the ability of two atmospheric density models, the modified Harris-Priester model and the Jacchia-Roberts model, to reproduce the decay histories of the Solar Mesosphere Explorer (SME) and Solar Maximum Mission (SMM) spacecraft in the 490- to 540-kilometer altitude range. Historical solar activity data were used in the input to the density computations. The period covered was January 1982 to June 1988.

For each spacecraft and atmospheric model, a drag scaling adjustment factor (i.e., a calibration) was determined for a high-solar-activity year, such that the observed annual decay in the mean semimajor axis was reproduced by an averaged variation-of-parameters (VOP) orbit propagation. The SME (SMM) calibration was performed using calendar year 1983 (1982). The resulting calibration factors differ by 20 to 40 percent from the predictions of the prelaunch ballistic coefficients.

The orbit propagations for each spacecraft were extended to the middle of 1988 using the calibrated drag models. For the Jacchia-Roberts density model, the observed decay in the mean semimajor axis of SME (SMM) over the 4.5-year (5.5-year) predictive period was reproduced to within 1.5 (4.4) percent. The corresponding figure for the Harris-Priester model was 8.6 (20.6) percent.

Detailed results of this study and conclusions regarding the importance of accurate drag force modeling for lifetime predictions are presented in the paper.

* This work was supported by the National Aeronautics and Space Administration (NASA)/Goddard Space Flight Center (GSFC), Greenbelt, Maryland, under Contract NAS 5-31500.

1. INTRODUCTION

A principal area of interest for mission planners and orbit analysts is the prediction of orbital decay. Accurate prediction of atmospheric density is the major challenge for long-term orbit decay predictions. The primary source of error in decay prediction for near-Earth spacecraft is the uncertainty in atmospheric density caused by solar activity prediction uncertainty. Even if the solar flux uncertainty is removed, the modeling of the atmospheric density remains a significant contributor of uncertainty to orbital decay predictions. The effect of atmospheric density modeling itself can be isolated from the solar activity prediction uncertainty by studying the past behavior of spacecraft for which measured solar activity can be substituted for uncertain predictions.

This paper compares two major atmospheric density models with regard to their ability to reproduce the decay histories of two representative near-Earth spacecraft. The atmospheric density models considered are the Jacchia-Roberts model (References 1 and 2) and the modified Harris-Priester model (References 3, 4, and 5). The spacecraft considered are the Solar Mesosphere Explorer (SME) and the Solar Maximum Mission (SMM).

The SMM orbit, during the period of study (January 1, 1982, to June 18, 1988), had an inclination of 28.5 degrees, a mean semimajor axis that decayed from 6914 to 6858 kilometers, and a mean eccentricity ranging from 3×10^{-4} to 7×10^{-4} . The SMM spacecraft is three-axis stabilized in a solar-oriented attitude, and thus has a drag cross-section that varies throughout an orbit. The orbital average cross-section depends on the season and the nodal precession. The SME orbit, during the period of study (January 4, 1983, to June 26, 1988), had an inclination of 97.5 degrees, a mean semimajor axis that decayed from 6903 to 6886 kilometers, and a mean eccentricity ranging from 1×10^{-3} to 1.5×10^{-3} . SME spins about an axis perpendicular to its orbit plane and thus presents an effectively constant drag cross-section.

For each of these spacecraft and atmospheric density models, a drag-force calibration factor was determined for the year with the highest available solar activity. The calibration factor was adjusted until the observed decay in the mean semimajor axis was accurately reproduced by an averaged variation-of-parameters (VOP) propagation of the mean equinoctial elements. The SMM calibration was performed for calendar year 1982, and the SME calibration was performed for calendar year 1983. The calibrated drag coefficients were then used in orbit propagations of several years duration. The amount of decay measured by the decrease in the mean semimajor axis at the end of the propagation was compared with that determined from operational orbit determination solutions for the two spacecraft. The calibration process was repeated for a year of low solar activity (1986) to test calibration consistency.

Section 2 of this paper discusses the VOP propagator, the atmospheric density models and solar activity data, the iterative drag coefficient calibration process, and the methods of obtaining definitive mean orbital elements for comparison with the calculations. Section 3 describes results of the calibrations and long-term decay predictions. Section 4 presents the conclusions. Modeling details are discussed in Appendix A.

2. METHODS OF ANALYSIS

This section describes the analytical methods for this study. Section 2.1 presents the orbit propagation methods, including all factors affecting force modeling such as solar activity and atmospheric density modeling. Section 2.2 describes the conversion of operational orbit solutions from osculating Cartesian elements to mean equinoctial elements comparable to our theoretical calculations. Section 2.3 details the procedures for calibrating drag constants.

2.1 ORBIT PROPAGATION METHODS AND MODELS

The averaged VOP propagator (AVGVOP) of the Goddard Mission Analysis System (GMAS) was used for long-term orbit propagation. GMAS (Reference 6) is a collection of computer programs used mainly for mission planning. AVGVOP is designed to efficiently compute moderately accurate values for the long-term motion of satellites. Since AVGVOP propagates mean equinoctial elements without including the short-term periodic perturbation effects, it can be used with far larger integration step sizes than an osculating element propagator (Reference 7). AVGVOP performs the numerical integration of the mean-element VOP equations of motion using a 12th-order Adams-Bashforth-Moulton method.

In Table 1, column 2 lists the parameters and options for the averaged VOP propagations. Those options that need explanation are described below. Detailed justification for the choice of options and values of the parameters is provided in Appendix A.

Sectorial and tesseral harmonics of the gravitational geopotential were excluded from the force model. Their long-term effects on the mean elements of the orbits considered are small, including those of the resonant tesseral harmonic of order 15.

An integration step size of 1 day was used. Since the drag-force model (see below) sampled at this rate is somewhat noisy, discretization was considered a potential source of error. Comparison tests (see Appendix A) using smaller step sizes demonstrated that the effect of discretization error on change in the mean semimajor axis is less than 0.5 percent at the end of a year.

The modified Harris-Priester atmospheric density model contains a term proportional to a power of the cosine of the angle between the radius vector and the direction of maximum densities, located 2 hours east of the Sun. Following the standard operational practice at Goddard Space Flight Center's (GSFC's) Flight Dynamics Facility (FDF), the power of the cosine used was 2 for the near-equatorial orbiting SMM and 6 for the near-polar orbiting SME .

An enhanced implementation (Reference 8) of the Harris-Priester atmospheric density model was used in this study. The standard modified Harris-Priester model uses density tables for only 10 values of the 10.7-centimeter solar flux, ranging from 65 to 275 (10^{-22} watts per meter² per hertz). This enhanced implementation uses special density tables, one for each integer value of the solar flux, constructed by interpolation among the standard Harris-Priester tables at each tabulated altitude. For each evaluation of the force

Table 1. Parameters and Options for Orbit Propagation

OPTION/PARAMETERS	LONG-TERM PROPAGATION	MEAN ELEMENT CONVERSION
Integration Type	Averaged VOP	Fixed-Step Cowell
Integration Step Size	86400 seconds	60 seconds
Geopotential Model	GEM-9 (21x0)	GEM-9 (21x21)
Drag Force	Included	Excluded
Coefficient of Drag, C_D	2.2	N/A
Cross-Sectional Area, A (square meters)	SMM: 17.5 SME: 1.129	SMM: 17.5 SME: 1.129
Spacecraft Mass, m (kilograms)	SMM: 2315.59 SME: 415.50	SMM: 2315.59 SME: 415.50
Atmospheric Density Model	Harris-Priester or Jacchia-Roberts	N/A
Power of Cosine in Harris-Priester Model	SMM: 2 SME: 6	N/A
Solar/Lunar Gravity	Included	Included
Solar Radiation Force	Included	Included
Solar Reflectivity Constant, C_R	1.2	1.2

Notes: GEM-9 = Goddard Earth Model-9
N/A = Not Applicable

model, the solar flux, obtained by linear time interpolation between fluxes tabulated at discrete times, is used to select the interpolated Harris-Priester density table for the nearest integer flux value. In the current application, the solar flux tables were identical to the daily measurements obtained from the National Geophysical Data Center, Boulder, Colorado, without subsequent smoothing or averaging. For the purposes of the current work, smoothing additional to that automatically accomplished by the integration of the laws of motion was considered to be unnecessary.

A standard implementation of the Jacchia-Roberts model was employed. In particular, the daily solar flux input values were the same as those used with the Harris-Priester model. The geomagnetic indices needed for the Jacchia-Roberts model were those obtained from the International Service of Geomagnetic Indices of the Institut für Geophysik, West Germany.

Drag coefficient calibration was performed for both a high solar activity year and a low solar activity year for each spacecraft and atmospheric density model. Calendar years 1982 and 1986 were used as the high and low solar activity years, respectively, for SMM. Calendar years 1983 and 1986 were used as the high and low solar activity years, respectively, for SME. The year of minimum solar activity in the last cycle was 1986; monthly average fluxes ranged from 68 to 84. The year 1982 had high solar activity; monthly averaged fluxes ranged from 145 to 214. A nominal high-activity year (1983) was used for

SME (because of temporary unavailability of operational solutions for 1982); monthly solar fluxes ranged from 93 to 142.

2.2 MEAN ELEMENT CONVERSION METHODS

To initialize the averaged VOP propagations and to provide mean semimajor axes for comparison with decay predictions, osculating elements corresponding to definitive operational orbit solutions were converted to mean equinoctial elements. These definitive solutions had been generated and archived in the FDF during operational navigation mission support. The conversion of these osculating elements to mean elements is described in this section. Mean elements for each spacecraft were obtained at the beginning and end of each year studied and at approximately 3-month intervals over the period studied.

The GMAS mean elements conversion (AVECON) process was used to numerically average (using 96-point Gaussian integration) the osculating equinoctial elements propagated from the definitive solution epoch. The time span of integration was 15 orbits centered on the epoch. The methods used in this propagation were distinct from those used in the longer propagations, as indicated in the last column of Table 1. The fact that atmospheric drag was omitted from the force model for these propagations did not produce a significant effect. Tests show that the effect of this omission on the converted mean semimajor axes is less than 1 meter.

2.3 DRAG CALIBRATION PROCEDURES

The drag force is calculated from the expression

$$F = \frac{1}{2} \rho v^2 (1 + \rho_1) C_D \frac{A}{m} \quad (1)$$

where

- ρ = modeled atmospheric density
- v = relative velocity of the spacecraft with respect to the atmosphere
- C_D = a priori drag coefficient
- A = a priori drag cross-sectional area
- m = a priori spacecraft mass
- ρ_1 = drag scaling adjustment parameter

The product of the last four factors in Equation (1) is known as the ballistic coefficient. The role of the factor involving ρ_1 is to compensate for all effective variations of ρ , C_D , A , and m from the nominal.

Calibration consists of finding a drag scaling adjustment factor, ρ_1 , that makes Equation (1) agree with the definitive orbital information for the spacecraft, as described below. This could alternately be described as the determination of an effective drag coefficient or as determination of the ballistic coefficient.

For each calibration, a 1-year averaged VOP orbital propagation was performed with one of the atmospheric density models. The propagations were initialized, at an epoch on or near the first day of the year, with mean elements converted from operational solutions as discussed above. The calculated decay in the mean semimajor axis at (or near) the end of the calendar year was then compared with the definitive equivalent. A new drag-scaling adjustment parameter, ρ_1 , was chosen and the process repeated until the final yearly decay was reproduced to within 0.2 percent. The definitive decay history, as sampled every few months throughout the year, was then plotted against the predictions of the final VOP propagations.

Finding the unique ρ_1 that duplicates the definitive decay in the mean semimajor axis at the end of the year amounts to solving a numerically defined equation in one unknown. The solution was performed by open-loop iteration of the method of the *regula falsi*. Initial values of ρ_1 were obtained in a variety of ways. The second endpoint for the initial *regula falsi* was obtained by assuming no decay for $\rho_1 = -1$. The entire year's propagation was repeated for each new ρ_1 . Convergence to within 0.2 percent of the amount of mean semimajor axis decay was obtained on the third iteration.

3. RESULTS

This section reports and interprets the results of the analytical procedures described in the previous two sections. Section 3.1 presents the results of the drag force calibrations and the consistency tests between the different years. Section 3.2 presents the results for the long-term (5- to 6-year) decay prediction studies using the calibrated drag force models.

3.1 CALIBRATION RESULTS

Altogether, eight calibrations were performed, one for each of the two spacecraft, the two atmospheric density models, and the two annual time spans. The results are summarized in Table 2. Decay curves (graphs of the mean semimajor axis versus time) are plotted in Figures 1 through 4 together with definitive points obtained as described in Section 2.2. The exact fit of the decay curves to the first and last definitive points occurs by design of the calibration process.

For each spacecraft and density model, results of three propagations are summarized in Table 2. The first uses the final converged ρ_1 for the high solar activity year (1982 or 1983), the second applies this same ρ_1 to the low solar activity year (1986) as a consistency check, and the third uses the final converged ρ_1 for 1986. The predicted yearly decay in column 5 is the total decrease in the mean semimajor axis from the beginning to the end of the 1-year propagation. Column 6 gives the corresponding quantity derived by converting the definitive elements. Column 7 gives the maximum difference between the definitive and propagated mean semimajor axes during the year (sampled as shown by the definitive points in the figures).

The tabulated maximum yearly discrepancy is a measure of how well each final ρ_1 value fits the definitive data in the mean semimajor axis and therefore is a measure of the

Table 2. Results of Calibration and 1-Year Consistency Tests

SPACECRAFT	ATMOSPHERIC DENSITY MODEL	YEAR	Q_1	PREDICTED YEARLY DECAY IN THE SEMIMAJOR AXIS (KILOMETERS)	DEFINITIVE YEARLY DECAY IN THE SEMIMAJOR AXIS (KILOMETERS)	MAXIMUM DISCREPANCY IN THE SEMIMAJOR AXIS (KILOMETERS)
SMM	Jacchia-Roberts	1982	-0.2120	20.629	20.651	0.470
		1986	-0.2120*	3.259	2.982	0.301
		1986	-0.2790	2.976	2.982	0.023
	Harris-Priester	1982	-0.3527	20.609	20.651	0.871
		1986	-0.3527*	4.850	2.982	1.868
		1986	-0.5960	2.984	2.982	0.134
SME	Jacchia-Roberts	1983	+0.2325	5.292	5.292	0.228
		1986	+0.2325*	1.418	1.408	0.090
		1986	+0.2230	1.408	1.408	0.082
	Harris-Priester	1983	+0.3762	5.291	5.292	0.319
		1986	+0.3762*	1.806	1.408	0.621
		1986	+0.0726	1.403	1.408	0.133

*Value for the earlier year applied to the current year (not a calibration result).

adequacy of the one-parameter calibration. The Jacchia-Roberts model performs better in this regard than the Harris-Priester model, by a factor of 2 for SMM and a factor of 1.5 for SME. It is also apparent in Figures 1 through 4 that the one-parameter calibrations were more effective at duplicating the annual decay curve for the Jacchia-Roberts model than for the Harris-Priester model.

Two results reflect the degree of consistency of each atmospheric density model among different years. One is the agreement between the final Q_1 solutions. Another is the accuracy of the prediction of the 1986 decay using the Q_1 value from the earlier year. Both of these are again markedly better for the Jacchia-Roberts atmospheric density model than for the Harris-Priester model and are somewhat better for SME than SMM.

3.2 LONG-TERM DECAY PREDICTION RESULTS

For each spacecraft and atmospheric density model, AVGVOP orbit propagations were performed extending from the initial epoch of the high solar activity year to June 1988. The calibration factors for the high solar activity years were used. SMM was propagated from January 1, 1982, to June 18, 1988. SME was propagated from January 4, 1983, to June 26, 1988. The parameters and options used in these propagations are those shown in column 2 of Table 1. Definitive mean semimajor axes with an epoch at the end of the long arc were converted and compared with the long propagation results for each spacecraft.

Table 3 summarizes the results of the comparisons between the predicted and definitive decay in the mean semimajor axis. Columns 4 and 5 give the decay in the mean semimajor axis over the period from the end of the initial calibrated year to the end of the

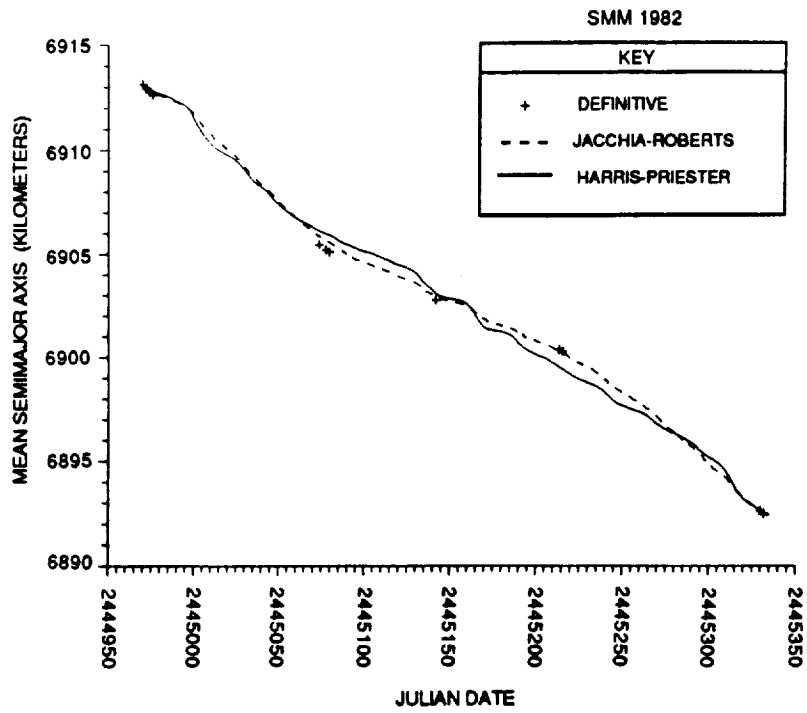


Figure 1. Definitive and Propagated Mean Semimajor Axis for SMM During 1982

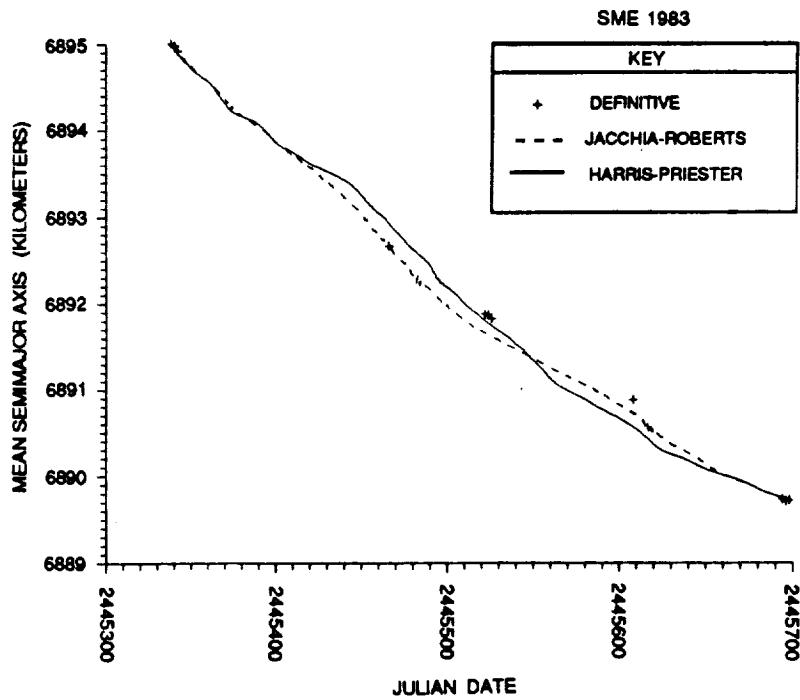


Figure 2. Definitive and Propagated Mean Semimajor Axis for SME During 1983

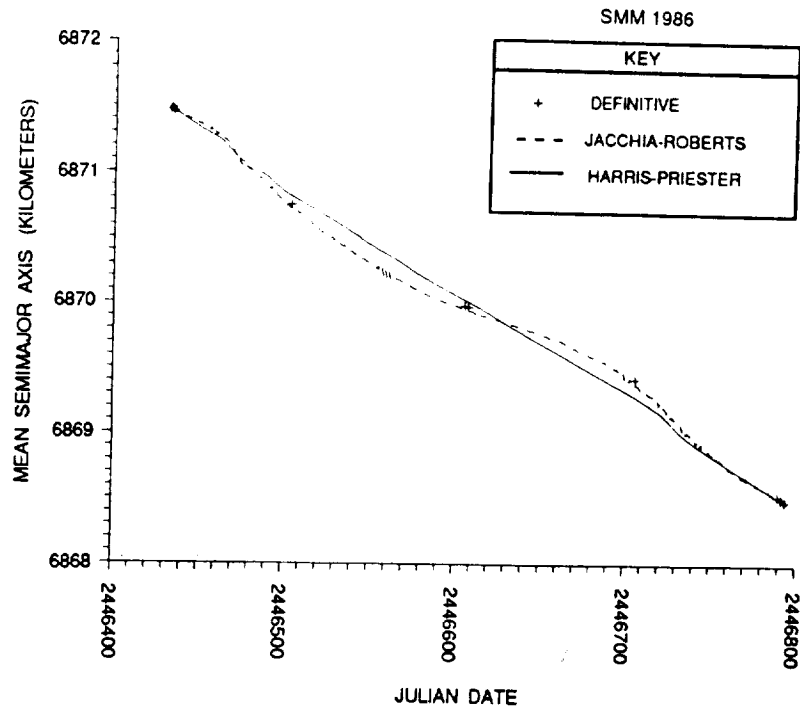


Figure 3. Definitive and Propagated Mean Semimajor Axis for SMM During 1986

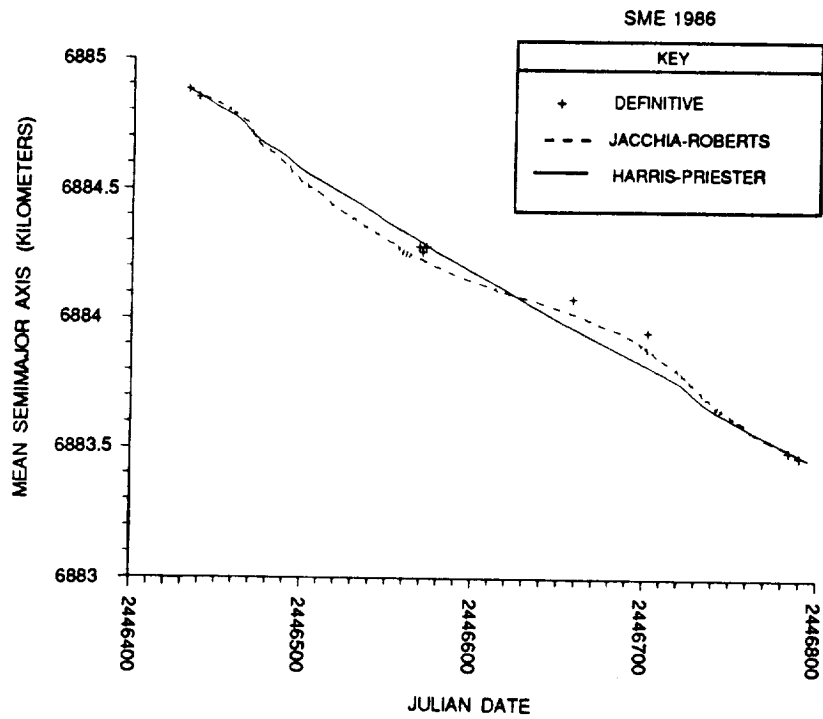


Figure 4. Definitive and Propagated Mean Semimajor Axis for SME During 1986

propagation interval, i.e., over the truly predictive interval. As in Section 3.1, the superiority of the Jacchia-Roberts model, demonstrated by the smaller percentages of discrepancy in the decay (column 6), is apparent. Once again, greater success in reproducing definitive semimajor axes was achieved with SME than SMM.

Table 3. Results of Multiyear Decay Prediction Tests

SPACECRAFT	ATMOSPHERIC DENSITY MODEL	ρ_1	PREDICTED DECAY IN THE SEMIMAJOR AXIS (KILOMETERS)	DEFINITIVE DECAY IN THE SEMIMAJOR AXIS (KILOMETERS)	DISCREPANCY IN THE DECAY
SMM	Jacchia-Roberts	-0.2120	33.54	35.08	4.4%
	Harris-Priester	-0.3527	42.33	35.08	20.6%
SME	Jacchia-Roberts	+0.2325	11.45	11.62	1.5%
	Harris-Priester	+0.3762	12.62	11.62	8.6%

4. CONCLUSIONS

The on-orbit calibration of the drag force model, performed in Section 3.1, was crucial to the relative success of the decay predictions of Section 3.2. The magnitudes of the drag scale adjustment factors, ρ_1 , demonstrate that conclusion. This may raise concern over the accuracy of prelaunch decay predictions made with uncalibrated ballistic coefficients.

While drag scale adjustments reflect a combination of errors affecting both atmospheric density model normalization and the ballistic coefficient, the pattern observed in this study suggests that ballistic coefficient error (caused by errors in the estimates of the drag coefficient, cross-sectional area, and/or mass) played a major role. Calibration results obtained with both atmospheric density models agree that the prelaunch ballistic coefficient was high for SMM and low for SME. The competing explanation is that both atmospheric density models are too dense over the tropics (SMM) and too rarified at higher latitudes (SME).

The mean ballistic coefficients suggested by the calibration results for the high solar activity year with both atmospheric density models are 28 percent below nominal for SMM and 30 percent above nominal for SME. If the factor ($C_D A/m$) in Equation (1) is adjusted to equal these mean ballistic coefficients for each of the spacecraft, new values of ρ_1 are required to give equivalent drag. Table 4 shows these adjusted ρ_1 values corresponding to each calibration in Table 2. These values are less than 10 percent, except for the 1986 Harris-Priester calibrations. Most of the observed drag scaling adjustment seems to have been a product of error in the a priori drag constants for the spacecraft.

The basis for the adopted operational values of C_D , A , and m is not well documented. Accurate theoretical calculation of C_D and A is nontrivial and requires some

Table 4. Calibration Results With Adjusted Ballistic Coefficients

SPACECRAFT	ATMOSPHERIC DENSITY MODEL	YEAR	ρ_1 (ADJUSTED)	ρ_1 (UNADJUSTED)
SMM	Jacchia-Roberts	1982	+0.098	-0.212
		1986	+0.005	-0.279
	Harris-Priester	1982	-0.098	-0.353
		1986	-0.437	-0.596
SME	Jacchia-Roberts	1983	-0.055	+0.232
		1986	-0.062	+0.223
	Harris-Priester	1983	+0.055	+0.376
		1986	-0.178	+0.073

compromise, in view of the contrasting uses to which such values may be put. (The effective values of these quantities are not necessarily the same for long-term decay prediction and short-arc definitive orbit determination, for example.) This is especially so for irregularly shaped, near-inertially oriented spacecraft such as SMM. Yet the state of the art of such calculations has undoubtedly advanced since the generation of the values for the spacecraft used here. It may not be necessary to assign a full measure of the observed 20- to 30-percent errors in a priori drag force normalization to the error budgets for prelaunch decay and lifetime predictions, even though such predictions cannot have the benefit of on-orbit calibration. Certainly, careful analysis of drag constants is a prerequisite for accurate decay and lifetime predictions.

There are several possible explanations for the apparently more consistent decay of SME, compared with SMM. The altitude range covered is twice as big for SMM as for SME and, since SMM was calibrated in a period of higher solar activity than SME, that calibration is required to serve over a larger range of solar activities. The previously noted differences between the configuration, orientation, and orbital inclination of these spacecraft all must have had their impact. In general, the expected effect is to make SMM decay more difficult to forecast. One consequence of the orbital inclination difference, however, should have had the opposite impact: the SME orbit is nearly, but not exactly, Sun-synchronous. While the orbital orientation with respect to the atmospheric diurnal bulge changes rapidly (eight cycles per year) for SMM, it changes slowly (11 degrees per year) for SME. Thus the high degree of calibration consistency between 1983 and 1986 observed for the Jacchia-Roberts atmospheric density model reflects both that model's accurate mean solar activity dependence and its apparently realistic diurnal bulge.

The Jacchia-Roberts atmospheric density model performed better than the Harris-Priester model in both the 1-year calibration tests and the long-term propagations. This is based on comparisons in four areas: (1) consistency of the final calibrated ρ_1 values for the high and low solar activity years, (2) agreement between the calculated and definitive

mean semimajor axes sampled quarterly throughout each calibration year, (3) prediction of the annual decay for 1986 using the calibration from the prior year of high solar activity, and (4) the discrepancy between the long-term predicted decay and the definitive decay.

The Jacchia-Roberts atmospheric density model substantially exceeded the Harris-Priester model in the consistency of calibration between the years of high and low solar activity and in its ability to fit the time dependence of the orbital decay during each year. The former model produced much better agreement between the final Q_1 values of the high and low solar activity years for both SMM and SME. When the Jacchia-Roberts model was used, the difference between the Q_1 values was -0.07 for SMM and 0.10 for SME. When the Harris-Priester model was used, the difference between the final Q_1 values was -0.24 for SMM and -0.30 for SME.

The percentage discrepancy of decay in the long-term propagations was much smaller using the Jacchia-Roberts model than using the Harris-Priester model. The propagations using the Jacchia-Roberts model had discrepancies of 4.4 percent for SMM and 1.5 percent for SME. The propagations using the Harris-Priester model had discrepancies of 20.6 percent for SMM and 8.6 percent for SME.

Solar activity forecasting will continue to dominate the error budget for lifetime prediction of low-altitude spacecraft. This study demonstrates that ballistic coefficient prediction error can also be significant. For the altitude range studied in this paper, use of the calibrated Jacchia-Roberts density model reduces the error due strictly to atmospheric density modeling to between 2 and 5 percent.

APPENDIX A

This appendix presents a justification of the modeling choices given in Table 1. In some cases, these choices have an impact on the accuracy of the results, as discussed below.

A step size of 1 day was used in both the 1-year calibrations and the long-term propagations. The use of a 1-day step size has been found to be generally satisfactory for long-term propagation (Reference 9). It was used in this study to reduce computer resource utilization and improve job turnaround time.

Tests of the 1-day step size were performed for the 1982 Jacchia-Roberts calibration and the 6-1/2-year Harris-Priester propagation for SMM. The tests used a one-orbit step size. In the Jacchia-Roberts calibration, the mean semimajor axes differed from the 1-day step size results by 76 meters at the end of the year and 63 meters in the root-mean-square (RMS) throughout the year. This error is 0.4 percent of the total yearly decay and could change q_1 by at most 0.004.

For the Harris-Priester propagation, the differences between the two step sizes were still less. The difference in the mean semimajor axis peaked at 44 meters (RMS = 12 meters) in 1982 and, for the entire arc, peaked at 53 meters (RMS = 27 meters). The difference was 16 meters at the calibration fiducial point at the end of 1982 and 33 meters on June 18, 1988; thus, the effects of discretization on the calibration and the total decay prediction were less than 0.1 percent for the Harris-Priester model.

Only zonal harmonics of the geopotential have been used in AVGVOP propagations. The effects of nonresonant tesseral and sectorial harmonics on the averaged VOP equations of motion are very small and are routinely neglected in such calculations (References 7 and 9). The effect of the 15th-order resonance has been investigated (through degree 21) using the AVGVOP implementation in the Research and Development version of the Goddard Trajectory Determination System (R&D GTDS). The effect on the mean semimajor axis is less than 3 meters, even for SMM when it approached exact resonance in June 1988. Some earlier GMAS calculations in which 15th-order resonance was included were found to have erroneously large resonant oscillations. As a result, resonant potential effects have been removed from all final results.

The modified Harris-Priester atmospheric density model simulates the diurnal bulge as a function of Φ , the angle from the spacecraft radius vector to the vector of maximum densities. The latter vector is displaced from the Sun vector by an adjustable amount (30 degrees throughout this study) in the right ascension. Densities are tabulated at $\Phi = 0$ degrees and $\Phi = 180$ degrees, with interpolation for intermediate values assumed to be linear in $\cos^N(\Phi/2)$ where N is a chosen integer. Standard practice at the FDF has been to take $N = 2$ for near-equatorial orbits and $N = 6$ for near-polar orbits; that tradition has been accepted in the present work.

REFERENCES

1. Jacchia, L. G., Smithsonian Astrophysical Observatory Special Report No. 332, *Revised Static Models of the Thermosphere and Exosphere with Empirical Temperature Profiles*, Cambridge, Massachusetts, May 1971
2. Roberts, E. R., Jr., "An Analytic Model for Upper Atmosphere Densities Based upon Jacchia's 1970 Models," *Celestial Mechanics*, Vol. 4, pp. 368-377, December 1971
3. Harris, I., and W. Priester, "Time Dependent Structure of the Upper Atmosphere," *Journal of Atmospheric Sciences*, Vol. 19, July 1952
4. Goddard Space Flight Center, NASA-TN-D-144, *Theoretical Models for the Solar-Cycle Variation of the Upper Atmosphere*, I. Harris and W. Priester, August 1962
5. Harris, I., and W. Priester, "Atmospheric Structure and Its Variations in the Region from 120 to 80 Km.," *COSPAR International Reference Atmosphere (CIRA) 1965*, Space Research IV. Amsterdam, Holland: North Holland Publishing Company, 1965
6. Computer Sciences Corporation, CSC/SD-86/6016 UD1, *Goddard Mission Analysis System (GMAS) Primer*, J. M. Roitz, May 1988
7. Computer Sciences Corporation, CSC/TR-77/6010, *A Recursively Formulated First-Order Semianalytic Artificial Satellite Theory Based on the Generalized Method of Averaging (Volume 1)*, W. D. McClain, November 1977
8. Computer Sciences Corporation, CSC/TM-85/6111, *Preliminary GRO Orbit Control Mission Analysis*, R. J. McIntosh, December 1985
9. McClain, W. D., A. C. Long, and L. W. Early, *Development and Evaluation of a Hybrid Averaged Orbit Generator*, Paper No. 78-1382, presented at the AIAA/AAS Astrodynamics Conference, Palo Alto, California, August 1978

LIFETIME PREDICTIONS FOR THE SOLAR MAXIMUM MISSION (SMM) AND SAN MARCO SPACECRAFT*

E. A. Smith, D. T. Ward, M. W. Schmitt, and M. C. Phenneger
Computer Sciences Corporation (CSC)

F. J. Vaughn and M. L. Lupisella
Goddard Space Flight Center (GSFC)

ABSTRACT

This paper describes lifetime prediction techniques developed by the Goddard Space Flight Center (GSFC) Flight Dynamics Division (FDD). These techniques were developed to predict the Solar Maximum Mission (SMM) spacecraft orbit, which is decaying due to atmospheric drag, with reentry predicted to occur before the end of 1989. Lifetime predictions have also been performed for the Long Duration Exposure Facility (LDEF), which was deployed on the 1984 SMM repair mission and is scheduled for retrieval on another Space Transportation System (STS) mission later this year. Concepts used in the lifetime predictions have been tested on the San Marco spacecraft, which reentered the Earth's atmosphere on December 6, 1988. Ephemerides predicting the orbit evolution of the San Marco spacecraft until reentry were generated over the final 90 days of the mission when the altitude was less than 380 kilometers. The errors in the predicted ephemerides are due to errors in the prediction of atmospheric density variations over the lifetime of the satellite. To model the time dependence of the atmospheric densities, predictions of the solar flux at the 10.7-centimeter wavelength ($F_{10.7}$) are used in conjunction with Harris-Priester (HP) atmospheric density tables.

Orbital state vectors, together with the spacecraft mass and area, are used as input to the Goddard Trajectory Determination System (GTDS). Propagations proceed in monthly segments, with the nominal atmospheric drag model scaled for each month according to the predicted monthly average value of $F_{10.7}$. Calibration propagations are performed over a period of known orbital decay to obtain the effective ballistic coefficient. Propagations using $\pm 2\sigma$ solar flux predictions are also generated to estimate the dispersion in expected reentry dates. Definitive orbits are compared with these predictions as time elapses. As updated vectors are received, these are also propagated to reentry to continually update the lifetime predictions. Noted trends can be used to infer the accuracy of initial and subsequent predictions of the reentry dates.

* This work was supported by the National Aeronautics and Space Administration (NASA)/Goddard Space Flight Center (GSFC), Greenbelt, Maryland, under Contract NAS 5-31500.

1. INTRODUCTION

This paper describes analysis performed by the Goddard Space Flight Center (GSFC) Flight Dynamics Division (FDD) to predict the reentry of the Solar Maximum Mission (SMM), San Marco, and Long Duration Exposure Facility (LDEF) spacecraft. An overview of the mission and orbit characteristics is given in Table 1.

Table 1. Spacecraft Mission and Orbit Characteristics

MISSION AND ORBIT CHARACTERISTICS	SPACECRAFT		
	SAN MARCO	SMM	LDEF
LAUNCH DATE	3/24/88	2/14/80	4/7/84
INITIAL ALTITUDE (KILOMETERS)	447	574	482
INCLINATION (DEGREES)	2.5	28.5	28.5
ECCENTRICITY	0.007	0.001	0.001
MASS (KILOGRAMS)	237	2315.59	6820
AREA (SQUARE METERS)	1.0	17.5	74.3
MISSION OBJECTIVE	DRAG STUDIES	SOLAR STUDIES	WEATHERING IN SPACE
REENTRY DATE	12/6/88	PREDICTED FOR LATE 1989	PLANNED FOR RETRIEVAL

SMM reentry support commenced in 1986 using the Rapid Orbit Prediction Program (ROPP) (References 1 and 2). Development of the present modeling for decay analysis using the Goddard Trajectory Determination System (GTDS) (References 3 and 4) began in 1987, and the SMM baseline reentry prediction was established in February 1988. Monthly update reporting began in August 1988. The San Marco lifetime analysis was performed from August 1988 to January 1989. Current activities include LDEF and SMM lifetime modeling.

For SMM, definitive altitude data and orbit solution initial state vectors for orbit propagation are obtained from daily orbit determination operational support provided by the FDD. For San Marco and LDEF, operational support is not provided by the FDD, and orbit solution state vectors were provided in the form of North American Aerospace Defense Command (NORAD) two-line elements. These are converted to Cartesian elements for use in ephemeris propagation, and they are also converted to Brouwer mean elements for the altitude representation. In this paper, orbital altitude is expressed as the mean altitude, which is the Brouwer mean semimajor axis minus the mean equatorial radius of the Earth (6378.14 kilometers).

For SMM, orbital lifetime estimates are important for planning science operations. For San Marco, reentry estimates were requested to coordinate San Marco measurements with sounding rocket measurements scheduled in November 1988. For LDEF, lifetime estimates are important for planning a Space Shuttle retrieval mission later this year.

Lifetime prediction techniques developed by the FDD employ a drag force calibration using historical data, followed by a GTDS lifetime prediction ephemeris propagated in monthly segments. In each segment, the Harris-Priester atmospheric density table and a drag force scaling parameter, Q_1 , are changed to accommodate variations in the drag force model due to predicted monthly average variations of the solar flux at the 10.7-centimeter wavelength ($F_{10.7}$).

Section 2 of this paper provides background information about the orbit propagators (ROPP and GTDS) and the aerodynamic drag models (Harris-Priester and Jacchia-Roberts) used in this analysis. Also discussed are the actual solar flux data and several predicted solar flux models, which drive the atmospheric density model. Section 3 presents the reentry analysis results for SMM, including the early ROPP results, the GTDS drag model calibration, and SMM lifetime predictions based on the various solar flux models. Section 4 describes the San Marco reentry analysis, and Section 5 presents the LDEF reentry analysis. Section 6 summarizes the key points of this study.

2. BACKGROUND

ROPP is designed to perform long propagations efficiently where high precision is unnecessary. It uses an eighth-order Adams-Moulton integrator with a Runge-Kutta starter, integrates in mean elements, and ignores short-period gravitational perturbations. The ROPP drag model allows for direct input of $F_{10.7}$ data and geomagnetic (K_p) data.

GTDS uses a 12th-order Cowell integrator with an iterative starter. The geopotential model is the Goddard Earth Model-9 (GEM-9) with terms up to order and degree 21. For SMM, this is truncated to maximum order and degree 16 and includes resonant harmonics above order and degree 16. For San Marco and LDEF, the GEM-9 is truncated to maximum order and degree 8 and also includes higher order resonant harmonics.

Two options for the GTDS atmospheric density model are applicable to the current analysis. The modified Harris-Priester (HP) atmospheric density model provides tables of density versus altitude corresponding to each of 10 discrete levels of $F_{10.7}$. The tabulated values are the global minimum and maximum density values (Q_{\min} and Q_{\max}) of the diurnal density variation cycle for each altitude. The density, Q , is a function of the angle ϕ between the spacecraft and the apex of the diurnal bulge, which is at a point 30 degrees east of the subsolar point. The diurnal bulge is modeled by

$$Q = Q_{\min} + (Q_{\max} - Q_{\min}) \cos^n \left(\frac{\phi}{2} \right) \quad (1)$$

The spatial shape of the diurnal density bulge is adjustable in GTDS by varying the power, n , of the cosine term. Both $n = 6$ and $n = 2$ have been used operationally, but $n = 2$ is preferred for low-inclination orbits.

The Jacchia-Roberts (JR) 1971 atmospheric density model includes effects correlated with the geomagnetic index, K_p , in its calculation of the exospheric temperature. It also requires 40 days of $F_{10.7}$ values beyond the day of analysis to accommodate an input for the 81-day $F_{10.7}$ average. Therefore, it is most reliable for use in past and near-current times, where $F_{10.7}$ and K_p data are known. The use of predicted $F_{10.7}$ and K_p data in the Jacchia-Roberts model is necessary for orbital lifetime predictions. The preliminary attempts described in this paper have resulted in limited success.

The definitive $F_{10.7}$ and A_p data used in this analysis are reported monthly by the National Geophysical Data Center. The solar flux data are determined each day from observations of the Sun. The K_p data are approximately logarithmic measurements made at 3-hour intervals around the world. The daily equivalent planetary amplitude, A_p , is derived by converting the K_p value to a linear index and averaging over 1 day. The $F_{10.7}$ and A_p data spanning the time period 1979 through 1988 are illustrated in Figure 1.

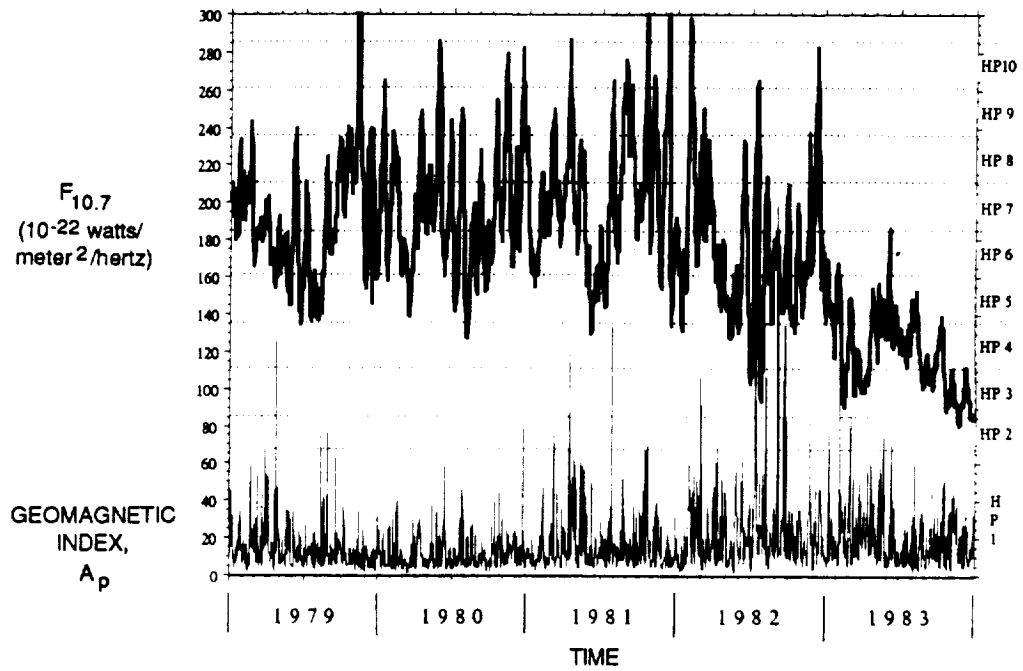
The principle source of predicted solar activity data for this analysis has been the GSFC Laboratory for Atmospheres (GSFC Code 610). Three sets of 1-year smoothed monthly $F_{10.7}$ predictions by Dr. Kenneth H. Schatten (References 5, 6, and 7) of GSFC are illustrated in Figure 2. Figure 3 illustrates the Schatten predictions in comparison with the actual solar flux activity. Each updated prediction supercedes the previous prediction.

Early analysis used predictions from the Marshall Space Flight Center (MSFC) (Reference 8). The MSFC data include a best estimate and 97.7-percent, 50-percent, and 2.3-percent probability intervals. The current work uses the Schatten predictions from February 1988, August 1988, and January 1989, hereafter referred to as SH 2/88, SH 8/88, and SH 1/89, respectively. These predictions include a nominal value, a $+2\sigma$ probability (high) value, and a -2σ probability (low) value, hereafter designated by appending a plus or minus sign, for example, (SH 2/88+) or (SH 2/88-).

The method for incorporating solar flux information into long-range GTDS ephemeris propagations using the Harris-Priester density model is described using San Marco as an example. Each monthly mean $F_{10.7}$ value is converted to a corresponding prediction of the atmospheric density represented by a Harris-Priester (HP) table number and a value of the drag scaling adjustment parameter, Q_1 , which also depends on the spacecraft altitude. Using Q_1 , the model of the atmospheric density is varied smoothly with the $F_{10.7}$ level between the HP tables. (In the discussion that follows, refer to Table 2.)

For an altitude of 380 kilometers, the minimum and maximum density values are retrieved from HP tables 3 through 7. The average density over one diurnal cycle is then determined by taking the arithmetic mean of the minimum and maximum values. The interpolation scheme for adjusting the HP table densities to solar fluxes between tables depends on the ratio of the average densities for the adjacent HP tables. This ratio is obtained by determining the Q_1 value that scales the lower table to the upper table value (see Table 2a, column 6) or scales the upper table to the lower table (see Table 2a,

a. 1979 - 1983



b. 1984 - 1988

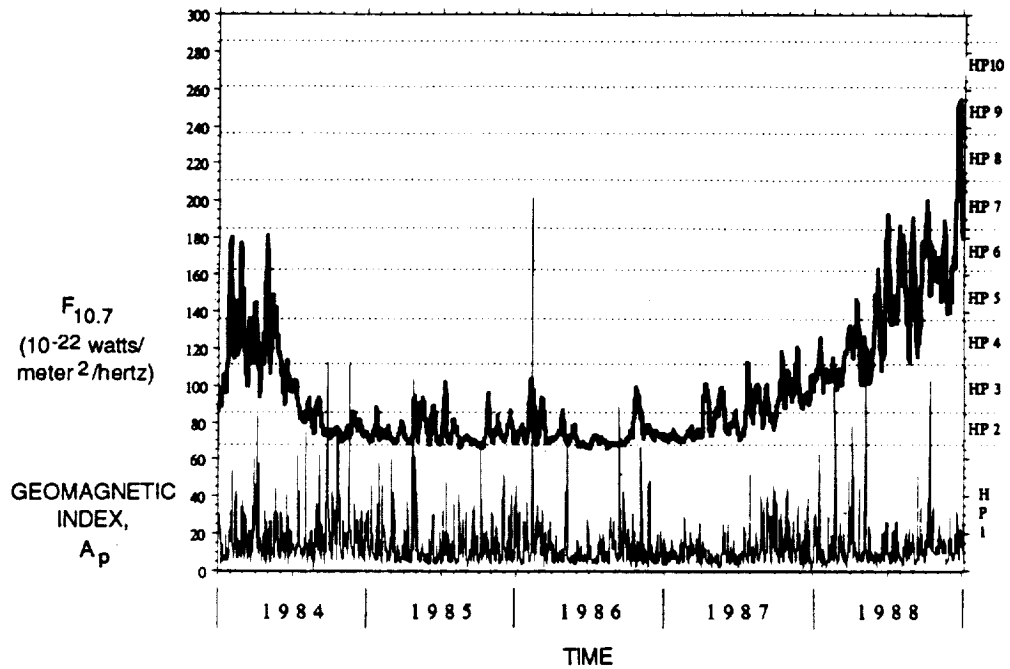


Figure 1. Solar Flux and Geomagnetic Index Profiles for 1979 Through 1988

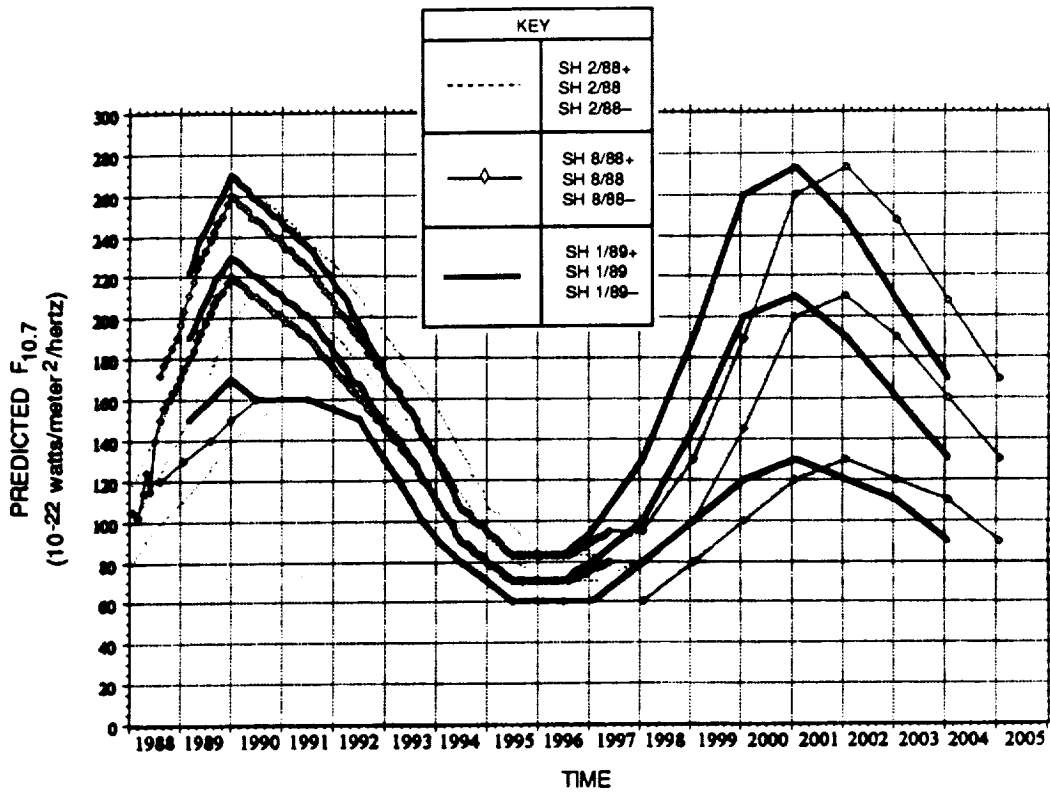


Figure 2. Schatten Solar Flux Predictions

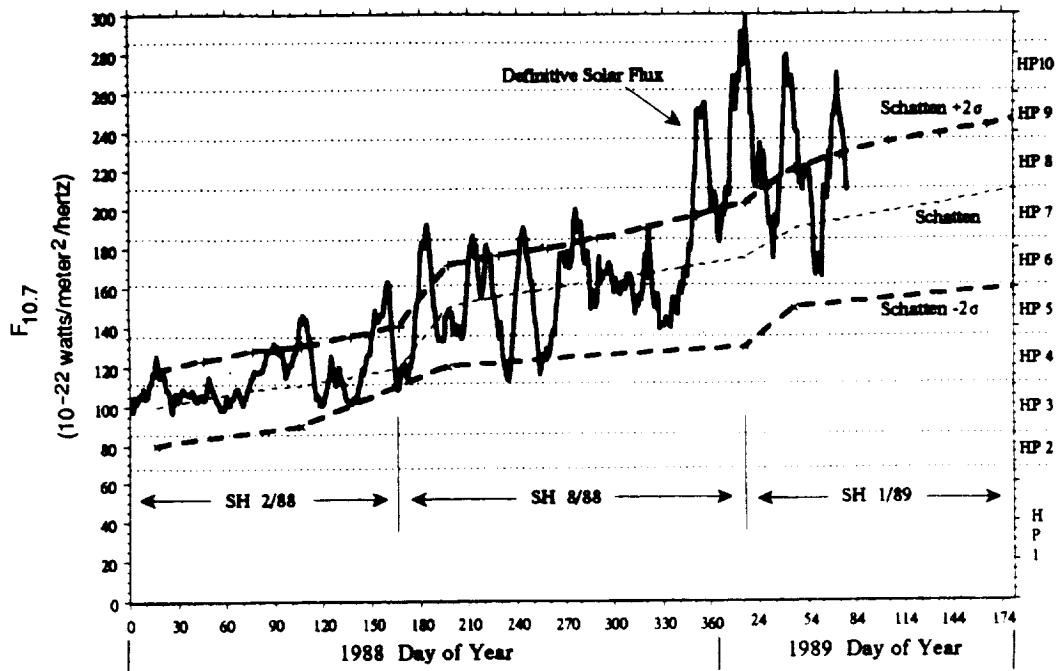


Figure 3. Definitive Solar Flux Values Versus the Schatten Solar Flux Predictions

column 7). For example, the Q_1 required to obtain the same density using HP table 3 as would be obtained for HP table 4 is 0.4223, because the average density for HP table 4 (4.688) is 42.23 percent greater than the average density for HP table 3 (3.296). In the other direction, the Q_1 needed to approximate HP table 3 from HP table 4 is -0.2969, because 3.296 is 29.69 percent less than 4.688.

Table 2. Drag Model Parameters for Cosine-Squared Diurnal Bulge

a. ATMOSPHERIC DENSITY AND INTERPOLATING VALUES OF Q_1 FOR SAN MARCO AT 380 KILOMETERS ALTITUDE

HP TABLE NO.	$F_{10.7}$ (10-22 watts/ meter ² / hertz)	ATMOSPHERIC DENSITY (grams/kilometer ³)			Q_1 FOR SHIFT OF ONE HP TABLE NO.	
		Q_{min}	Q_{max}	$Q_{average}$	UP	DOWN
3	100	1.382	5.210	3.296	0.4223	N/A
4	125	2.094	7.282	4.688	0.4109	-0.2969
5	150	3.274	9.955	6.615	0.2641	-0.2913
6	175	4.313	12.41	8.362	0.3039	-0.2089
7	200	6.205	15.60	10.903	N/A	-0.2331

NOTE: N/A = NOT APPLICABLE

b. MONTHLY AVERAGE SCHATTEN SOLAR FLUX PREDICTIONS AND ASSOCIATED Q_1 VALUES USED IN THE SAN MARCO LIFETIME RUNS

SOLAR FLUX MODEL	MONTH(S)	$F_{10.7}$ (10-22 watts/ meter ² / hertz)	HP TABLE NO.	Q_1
SH 8/88	9/88	159	5	0.0951
	10/88	163	6	-0.1003
	11/88	167	6	-0.0668
	12/88	171	6	-0.0334
SH 8/88+	9/88	180	6	0.0608
	10/88	185	6	0.1216
	11/88	190	7	-0.0932
	12/88	197	7	-0.0280
SH 8/88-	9/88 - 12/88	120	4	-0.0594
	1/89 - 2/89	130	4	0.0822

Once the Q_1 value to shift between adjacent tables has been obtained, the predicted $F_{10.7}$ level is compared with the standard tables, and the closest HP table is selected to approximate the density. Then, the Q_1 value required to adjust the HP table to the intermediate

$F_{10.7}$ value is determined by linear interpolation relative to the value determined for a shift of one table. For example, the SH 8/88 solar flux model predicted a level of 159 for September 1988. The HP table 5 ($F_{10.7} = 150$) is the closest table. A shift to HP table 6 ($F_{10.7} = 175$) can be accounted for by a q_1 value of 0.2641. The tabulated value of 0.0951 is obtained by taking 9/25 times 0.2641.

For other altitudes, the same procedure is used, but the numbers are different. Thus, the q_1 values are fixed quantities that fine-tune the Harris-Priester drag model to the predicted $F_{10.7}$ level for each month of a propagation.

3. SMM REENTRY ANALYSIS

For SMM, two events are of interest: reentry and decay of the orbit to an altitude corresponding to loss of attitude control. The loss of control is modeled to occur when the spacecraft's angular momentum management system cannot compensate for the effects of atmospheric torques. The adopted altitude for this is 370 kilometers (200 nautical miles) (Reference 9).

3.1 EARLY ROPP ANALYSIS

Early analysis using ROPP to predict the SMM reentry date utilized the technique of matching the observed orbital decay up to the date of the analysis to determine the ballistic coefficient ($C_D A/m$), where

- C_D = drag coefficient
- A = spacecraft cross-sectional area
- m = spacecraft mass

The ballistic coefficient determined by this approach was 0.01262 square meter per kilogram, which was somewhat lower than the value calculated from available spacecraft data, 0.01496 square meter per kilogram. Using this value, propagations to the reaction wheel saturation altitude (370 kilometers) and to reentry were performed. Starting with an orbital state vector determined for June 1, 1986, and using MSFC solar flux predictions (MSFC 4/86), the first prediction of the SMM reentry date by the FDD was for December 3, 1990.

3.2 GTDS CALIBRATION

SMM orbit solutions from launch through October 1987 were analyzed to establish that the atmospheric density variations, as measured by GTDS during orbit determination, were well correlated with observed solar flux variations (Reference 10). The drag model was then calibrated by adjusting the drag coefficient, C_D , to match the predicted and actual orbital decay over the history of the SMM mission. For the calibration runs, HP tables and q_1 values were determined for each definitive monthly mean $F_{10.7}$ value in the manner previously described. Then, for each year of the mission, the value of the C_D was adjusted to obtain agreement with the actual orbital decay. Year-to-year variations

were noted and were attributed to errors in the Harris-Priester atmospheric density model associated with different $F_{10.7}$ levels. For example, during the period of solar minimum (1984 through 1987), SMM orbital decay was very moderate and C_D estimates were atypically low. For solar flux levels in the range 150 to 200 during the declining portion of solar maximum period number 21 in 1981 and 1982, a C_D of 1.38 gave the best fit. This value was adopted since solar flux levels expected for the interval before reentry were in this range. The corresponding ballistic coefficient is 0.01043 square meter per kilogram, 20 percent lower than the value obtained in the ROPP calibration analysis.

3.3 SMM PREDICTION RESULTS FROM DIFFERENT SOLAR FLUX MODELS

Orbit decay predictions were performed using the most current solar flux prediction model available at the time. When a new model or an update to an old model was obtained, the prediction modeling switched. Overall, six models were used: three versions of the Marshall Space Flight Center (MSFC) model and three versions of the Schatten model. Reentry predictions for these models are summarized in Table 3.

Table 3. Summary of FDD Reentry Predictions for SMM

SOLAR FLUX MODEL	DATES		
	EPOCH	REENTRY	LOSS OF CONTROL
MSFC 12/87 BEST ESTIMATE	12/31/87	2/14/90	11/7/89
MSFC 4/88 BEST ESTIMATE	4/1/88	4/22/90	1/9/90
MSFC 6/88 BEST ESTIMATE	7/2/88	6/3/90	2/15/90
SH 2/88	12/31/87	7/24/90	4/18/90
SH 8/88+	10/2/88	12/9/89	9/21/89
SH 1/89+	2/1/89	10/7/89	8/3/89

3.3.1 DECAY PREDICTIONS WITH MSFC SOLAR FLUX MODELS

The first set of GTDS reentry predictions for SMM was based on the MSFC 12/87 solar flux predictions. Starting from an orbital solution vector of epoch December 31, 1987, the MSFC best estimate gave a reentry date of February 14, 1990, and loss of control on November 7, 1989. MSFC predictions are updated every 2 months, though subsequent MSFC models were used only for the purpose of comparison.

3.3.2 DECAY PREDICTIONS WITH THE SH 2/88 SOLAR FLUX MODEL

After completion of the work described in Section 3.3.1, the FDD adopted the Schatten solar flux predictions for all subsequent reentry predictions. The SH 2/88 solar flux

model was used for a propagation starting from an epoch of December 31, 1987. This resulted in the prediction of loss of control on April 18, 1990, and reentry on July 25, 1990. Because a period of constancy in solar flux prediction models occurred after February 1988, this propagation was established for reporting purposes as the FDD baseline reference.

The trend in these first predictions toward later reentry dates for later starting epochs is consistent with the fact that the later MSFC models and the first Schatten model predicted lower solar flux levels than the first MSFC models. Later updates to the Schatten model predicted higher solar flux levels, and the corresponding predicted reentry dates were earlier.

Following the establishment of a baseline prediction, comparisons were made between the mean altitude of the predicted and actual trajectories to monitor and report the orbit evolution and to assess trends in the actual orbit decay. Figure 4 shows the actual SMM mean altitude data from operational orbit determination in 1988 and also shows some of the predicted trajectories, including the baseline. Another trajectory is based on the definitive mean $F_{10.7}$ value for each month. These predicted trajectories are in close agreement until June 1988, when the actual $F_{10.7}$ values began to exceed the SH 2/88 model. The change in the decay rate for the actual SMM altitude data occurs 2 to 3 months later. At the end of 1988, the observed SMM orbital decay and the orbit predicted with the HP density table driven by the actual $F_{10.7}$ levels showed close agreement, in spite of discrepancies for several earlier months.

3.3.3 ANALYSIS USING THE JACCHIA-ROBERTS DENSITY MODEL

Subsequent work with the Jacchia-Roberts model resulted in a propagation that correctly predicted the shape of the orbital decay throughout 1988. Definitive $F_{10.7}$ and geomagnetic index (K_p) data were used as input up to December 1, 1988, after which predicted values from the SH 8/88 model were incorporated. A calibration performed using the interval from 1/1/88 to 12/1/88 requires a drag coefficient, C_D , of 3.35 to produce agreement. The fit to the anomalous downturn in the definitive SMM altitude data is quite good. By including the K_p data and incorporating the 81-day average $F_{10.7}$ into the density calculation, the Jacchia-Roberts model predicted the detailed time dependence of the definitive data. The Jacchia-Roberts model begins to show sizable discrepancies as soon as the definitive $F_{10.7}$ and K_p data run out and the predicted solar flux data begin. The cause of this is being investigated.

3.3.4 DECAY PREDICTIONS WITH THE SH 8/88 SOLAR FLUX MODEL

The SH 2/88 predictions were updated in August 1988 to accommodate the observed early rise to the solar maximum. The SH 8/88 predictions agreed well with the observed solar flux for several months, until the observations again increased beyond the predictions. The monthly mean $F_{10.7}$ value was 200.5 for December 1988, and 236.4 for January 1989, both above the SH 8/88 $+2\sigma$ levels. The original baseline propagation for SMM shows large differences with recent definitive data because solar activity has been much higher than the SH 2/88 model on which it was based. Month-by-month

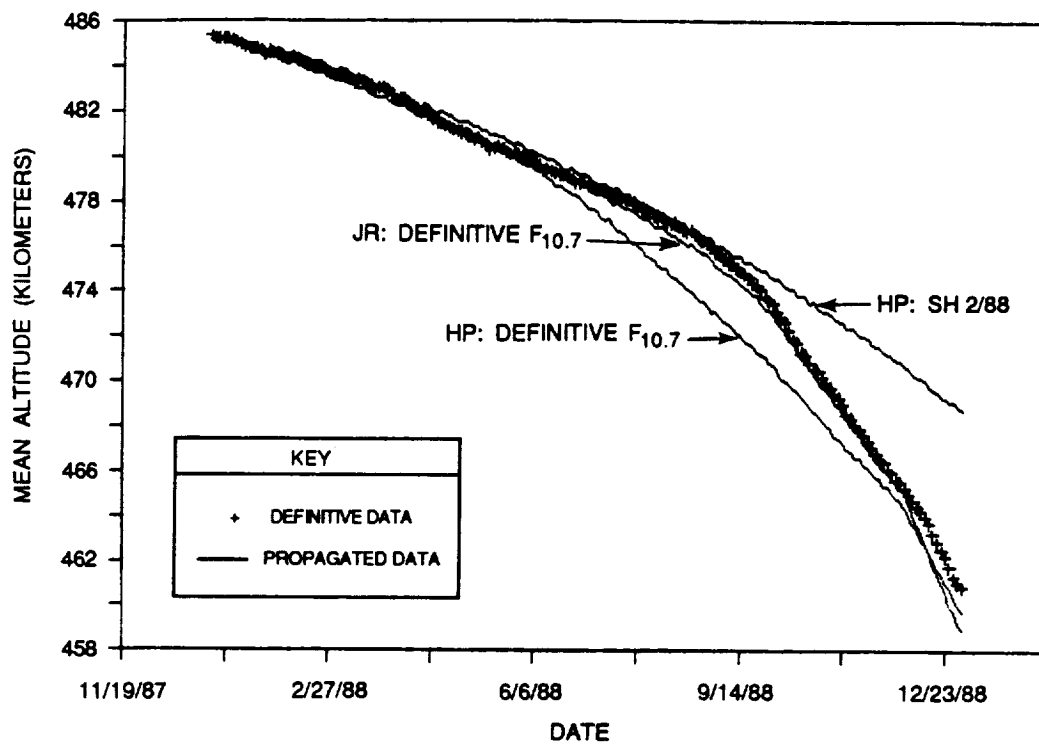


Figure 4. SMM Orbital Altitude for 1988

comparisons to the baseline reference ephemeris are given in Table 4. The angular difference between the predicted and actual spacecraft position now amounts to several orbits. The number of days that orbital decay is ahead of schedule is determined by noting when the predicted altitude will reach the current definitive altitude.

In January 1989, estimates of the SMM orbital decay trajectory were made using the SH 8/88 solar flux predictions. The epoch was set at October 2, 1988, since this was after the noticeable change in the decay rate. The definitive altitude data indicated that SMM closely followed the trajectory based on the $+2\sigma$ solar flux values and not the trajectory based on the nominal values. This is consistent, as the actual $F_{10.7}$ values were closer to the $+2\sigma$ predictions than to the nominal predictions. Based on the SH 8/88+ model, reentry was predicted to occur on December 9, 1989, and loss of control was predicted to occur on September 21, 1989.

3.3.5 DECAY PREDICTIONS WITH THE SH 1/89 SOLAR FLUX MODEL

A second update to the Schatten predictions, dated January 1989, differs from the SH 8/88 model by a shift of the $F_{10.7}$ levels upward by 10 units. The first entry is for February 1989; therefore, analysis with the SH 1/89 model is in the preliminary stages at this writing. There is evidence for another increase in the decay rate of the definitive

Table 4. Summary of the Predicted and Actual SMM Orbital Decay in Reference to the FDD Baseline Prediction

EPOCH DATE	MEAN ALTITUDE (kilometers)	OBSERVED ORBITAL DECAY (kilometers)	PREDICTED ORBITAL DECAY (kilometers)	OBSERVED MINUS PREDICTED (kilometers)	OBSERVED MINUS PREDICTED (percent)	OBSERVED MINUS PREDICTED POSITION (degrees)	OBSERVED ALTITUDE DECAY IS AHEAD BY (days)
12/31/87	485.383	--	--	--	--	--	--
8/1/88	477.597	7.786	7.583	.203	2.7	53.0	3
8/31/88	475.990	9.393	9.074	.319	3.5	59.5	5
9/30/88	473.458	11.925	10.732	1.193	11.1	84.9	21
11/1/88	469.299	16.084	12.671	3.413	26.9	180.8	52
12/1/88	465.574	19.809	14.425	5.384	37.3	345.7	71
12/31/88	460.832	24.551	16.677	7.874	47.2	582.2	91
2/1/89	454.067	31.316	19.099	12.217	64.0	N/A	122
3/1/89	446.830	38.553	21.587	16.966	78.6	N/A	150

SMM altitude data near January 10, 1989. The observed orbital decay exceeds the predicted decay using the SH 1/89+ model with $C_D = 1.38$. For February 1989, the monthly mean $F_{10.7}$ was 222.8, very close to the SH 1/89 +2 σ predicted value of 221. Matching the actual February orbital decay to predictions using the SH 1/89+ model requires $C_D = 1.64$. The corresponding ballistic coefficient is 0.01240 square meter per kilogram, which is close to the value obtained in the early ROPP calibration analysis. Using this C_D with the SH 1/89+ model and starting with a solution vector on February 1, 1989, reentry occurs on October 7, 1989 and loss of control is on August 4, 1989.

4. SAN MARCO REENTRY PREDICTIONS

In August 1988, the FDD was requested to predict the future orbital evolution of San Marco. Preliminary work had been done periodically during the mission using a drag model based on solar flux levels fixed at the value current at the prediction epoch. Predicted reentry dates changed uniformly with the later starting epochs, since the solar flux was steadily increasing during 1988. The consistency of the results was improved when the monthly solar flux variations were included in the propagations.

The results of the calibration runs for San Marco for the Jacchia-Roberts atmospheric model and two versions of the Harris-Priester atmospheric model are listed in Table 5. The interval for this propagation spanned from March 26, 1988, to September 1, 1988. Harris-Priester runs used the SH 2/88 solar flux model, since the actual solar flux levels closely matched this model over the calibration interval. Agreement between the predicted and actual orbital decay was quite good for $n = 6$; therefore, this bulge model was used

Table 5. Drag Model Calibration Runs for San Marco

DENSITY MODEL, BULGE MODEL, AND DRAG COEFFICIENT	MEAN ALTITUDE (kilometers)			ORBITAL DECAY (kilometers)		PREDICTION ERROR (percent)
	BEGINNING OF CALIBRATION INTERVAL	END OF CALIBRATION INTERVAL		PROPAGATED	DEFINITIVE	
		PROPAGATED	DEFINITIVE			
HARRIS-PRIESTER n = 6 C _D = 2.17	447.206	384.855	384.148	62.351	63.058	- 1.12
HARRIS-PRIESTER n = 2 C _D = 2.17	447.206	369.504	384.148	77.702	63.058	+23.2
JACCHIA-ROBERTS C _D = 1.67	447.206	384.494	384.148	62.712	63.058	-0.55

with the drag coefficient ($C_D = 2.17$) that was supplied with the spacecraft modeling parameters.

Reentry predictions for San Marco using the Harris-Priester models SH 2/88 and SH 8/88 nominal, $+2\sigma$, and -2σ solar flux levels are given in Table 6. Predictions using both $n = 6$ and $n = 2$ diurnal bulge models were performed for the starting epoch of September 1, 1988.

Table 6. San Marco Reentry Predictions

STARTING EPOCH	DIURNAL BULGE MODEL	SOLAR FLUX MODEL	REENTRY DATE
AUGUST 15, 1988	n = 6	SH 2/88	JANUARY 9, 1989
		SH 2/88+	DECEMBER 14, 1988
		SH 2/88-	FEBRUARY 21, 1989
SEPTEMBER 1, 1988	n = 6	SH 8/88	DECEMBER 12, 1989
		SH 8/88+	NOVEMBER 27, 1988
		SH 8/88-	JANUARY 23, 1989
	n = 2	SH 8/88	DECEMBER 2, 1989
		SH 8/88+	NOVEMBER 19, 1988
		SH 8/88-	JANUARY 7, 1989

The actual reentry was earlier than the predictions from the August 15 epoch because the actual solar flux was higher than the SH 2/88 model predictions. The September 1 predictions using SH 8/88+ and SH 8/88- models and a diurnal bulge model with $n = 6$ show a reentry envelope that brackets the actual reentry date. The actual $F_{10.7}$ levels in this timeframe closely matched the SH 8/88 model.

As propagations using the $n = 6$ diurnal bulge were repeated for subsequent NORAD vectors, there was a trend toward earlier reentry dates. The $n = 2$ diurnal bulge model resulted in increased consistency and eliminated the trend toward earlier reentry dates. Since these runs used $C_D = 2.17$, the calibration runs are called into question. In effect, this approach amounted to a recalibration by trial and error. The comparison of the definitive altitude data and the September 1 (SH 8/88; $n = 2$) predicted reentry trajectories is given in Figure 5.

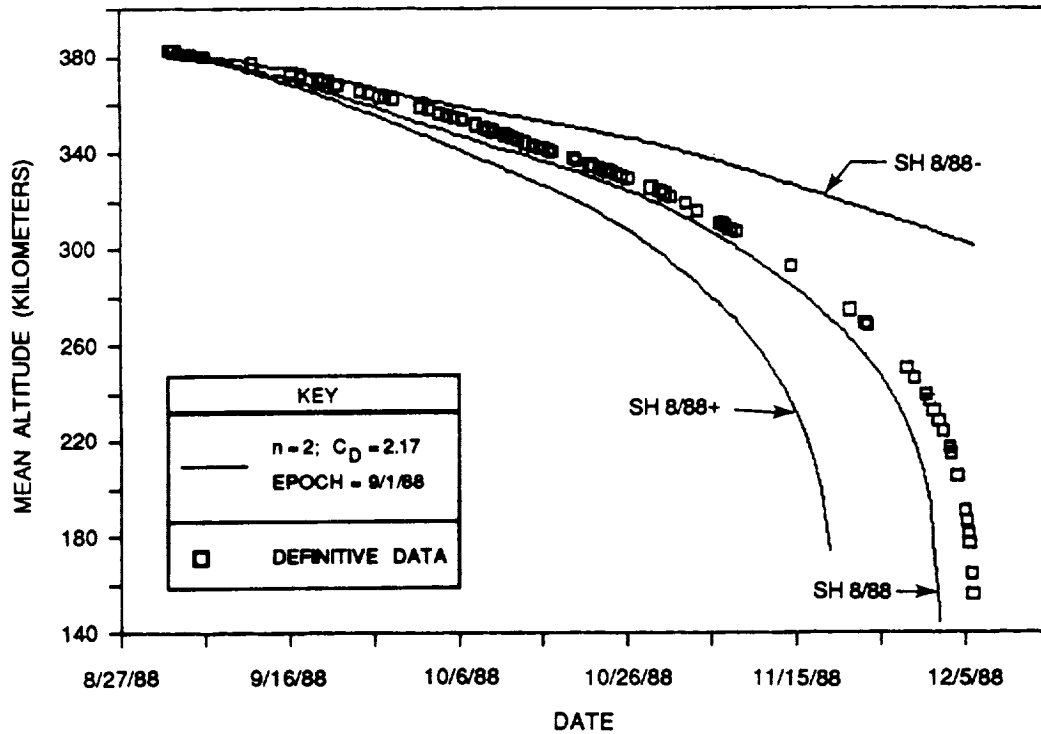


Figure 5. San Marco Orbital Altitude History

Another procedure was tried for San Marco. The drag model was calibrated by using a series of 5 to 10 NORAD vectors, spanning an interval of roughly 1 week, as input to a GTDS differential correction. The estimated solution state included the drag scaling parameter, ρ_1 . Propagations to reentry were performed with the same HP table and the solved-for value of ρ_1 . These results (listed in Table 7) were less consistent than those

Table 7. Differential Correction Reentry Predictions

EPOCH	DATA ARC	NO. OF NORAD VECTORS	HP TABLE NO.	ρ_1	F _{10.7} (10 ⁻²² watts/ meter ² / hertz)	REENTRY DATE
9/1/88	9/1 - 9/6	5	5	-0.0416	146.6	12/25/88
9/16/88	9/16 - 9/22	8	5	+0.0645	155.8	12/19/88
10/1/88	10/1 - 10/7	5	6	+0.0274	177.0	12/7/88
10/8/88	10/8 - 10/13	8	6	+0.2029	190.1	11/28/88
10/17/88	10/13 - 10/18	7	6	+0.0795	180.9	12/3/88

described above. This is as expected, since this procedure ignores F_{10.7} variations due to the 27-day rotation of the Sun and the gradual rise towards the solar maximum.

Reentry occurred on December 6, 1988, near 0130 coordinated universal time (UTC), with no visual confirmation. The last telemetry was received as San Marco passed over Kenya just prior to this time. Predictions made within 6 weeks of reentry were accurate to within 24 hours. Predictions made the day of the reentry were accurate to approximately one orbit. Five days before reentry, on December 1, the 2 σ extremes of the atmospheric density model predicted reentry times within 24 hours. Figure 6 shows a plot of predicted reentry dates versus the prediction epoch.

When the calibration and reentry prediction were repeated using the Jacchia-Roberts model with definitive F_{10.7} and K_p values, a markedly lower value of C_D = 1.67 was needed to match the observed decay for the calibration interval. The Harris-Priester model with n = 2 required C_D = 1.76 for agreement over this calibration interval. The predicted reentry date (December 16) using the calibrated Jacchia-Roberts model was late and was near the date for the Harris-Priester model with n = 2 and C_D = 1.76. During the calibration time interval, solar flux levels were in the range of 100 to 125; during the time interval until reentry, solar flux levels were in the range of 175 to 200. Similar inconsistencies in the Harris-Priester model dependence of the density on F_{10.7} for widely different values of the solar flux were also noted in the SMM analysis.

5. LDEF LIFETIME ANALYSIS

Calibration runs for LDEF were performed using NORAD two-line elements spanning October 18, 1988, to January 24, 1989. The calibration was done twice, once with actual monthly mean values of F_{10.7} and once with the SH 8/88+ solar flux model. For both solar flux models, agreement was obtained with C_D = 0.66, corresponding to a ballistic coefficient of 0.00719 square meter per kilogram.

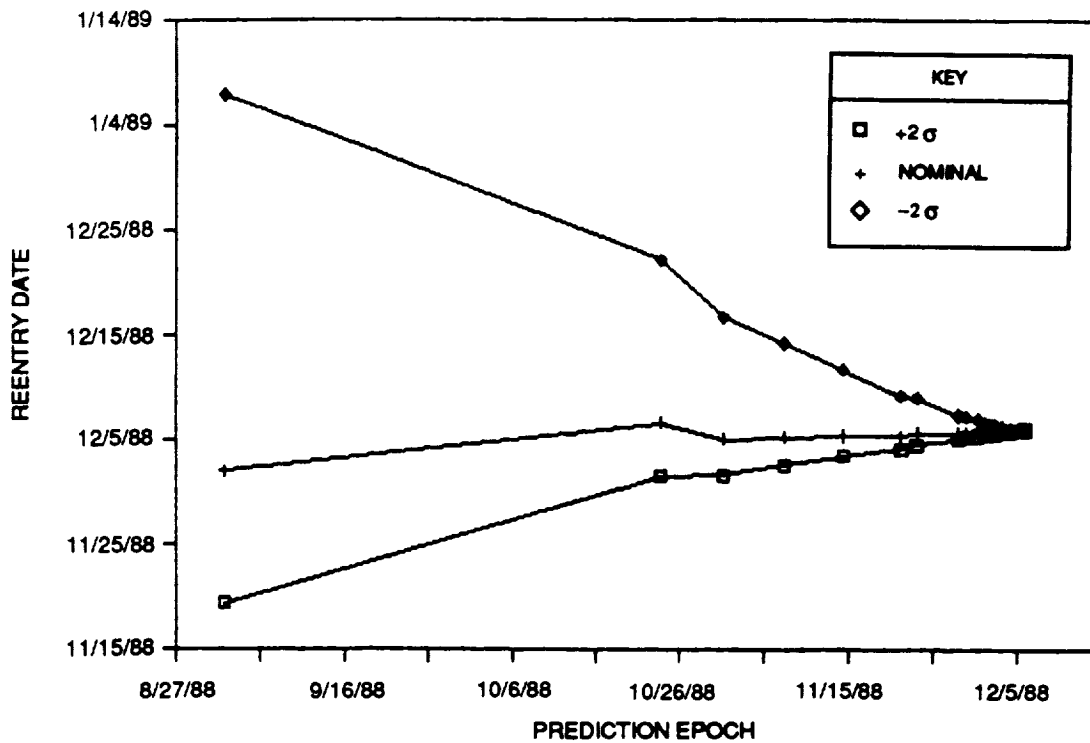


Figure 6. San Marco Reentry Dates Versus the Prediction Epoch

This effective ballistic coefficient was then used to predict the LDEF orbital evolution and the reentry date. Using an orbital state vector for February 1, 1989, and the SH 8/88+ solar flux model, the LDEF reentry is predicted to occur on February 16, 1990. SMM, though currently in a higher orbit than LDEF, is decaying more rapidly and will move lower than LDEF in June 1989 as it proceeds toward reentry. At the time of the planned retrieval in November 1989, the altitude of LDEF is predicted to be in the range of 370 to 350 kilometers.

Repeating the analysis with the SH 1/89+ solar flux model yields different results. A calibration over the month of February produced agreement with $C_D = 0.74$. When this propagation is extended forward in monthly segments based on the SH 1/89+ solar flux model, LDEF reentry is predicted for December 25, 1989. The margin for error is small if LDEF is to be successfully retrieved. A moderate increase in the solar flux beyond currently predicted values could easily threaten the planned November retrieval.

6. SUMMARY

Methods and results for spacecraft orbital lifetime prediction implemented in the GSFC FDD have been described. The procedure relies on a calibration of the ballistic coefficient over an interval of known orbital decay and solar activity. The calibration is followed by propagations to reentry, based upon a time-dependent atmospheric density driven by predicted $F_{10.7}$ models and starting with the most current orbital state.

As expected, the accuracy of the reentry prediction is strongly dependent upon the accuracy of the predicted solar flux model. The following additional observations can be made.

For long-term predictions, the use of the GTDS Harris-Priester atmospheric density model offers simplicity in the operational procedures and provides sufficient consistency and accuracy. This may occur because the calibration over the orbital decay intervals compensates for the limiting aspects of the Harris-Priester atmospheric density model. In particular, this model does not internally accommodate effects from the 81-day averaged $F_{10.7}$ value representing the solar disk radiance and the short-term geomagnetic index variations. Calibrations performed over intervals of the solar cycle similar to those expected in the propagation period may account for these limitations in the average sense.

Furthermore, the San Marco analysis and results provided an opportunity to practice for SMM and LDEF. When reentry is several months away, the present procedures are adequate. A baseline reference trajectory is established and used until comparisons with actual altitude data indicate that a modification is necessary. For the last few months of orbital decay, improved results can be obtained by repeating the propagations frequently and adjusting the drag model to obtain consistent reentry dates. For longer propagations, this is less practical, due not only to the longer computation time but also to the fact that errors in the predicted solar flux models dominate the uncertainties in reentry time.

Preliminary efforts to apply the Jacchia-Roberts atmospheric density model to orbital decay prediction led to mixed results, indicating that more work is necessary in this area. Good results were obtained in the calibration propagation for SMM in the 1-year interval of 1988. Less success was obtained in predicting the San Marco reentry and in predicting the SMM reentry in 1989. A successful implementation of an atmospheric density model based on the Jacchia-Roberts model should and did yield an intrinsically more accurate orbit prediction in comparison with the historical evolution where the solar flux data are well known. However, procedures are yet to be developed that are operationally simple and that can be used with predicted solar flux models.

Finally, based upon the analysis as of this writing and upon the current tendency for solar activity to often exceed the $+2\sigma$ levels of the $F_{10.7}$ predictions, SMM will reenter before December 1989 and LDEF could reenter as early as late December 1989.

REFERENCES

1. TRW Corporation, 08554-6001-R000, *Rapid Orbit Prediction Program (ROPP)*, D. M. Wexler, December 1967
2. Computer Sciences Corporation, CSC/TM-79/6214, *Rapid Orbit Prediction Program (ROPP) User's Guide*, W. M. Owen, Jr., September 1979
3. Goddard Space Flight Center, X-582-76-77, *Mathematical Theory of the Goddard Trajectory Determination System*, A. J. Fuchs, C. E. Velez, and J. O. Cappellari (editors), April 1976

4. Computer Sciences Corporation, CSC/SD-85/6738, *Goddard Trajectory Determination System (GTDS) User's Guide, Revision 2*, D. Squier and K. Byers, December 1987
5. Schatten, K. H., "Solar and Geomagnetic Prediction Data," memorandum from K. H. Schatten, GSFC Code 610.2, to GSFC Code 550, February 17, 1988
6. Schatten, K. H., "Update of Solar Flux and Geomagnetic Index Predictions," memorandum from K. H. Schatten, GSFC Code 610.2, to GSFC Code 550, August 24, 1988
7. Schatten, K. H., "January 1989 Solar and Geomagnetic Prediction Data," memorandum from K. H. Schatten, GSFC Code 610.2, to GSFC Code 554, January 31, 1989
8. Marshall Space Flight Center, "Solar Activity Inputs for Upper Atmospheric Models Used in Programs to Estimate Spacecraft Orbital Lifetime", MSFC memorandums, December 1987, April 1988, and June 1988
9. Computer Sciences Corporation, CSC/TM-80/6319, *Evaluation of SMM Attitude Stability at Low Spacecraft Altitudes*, S. D. Oh and J. M. Buckley, November 1980
10. Smith, E. A., "Correlations between Solar Activity and Operationally Determined Satellite Drag Variation Parameters," Paper No. 27, presented at the GSFC Flight Mechanics/Estimation Theory Symposium, Greenbelt, Maryland, May 1988





Report Documentation Page

1. Report No. NASA CP-3050		2. Government Accession No.		3. Recipient's Catalog No.	
4. Title and Subtitle Flight Mechanics/Estimation Theory Symposium - 1989				5. Report Date October 1989	
				6. Performing Organization Code 554	
7. Author(s) Thomas Stengle, Editor				8. Performing Organization Report No. 89B00261	
				10. Work Unit No.	
9. Performing Organization Name and Address Flight Dynamics Division Goddard Space Flight Center Greenbelt, Maryland 20771				11. Contract or Grant No.	
				13. Type of Report and Period Covered Conference Publication May 23-24, 1989	
12. Sponsoring Agency Name and Address National Aeronautics and Space Administration Washington, D. C. 20545-0001				14. Sponsoring Agency Code	
				15. Supplementary Notes Thomas Stengle is Head, Attitude Analysis Section, Flight Dynamics Analysis Branch, at Goddard Space Flight Center, Greenbelt, Maryland 20771	
16. Abstract This conference publication includes 27 papers and abstracts presented at the Flight Mechanics/Estimation Theory Symposium held on May 23-24, 1989, at Goddard Space Flight Center, Greenbelt, Maryland. Sponsored by the Flight Dynamics Division of Goddard Space Flight Center, this symposium featured technical papers on a wide range of issues related to orbit-attitude prediction, determination, and control; attitude sensor calibration; attitude determination error analysis; attitude dynamics; and orbit decay and maneuver strategy. Government, industry, and the academic community participated in the preparation and presentation of these papers.					
17. Key Words (Suggested by Author(s)) Flight Mechanics, Spacecraft Dynamics, Estimation Theory, Orbit Determination, Attitude Determination, Mission Analysis				18. Distribution Statement Unclassified - Unlimited Subject Category 13	
19. Security Classif. (of this report) Unclassified		20. Security Classif. (of this page) Unclassified		21. No. of pages 488	22. Price A21

